

**FAULT DETECTION, ISOLATION, AND
IDENTIFICATION FOR NONLINEAR SYSTEMS
USING A HYBRID APPROACH**

EHSAN SOBAHNI-TEHRANI

**A THESIS
IN
THE DEPARTMENT
OF
ELECTRICAL AND COMPUTER ENGINEERING**

**Presented in Partial Fulfillment of the Requirements
for the Degree of Master of Applied Science in
Electrical and Computer Engineering at
Concordia University
Montreal, Quebec, Canada**

August 2008

© Ehsan Sobhani-Tehrani, 2008



Library and
Archives Canada

Bibliothèque et
Archives Canada

Published Heritage
Branch

Direction du
Patrimoine de l'édition

395 Wellington Street
Ottawa ON K1A 0N4
Canada

395, rue Wellington
Ottawa ON K1A 0N4
Canada

Your file Votre référence
ISBN: 978-0-494-45478-7
Our file Notre référence
ISBN: 978-0-494-45478-7

NOTICE:

The author has granted a non-exclusive license allowing Library and Archives Canada to reproduce, publish, archive, preserve, conserve, communicate to the public by telecommunication or on the Internet, loan, distribute and sell theses worldwide, for commercial or non-commercial purposes, in microform, paper, electronic and/or any other formats.

The author retains copyright ownership and moral rights in this thesis. Neither the thesis nor substantial extracts from it may be printed or otherwise reproduced without the author's permission.

AVIS:

L'auteur a accordé une licence non exclusive permettant à la Bibliothèque et Archives Canada de reproduire, publier, archiver, sauvegarder, conserver, transmettre au public par télécommunication ou par l'Internet, prêter, distribuer et vendre des thèses partout dans le monde, à des fins commerciales ou autres, sur support microforme, papier, électronique et/ou autres formats.

L'auteur conserve la propriété du droit d'auteur et des droits moraux qui protègent cette thèse. Ni la thèse ni des extraits substantiels de celle-ci ne doivent être imprimés ou autrement reproduits sans son autorisation.

In compliance with the Canadian Privacy Act some supporting forms may have been removed from this thesis.

Conformément à la loi canadienne sur la protection de la vie privée, quelques formulaires secondaires ont été enlevés de cette thèse.

While these forms may be included in the document page count, their removal does not represent any loss of content from the thesis.

Bien que ces formulaires aient inclus dans la pagination, il n'y aura aucun contenu manquant.


Canada

Abstract

Fault Detection, Isolation, and Identification for Nonlinear Systems Using a Hybrid Approach

Ehsan Sobhani-Tehrani

This thesis presents a novel integrated *hybrid* approach for fault diagnosis (FD) of nonlinear systems; taking advantage of both system's mathematical model and the adaptive nonlinear approximation capability of computational intelligence techniques. Unlike most FD techniques, the proposed solution *simultaneously* accomplishes fault detection, isolation, and identification (FDII) within a unified diagnostic module. At the core of this solution are a bank of adaptive neural parameter estimators (NPE) and a set of single-parameterized fault models. The NPEs continuously estimate *unknown* fault parameters (FP) that are indicators of faults in the system. In view of the availability of full-state measurements, two NPE structures, namely series-parallel and parallel, are developed with their exclusive set of desirable attributes. The *parallel* scheme is extremely robust to measurement noise and possesses a simpler, yet more solid, fault isolation logic. On the contrary, the series-parallel scheme displays short FD delays and is robust to closed-loop system transients due to changes in control commands. Simple neural network architecture and update laws make both schemes suitable for real-time implementations. A fault tolerant observer (FTO) is then designed to extend the FDII schemes to systems with partial-state measurement. The proposed FTO is a neural state estimator that can estimate *unmeasured* states even in presence of faults. The estimated and the *measured* states then comprise the inputs to the FDII schemes. Simulation results for FDII of reaction wheels of a 3-axis stabilized satellite in presence of disturbances and noise demonstrate the effectiveness of the proposed FDII solution under both full and partial-state measurements.

Acknowledgement

I am grateful to my academic advisor, Professor K. Khorasani, for his support and guidance throughout my work. His inspiring advice and criticism has guided me not only during this thesis but throughout the years that I have been living in Montreal. This work would have never been done without his great vision, experience and insight. I also highly appreciate him for being *infinitely* kind and considerate towards me.

My special thanks go to Dr. Ali Talebi, my undergraduate teacher, friend, and spiritual brother, whose unconditional support and endless positive attitude has always been with me. I am deeply indebted to him for helping me to get the opportunity to pursue my graduate studies in Canada.

I would also like to thank all my friends, especially Hani Khoshdel, Dr. Nicolae Tudoroiu, Tao Jiang, Reza Pedrami, Aidin Mehdipour, and Houman Zarrabi who have been next to me at various situations and/or projects, and have made my time at Concordia University full of memorable, enjoyable, and wonderful moments.

I want to express my gratitude to Mrs. Armineh Garabedian, the President of GlobVision Inc., for her understanding, support, and encouragement during the last two and a half years that I have worked for her company. Her patience, passion for work, and wonderful optimistic attitude has always been a model and a source of inspiration for me.

Last, but not the least, I am sincerely thankful to my parents and my brother, Hessam, for their encouragement and incredible support. I am lucky to have such a wonderful, lovely and supportive family. Especially, I thank Hessam for being so generous in taking care of my parents and taking my place in the family so that my parents could better cope with the emotional sufferings over the years that I have been away from them.

*This thesis is dedicated to Zahra and Ahmad, my parents,
for their unwavering love.*

Contents

List of Figures	ix
List of Tables	xxiii
List of Abbreviations	xxvi
1 Introduction	1
1.1 Statement of the Work	2
1.2 Motivation of the Work	5
1.3 Objectives of the Research.....	12
1.4 Literature Review.....	13
1.5 Proposed Fault Diagnosis Scheme.....	23
1.6 Contributions of the Thesis.....	26
1.7 Outline of the Thesis.....	30
2 Fault Detection and Diagnosis	32
2.1 Problem Formulation	32
2.2 Desired Attributes of a Fault Diagnosis System	40
2.3 A Review of Analytical Redundancy-based FDI Approaches	43
2.3.1 Model-based Approaches to FDI	44
2.3.2 Computational Intelligence-based Approaches to FDI.....	61
2.4 Methodology Developed in This Thesis: Hybrid Approach to FDII.....	71
2.5 Robustness of FDI to Uncertainties	75
2.6 Conclusions.....	78
3 Proposed FDII for Nonlinear Systems with Full-State Measurement	80
3.1 Fault Modeling and Health Indicator Parameters	83
3.2 FDII Using Parameter Estimation.....	89
3.2.1 Conventional Linear and Nonlinear Parameter Estimation	92
3.2.2 Neural Network-based Parameter Estimation.....	96
3.3 FDII Using Series-Parallel Architecture of Neural Parameter Estimators	97
3.3.1 Weight Update Laws of the Series-Parallel Scheme	100
3.3.2 FDI Decision Logic of the Series-Parallel Scheme	102
3.4 Robust FDII Using Parallel Architecture of NPEs	104

3.4.1	Weight Update Laws of the Robust Parallel Scheme	107
3.4.2	Fault Isolation Policy of the Parallel Scheme	108
3.5	Conclusions.....	109
4	Proposed FDII for Nonlinear Systems with Partial State Measurement	112
4.1	FDII Using the Series-Parallel Scheme under Partial State Measurements ...	114
4.2	FDII Using the Parallel Scheme under Partial State Measurements.....	116
4.3	Fault Tolerant State Estimation	118
4.4	State Estimation of Nonlinear Dynamical Systems	121
4.4.1	Probabilistically Inspired Approaches to Nonlinear Filtering	123
4.4.2	Statistically Inspired Approaches to Nonlinear Filtering.....	126
4.5	Model-based State Estimation	129
4.6	Learning and Computational Intelligence-based State Estimation.....	130
4.6.1	Probabilistically Inspired Approaches to Neural Network-based Filtering	131
4.6.2	Statistically Inspired Approaches to Neural Network-based Filtering	134
4.7	Kalman Filter Structure Preserving Neural State Estimator (NSE).....	140
4.7.1	Update Laws for the NSE: Recursive On-line Backpropagation....	142
4.8	Conclusions.....	151
5	Application to a Satellite's Attitude Control Subsystem.....	153
5.1	Spacecraft Subsystems.....	155
5.2	Satellite Attitude Control Subsystem (ACS)	158
5.2.1	Fault Diagnosis in Satellite ACS	159
5.2.2	Satellite Attitude Dynamics	160
5.2.3	Mathematical Modeling of External Attitude Disturbances	177
5.3	Attitude Control	180
5.3.1	Three-Axis Active Attitude Control Design	181
5.4	Simulation Results of 3-Axis Stabilized ACS	183
5.4.1	Three-Axis Attitude Stabilization	183
5.4.2	Characterization of Possible Fault Scenarios in Reaction Wheels .	196
5.5	Simulation Results for FDII with Full-State Measurements	197

5.5.1	Simulation Results for FDII Using the Series-Parallel Scheme	203
5.5.2	Robustness Analysis of the Series-Parallel FDII Scheme with Respect to Measurement Noise.....	223
5.5.3	Simulation Results for FDII Using the Parallel Scheme	247
5.5.4	Robustness Analysis of the Parallel FDII Scheme with Respect to Measurement Noise.....	264
5.6	Simulation Results for FDII with Partial-State Measurement	285
5.6.1	State Estimation under Healthy Conditions	286
5.6.2	State Estimation in Presence of Faults.....	290
5.6.3	FDII Using Estimates of the Current from the NSE.....	294
5.7	Conclusions.....	315
6	Conclusions and Future Work	318
	References	327
	Appendix A.....	341
	Appendix B.....	344
	Appendix C.....	347

List of Figures

Figure 1-1. The role of FDII in an <i>active</i> fault tolerant control (FTC) system.....	7
Figure 1-2. Overview of the Swedish maintenance terminology standard <i>SSEN-13306</i> [7].	8
Figure 1-3. The role of FDII in DPHM module of a CBM system.	11
Figure 1-4. Analytical versus hardware redundancy based FDI as applied to the monitoring of a control system.	17
Figure 2-1. Decomposition of the open-loop system components and possible occurrence of faults in them.	34
Figure 2-2. The effect of various sensor faults on system measurements [73].....	35
Figure 2-3. Common types of actuator faults [73].....	37
Figure 2-4. Two schemes of structured residual set: (a) dedicated scheme and (b) generalized scheme for an example of isolating three faults [24].	49
Figure 2-5. Block diagram of IMM-based FDI approach [93].....	54
Figure 2-6. Generalized Observer Scheme (GOS) for (a) Sensor and (b) Actuator FDI..	55
Figure 2-7. Two-stage scheme for neural network-based fault detection and isolation. ..	66
Figure 2-8. A generic neural network-based multiple-model fault detection and isolation scheme.....	69
Figure 2-9. A conceptual structure of the integrated CI-based fault diagnosis [24].....	71
Figure 3-1. <i>Series-Parallel</i> scheme of the proposed hybrid FDII approach.....	98
Figure 3-2. <i>Parallel</i> scheme of the proposed hybrid FDII approach.....	105
Figure 4-1. The series-parallel FDII scheme under partial-state measurements using the integration of the <i>hybrid</i> NPEs and an FTO.	115
Figure 4-2. The robust parallel FDII scheme under partial-state measurements using the integration of the <i>hybrid</i> NPEs and an FTO.	117
Figure 4-3. The block diagram of the finite-memory neural state estimator [150] for sliding window of length $N=2$	137

Figure 4-4. The Kalman filter structure preserving neural state estimator (NSE) redrawn with modifications from [146].	141
Figure 4-5. The standard representation of a closed-loop nonlinear dynamical system [172].	144
Figure 5-1. A simplified block diagram of the space segment of a satellite, drawn with a number of modifications from Brown [153].	156
Figure 5-2: A detailed block diagram of a high fidelity reaction wheel model [167].	170
Figure 5-3. Validation of the discrete-time analytic model of the RW in response to the torque command voltage given in equation (5-32) at low speeds of the wheel.	176
Figure 5-4. Validation of the discrete-time analytic model of the RW in response to the torque command voltage given in equation (5-32) at high speeds of the wheel.	177
Figure 5-5. Closed-loop 3-axis stabilized attitude control subsystem (ACS) of the spacecraft.	183
Figure 5-6. Transient of Euler angles (Yaw-Pitch-Roll) for 3-axis attitude stabilization at low speeds of reaction wheel actuators.	185
Figure 5-7. Euler angles zoomed around the steady state for 3-axis attitude stabilization at low speeds of reaction wheel actuators.	185
Figure 5-8. Stabilization of quaternions.	186
Figure 5-9. Control signals during transient phase of attitude stabilization	187
Figure 5-10. Reaction torques generated by reaction wheels during transient phase of attitude stabilization.	187
Figure 5-11. Body angular rates of the satellite in the orbit reference frame during the transient phase of attitude stabilization.	188
Figure 5-12. Body angular rates of the satellite in the orbit reference frame during the steady state of attitude stabilization	189
Figure 5-13. Reaction wheel speeds during transient phase	190
Figure 5-14. Motor current of the reaction wheels during transient phase	190
Figure 5-15. Environmental attitude disturbances over one orbit of the satellite.	191
Figure 5-16. Yaw angle evolution in response to three slew-maneuvers	192

Figure 5-17. Pitch angle evolution in response to three slew-maneuvers.....	192
Figure 5-18. Roll angle evolution in response to three slew-maneuvers.....	193
Figure 5-19. The evolution of quaternions in response to three slew-maneuvers	193
Figure 5-20. Control signals in response to three slew-maneuvers	194
Figure 5-21. Reaction torques in response to three slew-maneuvers.....	194
Figure 5-22. Satellite body rates in response to three slew-maneuvers.....	195
Figure 5-23. The speeds of the three reaction wheels in response to three slew-maneuvers	195
Figure 5-24. The motor current of the three reaction wheels in response to three slew-maneuvers.	196
Figure 5-25. The estimated versus measured states using the series-parallel FDII scheme in presence of a time-varying fault in motor current over the time period $t \in [1000 \ 4250]$ second.	204
Figure 5-26. The residuals of the two NPEs of the series-parallel FDII scheme in presence of a time-varying fault in motor current over the time period $t \in [1000 \ 4250]$ second.	205
Figure 5-27. The estimated versus actual FPs using the series-parallel FDII scheme in presence of a time-varying fault in motor current over the time period $t \in [1000 \ 4250]$ second.	206
Figure 5-28. The health state of the RW using the series-parallel FDII scheme in presence of a time-varying fault in the motor current over the time period of $t \in [1000 \ 4250]$ second.	208
Figure 5-29. The estimated versus measured states using the series-parallel FDII scheme in presence of a sequence of low-severity bus voltage faults over the time period $t \in [1000 \ 5100]$ second.	211
Figure 5-30. The residuals of the two NPEs of the series-parallel FDII scheme a sequence of low-severity bus voltage faults over the time period $t \in [1000 \ 5100]$ second.....	212
Figure 5-31. The residuals of the two NPEs of the <i>series-parallel</i> FDII scheme in presence of a sequence of <i>low-severity bus voltage faults</i> over the time	

period $t \in [1000 \ 5100]$ second; zoomed in for the current residual of ‘the NPE for K_t fault’	213
Figure 5-32. The estimated versus actual FPs using the series-parallel FDII scheme in presence of a sequence of low-severity bus voltage faults over the time period $t \in [1000 \ 5100]$ second.	214
Figure 5-33. The health state of the RW using the series-parallel FDII scheme in presence of a sequence of low-severity bus voltage faults over the time period $t \in [1000 \ 5100]$ second.	215
Figure 5-34. The estimated versus measured states using the series-parallel FDII scheme in presence of a sequence of high-severity bus voltage faults over the time period $t \in [1000 \ 5100]$ second.	218
Figure 5-35. The residuals of the two NPEs of the <i>series-parallel</i> FDII scheme in presence of a sequence of <i>high-severity bus voltage faults</i> over the time period $t \in [1000 \ 5100]$ second; zoomed in for the current residual of “the NPE for K_t fault”.	219
Figure 5-36. The estimated versus actual FPs using the series-parallel FDII scheme in presence of a sequence of high-severity bus voltage faults over the time period $t \in [1000 \ 5100]$ second.	220
Figure 5-37. The health state of the RW using the series-parallel FDII scheme in presence of a sequence of high-severity bus voltage faults over the time period $t \in [1000 \ 5100]$ second.	221
Figure 5-38. The estimated versus actual FPs using the series-parallel FDII in presence of motor current fault over the period $t \in [1000 \ 4250]$ sec., subject to <i>medium</i> noise level (SNR=55 dB).	225
Figure 5-39. The health state of the RW using the series-parallel FDII scheme in presence of motor current fault over the period $t \in [1000 \ 4250]$ sec., subject to <i>medium</i> noise level (SNR=55 dB).	226
Figure 5-40. Moving-window filtered version of the estimated motor current FP versus its actual value using the series-parallel FDII scheme in presence of motor current fault over the time period $t \in [1000 \ 4250]$ sec., subject to <i>medium</i> noise level (SNR=55 dB).....	228
Figure 5-41. The health state of the RW using the series-parallel FDII scheme in presence of motor current fault over the time period $t \in [1000 \ 4250]$ sec, subject to <i>medium</i> noise	

level (SNR=55 dB) and with moving-window mean filtering of the motor current FP estimate.	228
Figure 5-42. The estimated versus actual FPs using the series-parallel FDII in presence of motor current fault over the time period $t \in [1000 \ 4250]$ sec., subject to <i>high</i> noise level (SNR=45 dB).	229
Figure 5-43. The estimated versus actual FPs using the series-parallel FDII in presence of a sequence of <i>low-severity</i> bus voltage faults over the time period $t \in [1000 \ 5100]$ sec., subject to <i>medium</i> noise level (Current SNR=54.57 dB and Speed SNR=54.76 dB). ...	233
Figure 5-44. The health state of the RW using the series-parallel FDII scheme in presence of a sequence of <i>low-severity</i> bus voltage faults over the time period $t \in [1000 \ 5100]$ sec., subject to <i>medium</i> noise level (Current SNR=54.57 dB and Speed SNR=54.76 dB).	234
Figure 5-45. Moving-window filtered version of the estimated motor current FP versus its actual value using the series-parallel FDII scheme in presence of a sequence of <i>low-severity</i> bus voltage faults over the time period $t \in [1000 \ 5100]$ sec., subject to <i>medium</i> noise level (Current SNR=54.57 dB and Speed SNR=54.76 dB).	235
Figure 5-46. The health state of the RW using the series-parallel FDII scheme in presence of a sequence of <i>low-severity</i> bus voltage faults over the time period $t \in [1000 \ 5100]$ sec., subject to <i>medium</i> noise level (Current SNR=54.57 dB and Speed SNR=54.76 dB), and with moving-window mean filtering of the motor current FP estimate.	236
Figure 5-47. The estimated versus actual FPs using the series-parallel FDII in presence of a sequence of <i>low-severity</i> bus voltage faults over the time period $t \in [1000 \ 5100]$ sec., subject to <i>high</i> noise level (Current SNR=44.57 dB and Speed SNR=44.76 dB).	237
Figure 5-48. The health state of the RW using the series-parallel FDII scheme in presence of a sequence of <i>low-severity</i> bus voltage faults over the time period $t \in [1000 \ 5100]$ sec., subject to <i>high</i> noise level (Current SNR=44.57 dB and Speed SNR=44.76 dB)..	238
Figure 5-49. The estimated versus actual FPs using the series-parallel FDII in presence of a sequence of <i>high-severity</i> bus voltage faults over the time period $t \in [1000 \ 5100]$ sec., subject to <i>medium</i> noise level (Current SNR=53.66 dB and Speed SNR=53.72 dB). ...	241
Figure 5-50. The health state of the RW using the series-parallel FDII scheme in presence of a sequence of <i>high-severity</i> bus voltage faults over the time period $t \in [1000 \ 5100]$ sec., subject to <i>medium</i> noise level (Current SNR=53.66 dB and Speed SNR=53.72 dB).	242

Figure 5-51. The estimated versus actual FPs using the series-parallel FDII in presence of a sequence of <i>high-severity</i> bus voltage faults over the time period $t \in [1000 \ 5100]$ sec., subject to <i>high</i> noise level (Current SNR=43.66 dB and Speed SNR=43.72 dB).....	243
Figure 5-52. The health state of the RW using the series-parallel FDII scheme in presence of a sequence of <i>high-severity</i> bus voltage faults over the time period $t \in [1000 \ 5100]$ sec., subject to <i>high</i> noise level (Current SNR=43.66 dB and Speed SNR=43.72 dB)..	244
Figure 5-53. The estimated versus measured states using the parallel FDII scheme in presence of a time-varying fault in motor current over the time period $t \in [1000 \ 4250]$ second.	248
Figure 5-54. The residuals of the two NPEs of the parallel FDII scheme in presence of a time-varying fault in motor current over the time period $t \in [1000 \ 4250]$ second.	249
Figure 5-55. The health state of the RW using the parallel FDII scheme in presence of a time-varying fault in motor current over the time period of $t \in [1000 \ 4250]$ second..	250
Figure 5-56. The estimated versus actual FPs using the parallel FDII scheme in presence of a time-varying fault in motor current over the time period $t \in [1000 \ 4250]$ second.	251
Figure 5-57. The estimated versus measured states using the parallel FDII scheme in presence of a sequence of low-severity bus voltage faults over the time period $t \in [1000 \ 5100]$ second.	253
Figure 5-58. The residuals of the two NPEs of the parallel FDII scheme in presence of a sequence of low-severity bus voltage faults over the time period $t \in [1000 \ 5100]$ second.	255
Figure 5-59. The health state of the RW using the parallel FDII scheme in presence of a sequence of low-severity bus voltage faults over the time period $t \in [1000 \ 5100]$ second.	256
Figure 5-60. The estimated versus actual FPs using the parallel FDII scheme in presence of a sequence of low-severity bus voltage faults over the time period $t \in [1000 \ 5100]$ second.	258
Figure 5-61. The estimated versus measured states using the parallel FDII scheme in presence of a sequence of high-severity bus voltage faults over the time period $t \in [1000 \ 5100]$ second.	260

Figure 5-62. The residuals of the two NPEs of the parallel FDII scheme a sequence of high-severity bus voltage faults over the time period $t \in [1000 \ 5100]$ second..... 261

Figure 5-63. The health state of the RW using the parallel FDII scheme in presence of a sequence of high-severity bus voltage faults over the time period $t \in [1000 \ 5100]$ second. 262

Figure 5-64. The estimated versus actual FPs using the parallel FDII scheme in presence of a sequence of high-severity bus voltage faults over the time period $t \in [1000 \ 5100]$ second. 263

Figure 5-65. The health state of the RW using the parallel FDII scheme in presence of motor current fault over the period $t \in [1000 \ 4250]$ sec., subject to *medium* noise level (SNR=55 dB). 266

Figure 5-66. The estimated versus actual FPs using the parallel FDII in presence of motor current fault over the period $t \in [1000 \ 4250]$ sec., subject to *medium* noise level (SNR=55 dB). 267

Figure 5-67. The health state of the RW using the parallel FDII scheme in presence of motor current fault over the period $t \in [1000 \ 4250]$ sec., subject to *high* noise level (SNR=45 dB). 268

Figure 5-68. The estimated versus actual FPs using the parallel FDII in presence of motor current fault over the time period $t \in [1000 \ 4250]$ sec., subject to *high* noise level (SNR=45 dB). 269

Figure 5-69. The health state of the RW using the parallel FDII scheme in presence of a sequence of *low-severity* bus voltage faults over the time period $t \in [1000 \ 5100]$ sec., subject to *medium* noise level (Current SNR=54.57 dB and Speed SNR=54.76 dB). ... 272

Figure 5-70. The estimated versus actual FPs using the parallel FDII in presence of a sequence of *low-severity* bus voltage faults over the time period $t \in [1000 \ 5100]$ sec., subject to *medium* noise level (Current SNR=54.57 dB and Speed SNR=54.76 dB). ... 273

Figure 5-71. The health state of the RW using the parallel FDII scheme in presence of a sequence of *low-severity* bus voltage faults over the time period $t \in [1000 \ 5100]$ sec., subject to *high* noise level (Current SNR=44.57 dB and Speed SNR=44.76 dB). 275

Figure 5-72. The estimated versus actual FPs using the parallel FDII in presence of a sequence of *low-severity* bus voltage faults over the time period $t \in [1000 \ 5100]$ sec., subject to *high* noise level (Current SNR=44.57 dB and Speed SNR=44.76 dB). 276

Figure 5-73. The health state of the RW using the parallel FDII scheme in presence of a sequence of <i>high-severity</i> bus voltage faults over the time period $t \in [1000 \ 5100]$ sec., subject to <i>medium</i> noise level (Current SNR=53.66 dB and Speed SNR=53.72 dB). ...	279
Figure 5-74. The estimated versus actual FPs using the parallel FDII in presence of a sequence of <i>high-severity</i> bus voltage faults over the time period $t \in [1000 \ 5100]$ sec., subject to <i>medium</i> noise level (Current SNR=53.66 dB and Speed SNR=53.72 dB). ...	280
Figure 5-75. The health state of the RW using the parallel FDII scheme in presence of a sequence of <i>high-severity</i> bus voltage faults over the time period $t \in [1000 \ 5100]$ sec., subject to <i>high</i> noise level (Current SNR=43.66 dB and Speed SNR=43.72 dB).	281
Figure 5-76. The estimated versus actual FPs using the parallel FDII in presence of a sequence of <i>high-severity</i> bus voltage faults over the time period $t \in [1000 \ 5100]$ sec., subject to <i>high</i> noise level (Current SNR=43.66 dB and Speed SNR=43.72 dB).	282
Figure 5-77. The current and speed estimates from the full-order FTO versus their actual values using only speed measurements subject to 3 satellite slew-maneuvers at low speeds of the wheel.	287
Figure 5-78. The current estimate from the full-order FTO versus its actual value using only speed measurements subject to 3 satellite slew-maneuvers at low speeds of the wheel; top figure: zoomed in on the y-axis, bottom figure: zoomed in on the time-axis for the first 2 seconds.	288
Figure 5-79. The current and speed estimates from the full-order FTO versus their actual values using only speed measurements subject to 1 slew-maneuver of the satellite at high speeds of the wheel.	289
Figure 5-80. The current estimate from the full-order FTO versus its actual value using only speed measurements subject to 1 slew-maneuver of the satellite at high speeds of the wheel; top figure: zoomed in on the y-axis, bottom figure: zoomed in on the time-axis for the first 3 seconds.	290
Figure 5-81. The current estimate from the full-order FTO versus its actual value using only speed measurements in presence of a time-varying fault in motor current over the time period of $t \in [1000 \ 4250]$ second.	291
Figure 5-82. The current estimate from the full-order FTO versus its actual value using only speed measurements in presence of a sequence of low-severity bus voltage faults over the time period $t \in [1000 \ 5100]$ second.	292

Figure 5-83. The current estimate from the full-order FTO versus its actual value using only speed measurements in presence of a sequence of high-severity bus voltage faults over the time period $t \in [1000 \ 5100]$ second..... 293

Figure 5-84. The estimated versus actual FPs using the series-parallel FDII scheme in presence of a time-varying fault in motor current over the time period $t \in [1000 \ 4250]$ second under partial-state measurements (i.e., measured speed and estimated current from the FTO)..... 296

Figure 5-85. The health state of the RW using the series-parallel FDII scheme in presence of a time-varying fault in motor current over the time period of $t \in [1000 \ 4250]$ second under partial-state measurements (i.e., measured speed and estimated current from the FTO)..... 297

Figure 5-86. The health state of the RW using the parallel FDII scheme in presence of a time-varying fault in motor current over the time period of $t \in [1000 \ 4250]$ second under partial-state measurements (i.e., measured speed and estimated current from the FTO)..... 299

Figure 5-87. The estimated versus actual FPs using the parallel FDII scheme in presence of a time-varying fault in motor current over the time period $t \in [1000 \ 4250]$ second under partial-state measurements (i.e., measured speed and estimated current from the FTO)..... 300

Figure 5-88. The estimated versus actual FPs using the series-parallel FDII scheme in presence of a sequence of low-severity bus voltage faults over the time period $t \in [1000 \ 5100]$ second under partial-state measurements (i.e., measured speed and estimated current from the FTO)..... 302

Figure 5-89. The health state of the RW using the series-parallel FDII scheme in presence of a sequence of low-severity bus voltage faults over the time period $t \in [1000 \ 5100]$ second under partial-state measurements (i.e., measured speed and estimated current from the FTO)..... 303

Figure 5-90. The health state of the RW using the parallel FDII scheme in presence of a sequence of low-severity bus voltage faults over the time period $t \in [1000 \ 5100]$ second under partial-state measurements (i.e., measured speed and estimated current from the FTO)..... 305

Figure 5-91. The estimated versus actual FPs using the parallel FDII scheme in presence of a sequence of low-severity bus voltage faults over the time period $t \in [1000 \ 5100]$

second under partial-state measurements (i.e., measured speed and estimated current from the FTO).....	307
Figure 5-92. The estimated versus actual FPs using the series-parallel FDII scheme in presence of a sequence of high-severity bus voltage faults over the time period $t \in [1000 \ 5100]$ second under partial-state measurements (i.e., measured speed and estimated current from the FTO).....	309
Figure 5-93. The health state of the RW using the series-parallel FDII scheme in presence of a sequence of high-severity bus voltage faults over the time period $t \in [1000 \ 5100]$ second under partial-state measurements (i.e., measured speed and estimated current from the FTO).....	310
Figure 5-94. The health state of the RW using the parallel FDII scheme in presence of a sequence of high-severity bus voltage faults over the time period $t \in [1000 \ 5100]$ second under partial-state measurements (i.e., measured speed and estimated current from the FTO).....	312
Figure 5-95. The estimated versus actual FPs using the parallel FDII scheme in presence of a sequence of high-severity bus voltage faults over the time period $t \in [1000 \ 5100]$ second under partial-state measurements (i.e., measured speed and estimated current from the FTO).....	313
Figure C-1. The residuals of the two NPEs of the <i>series-parallel</i> FDII scheme in presence of a sequence of <i>high-severity bus voltage faults</i> over the time period $t \in [1000 \ 5100]$ second.	347
Figure C-2. The estimated versus measured states using the <i>series-parallel</i> FDII scheme in presence of <i>motor current fault</i> over the time period $t \in [1000 \ 4250]$ sec., subject to <i>medium</i> noise level (SNR=55 dB).	348
Figure C-3. The residuals of the two NPEs of the series-parallel FDII scheme in presence of motor current fault over the period $t \in [1000 \ 4250]$ sec., subject to <i>medium</i> noise level (SNR=55 dB).	348
Figure C-4. The estimated versus measured states using the <i>series-parallel</i> FDII scheme in presence of <i>motor current fault</i> over the time period $t \in [1000 \ 4250]$ sec., subject to <i>high</i> noise level (SNR=45 dB).	349
Figure C-5. The residuals of the two NPEs of the series-parallel FDII scheme in presence of motor current fault over the time period $t \in [1000 \ 4250]$ sec., subject to <i>high</i> noise level (SNR=45 dB).	349

Figure C-6. The estimated versus measured states using the *series-parallel* FDII scheme in presence of a sequence of *low-severity* bus voltage faults over the time period $t \in [1000 \ 5100]$ sec., subject to *medium* noise level (Current SNR=54.57 dB and Speed SNR=54.76 dB)..... 350

Figure C-7. The residuals of the two NPEs of the *series-parallel* FDII scheme in presence of a sequence of *low-severity* bus voltage faults over the time period $t \in [1000 \ 5100]$ seconds, subject to *medium* noise level (Current SNR=54.57 dB and Speed SNR=54.76 dB)..... 350

Figure C-8. The estimated versus measured states using the *series-parallel* FDII scheme in presence of a sequence of *low-severity bus voltage faults* over the time period $t \in [1000 \ 5100]$ sec., subject to *high* noise level (Current SNR=44.57 dB and Speed SNR=44.76 dB)..... 351

Figure C-9. The residuals of the two NPEs of the *series-parallel* FDII scheme in presence of a sequence of *low-severity* bus voltage faults over the time period $t \in [1000 \ 5100]$ sec., subject to *high* noise level (Current SNR=44.57 dB and Speed SNR=44.76 dB).. 351

Figure C-10. The estimated versus measured states using the *series-parallel* FDII scheme in presence of a sequence of *high-severity* bus voltage faults over the time period $t \in [1000 \ 5100]$ sec., subject to *medium* noise level (Current SNR=53.66 dB and Speed SNR=53.72 dB)..... 352

Figure C-11. The residuals of the two NPEs of the *series-parallel* FDII scheme in presence of a sequence of *high-severity* bus voltage faults over the time period $t \in [1000 \ 5100]$ sec., subject to *medium* noise level (Current SNR=53.66 dB and Speed SNR=53.72 dB)..... 352

Figure C-12. The estimated versus measured states using the *series-parallel* FDII scheme in presence of a sequence of *high-severity* bus voltage faults over the time period $t \in [1000 \ 5100]$ sec., subject to *high* noise level (Current SNR=43.66 dB and Speed SNR=43.72 dB)..... 353

Figure C-13. The residuals of the two NPEs of the *series-parallel* FDII scheme in presence of a sequence of *high-severity* bus voltage faults over the time period $t \in [1000 \ 5100]$ sec., subject to *high* noise level (Current SNR=43.66 dB and Speed SNR=43.72 dB)..... 353

Figure C-14. The estimated versus measured states using the *parallel* FDII scheme in presence of *motor current fault* over the time period $t \in [1000 \ 4250]$ sec., subject to *medium* noise level (SNR=55 dB). 354

Figure C-15. The residuals of the two NPEs of the parallel FDII scheme in presence of motor current fault over the period $t \in [1000 \ 4250]$ sec., subject to <i>medium</i> noise level (SNR=55 dB).....	354
Figure C-16. The estimated versus measured states using the <i>parallel</i> FDII scheme in presence of <i>motor current fault</i> over the time period $t \in [1000 \ 4250]$ sec., subject to <i>high</i> noise level (SNR=45 dB).....	355
Figure C-17. The residuals of the two NPEs of the parallel FDII scheme in presence of motor current fault over the time period $t \in [1000 \ 4250]$ sec., subject to <i>high</i> noise level (SNR=45 dB).....	355
Figure C-18. The estimated versus measured states using the <i>parallel</i> FDII scheme in presence of a sequence of <i>low-severity bus voltage faults</i> over the time period $t \in [1000 \ 5100]$ sec., subject to <i>medium</i> noise level (Current SNR=54.57 dB and Speed SNR=54.76 dB).....	356
Figure C-19. The residuals of the two NPEs of the parallel FDII scheme in presence of a sequence of <i>low-severity bus voltage faults</i> over the time period $t \in [1000 \ 5100]$ seconds, subject to <i>medium</i> noise level (Current SNR=54.57 dB and Speed SNR=54.76 dB).....	356
Figure C-20. The estimated versus measured states using the <i>parallel</i> FDII scheme in presence of a sequence of <i>low-severity bus voltage faults</i> over the time period $t \in [1000 \ 5100]$ sec., subject to <i>high</i> noise level (Current SNR=44.57 dB and Speed SNR=44.76 dB).....	357
Figure C-21. The residuals of the two NPEs of the parallel FDII scheme in presence of a sequence of <i>low-severity bus voltage faults</i> over the time period $t \in [1000 \ 5100]$ sec., subject to <i>high</i> noise level (Current SNR=44.57 dB and Speed SNR=44.76 dB).....	357
Figure C-22. The estimated versus measured states using the <i>parallel</i> FDII scheme in presence of a sequence of <i>high-severity bus voltage faults</i> over the time period $t \in [1000 \ 5100]$ sec., subject to <i>medium</i> noise level (Current SNR=54.57 dB and Speed SNR=54.76 dB).....	358
Figure C-23. The residuals of the two NPEs of the parallel FDII scheme in presence of a sequence of <i>high-severity bus voltage faults</i> over the time period $t \in [1000 \ 5100]$ sec., subject to <i>medium</i> noise level (Current SNR=53.66 dB and Speed SNR=53.72 dB). ...	358
Figure C-24. The estimated versus measured states using the <i>parallel</i> FDII scheme in presence of a sequence of <i>high-severity bus voltage faults</i> over the time	

period $t \in [1000 \ 5100]$ sec., subject to <i>high</i> noise level (Current SNR=44.57 dB and Speed SNR=44.76 dB).....	359
Figure C-25. The residuals of the two NPEs of the parallel FDII scheme in presence of a sequence of <i>high-severity</i> bus voltage faults over the time period $t \in [1000 \ 5100]$ sec., subject to <i>high</i> noise level (Current SNR=43.66 dB and Speed SNR=43.72 dB).....	359
Figure C-26. Speed estimate from the full-order FTO versus its actual value using only speed measurements in presence of a time-varying fault in motor current over the time period of $t \in [1000 \ 4250]$ second.....	360
Figure C-27. Speed estimate from the full-order FTO versus its actual value using only speed measurements in presence of a sequence of low-severity bus voltage faults over the time period $t \in [1000 \ 5100]$ second.....	360
Figure C-28. Speed estimate from the full-order FTO versus its actual value using only speed measurements in presence of a sequence of high-severity bus voltage faults over the time period $t \in [1000 \ 5100]$ second.....	361
Figure C-29. The residuals of the two NPEs of the series-parallel FDII scheme in presence of a time-varying fault in motor current over the time period $t \in [1000 \ 4250]$ second under partial-state measurements (i.e., measured speed and estimated current from the FTO).....	362
Figure C-30. The residuals of the two NPEs of the parallel FDII scheme in presence of a time-varying fault in motor current over the time period $t \in [1000 \ 4250]$ second under partial-state measurements (i.e., measured speed and estimated current from the FTO).	362
Figure C-31. The residuals of the two NPEs of the series-parallel FDII scheme in presence of a sequence of low-severity bus voltage faults over the time period $t \in [1000 \ 5100]$ second under partial-state measurements (i.e., measured speed and estimated current from the FTO).....	363
Figure C-32. The residuals of the two NPEs of the series-parallel FDII scheme in presence of a sequence of low-severity bus voltage faults over the time period $t \in [1000 \ 5100]$ second under partial-state measurements (i.e., measured speed and estimated current from the FTO); zoomed in for the current residual of “the NPE for K_t fault”.	363
Figure C-33. The residuals of the two NPEs of the parallel FDII scheme in presence of a sequence of low-severity bus voltage faults over the time period $t \in [1000 \ 5100]$ second	

under partial-state measurements (i.e., measured speed and estimated current from the FTO)..... 364

Figure C-34. The residuals of the two NPEs of the *series-parallel* FDII scheme in presence of a sequence of *high-severity bus voltage faults* over the time period $t \in [1000 \ 5100]$ second under partial-state measurements (i.e., measured speed and estimated current from the FTO)..... 365

Figure C-35. The residuals of the two NPEs of the series-parallel FDII scheme in presence of a sequence of high-severity bus voltage faults over the time period $t \in [1000 \ 5100]$ second under partial-state measurements (i.e., measured speed and estimated current from the FTO); zoomed in for the current residual of “the NPE for Kt fault”. 365

Figure C-36. The residuals of the two NPEs of the parallel FDII scheme in presence of a sequence of high-severity bus voltage faults over the time period $t \in [1000 \ 5100]$ second under partial-state measurements (i.e., measured speed and estimated current from the FTO)..... 366

List of Tables

Table 5-1. Parameters of the attitude disturbance models used in the ACS simulations.	180
Table 5-2. The closed-loop ACS parameters including parameters of the RW model, the satellite attitude dynamics and the controller, used in the simulations.	184
Table 5-3. Specifications of the various measurement noise levels used in the simulations.	201
Table 5-4. Signal-to-noise ration (SNR) corresponding to the various noise intensities in Table 5-3 and calculated for different fault scenarios.	201
Table 5-5. The performance indices of motor current fault identification using the series-parallel FDII scheme in presence of intermittent motor current fault and with nominal noise levels.	210
Table 5-6. The performance indices of fault identification using the series-parallel FDII scheme in presence of low-severity bus voltage fault and with nominal noise levels.	217
Table 5-7. The performance indices of fault identification using the series-parallel FDII scheme in presence of high-severity bus voltage fault subject to nominal noise levels.	223
Table 5-8. Comparison of the RMSE of the motor current FP estimation using the series-parallel FDII scheme subject to various noise levels and in presence of intermittent motor current fault.	231
Table 5-9. Comparison of the ME of the motor current FP estimation using the series-parallel FDII scheme subject to various noise levels and in presence of intermittent motor current fault.	231
Table 5-10. Comparison of the STDE of FP estimation using the series-parallel FDII scheme subject to various noise levels and in presence of intermittent motor current fault.	232
Table 5-11. Comparison of the RMSE of the bus voltage FP estimation using the series-parallel FDII scheme subject to various noise levels and in presence of a sequence of low-severity bus voltage faults.	239
Table 5-12. Comparison of the ME of the bus voltage FP estimation using the series-parallel FDII scheme subject to various noise levels and in presence of a sequence of low-severity bus voltage faults.	239

Table 5-13. Comparison of the STDE of the bus voltage FP estimation using the series-parallel FDII scheme subject to various noise levels and in presence of a sequence of low-severity bus voltage faults.	239
Table 5-14. Comparison of the RMSE of the bus voltage FP estimation using the series-parallel FDII scheme subject to various noise levels and in presence of a sequence of high-severity bus voltage faults.	245
Table 5-15. Comparison of the ME of the bus voltage FP estimation using the series-parallel FDII scheme subject to various noise levels and in presence of a sequence of high-severity bus voltage faults.	245
Table 5-16. Comparison of the STDE of the bus voltage FP estimation using the series-parallel FDII scheme subject to various noise levels and in presence of a sequence of high-severity bus voltage faults.	245
Table 5-17. The performance indices of motor current fault identification using the parallel FDII scheme in presence of intermittent motor current fault and subject to nominal noise levels.	252
Table 5-18. The performance indices of fault identification using the parallel FDII scheme in presence of low-severity bus voltage fault and subject to nominal noise levels.	259
Table 5-19. The performance indices of fault identification using the parallel FDII scheme in presence of high-severity bus voltage fault and subject to nominal noise levels.	264
Table 5-20. Comparison of the RMSE of the motor current FP estimation using the parallel FDII scheme subject to various noise levels and in presence of intermittent motor current fault.	270
Table 5-21. Comparison of the ME of the motor current FP estimation using the parallel FDII scheme subject to various noise levels and in presence of intermittent motor current fault.	271
Table 5-22. Comparison of the STDE of FP estimation using the parallel FDII scheme subject to various noise levels and in presence of intermittent motor current fault.	271
Table 5-23. Comparison of the RMSE of the bus voltage FP estimation using the parallel FDII scheme subject to various noise levels and in presence of a sequence of low-severity bus voltage faults.	277
Table 5-24. Comparison of the ME of the bus voltage FP estimation using the parallel FDII scheme subject to various noise levels and in presence of a sequence of low-severity bus voltage faults.	277

Table 5-25. Comparison of the STDE of the bus voltage FP estimation using the parallel FDII scheme subject to various noise levels and in presence of a sequence of low-severity bus voltage faults.	277
Table 5-26. Comparison of the RMSE of the bus voltage FP estimation using the parallel FDII scheme subject to various noise levels and in presence of a sequence of high-severity bus voltage faults.....	283
Table 5-27. Comparison of the ME of the bus voltage FP estimation using the parallel FDII scheme subject to various noise levels and in presence of a sequence of high-severity bus voltage faults.....	283
Table 5-28. Comparison of the STDE of the bus voltage FP estimation using the parallel FDII scheme subject to various noise levels and in presence of a sequence of high-severity bus voltage faults.....	283
Table 5-29. The performance indices of motor current fault identification using the series-parallel FDII scheme in presence of intermittent motor current fault and under partial-state measurements (i.e., measured speed and estimated current from the FTO).	298
Table 5-30. The performance indices of motor current fault identification using the parallel FDII scheme in presence of intermittent motor current fault and under partial-state measurements (i.e., measured speed and estimated current from the FTO).....	301
Table 5-31. The performance indices of fault identification using the series-parallel FDII scheme in presence of low-severity bus voltage fault and under partial-state measurements (i.e., measured speed and estimated current from the FTO).	304
Table 5-32. The performance indices of fault identification using the parallel FDII scheme in presence of low-severity bus voltage fault and under partial-state measurements (i.e., measured speed and estimated current from the FTO).	308
Table 5-33. The performance indices of fault identification using the series-parallel FDII scheme in presence of high-severity bus voltage fault and under partial-state measurements (i.e., measured speed and estimated current from the FTO).	311
Table 5-34. The performance indices of fault identification using the parallel FDII scheme in presence of high-severity bus voltage fault and under partial-state measurements (i.e., measured speed and estimated current from the FTO).	314

List of Abbreviations

ACS	Attitude Control Subsystem
ADCS	Attitude Determination and Control Subsystem
ARR	Analytical Redundancy Relations
ART	Adaptive Resonance Theory
BP	Back-Propagation
CBM	Condition-Based Maintenance
C&DH	Command and Data Handling
CI	Computational Intelligence
DBP	Dynamic Back-Propagation
DES	Discrete Event System
DFT	Discrete Fourier Transform
DOS	Dedicated Observer Scheme
DPHM	Diagnosis, Prognosis and Health Management
DTW	Dynamic Time Warping
DWT	Discrete Wavelet Transform
EKF	Extended Kalman Filter
FA	Fault Accommodation
FD	Fault Diagnosis
FDA	Fault Diagnosis and Accommodation
FDAE	Fault Detection and Approximation Estimator
FDI	Fault Detection and Isolation
FDII	Fault Detection, Isolation and Identification
FDIR	Fault Detection, Isolation and Recovery
FF	Formation Flying
FFNN	Feedforward Neural Network
FIE	Fault Isolation Estimator
FMEA	Failure Mode and Effects Analysis
FMECA	Failure Mode, Effects and Criticality Analysis
FMSLF	Finite Multi-Severity Level Faults
FP	Fault Parameter
FPF	Fault Parameter Function
FSM	Finite State Machine
FTC	Fault Tolerant Control
FTO	Fault Tolerant Observer
FTSE	Fault Tolerant State Estimator
GD	Gradient Descent
GLR	Generalized Likelihood Ratio
GNC	Guidance, Navigation and Control
GOS	Generalized Observer Scheme
HEV	Hybrid Electric Vehicle
HMM	Hidden Markov Models
HOF	Hard-Over Failure
IMM	Interacting Multiple Models

ISLF	Infinite Severity Level Faults
KF	Kalman Filter
LEO	Low Earth Orbit
LIP	Lock-In-Place
LMI	Linear Matrix Inequality
LOA	Loss Of Accuracy
LOE	Loss Of Effectiveness
LS	Least Squares
LSE	Least Squares Estimator
ME	Mean of Error
MIMOSA	Machinery Information Management Open Systems Alliance
MIMO	Multi Input Multi Output
MISO	Multi Input Single Output
MLE	Maximum Likelihood Estimator
MLP	Multi Layer Perceptron
MM	Multiple Model
MSLF	Mono Severity Level Faults
MWMF	Moving Window Mean Filter
NARX	Nonlinear Autoregressive Exogenous
NN	Neural Network
NPE	Neural Parameter Estimator
NSE	Neural State Estimator
NUIO	Nonlinear Unknown Input Observer
OCS	Orbital Control System
OEM	Original Equipment Manufacturer
OSA-CBM	Open System Architecture – Condition Based Maintenance
PDF	Probability Distribution Function
PFM	Parameterized Fault Models
PID	Proportional, Integral, Derivative
PNN	Probabilistic Neural Network
QTA	Qualitative Trend Analysis
RBF	Radial Basis Functions
RHE	Receding Horizon Estimator
RLS	Recursive Least Squares
RMLP	Recursive Multi-Layer Perceptron
RMSE	Root Mean Square of Error
RPY	Roll-Pitch-Yaw
RUL	Remaining Useful Life
SML	Simulated Maximum Likelihood
SNR	Signal-to-Noise Ratio
SOC	State Of Charge
SOM	Self-Organizing Map
SPRT	Sequential Probability Ratio Test
STDE	Standard Deviation of Error
SVM	Support Vector Machines
TDL	Tapped Delay Line

TDNN	Time Delay Neural Network
T&TC	Telemetry and Telecommand
TTF	Time To Failure
UIO	Unknown Input Observer
UKF	Unscented Kalman Filter
UT	Unscented Transform
VSC	Variable Structure Control

Chapter 1:

1 Introduction

There is an increasing demand for man-made dynamical systems to operate autonomously in presence of faults and failures in sensors, actuators or components. Fault detection and identification are essential components of an autonomous system. Hence, a high demand exists for the development of intelligent systems that are able to autonomously detect the presence and isolate the location of faults occurring in different components of complex dynamical systems. Especially faults in a control loop are of particular importance since they may very quickly result in instability of the control system. Thus, it is crucial that faults are efficiently and timely detected and isolated while the system is in operation. This is essentially the concept of on-line health monitoring though, in general, health monitoring may also be performed off-line using stored data in a post-processing capacity to determine if the system overhaul is necessary. In general, autonomous on-line health monitoring and fault diagnosis is essential for mission-critical and safety-critical systems as opposed to fail-operational systems, where off-line health monitoring and fault diagnosis is usually sufficient – in order to perform maintenance. In this thesis, the main focus is on developing a fault diagnosis methodology that enables on-line health monitoring of nonlinear systems; however, the proposed approach can as well be applied for off-line monitoring purposes.

Furthermore, accurate identification of fault severities is an invaluable asset for system maintenance as well as development of reliable autonomous recovery procedures.

More precisely, accurate estimation of severities in case of incipient faults allows system operators and controllers to either very quickly schedule a maintenance service for the faulty component, to switch to the redundant component if maintenance is not possible, or to intelligently plan and execute preemptive actions in advance, in order to avoid catastrophic failures.

1.1 Statement of the Work

In this thesis, the problem of fault detection, isolation, and identification (FDII) in nonlinear dynamical systems is addressed. A "fault" is considered as an unpredicted or unexpected change of system behavior such that it either deteriorates the performance or demolishes the normal operation of the system. While the former is usually called an *incipient* fault, the later is usually considered as a total failure. A failure is usually the result of the progression of an incipient fault over time, and could lead to hazardous situations. Faults in a system are usually classified based on their time behaviour and their severity (i.e., their impact on system behaviour). From time behaviour point of view, faults can be classified into the following two groups:

- **Intermittent faults:** These faults persist for only a bounded period of time after their initiation. It should be noted, however, that even upon their termination the system may not behave in the same manner as before the fault initiation.
- **Permanent faults:** Once occurred, these faults exist forever unless the faulty component is replaced by a redundant one or serviced/repared, if possible.

As far as fault severity is concerned, the following three types of faults may occur in a system depending on the system or the component being monitored:

- **Mono severity level faults (MSLF):** These are the faults that occur only at one single state. For example, a stuck-closed fault in a valve can occur only in one configuration. Other examples include stuck-open fault in valves, and floating fault and hard-over failure (HOF) in electric motors.
- **Finite multi severity level faults (FMSLF):** FMSLFs are basically comprised of a set of MSLFs. Failures in a valve, which may be a two-state failure, being either stuck-open or stuck-closed, is a good example of FMSLFs. Other examples include hard-over failure (HOF) and float failure in actuators.
- **Infinite severity level faults (ISLF):** This type of faults can actually take place over a continuum, infinite level of severities. Examples of ISLFs include loss of effectiveness (LOE) and lock-in-place (LIP) in electric motors, and almost all types of sensor faults including bias, drift, loss of accuracy (LOA), freezing, and sensor calibration error.

The MSLFs and FMSLFs usually occur *abruptly*, hence the name *abrupt* faults. On the contrary, ISLFs usually develop (or grow) over time due to wear and tear of system components and thus they are often called *incipient* faults.

A "fault diagnosis system" is a system that is able to detect the presence of faults, determine their locations, and estimate their severities in a system. In other words, a fault diagnosis system is capable of performing the three tasks of *detection*, *isolation*, and *identification* of faults in a system, which are defined as follows [1]:

- **Fault detection:** To make a binary decision whether something has gone wrong or that everything is fine.

- **Fault isolation:** To determine the location of the fault, i.e., to identify which component, sensor, or actuator has become faulty.
- **Fault identification:** To estimate the severity, type or nature of the fault.

The relative importance of the above three tasks highly depends on the application and the system operator's objective of having a fault diagnosis system. However, the detection is essential for any practical system, isolation is almost equally important, and identification is crucial for fault recovery and reconfiguration as well as health monitoring and maintenance purposes. In this thesis, development of an integrated FDII scheme that is able to simultaneously detect the presence, isolate the location, and identify the severity of faults in the components of a nonlinear system is investigated.

Inevitable presence of measurement noise and system disturbances deteriorates the performance of an FDII scheme by generating *false alarms*. This is due to the fact that detailed characteristics of noise and disturbances are unknown and thus can not be modeled accurately. Reduction of the sensitivity of the FDII system to sensor noise and system disturbances does not necessarily fully solve the problem since it may be accompanied with insensitivity to faults and consequently too many missed alarms. So, it is highly desired to increase the insensitivity to noise and disturbances while keeping the FDII subsystem sensitive to faults. In this thesis, the sensitivity of the proposed FDII to measurement noise and system disturbances will be investigated and a solution will be proposed to increase the robustness of the FDII algorithm to measurement noise.

Furthermore, like many other existing FDII schemes, our initial FDII algorithm development is based on the assumption of full state measurement. However, in many practical situations, some of the system states are either not available for measurement or

their measurements are costly and highly prone to noise. This drives the need for FDII algorithms that are able to operate accurately under partial state measurement. As a result, development of a state estimation technique that is robust to the occurrence of faults in the system will be investigated. The robust state estimator will provide the FDII system with accurate and reliable estimates of unmeasured system states, allowing detection, isolation, and identification of faults even in presence of partial state measurements.

Eventually, the applicability of the developed algorithms will be verified for FDII of a spacecraft's attitude control system (ACS). The attitude control system (ACS) is composed of different components such as sensors (e.g. horizon sensors, sun sensors, magnetometers, etc.), and actuators (e.g. momentum wheels, torque rods, etc.). The proposed FDII algorithm can be applied for diagnosis of faults in any of the above ACS components; however, our focus in this thesis will be on reaction wheel actuators due to their vital role in maintaining and controlling the attitude of a 3-axis stabilized satellite.

1.2 Motivation of the Work

The consequences of faults can be extremely serious in terms of human fatalities, environmental impact, and economic loss. Furthermore, the ever-increasing demand for more safe, secure, and reliable operation of safety-critical, business-critical, and mission-critical systems has essentially made fault tolerance in such systems extremely important. In other words, there is a growing need for the so-called *autonomous fault tolerant systems* which are able to operate autonomously and reliably in presence of faults and failures in sensors, actuators, and components. Since FDII is an essential component of an autonomous fault-tolerant system, a high demand exists for development of intelligent

systems that are able to autonomously detect the presence, isolate the location, and estimate the severity of faults present and occurring in different components of a complex dynamical system while the system is in operation.

Figure 1-1 depicts the role of FDII in a fault tolerant control (FTC) system. As shown in this figure, once a fault is detected and the corresponding faulty component is located within the system, the FDII subsystem provides the reconfiguration mechanism with accurate estimates of the fault severity in order to allow proper reconfiguration or restructuring of the control system. If the estimated fault severities indicate a total loss of a component, then the (redundant) healthy/non-faulty components are chosen to take role in system operation. Otherwise, in case of a partial breakdown of a component (for example, loss of effectiveness in an actuator, a bias in a sensor, etc.), either a pre-calculated controller is switched into the system or some parameters of the controller are adjusted based on the fault severities, in order to control the new situation. More precisely, the objective of an FTC system is to modify the operation of the system based on its determined condition, which essentially establishes a tight coupling between the health monitoring or diagnostics algorithms and the controller.

In an *active* approach to FTC design, on-line restructuring of the control system or reconfiguration of the controller requires information on the location of faults (or faulty components), their severities, and their impacts on system operation. The task of FDII subsystem is to reliably and accurately acquire this information in order to successfully achieve a smooth and reliable autonomous recovery (or fault accommodation). For further details on this topic the reader can refer to the work of Yen and Ho [2], where the dependence between fault diagnosis (FD) and fault accommodation (FA) has been well

described and a model-based technique for on-line fault diagnosis and accommodation (FDA) has also been presented.

Finally, it should be mentioned that even though in *passive* FTC design, detailed information about the nature of faults is not essentially required for online reconfiguration of the controller, the safety and reliability of these systems can still be considerably improved and ensured through deployment of a reliable FDII subsystem.

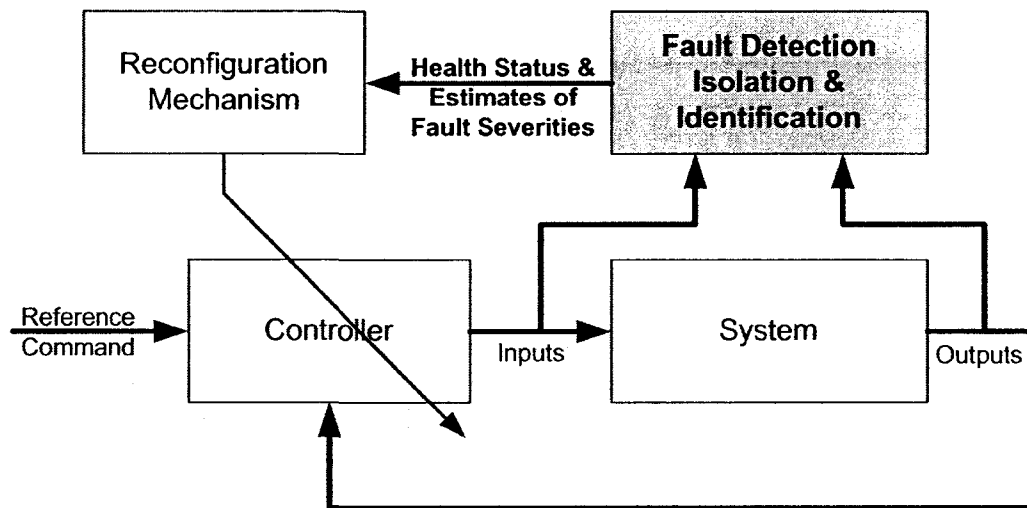


Figure 1-1. The role of FDII in an *active* fault tolerant control (FTC) system.

On the other hand, accurate identification of fault severities is an invaluable asset for system maintenance operations. Accurate estimation of fault severities facilitates the early detection of incipient faults and the identification of out-of-spec behaviors. This consequently allows system operators and controllers to intelligently plan and execute a priori preemptive actions to avoid system breakdown, catastrophic failures, and mission abortion. Furthermore, recent interest by aerospace industries in preventive maintenance (as opposed to corrective maintenance) systems, has called for a technological shift in system monitoring and maintenance operations from traditional scheduled time-based (or

distance-based) fixed interval maintenance practices (which tend to reduce system lifetime and increase system down-time, resulting in loss of profit) to condition-based maintenance (CBM) systems [3], [4]-[7].

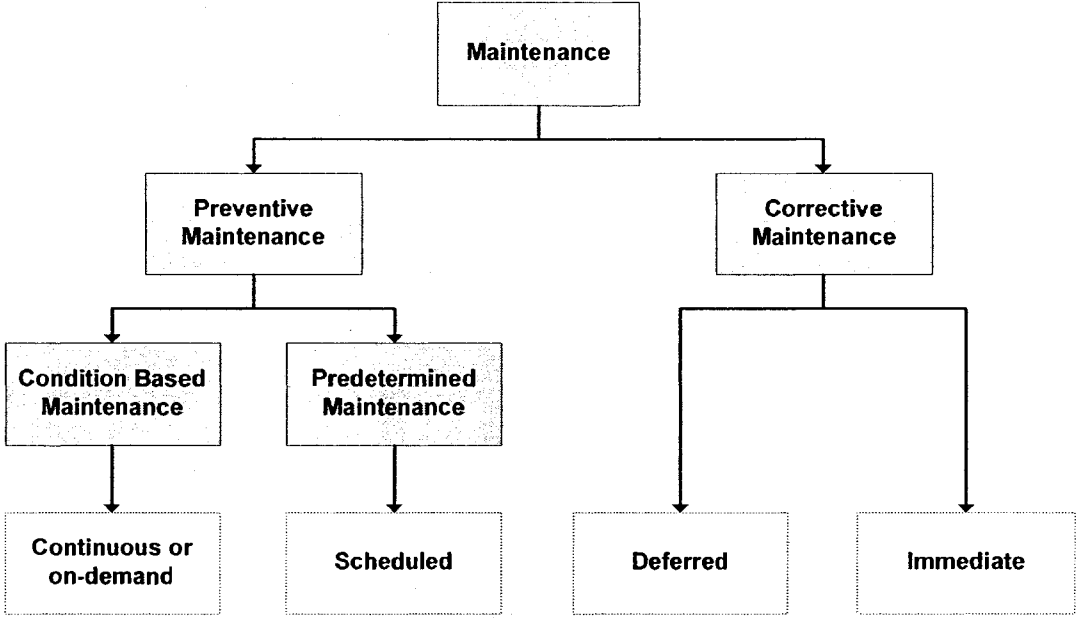


Figure 1-2. Overview of the Swedish maintenance terminology standard SSEN-13306 [7].

Figure 1-2, for example, depicts an overview of the Swedish maintenance terminology standard SS-EN 13306 [7]. According to this standard, maintenance is divided into *corrective* maintenance and *preventive* maintenance. With the corrective approach, maintenance is performed after a breakdown or whenever an obvious fault has occurred and detected in the system. Depending on the functionality and criticality of the failed component and the severity of the occurred fault, maintenance action must be performed immediately; while for others, the maintenance action can be deferred in time.

On the contrary, maintenance is performed in the preventive approach in order to prevent equipment breakdown by repairing, servicing, or exchanging the failed/faulty component. It can be seen in Figure 1-2 that in the Swedish standard preventive

maintenance has been divided into two categories including CBM and predetermined maintenance. The predetermined is scheduled in time based (or distance based) fixed intervals, while the CBM can have dynamic or on-demand intervals.

In CBM systems, maintenance actions are planned based on actual condition (objective evidence of need) of a component obtained from in-situ, non-invasive tests, and condition/health assessments [4]. In other words, the main idea behind CBM systems is to estimate the health status of a component under operation with the objective of deciding whether it is in need of maintenance or not, and if so at what time does the maintenance actions needs to be executed in order to avoid a breakdown or malfunction. The degree of automation in assessing the health condition can vary from human visual inspection to fully automated systems with sensors, diagnosis, prognosis, and health monitoring modules.

The pace of development in CBM systems has been increased over the past few years. As a result several products, standards, and standardization proposals have been developed within the CMB technical community. One of the most important of these standards is the open system architecture for condition-based maintenance (OSA-CBM) [8], which was originally developed by an organization with the same name but is currently managed by the MIMOSA (Machinery Information Management Open Systems Alliance) [9] standards body. OSA-CBM has been developed as a de facto standard that encompasses all the components essential to a functional CBM system. The OSA-CBM standard is modular solution that divides a CBM system into seven different layers including: (i) sensor module, (ii) signal processing module, (iii) condition monitoring

module, (iv) health assessment module, (v) prognostic module, (vi) decision support module, and (vii) presentation module.

Therefore, diagnosis, prognosis, and health management (DPHM) [3] is a crucial component of an autonomous CBM system. Diagnosis is essentially equivalent to FDII and is responsible for estimating the current health status of a system through the utilization of on-line sensing/measurement devices. Prognosis entails predicting the future health status of a system and its components using the system's current health state/diagnostics information provided by FDII subsystem, historical failure rate data, and appropriate fault evolution models. A reliable prognosis tool enables accurate prediction of fault evolution through accurate estimation of time-to-failure (TTF) and remaining useful life (RUL) of a component. TTF and RUL constitute the prognostics information of a system, which make it feasible to determine the future health status of the system and consequently provide indications of failure precursors. This essentially allows in-advance planning of optimal maintenance schedules in order to maximize system up-time, minimize time to repair (TTR), optimize maintenance costs, and avoid catastrophic failures. This can be achieved through development of a maintenance scheduler that can generate optimal maintenance schedules based on system prognostics information and future usage plans of the system taking into account the maintenance team objectives and constraints such as the number of available support crews and the availability of parts and resources needed to perform the required maintenance operation [3].

Figure 1-3 depicts an autonomous CBM system including the DPHM module and the maintenance scheduler. The figure also demonstrates the role of FDII within the DPHM module. As can be seen in the figure and as described above, the FDII system plays an

extremely important role in a CBM system. Any inaccuracies involved in estimation of system health status by the FDII system will simply propagate across the entire CBM system, which consequently deteriorates the overall performance of the CBM system even in presence of very precise prognosis and maintenance scheduler algorithms.

Thus, development of a reliable and accurate FDII system is extremely desirable for both FTC and CBM systems. The problem of FDII for linear systems has received considerable attention over the past three decades. Thus, the majority of fault diagnosis methods are based on either linear system models or linear approximation of nonlinear system models around an operating point. However, almost all practical systems operate around a wide dynamic operating range, thus showing nonlinear behavior that can not be accurately modeled with linear models. Therefore, it is necessary to design and develop FDII techniques that can tackle dynamic nonlinear systems directly.

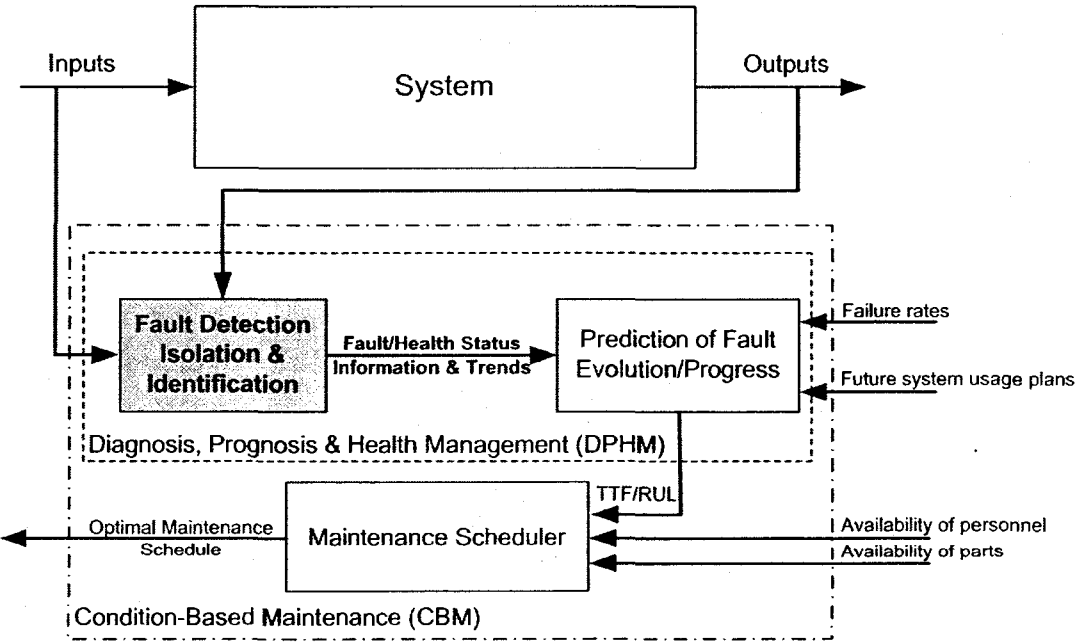


Figure 1-3. The role of FDII in DPHM module of a CBM system.

Furthermore, the problems of fault isolation and identification in nonlinear systems are even more complex than the detection problem and thus have remained less investigated. More specifically, identification of fault severities in nonlinear systems has received considerably less attention in the literature. However, with the recent increasing demand for FTC and CBM systems, accurate estimation of fault severities (i.e., fault identification) has become increasingly important.

Moreover, there is a lack of integration in the FDII approaches proposed in the literature. More precisely, most of the proposed techniques address only the fault detection and isolation (FDI) problem and tackle the fault identification issue using a separate subsystem, which essentially makes the FDII system structurally more complex. Thus, an integrated FDII solution that can simultaneously perform the three tasks of detection, isolation, and identification with minimum interaction among the tasks is highly desirable.

1.3 Objectives of the Research

The objectives of this thesis is to develop an integrated FDII scheme for nonlinear systems that is robust to sensor noise and system disturbances and that is able to operate even in presence of partial state measurements. The FDII scheme should not only be able to reliably detect the presence and isolate the location of anomalies in nonlinear systems but also accurately estimate their severities after their occurrence. Furthermore, the FDII system should be robust with respect to system disturbances and measurement noise in order to minimize false alarms while the system is under healthy mode of operation.

Moreover, the FDII system should be able to operate sufficiently accurate even in cases where some of the system states are not available for measurement (i.e., partial

state measurement). Thus, another objective of the research is to develop a state estimation algorithm that can provide accurate estimates of the unmeasured states of the system even in presence of faults or anomalies (that is robust to occurrence of faults) and can eventually be integrated into the FDII system.

Finally, the effectiveness of the developed integrated FDII scheme in diagnosis of faults in a practical engineering system has to be verified. For this purpose, the integrated FDII scheme will be applied for detection, isolation, and identification of faults in reaction wheel actuators of a satellite's attitude control system in presence of measurement noise, satellite and reaction wheel disturbances, and partial measurement of the states of the reaction wheel.

1.4 Literature Review

In the following, we will provide an overview of the fault diagnosis literature in general, and fault detection methodologies in particular. A more formal presentation of the FDII problem, further details on the issues involved, and some of the methodologies developed for FDII in the literature especially for fault isolation and identification tasks will be reviewed in Chapter 2.

Development of autonomous FDII algorithms and more specifically autonomous FDI algorithms has received considerable attention over the past two to three decades. The most traditional approach to FDI is primarily based on signal processing techniques as applied to system measurements. This is generally achieved using either of the following two approaches:

- (i) Time domain limit checking and/or trend analysis by comparing the statistics of the measurable states and outputs of the system with nominal operational limits

[1]. Dynamic trend analysis, also widely known as qualitative trend analysis (QTA), is one of the most common trend analysis techniques for fault diagnosis and classification [10]. The QTA technique involves the two steps of extraction of the trends/features from the data, and the interpretation of the trends to arrive at meaningful conclusions about the state of the process. A large number of methods have been developed in the literature for trend extraction and representation including, the fundamental work of [11] in developing a formal language for representing trends, a neural network-based extraction of primitive trends [12], a fuzzified symbolic representation of trends [13], and a wavelet-based method for the extraction of qualitative trends [14]. Trend interpretation has also received considerable attention over the last two decades and as a result a number of methods have been developed for estimation of similarity measures between extracted trends [10], also known as trend-matching algorithms. Some of the proposed algorithms include the use of hidden Markov models (HMM) for trend matching [15], the use of dynamic time warping (DTW) for similarity estimation [16], and most recently a fuzzy primitive-similarity-based approach for the estimation of trend similarity and consequently a fuzzy inference framework for fault diagnosis [17].

- (ii) Frequency or mixed time-frequency domain analysis of the time-series of system states and outputs measured by system sensors. The most popular signal processing algorithms that have been widely used for FDI purposes are the Discrete Fourier Transform (DFT) and the Discrete Wavelet Transform (DWT), which extract frequency and time-frequency features from time-series data,

respectively. More specifically, DWT has been extensively used over the last 15 years as a feature extraction tool for fault diagnosis [18], [19] of machinery components such as gearbox [20] and bearing [21], [22].

The major drawback of such signal processing techniques is that they do not consider the dynamic interrelationship between the measured signals of the system. This would essentially result in generation of numerous false alarms by the FDI system. To overcome this drawback and reliably detect and isolate faults (i.e., faulty components) in a system, some form of *redundancy* is required. The redundancy is basically employed to perform consistency checks between multiple measurements in the system that are mutually related.

Traditionally, redundancy and therefore fault diagnosis is achieved by using extra hardware, which is known as hardware (or physical/parallel) redundancy approach to fault diagnosis. In this approach, multiple lanes of a critical component such as an actuator (or a sensor) is used to control (or measure) a particular variable in the system. Typically a voting scheme is then applied to the hardware redundant system to perform consistency checks between signal levels and trends of the multiple identical components in order to decide if a fault has occurred and determine its location. The hardware redundancy is commonly used in mission and safety critical systems such as digital fly-by-wire flight systems and nuclear reactors. Even though hardware redundancy approach provides high performance and is known to be very reliable, it comes at the expense of (i) extra equipment and maintenance cost and (ii) extra space required for the extra hardware, which can be of significant importance for some applications (e.g., space applications). Furthermore, hardware redundancy approach becomes impractical and

unreliable in applications where identical duplication of some specific components is extremely difficult.

Consequently, another approach to create redundancy known as *analytical redundancy* was introduced in early 1970's by Beard [23], where instead of using extra hardware the redundancy is supplied by an analytical (or a mathematical) model of the component or the entire monitored process. Accordingly, fault diagnosis systems that are based on analytical redundancy are often called *model-based fault diagnosis* systems. The main advantage of the analytical redundancy-based approach is that no additional hardware copies of a component are needed for realizing a fault diagnosis algorithm.

Figure 1-4 depicts a general structure of the analytical redundancy-based versus the hardware redundancy FDI as applied to the monitoring of a control system. In the analytical redundancy approach, the mathematical relationship between different variables within the system, imposed by the analytical model of the system, serves as a reference point for fault diagnosis. More specifically, whenever system measurements are violating these relationships, the presence of a fault (or a faulty component) in the system is concluded. The violation from analytical relationships after the occurrence of faults is reflected in a set of signals known as *residuals*. Thus, the residual signals should ideally (i.e., under no process and measurement noise) be equal to zero when the system is healthy, and should deviate from zero when faults occur in the system. However, in presence of measurement noise and system disturbances, the residual signal shall remain in vicinity of zero under healthy system conditions and diverge from zero neighborhood (i.e., exceed a certain threshold band around zero) when faults occur in the system. Therefore, analytical redundancy-based fault diagnosis can be defined as the detection

and identification of faults in a system through evaluation and analysis of residual signals.

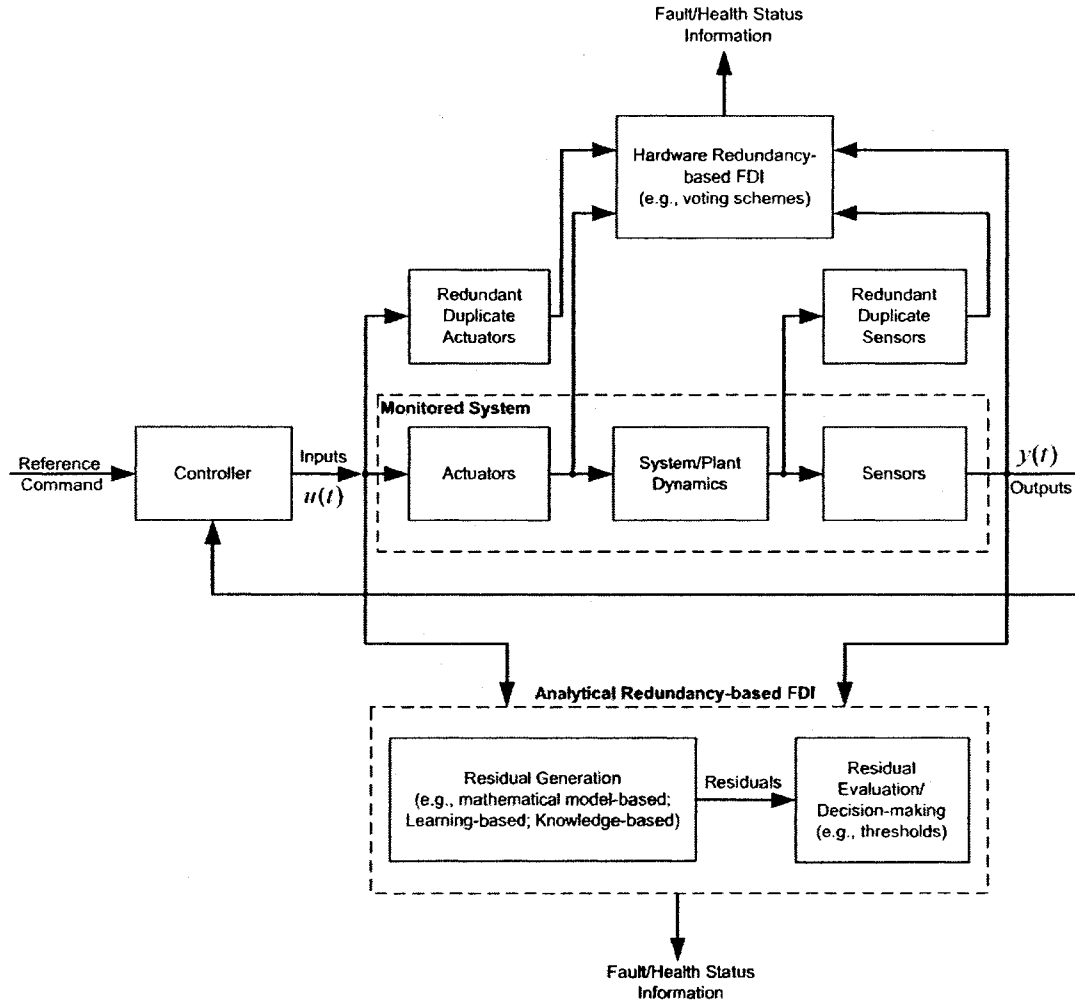


Figure 1-4. Analytical versus hardware redundancy based FDI as applied to the monitoring of a control system.

The analytical model in an analytical redundancy-based FDI system can take a variety of forms including ordinary differential equations, intelligent data-driven models, and expert system models. Hence, analytical redundancy-based fault diagnosis can broadly be pursued in three distinct frameworks based on the way the a priori knowledge about the system is being represented and utilized. The first one is the mathematical model-based

framework [1], [24]-[26], where a priori knowledge of the system is represented by the system's mathematical model derived using physical principles. The second one is the learning-based (or computational intelligence-based) framework [27]-[3] which relies heavily on a system's historical data and data-driven models of the system. References [28], [29] provide an extensive comparison of the various methods within the above two frameworks. Finally, the third framework includes the expert system-based (or fuzzy rule-based) approaches to FDI [30]-[34], which use an expert's knowledge of the system operation and its failure modes to obtain a qualitative model of the system.

As shown in Figure 1-4, the analytical redundancy-based FDI, in general, consists of two main stages of residual generation and residual evaluation (or decision making). This two-stage structure was first introduced in [35], and currently is widely accepted by the fault diagnosis community. The residual generation stage aims at generating residual signals using available input/output measurements from the monitored system. As mentioned previously, the residual signal should stay close to zero when no fault is present in the system, but should distinguishably diverge from the zero neighborhood (specified by appropriate thresholds) when a fault occurs. Thus, the residual generation stage is essentially a procedure for extracting fault symptoms from the system measurements.

In the residual evaluation stage, on the other hand, the generated residuals are inspected for the fault signatures, and their presence is determined by applying a decision rule. The decision rule may simply be a threshold test on the instantaneous values or moving window averages of the residuals, or it may consist of more complex statistical

methods such as generalized likelihood ratio (GLR) testing [36] or sequential probability ratio test (SPRT) [37], [38].

During the last two to three decades most of the research work in analytical redundancy-based fault diagnosis is focused on the residual generation problem due to its higher importance in the sense that well designed residuals make residual evaluation process fairly simple. As a result, most of the proposed FDI methods employ simple threshold techniques for decision-making based on residuals. Reference [39] provides a survey of the most widely used residual evaluation methods. However, there has also been some work reported in the literature on developing more advanced residual evaluation techniques using fuzzy logic [40], and more recently adaptive thresholds [41], [42]. Since in this thesis, we will use a simple, but widely used, threshold testing technique for residual evaluation, from now on we will focus on reviewing residual generation strategies that have been proposed in the literature.

Residual signal generation is generally achieved by comparing a measured signal with its estimate, where the estimate is obtained through a priori information and knowledge of the system being monitored. The a priori knowledge of the system can take a variety of forms including mathematical models, historical data saved into databases, and a set of rules stored in a rule or knowledge base. Hence, residual generation from system inputs and outputs can, in general, be achieved using mathematical model-based, learning-based, and knowledge-based methods, which employ physics-based mathematical models of the process, historical data of the process measured by sensors, and human expert knowledge of the system and its faults, respectively.

In general, mathematical model-based residual generation approaches aim at generating a set of residuals that reflect the discrepancies between the actual behaviour of a system and the expected behaviour given by its model. To enable fault isolation, usually a structured set of residuals is required, where each residual is affected only by a specific set of faults and remains insensitive or robust to the other faults. Furthermore, to ensure the robustness of the FDI system with respect to various sources of uncertainties including perturbations/disturbances, measurement noise, modeling inaccuracies, and unmodeled dynamics, the structured set of residuals must be designed in a way that remains insensitive to these uncertainties.

In general, three main model-based approaches are used to generate residuals. The first is the observer-based (or filter-based, or state estimation-based) methods [24], [43], which consist of a model-based reconstruction of the system outputs from sensor measurements (or a subset of system measurements), and defining the residuals as the difference between the actual measurements and the model-based estimates. The observer-based FDI techniques have been equally applied for both linear and nonlinear systems. The system outputs are estimated from the measurements by using, for example, linear or nonlinear observers [44], sliding-mode observers [45], and high-gain nonlinear observers [46] in a deterministic setting, and Kalman filters (including linear Kalman filter, Extended Kalman filter (EKF), and Unscented Kalman filter (UKF) [47], [48]) [49] or receding horizon estimators (RHE) [50]-[52], [53] in a stochastic setting. While the output estimation error is defined as the residual in the deterministic framework, the innovation sequence comprises the residual in the stochastic case.

The second is the parity space approach [54]-[55], [25], where the residual is generated using the so-called parity functions defined over a time window of system input and output data. Parity space method is based on simple algebraic projections and geometry and the basic idea behind this method is to provide an appropriate check of the parity or consistency of the various measurements within the monitored system [25]. Reference [55] provides a comprehensive description of the parity space method and reference [54] demonstrates its application to fault diagnosis of an operating nuclear reactor. Parity space technique has also been successfully applied to fault diagnosis of inertial navigation systems [56]. Although parity space method has been primarily developed and applied for linear systems, it has been recently applied for fault estimation of nonlinear systems [57]. Furthermore, it has been shown in [58] and [59] that the parity space approach is equivalent to the high gain observer-based method. However, it should be noted that the parity space method is more sensitive to measurement noise and process noise (or disturbance) as compared to observer-based methods, which are more robust to noise and disturbances due to their closed-loop structure.

Finally, the third approach to residual generation is parameter estimation [26], [60]. This approach is based on the assumption that the faults are reflected in the physical parameters of the system. Hence, in order to identify faults, the system parameters are estimated on-line using well-known parameter estimation techniques. The residuals in this approach are essentially the difference between the on-line estimates of the system parameters and their corresponding values under fault-free conditions. The parameter estimation approach was initially developed for linear systems due to availability of very well-known linear parameter estimation methods. However, recent advances in nonlinear

parameter estimation using, for example, UKF and adaptive neural networks, has made it possible to use parameter estimation approach for FDII of nonlinear dynamic systems [53], [61].

An alternative to the model-based residual generation approach is the so-called learning-based method, which has the potential to learn the plant model from historical input-output data of the system. The learned data-driven model can then be used to serve as the analytical model for residual generation. This approach becomes increasingly more appealing for situations where high-fidelity mathematical model of the monitored system does not exist or is extremely difficult to obtain. The main challenge though is to ensure that sufficient amount of data from the healthy operational mode of the system is available. References [62]-[64] provide detailed surveys of fault diagnosis using learning-based methods, which are often also called as computational intelligence-based methods, artificial intelligence-based methods, soft-computing approaches, or simply intelligent methods. According to the FDI literature, artificial neural networks, fuzzy logic, and neuro-fuzzy systems are the most widely used intelligent approaches to fault diagnosis. Wherever fuzzy logic is employed, the availability of expert knowledge of the system encoded as a set of fuzzy “*if-then*” rules is implicitly assumed. Whenever expert knowledge is not available and the fuzzy rules are obtained using qualitative physics, neural networks are profoundly used for learning (or determining) the parameters of those rules using historical input-output data of the system, hence the neuro-fuzzy systems.

As mentioned above, neural networks are among the most widely used intelligent techniques for FDII. This is mainly due to their distinguished ability to approximate, to an arbitrary level of accuracy, any continuous nonlinear function, given suitable network

parameters (or weights), architecture and learning algorithm [65]. Indeed, neural networks are able to learn nonlinear functions from examples. They have the ability to make intelligent decisions even in cases where system data is corrupted with noise. They also have a highly parallel structure, which is expected to achieve a higher degree of fault-tolerance than conventional function approximation schemes and, last but not the least, they are readily applicable to multivariable systems. Neural networks can also be applied for process condition/health monitoring, where the focus is on identification of small irreversible changes (i.e., incipient faults) in the process that develop into bigger faults. Reference [3] takes a look at the cutting-edge discipline of intelligent and in particular neural network-based DPHM technologies for predictive maintenance or CBM of engineering systems. Practical case studies of especially DPHM in rotating machinery are also provided therein to illustrate the enabling technologies.

1.5 Proposed Fault Diagnosis Scheme

The FDII scheme proposed in this thesis is a nonlinear fault diagnosis method, which is based on a synergy of multiple frameworks and approaches to fault diagnosis. This synergy takes place at various levels and can be described from different perspectives. The first and possibly the most important aspect of this synergy is that the proposed FDII technique is a *hybrid* solution in the sense that it benefits from both mathematical model of the system and adaptive nature of intelligent techniques, especially neural networks. In essence, the proposed hybrid framework to FDII is an integration of the previously introduced model-based and computational intelligence-based approaches to fault diagnosis.

The mathematical models employed in this hybrid solution involve models of healthy as well as faulty operation of the system. More precisely, a multi-parameterized fault model is defined and developed, which is basically a parameterized dynamic nonlinear model. The parameters of this model are called fault parameters (FPs) and are defined in a way that a one-to-one correspondence can be established between their values and the health status of the physical system components. Thus, the proposed FDII solution aims at an on-line estimation of the fault parameters from system measurements (under full-state measurement assumption) in order to determine the health state of the system. This essentially connects the proposed method to the formerly mentioned parameter estimation approach to fault diagnosis that is based on the assumption that system component faults are reflected in the physical system parameters. However, a modified version of the proposed FDII method is also presented that is applicable to systems with partial state measurements. This leads us to the second aspect of the synergy, where not only the fault parameters have to be estimated but also the unmeasured states of the system. In essence, a combination of online state and parameter estimation (also called dual estimation) is developed to achieve FDII under partial state measurement condition. Since state estimation is achieved using a special type of adaptive filters, the proposed FDII method can also be viewed as an integration of the filter-based and the parameter estimation-based approaches to fault diagnosis.

The third aspect of the synergy is the use of multiple models to enable fault isolation. Over the last decade the multiple-model (MM) approach has become very popular and widely applied for estimation, health monitoring, and control of dynamical systems (see references [66], [67], and [68], respectively). The MM approach is based on a set (or a

bank) of models that represent possible patterns of system behaviour or system structure. The model set (or the bank of models) thus includes models corresponding to healthy as well as faulty modes of system operation. Usually one model in the bank is associated to the healthy operational mode and the rest of the models correspond to various possible fault scenarios in the system. However, multiple models associated to healthy operational mode can also co-exist in the bank if the system structure changes during healthy operations. Nevertheless, the MM approach enables explicit modeling of changes in the system behavior by “switching” from one model to another. Changes in the system behavior may involve structural as well as parametric changes, and take place due to occurrence of faults and/or changes in the system’s operating point.

The MM approach to fault diagnosis traditionally includes a finite number of nonparametric models, which can essentially represent only a finite set of system behaviour. Then, a bank of filters or state estimators is designed to operate in parallel at each instant of time, where each filter is designed based on a particular model in the model set. This works absolutely well for systems with finite number of fault severity levels (for example, stuck-closed and stuck-open failures in control valves, and hard-over and float faults in motor actuators). However, in many engineering systems, occurrence of faults only degrades the performance of a component, actuator, or sensor, and the degradation can take place with a continuum, infinite level of severities. Examples of these kinds of faults include loss-of-effectiveness (LOE) and lock-in-place (LIP) faults in motor actuators, and most types of sensor faults such as bias, drift, loss of accuracy, and freezing. Many component faults also fall into this category such as body damage fault in an aircraft. Accurate and reliable severity identification of these faults, especially at early

stages of their development, is of utmost importance in order to avoid catastrophic failures, and also to plan, in advance, maintenance actions and perform them in time.

Ideally, the traditional MM-based approaches to fault diagnosis would be able to accurately identify fault severities *only if* infinite number of models (or quantization levels) coexists in the model bank, which makes them computationally unfeasible and thus impractical. The fault diagnosis approach proposed in this thesis resolves this practical problem by defining multiple parameterized fault models (PFM), where the parameters can take essentially infinite number of values (i.e., the parameter values can vary over a continuum). Thus, the PFM set (or bank) is implicitly unbounded.

Putting all the synergistic aspects together, we can assert that the FDII methodology proposed in this thesis is a *hybrid*, multiple-model, dual (state and parameter) estimation based approach to fault diagnosis of nonlinear systems.

1.6 Contributions of the Thesis

In this thesis, a novel fault detection, isolation, and identification (FDII) methodology for nonlinear systems is proposed that possesses a number of noble features that distinguishes it from most of the existing fault diagnosis techniques. First, the proposed FDII solution provides an *integrated* framework to *simultaneously* detect, isolate, and identify (i.e., estimate the severity of) faults in the components of a general nonlinear system. More precisely, while most of the standard FDII approaches in the literature incorporate either two or three separate subsystems (or subroutines) to accomplish the three tasks of detection, isolation, and identification, our integrated solution enables us to accomplish the three tasks within a unified, integrated module (or FDII system). For example, FDII techniques traditionally consist of three sub-modules including a residual

generation module for detection, a residual post-processing module for isolation, and an extra identification module for estimating the severity of faults based on system measurements and the information provided FDI. Even though some of the more advanced FDII approaches in the literature have merged the detection and isolation sub-modules into a single subsystem through generation of special types of residual signals (for example, directional residuals), they still use a separate module for fault identification.

Second, the proposed novel FDII methodology is a *hybrid* approach to nonlinear fault diagnosis, which efficiently and effectively utilizes both the *a priori* mathematical model information of the system, and adaptive and self-learning capabilities of computational intelligent techniques within a unified framework. Even though *hybrid* diagnostic methods are recently being more developed in the literature, but the domain of *hybrid* fault diagnosis still needs to be much further investigated and explored.

The third innovative aspect of the proposed FDII methodology is in its power of accurate and reliable estimation of the severity of incipient faults in nonlinear systems. In fact, there are very few fault diagnosis techniques in the literature that address the problem of incipient fault identification in nonlinear systems since this domain of research, despite its undeniable importance, has received considerably less attention as compared to fault detection and isolation.

The fourth novelty of this thesis is the development of two schemes of the proposed hybrid nonlinear FDII technique, namely *series-parallel* and *parallel*, which respectively enable *robustness* of fault diagnosis with respect to measurement noise and the closed-loop system transients due to changes in the control command inputs. More specifically,

the proposed *series-parallel* FDII scheme, though being very sensitive to measurement noise, very quickly detects and isolates faults (i.e., with a very short delay) and also exhibits robustness to the changes in the control command signal. Therefore, the series-parallel scheme is very well suited for monitoring of high signal-to-noise ratio (SNR) systems with frequent control commanding and stringent, safety- and reliability-related requirements on delays in FDI. On the other hand, the parallel scheme is extremely robust to measurement noise and it can very reliably perform FDI and very accurately estimate fault severities even in presence of large measurement noise. This makes the parallel scheme a definitive choice for reliably monitoring systems with low SNR specifications. The enhanced reliability of the parallel FDII scheme as compared to its series-parallel counterpart is due to its rigorous fault isolation capability as well as the simplicity of its fault isolation decision logic. It should be noted that the robust *parallel* FDII scheme proposed in this thesis is an entirely new development in the literature. On the other hand, the novel aspects of the series-parallel scheme as compared to other two similar FDI methods proposed in the literature (Alessandri [69] and Sobhani-Tehrani [70]) are in (i) remarkably simpler neural network architecture and adaptation laws, (ii) more solid fault isolation results due to the first-time use of a bank of *single-parameter* fault models, and (iii) fault severity identification capability.

Both the series-parallel and the robust parallel hybrid nonlinear FDII techniques discussed in the above rely on the availability of full state measurements of the system. The full-state measurement assumption is, in fact, very popular among most of the nonlinear diagnostic methodologies proposed in the literature. However, there are a few reasons – provided and discussed in details in Chapter 4 – as why this can be a relatively

restrictive assumption, which can eventually render a fault diagnosis system designed as per assumption impractical or unreliable. The fifth contribution of this thesis essentially addresses this issue by extending the proposed series-parallel and parallel FDII schemes to systems with partial state measurement. This is achieved through development and deployment of a fault-tolerant observer (FTO) that estimates the states of the system using system input and output signals (or measurements) even in presence of faults in system components. The estimated states are then employed as inputs to the proposed FDII subsystem. If some of the system states are directly *measured*, then the estimates of the *unmeasured* states – obtained from an essentially a *reduced-order* FTO – and the actual *measured* states – obtained from sensors – comprise the inputs to the FDII module.

A fault-tolerant observer (FTO) *terminology* or notion is proposed in this thesis for the first time in the literature, though a very similar *concept* has been previously proposed and extensively investigated in the literature under the terminology of *unknown input observers* (UIO). The UIOs have the capability of estimating the states in presence of unknown inputs. Thus, considering faults as *unknown inputs* to the system, the UIOs may be employed to provide state estimates that are *decoupled* from faults. However, in the literature, the UIOs have been mainly developed within the context of robust control and robust fault diagnosis, where modeling uncertainties and external disturbances – rather than faults – are modeled as unknown inputs. Consequently, the objective in UIO design is to make the control system and fault diagnosis subsystem *robust* with respect to modeling errors and external disturbances, which is basically different from the purpose of FTO described above.

The FTO method developed in this thesis is called the Kalman filter structure preserving neural state estimator (NSE). It should be noted, however, that the structure/architecture of this NSE is not a novelty of this thesis and has been borrowed from the *optimal filtering and state estimation* literature. Instead, it is the *new* weight update laws of the NSE that comprises another contribution of this thesis.

Finally, the application of the proposed algorithms to fault diagnosis of reaction wheel actuators of spacecraft attitude control system (ACS) comprises the practical – as opposed to theoretical – contribution of this thesis. Reaction wheels, although being largely deployed on-board numerous modern satellites, are very sensitive devices and are susceptible to various anomalies. Hence, there is high demand for fault diagnosis algorithms to monitor these devices. As a result, fault detection and isolation (FDI) in reaction wheels has been extensively investigated over the last few years. However, they have entirely missed addressing incipient fault identification or severity estimation in these devices, which thus can essentially be considered as a practical contribution of this thesis.

1.7 Outline of the Thesis

This thesis is organized as follows. Chapter 2 formally defines the fault diagnosis problem in nonlinear systems and presents a comprehensive literature review and analysis of different approaches to fault detection, isolation, and identification (FDII) of both linear and nonlinear systems. Both model-based and computational intelligence-based approaches to fault diagnosis have been extensively reviewed and analyzed, and a number of well-known methodologies within each framework are further demonstrated and their respective pros and cons are cited. Chapter 3 demonstrates both the series-

parallel and the robust parallel structures of the *hybrid* nonlinear FDII methodology under full-state measurement assumption, which is the core contribution of this thesis. Chapter 3 also introduces a specific formulation of the problem of FDII in nonlinear systems as a nonlinear parameter estimation problem using the notion of parameterized fault models (PFMs). A short survey of various model-based and computational intelligence-based nonlinear parameter estimation techniques is also performed in this chapter. In Chapter 4, first the theory of state estimation or filtering has been comprehensively reviewed in order to design and develop a fault tolerant state estimator that enables FDII under partial-state measurement conditions. A specific adaptive neural state estimator (NSE) is then designed and its integration with the proposed *hybrid* FDII schemes are described in this chapter. Chapter 5 explains the spacecraft attitude control system and reaction wheel actuators to which the proposed fault diagnosis algorithms are applied. Simulation results demonstrating the effectiveness and validating the properties (such as robustness) of the proposed FDII algorithms have also been proposed in this chapter. Finally concluding remarks and future work are included in Chapter 6.

Chapter 2:

2 Fault Detection and Diagnosis

In this chapter, we start with formal definition and formulation of the fault detection and diagnosis problem in nonlinear systems. Then, desired attributes of a fault diagnosis system and the rationale behind each attribute are discussed. A comprehensive survey and analysis of the literature on model-based and computational intelligence-based approaches to fault diagnosis is then presented with individual emphasis on sometimes tightly connected tasks of fault detection, isolation and identification. A number of well-known methodologies within each approach are further demonstrated and their respective advantages and disadvantages are highlighted. Finally, the issue of robustness in fault diagnosis is introduced and briefly discussed.

2.1 Problem Formulation

In this section, the problem of detecting, isolating, and identifying faults in a general nonlinear system is formulated. Towards this end, consider a general nonlinear dynamic system described by the following nonlinear discrete-time state space representation:

$$\begin{aligned}x_{k+1} &= f(x_k, u_k) + \Gamma(x_k)w_k \\ y_k &= h(x_k) + v_k\end{aligned}\tag{2-1}$$

where $x_k \in \mathfrak{R}^n$ is the system state vector, $f: \mathfrak{R}^n \times \mathfrak{R}^r \rightarrow \mathfrak{R}^n$, $h: \mathfrak{R}^n \rightarrow \mathfrak{R}^m$ are smooth nonlinear vector-valued functions (or vector fields) on their respective domains, $u_k \in \mathfrak{R}^r$ is the control input vector, $y_k \in \mathfrak{R}^m$ is the system output vector, and w_k and v_k

represent system disturbances and measurement noise, respectively. The vector fields f and h represent the dynamics and output equation of the nominal model of the system. The state-dependent function $\Gamma(\cdot)$ essentially represents the channel over which the external disturbances are applied to the system. In many systems this function is simply a matrix gain. It is assumed that all system states are available for measurement. It is also assumed that disturbances and measurement noise are bounded signals, that is

$$\|w_k\| \leq D_{\max}, \|v_k\| \leq N_{\max} \quad \forall k \in N \quad (2-2)$$

Under full-state measurement assumption, the output equation in (2-1) can be redefined as $y_k = C x_k + v_k$, where C is an $n \times n$ identity matrix.

In this thesis, we are concerned with diagnosis of faults that occur in components of the open-loop system. More precisely, even though the performance of the proposed FDII technique will be assessed in an operational closed-loop setting, we assume that no faults may occur in the system controller. There are two main reasons for this assumption. First, modern control systems are computer-controlled and are thus more reliable and less prone to errors particularly due to hardware wear and tear. Second, faults/errors that may occur in the controller software are usually handled using an entirely different error handling and accommodation mechanisms, which are mostly developed by researchers in the computer science community.

As far as the open-loop system is concerned, the system under consideration can be decomposed into three parts including sensors, actuators, and system dynamics. Figure 2-1 shows this decomposition that is also often used in practice. As can be observed from this figure, faults may occur in any of the three components of the open-loop system as described below. Furthermore, the plant dynamics and the sensor measurements are

always affected by external system disturbances (or process noises) and measurement noises, respectively. A reliable fault diagnosis system should be able to distinguish faults from system disturbances and measurement noise. More precisely, the fault diagnosis system must be robust to these uncertainties while remaining sensitive to faults. The robustness of an FDI system to various sources of uncertainties is of utmost importance, which will be further discussed in Section 2.5. In the following we will describe the various sources of faults in the open-loop system.

(i) Sensor faults: Sensors are basically the output interface of a system to the external world, and convey information about a system's behaviour and internal states. Therefore, sensor faults may cause substantial performance degradation of all decision-making systems or processes that depend on data integrity for making decisions. Such systems include, but not limited to, feedback control systems, safety control systems, quality control systems, navigation systems, surveillance and reconnaissance systems, state estimation systems, optimization systems, and interestingly health monitoring and fault diagnosis systems. For example, in a feedback control system sensors are used either to directly measure system states or to generate state estimates for the feedback control law. Thus, presence of faults in sensors may deteriorate state estimates and consequently result in inefficient and/or inaccurate control.

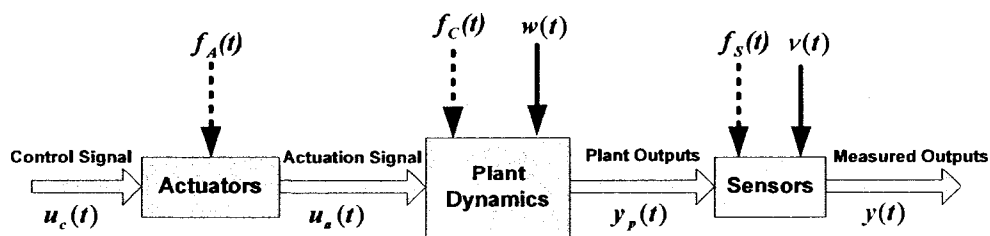


Figure 2-1. Decomposition of the open-loop system components and possible occurrence of faults in them.

Common sensor faults/failures include: (a) bias; (b) drift; (c) performance degradation (or loss of accuracy); (d) sensor freezing; and (e) calibration error [71].

Figure 2-2 depicts the effect of the above faults on system measurements.

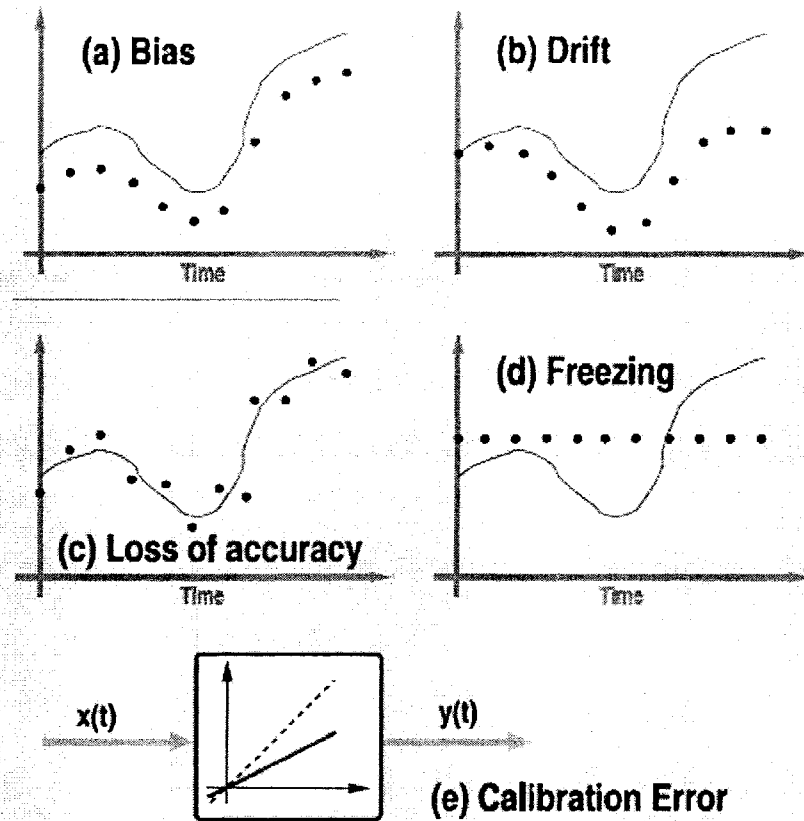


Figure 2-2. The effect of various sensor faults on system measurements [73].

Moreover, the mathematical representation of the above sensor faults is as follows [71]:

$$y_i(t) = \begin{cases} x_i(t) & \forall t \geq t_0 & \text{No failure} \\ x_i(t) + b_i & \dot{b}_i(t) = 0, b_i(t_{Fi}) \neq 0 & \text{Bias} \\ x_i(t) + b_i(t) & |b_i(t)| = c_i t, 0 < c_i \ll 1 & \forall t \geq t_{Fi} & \text{Drift} \\ x_i(t) + b_i(t) & |b_i(t)| \leq \bar{b}_i, \dot{b}_i(t) \in L^\infty & \forall t \geq t_{Fi} & \text{Loss of accuracy} \\ x_i(t_{Fi}) & & \forall t \geq t_{Fi} & \text{Sensor freezing} \\ k_i(t)x_i & 0 < \bar{k}_i \leq k_i(t) \leq 1 & \forall t \geq t_{Fi} & \text{Calibration error} \end{cases} \quad (2-3)$$

where t_{Fi} denotes the time of fault occurrence on the i^{th} sensor, and b_i denotes its accuracy coefficient such that $b_i \in [-\bar{b}_i, \bar{b}_i]$ where $\bar{b}_i > 0$. Furthermore, it is seen that $k_i \in [\bar{k}_i, 1]$, where $\bar{k}_i > 0$ denotes the minimum sensor effectiveness. We can represent the above cases, except the freezing case, with the following mathematical model:

$$y = K_m x + B \quad (2-4)$$

where K_m is a positive definite diagonal matrix whose elements are slowly varying within $[\bar{k}_i, 1]$, and elements of vector B slowly vary within $[-\bar{b}_i, \bar{b}_i]$.

(ii) Actuator faults: In many electromechanical or electrochemical systems, control signals from the controller (for example, a microprocessor or a microcontroller) cannot be directly applied to the system. Actuators are needed to transform control signals to proper actuation signals such as torques and forces to drive the system. Actuators are thus the control hubs of a system. Therefore, consequences of the occurrence of anomalies in a system's actuators or control effectors may vary from higher energy consumption (due to an incipient fault) to total loss of control (due to total failure of an actuator).

Actuator faults are usually dependent on the actuator type. However, common types of faults have been identified for specific types of actuators. For example, common faults in control valve actuators include stuck-open, stuck-closed, and abnormal leakage. Another common set of actuator faults especially in servomotors include: (a) lock-in-place (LIP) or freezing; (b) float; (c) hard-over-failure (HOF); and (d) loss of effectiveness (LOE) [72].

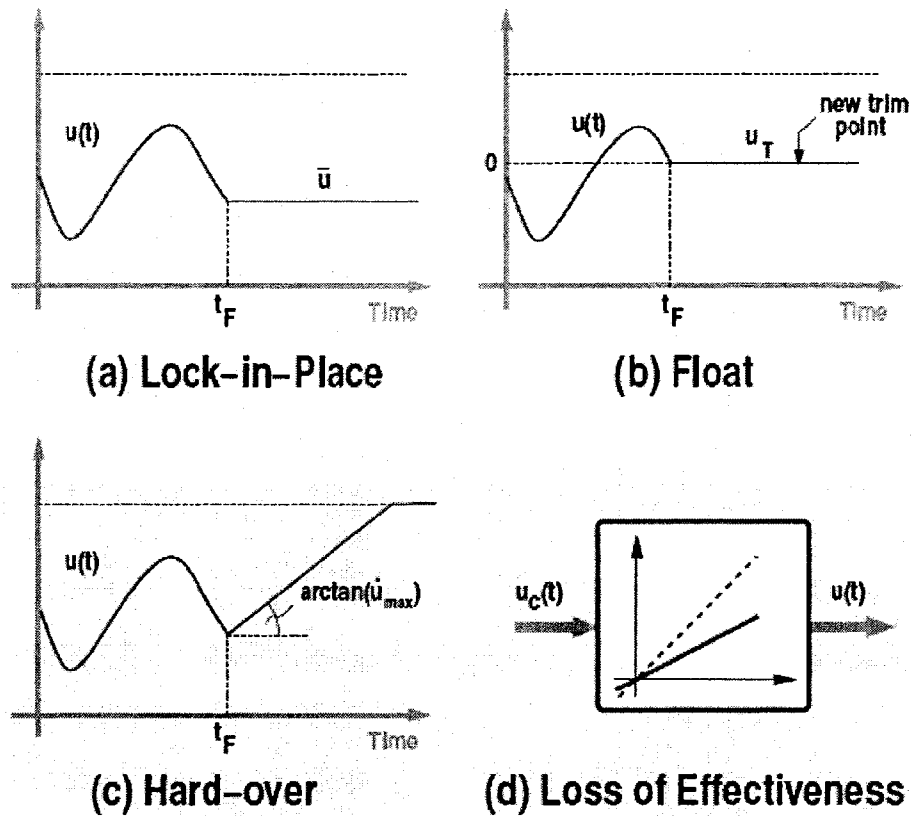


Figure 2-3. Common types of actuator faults [73].

In the case of LIP faults, the actuator "freezes" at a certain condition and does not respond to subsequent commands. HOF is characterized by the actuator moving to the upper or lower position limit regardless of the command. The speed of response is limited by the actuator rate limit. Float fault occurs when the actuator "floats" with zero moment and does not contribute to the control authority. LOE is characterized by lowering the actuator gain with respect to its nominal value. Different types of actuator faults can be mathematically represented by:

$$u_a^i(t) = \begin{cases} u_c^i(t) & \text{Absence of Faults/Failures} \\ k_i(t)u_c^i(t) & 0 < \varepsilon_i \leq k_i(t) < 1, \forall t \geq t_{Fi}; \text{ (LOE)} \\ 0 & \forall t \geq t_{Fi}; \text{ (Float)} \\ u_c^i(t_{Fi}) & \forall t \geq t_{Fi}; \text{ (LIP)} \\ u_{i\min} \vee u_{i\max} & \forall t \geq t_{Fi}; \text{ (HOF)} \end{cases} \quad (2-5)$$

where $u_a^i(t)$ denotes the actuation signal (or actuator output) from the i^{th} actuator, $u_c^i(t)$ is the control command signal (or actuator input) to the i^{th} actuator, t_{Fi} denotes the time of fault occurrence on the i^{th} actuator, $k_i(t) \in [\varepsilon_i, 1]$ is the actuator effectiveness coefficient of the i^{th} actuator with $\varepsilon_i > 0$ being the minimum effectiveness, and $u_{i\min}$ and $u_{i\max}$ are the lower and upper limits on the actuation level of the i^{th} actuator, respectively.

We can represent the above cases with the following mathematical model:

$$u_a^i(t) = \delta_i k_i u_c^i(t) + (1 - \delta_i) \bar{u}_i \quad (2-6)$$

where $\delta_i = 1, k_i = 1$ in absence of faults/failures, $\delta_i = 1, 0 < k_i < 1$ in presence of LOE, and $\delta_i = 0$ in other types of faults (i.e., float, LIP, and HOF) with \bar{u}_i being the position at which the actuator is locked.

(iii) Components faults: The component faults are usually represented as cases where some condition changes in the system rendering the nominal dynamic equation of the system invalid. Component faults are also dependent on the system being monitored. Some examples include: power source (e.g., battery, solar arrays) failures in satellites; leak in a tank in chemical systems or propulsion systems; body damage (e.g., wing damage, control surface damage) faults in aerial vehicles; bearing faults in rotational equipments (e.g., aircraft engines); friction faults due to lubricant deterioration; and tooth breakage and crack in gears of a gearbox system (especially in helicopters). Mathematical representation or modeling of these faults is some times very difficult and extensive

experimentation may be needed before constructing a model. Yet, in general, components faults can be represented by a change in the system's state equation (i.e., a change in the nonlinear function f in equation (2-1)), being either a parametric change or a structural/functional change. We will further discuss the important issue of fault modeling in Section 3.1.

Component faults may have minor to very severe consequences. For example, an unexpected failure of the gearbox in a helicopter may cause significant economic as well as fatal loss. Nonetheless, these types of faults usually occur due to wear and tear of the system components. Thus, it is extremely crucial to diagnose these faults at early stages of component degradation in order to avoid catastrophic consequences. Early diagnosis of incipient component faults allows performing timely, on-demand maintenance operations on the degraded component, which may also involve component replacement.

Now that we have identified the general sources of faults in a general nonlinear system with nominal dynamics given in equation (2-1), we can state the fault diagnosis problem as follows:

Fault diagnosis is the problem of autonomously detecting the presence, isolating the location, and identifying the type and severity of any of the three afore-mentioned faults in a system. Our objective in this thesis is to simultaneously achieve fault detection, isolation and identification (FDII) within a unified framework. In this thesis, we will mainly focus on FDII of component faults and actuator faults, since accurate FDII of incipient faults in components and actuators of a system is vital for enhancement of the reliability and safety of the system as well as fault prognosis and consequently condition-based maintenance (CBM). In particular, the CBM technology has recently received

considerable attention from various industries and OEMs (Original Equipment Manufacturers) such as Pratt & Whitney in aircraft engines, production chain of automotive industry, etc. Nevertheless, the proposed FDII approach can be easily extended to sensor and actuator faults, since they can also be represented by the fault models developed in this thesis, which are described in Section 3.1.

2.2 Desired Attributes of a Fault Diagnosis System

A fault diagnosis system should ideally meet some expectations. Some of the most important desirable attributes of a diagnostic system are explained in the following:

- **Early detection and diagnosis:** This refers to the capability of a diagnostic system in detecting and isolating incipient faults. Early detection and isolation of faults prior to their full manifestation into a failure is of utmost importance for fault tolerant control of safety critical systems as well as condition-based maintenance practices. While being sensitive to incipient faults, the diagnostic system should keep false alarms under healthy operational modes of the system minimized, which poses a major challenge in achieving early detection capability.
- **Isolability:** This is the capability of a diagnostic system in distinguishing the origins of a fault from other potential fault sources or to locate a faulty component among various components of a system. While being absolutely necessary for CBM, isolation capability is also crucial to obtain fault tolerance, since proper counter-measures cannot be taken without knowing the source of an anomaly in system. Isolability of a fault does not depend only on the diagnostic system design but also on the way the fault affects system outputs (i.e., fault observability). Moreover, various sources of uncertainties such as modeling uncertainty/errors

and system disturbances pose a serious challenge to achieve a high degree of isolability. More precisely, a diagnostic system with a high degree of isolability may be so sensitive to these uncertainties.

- **Fault Identifiability:** To estimate the severity, type or nature of the fault. While being useful for fault accommodation purposes, fault indentifiability is a definitive requirement for fault prognosis and eventually CBM. Accurate fault identification is usually very difficult to achieve due to presence of measurement noise, system disturbances, modeling uncertainties, and last but not the least coupling/interactions between potential fault sources in the system being monitored.
- **Robustness:** Uncertainties are inevitable in practical settings. Therefore, robustness to measurements noise, system disturbances, and modeling uncertainties is one of the most highly desirable attributes of a diagnostic system intended for practical implementations. Robustness essentially augments diagnostic system reliability and effectiveness. Due to its utmost importance, in Section 2.5 we discuss the issue of robustness of the fault diagnosis system in more details.
- **Novelty Identifiability:** Although the well-known, industry standard failure analysis tools such as FMEA (failure mode and effects analysis) (which was formally introduced in the late 1940s, with military purposes, by the US Armed Forces) and, its recent extension, FMECA (failure mode, effects, and criticality analysis) provide fruitful information on potential failure modes within a system and their effects/impacts upon it, as well as charting the probability of failure

modes against the severity of their consequences (i.e., criticality analysis), there is still a chance of novel anomalies occurring in the system. It is expected from a diagnostic system *not* to wrongly classify novel malfunctions in the system as other *a priori* known type of malfunctions or to treat them as being a healthy operational mode. While detection of novel faults is relatively easy to achieve, isolation and identification of them is extremely difficult to accomplish, especially because these faults cannot be modeled due their unknown nature.

- **Multiple Fault Identifiability:** This refers to the ability of a diagnostic system to identify and correctly classify multiple faults that may even coexist in a system. This is a rather difficult requirement mainly due to nonlinearities and coupling/interactions that generally exist between the states and the potential fault sources of a dynamical system. Another reason is that some faults in an engineering system are extremely difficult to model because of their complexity.
- **Explanation Facility:** A diagnostic system should be able to explain where a fault originated and how it propagated in the system.
- **Adaptability:** The operating conditions of the system change due to disturbances and environmental changes. Furthermore, a system's components experience performance degradation over time. Hence, a fault diagnosis should intelligently adapt to these changes in order to maintain its diagnostic performance.
- **Reasonable storage and computational requirement:** Memory and computational requirements are the two fundamental characteristics of any algorithm intended for on-line, real-time implementation. Diagnostic algorithms, especially the ones intended for embedded on-board fault diagnosis, are by no

means an exception. Therefore, while designing a fault diagnosis system, it is necessary to keep in mind that the computational and memory requirements must always meet the specifications of the application, also including power consumption specifications. Moreover, depending on the application, a reasonable compromise between these two requirements should be made.

2.3 A Review of Analytical Redundancy-based FDI Approaches

In Chapter 1, the two fundamentally distinct approaches to the general problem of fault detection and isolation, namely the hardware redundancy-based and analytical redundancy-based approaches, were discussed and compared in details. Furthermore, a general overview of some of the analytical redundancy-based methods was provided. In this section, however, we formally investigate the analytical redundancy-based approaches and explore some of the well-known FDI techniques proposed in the literature within each approach.

The investigation of various analytical redundancy-based diagnostic approaches starts essentially with classifying them into different categories according to the form of system information (or process knowledge) utilized within each approach. In view of this, most of the existing FDI methodologies can essentially be divided into model-based and computational intelligence-based approaches. In the former, the mathematical model of the system is being used as an *a priori* source of information on the system being monitored. However, the latter approach utilizes either quantitative historical data of the system or qualitative information on the system in the form of *if-then* rules.

In this section, we investigate these two fundamentally and conceptually different approaches to FDI and some of the specific FDI methods developed within each approach will also be reviewed and analyzed.

2.3.1 Model-based Approaches to FDI

Model-based fault diagnosis approaches can, in general, be classified into two mathematically distinct categories with respect to the dynamical model and the on-line information/data that they use. These two category approaches include:

- **Discrete-event system (DES) based approaches:** These methods are pursued whenever the behaviour of the system being monitored can be modeled as a finite-state machine (FSM) (or described as a discrete-event system), and the system can be observed merely as a sequence of events. Techniques under this category solve the diagnostics task by comparing the observed event sequence with the discrete-event dynamics of the model. DES-based systems and diagnostic methods are not of interest in this thesis, however, a very good treatment of the subject can be found in [74] and [75].
- **Differential or difference equation model-based approaches:** These methods are used whenever the system being monitored can be represented by a mathematical model in form of a differential or difference equation and the system outputs can be measured numerically. Since these systems are under consideration in this thesis, the model-based portion of the proposed hybrid fault diagnosis method falls under this category. Hence, in the following we will focus on reviewing the literature along this line of research.

Before proceeding with the specific and focused literature review, it is worthwhile to mention that the above two groups of model-based diagnostic methods differ significantly in terms of their mathematical background and their associated diagnostic steps. This is due to fundamental differences between the properties of the systems that they monitor. For example, fault diagnosis approaches for continuous-variable systems are usually decomposed into two steps of residual generation and residual evaluation (see also Section 1.4), whereas in discrete-event systems these steps cannot be defined (because the notion of a difference between events is not defined [75]). Instead, DES-based diagnostic approaches check the consistency between the current system behaviour and the DES model in a different way [74].

A quick review of literature on fault diagnosis reveals that the three tasks of fault detection, isolation and identification have not been equally investigated in the literature. This is partly due to the different levels of complexity involved in each task. In general, fault isolation and especially fault identification are more complicated than fault detection. Therefore, we need to separately review the literature corresponding to each task.

2.3.1.1 Model-based Fault Detection

Fault detection is essentially the first step of fault diagnosis. It basically detects the presence of faults, and the detection of incipient faults (or early detection of faults) is extremely important for the safety of the system as well as efficient implementation of a CBM system. As was mentioned in Chapter 1, model-based fault detection is based on residual generation, where the residuals are quantities that represent the inconsistency between the actual system behaviour and the mathematical model of the system.

Many residual generation methods have been proposed by various researchers in the field, some of which were reviewed in Section 1.4. Among them, nonlinear observer-based residual generation has been the most extensively studied. Observers are dynamical systems that estimate the states and consequently the outputs of a process. An observer-based residual is simply the output estimation error itself or a combination of the output estimation errors. Various nonlinear observer design techniques have been used for observer-based residual generation, since there does not exist a universal, optimal nonlinear observer for *all* nonlinear systems. The existing nonlinear observers have to be designed usually under certain assumptions on system structure, system inputs, and/or the degree of the system nonlinearity.

In a deterministic framework, Frank *et al.* [44] provide a survey of the use of nonlinear observers for fault detection and isolation. More specifically, Hammouri *et al.* [43], [46] discuss the use of high-gain observers for fault detection of control affine nonlinear systems. Besancon and Hammouri [76] studied the observer design problem utilizing the solution of Riccati equation for Lipschitz nonlinear systems. Seliger and Frank [77] proposed nonlinear unknown input observers (UIO) as an extension of the linear UIO to a class of nonlinear systems. Ding and Frank [78], and Yang and Saif [79] proposed the use of adaptive nonlinear observers for fault detection. Sreedhar *et al.* [80] designed fault detection for nonlinear systems based on sliding mode observer.

In a stochastic setting to observer-based fault detection, Alessandri *et al.* [81] used extended Kalman filter (EKF) for detection of actuator faults in unmanned underwater vehicles. Caliskan and Hajiyev [82] developed an EKF-based fault detection algorithm for surface faults in aircraft. Okatan *et al.* [83] developed a fault detection algorithm for

magnetometers and sun sensors of the attitude determination and control system of Low Earth Orbit (LEO) satellites using an approach for checking the statistical characteristics of EKF innovation sequence. Tudoroiu *et al.* [84] used unscented Kalman filter (UKF) for fault detection in actuators of satellite attitude control system (ACS). Finally, Li and Kadiramanathan [85] developed a likelihood ratio approach based on particle filters [49] for fault diagnosis in nonlinear stochastic systems.

The second classical method to residual generation for fault detection is the parity space approach, which relies on analytical redundancy relations (ARR) that link a subset of selected variables of the system under consideration. The ARR relations can be automatically obtained from the model equations using various elimination algorithms [58]. The ARR relations can be separated into two parts. The first part depends only on known (measured) variables, while the second one, namely evaluation part, depends on the fault components. Parity residuals are generated by computing on-line the known part of these relations. The residual value can be interpreted by the evaluation part of the ARR [58]. Christophe *et al.* [58], [59] have proven that for a class of nonlinear multi input single output (MISO) systems a relationship exists between parity residuals and residuals generated by high-gain observers. The major drawback of the parity space approach, however, is that the residuals are computed using time derivatives of measured variables, which makes the approach very sensitive to measurement noise and system disturbances. Thus, to make it useful in a noisy environment, extra filtering and pre-processing are required. A good survey on the applications of parity space approach to nonlinear system fault detection was provided in Section 1.4.

2.3.1.2 Model-based Fault Isolation

Once a fault is detected in a system, it should be followed by fault isolation which will distinguish (or isolate) a particular fault from others or locate the faulty component within the system. While a single residual signal is sufficient for fault detection, fault isolation requires usually a set of residuals (or a residual vector). If a residual vector can isolate *all* faults, it has the required fault isolability property.

Basically, there are two fundamental frameworks to create a residual set to enable fault isolation, including *structured residual set* and *directional residual set*. Almost all model-based fault isolation methodologies can be classified to belong to either of these two frameworks. In the following, we will individually review the overall concept of each framework and some of the well-known model-based fault isolation techniques associated to each framework will be discussed.

(A) Structured Residual Set: One approach to fulfill the fault isolation task is to design a set of structured residuals, where each residual is designed to be sensitive to a subset of faults, whilst remaining insensitive to the remaining faults. The design procedure consists of two steps; the first step is to specify the sensitivity and insensitivity relationships between residuals and faults according to the assigned isolation task, and second is to design a set of residual generators according to the desired sensitivity and insensitivity relationships [24].

The structured residuals can be designed in two conceptually different ways, namely *dedicated residual set* and *generalized residual set*. These two schemes are shown in Figure 2-4 for an example of isolating three different faults $\{f_1, f_2, f_3\}$.

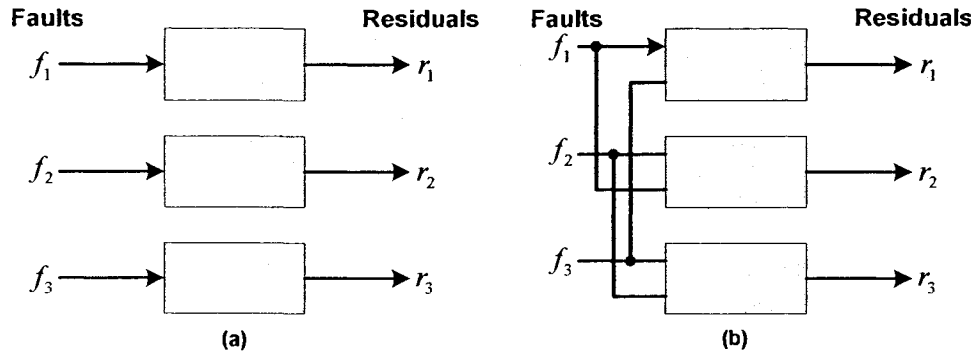


Figure 2-4. Two schemes of structured residual set: (a) dedicated scheme and (b) generalized scheme for an example of isolating three faults [24].

A-1) Dedicated Scheme of the Structured Residual Set: In the dedicated scheme, the following simple threshold logic [24] can be used to make decision about the appearance of a specific fault:

$$r_i(t) > T_i \Rightarrow f_i(t) \neq 0; \quad i \in \{1, 2, \dots, L\} \quad (2-7)$$

where L is the total number of faults (f_i) to be isolated, and T_i ($i = 1, 2, \dots, L$) are thresholds corresponding to residuals r_i ($i = 1, 2, \dots, L$). The dedicated residual set is very simple and all faults can be detected simultaneously, however, there is normally no design freedom left to achieve other desirable attributes of a fault diagnosis system such as robustness to various sources of uncertainties (i.e., measurement noise, system disturbances, and modeling errors). As will be seen in Chapter 3 and demonstrated in Chapter 5, some of the characteristics of the *series-parallel* FDI scheme proposed in this thesis are similar to that of the dedicated scheme. In particular, a portion of the fault isolation decision logic of the series-parallel scheme is analogous to that of the dedicated scheme. Furthermore, both methods are equally *sensitive* (or *non-robust*) to measurement noise.

Various fault isolation techniques have been developed in the literature under the dedicated scheme. Clark [86], in his pioneering work, designed a *dedicated observer scheme* (DOS) for sensor fault detection, which was actually (and surprisingly) the original inspiration for the concept of dedicated residual set (or dedicated scheme). In DOS an observer reconstructs all of the system outputs except one (i.e., $y_j(t), j = 1, \dots, m, j \neq i$) using all of the system inputs and the only left-out output, namely y_i . Then, the difference between the estimate and the measurement indicates the possibility of a fault in the i^{th} sensor. If this technique is applied for all m outputs of the system, namely $y_i, i = 1, \dots, m$, then a bank of m dedicated observers are needed to monitor m sensors of the system. Chen and Saif [87] recently extended Clark's DOS to actuator fault isolation. Their scheme is able to detect and isolate multiple actuator faults using a bank of r observers, where r is the total number of the actuators in the system under consideration.

Another very important group of fault isolation methods that essentially fall under the dedicated scheme are the multiple model (MM) approaches. Over the past few decades the use of multiple models has become very popular and widely applied across various domains of research including estimation, control, target tracking, and fault diagnosis of stochastic systems. In the literature, there are mainly two types of MM algorithms, namely non-interacting MM and interacting MM (IMM). Non-interacting MM approach was originally proposed by Magill [87] for optimal adaptive estimation of sampled linear stochastic processes. As mentioned therein, the MM estimator is composed of a set of elemental estimators and a corresponding set of weighting coefficients. However, the model-based elemental filters independently operate in parallel at all times without any

interaction between them. Such an approach is not suitable for fault diagnosis problem since it assumes that there are no mutual interactions among the multiple models, whereas in general, the system structure or parameters do indeed change as a system component (as well as a sensor or an actuator) fails. Nonetheless, the MM approach has also been developed for fault diagnosis in different engineering applications but mainly for the purpose of detection rather than isolation. For example, see Laparo *et al.* [88] on leak detection in heat exchanger systems, and Manke and Maybeck [89] on sensor/actuator failure detection in the Vista F-16 fighter aircraft. Furthermore, Alessandri *et al.* [81] used a bank of non-interacting extended Kalman filters (EKF) for isolation of faults in actuators of unmanned underwater vehicles.

The interacting multiple-model (IMM) approach, initially proposed by Blom and Bar-Shalom [90] for state estimation of stochastic systems, presented a notable advance to MM-based estimation (also see the book by Bar-Shalom *et al.* [91] for more details on IMM and its application to tracking and navigation). The IMM approach uses modal probabilities to weight the inputs and outputs of a bank of parallel filters at each instant of time. Furthermore, the IMM approach overcomes the weakness of the non-interacting MM approach by explicitly modeling the abrupt changes of the system by “switching” from one model to another in a probabilistic manner. This approach is one of the most cost-effective adaptive estimation techniques for systems involving structural as well as parametric changes [67].

Faults/failures usually create structural and parametric changes in the system. Since the IMM approach explicitly models and effectively handles the structural and/or parametric changes in the system, it presents a very promising and effective candidate

approach for fault detection and isolation. Mehra *et al.* [92], and Zhang and Xiao [93] independently and almost simultaneously proposed IMM approach for fault detection and diagnosis for the first time. The IMM-based nonlinear fault diagnosis assumes that the system being monitored can be modeled, at any time, sufficiently accurately by the following jump Markov hybrid nonlinear system [67]:

$$\begin{aligned} x(k+1) &= f(k, m(k+1), x(k), u(k)) + T(k, m(k+1)), w(k, m(k+1)) \\ z(k) &= g(k, m(k), x(k), u(k)) + v(k, m(k)) \end{aligned} \quad (2-8)$$

with $x_0 \sim N(\hat{x}_0, P_0)$; where the mode of the system at time k is selected by a discrete process $m(k)$ that is modeled as a discrete-time, L -state, first-order Markov chain with transition probabilities $\pi_{ij}(k)$ given by:

$$\pi_{ij}(k) = P\{m_j(k+1) | m_i(k)\}, \forall m_i, m_j \in S \quad (2-9)$$

where $\pi_{ij}(k)$ is the probability of the transition from mode i at time-step k to mode j at time-step $k+1$, and

$$0 \leq \pi_{ij}(k) \leq 1, \quad i=1, \dots, N; \quad j=1, \dots, N; \quad \sum_j \pi_{ij}(k) = 1, \quad i=1, \dots, N \quad (2-10)$$

where $S = \{m_1, m_2, \dots, m_L\}$ is the set of all possible modes of the system including healthy and various faulty modes, and L is the total number of modes in S .

In IMM-based fault diagnosis, one mathematical model has to be designed per each mode in the set S . This is the so-called “model set design” step of the IMM approach. This is the initial and a key step in IMM approach because the model set has to be designed such that it represents as many system modes as possible. Therefore, the design of a proper model set requires *a priori* knowledge of the potential system faults/failures.

Once a model set is designed, a model-based recursive filter has to be designed based on each model in the IMM model set in order to estimate system states. Various stochastic filtering techniques can be used for this purpose. The filter that has been commonly used for nonlinear systems is the extended Kalman filter (EKF) (see, for instance, Zhang and Xiao [67], and Tuduroiu and Khorasani [94]). More recently, Tuduroiu *et al.* [84] developed an interactive bank of unscented Kalman filters for fault detection and isolation in actuators of satellite attitude control system.

Each filter in the IMM bank recursively calculates a model-conditional estimate of the system states and then these estimates are combined to obtain an overall estimate, also called *mixed* estimate, of system states. The mixed estimates are calculated using the so-called model (or mode) probabilities. It should be noted that the model probabilities are different from transition probabilities introduced above. The transition probabilities comprise a matrix that is a parameter of the IMM algorithm and is usually set to a fixed value; however, the model probabilities comprise a vector $(\mu_i, i = 1, 2, \dots, N$ in Figure 2-5) that is essentially part of the state vector of the IMM algorithm and is recursively updated at each time-step of the algorithm operation. The model probabilities at each instant of time represent the probability of each mode currently in effect. Therefore, the largest model probability indicates clearly the mode in effect at that instant, hence fault is isolated. Furthermore, the value of the largest model probability provides a quantitative measure of the *confidence* level of IMM-based diagnoser in its decision, which is almost an exclusive property of IMM-based fault diagnosis. This can definitely be considered as an advantage IMM, since the confidence information can be very effectively used for information fusion in fault diagnosis systems comprising of more than one diagnoser (or

decision-makers). Figure 2-5 depicts the block diagram representation of the IMM-based fault diagnosis algorithm.

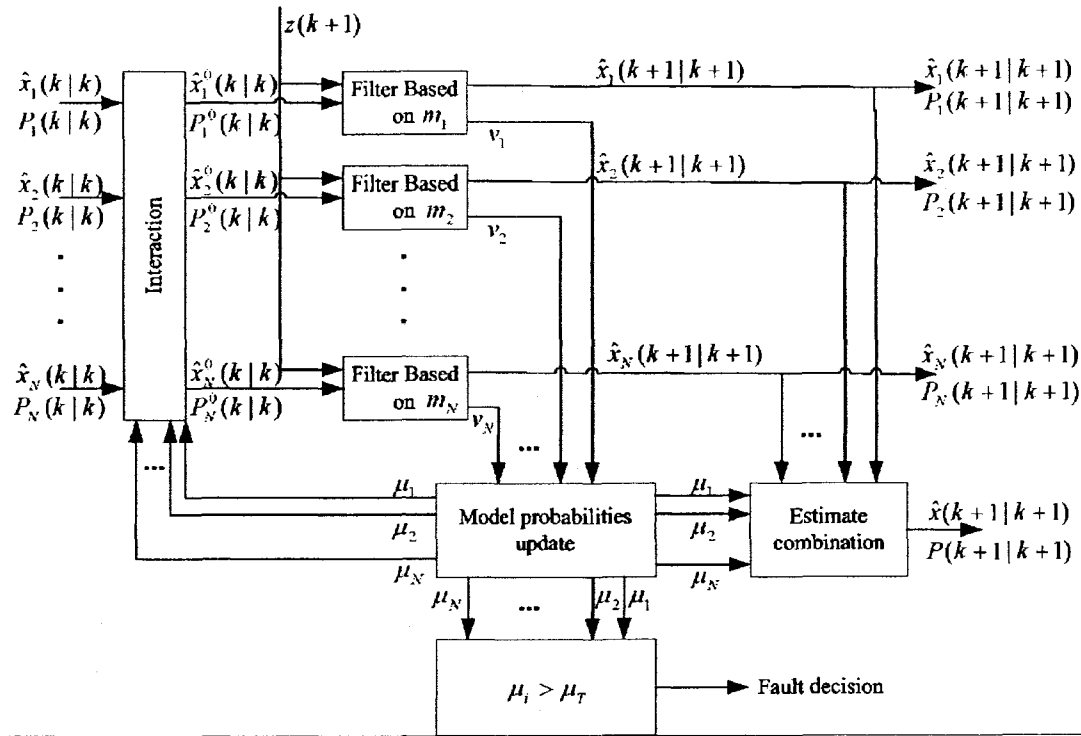


Figure 2-5. Block diagram of IMM-based FDI approach [93]

A-2) Generalized Scheme of the Structured Residual Set: The generalized scheme for designing the structured residual consists of making each residual sensitive to all but one faults, i.e. [24],

$$\begin{cases}
 r_1(t) = R(f_2(t), \dots, f_L(t)) \\
 \vdots \\
 r_i(t) = R(f_1(t), \dots, f_{i-1}(t), f_{i+1}(t), \dots, f_L(t)) \\
 \vdots \\
 r_L(t) = R(f_1(t), \dots, f_{L-1}(t))
 \end{cases} \quad (2-11)$$

The above set of residuals is defined as *generalized residual set*. If a bank of observers are used for generation of all residuals in the generalized residual set (i.e., a bank of observer-based residual generators), the structure is known as the *generalized observer scheme* (GOS) (see survey paper of Frank [95], and Lunze and Schroder [75] for application of GOS to sensor and actuator fault diagnosis of discrete-event systems). The isolation in generalized scheme can be performed by using the following logic [24]:

$$\left. \begin{aligned} r_i(t) &\leq T_i \\ r_j(t) &> T_i \quad \forall j \in \{1, \dots, i-1, i+1, \dots, L\} \end{aligned} \right\} \Rightarrow f_i(t) \neq 0 \quad (2-12)$$

for $i=1,2,\dots,L$.

The GOS-based FDI, depicted in Figure 2-6 for both sensor and actuator fault detection and isolation, is more robust than DOS with respect to parameter uncertainties and measurements noise. This is mainly due to the fact that in GOS, more than one output y_i is fed into the observers [95], as can also be seen in Figure 2-6.

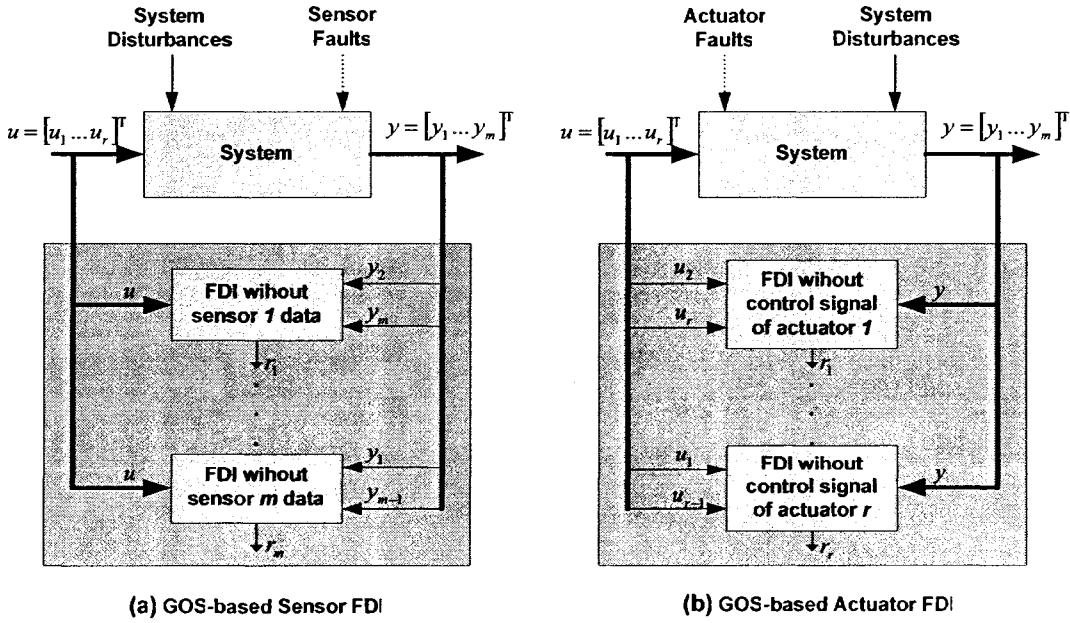


Figure 2-6. Generalized Observer Scheme (GOS) for (a) Sensor and (b) Actuator FDI

It will be seen in Chapter 3 and shown in Chapter 5 that the *robust parallel* scheme of the hybrid nonlinear FDI approach proposed in this thesis exhibits properties similar to the generalized scheme. More precisely, we will see that the fault isolation decision logic of the proposed parallel scheme is very similar to that of the generalized scheme, and it is extremely robust to measurement noise.

(B) Directional Residual Set: An alternative approach to fault isolation is to address the residual set generation problem within a geometric framework. More precisely, we have to define a *residual space* as the space spanned by the residual vector and then achieve fault isolation through designing a *directional* residual vector, also called *detection filters* (see Beard [96] and Jones [97]). A *directional* residual set is a vector that lies in a fixed and fault-specific direction (or subspace) in the residual space, in response to that particular fault [24]. In mathematical notation, we want to have:

$$r(t|f_i(t)) = \beta_i(t)\bar{l}_i; \quad i = 1, 2, \dots, L \quad (2-12)$$

where the constant vector \bar{l}_i is the *signature direction* of the i^{th} fault in the residual space and β_i is a scalar that depends on the fault size and dynamics [24]. A fault is then isolated by determining the fault signature direction that is the closest to the generated residual vector. Therefore, in order to isolate faults reliably (i.e., to reduce both incorrect isolation rate) there must be a one-to-one correspondence between fault signatures and potential fault sources (i.e., each fault signature must be uniquely associated with one fault).

Although directional residual set is simpler to implement (not necessarily to design, which is more problem dependent) than the structured residual set, and it also provides more reliable fault isolation capability under ideal conditions, it is really difficult to make

it robust against various sources of uncertainties, especially modeling errors and system disturbances.

A number of fault isolation methods have been proposed in the literature within the model-based directional residual generation framework. *Fault detection filters* proposed by Beard [96] and Jones [97] (also known as Beard-Jones fault detection filter) is one of the pioneering methods that has actually inspired the *directional* residual concept. Being originally designed for FDI of linear systems, fault detection filter is a Luenberger observer-based method, where the observer gain is chosen so that the direction of the residual vector in the output residual space can be used to identify the failed component. Note that in the Beard-Jones detection filter design faults are viewed as inputs and the residuals are viewed as outputs.

The Beard-Jones *detection filter*, developed following the *directional residual set* concept, has also inspired the celebrated *geometric approach* to fault isolation which indeed falls indeed under the *dedicated residual set* category. Massoumnia [98] first proposed a geometric formulation of the Beard-Jones fault detection filter problem for linear systems using the concept of *unobservability subspaces*, which is a subspace in the residual space that can be made “unobservable” via “output-reduction” and “output-injection” leading to a *quotient* (observable) subsystem unaffected by all faults except one. This approach is known in the literature as the geometric approach to FDI. Later, Massoumnia *et al.* [99] proved that a basic *necessary and sufficient* condition for the fault isolation problem to be solvable is the existence of an unobservability subspace. The unobservability subspace can be determined by means of simple recursive algorithm.

Massoumnia *et al.* [99] also showed that the geometric approach to FDI is the dual version of the problem of non-interacting control by means of dynamic feedback.

De Persis and Isidori [100] extended Massoumnia's geometric approach to nonlinear systems by proposing a *differential-geometric* approach that gives the necessary and sufficient conditions for solving the problem of nonlinear FDI. Detailed description of their approach requires many background mathematical definitions and concepts, which is out of the scope of this thesis but the interested reader can refer to [100] for the details and further information. The background mathematical concepts and definitions can also be found in Isidori's book [101]. However, to put it in a nutshell, in nonlinear geometric approach an *unobservability distribution* is computed by means of suitable algorithms, which results in a coordinate transformation in the state and the output space of the system that induces an "observable" *quotient* subsystem unaffected by all faults but one. Then, a fault detection filter (i.e., a nonlinear observer) is designed for the quotient subsystem.

In mathematical notations, in the nonlinear geometric approach it is assumed that the nonlinear system can be described by the following model:

$$\begin{aligned} \dot{x} &= f(x) + \sum_{i=1}^r g_i(x)u_i + \sum_{i=1}^L l_i(x)m_i + \Gamma(x)w \\ y &= h(x) \end{aligned} \quad (2-13)$$

where $u_i, i = 1, \dots, r$; $m_i, i = 1, \dots, L$; and w denote the input channels for control purposes, the fault/malfunction signals whose occurrence has to be detected and isolated, and system disturbance signals, respectively. The objective is then to find for each fault signal $m_i, i = 1, \dots, L$, a *quotient* subsystem that is affected by the fault signal m_i and decoupled from other faults $m_j, j = 1, \dots, L; j \neq i$ (and, if possible, decoupled from

disturbance w to also achieve robustness with respect to disturbance). The algorithm that verifies the existence of such a *quotient* subsystem is a constructive algorithm that provides the state coordinate transformation $z = \Phi(x)$ required for fault isolation. Once the coordinate transformation function $\Phi(\cdot)$ is found and applied to the system's state space equations, the new state space representation of the system in terms of the transformed coordinate z is obtained. Then, a nonlinear observer is designed for estimating z , with the residual defined as $r = z - \hat{z}$, where \hat{z} is the estimate from the observer.

The main power of the nonlinear geometric approach is in providing necessary and sufficient conditions for the solution of fault isolation problem, supported by unprecedented rigorous mathematical proofs. Furthermore, under full-state measurement conditions (i.e., the function $h(\cdot)$ in equation (2-13) is simply a unity matrix), finding the coordinate transformation $\Phi(\cdot)$ is fairly simple (though, this is not always the case under partial state measurement). However, it also possesses some drawbacks. A major drawback is lack of robustness to modeling errors. Since the transformation $\Phi(\cdot)$ is obtained based on system's nominal equations, any discrepancies between the actual system and its nominal model of the system (due to unmodeled dynamics, parameter uncertainties, parameter variations, etc.) may render the analytical results invalid. To a lesser extent, the measurement noises will also affect the performance of the geometric approach. As far as robustness to system disturbances are concerned, sometimes little design freedom is left to decouple residuals from disturbances.

2.3.1.3 Model-based Fault Identification

Despite its undeniable importance, model-based fault identification has received less attention from the research community as compared to model-based FDI. This is especially true for nonlinear systems. Nonetheless, possibly the first formal effort to estimate the severity of faults is in the seminal works of Isermann [60], [26]. In his work it is assumed that faults are reflected in the physical parameters of the system, hence, faults can be identified through on-line estimation of system parameters. However, the parameter estimation approach of Isermann was developed for linear systems due to availability of very well-known linear parameter estimation methods. More recently, Tan and Edwards [102] applied the concept of “equivalent output estimation error injection” - proposed by Edwards [45] - to reconstruct faults for linear systems using sliding mode observers. Once again, however, their approach was developed for linear systems.

Chen and Saif [87] recently extended the approach proposed by Tan and Edwards [102] to actuator fault identification in a class of nonlinear systems. More specifically, they modified the approach proposed Tan and Edwards [102] in two ways. First, instead of linear systems they consider a specific class of uncertain nonlinear systems. Second, instead of reconstructing only faults, they reconstruct the inputs and the faults at the same time. They estimate actuator faults using equivalent control method in sliding mode observer design. Nevertheless, their approach also has two limitations. First, it has been developed specifically for actuators faults and its application to identification of component faults in a nonlinear system has not been discussed. Second, it is applicable only to a specific class of nonlinear systems rather than a general one.

One may also use multiple model (MM) approach for fault identification, where multiple models in the model bank correspond to different levels of fault severity. However, this will introduce an inevitable quantization error in fault estimation. This quantization error can be reduced as more models are used in the bank. But the use of more models will increase the computational requirements of the algorithm. In order to very precisely identify faults, *ideally* infinite number of models (or quantization levels) should coexist in the model bank, which makes the approach computationally unfeasible and thus impractical. The IMM approach, to a lesser extent, has a similar problem, though Zhang and Xiao [93] suggest that in the IMM approach, the magnitude (size) of a fault can be determined by the probabilistically weighted sum of the fault magnitudes of the corresponding partial fault models. However, this idea has not been well elaborated and, as was mentioned previously, the fine-tuning of the IMM approach is not easy to accomplish especially if precise fault identification is required. Zhang and Jiang [173] have also developed a two-stage adaptive Kalman filter (or a *dual* Kalman filter) for simultaneous (or *joint*) state and fault parameter estimation, which is applicable to identification of *only* actuator (not component) faults.

2.3.2 Computational Intelligence-based Approaches to FDI

The model-based approaches to fault diagnosis rely on the analytic mathematical model of the process being monitored. This implies that the accuracy of the model has direct impact on diagnostic system performance and reliability. More precisely, the more accurate the model, the more reliable will be the model-based fault diagnosis scheme. However, for complex and uncertain systems, the derivation of high-fidelity mathematical models from physical principles can become very complicated, time

consuming, and even sometimes unfeasible (for instance, some systems cannot be represented accurately enough by a lumped parameter system). Moreover, even with the possibility of deriving a mathematical model using first principles, obtaining accurate model parameter values may become a very tedious job or even practically impossible due to proprietary issues regularly imposed by OEMs and/or system integrators. Last but not the least, some systems exhibit uncertain behaviors such as higher order dynamics and high-frequency oscillations, collectively called unmodeled dynamics, which cannot be precisely modeled.

Mathematical methods in computational intelligence and learning theory – neural networks, fuzzy logic, neuro-fuzzy systems, and genetic algorithms – represent a promising way of circumventing the above-mentioned modeling precision problems in model-based fault diagnosis. Indeed, during the past decade computational intelligence (CI)-based fault diagnosis methods have been extensively developed and successfully applied to various engineering systems. A number of survey papers and books in the literature review the use of computational intelligence techniques in fault diagnosis. Among the pioneers is the survey paper of Patton *et al.* [27] that outlines some of the residual generation methods based upon artificial intelligence techniques, which integrate both quantitative and qualitative knowledge of the system in fault diagnosis. More recently, Palade *et al.* [103] published a book consisting of a set of papers reviewing the main computational intelligence techniques and their applications to fault diagnosis. They have also discussed the main advantages and disadvantages of each methodology and it is shown that many times hybrids of CI-based diagnostic techniques are used in practice to utilize their advantages and overcome their disadvantages. Two other recent books,

namely Korbics *et al.* [63] and Vashtsevanos *et al.* [3] also review intelligent fault diagnosis methods.

Using CI-based techniques enables one to exploit both quantitative (numerical) and qualitative (symbolic) information about the system being monitored. Qualitative information is normally expressed in the form of Boolean or fuzzy “*if-then*” rules. For systems represented by Boolean rules, causal reasoning and fault tree analysis methods have been historically used especially in aerospace and nuclear industries (see Zampino [104] and the pioneering work of Crosetti [105], respectively). On the other hand, fuzzy logic is the right tool for fault diagnosis whenever the system behaviour is described by a set of fuzzy “*if-then*” relations derived either by an expert or using qualitative physics. More details regarding the use of fuzzy models for fault diagnosis can be found in Dexter [106] and Mendonca *et al.* [107]. The key advantage of the qualitative CI-based approaches is that they can provide valuable information for the system operators to identify the root cause of anomalies (i.e., the series of events/anomalies that ended up to a failure).

Though seemingly attractive, qualitative CI-based fault diagnosis methods also suffer from a major drawback. In many engineering applications, deriving Boolean and/or fuzzy “*if-then*” rules is by no means straightforward and requires extensive expert knowledge of the system. Instead, the knowledge that describes the system behaviour is contained in large quantitative datasets stored in data bases. Neural networks are ideal mathematical tools for such situations due to their universal nonlinear function approximation property (Cybenko theorem; see Cybenko [108]), and their ability to learn and reproduce system behaviour from quantitative system datasets (i.e., historical system input-output data).

Neural networks do indeed provide an excellent framework for identification of nonlinear systems (see the seminal work of Narendra and Parthasarathy [65]).

All these properties make neural networks a promising tool for applications as diverse as feature extraction, pattern recognition, clustering, classification, information integration, and as mentioned above in system identification, which all can effectively be applied for fault diagnosis and health monitoring. As a result, neural networks have been applied to fault diagnosis in different ways. In the following, we will review three of the most commonly used neural network (NN)-based approaches to fault diagnosis.

I) Neural Network-based Pattern Recognition Approach to Fault Diagnosis: In pattern recognition approaches, neural networks are used mainly for feature classification. In other words, the neural network is only used as a *fault classifier*. For example, in Li *et al.* [109] the bearing vibration frequency features and time-domain characteristics are applied to a neural network to build an automatic motor bearing fault diagnosis machine. In these applications, neural networks are merely used to examine the possibility of a fault or abnormal features in system measurements and give a fault classification signal to declare the health state of the system. This approach of using only system output measurements produces valid fault diagnosis results mainly for static systems or steady-state processes. However, this is not usually the case for fault diagnosis of dynamic systems (especially nonlinear ones), where a change in system inputs can also affect certain features of system outputs. Therefore, the NN-based pattern recognition approach to fault diagnosis of nonlinear dynamic systems can generate incorrect fault information while only the system inputs have been changed. This problem has been resolved by the following second approach to NN-based fault diagnosis.

II) Neural Network-based Residual Generation Decision-Making Scheme: This NN-based diagnostic scheme was initially proposed by Patton *et al.* [110]. In this scheme, depicted in Figure 2-7, neural networks are utilized at two stages: *residual generation* and *decision-making* (for fault isolation). At residual generation stage, neural networks are used as prediction models. An important feature of a neural network-based prediction model is that it will automatically “learn” the nonlinear system dynamics during training process made over several training cycles, with training data coming from historical input-output data of the system. Neural network-based prediction models have potential advantages over traditional prediction and estimation methods, including powerful nonlinear mapping properties, noise tolerance, self-learning and self-adapting, and parallel processing capabilities.

Various NN-based nonlinear system identification architectures can be used as prediction model at residual generation stage. Three widely used architectures include nonlinear autoregressive exogenous (NARX) model neural networks, recurrent neural networks, and dynamic neural networks, as shown in Figure 2-7. These architectures differ in terms of the way dynamics has been introduced into the network architecture. In the following, we will briefly review the literature on NN-based identification of nonlinear dynamic systems.

A large body of literature has been dedicated to the identification of nonlinear dynamic systems using neural networks. These efforts are justified by the following four important features of neural networks, namely (i) their nonlinear characteristics that make them suitable for dealing with nonlinear systems, (ii) their parallel and pipeline processing characteristics that allow them to perform computations more efficiently, (iii)

their self-learning and self-adapting characteristics that are ideal for adapting to different environmental conditions, and (iv) their tolerance to noise.

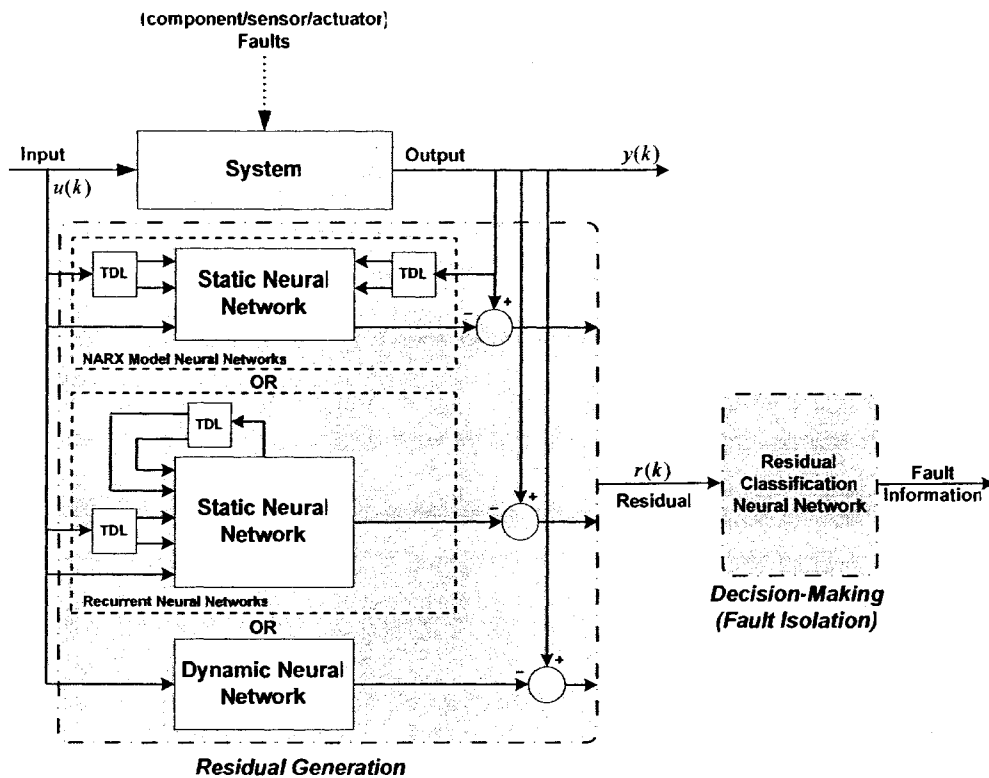


Figure 2-7. Two-stage scheme for neural network-based fault detection and isolation.

One may classify NN-based nonlinear dynamic system identification schemes into four main categories. The first category utilizes tapped delay lines (TDL) along with a static neural network in its structure. The TDLs are used to introduce dynamics into the network by generating delayed inputs and outputs of the system that are then fed to a static network as the regressor vector. The network then performs a static nonlinear map on this regressor vector so that the desired output is obtained. This model is called nonlinear autoregressive exogenous (NARX) model. For further details, refer to Narendra and Parthasarathy [65].

The second category is recurrent neural networks. In this approach, a dynamic input-output representation is constructed using a recurrent structure. This method has been investigated in Funahashi and Nakamura [111], and Ku and Lee [112]. More specifically, Funahashi and Nakamura [111] proved that the proposed recurrent neural network is capable of identifying any nonlinear dynamic system provided that the initial states of the network are chosen appropriately with respect to the initial conditions of the system.

The third category is embedded dynamic neural networks. The embedded dynamic neural networks are constructed by utilizing dynamic neurons whose model is different from that of static neurons. In the former, one or more dynamic elements are utilized to obtain a specific dynamical input-output map. Several dynamic neuron structures have been reported in the literature. Atiya and Parlos [113] introduced a spatio-temporal neuron in which the conventional weight multiplication operation was replaced by a linear filtering (an all zero filter) operation. Gamma neuron model was developed by Principe and Motter [114] for identification of nonlinear systems. The structure of the Gamma model is similar to the tapped delay line structure but instead of using simple shift elements in the line, a first order linear filter is utilized to generate a dynamic input-output map. Yazdizadeh and Khorasani [115] introduced an embedded dynamic neural network in which adaptive linear filters are augmented before the NN's hidden-layer activation functions in order to generate a dynamic input-output map. In this network, learning takes place by adapting both the embedded linear filter parameters and the neural network weights. The well-known time delay neural network (TDNN) was first introduced by Waibel *et al.* [116] for phoneme recognition. In TDNN, each weight is associated with a delay. The adaptive version of TDNN was introduced by Yazdizadeh

[117] for identifying two classes of nonlinear dynamic systems denoted as “the first” and “the fourth” class of nonlinear systems by Narendra and Parthasarathy [65].

The fourth category of dynamic neural identifiers, which is proposed by Abdollahi *et al.* [118], consists of a feed-forward static neural network architecture cascaded/ followed by a fixed stable linear filter. During the training/learning process, neural network weights comprise the only adaptive parameters of the proposed dynamic neural identifier and the parameters of the stable linear filter remain unchanged.

In the second stage of the NN-based fault diagnosis scheme, namely *decision-making* stage, a neural network-based classifier is used to partition the residual vector to patterns corresponding to different system healthy and faulty situations. The NN-based classifier is trained to recognize complex features in residuals and then generates fault detection and isolation information. The training can take place in both supervised and unsupervised modes; however, supervised classifiers are generally more accurate. Nonetheless, they have a major disadvantage of requiring data from *all* possible fault situations for classifier training. A supervised NN-based classifier trained using only fault-free situations cannot be expected to perform well for faulty situations.

III) Neural Network-based Multiple-Model Residual Generation and Classification:

This NN-based fault diagnosis scheme, originally proposed by Patton *et al.* [27], follows the idea of multiple model-based FDI scheme described in Section 2.3.1.2, where the mathematical models have been replaced by parallel NN-based dynamic identifiers. This scheme, depicted in Figure 2-8, also consists of two stages: *NN-based multiple-model residual generation* and *isolation decision-making*. In the former stage, each fault model in the residual generation block is a *dynamic neural network* that identifies a class of

system behavior. The dynamic neural identifiers that were discussed in the previous NN-based fault diagnosis scheme are equivalently applicable to in here. The major difference is that, as opposed to residual generation decision-making scheme, the NN-based multiple-model scheme requires data from all healthy and faulty situations at *residual generation* stage in order to be able to learn all classes of system behaviour. This can be considered as one of the main drawbacks of the NN-based multiple-model approach.

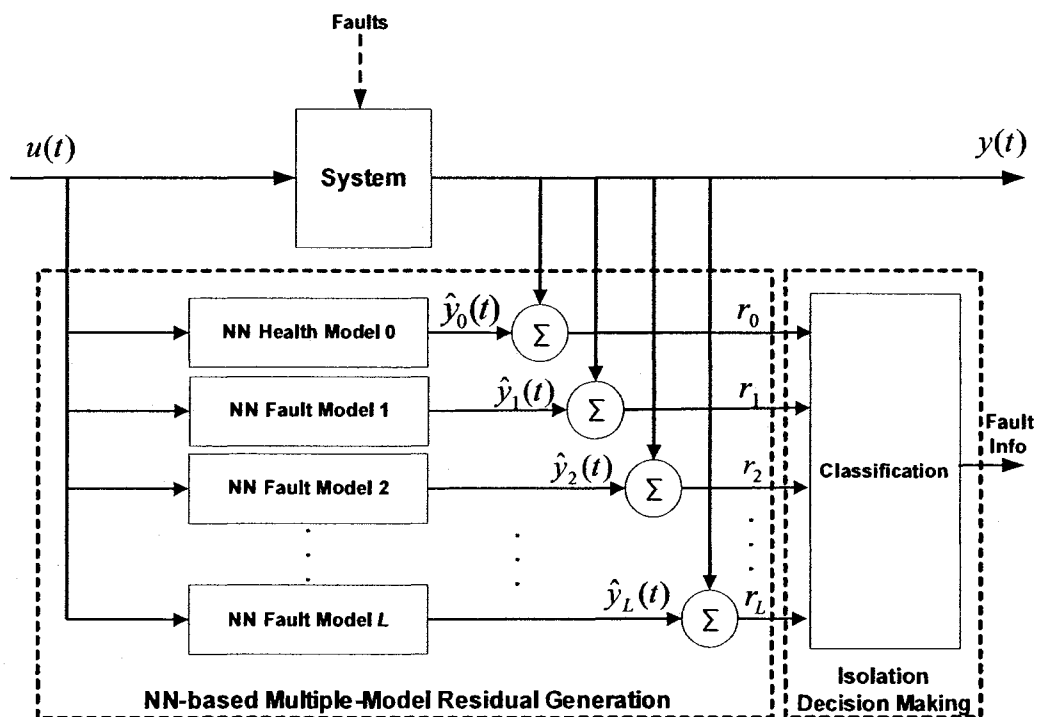


Figure 2-8. A generic neural network-based multiple-model fault detection and isolation scheme.

In the isolation decision making stage, the main task is to classify the generated residuals into a number of distinguishable patterns corresponding to different healthy as well as faulty situations. Thus, another neural network is used for this purpose based on the *classification* capability of neural networks. Once again, various NN-based classifier architectures and algorithms can be utilized at this stage. These include multi-layer

perceptron (MLP) network, radial basis function (RBF) network, support vector machines (SVM), probabilistic neural networks (PNN), and fuzzy neural networks for supervised classification; and competitive neural networks (e.g., Kohonen network, self-organizing maps (SOM)), and adaptive resonance theory (ART) networks (i.e., ART-II, fuzzy-ART) for unsupervised classification.

The above-mentioned CI-based diagnostic methods use either qualitative or quantitative information about a system in order to achieve fault diagnosis. Both methodologies have been successfully applied to fault diagnosis of various engineering systems; however, integrating both quantitative and qualitative information can greatly enhance the diagnostic system performance and robustness. Such diagnostic systems are collectively called *integrated computational intelligence*-based fault diagnosis systems. There are basically two main ideas within the integrated CI-based framework. One is to generate residuals using NN-based methods and then allocate the decision-making (or isolation decision-making) process to a fuzzy-logic inference engine. This approach allows system operators to describe the system behaviour or the fault-symptom relationship with simple *if-then* rules.

The second integrated CI-based diagnostic concept, depicted in Figure 2-9 from Chen and Patton [24], revolves around using neural networks for two main purposes: (i) residual generation using *quantitative* historical input-output data of the system, and (ii) learning (or determining) from quantitative information of the system the parameters of the fuzzy model of the system (i.e., the fuzzy "*if-then*" rules *qualitatively* describing the system behaviour). This integration of quantitative and qualitative knowledge of the system is accomplished through a neuro-fuzzy system (or a fuzzy neural network) that

makes it feasible to combine the learning ability of neural networks with the explicit knowledge representation of fuzzy logic. According to Patton *et al.* [27], a potential way of implementing a neuro-fuzzy system is to use B-Spline neural networks. For further information on neurofuzzy modeling, refer to Brown and Harris [119].

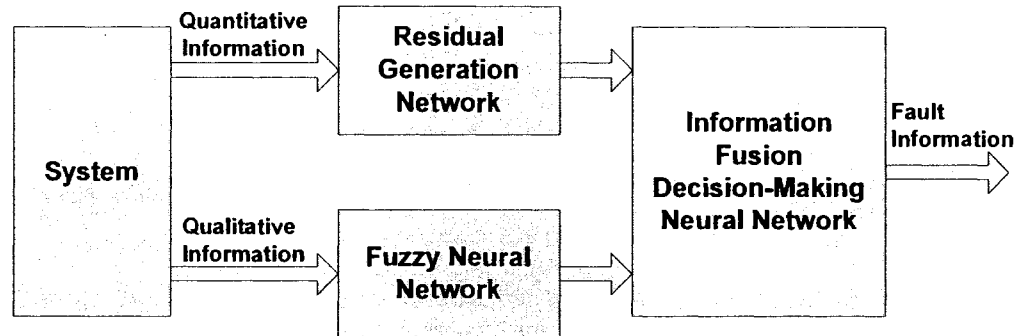


Figure 2-9. A conceptual structure of the integrated CI-based fault diagnosis [24].

Moreover, a trained neural network can be used to evaluate the reliability of information provided by either quantitative or qualitative methods and decide which has to be accordingly weighted in the information fusion, as depicted in Figure 2-9.

2.4 Methodology Developed in This Thesis: Hybrid Approach to FDII

The approach proposed in this thesis is essentially a hybrid approach to fault diagnosis. More precisely, the proposed fault diagnosis methodology simultaneously exploits both the *a priori* mathematical model information of the system and the nonlinear approximation and adaptation capability of neural networks. Specifically, mathematical model of the system is used as a basis for *fault modeling* and *isolation*, and the capability of neural networks in adaptive nonlinear function approximation is used as a basis for on-line *fault severity identification*.

Only a few fault diagnosis methodologies exist in the literature, which simultaneously take advantage of mathematical model of a system and exclusive capabilities of computational intelligence techniques, especially neural networks, in a hybrid framework. For example, Alessandri [69] proposed a hybrid approach to fault detection in nonlinear systems. In his work, fault detection and isolation is accomplished by means of a bank of estimators, which provide estimates of parameters that describe actuator, plant, and sensor faults. These estimators, also called finite-memory filters, perform according to a receding-horizon strategy and are designed using nominal *mathematical model* of the system and the models of the failures. The problem of designing such estimators for general nonlinear systems is solved by searching for optimal estimation functions. These functions are approximated by *feedforward neural networks* and the problem is reduced to finding the optimal neural weights, hence the name *finite-memory neural filters*. The learning process of the neural filters is split into two phases: an off-line initialization phase using any possible “*a priori*” knowledge on the statistics of the random variables affecting the system states, and an on-line training phase for on-line optimization of neural weights.

In another example of *hybrid* approach to diagnostics, Xiaodong *et al.* [120] presented a robust fault detection and isolation scheme for abrupt and incipient faults in nonlinear uncertain dynamic systems. The diagnostic architecture proposed therein consists of a bank of $N+1$ nonlinear adaptive estimators, where N is the number of potential faults that may affect the nonlinear system. One of the nonlinear adaptive estimators is the *fault detection and approximation estimator* (FDAE) used to detect faults. The remaining ones are *fault isolation estimators* (FIEs) that are used for isolation

purposes only after a fault has been detected. Under normal operating conditions (without faults), the FDAE is the only estimator monitoring the system. Once a fault is detected, the bank of FIEs is activated and the FDAE adopts the mode of approximating the fault function. The nominal *mathematical model* of the system is explicitly used for designing both FDAE and FIEs. Furthermore, a key component of FDAE is an *online approximator*, which, in presence of a fault, provides the adaptive structure for approximating online the *unknown* nonlinear fault function. This is where the extreme capability of neural networks in adaptively representing nonlinear multivariable functions is employed to implement the *online approximator* of FDAE.

Very recently, Talebi and Khorasani [121] presented a *hybrid* intelligent fault detection and isolation scheme for a general nonlinear system using a *neural network*-based observer. The proposed NN-based observer employs nominal *mathematical model* of the system in conjunction with two *recurrent neural networks*, which are used to identify general *unknown* actuator and sensor faults. The distinct advantage of their method is that, unlike many previous methods in the literature, it does not rely on the availability of full state measurements.

The above works, however, either have not addressed the important problem of fault severity estimation (or fault identification) or have addressed it in a way that is not of use to fault prognosis and consequently condition-based maintenance (CBM). More precisely, the approach proposed by Alessandri [69] is only a fault detection and isolation method, leaving fault identification problem unsolved. On the other hand, the approaches proposed by Xiaodong *et al.* [120], and Talebi and Khorasani [121] estimate/identify the *fault function* that represents the *overall* impact of faults on system states. Though

estimating this overall impact is often sufficient for fault accommodation (and thus achieving fault tolerant control) and is also useful for identifying actuator faults (especially, static actuators or actuators with negligible dynamics), it is not appropriate for fault prognosis and CBM of system components. The reason is that it is either impossible or extremely difficult to obtain fault trend information for a specific system component from the aforementioned fault function estimate.

The *hybrid* fault diagnosis approach presented in this thesis, however, is able to detect, isolate, and identify the severity of faults in components of a general nonlinear system within a unified, integrated framework. This is achieved through the use of a bank of parameterized fault models and a corresponding bank of adaptive neural parameter estimators (NPEs) to estimate fault parameter (FP) vector and thus fault severities. The nominal *mathematical model* of the system is used in both PFM bank and NPE design, and neural networks are used in NPE design; hence being a *hybrid* approach to fault diagnosis.

Finally, in order to achieve FDII under partial-state measurement, a separate nonlinear observer is designed to continuously estimate system's states from inputs and measurements even in presence of faults in system components. We call such an observer a *fault-tolerant observer* (FTO) or a *fault tolerant state estimator* (FTSE). To the best of our knowledge, the FTO *terminology* proposed in this thesis appears for the first time in the literature. A similar *concept* of fault tolerance in state estimation has been investigated in the literature under the *unknown input observer* (UIO) terminology. However, the UIOs have been developed and employed in the literature as a means to make fault diagnosis algorithms robust with respect to unknown uncertainties such as

modeling errors and *external disturbances*. In other words, instead of faults the modeling errors and external disturbances are modeled as unknown inputs and the UIOs are designed in order to decouple the state estimates from these uncertainties.

The FTSE method proposed in this thesis is a Kalman filter structure preserving neural state estimator (NSE). It is a *hybrid* approach to nonlinear filtering, since it utilizes both mathematical model of the system and the adaptive nonlinear function approximation capability of neural networks. Chapter 4 discusses, in details, the proposed NSE and its integration with the proposed FDII method in order to achieve fault diagnosis under partial state measurement.

2.5 Robustness of FDI to Uncertainties

Model-based fault diagnosis (FD) approaches rely on the key assumption that a perfectly accurate and complete mathematical model of the system under supervision is available. However, such assumption is usually not valid in practice since it is difficult to obtain the necessary modeling accuracy required for construction of reliable analytical redundancy-based FD architectures. Unavoidable modeling and environmental uncertainties that arise due to modeling errors, parameter variations, time variations, unknown external disturbances, and measurement noise deteriorate the performance of the FD schemes by causing false alarms. This performance deterioration can happen to an extent that makes the model-based FD scheme totally useless. This necessitates the development of FD algorithms, which have the ability to reliably detect, isolate, as well as identify faults and failures in presence various sources of uncertainties. Such algorithms are referred to as *robust fault diagnosis* algorithms.

To overcome the difficulties introduced by modeling and environmental uncertainties, a model-based FDI has to be made robust, i.e. insensitive to uncertainty [24]. However, sometimes, merely reducing the sensitivity to uncertainties does not solve the problem because such a sensitivity reduction may be undesirably accompanied by a reduction of sensitivity to faults. Thus, a more meaningful formulation of the robust FDI problem is to increase the robustness to various sources of uncertainty without losing sensitivity to faults. In other words, an FDI scheme designed to provide satisfactory sensitivity to faults, associated with the necessary robustness with respect to modeling and environmental uncertainties, is called a *robust FDI scheme*.

The importance of robustness in model-based FDI has been widely recognized by both academia and industry. More specifically, robust FDI for linear systems has been extensively investigated by many researchers during the last two to three decades. As a result, a number of methods have been proposed to tackle the linear robust FDI problem [24] such as the UIO method [122], eigen-structure assignment [123], and optimally robust parity relation methods [124].

Traditionally, the robust FDI problem for nonlinear dynamic systems has been approached in two steps. The model is first linearized around an operating point, and then robust linear FDI techniques are applied to generate residuals that are insensitive to uncertainties but responsive to faults. This method only works well when the linearization does not cause a large mismatch between linear and nonlinear models and the system operates close to the specified operating point. As another alternative to robust nonlinear FDI, one might think of just simply increasing the threshold levels of the residuals generated by the nonlinear FDI scheme and thus reducing the number of false

alarms. However, the increase in the threshold levels will at the same time decrease the fault sensitivity of the FDI scheme.

This imposes a tradeoff between reducing the number of false alarms and the number of missed alarms (i.e., missing to detect the presence of an actually occurred fault). A reliable solution to such a trade-off problem is not trivial in practice especially due to the nonlinear behavior of the system dynamics and the presence of different sources of unknown uncertainties. Therefore, there is a high demand for development of techniques that make the nonlinear FDII problem robust to modeling and environmental uncertainties to remarkably reduce the number of false alarms when the nonlinear system is under healthy mode of operation, whilst reliably diagnosing faults or failures.

However, the problem of robust FDII for nonlinear systems has not been investigated as extensively as its linear counterpart. In particular, very few works have been reported in the literature on robust fault isolation and severity identification - rather than just detection - for nonlinear systems. Some examples of robust fault detection and isolation (but not identification) techniques for uncertain nonlinear systems can be found in the works of Xiaodong et al. [120], Talebi and Khorasani [121], Chen and Saif [87], and Wu and Saif [125].

In this thesis, we address the robustness of FDII with respect to external disturbances and particularly measurement noise. Robustness of FDII to measurement noise is of utmost importance especially in applications with low SNR. Robustness in the analytical redundancy-based framework to FDII is, in general, achieved by either making the *residual generation* process or the *residual evaluation* process insensitive to uncertainties. In this thesis, we adopt the former approach by reconfiguring the

architecture of the proposed FDII scheme from *series-parallel* into *parallel*. The robustness of the *parallel* FDII scheme will be further explained in Chapter 3 and demonstrated in Chapter 5.

2.6 Conclusions

In this chapter, the problem of fault detection, isolation, and identification (FDII) in nonlinear systems was defined and formulated. Potential sources of faults in an open-loop system were also introduced including actuator, sensor, and component faults and some common types of faults in them were identified. Simple mathematical models of common types of sensor and actuator faults were also presented.

Based upon the formal definition of the FDII problem, various analytical redundancy-based fault diagnosis approaches and methodologies in the literature were reviewed. Based on the *a priori* source of information on the system being used for diagnostic purposes, these approaches were divided into two categories, namely model-based and computational intelligence (CI)-based. While the model-based approaches exploit the mathematical model of the system for FDII design, the CI-based approaches use quantitative data or qualitative information (i.e., *if-then*) or a combination of both.

The literature on model-based approaches to fault diagnosis was reviewed separately for the three tasks of detection, isolation and identification. The reason for this individual investigation was said to be the different levels of complexity associated with each task and the varying number of contributions that have been within each domain. Specifically, model-based fault isolation methods were very comprehensively reviewed and analyzed in terms of the concepts behind each method and some examples of FDI techniques developed based upon each concept were also mentioned and analyzed. Even though

being less investigated and researched, some recent efforts in model-based fault identification or severity estimation were also reviewed.

For the CI-based diagnostic approaches, the literature survey was not separated based on the specific task in the FDII problem, since such a distinction can hardly be made within the CI-based fault diagnosis domain. Instead, some extensively used concepts and schemes to achieve fault diagnosis without having a mathematical model of the system were introduced. More precisely, methods that use quantitative data of the system for residual generation based on the learning capability of neural networks were extensively reviewed. Diagnostic methodologies that use qualitative information of the system (mainly in the form of *if-then* rules) were also explored, which are mostly based on fuzzy logic theory. Furthermore, a general scheme for integrating both quantitative data and qualitative information of the system for fault diagnosis purposes was proposed. It was shown that this integrated scheme consists of various techniques from computational intelligence domain such as neural networks, fuzzy systems, and neuro-fuzzy systems.

Eventually, the proposed approach to fault diagnosis in this thesis was reviewed, which is essentially a *hybrid* approach to FDII. It is called *hybrid* in the sense that both *a priori* mathematical model information of the system and the adaptive nonlinear function approximation capability of neural networks are simultaneously used to accomplish FDII. It was mentioned that the *hybrid* approach to fault diagnosis is relatively new to the research community and actually few works have been reported in the literature following this approach (which were also reviewed in this chapter). However, it is certainly a very promising approach and sounds to be the inevitable choice of future in the fault diagnosis domain.

Chapter 3:

3 Proposed FDII for Nonlinear Systems with Full-State Measurement

In this thesis, a new integrated solution to the problem of FDII for nonlinear systems is proposed. The proposed fault diagnosis methodology benefits from both *a priori* mathematical model information of the system, and the nonlinear function approximation and adaptation capability of neural networks in a hybrid framework. More specifically, mathematical model of the system is used to construct a bank of parameterized fault models, which enables fault isolation.

As mentioned earlier in Chapter 2, the idea of using a bank of estimators/observers/models for fault detection and isolation has been previously pursued in the literature by many researchers (see, for example, Mehra *et al.* [92], Zhang and Xiao [93], Alessandri [69], Tudoroiu and Khorasani [94], and Tudoroiu *et al.* [84] in chronological order). However, they have neither addressed the problem of fault severity identification nor performed a comprehensive robustness analysis with respect to measurement noise, which considerably affects the performance of FDII algorithms in real-world applications.

Once a bank of PFMs is constructed, a corresponding bank of neural parameter estimators (NPE) is designed to estimate fault parameters (FPs) and thus accomplish fault

identification. Therefore, even in terms of methodology, the proposed *hybrid* fault diagnosis approach can be viewed as an *integration* of multiple-model (MM) method and parameter estimation method, two well-known fault diagnosis methods that were both extensively reviewed in Chapters 1 and 2.

Furthermore, two NPE structures, namely *series-parallel* and *parallel*, are proposed with their respective fault isolation policies, where each structure shows an exclusive set of desirable properties. For example, the proposed *parallel* scheme is extremely robust to measurement noise, hence making it suitable for low SNR applications. On the other hand, the *series-parallel* scheme displays very fast convergence rates desirable for systems requiring short delay in fault diagnosis. Thus, the choice of the appropriate FDI structure really depends on the specifications and requirements of the specific problem at hand.

The robust *parallel* FDII scheme proposed in this thesis is an entirely novel development in the literature. On the contrary, Alessandri [69] and Sobhani-Tehrani *et al.* [70], have previously developed FDI techniques similar to the *series-parallel* scheme. However, the *series-parallel* scheme proposed in this thesis possesses the following three novelties: (i) more solid fault isolation results due to the first-time use of a bank of *single-parameter* fault models (equation (3-7) in Section 3.1) extracted from the *multi-parameter* fault model (equation (3-3) Section 3.1) employed by Alessandri [69], (ii) remarkably simpler neural network architecture and adaptation laws than those employed by Alessandri [69] and Sobhani-Tehrani *et al.* [70], which makes the proposed methodology more suitable for real-time implementation, and (iii) fault identification

capability – the simulation results presented in Alessandri [69] do not demonstrate such capability.

The *series-parallel* and robust *parallel* FDII schemes, presented in this chapter, are developed based on the availability of full state measurements. Nonetheless, the extension of the two FDII schemes to partial-state measurement conditions has also been partially achieved through the use of a *hybrid* fault tolerant state estimator, which is the subject of Chapter 4.

In this thesis, we make the following assumptions regarding the system states and the occurrence of faults in the system, which comprise the basis for fault diagnosis design, development, and verification:

Assumption (i). The control input signals and the state vector remain bounded prior to and after the occurrence of a fault.

Assumption (ii). The faults do not occur at the same time; i.e., at each instant of time only one fault may occur in the system. This is a very reasonable assumption because the chance of two faults taking place at the same time is highly unlikely. Note that this does *not* exclude *existence* of concurrent faults in the system. More precisely, two faults may overlap each other. Since there is always some delay in fault diagnosis, a more practical assumption should be as follows: once a fault has occurred in the system, a second fault won't occur in a time period equal to the time-delay in FDII after the first fault occurrence. Although the probability of such an assumption *not* being true is not zero but is infinitely small due to the very short duration of fault diagnosis delay relative to the life time of the system or component being monitored.

Assumption (iii). The time variation of fault severities is “slow” compared to the dynamics of the states of the system. The rationale behind this assumption will be clarified in Section 3.2. Yet, this is a reasonable assumption for most engineering systems. Because for *abrupt* faults, once they occur it is not likely that their severity changes over time and for *incipient* faults, since they occur due to wear and tear of system components, the fault growth rates are often much slower than system dynamics.

3.1 Fault Modeling and Health Indicator Parameters

Generally speaking, different models of a faulty system may be constructed. Consequently, a number of perspectives and concepts on fault modeling have been developed by different researchers in the field. For example, Patton *et al.* [27] and Korbicz *et al.* [126] developed computational intelligence (CI)-based, data-driven models of faulty system. They used dynamic neural networks to identify full system dynamics including nominal and faulty dynamics, under different fault scenarios. The major drawback of their fault modeling approach is that data from different fault scenarios is required to train the CI-based models, while such data does not usually exist in practice. One way to resolve this problem is to inject faults into a simulation model of the system and generate faulty data using simulations. However, this applies only to situations where either a high-fidelity simulator of the system is available or is easy and cost-effective to develop.

Mathematical modeling techniques have also been extensively applied to model faults and/or faulty systems. In Section 2.1, simple mathematical models of sensor and actuator faults/failures were presented in equations (2-3), (2-4), (2-5), and (2-6), respectively. However, as discussed in Gertler [127], most practical faults are nonlinear functions of

system states and inputs. For example, the magnitude of a thermal system or a chemical process is, in general, a nonlinear function of the pressure and the temperature. Consequently, more general mathematical formulations of fault models have also been proposed in the literature. For example, Xiaodong *et al.* [120] describe a general multivariable nonlinear dynamic system, with full-state measurement, by the following differential equation:

$$\begin{aligned} \dot{x} &= f(x, u) + \eta(x, u, t) + B(t - T_0)\phi(x, u) \\ y &= x \end{aligned} \quad (3-1)$$

where $x \in \mathfrak{R}^n$ is the state vector of the system, $u \in \mathfrak{R}^r$ is the control input vector, $f, \phi: \mathfrak{R}^n \times \mathfrak{R}^r \rightarrow \mathfrak{R}^n$, and $\eta: \mathfrak{R}^n \times \mathfrak{R}^r \times \mathfrak{R}^+ \rightarrow \mathfrak{R}^n$ are smooth vector fields, and $B(t - T_0)$ is a matrix function representing the time profiles of the faults, where T_0 denotes the unknown fault occurrence time. The vector fields f, η , and ϕ represent the dynamics of the nominal model, the modeling uncertainty (including external disturbances as well as modeling errors), and the change in the system dynamics due to a fault, respectively. Thus, as can be seen in equation (3-1), faults have been modeled as an unknown nonlinear function of the system states and inputs that affects the nominal system dynamics. More precisely, from a qualitative viewpoint, the term $B(t - T_0)\phi(x, u)$ represents the deviation in the system dynamics due to a fault.

The matrix $B(t - T_0)$ characterizes the time profile of a fault that occurs some *unknown* time T_0 , and is defined in Xiaodong *et al.* [120] as follows:

$$B(t - T_0) = \text{diag}[B_1(t - T_0), \dots, B_n(t - T_0)]$$

where $B_i: \mathfrak{R} \rightarrow \mathfrak{R}$ is a function representing the time profile of a fault affecting the i^{th} state equation, for $i = 1, 2, \dots, n$; and modeled as follows:

$$B_i(t-T_0) = \begin{cases} 0 & \forall t < T_0 \\ 1 - e^{-\lambda_i(t-T_0)} & \forall t \geq T_0 \end{cases}$$

where the scalar $\lambda_i > 0$ denotes the unknown fault evolution rate. While small values of λ_i characterize slowly developing or *incipient* faults, large values of λ_i make function B_i approach a step function and thus model *abrupt* faults.

The model in equation (3-1) allows characterization of both additive and multiplicative faults as well as more general nonlinear faults. However, it represents only the *overall* impact of faults on system states, which, even though being useful for fault accommodation purposes, is of limited use for fault prognosis and CBM of system components. The reason is that, in general, it is very difficult to establish a one-to-one correspondence between the nonlinear fault function ϕ and the health state of the actual physical components - excluding actuators - of the system. Indeed, the proposed model is useful for fault severity estimation and prognosis of system actuators. For example, the model used by De Persis and Isidori [100] (given in equation 2-13), which is very suitable for isolation as well as identification of actuator faults, is actually a special case of the model in equation (3-1) with B_i being a step function and the nonlinear function ϕ being a superposition of bilinear terms.

Talebi and Khorasani [121] have recently generalized the model in equation (3-1) to the case of sensor faults and extended it to systems with partial state measurement as follows:

$$\begin{cases} \dot{x} = f(x, u) + \eta_x(x, u, t) + \phi_a(x, u, t) \\ y = Cx + \eta_y(x, u, t) + \phi_s(x, u, t) \end{cases} \quad (3-2)$$

where $\eta_x : \mathfrak{R}^n \times \mathfrak{R}^r \times \mathfrak{R}^+ \rightarrow \mathfrak{R}^n$ represents the plant unmodeled dynamics and disturbances, $\eta_y : \mathfrak{R}^n \times \mathfrak{R}^r \times \mathfrak{R}^+ \rightarrow \mathfrak{R}^m$ is the sensor modeling uncertainties and noise, and $\phi_a : \mathfrak{R}^n \times \mathfrak{R}^r \times \mathfrak{R}^+ \rightarrow \mathfrak{R}^n$ is the *unknown* actuator faults, $\phi_s : \mathfrak{R}^n \times \mathfrak{R}^r \times \mathfrak{R}^+ \rightarrow \mathfrak{R}^m$ represents the *unknown* sensor faults. Nonetheless, although being more general, it has the same disadvantage of the model in equation (3-1) for fault identification of system components (other than sensors and actuators).

In this thesis, following the pioneering work of Isermann [60] on fault diagnosis of linear systems and more recent work of Alessandri [69] on fault detection and isolation of nonlinear systems, we have assumed that the system component faults are reflected in the physical system parameters. Some examples of these physical parameters include friction, torque gain, damper coefficient, etc. Furthermore, we use the notion of fault parameters (FP), which was first introduced in Alessandri [69], to parameterize the *a priori* known mathematical model of the system with *unknown* parameters that actually represent faults in system components.

We assume that the occurrence of faults in the system can be represented by changes in the FPs that affect, in one way or the other, the actual physical parameters of the mathematical model of the system. In other words, the FPs shall be defined in a way that a one-to-one correspondence can be established between their values and the health status of the physical system components. Consequently, the faulty system can be described by the following discrete-time parameterized nonlinear fault model, called *multi-parameter* fault model (the discrete-time model of the system is used, since the proposed hybrid FDII algorithm is developed in a discrete-time framework):

$$\Omega: \begin{cases} x_{k+1} = f(x_k, u_k, \alpha_k) + \Gamma(x_k)w_k \\ y_k = h(x_k) + v_k \end{cases} \quad (3-3)$$

where the vector fields $f: \mathfrak{R}^n \times \mathfrak{R}^r \times \mathfrak{R}^+$ and $h: \mathfrak{R}^n \rightarrow \mathfrak{R}^m$ respectively represent the nominal system dynamics and output measurement channel; k is the discrete time-step; $\alpha_k \in \mathfrak{R}^L$ (or $\alpha_k: \mathfrak{R}^+ \rightarrow \mathfrak{R}^L$) denotes the time-dependent fault parameter (FP) vector containing L elements; w_k and v_k denote external disturbances and measurement noise, respectively; and the nonlinear function $\Gamma(x_k)$ represents the generally state-dependent channel through which the external disturbances are applied to the system. Since we are *not* investigating the robustness of FDII to modeling errors, we have not incorporated a term corresponding to modeling errors in equation (3-3). It should be noted that under full-state measurement assumption of this chapter, the nonlinear vector-valued function h becomes essentially an $n \times n$ identity matrix.

Furthermore, $\alpha_k = \alpha_H$ implies the absence of faults in the system, i.e., healthy mode of operation. The value of α_H depends on the way that the FP vector affects the physical system parameters in equation (3-3); usually being either additive or multiplicative. The representation adopted in this thesis is the additive form, hence making $\alpha_H = [0]_{L \times 1}$.

It should be noted that the time-dependent fault parameter vector α_k can also, in general, be a function of system states and inputs. However, in this thesis, without loss of generality we assume that it is only a function of time. Indeed, it can be easily shown that the model in equation (3-3) is equivalent to the state- and input-dependent fault function models given in equations (3-1) and (3-2).

Consider the model in equation (3-3). Let us add and subtract to and from the right-hand side of the state equation the nominal state dynamics of the system with $\alpha_k = \alpha_H$; i.e.,

$$\Omega: \begin{cases} x_{k+1} = f(x_k, u_k, \alpha_k) + \Gamma(x_k)w_k + f(x_k, u_k, \alpha_H) - f(x_k, u_k, \alpha_H) \\ y_k = h(x_k) + v_k \end{cases} \quad (3-4)$$

By re-arranging the terms, we have:

$$\Omega: \begin{cases} x_{k+1} = f(x_k, u_k, \alpha_H) + \Gamma(x_k)w_k + f(x_k, u_k, \alpha_k) - f(x_k, u_k, \alpha_H) \\ y_k = h(x_k) + v_k \end{cases} \quad (3-5)$$

By replacing the term $f(x_k, u_k, \alpha_k) - f(x_k, u_k, \alpha_H)$ with the function $\phi(x_k, u_k, \alpha_k)$, we have:

$$\Omega: \begin{cases} x_{k+1} = f(x_k, u_k, \alpha_H) + \Gamma(x_k)w_k + \phi(x_k, u_k, \alpha_k) \\ y_k = h(x_k) + v_k \end{cases} \quad (3-6)$$

Neglecting the terms corresponding to the modeling errors in equations (3-1) and (3-2), one can easily see that they are equivalent to model in equation (3-6), especially that in absence of faults in the system (i.e., healthy operational mode of the system) we have:

$$\phi(x_k, u_k, \alpha_k) \Big|_{\alpha_k = \alpha_H} = f(x_k, u_k, \alpha_H) - f(x_k, u_k, \alpha_H) \equiv 0$$

The fault model in equation (3-3), with output equation as $y_k = x_k + v_k$ due to full-state measurement assumption, enables us to state the problem of fault diagnosis for nonlinear systems in the form of an on-line nonlinear parameter estimation problem, where the unknown fault parameters (FPs) are being estimated using system inputs and measurements. If *all* of the system states were not available for measurement, then the fault diagnosis problem shall be stated as an on-line *dual* estimation (i.e., state and parameter estimation) problem.

Within the proposed fault diagnosis framework, fault detection can be accomplished by simply comparing the estimated FP vector against α_H . However, for fault isolation and fault severity estimation purposes, we propose a bank of parameter estimators where each estimator is designed based on a *single-parameter* fault model.

Consider the *multi-parameter* fault model of equation (3-3) with L fault parameters. We extract L *single-parameter* fault models, $\Omega_i, i = 1, \dots, L$, from model (3-3) as follows:

$$\Omega_i : \begin{cases} x_{k+1} = f(x_k, u_k, \alpha_k^i) + \Gamma(x_k) w_k \\ y_k = h(x_k) + v_k \end{cases} ; i = 1, \dots, L \quad (3-7)$$

A bank of L parameter estimators may then be designed based on each *single-parameter* fault model in equation (3-7), where the i^{th} parameter estimator will essentially estimate the i^{th} fault parameter, namely α_k^i . It should be noted that the extraction of *single-parameter* fault models from the *multi-parameter* fault model to enable fault isolation is unprecedented in the literature.

3.2 FDII Using Parameter Estimation

The formulation of the fault diagnosis problem presented in the previous section necessitates developing appropriate nonlinear parameter estimation techniques to accomplish FDII objectives. The use of parameter estimation approach for fault diagnosis has been previously reviewed on numerous occasions in the thesis. So, we focus on the nonlinear parameter estimation problem itself and very briefly review some of its potential solutions.

The problem of parameter estimation, in its most general form, is defined as follows (with slight modification from Bar-Shalom *et al.* [91]):

The term *parameter* is used to designate a quantity (scalar or vector-valued) that is assumed to be *time invariant*. If it does change with time, it can be designated (with a slight abuse of language) as a “time-varying parameter,” but its time variation must be “slow” compared to the state variables of a system. Then the problem of estimating a parameter p is the following. Given the measurements

$$y_j = G(j, u_j, w_j, p) \quad j = 1, \dots, k \quad (3-8)$$

made in presence of the known exogenous (or control) inputs u_j and *unknown* disturbances (noises) w_j , find a function of the k observations and control inputs

$$\hat{p}_k = \hat{P}(k, Z_1^k) \quad (3-9)$$

that estimates the value of p in some sense, where the measurements and observed exogenous (or known control) inputs from the current time-step k all the way to the initial moment, are denoted compactly as

$$Z_1^k = \{y_j, u_j\}_{j=1}^k \quad (3-10)$$

The function \hat{P} in equation (3-9) is called the *parameter estimator function*. The value of this function \hat{p}_k is the *parameter estimate*. The vector-valued function G is the observation function, which, in case of a general nonlinear dynamic system (given in equation (2-1)) with full-state measurement becomes equivalent to the system’s state dynamics (i.e., the vector-valued function f in equation (3-3)). It is thus the linearity or *nonlinearity* of the function G with respect to the parameter p (or equivalently, the function f in equation (3-3), with full-state measurement, with respect to FP vector α_k) that determines the linearity or nonlinearity of the parameter estimation problem.

The above definition justifies the necessity of the *Assumption (iii)* of FDII, stated at the beginning of this chapter, for the FP estimation problem to be solvable. Furthermore, the above definition suggests that the solution to the problem of estimating the FP vector α_k – and thus solving the FDII problem – is a parameter *estimator function* \hat{A} as a function of system observations/measurements, control inputs, and time, whose value at each instant of time determines the FP estimate $\hat{\alpha}_k$; i.e.,

$$\hat{\alpha}_k = \hat{A}(Y_1^k, U_1^k, k) \quad (3-11)$$

where $Y_1^k = \{y_j\}_{j=1}^k$ and $U_1^k = \{u_j\}_{j=1}^k$ are respectively the system measurements and control inputs from the initial moment to the current time-step k . The estimator function \hat{A} is called *fault parameter function* (FPF) throughout this thesis. It should be noted that the FPF in equation (3-11) requires the entire past observed data. Such a formulation of the parameter estimator function is useful only for *finite-horizon problems* such as finite-horizon tracking problem. However, it is impractical and computationally unfeasible for *infinite-horizon problems* such as online monitoring and fault diagnosis, since the dimension of the input space of the estimator function increases linearly in time. Therefore, we need to limit the memory of the estimator to a fixed, limited number of previous measurements and control inputs. Here, at each time-step k , we take the measurements and control signals from only the previous time-step $k-1$. Thus, we have:

$$\hat{\alpha}_k = \hat{A}(y_{k-1}, u_{k-1}, k) \quad (3-12)$$

There are two fundamental approaches one can use for estimating a parameter:

- (i) **Nonparametric (or distribution free) approaches:** There is a true *unknown* value p_0 for the parameter, which does not obey a specific distribution. These are also called the *non-Bayesian* or *Fisher* approaches.
- (ii) **Parametric random approaches:** The parameter is a realization of a random variable with an *a priori* known probability distribution function (PDF). These are also called *Bayesian* approaches.

However, the FP vector does not have any *a priori* known PDF because faults in a system, in general, do not occur according to a specific distribution (or stochastic model). Therefore, the problem of nonlinear FP vector estimation has to be solved using a *non-parametric* or *non-Bayesian* approach.

3.2.1 Conventional Linear and Nonlinear Parameter Estimation

In this subsection, we will very briefly mention some of the conventional *non-Bayesian* parameter estimation methods applicable to both linear and nonlinear parameter estimation problems. For further details, refer to Bar-Shalom *et al.* [91] and Haykin [49]. These methods include:

(a) Maximum Likelihood Estimator (MLE): This method maximizes the so-called *likelihood* function (LF) of the parameter, namely $\Lambda_z(p) = P(Z|p)$, defined as the PDF of the measurements conditioned on the parameter; i.e.,

$$\hat{p}^{ML}(Z) = \arg \max_p \Lambda_z(p) = \arg \max_p P(Z|p) \quad (3-13)$$

where the LF is a measure of how “likely” a parameter value is given the obtained observations [91]. The likelihood function serves as a measure of the *evidence from the data* [91]. MLE has been extensively used for linear parameter estimation. The use of

MLE for nonlinear parameter estimation essentially entails solving a nonlinear optimization (maximization) problem, which cannot often be solved analytically and thus should be solved approximately. However, most conventional searching algorithms are likely to converge to local *maxima*. Nevertheless, the genetic algorithm (GA) poses as a good candidate for solving the nonlinear MLE problem, since it tends to find the globally optimal solution without being trapped at local minima. For example, Abutaleb [128] applied GA to MLE of the parameters of a nonlinear system in a noisy environment. For pure GA-based nonlinear parameter estimation, refer to Yao and Sethares [129].

Singer [130] proposed another approach to solving the nonlinear MLE problem through the use of Monte Carlo simulations; hence the name *simulated maximum likelihood* (SML). Nonetheless, both GA-based MLE and SML are computationally extensive, which makes them inappropriate for real-time, on-line FP vector estimation required to accomplish FDII of nonlinear systems.

(b) Least Squares Estimator (LSE) [91]: In equation (3-8), assume that the *unknown* disturbances (noises) appear in additive form; thus,

$$y_j = G(j, u_j, p) + w_j \quad j = 1, \dots, k \quad (3-14)$$

Then, the LSE method minimizes the *cumulative* squared of the estimation error as a function of the parameter p ; i.e.,

$$\hat{p}_k^{LS} = \arg \min_p \left\{ \sum_{j=1}^k \|y_j - G(j, u_j, p)\|^2 \right\} \quad (3-15)$$

If the function G is linear in p , then one has *linear* LS problem. Accordingly, a nonlinear function G results in the *nonlinear* LS problem. It should be emphasized that the LSE

coincides with the MLE if the measurement/process noises w_j are independent and identically distributed zero-mean Gaussian random variables; i.e., $w_j \sim N(0, \sigma^2)$ [91].

Once again, the use of *cumulative* error over the entire past observed data makes LSE inappropriate for *infinite-horizon* problems such as on-line FDI. However, a useful feature of the LSE is that it can be rewritten in recursive form, which is useful for sequential, online processing. Recursive Least Squares (RLS) is commonly used for parameter estimation of linear systems (see Houacine [131]). For application of RLS to nonlinear systems, see Haupt *et al.* [132], where the authors have developed an optimal iterative algorithm for discrete nonlinear least-squares estimation.

(c) Kalman Filter-based Estimation: The celebrated Kalman filter (KF) [49], rooted in the state-space representation of dynamical systems, provides an optimal (in the sense of minimum variance) recursive solution to the problem of parameter estimator under the hypotheses of Gaussian measurement and process noises, and the linearity of state and measurement equations. The KF is also capable of optimal *dual* estimation for linear systems, in which both the states of the dynamical system and its parameters are estimated simultaneously, given only noisy observations. It should be noted that the KF-based parameter estimators are distribution-free (or non-parametric) only with respect to the unknown parameters that need to be estimated, but they all depend on the Gaussian distribution assumption of system states as well as process and measurement noise.

Two extensions of the KF to nonlinear systems include the extended Kalman filter (EKF) and the unscented Kalman filter (UKF). For complete mathematical description of the EKF and the UKF algorithms, refer to Haykin [49]. The EKF is being extensively used as an industry standard technique for recursive parameter estimation, state

estimation, and *dual* estimation of nonlinear systems. However, it suffers from suboptimal performance and sometimes divergence due to errors introduced by “first-order” approximation of the true nonlinear dynamics. Although “second-order” versions of the EKF exist, their increased implementation and computational complexity tend to prohibit their use.

The UKF algorithm addresses the “first-order” approximation issue of the EKF through the use of *unscented transformation* (UT). The UT is a method for calculating the statistics of a random variable that undergoes a nonlinear transformation (Julier and Uhlmann [48]). From Julier *et al.* [133], it is known that UKF can predict the state estimate and error covariance to 4th order accuracy while the EKF only predicts with accuracy up to 2nd order for the state estimate and 4th order for the error covariance. Another advantage of the UKF is its ease of implementation. In contrast to the EKF, the UKF algorithm does not require calculation of the Jacobian matrices that could sometimes lead to implementation difficulties.

Despite its clear advantages over the EKF, the UKF algorithm also possesses a major implementation difficulty. It has more number of parameters than the EKF, which makes the UKF relatively difficult to tune. This is due to the three extra parameters associated to the unscented transform. While some guidelines exist on how to choose these parameters, the optimal selection clearly depends on the specifics of the problem at hand, and is not fully understood [49].

Nevertheless, both the EKF and the UKF algorithms suffer from common limitations. Both algorithms make a Gaussian assumption on the probability density of the process and measurements noises and the state random variable. Although being often valid, a

Gaussian assumption will not suffice for certain problems and applications, and thus the UKF and the EKF cannot be applied with confidence. Moreover, the author's numerous experiences with both the EKF and the UKF in different state estimation and fault diagnosis applications has revealed that it is sometimes very time-consuming and difficult to optimally tune the two algorithms. Thus, one needs to resort to algorithms that are more powerful in dealing with nonlinearities and non-Gaussian situations, and are also easier to tune. It is strongly believed that neural networks provide such an alternative strategy that can resolve the above-mentioned limitations of KF-based algorithms.

3.2.2 Neural Network-based Parameter Estimation

To overcome the aforementioned limitations and/or shortcomings, we choose multi-layer feed-forward (static) neural networks for parameter estimation. The neural networks are a promising alternative to the conventional parameter estimation methods due to: (i) their universal function approximation property that allows approximating any continuous, multivariate nonlinear function to any desired degree of accuracy; (ii) their ability to approximate *unknown* nonlinear functions without any explicit specification of functional or distributional assumption (such as the Gaussian distribution assumption of KF-based methods) for the underlying model; and (iii) the availability of effective, well-studied, and well understood on-line adaptation (or weight optimization) algorithms, which make the adaptation algorithm fairly simple to tune. The neural weight adaptation algorithms are so well-established that even numerous modifications and enhancements to the basic algorithms have also been proposed in the literature.

Consequently, in this thesis we develop neural parameter estimators (NPE) for adaptively estimating the fault parameter function (FPF) and thus to estimate the FP

vector. We propose two NPE schemes, namely “series-parallel” and “parallel” that differ mainly in their structure. These terminologies are borrowed from the system identification literature (see Narendra and Parthasarathy [65]). To accomplish fault isolation, we develop a *bank* of L NPEs, where each NPE in the bank is designed according to one of the L *single-parameter* fault models in equation (3-7). Hence, the i^{th} NPE in the bank is responsible for estimating the i^{th} fault parameter α_k^i , for $i = 1, \dots, L$. It should be noted, however, that the idea of developing a bank of NPEs is entirely independent from the NPE structure, being “series-parallel” or “parallel”. Nonetheless, the fault isolation decision logic depends on the NPE structure being used, as will be shown in the following sections.

3.3 FDII Using Series-Parallel Architecture of Neural Parameter Estimators

Figure 3-1 depicts the structure of a bank of series-parallel NPEs designed and developed to simultaneously achieve the three objectives of fault detection, isolation, and fault severity estimation. As can be seen in this figure, residual signals $r_k^i, i = 1, \dots, L$ and the FP estimates $\hat{\alpha}_k^i, i = 1, \dots, L$ comprise the outputs of the series-parallel scheme and the three tasks of FDII are achieved by examining all these quantities. Fault detection and isolation (FDI) decision logic of this scheme are presented in Section 3.3.2.

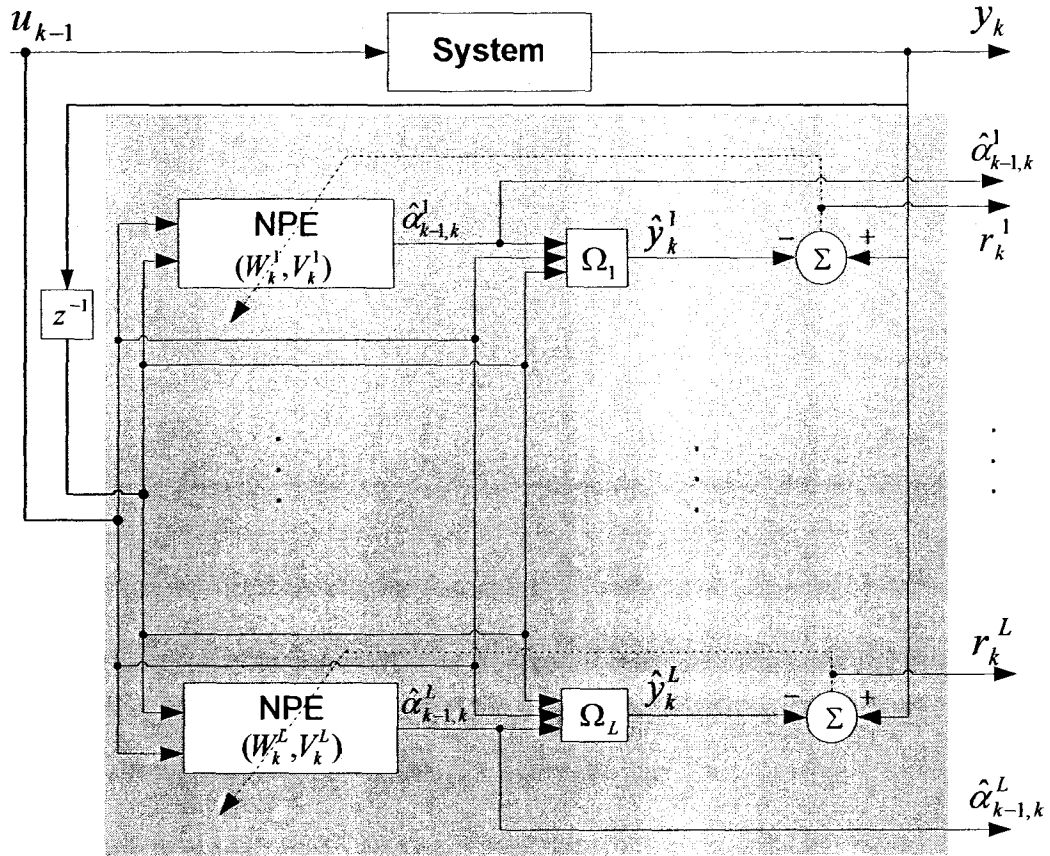


Figure 3-1. Series-Parallel scheme of the proposed hybrid FDII approach.

The series-parallel structure is composed of two major subsystems: 1) the feed-forward (static) neural networks (FFNN) (i.e., the NPEs) utilized to adaptively approximate nonlinear FP estimation functions and 2) the nonlinear *single-parameter* fault models given in equation (3-7) utilized for state/output estimation (or prediction) based on FP estimates. Accordingly, at each time-step k , the following two set of calculations are performed associated with each NPE in the bank:

1) Calculation of FP estimates:

$$\hat{\alpha}_{k-1,k}^i = g(\bar{y}_k, W_k^i, V_k^i) ; i = 1, \dots, L \quad (3-16)$$

and
$$\bar{y}_k = [y_{k-1} \quad u_{k-1}]^T \quad (3-17)$$

where $\hat{\alpha}_{k-1,k}^i$ is the estimate of the i^{th} fault parameter at time $k-1$ calculated at time k , W_k^i, V_k^i are respectively the output and the hidden layer weight matrices of the i^{th} NPE, \bar{y}_k is the input vector of all NPEs, and g is the nonlinear mapping implemented by a single hidden layer FFNN with linear activation functions for the neurons at the output layer and the nonlinear activation functions for the neurons at the hidden-layer. Thus,

$$g(\bar{y}_k, W_k^i, V_k^i) = W_k^i \sigma(V_k^i \bar{y}_k) \quad (3-18)$$

where $\sigma(\cdot)$ is the activation function of the hidden-layer neurons that is usually set to be a *sigmoidal* function:

$$\sigma_j(V_k^i \bar{y}_k) = \frac{2}{1 + \exp(-2V_{kj}^i \bar{y}_k)} - 1 \quad (3-19)$$

where V_{kj}^i is the j^{th} row of V_k^i and $\sigma_j(V_k^i \bar{y}_k)$ is the j^{th} element of $\sigma(V_k^i \bar{y}_k)$.

2) State/Output estimation (or prediction) based on FP estimates: In this step, the states and consequently the outputs of the system are estimated (or predicted) using the known part of the *single-parameter* fault models in equation (3-7) (i.e., without *unknown* external disturbances w_k and measurement noise v_k) and based on the FP vector estimate from step 1, namely $\hat{\alpha}_{k-1,k}$. Hence,

$$\begin{cases} \hat{x}_k^i = f(x_{k-1}, u_{k-1}, \hat{\alpha}_{k-1,k}^i) \\ \hat{y}_k^i = \hat{x}_k^i \end{cases} ; i = 1, \dots, L \quad (3-20)$$

where $x_{k-1} = y_{k-1}$ are the measured states of the system.

3.3.1 Weight Update Laws of the Series-Parallel Scheme

The weights of NPEs are updated with the objective of minimizing the weighted L_2 norm of the instantaneous output estimation error vector defined as:

$$\tilde{y}_k^i = y_k - \hat{y}_k^i \quad ; i = 1, \dots, L \quad (3-21)$$

Thus, the objective function, at time-step k , of the i^{th} NPE is the instantaneous output error:

$$J_k^i = \frac{1}{2} \|\tilde{y}_k^i\|_Q^2 = \frac{1}{2} \tilde{y}_k^{i\text{T}} Q \tilde{y}_k^i \quad (3-22)$$

where $Q \in \mathbb{R}^{n \times n}$ is the estimation error weight matrix.

The weights of NPEs are updated using the well-known gradient descent (GD) algorithm:

$$\begin{aligned} W_{k+1}^i &= W_k^i - \eta_w^i \left(\frac{\partial J_k^i}{\partial W_k^i} \right) \\ V_{k+1}^i &= V_k^i - \eta_v^i \left(\frac{\partial J_k^i}{\partial V_k^i} \right) \end{aligned} \quad ; i = 1, \dots, L \quad (3-23)$$

where $\eta_w^i, \eta_v^i > 0; i = 1, \dots, L$ are the learning rates.

In order to precisely derive the weight update laws, let us define for $i = 1, \dots, L$:

$$net_{v_k}^i = V_k^i \bar{y}_k \quad (3-24)$$

$$net_{w_k}^i = W_k^i \sigma(V_k^i \bar{y}_k) \quad (3-25)$$

Thus, the partial derivatives $\partial J_k^i / \partial W_k^i, \partial J_k^i / \partial V_k^i$ can be computed according to the following equations:

$$\frac{\partial J_k^i}{\partial W_k^i} = \frac{\partial J_k^i}{\partial net_{w_k}^i} \frac{\partial net_{w_k}^i}{\partial W_k^i} \quad (3-26)$$

$$\frac{\partial J_k^i}{\partial V_k^i} = \frac{\partial J_k^i}{\partial net_{v_k}^i} \frac{\partial net_{v_k}^i}{\partial V_k^i} \quad (3-27)$$

where

$$\frac{\partial J_k^i}{\partial net_{w_k}^i} = \frac{\partial J_k^i}{\partial \tilde{y}_k^i} \frac{\partial \tilde{y}_k^i}{\partial \hat{y}_k^i} \frac{\partial \hat{y}_k^i}{\partial \hat{x}_k^i} \frac{\partial \hat{x}_k^i}{\partial \hat{\alpha}_{k-1,k}^i} \frac{\partial \hat{\alpha}_{k-1,k}^i}{\partial net_{w_k}^i} = -\tilde{y}_k^{i\top} Q \frac{\partial \hat{x}_k^i}{\partial \hat{\alpha}_{k-1,k}^i} \frac{\partial \hat{\alpha}_{k-1,k}^i}{\partial net_{w_k}^i} \quad (3-28)$$

$$\frac{\partial J_k^i}{\partial net_{v_k}^i} = \frac{\partial J_k^i}{\partial \tilde{y}_k^i} \frac{\partial \tilde{y}_k^i}{\partial \hat{y}_k^i} \frac{\partial \hat{y}_k^i}{\partial \hat{x}_k^i} \frac{\partial \hat{x}_k^i}{\partial \hat{\alpha}_{k-1,k}^i} \frac{\partial \hat{\alpha}_{k-1,k}^i}{\partial net_{v_k}^i} = -\tilde{y}_k^{i\top} Q \frac{\partial \hat{x}_k^i}{\partial \hat{\alpha}_{k-1,k}^i} \frac{\partial \hat{\alpha}_{k-1,k}^i}{\partial net_{v_k}^i} \quad (3-29)$$

$$\frac{\partial net_{w_k}^i}{\partial W_k^i} = \sigma(V_k^i \bar{y}_k), \quad \frac{\partial net_{v_k}^i}{\partial V_k^i} = \bar{y}_k \quad (3-30)$$

The partial derivative $\partial \hat{x}_k^i / \partial \hat{\alpha}_{k-1,k}^i$; $i = 1, \dots, L$ is calculated using the i^{th} state estimation equation of equation (3-20) as follows:

$$\frac{\partial \hat{x}_k^i}{\partial \hat{\alpha}_{k-1,k}^i} = \frac{\partial f(x_{k-1}, u_{k-1}, \hat{\alpha}_{k-1,k}^i)}{\partial \hat{\alpha}_{k-1,k}^i} \quad (3-31)$$

which is essentially the Jacobian of the vector-valued function f with respect to the *scalar* parameter $\hat{\alpha}_{k-1,k}^i$. However, it should be noted that we do not need to calculate the Jacobian matrix of the system with respect to the states, which is an advantage from implementation point of view.

Finally, the well-known standard back-propagation (BP) algorithm is used to calculate the partial derivatives $\partial \hat{\alpha}_{k-1,k}^i / \partial net_{w_k}^i$, $\partial \hat{\alpha}_{k-1,k}^i / \partial net_{v_k}^i$ for $i = 1, \dots, L$. Due to the *linearity* of the output layer of the NPEs, we simply have

$$\frac{\partial \hat{\alpha}_{k-1,k}^i}{\partial net_{w_k}^i} = 1 \quad (3-32)$$

and taking into account the sigmoidal activation functions of the hidden layer of the NPEs, we have:

$$\frac{\partial \hat{\alpha}_{k-1,k}^i}{\partial net_{v_k}^i} = W_k^i \left(I - \Lambda \left(V_k^i \bar{y}_k \right) \right) \quad (3-33)$$

where $\Lambda(V_k^i \bar{y}_k) = \text{diag}[\sigma_j^2(V_k^i \bar{y}_k)]$, $j = 1, \dots, S^i$; and S^i is the number of neurons in the hidden-layer of the i^{th} NPE and V_k^i is, once again, the j^{th} row of V_k^i .

3.3.2 FDI Decision Logic of the Series-Parallel Scheme

To formulate the FDI decision logic, we need to define a set of residual vectors as – a total of L residual vectors can be defined; one per state estimator in the bank:

$$r_k^i = y_k - \hat{y}_k^i ; i = 1, \dots, L \quad (3-34)$$

Given *Assumption (ii)*, the fault detection and isolation (FDI) decision logic for the series-parallel scheme is quite straight-forward and can be stated as follows:

$$\begin{aligned} (C_k^F, T_F^C) = \{ (i, k, T_s) \mid |r_k^{i,j}| \leq \delta^j \wedge |\hat{\alpha}_k^i - \alpha_H^i| > \varepsilon^i \} \\ l = 1, \dots, L; l \neq i; j = 1, \dots, n \end{aligned} \quad (3-35)$$

where $|r_k^{i,j}|$ is the absolute value of the j^{th} element of the residual vector corresponding to the i^{th} NPE in the bank; δ^j ; $j = 1, \dots, n$ denote the thresholds associated to the output (or state) residuals of the NPEs; ε^i ; $i = 1, \dots, L$ denote the thresholds corresponding to the FP estimate of the i^{th} NPE in the bank; C_k^F specifies at each instant of time (the index of) the faulty component(s) (or the *health state* of the system); T_s is the *sampling time* of the system; α_H^i is the value of the i^{th} FP under nominal, healthy conditions (which is “zero”

for additive FPs and “one” for multiplicative FPs); and T_F^C represents the detection and isolation time of the occurred fault(s). Under healthy conditions, C_k^F should ideally (i.e., under *perfect detection*) be an *empty set* (i.e., $C_k^F = \emptyset$). On the other hand, in presence of *only one* faulty component in the system, C_k^F should ideally (i.e., under *perfect isolation*) belong to the set $\{1, \dots, L\}$. However, in case of *imperfect isolation*, C_k^F would be a subset of the set $\{1, \dots, L\}$, consisting of more than one elements.

It should be noted that, as opposed to the thresholds $\varepsilon^i; i = 1, \dots, L$, the thresholds $\delta^j; j = 1, \dots, n$ are common (or equal) across all NPEs in the bank. As mentioned at the beginning of Section 3.3 and can also be seen from the FDI decision logic in equation (3-35), both the *residual* signals and the FP estimates $\hat{\alpha}_k^i; i = 1, \dots, L$ are examined in the series-parallel scheme to detect the presence and isolate the location of faults in the monitored system. Once a fault is detected and the faulty component is isolated, the severity of the fault is essentially the value of the corresponding FP estimate, namely $\hat{\alpha}_{k-1,k}^{C_k^F}$.

Finally, the FDI decision logic of the series-parallel scheme shows resemblance with that of the dedicated observer scheme (DOS) presented in Section 2.3.1.2. In particular, careful comparison of equations (3-35) and (2-7) clearly reveals *partial* equivalence between the two FDI decision logics; except that the residuals in the FDI decision rule of the DOS are replaced by the FP estimates in the *last condition* of the FDI decision rule of the series-parallel scheme.

3.3.2.1 Threshold Selection Criteria

In the series-parallel scheme, fault detection can be ensured if the well-known worst-case noise/disturbance analysis is employed for assigning the thresholds $\delta^j; j = 1, \dots, n$ in equation (3-35). However, this does not guarantee that fault isolation will be *perfectly* achieved. More precisely, the i^{th} FP estimate $\hat{\alpha}_{k-1,k}^i$ is not *perfectly* decoupled from *all* fault sources but the i^{th} one (i.e., the fault sources $j = 1, \dots, i-1, i+1, \dots, L$). In fact, there is always a *weak* impact from the fault sources $j = 1, \dots, i-1, i+1, \dots, L$ on the i^{th} FP estimate $\hat{\alpha}_{k-1,k}^i$, as will be demonstrated using simulations in Section 5.5.1. However, this *weak* impact can be resolved by properly setting the thresholds $\varepsilon^i; i = 1, \dots, L$. A good rule of thumb that augments the reliability of FDII and ensures the safety of the system is to select the thresholds $\varepsilon^i; i = 1, \dots, L$ in a way that the occurrence of the i^{th} fault with a severity level below its respective threshold ε^i does not significantly deteriorate the closed-loop system performance.

3.4 Robust FDII Using Parallel Architecture of NPEs

The series-parallel scheme developed in the previous section possesses several advantages including simple FDI decision logic (as discussed earlier) and fast convergence (which will be demonstrated in Section 5.5.1). It should be noted that fast convergence essentially results in short delay in FDI. However, as mentioned previously, it may incorrectly isolate faults specially when there is a strong coupling between two fault sources. Furthermore, as will be illustrated in the simulation results of Section 5.5.2, the series-parallel scheme suffers from lack of robustness to measurement noise. Indeed,

measurement noise significantly deteriorates, in particular, the fault isolation and identification performance of the series-parallel scheme. This is due to the fact that measurement noise directly propagates through the network, directly affecting the FP estimates as can be observed from Figure 3-1. As mentioned in Section 2.3.1.2, the non-robustness to measurement noise is also an inherent property of the DOS FDI method. This, once again, emphasizes the similarity of the two methods.

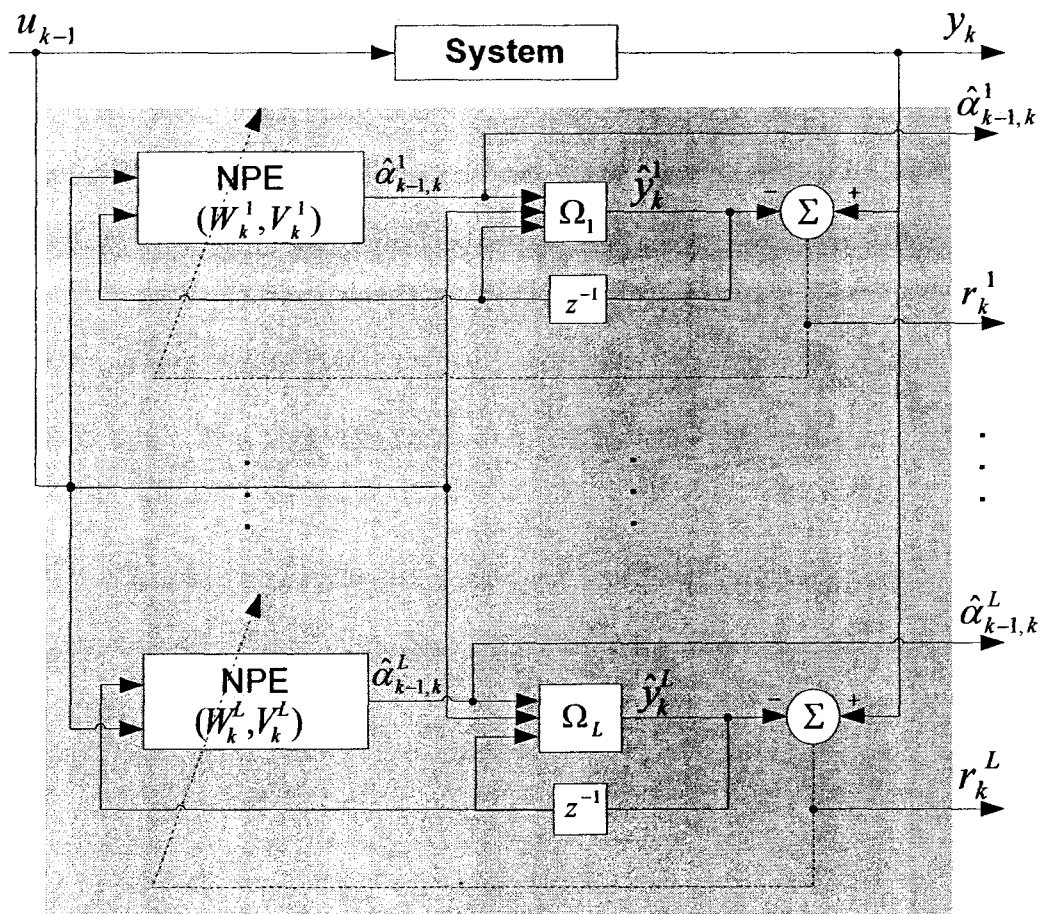


Figure 3-2. Parallel scheme of the proposed hybrid FDI approach.

The sensitivity of the series-parallel scheme to measurement noise makes it impractical and unreliable for fault diagnosis in low SNR applications. The parallel

scheme developed in this section intelligently resolves this issue by feeding back the estimated rather than the measured outputs to the NPE input. This slight restructuring of the series-parallel scheme makes the measurement noises to be filtered out in the NPE weight adaptation process of the parallel FDII scheme, hence making it extremely robust to measurement noise. The extreme insensitivity of the FDII performance of the parallel scheme to measurement noise will be demonstrated in Section 5.5.4. The schematic of the *robust* parallel structure of the proposed *hybrid* FDII methodology is shown in Figure 3-2.

Furthermore, using a special formulation of the FDI decision logic, the parallel scheme allows fault isolation to be *perfectly* achieved in contrast to the series-parallel scheme. The reason for *perfect* isolation in the parallel scheme is that, as opposed to the series-parallel structure, the only signal common among the inputs of all state estimators (or predictors) and the NPEs in the bank is the control input signal. More precisely, each NPE and state estimator in the bank utilizes its own state estimate (or prediction), which automatically enforces a structural decoupling between the units. Clearly, this restructuring also has a disadvantage of slower convergence rate for the state estimators and the NPEs of the parallel scheme as compared to its series-parallel counterpart. This slower convergence rate causes longer fault diagnosis delays and makes the parallel scheme sensitive to transients of the closed-loop system (due to changes in the control command). More precisely, while the state estimates from the series-parallel scheme very quickly converge to the measured states and thus it is extremely robust to closed-loop system transients, the parallel scheme generates false alarms during the transients until the closed-loop system stabilizes at the steady state. All of the above-mentioned

characteristics of each FDII scheme are further demonstrated and verified in Chapter 5 using simulations.

The NPE calculations and weight adaptation laws of the parallel structure remain essentially similar to that of the series-parallel scheme with only slight modifications; however, the FDI decision logics of the two are a bit different. These changes and differences are reflected in the following.

Since instead of the actual measurements, the output estimates (or predictions) are fed back to the NPEs' and state estimators, y_{k-1} in equation (3-17) should be replaced by \hat{y}_{k-1}^i , and x_{k-1} (equal to y_{k-1} under full-state measurement assumption) in equation (3-20) must be replaced also by \hat{x}_{k-1}^i both for $i = 1, \dots, L$. Hence, for the robust parallel FDII scheme we have:

$$\hat{\alpha}_{k-1,k}^i = g(\bar{y}_k^i, W_k^i, V_k^i) ; i = 1, \dots, L \quad (3-36)$$

and

$$\bar{y}_k^i = [\hat{x}_{k-1}^i \quad u_{k-1}]^T ; i = 1, \dots, L \quad (3-37)$$

Moreover,

$$\begin{cases} \hat{x}_k^i = f(\hat{x}_{k-1}^i, u_{k-1}, \hat{\alpha}_{k-1,k}^i) \\ \hat{y}_k^i = \hat{x}_k^i \end{cases} ; i = 1, \dots, L \quad (3-38)$$

3.4.1 Weight Update Laws of the Robust Parallel Scheme

Once the above adjustments are applied to equations (3-20) and (3-17), the weight update laws remain practically intact, since they are written in terms of \bar{y}_k in equation (3-17), which represents the input vector of the NPEs. The only required adjustment to the weight update laws of the series-parallel scheme that may need to be explicitly re-

emphasized is in equation (3-31). For the robust parallel structure, this equation should be reinstated for $i = 1, \dots, L$ as follows:

$$\frac{\partial \hat{x}_k^i}{\partial \hat{\alpha}_{k-1,k}^i} = \frac{\partial f(\hat{x}_{k-1}^i, u_{k-1}, \hat{\alpha}_{k-1,k}^i)}{\partial \hat{\alpha}_{k-1,k}^i} \quad (3-39)$$

3.4.2 Fault Isolation Policy of the Parallel Scheme

Once again, we need to define a set of L residual vectors – one per state estimator in the bank – as follows:

$$r_k^i = y_k - \hat{y}_k^i; \quad i = 1, \dots, L \quad (3-40)$$

In sequel, the FDI decision strategy can be stated as follows:

$$(C_k^F, T_F^C) = \left\{ (i, kT_s) \mid |r_k^{i,j}| \leq \delta^j \wedge |r_k^{l,j}| > \delta^j; l = 1, \dots, L; l \neq i; j = 1, \dots, n \right\} \quad (3-41)$$

where $r_k^{i,j}$ denotes the j^{th} element of residual vector r_k^i and $\delta^j; j = 1, \dots, n$ are the thresholds corresponding to the state residuals of the NPEs. It should be noted that the thresholds $\delta^j; j = 1, \dots, n$ are common (or equal) across all NPEs in the bank. The above fault isolation policy states that the fault model with residuals within the threshold bounds is actually the current active mode of the system. In the parallel scheme, threshold values are determined using the worst-case disturbance/noise analysis. Once the fault source is isolated, the severity of the fault is essentially the value of the corresponding FP estimate. It should be noted that the FDI decision logic of the robust parallel scheme is simpler to implement than that of the series-parallel scheme. This can be simply observed by comparing equation (3-41) with equation (3-35). As can be seen from those equations, the FDI logic of the parallel scheme has only n parameters to be specified corresponding to the residual thresholds $\delta^j; j = 1, \dots, n$, with n being the order of the monitored system.

On the other hand, in the series-parallel scheme $n+L$ parameters need to be specified, where in addition to the residual thresholds, the thresholds associated to FPs $\varepsilon^i; i = 1, \dots, L$ have to be determined; L being the number of faults modeled in the system. Interestingly, the simplicity of the FDI logic of the robust parallel scheme comes along with solid fault isolation capability. This is intrinsic to the parallel scheme, where fault isolation is essentially enforced in its structure. This was already discussed in more details on pages 106 and 107, and is also demonstrated through simulations in Chapter 5.

3.5 Conclusions

The *hybrid* nonlinear fault detection, isolation, and identification (FDII) approach proposed in this thesis was presented in this chapter. In order to achieve fault identification, faults were modelled through parameterization of the nominal mathematical model of the system with a set of fault parameters (FPs), where each FP is an indication of a particular fault in the system. It was explained, however, that such a *multi-parameter* fault model does not allow fault isolation. Hence, a set of *single-parameter* fault models were extracted from the *multi-parameter* ones in order to achieve fault isolation. Once the set of single-parameter fault models were derived, the problem of FDII in nonlinear systems was formulated as an on-line nonlinear parameter estimation problem with FPs as the *unknown* parameters that need to be estimated. Various nonlinear parameter estimation methods were then reviewed and a solution based on neural networks was then proposed. The universal function approximation capability of neural networks and the availability of well-established and well-understood weight adaptation laws were the rationales behind choosing neural networks for solving the on-line nonlinear parameter estimation problem.

Hence, the core of the proposed *hybrid* nonlinear FDII solution was a bank of adaptive neural parameter estimators (NPE), where each NPE in the bank was designed based on a separate single-parameter fault model. At each instant of time, the NPEs provide estimates of the *unknown* fault parameters (FP), which in conjunction with the output residuals determine the health state of the system being monitored. The residuals were defined as the difference between the actual measurements and the output estimates (or predictions) generated by the single-parameter fault models using their respective FP estimates from the NPEs. The fault parameter estimation was based on on-line minimization of instantaneous output estimation error.

Under full-state measurement assumption, two NPE structures including the series-parallel and the parallel were proposed and their respective FDI decision logics and weight update laws were derived. Each FDII scheme was shown to exhibit an exclusive set of desirable attributes. More specifically, it was discussed that the FDII performance of the *parallel* scheme is extremely robust to measurement noise, hence making it suitable for health monitoring of systems with even very low SNR values. Furthermore, it was discussed that the smaller number of thresholds makes the FDI decision logic of the parallel scheme simpler than that of the series-parallel scheme. On the contrary, it was discussed that the series-parallel scheme displays fast convergence rates and is very robust to the closed-loop system transients, which are due to changes in the control command signal. Hence, the series-parallel scheme is desirable for (high SNR) systems requiring very short delays in fault diagnosis and/or systems requiring frequent commanding. In practice, the choice of the appropriate FDII scheme is imposed by the specifications and the requirements of the specific problem at hand. Furthermore, simple

neural network architecture and straightforward weight adaptation laws make both proposed FDII schemes suitable for real-time implementation of on-line health monitoring systems. It should be noted that the robust parallel FDII scheme is a major contribution of this thesis, being proposed for the first time in the literature. Furthermore, the novelty aspects of the series-parallel scheme were also mentioned in this chapter.

Chapter 4:

4 Proposed FDII for Nonlinear Systems with Partial State Measurement

Similar to many of the existing fault diagnosis methods, the two FDII schemes developed in the previous chapter relied on the availability of full-state measurements. However, even with recent advances in sensor and instrumentation technology, *all* the states of a dynamical system may not be directly measurable. This might be due to unavailability of operational, accurate, or reliable (on-board) sensors for measurement of some specific physical variables. For example, the state of charge (SOC) in batteries – employed almost everywhere from portable electronics to hybrid electric vehicles (HEV) – cannot be directly measured while the battery is in operation. Some experimental methods certainly exist for measuring the SOC but such measurements have to be taken under a controlled experimental setup and cannot be achieved while the battery provides power to the system (i.e., laptop, HEV, etc.).

Furthermore, sensors are often prone to permanent or intermittent faults/failures. This essentially makes their measurements at least temporarily unavailable. For example, sensors regularly require recalibration after certain amount of time/deployment due to bias or drift. Until the recalibration is performed, both the control system and the fault diagnosis subsystem are expected to continue their operation in order to monitor, ensure, and maintain the safety of the entire system. Needless to say that even for systems where

complete shutdown is possible, economic loss due to system shutdown is irrefutable. Finally, it should also be noted that for some sensors, the amount of measurement noise can be relatively high and also the measurement noise and sensor accuracy may well depend on the dynamic range of the variable being measured. For example, current sensors usually exhibit varying level of accuracy over different ranges of current. Therefore, the reliability of measurements from these sensors changes accordingly. In conclusion, to augment the reliability of control and health monitoring systems, one needs to estimate system estimates that are either intrinsically non-measurable or have temporarily or permanently turned out to be non-measurable due to occurrence of sensor faults/failures.

As mentioned previously, both the series-parallel and the parallel FDII schemes proposed in Chapter 3 rely on full-state measurements. More precisely, state measurements comprise the inputs to the FDII subsystem. Consequently, any inaccuracies in state measurements eventually affect diagnostic performance. When some of the system states are not directly measurable (or may temporarily become non-measurable) then their corresponding estimates shall be provided to the FDII unit. Therefore, the accuracy of state estimates becomes crucial for successful and reliable fault diagnosis just as the accuracy of the measurements in full-state measurements conditions.

Furthermore, the state estimates should not only be accurate during healthy operational mode of the system to avoid false alarms, but also during faulty periods. Here, “faulty periods” refer to presence of faults in system components and/or actuators assuming that sensor faults won’t occur. The inaccuracy of state estimates during faulty

periods, at its worst possibility, may cause faults to be missed (i.e., misdetection), or more likely to be incorrectly isolated and/or inaccurately identified. Thus, it is highly desirable that state estimators or observers should accurately estimate unmeasured system states using inputs and available sensor measurements even in presence of faults in the system. In other words, the state estimator or observer must be fault tolerant. It is important to note that, to the best of our knowledge, the *terminology* of *fault tolerant observer* (FTO) has been introduced in this thesis for the first time in the literature. Though, the *concept* has been previously proposed and fairly well investigated under the terminology of *unknown input observers* (UIO), which will be further discussed in Section 4.3.

In the following, we first assume that an FTO exists that can accurately estimate unmeasured system states in both presence and absence of faults. Based on this assumption, the extension of the series-parallel and parallel FDII schemes to systems with partial state measurements is presented. Then, in the rest of this Chapter, we focus on developing a fault tolerant observer that essentially enables this extension.

4.1 FDII Using the Series-Parallel Scheme under Partial State Measurements

Figure 4-1 depicts a block diagram representing the extension of the series-parallel FDII scheme to partial-state measurement conditions. As shown in this figure and described in the above, this extension based upon integration of the *hybrid* NPEs of the series-parallel FDII scheme with a fault tolerant observer.

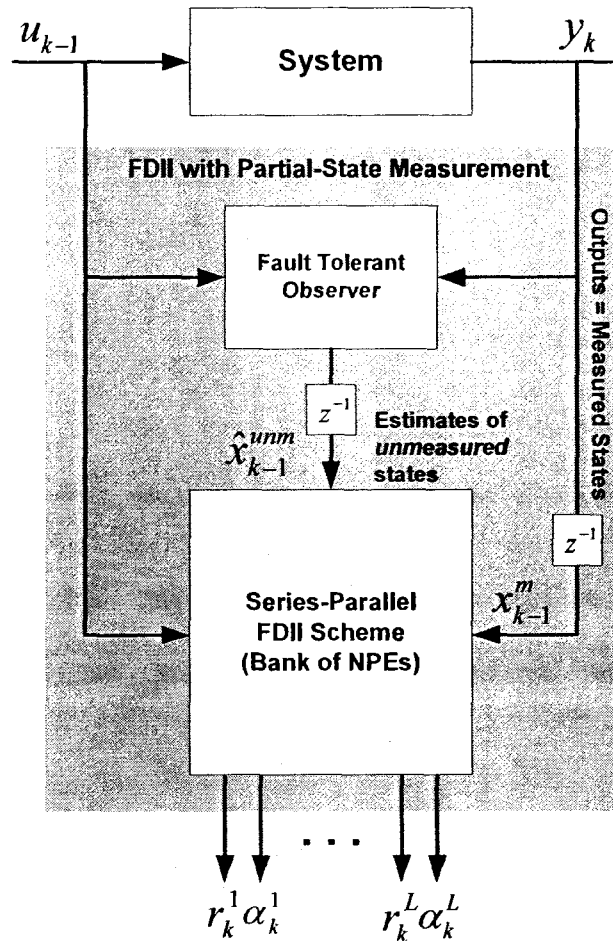


Figure 4-1. The series-parallel FDI scheme under partial-state measurements using the integration of the *hybrid* NPEs and an FTO.

Let us first assume that the system states can be divided into measured and unmeasured states as follows:

$$x = \begin{bmatrix} x^m & x^{unm} \end{bmatrix} = \begin{bmatrix} y & x^{unm} \end{bmatrix} \quad (4-1)$$

where x^m denotes the subset of system states directly measured by sensors (i.e., system outputs) and x^{unm} represents the subset of *unmeasured* states of the system.

Then, as can be seen from Figure 4-1, the measured states $x_k^m = y_k$ are fed directly to the series-parallel FDI scheme, while the unmeasured states are first estimated by the

FTO using system inputs and output measurements and then these estimates \hat{x}_k^{unm} are fed as inputs to the bank of NPEs of the FDII module. Accordingly, the equations, the NPE update laws, and the FDI decision logic of the series-parallel FDII scheme have to be slightly modified as follows:

(i) In equation (3-17), y_{k-1} must be replaced by $\begin{bmatrix} x_{k-1}^m & \hat{x}_{k-1}^{unm} \end{bmatrix}$; hence,

$$\bar{y}_k = \begin{bmatrix} \begin{bmatrix} x_{k-1}^m & \hat{x}_{k-1}^{unm} \end{bmatrix} & u_{k-1} \end{bmatrix}^T \quad (4-2)$$

(ii) In equation (3-20), x_{k-1} must be replaced by $\begin{bmatrix} x_{k-1}^m & \hat{x}_{k-1}^{unm} \end{bmatrix}$; hence,

$$\begin{cases} \hat{x}_k^i = f\left(\begin{bmatrix} x_{k-1}^m & \hat{x}_{k-1}^{unm} \end{bmatrix}, u_{k-1}, \hat{\alpha}_{k-1,k}^i\right) \\ \hat{y}_k^i = \hat{x}_k^i \end{cases} ; i = 1, \dots, L \quad (4-3)$$

(iii) The instantaneous output estimation error of the NPEs in equation (3-21) must also be redefined as follows:

$$\tilde{y}_k^i = \begin{bmatrix} x_{k-1}^m & \hat{x}_{k-1}^{unm} \end{bmatrix} - \hat{y}_k^i ; i = 1, \dots, L \quad (4-4)$$

Eventually, (iv) the residual vectors corresponding to the L NPEs in the bank given in equation (3-21) should be redefined as follows:

$$r_k^i = \begin{bmatrix} x_{k-1}^m & \hat{x}_{k-1}^{unm} \end{bmatrix} - \hat{y}_k^i ; i = 1, \dots, L \quad (4-5)$$

The rest of the equations for the weight update laws and the FDI decision logic remain essentially the same as the ones given in Chapter 3 for the series-parallel FDII scheme.

4.2 FDII Using the Parallel Scheme under Partial State Measurements

FDII using the parallel scheme can be accomplished under partial-state measurements using exactly the same principle as the one described for the series-parallel scheme. More

specifically, an FTO is integrated with the parallel NPEs to achieve FDII under partial availability of system states, as depicted in Figure 4-2.

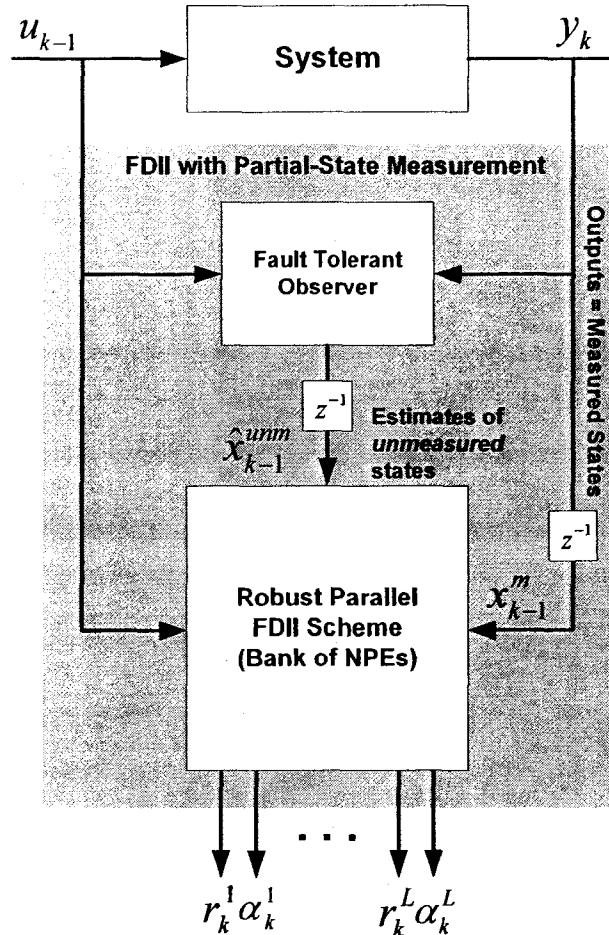


Figure 4-2. The robust parallel FDII scheme under partial-state measurements using the integration of the *hybrid* NPEs and an FTO.

It is important to note that Figure 4-2 looks exactly the same as Figure 4-1, except for the internal structure of the two FDII schemes, which has not been shown in these two figures. More precisely, the difference between the two figures is internal to the FDII blocks and is in the way the vector $\begin{bmatrix} x_{k-1}^m & \hat{x}_{k-1}^{umm} \end{bmatrix}$ is being used within each scheme. The equations (4-2) to (4-5) essentially described how the vector $\begin{bmatrix} x_{k-1}^m & \hat{x}_{k-1}^{umm} \end{bmatrix}$ affects (or is being used in) the equations governing the series-parallel scheme. For the robust parallel

scheme, however, the changes (i) and (ii) mentioned for the series-parallel scheme in equations (4-2) and (4-3) are *not* required and the equations (3-36) to (3-38) still remain valid even in presence of partial state measurements. Indeed, for the robust parallel scheme *only* the instantaneous output estimation error and the residual vector have to be redefined as exactly the same way for the series-parallel scheme shown in equations (4-4) and (4-5), respectively.

The aforementioned FDII schemes under partial state measurements (depicted in Figure 4-1 and Figure 4-2) consist of two main modules, namely the *hybrid* NPEs and an FTO. The design and development of hybrid NPEs was the subject of Chapter 3 and both series-parallel and parallel NPE schemes were thoroughly treated in that chapter. Hence, the focus of the rest of this chapter is on the design and development of an FTO, which enables FDII under partial state measurements.

4.3 Fault Tolerant State Estimation

To the best of our knowledge, the *terminology* of *fault tolerant observer* (FTO) introduced in this thesis appears for the first time in the literature. Though, the *concept* has been previously proposed and fairly well investigated under the terminology of *unknown input observers* (UIO). The UIOs have the capability of estimating the states in presence of unknown inputs. The unknown inputs may include certain immeasurable input signals of the system, uncertainties of certain parameters of the system, modeling errors, external/environmental disturbances, and even faults.

Many researchers have successfully designed and developed a variety of UIOs for both linear and nonlinear systems. For example, Darouach *et al.* [134] presented a full-order Luenberger observer for linear systems with unknown inputs. Based on a consensus

in the UIO literature, one of the first direct extensions of the linear UIO to the non-linear case was proposed by Wunnenberg [135]. His approach was referred to as the NUIO (nonlinear UIO) and was applicable to a specific class of nonlinear systems, where nonlinearity is a function of only inputs and outputs. However, this class of nonlinear systems is rather limited and many physical systems cannot be modeled as such. Moreover, it is also very difficult to transform a general nonlinear system into this required form.

In other efforts to nonlinear UIO, Koenig and Mammar [136] designed a reduced-order nonlinear UIO for robust fault detection in a class of nonlinear systems, where both linear and nonlinear terms are present. Their approach essentially extends the UIO-based *robust fault diagnosis* in linear systems to nonlinear system. Pertew *et al.* [137] developed an unknown input observer for nonlinear systems using H_∞ approach. However, they consider modeling errors and system disturbances as *unknown* inputs, hence designing a *robust* rather than a *fault tolerant* observer. More recently, Koenig [138] developed a nonlinear observer for descriptive type of nonlinear systems with unknown inputs based on linear matrix inequality (LMI) approach. Finally, in a very recent work, Mondal *et al.* [139] proposed a full-order Luenberger-like UIO for a class of nonlinear systems with both linear and nonlinear terms, whose nonlinear function satisfies Lipschitz conditions. Once again, however, their proposed UIO is more like a robust observer with potential applications in robust control.

Considering faults as *unknown inputs* to the system, the UIOs can be designed to provide state estimates that are *decoupled* from faults. Nonetheless, as implied by the short survey in the above, UIOs have been mainly designed within the context of robust

control and robust fault diagnosis, in which modeling uncertainties and external disturbances – rather than faults – are modeled as unknown inputs. Accordingly, the objective had been to make the control and/or fault diagnosis system *robust* with respect to these unknown (uncertain) inputs (i.e., modeling errors and external disturbances). This is clearly different from our objective of designing a FTO described at the beginning of this chapter.

In this thesis, we do not use UIOs to design a FTO. In fact, we do not even take a deterministic approach to state estimation known as “observer design” in the literature. Instead, we follow a stochastic approach to state estimation, better known as “*filter design*” or simply “*filtering*”. More specifically, we take a *hybrid* approach to FTO design by simultaneously exploiting the model-based optimal filtering theory and the self-adapting and self-learning capabilities of computational intelligence (CI) techniques especially neural networks to achieve *fault tolerance* in state estimation.

Hence, we start first by defining the state estimation (or filtering) problem in nonlinear dynamical systems. We then review the optimal filtering theory within two separate frameworks, namely probabilistic and statistical, and review a few methods within each. We will then explore how the exclusive capabilities of CI techniques are employed within each framework to nonlinear filtering problem. Eventually, a fault tolerant state estimation solution based on the *prediction-correction* structure of the Kalman filter and adaptive learning and nonlinear approximation capability of neural networks will be presented. The proposed solution is called the Kalman filter structure preserving neural state estimator (NSE). It should be noted, however, that the structure of the proposed NSE solution has been taken from the *robust optimal filtering* literature and

is not a contribution of this thesis. Rather, it is the *novel* recursive weight update laws of the NSE that comprises one of the contributions of this thesis. Moreover, the use of this NSE as a fault tolerant observer has not also been previously reported in the literature.

4.4 State Estimation of Nonlinear Dynamical Systems

The problem of estimating the states of a stochastic dynamical system from noisy observations is of central importance in engineering. The optimum estimation has been a focus of research in signal processing and control since the pioneering works of Weiner [140] and Kolmogorov almost half a century ago [141]. However, our purpose is not to give a historical account of the development of the estimation theory. Thus, we will focus on the definition of the state estimation problem and demonstrate the two fundamentally different mathematical frameworks for solving this problem. We will also show how the exclusive nonlinear approximation capability of neural networks can be exploited as a tool for nonlinear estimation within each framework.

Problem Definition [49], [141]: Consider the discrete-time stochastic dynamical system described by the stochastic vector difference equation:

$$x_{k+1} = f(x_k) + \Gamma(x_k)w_k \equiv F(x_k, w_k), \quad k = 0, 1, \dots \quad (4-6)$$

where $x_k \in \mathfrak{R}^n$ is the state vector at time-step k , $f: \mathfrak{R}^n \rightarrow \mathfrak{R}^n$ is a vector field representing the nominal nonlinear system dynamics, $\{w_k, k = 0, 1, \dots\}$ denotes the process noise sequence (or external disturbance from control engineering perspective), Γ is a vector-valued function representing the state-dependent channel through which the process noise affects the system states, and F is a vector-valued function representing the collective effect of the system dynamics and the process noise on the evolution of

system states in time. The distribution of the initial condition x_0 is assumed given, and it is independent from w_k . Let the discrete, noisy, m -vector observations (measurements) y_k be given by

$$y_k = h(x_k) + v_k, \quad k = 1, 2, \dots \quad (4-7)$$

where $h: \mathcal{R}^n \rightarrow \mathcal{R}^m$ denotes the system measurement function and $\{v_k, k = 0, 1, \dots\}$ is the m -dimensional measurement noise sequence. For simplicity, process noise w_k and measurement noise v_k are assumed to be independent. Generally, in the optimal filtering theory (and development here as well), without loss of generality it is initially assumed that there is no control input u_k acting on the system. It should be noted that this assumption will not alter the generality of the problem and its solution since we always have a complete knowledge of the control input.

Let $Y_l^l = \{y_1, \dots, y_l\}$ be the sequence of observations (or measurements) from system sensors. Given a realization of the sequence of observations, the *discrete-time estimation* problem consists of computing an estimate of x_k based on observations Y_l^l . If $k < l$, the problem is called the discrete-time *smoothing* problem; if $k = l$, it is called the discrete-time *filtering* problem; and if $k > l$, it is called the discrete-time *prediction* problem.

Since most of the health monitoring and FDII systems (especially on-board FDII systems) aim at *on-line monitoring* and identification of the present health state of the system on the basis of current observations and available data, the state estimation problem of interest to FDII is essentially a *filtering* problem. Hence, in subsequent sections we exclusively focus on the filtering problem as a special case of the state

estimation problem. Also, we describe the two different mathematical frameworks for solving the filtering problem, namely *probabilistic* and *statistical* frameworks.

4.4.1 Probabilistically Inspired Approaches to Nonlinear Filtering

This framework is adopted whenever the probability density functions of all the random variables in the system are exactly known. This knowledge enables one to describe completely the uncertainty in the process and measurement noises as well as in the initial state of the system. Thus, all filtering methodologies developed within this framework assume that the process noise w_k and measurement noise v_k of equations (4-6) and (4-7) are both white Gaussian noise sequences; i.e., $w_k \sim N(0, Q_k)$ and $v_k \sim N(0, R_k)$, where $Q_k, R_k > 0$ are positive definite covariance matrices of process and measurement noise, respectively. The estimation (or filtering) problem in probabilistic framework is usually formulated in terms of some optimality criteria such as *maximum likelihood (Bayesian)*, *minimum variance* or *minimum mean square error*, etc.

It is well-known in the estimation literature that the *conditional probability density* function of x_k given observation sequence $Y_1^k = \{y_1, \dots, y_k\}$, which is written as $p(x_k | Y_1^k)$, is the complete *optimal* solution to the filtering problem. The reason is that this conditional density contains all the necessary statistical information about x_k that exists in the available observations and the initial condition $p(x_0)$.

In the special case of linear filtering problem, where both functions f and h in equations (4-6) and (4-7) are linear (i.e., f, h are matrices of dimensions $[n \times n]$, $[m \times n]$, respectively), the proposed conditional probability density is Gaussian. This is due to the

fact that linear transformation of a Gaussian random variable is always Gaussian (see Papoulis and Pillai [142]). Therefore, the state of the system can be completely represented by its mean vector and covariance matrix. Then, the optimal solution to the filtering problem would be the Kalman filter which gives the recursive equations of the evolution of the conditional mean as the optimal estimate and the covariance matrix as a representative of our confidence in the goodness of the estimates. Nonetheless, in the general nonlinear case the situation is far more difficult. This is mainly due to the fact that the nonlinear transformation of a Gaussian random variable is not necessarily Gaussian. Therefore, the conditional density function cannot in general be characterized by a finite set of parameters like mean and covariance. In other words, in the linear filtering problem the dimension of filter state space (i.e., filter order) is finite and the elements of the mean vector and the covariance matrix comprise the states of the filter. However, in the nonlinear case the filter order is infinite, that is the whole conditional density function needs to be estimated.

Although the conditional density function provides the complete solution to the optimal filtering problem, there still remains this question that what statistics, like the mode, the mean or the median, of that density function should be regarded as the state estimate. To answer this question we need to define a criterion that will let us compare the different possible estimates. Clearly the best criterion would be the estimation error defined as

$$\tilde{\mathbf{x}}_k = \mathbf{x}_k - \hat{\mathbf{x}}_k \quad (4-8)$$

Now, a good estimate would be the one with a small estimation error itself or a small statistical measure of the error. So we need to define a loss or cost function $J(\tilde{\mathbf{x}}_k)$ in

terms of the estimation error. A very well known cost (or loss) function in the literature is the quadratic form given as follows:

$$J(\tilde{x}_k) = \tilde{x}_k^T S \tilde{x}_k \quad (4-9)$$

where $S \geq 0$ is a positive semi-definite matrix. The estimate that minimizes the average or expected loss, $E\{J(\tilde{x}_k)\}$, for a quadratic cost function given in (4-9) is called the *minimum variance* or *minimum mean square error* estimate. It can be shown (see Jazwinski [141]) that the conditional mean of the state vector, namely $E\{x_k | Y_1^k\}$, is the minimum variance estimate for *all* filtering problems, regardless of the conditional probability density function of the state $p(x_k | Y_1^k)$. Thus the optimal estimate, in the sense of minimum error variance is as follows:

$$\hat{x}_k = E\{x_k | Y_1^k\} \quad (4-10)$$

It should be noted that the minimum variance estimate given in the above is an *unbiased* estimate.

Based on the discussions so far, it can be concluded that in the probabilistic approach to filtering, the main objective is to determine the *conditional density function* of the state $p(x_k | Y_1^k)$, based on which the optimal estimate (the mean, the mode, the median, etc.) can be calculated for any desired loss function. However, as was mentioned previously, determination of the equations of evolution of the probability density function, in general, entails the derivation of the update equations of a filter with infinite-dimensional state space, except for some special cases like filtering of linear systems with Gaussian distributions. Thus, in general, it is not computationally feasible to determine

the equations of evolution of $p(x_k | Y_1^k)$. As an approximate remedial solution, however, one may directly use the *conditional mean instead of the conditional density function* and try to find its equations of evolution to end up with the minimum variance estimate of the state. Further details of this approach are out of the scope of this thesis but the interested reader may refer to Jazwinski [141] and Haykin *et al.* [143].

In the next section, the statistical approach to the filtering problem and its connection with the probabilistic framework will be presented. Also, it will be shown as how the statistical framework has inspired the use of neural networks in the nonlinear estimation or filtering problem.

4.4.2 Statistically Inspired Approaches to Nonlinear Filtering

In the discrete-time filtering problem defined in Section 4.4, the process noise w_k and the measurement noise v_k can be considered simply as *errors of unknown nature* instead of random variables with predefined distributions. Now assuming \bar{x}_0 as an *a priori* estimate of the initial state x_0 , we wish to estimate the state sequence $\{x_0, \dots, x_N\}$ based on the observation sequence $\{y_0, \dots, y_N\}$ so that the errors in the state and observations are small. Taking the classical *least squares* approach, we have to minimize the cost function J_N given in the following with respect to $\{x_0, \dots, x_N; w_0, \dots, w_N\}$

$$J_N = \frac{1}{2} \|x_0 - \bar{x}_0\|_{P_0}^2 + \frac{1}{2} \sum_{k=1}^N \|y_k - h(x_k)\|_{R_k}^2 + \frac{1}{2} \sum_{k=1}^N \|w_k\|_{Q_k}^2 \quad (4-11)$$

subject to the constraint

$$x_{k+1} = F(x_k, w_k), \quad k = 0, 1, \dots, N-1 \quad (4-12)$$

where F is the vector-valued function in equation (4-6), and P_0 , R_k , and Q_k are some positive definite *weighting* matrices; quantitatively representing our belief in the *a priori* estimate of the initial condition, the measurement equation (i.e., equation (4-7)), and the nominal noise-free dynamical system model (i.e., equation (4-6) without the additive process noise and with only the function f), respectively. The reason for the last term in equation (4-11) being an indication of our belief in the nominal dynamical system model is due to the fact that the process noise w_k may represent an error in modeling the dynamical system via the state equation (4-6).

It is evident from equation (4-11) that the minimization of the cost J_N requires *all* observations up to time N ; thus the memory as well as computational requirements of solving the least squares minimization is growing linearly with time making it unfeasible for real-time implementations. One way to overcome this drawback is to solve the minimization of J_N in a recursive form, which is called the *recursive least squares*. In this procedure the minimization of J_{N+1} would be done based on the current observation y_{N+1} and the solution to the minimization problem of J_N , namely \hat{x}_N . In other words, an evolution equation of \hat{x}_k would be derived in the form of a difference equation with the current observation y_k as a forcing term. As discussed later in Sections 4.6.2 and 4.7, this constitutes one of the conceptual inspirations for the structure of the neural state estimator (or neural filter) originally proposed by Parisini and Zoppoli [146], and enhanced and employed as an FTO in this thesis.

However, another way of resolving the computational limitation of the original least squares is through limiting the filter memory to a window of size N containing only the

last N observations $Y_{k-N+1}^k = \{y_{k-N+1}, \dots, y_k\}$. To the best of our knowledge, this concept of *limited memory filtering* was originally proposed and rigorously derived in the late 1960's by Jazwinski [147]. However, his main intention was to solve the problem of filter divergence in extended Kalman filter (EKF) in presence of modeling uncertainties. Nevertheless, the concept of limited (or finite) memory filtering has later been followed by many researchers in the field. For example, Houacine [131] proposed regularized fast recursive-least squares algorithms for finite memory filtering; Manolakis *et al.* [144] also proposed efficient time-recursive least-squares algorithms for finite-memory adaptive filtering; and Niedzwiecki [145] proposed a multiple-model approach to finite memory adaptive filtering.

Before concluding this section, it is necessary to imply the connection between the probabilistic and the statistical frameworks. This necessity comes from the fact that although statistical approach is conceptually and theoretically simpler than the probabilistic one, the meaning and interpretation of its results is more difficult. Hence, once a probabilistic interpretation of the statistical methods is made, which is basically the connection between the two frameworks, they could be set as formal approaches to the estimation problem. This connection was implicitly made by Jazwinski in his book [141], where he mentioned that the discrete least squares approach is equivalent to maximizing the conditional probability density function

$$p(x_0, \dots, x_N | y_1, \dots, y_N) \quad (4-13)$$

with respect to $\{x_0, \dots, x_N\}$, provided that Γ in equation (4-6) is independent of the state vector x_k . This is obviously the case for simple additive process noise assumption, which is a valid assumption for many practical systems (i.e., in many systems the channel over

which the disturbance affects the system states can be sufficiently accurately modeled as simply a gain). In the probabilistic framework the estimation based on the maximization of (4-13) is called *joint maximum likelihood (Bayesian)* estimation. Furthermore, the maximum likelihood (Bayesian) estimate is the same as the minimum variance estimate, proposed in Section 4.4.1, provided that the density function of the state is *unimodal* and concentrated near the mode, as in for example, the Gaussian distribution.

4.5 Model-based State Estimation

The renowned Kalman filter provides a model-based recursive solution to the *linear* optimal filtering problem. It is, in fact, the *minimum mean-square (variance) estimator* of the states of a linear dynamical system. However, most physical systems are inherently nonlinear in nature. In consequence, a number of extensions of the Kalman filter to dynamical systems with nonlinear model have been proposed in the literature. The extended Kalman filter is basically the most well-known of all, which is, indeed, an industry standard technique for nonlinear filtering. The EKF extends the use of Kalman filter to nonlinear systems through a linearization procedure. However, unlike its linear counterpart, it is *not* an optimal estimator. In addition, the EKF may quickly diverge if the initial state estimation error is relatively large (i.e., the initial estimate of the state is very different from the actual initial conditions of the system). More importantly, any modeling errors or parameter variations in the system may make the EKF to quickly diverge, owing to its linearization procedure.

Unscented Kalman filter (UKF) is a more recent extension of the Kalman filter to nonlinear systems. Instead of linearization, the UKF uses a deterministic sampling technique known as the *unscented transform* to extend the KF to nonlinear dynamical

models. Both EKF and UKF algorithms were referred to on various occasions in Chapters 1 to 3 of the thesis (e.g., state estimation for residual generation in nonlinear systems, nonlinear parameter estimation, etc.). Accordingly, their corresponding references in the literature were also provided. Nevertheless, Haykin [49] provides the details of the two techniques (and also the particle filters as another model-based nonlinear filtering method) and very well describes the specific advantages and disadvantages of each.

The point that must be strongly emphasized is that the model-based filtering methods such as the EKF and the UKF, though being very well suited for state estimation, do not provide good candidates for implementing a fault tolerant observer. The reason being that the filter equations are all based on the nominal mathematical model of the nominal system, while faults, in general, render these equations invalid. Therefore, once fault occur, the filter equations are no longer valid for the faulty system. Furthermore, there is usually no design freedom left in the EKF and the UKF equations to compensate for this model mismatch during the faulty periods. In fact, the UKF and especially the EKF are not even *robust* to system parameter variations, let alone faults, and very quickly diverge as parameter variations take place. In the next sections, we will observe how the exclusive capabilities of computational intelligence techniques and more specifically, neural networks can be employed to address the issue of filter robustness to faults (and/or parameter variations).

4.6 Learning and Computational Intelligence-based State Estimation

So far we have provided the foundations for optimal filtering and the existing frameworks to solve it. Our goal in this section is to investigate the possible ways of incorporating neural networks as a tool in solution of the optimal filtering problem, in

general, and in addressing the robustness issue of filters, in particular. Computational intelligence and learning-based techniques such as neural networks deal with “approximation” of the nonlinear maps. Equipped with the universal approximation theorem, neural networks have been largely and successfully applied to the very similar problem of nonlinear system identification, being able to produce excellent results.

These excellent results may be attributed to the three important features of neural networks, namely, (i) their nonlinear characteristics that make them suitable for dealing with nonlinear systems, (ii) their parallel and pipeline processing characteristics that allow them to perform different tasks more efficiently, and, the most important of all to our objective of fault tolerance, (iii) their self-learning and self-adapting capabilities that are ideal for adapting to different and possibly unseen environmental conditions (for example, occurrence of faults).

The investigation of the use of neural networks in adaptive filtering is carried out separately for the probabilistic and statistical frameworks. Moreover, the inspirations for each method together with its advantages and drawbacks will be explained. We will finally take the neural state estimation method proposed by Parisini and Zoppoli [146] for real-time, on-line implementation of a fault tolerant observer. The supporting arguments for selecting this specific method will also be provided.

4.6.1 Probabilistically Inspired Approaches to Neural Network-based Filtering

Inspired by the probabilistic approach to nonlinear filtering – described in Section 4.4.1 – and the universal function approximation capability of artificial neural networks, Lo [148] proposed a synthetic approach to optimal filtering problem. As was mentioned in

Section 4.4.1, the optimal solution to the filtering problem would be a filter with the conditional density *function* as its state. It was then argued that since, in general, the conditional density function can not be parameterized by a finite number of parameters, the filter state would be infinite-dimensional and thus computationally unfeasible and impractical. Even in case filter parameters are finite, the analytical derivation of filter equations is, in general, a difficult problem to solve, except for the Gaussian case with the EKF and the UKF as its typical solutions.

As briefly mentioned in Section 4.4.1, one way to overcome this situation is to consider the conditional mean (or any other desired statistics of the conditional density function) as the final solution to the filtering problem. Then, the output of the conditional mean function is used as a point estimate of the state. However, it is still, in general, difficult to derive the analytical filter equations for such an estimator. Hence, approximations to the equations of evolution of the conditional mean are required. In particular, we seek an estimate $\hat{\mu}$ of the conditional mean $\mu(\cdot) = E[x_k | Y_{k-m+1}^k]$ that enables us to calculate the plug-in estimate of x_k as $\hat{x}_k = \hat{\mu}(Y_k^m)$, where $Y_{k-m+1}^k = [y_{k-m+1}, \dots, y_{k-1}, y_k]^T$ denotes the last m observations/measurements of the system.

This is conceptually the main probabilistic point of the method proposed by Lo [148]. Note that it has been implicitly assumed that the filter memory is limited because of practical considerations. Lo tries to estimate the conditional mean by a recurrent multi-layer perceptron (RMLP) neural network. The two main results of his work can be stated as follows [148]:

Consider the n -dimensional random state process x_k and m -dimensional observation process y_k for $k = 0, \dots, T$. Then, defining \hat{x}_k as the network's output at time k , we have:

R.1) Given $\varepsilon > 0$, there exists a sufficiently large RLMP such that

$$\frac{1}{T} \sum_{k=1}^T E \left[\left\| \hat{x}_k - E \left[x_k | Y_1^k \right] \right\|^2 \right] < \varepsilon \quad (4-14)$$

where $Y_1^k = \{y_1, \dots, y_k\}$ are the network's input in the given order.

R.2) If the RMLP has one hidden layer of fully interconnected neurons and the network output is written as $\hat{x}_k(N)$ to indicate its dependency on N , then

$$\bar{x}(N) = \min_W \frac{1}{T} \sum_{k=1}^T E \left[\left\| \hat{x}_k(N) - E \left[x_k | Y_1^k \right] \right\|^2 \right] \quad (4-15)$$

is monotonically decreasing and it converges to 0 as N approaches to infinity. In equation (4-15), W is the set of parameters (or weights) of the neural filter.

The above results state that the proposed RMLP architecture is sufficiently flexible to approximate the desired conditional mean function in mean square sense to an arbitrary degree of accuracy over any given finite set of time steps. Also, the neural filter converges to the minimum variance estimate (i.e., the *conditional mean* $E \left[x_k | Y_1^k \right]$), as the number of fully interconnected hidden neurons increases.

The synaptic weights of such a neural filter are determined by training the network using the input/output data. In other words, the realizations of x_k and y_k are utilized to synthesize the neural filter. Since these realizations are often collected from actual experiments, no specific assumptions about the mathematical models (4-6) and (4-7), or about the distribution of the random variables are required. Therefore, a clear advantage of this method is that no *a priori* knowledge of the state and observation equations is

required other than having *sufficient* data to properly train the RMLP network via dynamic back-propagation (DBP) (see Werbos [149]). Furthermore, unlike many probabilistic approaches, no assumptions such as the states being Markovian or the process and measurement noises being Gaussian are anymore required. Lo [148] showed that his neural filter is significantly superior to the EKF using two types of nonlinear systems as test cases, with one having a chaotic behavior. However, his work also suffers from the following drawbacks:

1. Given a finite training set, there is no guideline for selecting an appropriate size of the hidden layer neurons to yield the best generalization performance.
2. The optimization or training methods used are not well suited for the incremental learning required in a non-stationary or time-varying environment (due to, for example, occurrence of faults).
3. The operating time, T , of the filter is not always known beforehand in many applications (for example, on-line health monitoring and diagnosis).

Clearly, the last two drawbacks significantly confine the application of this neural filter to FTO design and consequently to on-line FDII under partial-state measurement.

4.6.2 Statistically Inspired Approaches to Neural Network-based Filtering

In view of the shortcomings of the Lo's work as mentioned above, this section presents two statistically inspired neural filters that are more compatible with the requirements and specifications of a fault tolerant state estimator.

First is the so-called *finite-memory neural estimator* originally proposed by Alessandri *et al.* [150]. This neural filter is basically a least-squares limited memory

filter. Assuming a nonlinear dynamical system governed by equations (4-6) and (4-7) and with known control inputs u_k , the filter design starts with considering the non-quadratic generalization of the classical least squares loss criterion (or cost function) evaluated over the finite length of a sliding window in order to limit the memory of the filter

$$J_k = \chi(\|\hat{x}_{k-N,k} - \hat{x}_{k-N,k-1}\|) + \sum_{i=k-N}^k \varphi\left[\|y_i - (h(\hat{x}_{i,k}) + \hat{v}_{i,k})\|\right] + \sum_{i=k-N}^k \varphi_1(\|\hat{v}_{i,k}\|) + \sum_{i=k-N+1}^k \psi\left[\|\hat{x}_{i,k} - F(\hat{x}_{i-1,k}, \hat{w}_{i-1,k}, u_{i-1})\|\right] + \sum_{i=k-N}^{k-1} \psi_1(\|\hat{w}_{i,k}\|), \quad k = N, N+1, \dots \quad (4-16)$$

where $N \geq 1$ is the number of measurements made within the sliding window, and $\hat{x}_{i,k}$, $\hat{w}_{i,k}$ and $\hat{v}_{i,k}$ are the estimates of the states, the process noise, and the measurement noise, at time-step k , respectively. The estimates are obtained using the measurements $Y_{k-N}^k = \{y_{k-N}, \dots, y_k\}$, the control inputs $U_{k-N}^{k-1} = \{u_{k-N}, \dots, u_{k-1}\}$, and the *a priori* estimate of \hat{x}_{k-N} , (i.e., $\hat{x}_{k-N,k-1}$). The scalar functions χ , φ , φ_1 , ψ , and ψ_1 are increasing functions for positive values of their arguments, all equal to zero at zero values of their respective arguments; i.e., $\chi(0) = \varphi(0) = \varphi_1(0) = \psi(0) = \psi_1(0) = 0$. These functions have to be regarded as penalty functions by which we express our confidence in the *a priori* estimate $\hat{x}_{k-N,k-1}$, in the observation model (equation (4-7)), in the state equation model (equation (4-6)), and in the magnitudes of the measurement and the process noises, respectively.

Defining the information vector at time-step k – based on which the new estimates will be evaluated – as

$$I_k^N = \text{col}(\hat{x}_{k-N,k-1}, y_{k-N}, \dots, u_{k-N}, \dots, u_{k-1}) \quad (4-17)$$

and considering *estimation functions* of the forms $\hat{x}_{i,k} = \mu_{i,k}(I_N^k)$, $\hat{w}_{i,k} = \xi_{i,k}(I_N^k)$, $\hat{v}_{i,k} = \eta_{i,k}(I_N^k)$, Alessandri *et al.* [150] first state the nonlinear state estimation problem as that of finding the *optimal estimation functions*

$$\begin{cases} \hat{x}_{i,k}^o = \mu_{i,k}^o(I_N^k), i = k - N, \dots, k \\ \hat{w}_{i,k}^o = \xi_{i,k}^o(I_N^k), i = k - N, \dots, k - 1 \\ \hat{v}_{i,k}^o = \eta_{i,k}^o(I_N^k), i = k - N, \dots, k \end{cases} \quad (4-18)$$

that minimize the cost function in (4-16) for $k = N, N + 1, \dots$.

However, they argue that the solution to the above statement of the filtering problem entails solving a nonlinear non-quadratic functional optimization problem (see Zoppoli *et al.* [151]), in which the unknowns are the optimal estimation functions. Clearly, such a functional optimization problem cannot, in general, be solved analytically. However, the universal function approximation capability of neural networks is utilized to resolve this issue in an approximate way. More precisely, to make the optimization feasible for on-line applications, they *approximate* the optimal estimation functions in equation (4-18) MLP neural networks thus reducing the functional optimization problem to a nonlinear programming problem (i.e., the optimization of the neural weights). They also derived a *simplified* structure of the optimal estimation functions of equation (4-18) in order to make them appropriate for the use of nonlinear approximators such as neural networks. The simplification was performed using a *proposition* stated in [150], which was based on the global implicit function theorem. Further details of this proposition can be found therein. Finally, the *finite-memory state estimation* problem is reinstated as that of finding the following *suboptimal* neural estimation functions:

$$\begin{cases} \hat{x}_{k-N} = \bar{\mu}_{k-N} (I_N^k, W_{k-N}^1) \\ \hat{w}_i = \bar{\xi}_i (\hat{x}_i, Y_{i+1}^k, U_i^{k-1}, W_i^2), i = k-N, \dots, k-1 \\ \hat{v}_i = \bar{\eta}_i (\hat{x}_i, y_i, W_i^3), i = k-N, \dots, k \end{cases} \quad (4-19)$$

where W_{k-N}^1 , $W_i^2, i = k-N, \dots, k-1$, and $W_i^3, i = k-N, \dots, k$ are the set of parameters (or weights) of the suboptimal neural estimation functions, and $Y_{i+1}^k = \{y_{i+1}, \dots, y_k\}$. Careful comparison of equations (4-18) and (4-19) indicates that the suboptimal estimation functions differ from the optimal ones in two ways: (i) due to the aforementioned *simplification*, the dimension of the input spaces of the optimal estimation functions are reduced in the suboptimal ones, thus making them simpler to be approximated by neural estimators (the *curse of dimensionality*) and (ii) the suboptimal estimation functions are now parameterized, where the optimal *parameters*, rather than the *functions*, have to be found as a solution to the filtering problem. Figure 4-3 depicts the *suboptimal* finite-memory neural state estimator for a sliding window of $N = 2$.

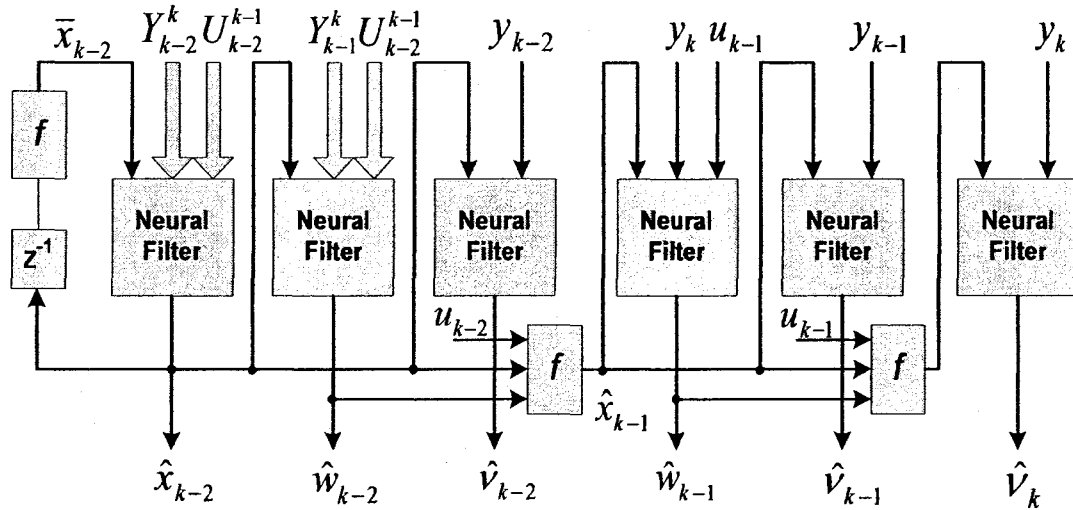


Figure 4-3. The block diagram of the finite-memory neural state estimator [150] for sliding window of length $N=2$.

The weight optimization (or training) of the neural approximating functions in equation (4-24) is achieved in two phases: 1) optimization at time step $k = N$, which is called *off-line initialization* (OFI) procedure and 2) optimization at time steps $k = N + 1, N + 2, \dots$, which is called the *on-line adaptation* (ONA) procedure. The OFI is used to exploit all *a priori* available information on the statistics of the random variables in the system, like the initial state x_0 and the process and the measurement noises. During the ONA phase the neural weights will be confirmed (in case of a known stationary environment) or *adapted* (in case of a stochastic non-stationary environment such as occurrence of faults).

Alessandri *et al.* [150] have also shown through numerous simulations that the finite-memory neural filter described in the above significantly outperforms the EKF filter, especially in presence of variations in nominal system parameters. In other words, the finite-memory neural filter is much more robust to model parameter variations than the EKF. Hence, it can be considered as a potential solution to the fault tolerant observer design problem. Nonetheless, this filtering technique has *not* been selected for FTO implementation in this thesis due to following four reasons:

1. It is computationally heavy due to a relatively large number of neural filters required to implement the filter. This can also be seen from Figure 4-3, where the scheme consists of six neural filters for a window length of only $N = 2$.
2. The large number of neural filters makes the fine-tuning of the finite-memory filter time-consuming and complicated.
3. The filter optimization involves two phases, where each stage usually requires a specific set of parameter values. This even makes the number of algorithm parameters bigger and thus tuning the algorithm more difficult.

4. Though the window length often considerably affects filter performance, there are no rigorous guidelines as how to set its value.

The above limitations enforce us to resort to another slightly less powerful, yet computationally simpler, neural state estimation method proposed by Parisini and Zoppoli [146]. They were basically inspired by the solution to the linear quadratic (LQ) optimal control or estimation problem in a statistical context. It is well known that under the LQ assumptions, the optimal least squares estimate \hat{x}_k^o of the states x_k of a linear dynamical system can be obtained by the following recursive equation, called linear recursive least squares (RLS)

$$\begin{cases} \hat{x}_k^o = x_k^- + K_k (y_k - H_k x_k^-), & k = 0, 1, \dots, N-1 \\ x_0^- = E\{x_0\} \end{cases} \quad (4-20)$$

where x_k^- is the one-step state prediction and K_k is a time-varying gain matrix determined at each time step by means of a suitable model-based recursive equation. Indeed, the optimal linear least squares minimizes the cost function

$$J_k = \|x_0 - \bar{x}_0\|_M^2 + \sum_{k=0}^N \|y_k - H_k x_k\|_{V_k}^2 + \sum_{k=1}^N \|x_k - A_{k-1} x_{k-1}\|_{T_{k-1}}^2 \quad (4-21)$$

with respect to $\{x_0, \dots, x_N\}$, where \bar{x}_0 is an *a priori* estimate of the initial state x_0 ; and M , V_k , and T_{k-1} are positive definite symmetric matrices. It should be noted that the cost in (4-21) is a special case of the more general cost function given in (4-11) with linear dynamical model equations.

It should also be noted that the optimal linear RLS is actually the statistical counterpart of the standard Kalman filter that was originally developed in the probabilistic framework to optimal filtering. Indeed, a very interesting relationship exists

between the two filters. More specifically, if the matrix M in equation (4-21) is chosen as the inverses of the initial covariance matrix; V_k and T_k in equation (4-21) are selected as the inverse of the measurement noise covariance and the process noise covariance, respectively; and the initial state and the noises are mutually independent and Gaussian, the linear RLS estimator and the Kalman filters coincide with each other.

4.7 Kalman Filter Structure Preserving Neural State Estimator (NSE)

To solve the filtering problem for nonlinear dynamical systems, Parisini and Zoppoli [146] used the so-called concept of “linear-structure preserving principle” (LISP), which is designed to imitate the structure of an optimal linear RLS or similarly the standard Kalman filter. It can briefly be stated as follows [146]:

Once the LQ structure has been found, maintain the same linear structure that implements the solution to the LQ problem. Then: (a) replace the linear state equation and the linear observation channel with the ones appearing in the original non-LQ problem, and (b) replace the filter gain matrix with a nonlinear mapping, which becomes the unknown of the new non-LQ problem.

Thus, the linear state prediction (as well as measurement prediction) is replaced by a nonlinear one, using the *exact* nonlinear dynamics of the system. Furthermore, the filter gain matrix is replaced by a parameterized nonlinear function that is a function of the prediction error. For the parameterized nonlinear function, we use an MLP neural network with neural weights as the parameters that are continuously adapted; hence the name Kalman filter structure-preserving neural state estimator (NSE). To sum up, the recursive state equations of the NSE are as follows:

$$\begin{cases} \text{Prediction Step: } \hat{x}_k^- = f(\hat{x}_{k-1}, u_{k-1}) \\ \text{Correction Step: } \hat{x}_k = \hat{x}_k^- + g(e_k^-, W_k^{obs}, V_k^{obs}) \end{cases} \quad (4-22)$$

With the output equation defined as:

$$\hat{y}_k = h(\hat{x}_k) = H \hat{x}_k \quad (4-23)$$

where $e_k^- = y_k - \hat{y}_k^- = y_k - h(\hat{x}_k^-)$ is the prediction error, $g(e_k^-, W_k^{obs}, V_k^{obs})$ is a multilayer feed-forward neural network with prediction error e_k^- as the input and with sigmoidal activation functions for the hidden-layer neurons and linear neurons in the output layer. The parameters W_k^{obs} and V_k^{obs} denote the weights of the output and hidden layers of the network, respectively.

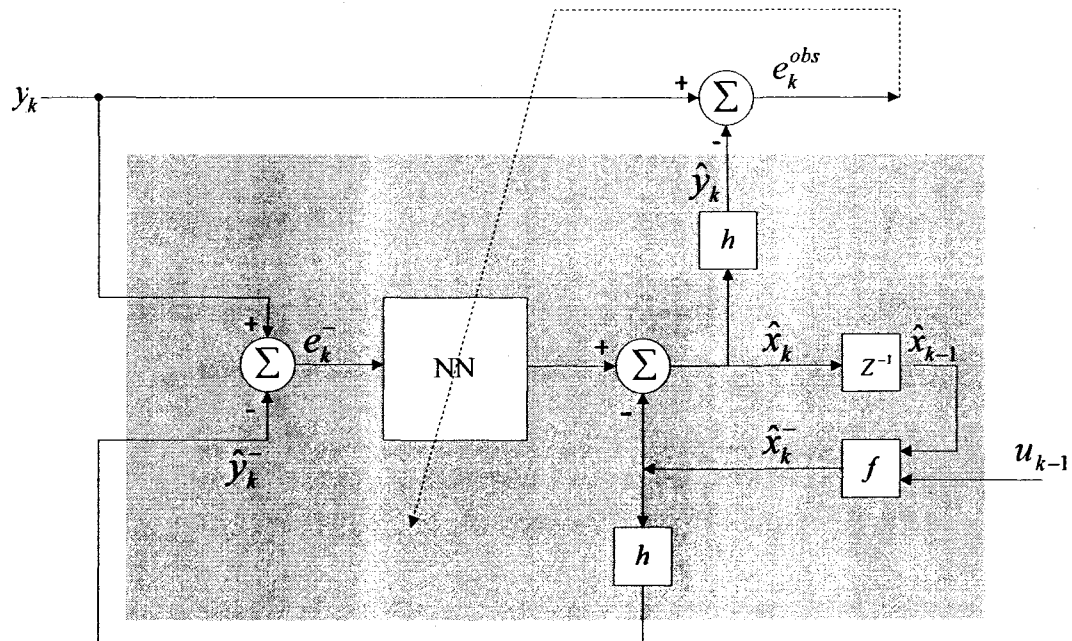


Figure 4-4. The Kalman filter structure preserving neural state estimator (NSE) redrawn with modifications from [146].

The recursive equation of the NSE, given in equation (4-22), can also be compactly written as follows:

$$\hat{x}_k = f(\hat{x}_{k-1}, u_{k-1}) + g(e_k^-, W_k^{obs}, V_k^{obs}) \quad (4-24)$$

The block diagram representation of the Kalman filter structure preserving NSE is shown in Figure 4-4. The only assumption made in this scheme is that the process and measurement noise are zero mean, i.i.d., and mutually independent. Parisini and Zoppoli [146] applied this neural filter to a subclass of *target motion analysis* problems. Simulation results presented therein revealed that this neural filter outperforms the EKF algorithm especially in presence of model uncertainties or model parameter variations. The results showed significant performance gains over the EKF filter, especially in situations that EKF diverges due to numerical instability of the covariance matrix. The other advantage of this recursive scheme is that it does not have the computational complexity issues of the Lo's approach [148] when the observation period is too large or has essentially no *a priori* bound as in on-line health monitoring and fault diagnosis applications. It is extremely important to note that the structure/architecture of the developed NSE is *not* a novelty of this thesis and has been borrowed from Parisini and Zoppoli [146]. However, the development of *new* weight update laws for the NSE comprises another contribution of this thesis, which is the subject of the next section.

4.7.1 Update Laws for the NSE: Recursive On-line Backpropagation

Parisini and Zoppoli [146] update the neural filter weights using the standard backpropagation algorithm. They argued that the neural weight adaptation can be performed according to the following procedure. At time-step $k+1$, a nonlinear optimization is

performed on the set of weights $W_{k+1}^{obs}, V_{k+1}^{obs}$, while freezing the set of k previously computed weights $\{W_i^{obs}, V_i^{obs}\}_{i=1}^k$. However, this optimization philosophy may result in suboptimal performance or even filter divergence due to presence of feedback in the proposed NSE architecture (as can be seen in Figure 4-4, where the neural network output is fed back to its input after passing through system dynamics).

In order to adapt *closed-loop* discrete-time dynamical systems (for example, closed-loop nonlinear controllers and nonlinear infinite impulse response (IIR) filters) using steepest descent, a partial derivative of the associated dynamical system must be calculated. Due to presence of feedback in a dynamical system, the calculation of this derivative can be quite complex. However, Piche [172] correctly argues that the *ordered partial derivative*, which is a partial derivative whose constant and varying terms are defined using ordered set of equations, provides a mathematical tool for easily finding derivatives of complex dynamical systems. The *ordered partial derivative* is further explained in Appendix A.

The neural state estimator depicted in Figure 4-4 is essentially a closed-loop nonlinear dynamical system. Hence, instead of the standard back-propagation algorithm, steepest descent algorithms based on the *ordered partial derivatives* have to be employed for obtaining the most accurate weight update laws of the NSE. This essentially enhances the accuracy, reliability, and robustness of the neural state estimator.

As demonstrated by Piche [172], two class of steepest descent adaptation (or training) algorithms based on ordered partial derivatives can be derived for a general closed-loop nonlinear discrete-time dynamical system with standard representation shown in Figure 4-5. These include: (i) *epochwise training algorithms* and (ii) *on-line training algorithms*.

An *epochwise training algorithm* is any algorithm in which the adaptation takes place after each epoch or after a number of epochs, where an *epoch* is an iteration to iteration cycling of a discrete-time dynamical system from initial to final iteration (i.e., $k = k_f$).

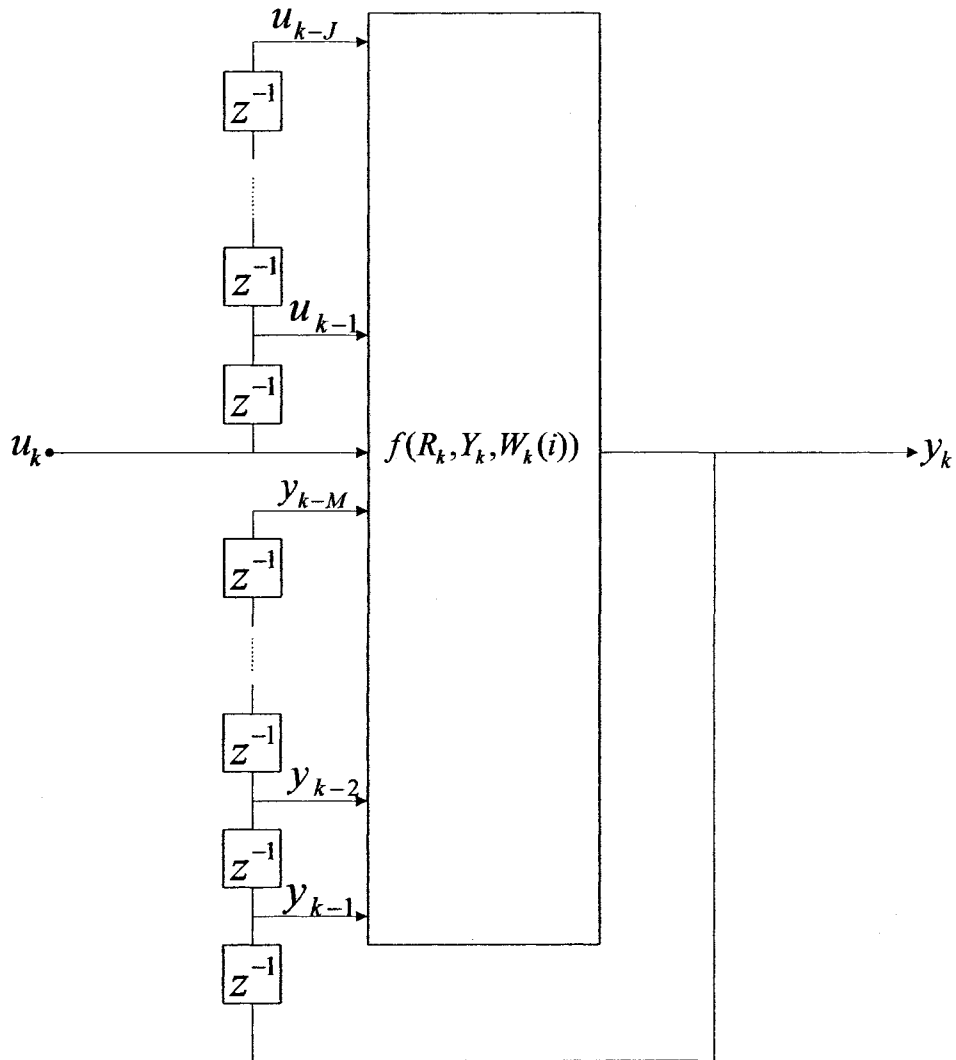


Figure 4-5. The standard representation of a closed-loop nonlinear dynamical system [172].

Epochwise systems are encountered much more frequently in control applications than in filtering applications. Furthermore, the error function in epochwise systems is

usually defined as the *cumulative* error between the desired values and the outputs of the adaptive dynamical system as follows:

$$E = \sum_{k=0}^{k_f} \frac{1}{2} (d_k - y_k)^T (d_k - y_k) \quad (4-25)$$

where k_f is the terminal time, d_k is the desired response and y_k is the output of the adaptive closed-loop nonlinear dynamical system as depicted in Figure 4-5.

Utilizing steepest descent, epochwise algorithms update the weights using [172]:

$$W(i+1) = W(i) - \eta \frac{\partial^+ E}{\partial W(i)} \quad (4-26)$$

where η is the learning rate, i is the index of the current epoch, and $\partial^+ E / \partial W(i)$ is the *ordered partial derivative* of the error in equation (4-24) with respect to the weight vector at the i th epoch. Nonetheless, the epochwise adaptation algorithms are not suitable for real-time implementation of adaptive filters. Hence, these algorithms are *not* of interest for derivation of update laws for the neural state estimator required for on-line FDII under partial state measurements.

On the other hand, *on-line training algorithms* can be used for both adaptive control and filtering applications [172]. In adaptive control and filtering applications, on-line training allows a controller or a filter to either adapt to unknown plant characteristics or track slow changes in plant dynamics. On-line training also enables real-time implementation of adaptive controllers and filters. In on-line adaptation algorithms, the error is usually defined at each iteration as the instantaneous error between the desired response and the output of the adaptive system:

$$e_k = \frac{1}{2} (d_k - y_k)^T (d_k - y_k) \quad (4-27)$$

where k is the current time step (or iteration) of the discrete-time dynamical system. Using the error in equation (4-26), the *on-line training algorithms* update the weights at each time step k . However, calculation of the exact *ordered partial derivative* of the error with respect to the weight vector (i.e., error gradient) is not possible. Instead, an approximation of the error gradient must be used to update the weights. Therefore, the on-line update rule at time step k is expressed as [172]:

$$W_{k+1} = W_k - \eta \frac{\partial^+ \widehat{E}_k}{\partial W_k} \quad (4-28)$$

where $\partial^+ \widehat{E}_k / \partial W_k$ is the approximate error gradient.

According to Piche [172], two versions of *on-line training algorithms* exist including: (i) on-line backswep algorithm and (ii) on-line recursive algorithm. Among the two, the on-line *recursive* algorithm can be used to adapt the weights of the neural network IIR filters and controllers. Using the on-line recursive algorithm for the standard representation of a closed-loop nonlinear dynamical system, depicted in Figure 4-5, the approximate error gradient in equation (4-27) can be calculated as follows [172]:

$$\frac{\partial^+ \widehat{E}_k}{\partial W_k} = -(d_k - y_k)^T \frac{\partial^+ y_k}{\partial W_k} \quad (4-29)$$

where the *approximate* output derivative $\partial^+ y_k / \partial W_k$ is *recursively* calculated as:

$$\frac{\partial^+ y_k}{\partial W_k} = \frac{\partial y_k}{\partial W_k} + \sum_{m=1}^M \beta^m \frac{\partial y_k}{\partial y_{k-m}} \frac{\partial^+ y_{k-m}}{\partial W_{k-m}} \quad (4-30)$$

where $0 < \beta < 1$.

Since recursive learning is well-suited for real-time applications such as on-line health monitoring and FDII, in this thesis the recursive on-line back-propagation

algorithm based on equations (4-28) and (4-29) is used to derive the weight update laws of the Kalman filter structure preserving NSE.

First, let's define the observer error as:

$$e_k^{obs} = y_k - \hat{y}_k \quad (4-31)$$

where y_k denotes the outputs (i.e., the measured states) of the system and \hat{y}_k are the output estimates from the FTO (i.e., the NSE). Then, using the observer error in equation (4-31) and equation (4-23), the cost function of the NSE is defined as:

$$J_k^{obs} = \frac{1}{2} \|e_k^{obs}\|^2 = \frac{1}{2} \|y_k - \hat{y}_k\|^2 = \frac{1}{2} \|y_k - h(\hat{x}_k)\|^2 \quad (4-32)$$

Utilizing the *on-line training algorithm*, given in equation (4-27), the weights of the NSE must be updated as follows:

$$\begin{aligned} W_{k+1}^{obs} &= W_k^{obs} - \eta_w^{obs} \left(\frac{\partial^+ J_k^{obs}}{\partial W_k^{obs}} \right) \\ V_{k+1}^{obs} &= V_k^{obs} - \eta_v^{obs} \left(\frac{\partial^+ J_k^{obs}}{\partial V_k^{obs}} \right) \end{aligned} \quad (4-33)$$

where W_k^{obs} and V_k^{obs} are respectively the output layer and hidden layer weights of the NSE, and η_w^{obs} and η_v^{obs} are the learning rates corresponding to the output layer and hidden layer, respectively.

Using equation (4-32), the *approximate* gradient of the cost function with respect to output layer weights W_k^{obs} is as follows:

$$\begin{aligned}
\frac{\partial^+ \widehat{J}_k^{obs}}{\partial W_k^{obs}} &= -e_k^{obs} \cdot \frac{\partial h(\widehat{x}_k)}{\partial \widehat{x}_k} \cdot \frac{\partial^+ \widehat{x}_k}{\partial W_k^{obs}} \\
&= -e_k^{obs} \cdot H \cdot \frac{\partial^+ \widehat{x}_k}{\partial W_k^{obs}} \\
&= -e_k^{obs} \cdot \sum_{j=1}^n h_j \frac{\partial^+ \widehat{x}_k^j}{\partial W_k^{obs}}
\end{aligned} \tag{4-34}$$

Similarly, the *approximate* gradient of the cost function with respect to hidden layer weights V_k^{obs} is as follows:

$$\begin{aligned}
\frac{\partial^+ \widehat{J}_k^{obs}}{\partial V_k^{obs}} &= -e_k^{obs} \cdot \frac{\partial h(\widehat{x}_k)}{\partial \widehat{x}_k} \cdot \frac{\partial^+ \widehat{x}_k}{\partial V_k^{obs}} \\
&= -e_k^{obs} \cdot H \cdot \frac{\partial^+ \widehat{x}_k}{\partial V_k^{obs}} \\
&= -e_k^{obs} \cdot \sum_{j=1}^n h_j \frac{\partial^+ \widehat{x}_k^j}{\partial V_k^{obs}}
\end{aligned} \tag{4-35}$$

Now, utilizing the on-line *recursive* algorithm in equation (4-30) for the Kalman filter structure preserving neural state estimator, depicted in Figure 4-4, we have:

$$\begin{cases} \frac{\partial^+ \widehat{x}_k^j}{\partial W_k^{obs}} = \frac{\partial \widehat{x}_k^j}{\partial W_k^{obs}} + \beta \frac{\partial \widehat{x}_k^j}{\partial \widehat{x}_{k-1}} \frac{\partial^+ \widehat{x}_{k-1}}{\partial W_{k-1}^{obs}} \\ \frac{\partial^+ \widehat{x}_k^j}{\partial V_k^{obs}} = \frac{\partial \widehat{x}_k^j}{\partial V_k^{obs}} + \beta \frac{\partial \widehat{x}_k^j}{\partial \widehat{x}_{k-1}} \frac{\partial^+ \widehat{x}_{k-1}}{\partial V_{k-1}^{obs}} \end{cases} ; j = 1, \dots, n \tag{4-36}$$

where $\widehat{x}_k \in \mathcal{R}^n$ is the estimate of the state vector of the system at time step k , \widehat{x}_k^j is the estimate of the j th state of the system, and, once again, $0 < \beta < 1$. It is important to note that M in equation (4-30) is equal to 1 in equation (4-36) of the Kalman filter structure preserving NSE. This is due to the fact that in the NSE architecture, only the last state estimate generated at the output of the NSE, namely \widehat{x}_{k-1} , is fed back to the NSE input, as can also be seen from Figure 4-4. Furthermore, it is very important to note that equation

(4-36) is a *recursive* equation. More precisely, the terms $\partial^+ \widehat{x}_{k-1} / \partial W_{k-1}^{obs}$ and $\partial^+ \widehat{x}_{k-1} / \partial V_{k-1}^{obs}$ on the right-hand side of equation (4-36) are indeed the previously calculated values (i.e., calculated at the previous time step $k-1$) of the *approximate ordered partial derivatives* $\partial^+ \widehat{x}_k / \partial W_k^{obs}$ and $\partial^+ \widehat{x}_k / \partial V_k^{obs}$ on the left-hand side of equation (4-36), respectively.

The terms $\partial \widehat{x}_k^j / \partial W_k^{obs}$ and $\partial \widehat{x}_k^j / \partial V_k^{obs}$ are the partial derivatives of the neural network output at time step k with respect to its weights used at time step k . Hence,

$$\begin{cases} \frac{\partial \widehat{x}_k^j}{\partial W_k^{obs}} = \frac{\partial g_j(e_k^-, W_k^{obs}, V_k^{obs})}{\partial W_k^{obs}} \\ \frac{\partial \widehat{x}_k^j}{\partial V_k^{obs}} = \frac{\partial g_j(e_k^-, W_k^{obs}, V_k^{obs})}{\partial V_k^{obs}} \end{cases} ; j = 1, \dots, n \quad (4-37)$$

These two terms can be easily calculated using the standard back-propagation (BP) algorithm as follows:

$$\begin{cases} \frac{\partial g_j(e_k^-, W_k^{obs}, V_k^{obs})}{\partial W_k^{obs}} = \sigma(V_k^{obs} \cdot e_k^-) \\ \frac{\partial g_j(e_k^-, W_k^{obs}, V_k^{obs})}{\partial V_k^{obs}} = \left(W_{k_j}^{obs} \cdot \left(I - \Lambda(V_k^{obs} \cdot e_k^-) \right) \right)^T e_k^- \end{cases} ; j = 1, \dots, n \quad (4-38)$$

Furthermore, the term $\partial \widehat{x}_k^j / \partial \widehat{x}_{k-1}^i$ in equation (4-36) is defined as follows:

$$\frac{\partial \widehat{x}_k^j}{\partial \widehat{x}_{k-1}^i} \triangleq \left[\frac{\partial \widehat{x}_k^j}{\partial \widehat{x}_{k-1}^1}, \dots, \frac{\partial \widehat{x}_k^j}{\partial \widehat{x}_{k-1}^i}, \dots, \frac{\partial \widehat{x}_k^j}{\partial \widehat{x}_{k-1}^n} \right]; j = 1, \dots, n \quad (4-39)$$

where $\partial \widehat{x}_k^j / \partial \widehat{x}_{k-1}^i$; $j = 1, \dots, n$; $i = 1, \dots, n$ is the (j, i) element of the above matrix. Consider the Jacobian matrix of the nonlinear system in equation (4-6) defined as:

$$F_{k-1} = \frac{\partial f(\hat{x}_k, u_k)}{\partial \hat{x}_{k-1}} = \begin{bmatrix} \frac{\partial f_1(\hat{x}_k, u_k)}{\partial \hat{x}_{k-1}^1} & \cdots & \frac{\partial f_1(\hat{x}_k, u_k)}{\partial \hat{x}_{k-1}^n} \\ \vdots & \ddots & \vdots \\ \frac{\partial f_n(\hat{x}_k, u_k)}{\partial \hat{x}_{k-1}^1} & \cdots & \frac{\partial f_n(\hat{x}_k, u_k)}{\partial \hat{x}_{k-1}^n} \end{bmatrix} \quad (4-40)$$

with the (j,i) element of the Jacobian matrix defined as follows:

$$F_{k-1}^{ji} = \frac{\partial f_j(\hat{x}_k, u_k)}{\partial \hat{x}_{k-1}^i}; \quad j = 1, \dots, n; \quad i = 1, \dots, n \quad (4-41)$$

Then, the (j,i) element of the matrix in equation (4-39) – and correspondingly in equation (4-36) – can be calculated as follows using the definition of the Jacobian matrix in equation (4-41) in conjunction with equation (4-24):

$$\frac{\partial \hat{x}_k^j}{\partial \hat{x}_{k-1}^i} = F_{k-1}^{ji} + W_{k_j}^{obs} \cdot \left(I - \Lambda(V_k^{obs} e_k^-) \right) \frac{\partial e_k^-}{\partial \hat{x}_{k-1}^i} \quad (4-42)$$

where the term $W_{k_j}^{obs} \cdot \left(I - \Lambda(V_k^{obs} e_k^-) \right)$ on the right-hand side of equation (4-42) is the partial derivative of the neural network output with respect to its input, which is obtained using the standard back-propagation algorithm. Furthermore, the partial derivative $\partial e_k^- / \partial \hat{x}_{k-1}^i$ on the right-hand side of equation (4-42) can simply be calculated as follows:

$$\frac{\partial e_k^-}{\partial \hat{x}_{k-1}^i} = \frac{\partial (y_k - h(\hat{x}_k^-))}{\partial \hat{x}_{k-1}^i} = - \frac{\partial h(\hat{x}_k^-)}{\hat{x}_k^-} \cdot \frac{\partial \hat{x}_k^-}{\partial \hat{x}_{k-1}^i} \quad (4-43)$$

where $\partial h(\hat{x}_k^-) / \hat{x}_k^- = H$, assuming the linearity of the output equation.

4.8 Conclusions

The objective of this chapter was to extend the applicability of the two FDII schemes proposed in Chapter 3 under full-state measurement assumptions, to systems with partial state measurement. In order to accomplish this goal, we introduced the notion of fault tolerant observer (FTO) that enables accurate estimation of unmeasured states of the system even in presence of faults or anomalies in the system. It was mentioned that such a fault tolerant state estimator allows us to directly use the same FDII schemes proposed in Chapter 3, but this time with the estimated states instead of the actual measurements for the unmeasured states of the system. Needless to say, the measured states would directly be used as inputs to the FDII scheme. Two FDII schemes under partial state measurements were proposed, which consist of the integration of the series-parallel and the parallel *hybrid* NPEs and a fault tolerant observer. The respective modifications in the weight update laws of both NPE schemes due to this *integration* were also highlighted.

As far as the design of an FTO is concerned, it was noted that in the literature a similar concept has been extensively pursued under the notion of unknown input observers (UIO). A few of the work in the literature on UIO design for nonlinear systems were reviewed. It was argued, however, that the UIOs have been mainly designed within the context of robust fault diagnosis, in which modeling uncertainties and external disturbances – rather than faults – are modeled as unknown inputs. Consequently, it was mentioned that the UIOs have been utilized to make the fault diagnosis system *robust* with respect to these unknown (uncertain) inputs. Hence, instead of UIOs, a stochastic approach to state estimation, better known as “*filtering*”, was selected to design an FTO. More specifically, a *hybrid* approach to FTO design was taken, which simultaneously

exploits the model-based optimal filtering theory and the self-adapting and self-learning capabilities of neural networks to achieve *fault tolerance* in state estimation.

Firstly, the state estimation (or filtering) problem in nonlinear dynamical systems was defined. Then, two distinct frameworks to optimal filtering theory, namely probabilistic and statistical, were reviewed and some of the well-known, important methods within each framework were mentioned and analyzed. The exclusive capabilities of CI techniques as employed within each framework of the nonlinear filtering problem were then explored. Eventually, a fault tolerant state estimation solution based on the *prediction-correction* structure of the Kalman filter and adaptive learning and nonlinear approximation capability of neural networks, known as the Kalman filter structure preserving neural state estimator (NSE), was presented. It was noted that even though the use of this NSE as an FTO is a novelty of this thesis, the structure of the NSE solution itself has been taken from the *robust optimal filtering* literature and is not a contribution of this thesis. However, instead of the standard back-propagation algorithm, a *novel* recursive weight update law for the NSE was derived based on the *on-line recursive back-propagation* algorithm and the concept of *ordered partial derivatives*. It was argued that the use of standard back-propagation algorithm to adapt the weights of the NSE results in suboptimal performance due to presence of feedback in the NSE architecture. More precisely, the newly developed weight update law based on the *ordered partial derivatives* enhances the accuracy and robustness of the neural state estimator. Hence, this novel weight adaptation algorithm constitutes one of the contributions of this thesis.

Chapter 5:

5 Application to a Satellite's Attitude Control Subsystem

Like many other man-made dynamical systems, spacecraft are potentially subjected to unexpected anomalies and failures in subsystems and components during their mission lifetime. Future generations of spacecraft need to show proper reaction to unexpected events such as component/subsystem failures or environmental interactions. Most currently used spacecraft controllers react to different situations according to some, often, hard-coded routines. This is impractical when the spacecraft is facing an unexpected event. On the other hand, the probability of fault occurrence increases with the time needed to accomplish the mission. Hence, the development of technologies that enable the spacecraft to *automatically* detect, isolate, identify and eventually respond and recover from (unexpected) faults/failures in its components, subsystems or mission goals are highly desirable. The main goal of an autonomous operation should be to maintain the spacecraft's safety and to perform the critical functions in priority.

Current methodologies that are utilized in health monitoring of Earth-orbiting satellites and space probes rely heavily on the ground support and operations. Spacecraft telemetry from the orbiting satellites is regularly down-linked to ground stations at appropriate locations and times. At the ground station the trained operators will then

evaluate and analyze a significant amount of data in order to determine the current state as well as the health status of the satellite. This is clearly a time-consuming, labor-intensive operation that is significantly prone to various human-initiated errors and misjudgements. Therefore, *autonomy* in satellite diagnostics and health monitoring is highly desirable in order to have a more efficient and effective operation for all the existing as well as future satellite missions. This *autonomy* can, in general, be achieved in two ways: (i) *on-board* the satellite using an embedded fault diagnosis system that identifies presence of anomalies and reports them to satellite controllers for recovery and/or reconfiguration, and (ii) through a decision support system that can provide informative advise to the operational people regarding the health of the satellite subsystems and components and in them.

The distance may be the most significant factor that makes the existence of an *onboard* autonomy more demanding. The farther the spacecraft is from the ground, the less knowledge is available about its present environment. Also, the distance causes huge delays in communication between the ground and the spacecraft, especially for deep space probes. Fortunately, recent advances in computer hardware and computational techniques have allowed for more tasks to be accomplished onboard the space vehicles. Many of the ground activities such as navigation and maneuver planning; command planning and sequencing; and fault diagnosis and recovery can, to a large extent, be accomplished autonomously onboard spacecraft. More specifically, *onboard* diagnostics enables detection and diagnosis of spacecraft faults in a relatively short period of time, which consequently allows the spacecraft to reschedule its mission and re-allocate its resources to still maintain as many mission objectives as possible.

In conclusion, the advantages of autonomous, especially on-board, health monitoring and fault diagnosis and recovery may be summarized as follows:

- It enables short fault diagnosis delays and consequently faster response times under both normal and faulty situations.
- Significantly reduces the cost of ground-based operations and support especially for long duration missions.
- Eliminates the long round trip delays due to large distance between the spacecraft – especially deep space probes – and the ground.
- Allows continuous operations even in loss of communication with the ground due to the unpredictable events and environment around the space vehicle.

5.1 Spacecraft Subsystems

Satellites are complex engineering systems consisting of various electrical, electromechanical, mechanical, and thermal components/subsystems that continuously interact and cooperate with each other to maintain and successfully accomplish satellite mission objectives.

Monolithic spacecraft are typically divided into seven subsystems including command and data handling (C&DH), attitude determination and control (ADCS), orbital control, navigation and orbital control, power, telemetry and telecommand (T&TC), thermal, and propulsion subsystems. Each subsystem is responsible for performing a specific set of functions. Furthermore, many of these subsystems always communicate with each other to collectively ensure the execution of satellite commands. A highly simplified, yet informative, block diagram of the space segment (counter to ground segment) of a satellite mission, including payload instruments and satellite bus with its

associated subsystems is shown in Figure 5-1. Extensive details to each subsystem can be found in the renowned book of Wertz and Larson [152], known as the Bible of spacecraft mission analysis and design, and also in Brown [153].

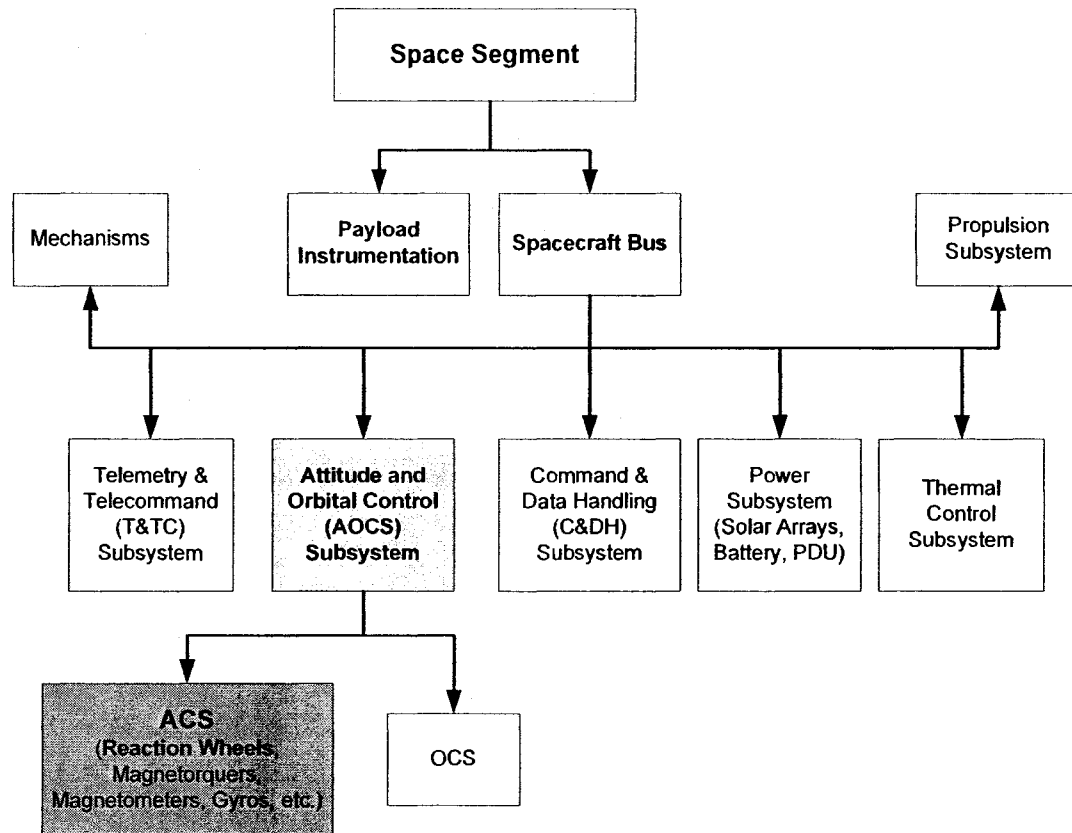


Figure 5-1. A simplified block diagram of the space segment of a satellite, drawn with a number of modifications from Brown [153].

Because of the aforementioned complexity of satellite systems, diverse set of diagnostic autonomy requirements and specifications are often set for a satellite at different levels of abstraction. Hence, to be able to effectively and efficiently address the problem of autonomous fault diagnosis and recovery in spacecraft, one may consider the following hierarchical decomposition of the problem into three levels:

- (i) **Component level:** This involves detection and diagnosis of faults and failures in sensors, actuators, and internal system components of a satellite;

- (ii) **Subsystem level:** This involves dealing with the sequencing of commands and events in between the satellite subsystems (such as the attitude control subsystem (ACS), propulsion, thermal, GNC, communication, power, etc.) and the impact of faults at this level; and
- (iii) **Mission level:** This involves all the activities that are related to the overall mission safety and objectives/goals that lead to re-scheduling and/or re-planning of the satellite mission – if needed – due to occurrence of faults/failures.

Indeed, hierarchical FDIR concept is being currently pursued by most of the world's renowned space agencies. For example, European Space Agency has put into place their own hierarchical FDIR architecture, consisting of four levels, to support the overall spacecraft system autonomy during both normal operations (“nominal autonomy”) and during off-nominal operations (“failure case autonomy”) [154]. More recently, Barua and Khorasani [155] developed an intelligent model-based hierarchical fault diagnosis technique for satellite formations that essentially extends the *hierarchical* diagnostic concept to formation flying of multiple satellites.

Going back to the three-level architecture mentioned in the above, the behaviour of a satellite at mission level, the highest level of the proposed diagnostic hierarchy, can be modeled as a discrete-event system (DES). Thus, DES-based diagnostic methods using finite state automata (see for example, [157] and [158]) show great potential for fault diagnosis at this level. One of the most important and successful applications of DES-based autonomous fault diagnosis is in the NASA's Deep Space One mission [159].

Numerous fault diagnosis methods are applicable to the lowest level of the hierarchy (i.e., the component level). In fact, most of the reviewed (in Chapters 1 and 2) diagnostic

techniques in the literature including both model-based and computational intelligence-based approaches have the potential to be applied for satellite fault diagnosis at the component level. Among various existing contributions in the literature, one may refer to the works of Talebi and Khorasani [160] on fault detection and isolation of magnetorquer type actuators of satellite ACS using an intelligent robust FDI scheme; Tudoroiu and Khorasani [94] on fault detection and diagnosis of satellite ACS using an interactive multiple model approach; Tao *et al.* [161] on fault detection, isolation and recovery of satellite orbital control system (OCS) using a parameter estimation-based approach; and Wu and Saif [162] on fault diagnosis of a satellite system with flexible appendages using a robust observer-based methodology.

5.2 Satellite Attitude Control Subsystem (ACS)

In this thesis, our focus is on testing and validating the proposed *hybrid* FDI methodology for fault diagnosis of reaction wheel actuators of the satellite ACS. Attitude control deals with the orientation of a spacecraft with respect to a desired reference frame. The attitude control task can basically be divided into three subtasks including: (i) attitude determination, which is done with the help of attitude sensors such as gyros, star trackers, and sun sensors; (ii) attitude correction, which is achieved by torques applied to the satellite body and generated by actuators such as reaction wheels, momentum wheels, control moment gyros, magnetic torquers, sometimes thrusters; (iii) attitude control, which is software-based algorithm that essentially the magnitude and direction of torque to be applied to the satellite in response to an attitude command or in compensation of attitude disturbances.

5.2.1 Fault Diagnosis in Satellite ACS

Faults in a satellite's attitude control system (ACS) due to malfunctions in components, actuators, or sensors, could result in higher energy consumption, loss of control, and eventually mission abortion. Faults may, in general, result from unexpected interferences or gradual aging of the ACS components, actuators, and/or sensors. In order to increase the energy efficiency, ensure the equipment safety, and enhance the reliability and overall fault tolerance of any space-based mission it is necessary to develop robust fault diagnosis techniques for components, actuators, and sensors of the ACS so that remedial actions are taken as soon as possible.

Faults in actuators require special attention due to their direct impact on and determining role in the satellite station-keeping and attitude control. Moreover, long time experience with ACS actuators in different satellite missions has revealed that they are highly prone to faults and malfunctions.

Current methods for detecting and correcting anomalies onboard a satellite and on the ground are primarily based on simple limit checking and trend analysis techniques, which are not reliable and are error-prone. On the other hand, anomaly detection based on manual telemetry data analysis is very time-consuming and subject to human mistakes. It should be noted, however, that satellite monitoring and diagnostics can be automated without compromising reliability using advanced decision support systems that utilize model-based, rule-based, and intelligent-based methodologies. The development of more reliable automatic health monitoring and fault diagnosis tools is even more crucial for satellite constellation and formation flying (FF) missions due to the much larger amount of telemetry data (because of multiple number of satellites) and due to the stringent

constraints that are imposed by the constellation or FF mission requirements. In the past few years, a significant number of model-based and computational intelligence-based approaches have been proposed by research community for fault diagnosis in satellite ACS subsystem, in general, and actuators and sensors, in particular. Some of these were already mentioned at the end of Section 5.1. For few other references especially on fault diagnosis of reaction wheel actuators of ACS, refer to Talebi and Patel [163] using an intelligent detection and recovery scheme, Li *et al.* [164] for a dynamic neural network-based method, and Meskin and Khorasani [165] based on the nonlinear geometric approach.

Despite their own contributions, almost all of the above work have three limitations in common: (i) they have *not* addressed the problem of fault severity estimation in reaction wheels, which could be very beneficial to avoid catastrophic failures; (ii) *none* of them have performed a comprehensive robustness analysis with respect to measurement noise; and (iii) most of them assume full-state measurements. In this chapter, we intend to first validate the *hybrid* FDII methodology proposed in Chapter 3 by applying it to fault diagnosis of reaction wheels of ACS. This essentially allows us to also address the first two limitations mentioned above. Second, we consider partial state measurements from the reaction wheel to test and validate the fault tolerant observer proposed in Chapter 4 and, at the same time, address the third limitation above of the existing methods.

5.2.2 Satellite Attitude Dynamics

Prior to fault diagnosis design and implementation, we need to develop mathematical models of ACS with reaction wheels as actuators. These models are needed for two purposes: (i) to simulate the satellite ACS and be able to inject and simulate faults and (ii)

to use some of the models for fault diagnosis design since the proposed *hybrid* FDI method also utilizes the mathematical model of the system being monitored. Hence, we start by developing an ACS simulator by modeling and design of various elements of the ACS closed-loop system. It should be noted that the materials corresponding to modeling presented in this and/or the subsequent sections are gathered from various references from [152] to [166]. In the following, we naturally start with modeling the satellite's attitude dynamics.

The attitude dynamics of a rigid body satellite controlled by reaction wheels and thrusters can in general be described by the following nonlinear differential equation:

$$I_{sat}\dot{\omega} + \omega \times (I_{sat}\omega + I_{rw}\omega_{rw}) + \tau_{rw} + \tau_{Thruster} = \tau_{dist} \quad (5-1)$$

where I_{sat}, I_{rw} denote the inertia of the satellite and the reaction wheels, respectively, $\omega = [\omega^x \ \omega^y \ \omega^z]^T$ denotes the angular velocity vector of the satellite, and ω_{rw} is the angular velocity (or speed) of the reaction wheel(s). It should be noted that for the rest of this thesis, the wheel speed ω_{rw} is represented without its subscript simply as ω , not to be confused with the satellite's angular velocity that is always represented by ω or any of its components, namely ω^x , ω^y , or ω^z . The inputs τ_{rw}, τ_{dist} , and $\tau_{Thruster}$ respectively represent the torque vectors exerted on the satellite body by reaction wheels, external disturbances, and attitude control thrusters. Here, we assume that *no* thrusters are employed for attitude control, hence $\tau_{Thruster} = 0$.

Moreover, assume that the spacecraft body-fixed frame is aligned with the principal axes (for the definition of the spacecraft principal axes reference frame refer to Appendix

B), in which case the products of inertia are zero. Three reaction wheels exist in the ACS, one per each principal axis (assuming alignment of the spacecraft's body-fixed frame and the principal axes); and the components of the reaction wheel Inertia matrix are very small compared to that of the satellite Inertia matrix, namely $I_w \ll I_{sat}$. We may then expand the attitude vector differential equations in (5-1) in discrete-time form as follows:

$$\begin{aligned}\varpi_k^x &= k_{xx}(\varpi_{k-1}^y \varpi_{k-1}^z) + T_k^x / I_{sat}^{xx} \\ \varpi_k^y &= k_{yy}(\varpi_{k-1}^z \varpi_{k-1}^x) + T_k^y / I_{sat}^{yy} \\ \varpi_k^z &= k_{zz}(\varpi_{k-1}^x \varpi_{k-1}^y) + T_k^z / I_{sat}^{zz}\end{aligned}\quad (5-2)$$

where k is the discrete time-step, I_{sat}^{xx} , I_{sat}^{yy} , and I_{sat}^{zz} are the diagonal elements of the spacecraft's Inertia matrix, and T_k^x, T_k^y, T_k^z denote the instantaneous net torques exerted on the principal axes of the satellite body (x -axis, y -axis and z -axis) due to combined effect of external disturbances and reaction torques exerted by the wheels; hence

$$\begin{aligned}T_k^x &= \tau_k^{distx} - \tau_k^{wx} \\ T_k^y &= \tau_k^{disty} - \tau_k^{wy} \\ T_k^z &= \tau_k^{distz} - \tau_k^{wz}\end{aligned}\quad (5-3)$$

and the coefficients k_{xx}, k_{yy}, k_{zz} are given by

$$k_{xx} = \frac{I_{sat}^{yy} - I_{sat}^{zz}}{I_{sat}^{xx}}, k_{yy} = \frac{I_{sat}^{zz} - I_{sat}^{xx}}{I_{sat}^{yy}}, k_{zz} = \frac{I_{sat}^{xx} - I_{sat}^{yy}}{I_{sat}^{zz}}\quad (5-4)$$

It should be noted that the components of the satellite angular velocity with respect to the inertial reference frame \mathfrak{I}_N (see Appendix B for the definition of this frame), namely $\varpi_k^x, \varpi_k^y, \varpi_k^z$ are expressed in the spacecraft fixed/body reference frame \mathfrak{I}_B (see Appendix B), and are measured by gyroscopes installed in strap-down systems. Also, in order to

implement an attitude control law it is more convenient to use an orbital rotating frame attached to the orbit, such as the RPY (Roll, Pitch, Yaw) frame, also called orbital frame (see Appendix B). It is also very important to note that if spacecraft attitude is represented with respect to the non-rotating inertial reference frame \mathfrak{S}_N , then the attitude commands even under *no* slew-maneuvering (i.e., a maneuver to change the orientation of a satellite) should always be nonzero, time-varying signals in order to compensate the effect of satellite rotation around the Earth. While representing spacecraft's attitude with respect to the *rotating* orbital reference frame automatically solves this problem and makes attitude commands more comprehensible; i.e., under *no* slew-maneuvering (or attitude stabilization) the attitude commands are zero and spacecraft slew-maneuvering can be commanded by simply one or a series of step functions.

In general, the instantaneous attitude of a spacecraft can be described or represented in various ways. However, the Euler angles are the most visually comprehensible set of attitude parameters and have been commonly used in attitude representation of rigid bodies including satellites. The Euler angles (φ, θ, ψ) consist of three successive rotation angles that can describe the orientation of any rotating object, in general, and a satellite, in particular. The rotations may occur about any of three orthogonal axes, but there cannot be two rotations about the same axis in a row.

The order of the rotations, however, is very important to the orientation and the most commonly used order is the asymmetric 3-2-1 rotations, which correspond to Yaw-Pitch-Roll rotations also commonly used in the aircraft dynamics. This asymmetric set of Euler angles is used since there are no repeated rotations. However, it has singularities whenever the pitch angle (θ) has a value of $\pm 90^\circ$, which limits the applicability of

Euler angles description to only small rotations. It should be noted though that the singularity at a specific angle is an *inherent* property of Euler representation regardless of the sequence of rotations. The main advantage of the Euler angles, however, is the ability to clearly visualize the orientation of the vehicle as it undergoes a series of rotations. The 3-2-1 Euler angle rotation sequence is equivalent to the following *direction cosine matrix*:

$$[C(\varphi, \theta, \psi)] = \begin{bmatrix} \cos\theta\cos\psi & \cos\theta\sin\psi & -\sin\theta \\ \sin\varphi\sin\theta\cos\psi - \cos\varphi\sin\psi & \sin\varphi\sin\theta\sin\psi + \cos\varphi\cos\psi & \sin\varphi\cos\theta \\ \cos\varphi\sin\theta\cos\psi + \sin\varphi\sin\psi & \cos\varphi\sin\theta\sin\psi - \sin\varphi\cos\psi & \cos\varphi\cos\theta \end{bmatrix} \quad (5-5)$$

The Euler angles could be obtained from the rotation matrix by using the following set of nonlinear inverse transformations:

$$\begin{aligned} \varphi &= \text{atan}\left(\frac{C_{23}}{C_{33}}\right) \\ \theta &= -\text{asin}(C_{13}) \\ \psi &= \text{atan}\left(\frac{C_{12}}{C_{11}}\right) \end{aligned} \quad (5-6)$$

To avoid the singularities in the Euler angles (φ, θ, ψ) the satellite dynamics has to be expressed in the quaternion representation. Defining the unit quaternion set as

$$q(t) = [q_0(t) \quad q_1(t) \quad q_2(t) \quad q_3(t)]^T = [q_0(t) \quad \bar{q}_{13}(t)]^T \quad (5-7)$$

where the first quaternion $q_0(t)$ component represents the scalar component and the last three components $[q_1(t), q_2(t), q_3(t)]^T$ represent the quaternion vector \bar{q}_{13} . To formally define the quaternions, let's denote the unit vector along the Euler axis as $\bar{\lambda} = [\lambda_1 \quad \lambda_2 \quad \lambda_3]^T$, where λ_i are the direction cosines of the Euler axis relative to the

axes of the inertial reference frame \mathfrak{S}_N . Then, the four elements of the quaternion set are defined as:

$$\begin{aligned} q_0(t) &= \cos(\Theta/2) \\ q_1(t) &= \lambda_1 \sin(\Theta/2) \\ q_2(t) &= \lambda_2 \sin(\Theta/2) \\ q_3(t) &= \lambda_3 \sin(\Theta/2) \end{aligned} \quad (5-8)$$

where Θ represents the principal rotation angle about the Euler axis and given by:

$$\Theta = \text{acos}\left(\frac{C_{11} + C_{22} + C_{33} - 1}{2}\right) \quad (5-9)$$

and

$$\begin{aligned} \lambda_1 &= \frac{C_{23} - C_{32}}{2 \sin \Theta} \\ \lambda_2 &= \frac{C_{31} - C_{13}}{2 \sin \Theta} \\ \lambda_3 &= \frac{C_{12} - C_{21}}{2 \sin \Theta} \end{aligned} \quad (5-10)$$

where C_{ij} is the element on the i^{th} row and j^{th} column of the direction cosine matrix for $i, j = 1, 2, 3$. For the unit quaternion representation, the quaternion parameters are *constrained* to form a hypersphere given by the following equation:

$$\bar{q}_{13}^T \bar{q}_{13} + q_0^2 = 1 \quad (5-11)$$

Due to lack of singularities, the quaternion representation is useful for both small and large rotations (i.e., satellite slew-maneuvers). The direction cosine matrix can also be obtained from the quaternion parameters as follows:

$$[C_q] = \begin{bmatrix} q_0^2 + q_1^2 - q_2^2 - q_3^2 & 2(q_1q_2 + q_0q_3) & 2(q_1q_3 - q_0q_2) \\ 2(q_1q_2 - q_0q_3) & q_0^2 - q_1^2 + q_2^2 - q_3^2 & 2(q_2q_3 + q_0q_1) \\ 2(q_1q_3 + q_0q_2) & 2(q_2q_3 - q_0q_1) & q_0^2 - q_1^2 - q_2^2 + q_3^2 \end{bmatrix} \quad (5-12)$$

Since direction cosine matrix of a specific rotation is always *unique*, by comparing equations (5-5) and (5-11), one can obtain the static nonlinear transformation from quaternion to Euler angles:

$$\begin{aligned}\varphi &= \text{atan}\left(\frac{C_{23}}{C_{33}}\right) = \text{atan}\left(\frac{2(q_2q_3 + q_0q_1)}{q_0^2 - q_1^2 - q_2^2 + q_3^2}\right) \\ \theta &= -\text{asin}(C_{13}) = -\text{asin}(2(q_1q_3 - q_0q_2)) \\ \psi &= \text{atan}\left(\frac{C_{12}}{C_{11}}\right) = \text{atan}\left(\frac{2(q_1q_2 + q_0q_3)}{q_0^2 + q_1^2 - q_2^2 - q_3^2}\right)\end{aligned}\quad (5-13)$$

The quaternion kinematics differential equations are given by:

$$\dot{q}(t) = \begin{bmatrix} \dot{q}_0(t) \\ \dot{q}_1(t) \\ \dot{q}_2(t) \\ \dot{q}_3(t) \end{bmatrix} = \begin{bmatrix} \dot{q}_0(t) \\ \dot{q}_{13}(t) \end{bmatrix} = \frac{1}{2} \begin{bmatrix} 0 & -\varpi^x & -\varpi^y & -\varpi^z \\ \varpi^x & 0 & \varpi^z & -\varpi^y \\ \varpi^y & -\varpi^z & 0 & \varpi^x \\ \varpi^z & \varpi^y & -\varpi^x & 0 \end{bmatrix} \begin{bmatrix} q_0(t) \\ q_1(t) \\ q_2(t) \\ q_3(t) \end{bmatrix}\quad (5-14)$$

or, equivalently

$$\dot{q}(t) = \begin{bmatrix} \dot{q}_0(t) \\ \dot{q}_1(t) \\ \dot{q}_2(t) \\ \dot{q}_3(t) \end{bmatrix} = \begin{bmatrix} \dot{q}_0(t) \\ \dot{q}_{13}(t) \end{bmatrix} = \frac{1}{2} \begin{bmatrix} q_0 & -q_1 & -q_2 & -q_3 \\ q_1 & q_0 & -q_3 & q_2 \\ q_2 & q_3 & q_0 & -q_1 \\ q_3 & -q_2 & q_1 & q_0 \end{bmatrix} \begin{bmatrix} 0 \\ \varpi^x(t) \\ \varpi^y(t) \\ \varpi^z(t) \end{bmatrix}\quad (5-15)$$

The kinematics differential equation in (5-15) essentially connects the spacecraft's attitude to its angular velocity vector $\varpi = [\varpi^x \ \varpi^y \ \varpi^z]^T$, which is obtained from gyroscope measurements. It should be noted that ϖ represents the angular velocity of the body-fixed frame with respect to the inertial frame ϖ_B^N . However, the quaternion components represent orientation/attitude of the satellite body fixed frame with respect to the orbital frame. Thus, we need to calculate the angular velocity of the body-fixed frame

with respect to the orbital frame, namely ϖ_B^O . Consider the following general equation from vector calculus:

$$\varpi_B^N = \varpi_B^O + \varpi_O^N = \varpi_B^O + R_O^B \begin{bmatrix} 0 \\ -n_c \\ 0 \end{bmatrix} \quad (5-16)$$

where n_c is the orbital frequency of the satellite given by:

$$n_c = \sqrt{\frac{\mu}{R_c^3}} \quad (5-17)$$

where μ represents the gravitational parameter of the Earth, and R_c is the distance from the center of the Earth and the satellite.

Finally, R_O^B is the rotation matrix transforming any vector represented in orbital frame to a vector in body fixed frame and can be obtained from the quaternion set, which is actually the direction cosine matrix corresponding to the quaternion set representing the orientation of the body-fixed frame with respect to the orbital frame. Therefore, we have:

$$\varpi_B^O = \varpi_B^N + \begin{bmatrix} q_0^2 + q_1^2 - q_2^2 - q_3^2 & 2(q_1q_2 + q_0q_3) & 2(q_1q_3 - q_0q_2) \\ 2(q_1q_2 - q_0q_3) & q_0^2 - q_1^2 + q_2^2 - q_3^2 & 2(q_2q_3 + q_0q_1) \\ 2(q_1q_3 + q_0q_2) & 2(q_2q_3 - q_0q_1) & q_0^2 - q_1^2 - q_2^2 + q_3^2 \end{bmatrix} \begin{bmatrix} 0 \\ n_c \\ 0 \end{bmatrix} \quad (5-18)$$

Using the above equation and the angular speeds of the satellite measured by all three Gyros we can calculate the angular velocity of the body-fixed frame with respect to the orbital frame as follows:

$$\varpi_B^O = \begin{bmatrix} \varpi^x \\ \varpi^y \\ \varpi^z \end{bmatrix} + n_c \begin{bmatrix} 2(q_1q_2 + q_0q_3) \\ 1 - 2(q_1^2 + q_3^2) \\ 2(q_2q_3 - q_0q_1) \end{bmatrix} \quad (5-19)$$

5.2.2.1 Dynamic Modeling of Reaction Wheel Actuators

The selection of reaction wheels for attitude control is well justified due to their popularity in active satellite attitude control. The ACS can be considered as a MIMO control system. A high fidelity nonlinear model of a reaction wheel has been obtained from Bialke [167] and has been integrated into the ACS dynamics. This high-fidelity model is also required for enhancing the robustness of the FDII schemes proposed in this thesis with respect to modeling errors. A block diagram representation of this high-fidelity reaction wheel model is shown in Figure 5-2.

The reaction wheels considered in this thesis are ITHACO ‘type A’ reaction wheels that are currently being manufactured by Goodrich Corporation. The values of model parameters for this type of wheel are also obtained from Bialke [167] and are given Table 5-2. Closed-loop ACS simulation results verified the validity of this parameter selection (refer to the torque levels in Figure 5-10 presented in Section 5.4.1, where the torque levels are consistent with nominal torque levels of ITHACO ‘type A’ wheels).

Each reaction wheel consists of several internal and external loops that have to be integrated to yield an accurate overall high-fidelity model of the wheel, which is highly nonlinear especially at high speeds of the wheel. The following loops play an important role in the dynamics of each reaction wheel (refer to Figure 5-2 and reference [167] for further details):

- (i) The negative feedback EMF torque limiting loop τ_{EMF} due to low bus voltage V_{bus} condition that may limit the motor torque at high speeds due to increasing back-EMF voltage gain k_e of the motor. Note the nonlinear relationship between I_{bus} and V_{bus} (i.e., the current and the voltage of the bus).

$$I_{bus} = \left(\frac{1}{V_{bus} - 1} \right) (I_m^2 R_B + 0.04 |I_m| V_{bus} + P_q + \omega I_m k_e) \quad (5-20)$$

As can also be observed from equation (5-20), the motor current of the wheel is a highly nonlinear function of the bus current I_{bus} . Consequently, motor current of the wheel becomes a highly nonlinear function of the bus voltage V_{bus} .

- (ii) The negative feedback viscous and coulomb frictions generated in bearings. Viscous friction is generated due to the bearing lubricant, and it has a strong sensitivity to temperature T . The bi-linear dependence between temperature, reaction wheel angular speed and the viscous torque is given by:

$$\tau_v = (0.0049 - 0.00002(T+30))\omega \quad (5-21)$$

- (iii) Coulomb friction is caused by friction within bearings, and is independent of the wheel speed and temperature, and therefore is primarily of interest as a disturbance source.
- (iv) The negative feedback speed limiter loop that prevents the flywheel from reaching unsafe speeds.
- (v) The motor torque control is included since the motor driver is essentially a voltage controlled current source with a gain G_d . The motor has a torque constant gain k_t , which delivers a torque proportional to the current driver. Thus, to inject faults in the motor current to validate and test the FDII algorithms, one may simply change the torque constant gain k_t . This is basically an alternative way of representing unexpected changes in motor current value.

- (vi) The torque noise disturbance τ_{noise} is a very low frequency torque variation from bearings due to lubricant dynamics. The torque noise is modeled as a sine wave having a high pass filter frequency w_n

$$\tau_{noise} = J_w \theta_{noise} w_n^2 \sin(w_n t) \quad (5-22)$$

where θ_{noise} represents the torque noise angle.

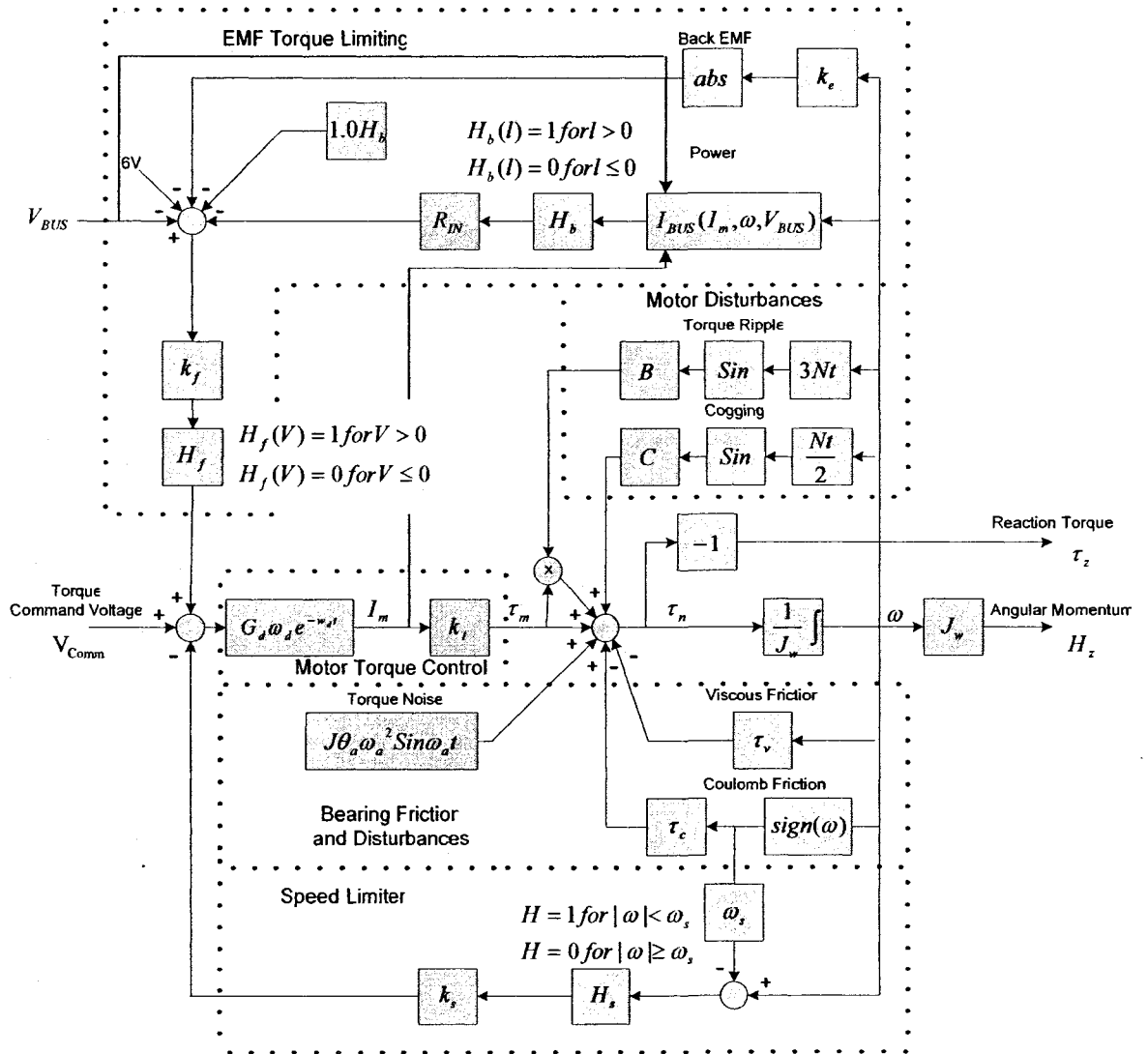


Figure 5-2: A detailed block diagram of a high fidelity reaction wheel model [167]

Few remarks on the reaction wheel (RW) model:

- The speed limiter and the EMF torque limiting loops use three discontinuous Heaviside step functions to enable the high-gain negative feedback k_f , when the reaction wheel exceeds an established speed threshold ω_s , to eliminate the voltage drop when the power is not being drawn from the bus during a deceleration since the energy is being removed from the wheel.
- The EMF torque-limiting loop could be controlled by the voltage feedback gain, k_f .
- The torque command voltage is restricted to be within $\pm 5V$. Therefore, a saturation block is incorporated into the closed-loop ACS simulator after the controller to limit the control signal within these bounds.

It is important to note that the reaction wheel model depicted in Figure 5-2 consists of a few discontinuous functions such as the Heaviside functions, the sign function and the absolute value functions that essentially make the entire reaction wheel model discontinuous. However, an analytical approximation of the reaction wheel is required specifically for designing the fault tolerant observer, which requires calculation of the Jacobian matrix of the system. Hence, all discontinuities in the model need to be approximated by appropriate analytical functions. For this purpose, one or combinations of parameterized sigmoidal functions are employed to approximate the discontinuous functions to an arbitrarily level of accuracy. These parameterized sigmoidal functions are of the following form:

$$\text{sigmoid}(x) = \frac{1}{1 + e^{-ax}} \quad (5-23)$$

where $a \gg 1$ determines the accuracy of the approximation. The larger the value of this parameter, the more accurate will be the approximation, however, very large values of a may also cause numerical singularities particularly in calculating the Jacobian matrix of the system. In this thesis, a value of $a = 10$ has been selected to achieve a sufficiently accurate approximation. In the model shown in Figure 5-2, the Heaviside functions H_b and H_f can be approximated as follows:

$$H_b(I) \cong \frac{1}{1 + \exp(-aI)} \quad (5-24)$$

$$H_f(V) \cong \frac{1}{1 + \exp(aV)} \quad (5-25)$$

The sign function and the absolute value function can also be approximated as follows:

$$\text{sign}(\omega) = \frac{1 - \exp(-a\omega)}{1 + \exp(-a\omega)} \quad (5-26)$$

$$\text{abs}(k_e \omega) = \frac{1 - \exp(-ak_e \omega)}{1 + \exp(-ak_e \omega)} k_e \omega \quad (5-27)$$

It should be noted that the approximation (5-27) of the absolute value function is not in fact necessary, since the derivative of the absolute value function can, in general, be calculated as:

$$\frac{d}{dx} \text{sign}(x) = \begin{cases} 1, & \text{if } x > 0 \\ -1, & \text{if } x < 0 \\ 0, & \text{if } x = 0 \end{cases} \quad (5-28)$$

where the inherently undefined value of the derivative at $x = 0$ is intentionally set to zero. Eventually, the Heaviside function H_s can be approximated as follows:

$$H_s(\omega) = \frac{1}{1 + \exp(-a(\omega - \omega_s))} + \frac{1}{1 + \exp(a(\omega + \omega_s))} \quad (5-29)$$

In conclusion, the mathematical state-space representation of the analytical model of the reaction wheel employed in both FDII and FTO design may now be expressed as follows:

$$\begin{aligned} \dot{I}_m &= G_d \omega_d (f_3(\omega, I_m) - f_5(\omega)) - \omega_d I_m + G_d \omega_d V_{Comm} \\ \dot{\omega} &= \frac{1}{J_w} [f_1(\omega) + k_t I_m (f_2(\omega) + 1) - \tau_v \omega - \tau_c f_4(\omega) + \tau_{noise}] \end{aligned} \quad (5-30)$$

in which:

$$\begin{aligned} f_1(\omega) &= C \sin \frac{Nt}{2} \omega \\ f_2(\omega) &= B \sin 3Nt\omega \\ f_3(\omega, I_m, V_{bus}) &= \frac{\exp(-aV(\omega, I_m, V_{bus}))}{1 + \exp(-aV(\omega, I_m, V_{bus}))} V(\omega, I_m, V_{bus}) \\ f_4(\omega) &= \frac{1 - \exp(-a\omega)}{1 + \exp(-a\omega)} \\ f_5(\omega) &= \frac{k_s(\omega - \omega_s f_4(\omega))}{2} \left(\frac{1}{1 + \exp(-a(\omega - \omega_s))} + \frac{1}{1 + \exp(a(\omega + \omega_s))} \right) \\ V(\omega, I_m, V_{bus}) &= k_f \left[V_{bus} - 6 - \frac{1}{1 + \exp(-aI_{bus})} (1 + R_{in} I_{bus}) - \frac{1 - \exp(-ak_e \omega)}{1 + \exp(-ak_e \omega)} k_e \omega \right] \end{aligned} \quad (5-31)$$

where f_1 and f_2 are functions due to motor disturbances, f_3 is derived from the EMF torque limiting block, f_4 is a sigmoidal function replacing the discontinuous sign function in the Coulomb friction block, f_5 represents the speed limiter block, and V_{Comm} is the torque command voltage generated by the attitude controller. As can be seen from equations (5-30) and (5-31), the reaction wheel model is a second-order highly nonlinear model with motor current and wheel speed as the states and the command torque voltage as the input.

Furthermore, since the proposed FDII algorithm is developed based on a discrete-time model of the system being monitored, the analytical nonlinear model of (5-30) was discretized using Euler's backward difference method with a sampling time of

$T_s = 50msec$. This value of the sampling time ensures the validity of the Nyquist-Shannon sampling theorem for the linearized model of the reaction wheel. More precisely, the fastest changing signal within the reaction wheel is the motor current corresponding to electrical, as opposed to, mechanical subsystems of the wheel. The bandwidth of the motor current is limited by the frequency ω_d in the transfer function between the torque command voltage and the motor current in the linearized model of the reaction wheel. This transfer function and its associated frequency, namely ω_d , can also be observed in the “motor torque control” block of the wheel model depicted in Figure 5-2. The value of ω_d is given in Table 5-2 as $9 rad/s$, which is equivalent to $9/2\pi \cong 1.43 Hz$. By selecting the sampling frequency to be 14 times of the bandwidth of the current signal, the *sampling frequency* becomes almost equal to 20 Hz, which is equivalent to $T_s = 50msec$.

It should be emphasized that the analytical approximation model of the reaction wheel given in equations (5-30) and (5-31) is utilized only for FDII and FTO design. For fault injection and simulation as well as data generation purposes, the original continuous-time discontinuous model of the reaction wheel presented in Figure 5-2 is used in the closed-loop ACS simulator.

Validation of the discrete-time analytical model of the reaction wheel: The discrete-time analytic approximation of the reaction wheel model needs to be validated against the original continuous-time discontinuous model prior to its use for FDII and FTO design purposes. Hence, the two reaction wheel models are run in parallel with the same torque command voltage given in the following:

$$V_{\text{Comm}}(t) = 3 \sin(t) + 2 \sin(4t) + v(t) \quad (5-32)$$

where $v(t)$ is sampled from a random process with uniform distribution over the interval $[-0.5, 0.5]$. Thus,

$$-0.5 \leq v(t) \leq 0.5, \quad \forall t \in \mathfrak{R}^+ \quad (5-33)$$

The command voltage in equation (5-32) is selected in order to first span the entire possible range of the torque command voltage (i.e., $\pm 5\text{V}$) and second to stimulate (or excite) the internal modes of the reaction wheel using a random input signal $v(t)$. Furthermore, the frequencies of the sinusoids in equation (5-32) are set to 1 and 4 rad/s , which are considerably smaller than the bandwidth of the motor current signal imposed by the value of $\omega_d = 9 \text{ rad/s}$.

Furthermore, the model has been validated at both high and low speeds of the wheel, especially that the reaction wheel performance and characteristics are highly dependent on the speed of the wheel. Figure 5-3 depicts the validation results for the states of the reaction wheel (i.e., current and speed) as well as the reaction torque generated by the wheel. In theory, comparing the results for current and speed would have been sufficient to verify the validity of the discrete-time analytic model (remember that the states of a system carry all the information about that system). However, due to the extreme importance of the generated reaction torque by the wheel (note that reaction wheel is the actuator of ACS), the validation results are also depicted for reactions torque.

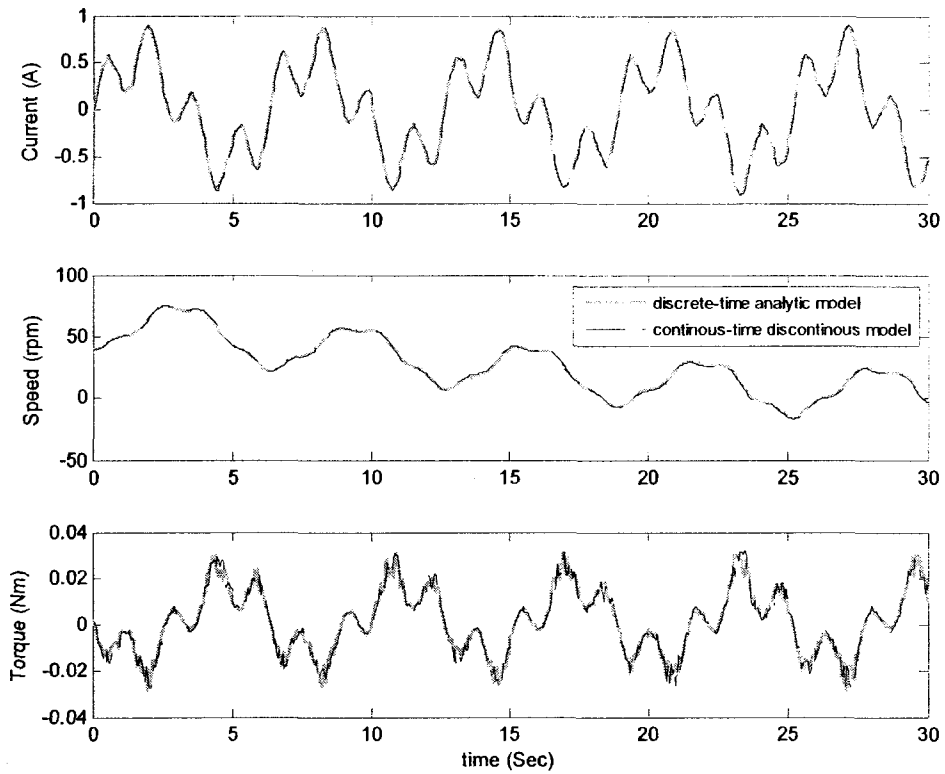


Figure 5-3. Validation of the discrete-time analytic model of the RW in response to the torque command voltage given in equation (5-32) at low speeds of the wheel.

The results of Figure 5-3 clearly indicate that the discrete-time analytic model of equations (5-30) and (5-31) very closely matches the continuous-time discontinuous model of Figure 5-2 at low speeds of the wheel. The same conclusion can be drawn from Figure 5-4 at high speeds of the wheel. In this figure, the back EMF signal of the two models has also been shown and compared due to its importance at high speeds of the wheel.

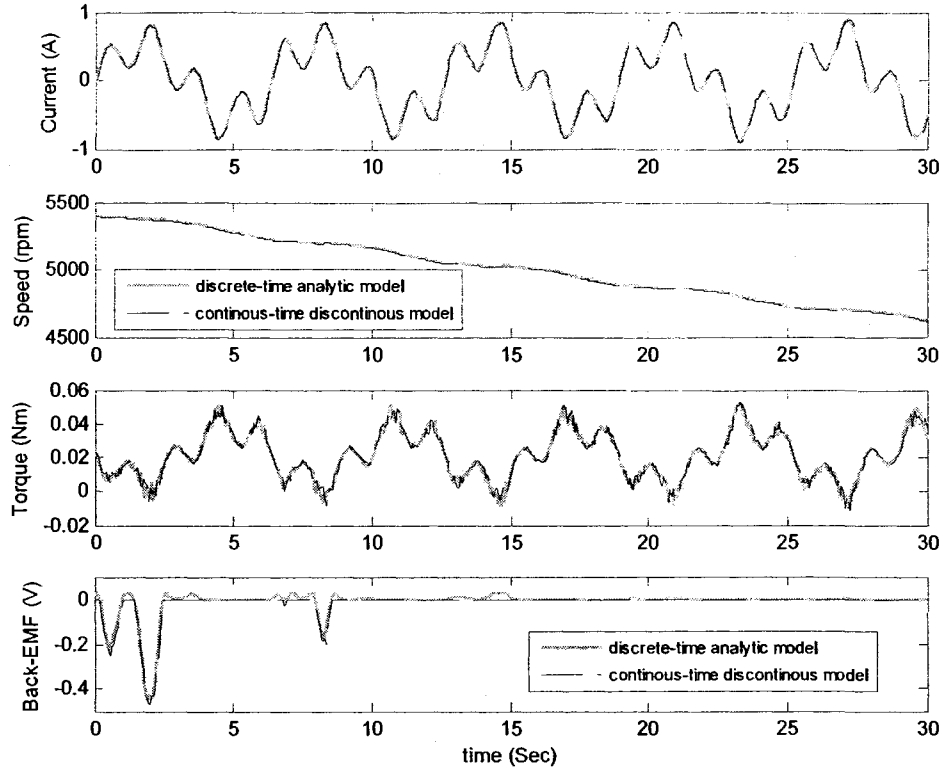


Figure 5-4. Validation of the discrete-time analytic model of the RW in response to the torque command voltage given in equation (5-32) at high speeds of the wheel.

5.2.3 Mathematical Modeling of External Attitude Disturbances

The attitude control subsystem of an Earth-orbiting satellite must tolerate the typical external disturbance torques due to the gravity-gradient effects, the Earth's magnetic field, aerodynamic torques (dominant in low-altitude orbits) and solar radiation torque. Furthermore, the robustness of the FDII subsystem to these external disturbances has to be investigated, ensured and verified. Otherwise, the FDII subsystem would generate false alarms due to presence of these disturbances. Therefore, all these environmental disturbances need to be modeled and properly incorporated into the ACS simulator to be able to evaluate the robustness of the proposed FDII algorithms with respect to them. As

a result, the following mathematical models of these disturbances are obtained from Wertz and Larson [152] and are incorporated into the ACS simulator.

5.2.3.1 Gravity Gradient Torque

Gravity gradient torque is primarily influenced by spacecraft inertias and orbit altitude. The worst-case gravity gradient torque is estimated as:

$$\tau_g = \frac{3\mu}{2R^3} |I_{sat}^{xx} - I_{sat}^{yy}| \sin 2\theta \quad (5-34)$$

where θ is the maximum deviation in the local-vertical pointing (in radians), μ is the Earth's gravity constant in m^3/s^2 , R is the orbit radius in meters, I_{sat}^{yy} is the moment of inertia of the satellite about y -axis in $\text{kg}\cdot\text{m}^2$, and I_{sat}^{xx} is the moment of inertia about x -axis in $\text{kg}\cdot\text{m}^2$.

5.2.3.2 Magnetic Torque

Magnetic torque is primarily influenced by orbit altitude, residual spacecraft magnetic dipole and the orbit inclination. The worst-case magnetic torque is estimated as:

$$\tau_m = D_r E_{mf} \quad (5-35)$$

where D_r is the residual Dipole of the satellite in $\text{amp}\cdot\text{turn}\cdot\text{m}^2$, $E_{mf} = \frac{2M}{R^3}$ is the Earth's magnetic field in Tesla, M is the magnetic moment of the Earth in $\text{Tesla}\cdot\text{m}^3$, and R is the orbit radius or radius from the dipole (Earth) center to the satellite (in meter).

5.2.3.3 Aerodynamic Torque

Aerodynamic torque is primarily influenced by orbit altitude, spacecraft geometry and the location of the centre of gravity of the spacecraft. The worst-case aerodynamic torque is estimated as:

$$\tau_a = F_{aero}(c_{pa} - c_g) \quad (5-36)$$

where $F_{aero} = 0.5[\rho C_D A_{aero} V^2]$ is the aerodynamic force, ρ is the atmospheric density in kg/m^3 , C_D is the drag coefficient, which is between 2 and 2.5, A_{aero} is the surface area for aerodynamic pressure in m^2 , V is the satellite velocity, c_{pa} is the centre of aerodynamic pressure, and c_g is the centre of gravity.

5.2.3.4 Solar Radiation Torque

Solar radiation torque is primarily influenced by spacecraft geometry; spacecraft surface reflectivity and the location of the centre of gravity of the spacecraft. The worst-case solar radiation torque is estimated as:

$$\tau_s = F_{solar}(c_{ps} - c_g) \quad (5-37)$$

where in the force $F_{solar} = \frac{F_s}{c} A_s (1+r) \cos i_s$, F_s is the solar constant, c is the speed of light in m/s , A_s is the surface area for solar radiation in m^2 , r is the coefficient of reflectivity, i_s is the Sun incidence angle, c_{ps} is the location of the centre of solar pressure, and c_g is the centre of gravity. Coefficient of reflectivity r is a number between 0 and 1 with usual value of 0.6 for most of the satellites. However, in order to consider the worst-case scenario, we selected the maximum possible value of 1 in the simulations.

The values of the entire set of parameters of the environmental models (i.e., the environmental parameters) are provided in Table 5-1. It is important to note that some of these parameters are universal constants but some are specific to the LEO satellite that has been simulated.

Table 5-1. Parameters of the attitude disturbance models used in the ACS simulations.

Parameter	Description	Units	Value
ρ	Atmospheric density	kg / m^3	1.04×10^{-13}
A_{aero}	Contact surface area for aerodynamic pressure	m^2	1
A_s	Contact surface area for solar radiation	m^2	1
C_D	The drag coefficient	-	2.2
c_{pa}	The center of aerodynamic pressure	-	0.1
c_g	The center of gravity	-	0
c_{ps}	The center of solar pressure	-	0.1
C_D	The drag coefficient	-	2.2
M	Magnetic moment of earth	$T.m^3$	7.96×10^{15}
D_r	Residual Dipole of the satellite	$Amp-turn.m^2$	0.8
F_s	Solar constant	W/m^2	1366
r	Reflectance factor	-	1
θ	Maximum deviation in the local-vertical pointing	rad	1.74×10^{-4}
i_s	Incidence angle	deg	0
$T_{grg\ max}$	The maximum gravity gradient torque	Nm	7.4119×10^{-6}
$T_{aero\ max}$	Maximum aerodynamic drag torque	Nm	6.4617×10^{-7}
$T_{mgn\ max}$	Maximum magnetic torque	Nm	3.7694×10^{-5}
$T_{solar\ max}$	Maximum Solar radiation torque	Nm	9×10^{-7}

5.3 Attitude Control

Various techniques to control the attitude of a spacecraft including passive methods such as spin stabilization and gravity gradient, and active methods such as momentum bias and three-axis (3-axis) attitude stabilization. The criteria for choosing a specific attitude control technique mainly depend on accuracy requirements and specifications as well as the budget of the ACS. The 3-axis active attitude control technique, though being costly,

is the most precise technique among the others. It is also the most common attitude control technique in modern satellites. Therefore, in this thesis, this control technique is employed to stabilize the attitude of the satellite. For further details on each attitude control technique refer to Wertz and Larson [152], and Sidi [168].

5.3.1 Three-Axis Active Attitude Control Design

The spacecraft attitude control is achieved using three reaction wheels that generate control torques $\tau_{wx}, \tau_{wy}, \tau_{wz}$ about the three principal axes of the satellite. The torque vector appears explicitly in the attitude dynamics of the satellite given in equation (3-3). We have developed and implemented variable structure control (VSC) strategy [169], [170], [171] for attitude control, which performs extremely well in presence of an ideal reaction wheel model (i.e., a simple gain factor). However, as soon as we inject the nonlinear dynamics of the reaction wheel into the attitude control loop, the VSC controller fails to stabilize and control the spacecraft slew-manoevres. The same phenomenon was observed using linear state feedback control strategy designed based on the linearized attitude dynamics of the satellite.

Interestingly, however, we designed and implemented a decentralized PID control strategy that performs extremely well for both attitude regulation and tracking even in presence of nonlinear reaction wheel dynamics and physical constraints on control signal (i.e., control signal saturation). All of the above-mentioned control strategies were designed based on the quaternion representation of satellite attitude (i.e., using quaternion-based kinematics differential equations) in order to avoid dynamic singularities of the Euler representation.

In both VSC and state feedback control strategies, the attitude control error $e_{att} = [e_1 \ e_2 \ e_3]^T$ was defined based on the quaternions as follows:

$$e_{att} = \begin{bmatrix} q_{0c} & q_{3c} & -q_{2c} & -q_{1c} \\ -q_{3c} & q_{0c} & q_{1c} & -q_{2c} \\ q_{1c} & q_{2c} & q_{3c} & -q_{0c} \end{bmatrix} \begin{bmatrix} q_1 \\ q_2 \\ q_3 \\ q_{0c} \end{bmatrix} \quad (5-38)$$

where $q_{ic}, q_i; i = 0,1,2,3$ are the commanded and current attitude quaternions, respectively. The PID control design based on the quaternion error given above, however, will require MIMO PID controllers that are not straightforward to design and tune. Thus, to simplify the PID parameter tuning, the attitude error in PID control is defined based on the Euler angles. Three separate decentralized PID controllers are designed for each angle. A quaternion to Euler angle transformation is needed to close the loop. This nonlinear transformation is, in fact, given in equation (5-13). This equation allows us to obtain the Euler angles from the quaternions. This would not impose singularity problems because of the static nature of this transformation. More precisely, the quaternion kinematics differential equations are still integrated to obtain the quaternions. Thus, no dynamic singularities will occur in the closed-loop attitude control system.

Furthermore, the above-mentioned definition of control error in the PID control strategy design also enables better visualization of the satellite manoeuvre control commands. To take the actuator saturation into account, saturation blocks were applied to the outputs of the PID controllers. Accuracies in the order of less than of 5 *mdeg* can be achieved for thee axes using this decentralized PID control strategy. Figure 5-5 depicts the block diagram representation of the closed-loop ACS subsystem that has been developed in this thesis.

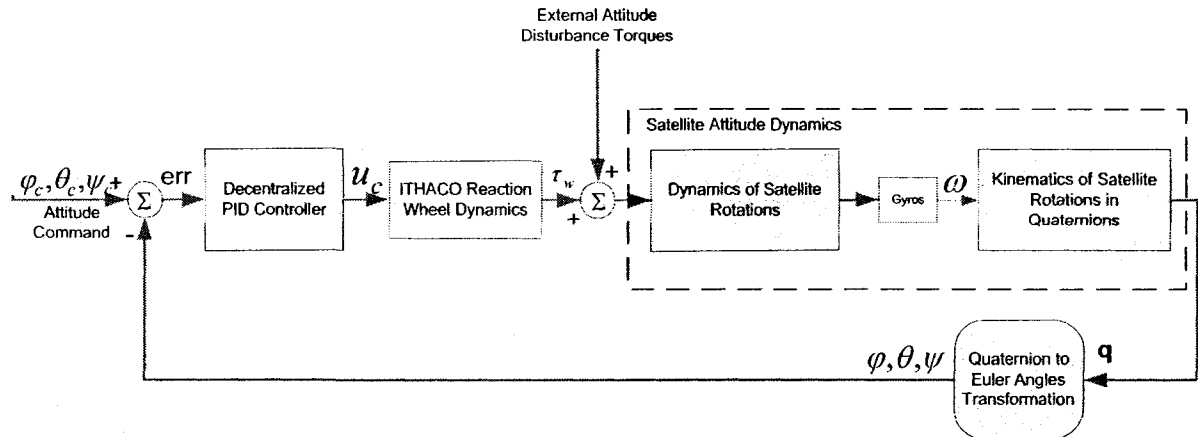


Figure 5-5. Closed-loop 3-axis stabilized attitude control subsystem (ACS) of the spacecraft.

5.4 Simulation Results of 3-Axis Stabilized ACS

In this section, we present attitude stabilization as well as slew-maneuvring capabilities of the ACS under healthy (or nominal) mode of operation and in presence of external disturbances, reaction wheel dynamics, and control (or equivalently actuation) signal saturation. As mentioned previously, Table 5-2 and Table 5-1 show the model parameter values used in ACS simulations for the components of ACS and the environmental disturbances, respectively.

5.4.1 Three-Axis Attitude Stabilization

We first start with the attitude regulation capability of the ACS, where the asymptotic stability of the satellite attitude is shown in response to a non-zero initial attitude, no attitude commands, and in presence of environmental disturbances. The evolution of the Euler angles under such scenario can be seen in Figure 5-6 and Figure 5-7. More specifically, Figure 5-6 shows that the three Euler angles asymptotically approach to zero starting from nonzero initial conditions. It can be seen from this figure that the settling

time of the closed-loop ACS is about 8.3 minutes. Figure 5-7 depicts the Euler angles at steady-state. It can be seen from this figure that the attitude stabilization error is in the order of less than 5 *mdeg*. Figure 5-8 shows the same attitude stability property for the quaternions.

Table 5-2. The closed-loop ACS parameters including parameters of the RW model, the satellite attitude dynamics and the controller, used in the simulations.

Parameter	Description	Units	Value
J_{xx}	Satellite inertia about x-axis	$N.m.s^2$	450
J_{yy}	Satellite inertia about y-axis	$N.m.s^2$	200
J_{zz}	Satellite inertia about z-axis	$N.m.s^2$	440
J_w	Wheel inertia	$N.m.s^2$	0.0077
G_d	RW driver gain	A/V	0.19
k_t	Motor torque constant	$N.m/A$	0.029
k_e	Motor Back-EMF	$V/rad/s$	0.029
k_s	Overspeed circuit gain	$V/rad/s$	95
k_f	Voltage feedback gain	V/V	0.5
ω_s	Overspeed circuit threshold	rad/s	690
τ_c	Coulomb friction	$N.m$	0.002
N	Number of motor poles	-	36
R_{in}	Input resistance	Ω	2
ω_d	Frequency	rad/s	9
K_P	PID proportional coefficient	-	100
K_I	PID integral coefficient	s^{-1}	2
K_D	PID derivative coefficient	s	4000

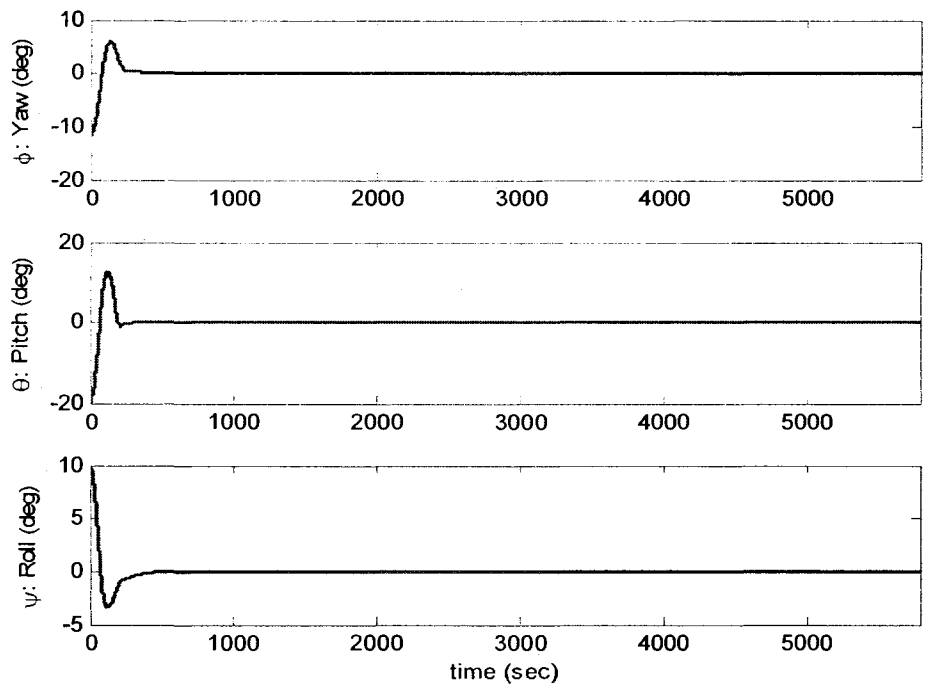


Figure 5-6. Transient of Euler angles (Yaw-Pitch-Roll) for 3-axis attitude stabilization at low speeds of reaction wheel actuators

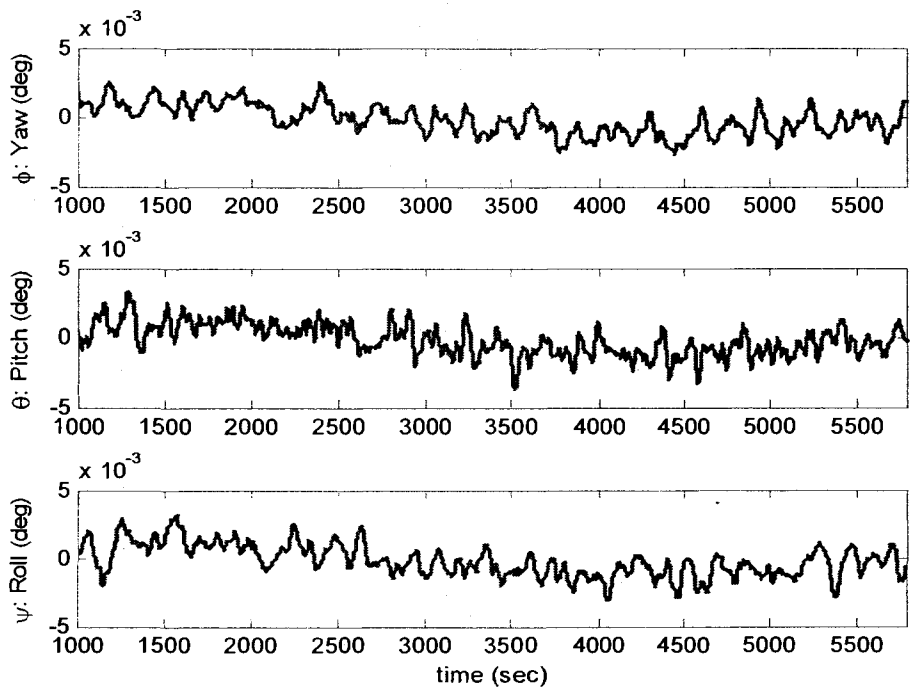


Figure 5-7. Euler angles zoomed around the steady state for 3-axis attitude stabilization at low speeds of reaction wheel actuators

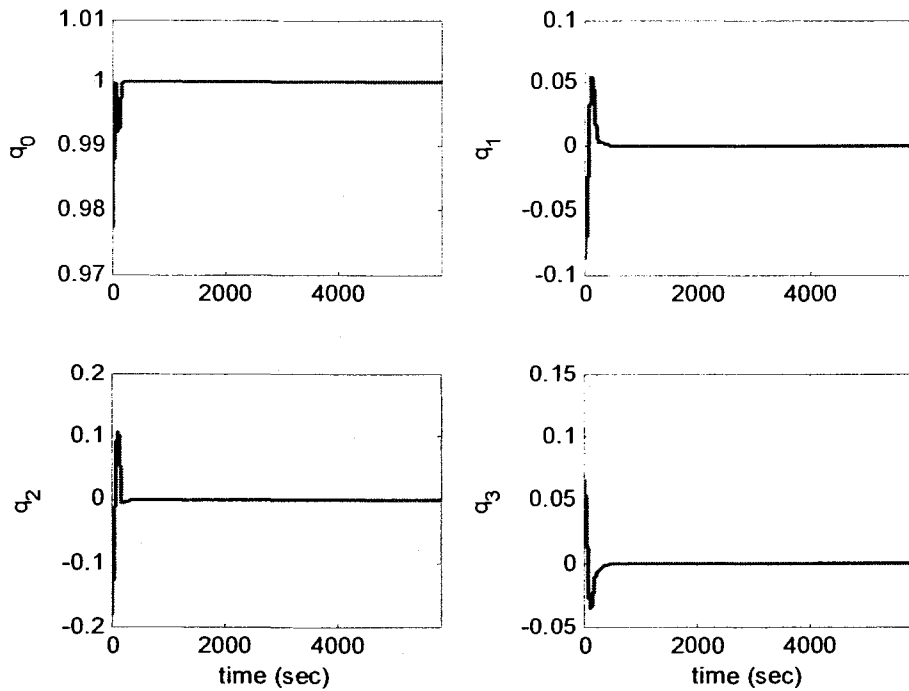


Figure 5-8. Stabilization of quaternions.

Figure 5-9 and Figure 5-10 show the control signals and the reaction torques generated by the reaction wheels, respectively. As can be seen in these figures, even though the control signal has got saturated over some time intervals, but the ACS performs very well. Furthermore, the magnitude of the reaction torques is consistent with the nominal specifications of the ITHACO 'type A' reaction wheels mentioned in spec sheets of this wheel.

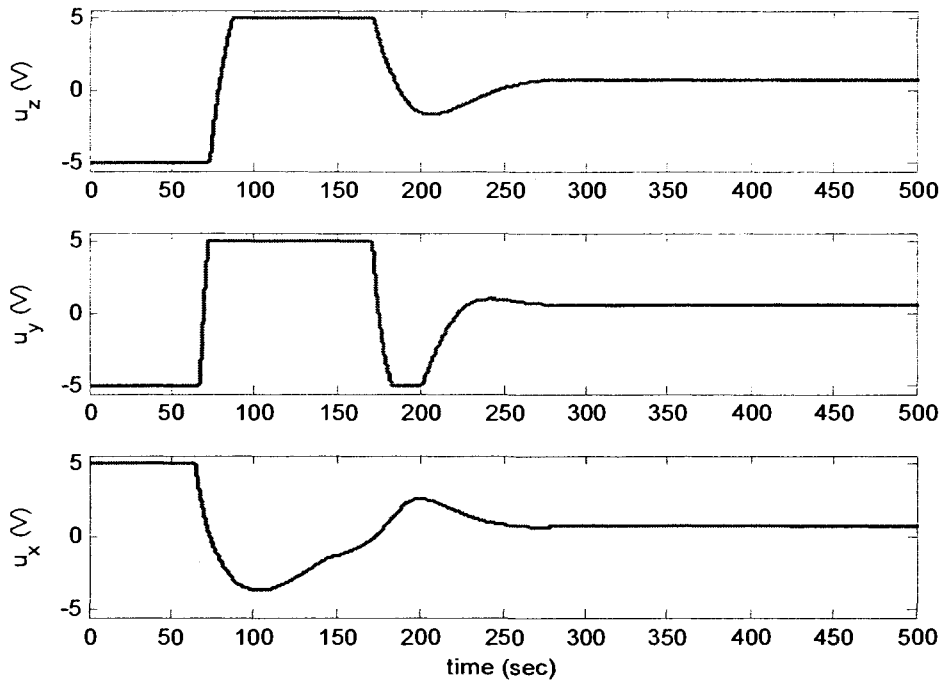


Figure 5-9. Control signals during transient phase of attitude stabilization

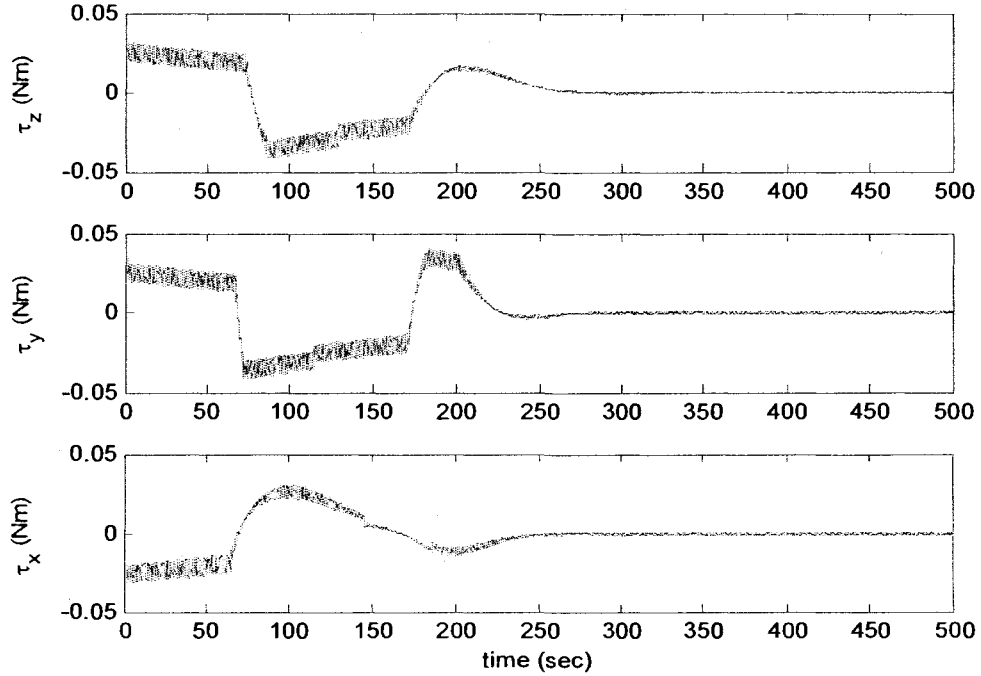


Figure 5-10. Reaction torques generated by reaction wheels during transient phase of attitude stabilization.

Figure 5-11 and Figure 5-12 depicts the spacecraft's body angular rates during the transient and steady state, respectively. The variations in satellite angular rates during the transient are due to satellite rotations until it reaches a stable attitude. However, it can be seen from Figure 5-12 that during steady state, the angular velocity of the satellite around the y -axis does not converge to zero and instead it converges to a nonzero value almost equal to -1.1×10^{-3} (rad/sec). This is, indeed, due to the satellite rotation around the Earth and that specific value is actually the speed of that rotation (or orbital frequency of the satellite n_c), which is dependent on satellite altitude in the orbit and is given by equation (5-17). This observation is also consistent with equation (5-18), where the term $-n_c$ appears on the right-hand side of the equation.

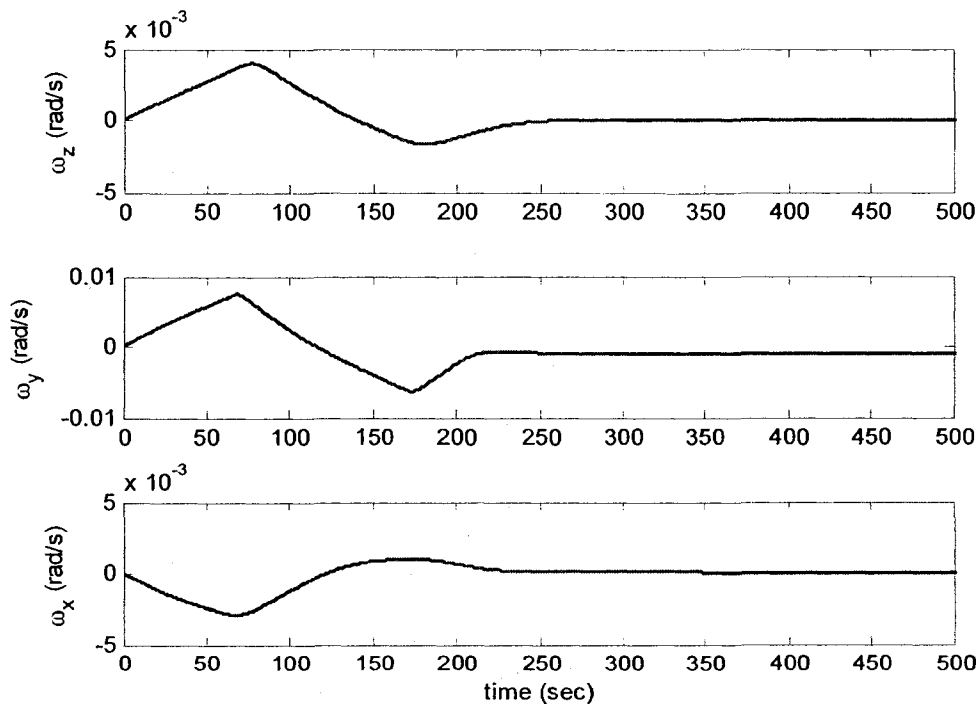


Figure 5-11. Body angular rates of the satellite in the orbit reference frame during the transient phase of attitude stabilization

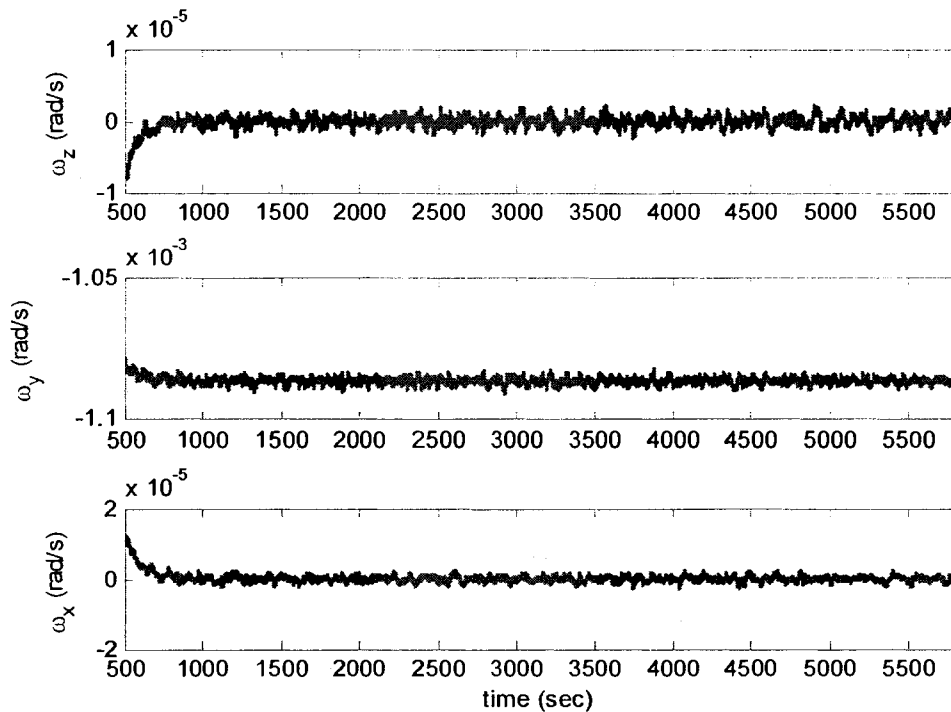


Figure 5-12. Body angular rates of the satellite in the orbit reference frame during the steady state of attitude stabilization

Figure 5-13 and Figure 5-14 depict the angular speeds of the three reaction wheels and the motor currents of the three wheels, respectively. Eventually, the cumulative effect (or torque) of different external attitude disturbances is depicted in Figure 5-15 for one complete orbit of the satellite.

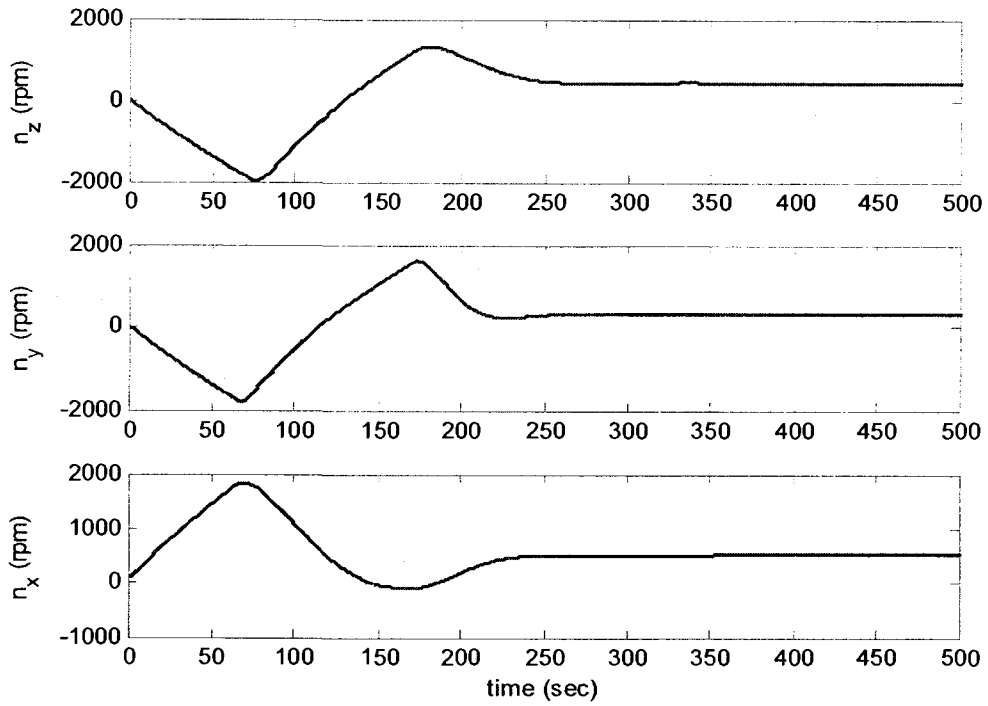


Figure 5-13. Reaction wheel speeds during transient phase

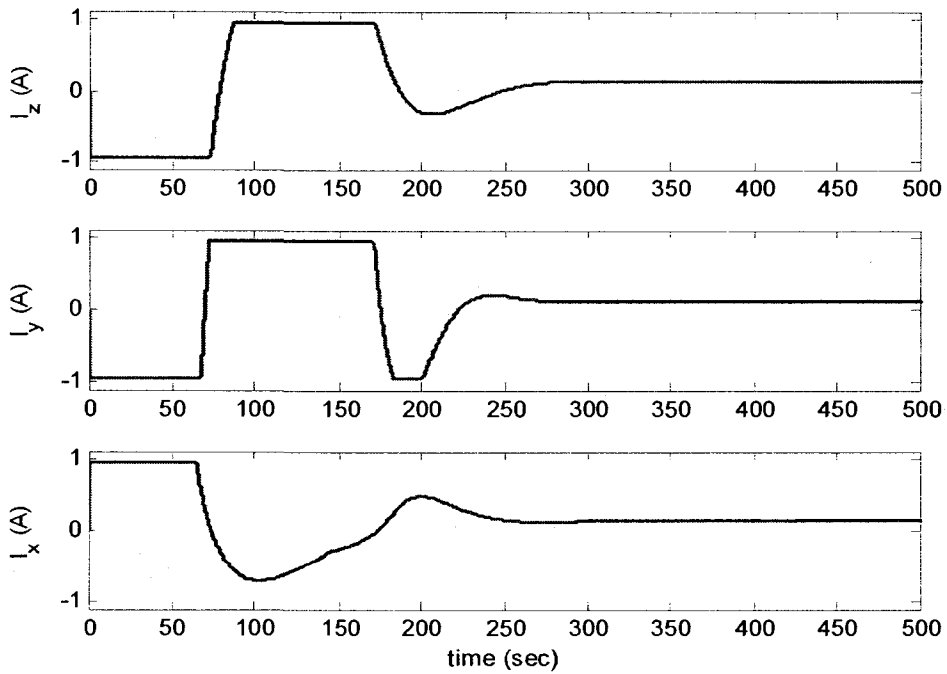


Figure 5-14. Motor current of the reaction wheels during transient phase

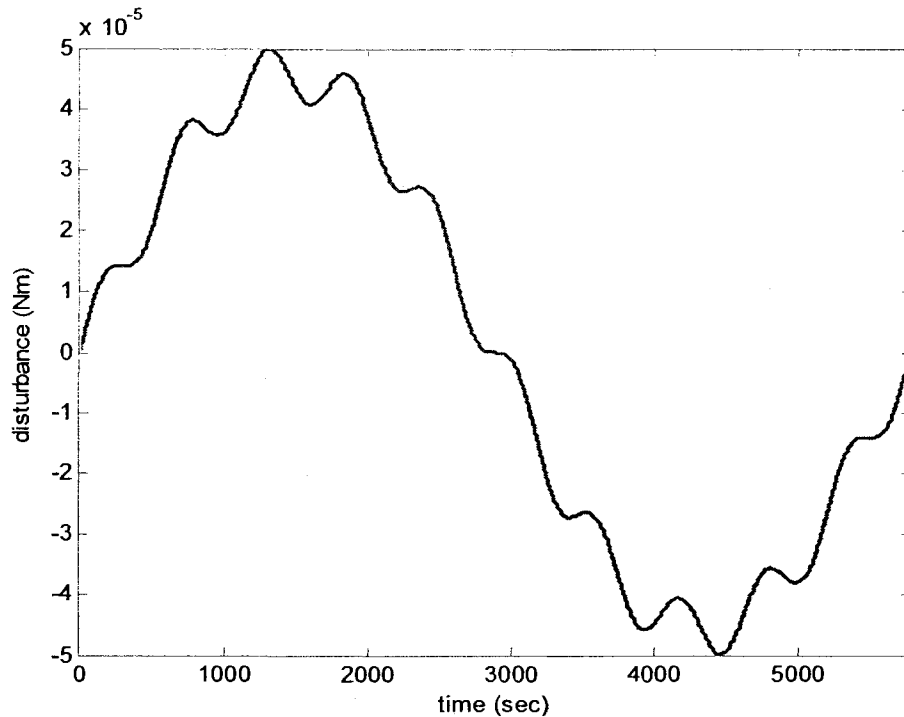


Figure 5-15. Environmental attitude disturbances over one orbit of the satellite

In order to investigate the slew-maneuvering capability of the ACS, the satellite was commanded to perform three slew maneuvers within almost half of an orbit period. Therefore, the attitude of the satellite was commanded at three different times within this period of time. The attitude commands were sent to all the three Euler angles simultaneously. Figure 5-16 to Figure 5-18 respectively represent the evolution of yaw, pitch and roll angles versus their commanded values. It can be easily seen from these figures that all the commanded attitudes have been perfectly achieved by the ACS. The response of other major quantities/variables of the ACS, including the quaternions, the control signals, the reaction torques generated by the wheel actuators, the spacecraft body rates and the speeds and current of the reaction wheels, to the three slew maneuvers are depicted in Figure 5-19 to Figure 5-24, respectively.

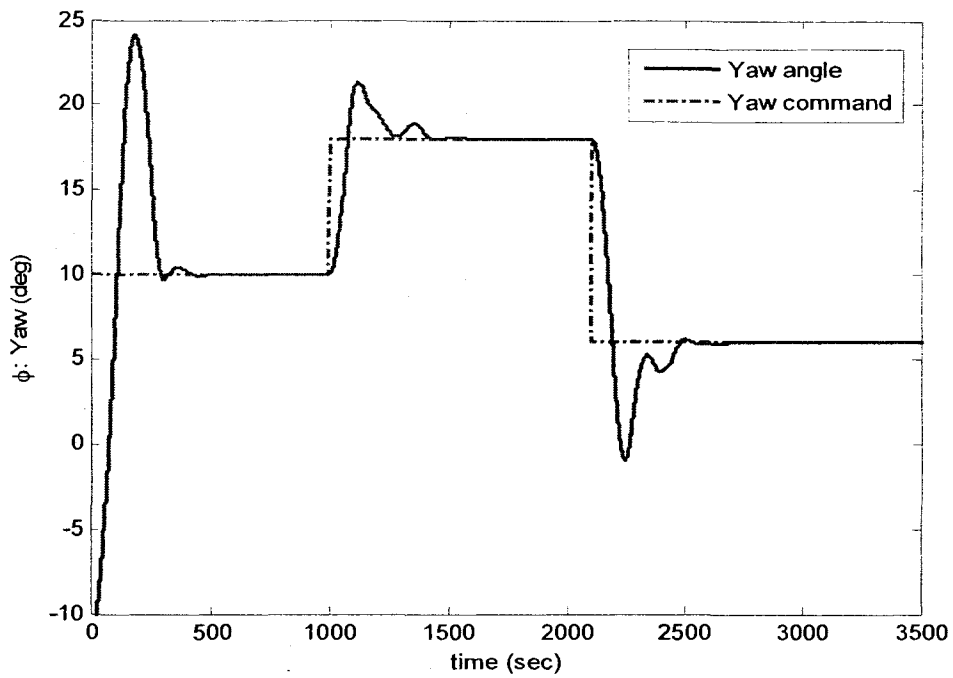


Figure 5-16. Yaw angle evolution in response to three slew-maneuvers

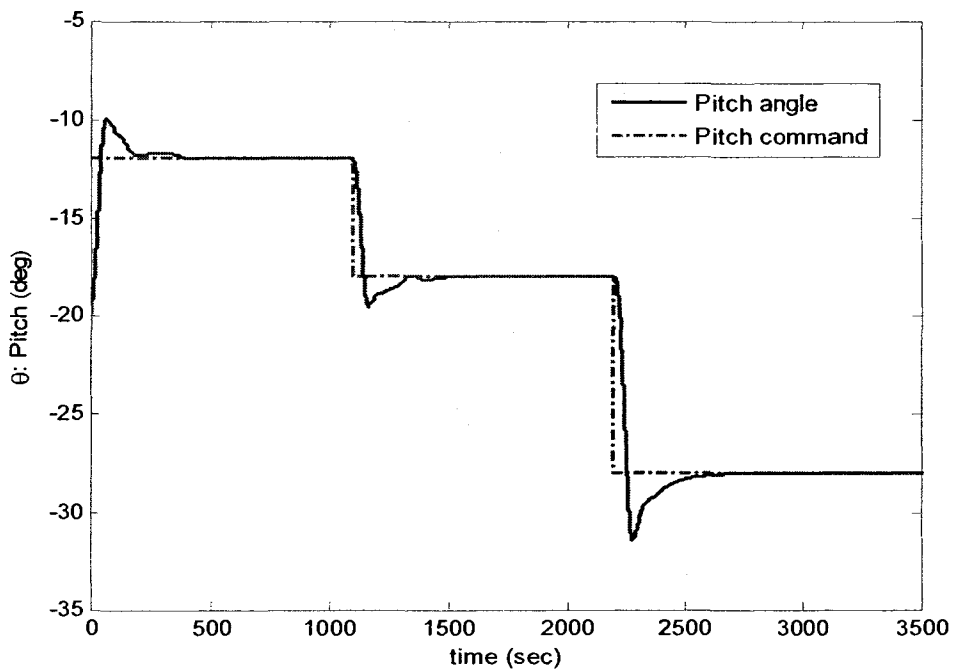


Figure 5-17. Pitch angle evolution in response to three slew-maneuvers

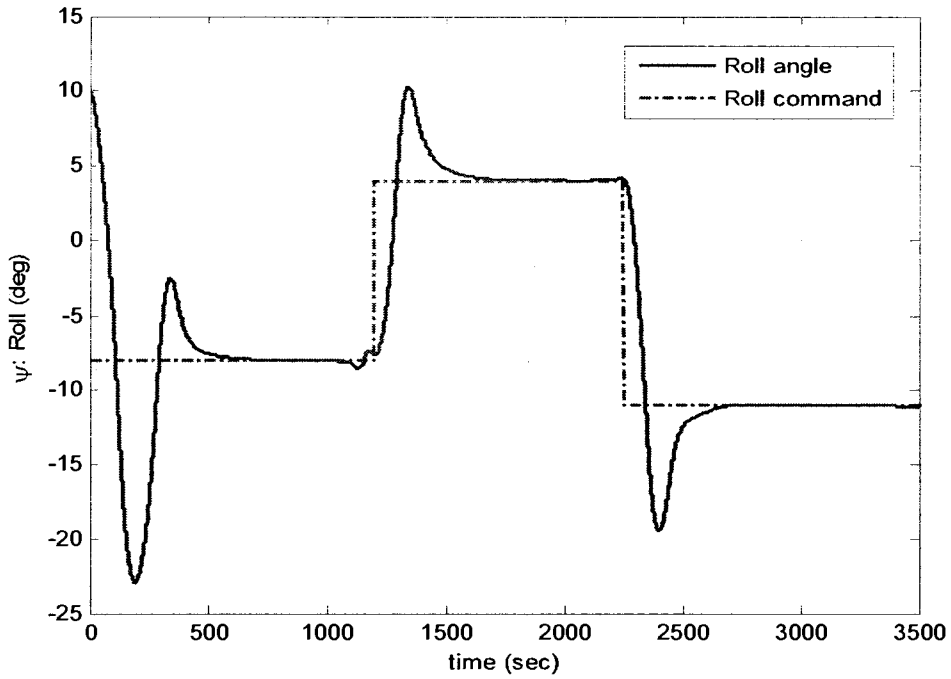


Figure 5-18. Roll angle evolution in response to three slew-maneuvers

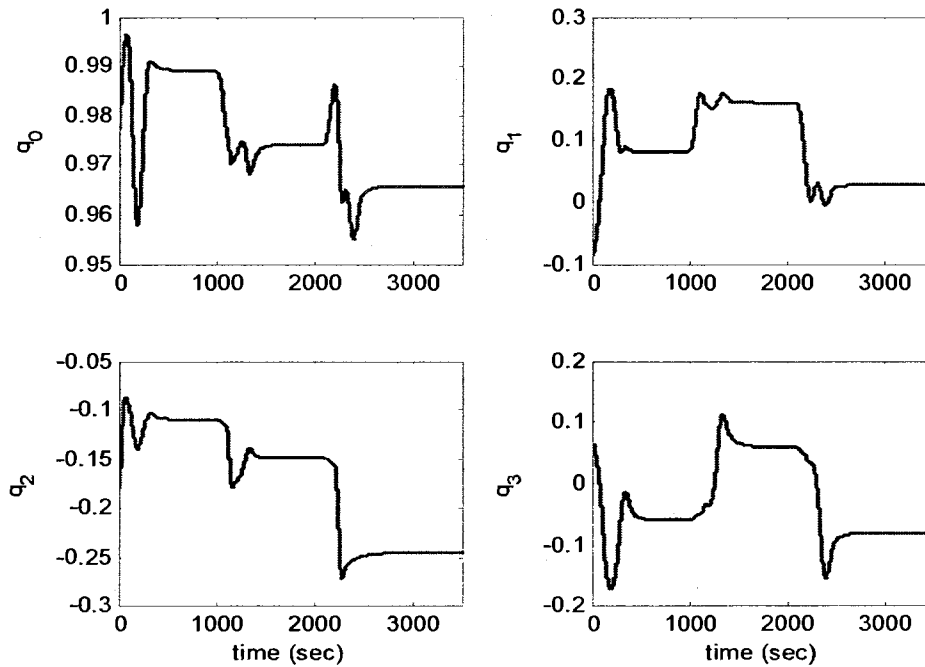


Figure 5-19. The evolution of quaternions in response to three slew-maneuvers

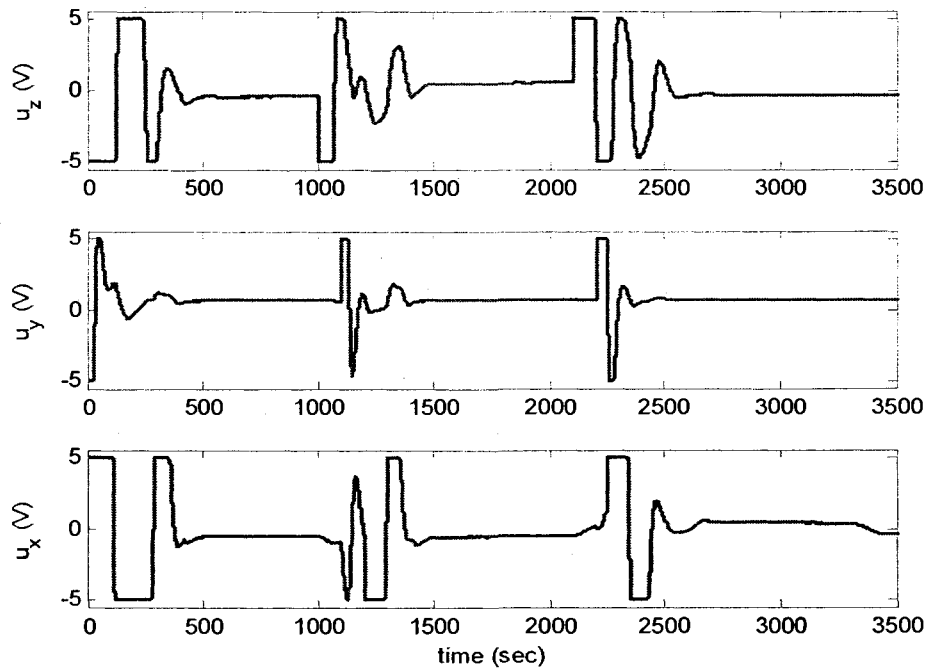


Figure 5-20. Control signals in response to three slew-maneuvers

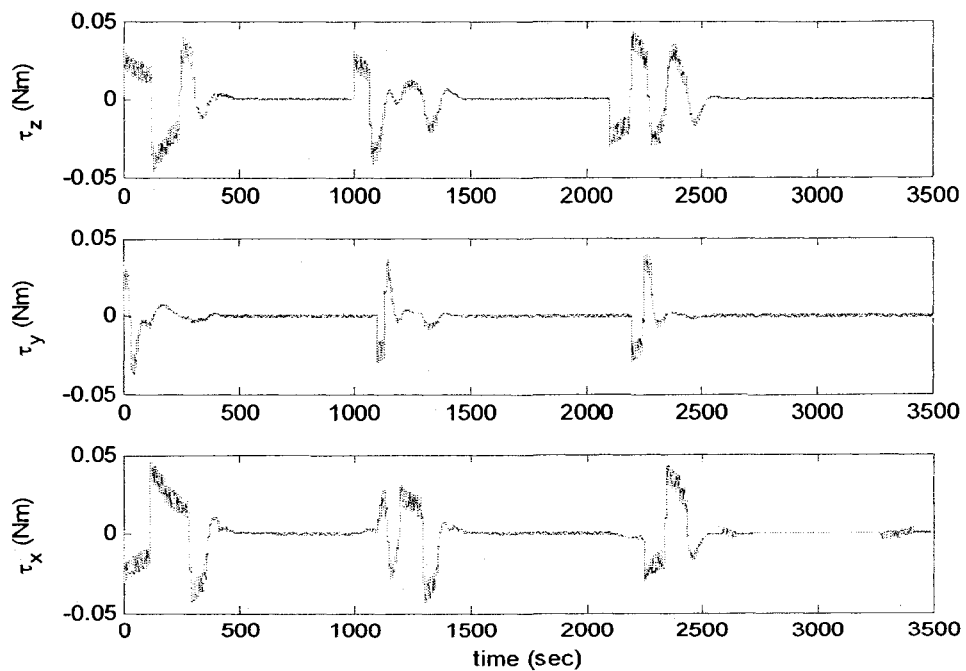


Figure 5-21. Reaction torques in response to three slew-maneuvers

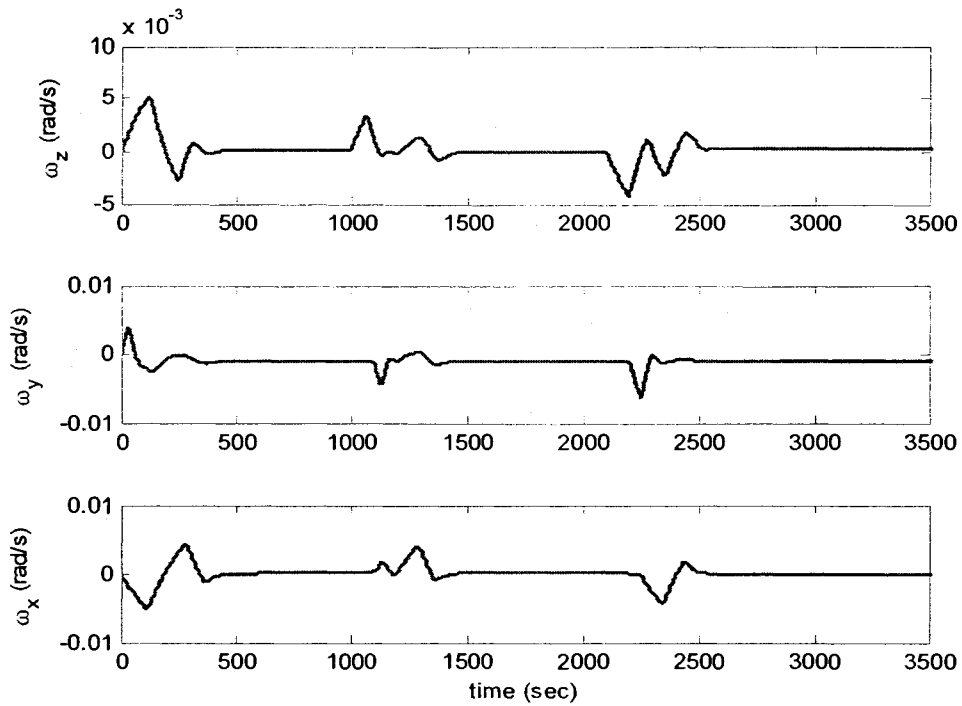


Figure 5-22. Satellite body rates in response to three slew-maneuvers

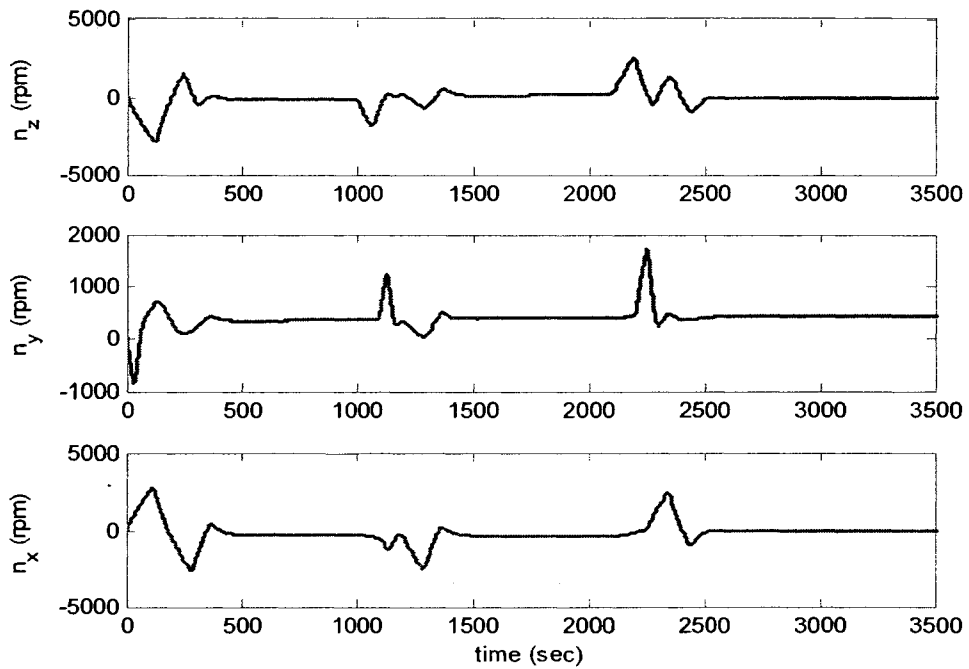


Figure 5-23. The speeds of the three reaction wheels in response to three slew-maneuvers

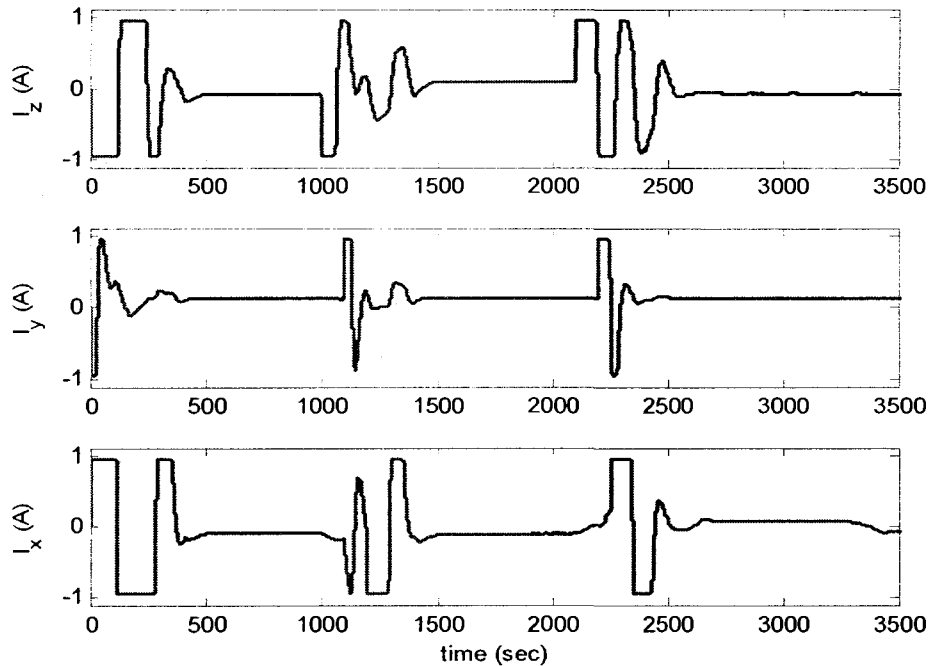


Figure 5-24. The motor current of the three reaction wheels in response to three slew-maneuvers.

5.4.2 Characterization of Possible Fault Scenarios in Reaction Wheels

In order to be able to develop the FDI algorithms and to inject faults in the ACS, the potential sources of anomalies in the reaction wheels have to be identified. Extensive experimental experience with reaction wheels on-board different satellite missions has revealed that the following potential failures may occur in these attitude actuators:

- (i) **Unexpected changes in the bus voltage V_{bus} (i.e., bus voltage drop), and**
- (ii) **Unexpected changes in the motor current, which can be represented (or modeled) by changes in the motor torque constant k_t .**

5.5 Simulation Results for FDII with Full-State Measurements

In this section, we present simulation results of FDII in reaction wheel actuators of ACS subject to faults in motor current and bus voltage and under the availability of full-state measurements. It is very important to note that for FDII purposes, the reaction wheel itself, though being an actuator of ACS, is considered as the system being monitored. More precisely, the second-order nonlinear model of the reaction wheel acts as the system (or plant) under consideration and consequently the wheel's signals, namely voltage, current, and speed, comprise the inputs of the FDII subsystem. Therefore, the satellite attitude model and controller are used to provide a near-realistic simulation of reaction wheel operation in a closed-loop ACS operation and they are not used in FDII design.

As mentioned previously, three identical reaction wheels are used in a 3-axis stabilized satellite for attitude control. According to the aforesaid philosophy of monitoring the wheels, one FDII modules need to be dedicated to each reaction wheel, thus requiring a total of 3 FDII modules for health monitoring of the whole reaction wheel assembly of the ACS. Since it is assumed that the reaction wheels are identical their corresponding FDII modules would also be essentially identical. Hence, in this section we show the results of FDII for only one of the wheels in ACS, corresponding to the Pitch axis. The simulation data, however, are obtained from the closed-loop ACS simulation of a 3-axis stabilized LEO satellite. The simulations are carried out for 6000 seconds (or 100 minutes) of ACS operation, which is just slightly larger than the period of the simulated LEO satellite (the simulated LEO satellite was in an altitude of 586.91 km with an orbit period of 96.4144 minutes).

Intermittent time-varying faults are injected into two of the reaction wheel components, namely motor current and bus voltage. Faults in motor current are modeled and injected as variations in motor torque gain k_t . Faults in bus voltage are modeled and injected as drops in the voltage of the power bus V_{bus} in equations (5-30) and (5-31). In consequence, two fault parameters (FPs) are defined that affect the bus voltage and the motor gain in additive form. Therefore, the multi-parameterized fault model is obtained by replacing V_{bus} in equations (5-30) and (5-31) by $V_{bus} + \alpha^1$, and replacing k_t in equation (3-30) by $k_t + \alpha^2$, where α^1 and α^2 are *unknown* fault parameters that indicate possible presence of faults in bus voltage and motor current respectively. Due to additive formulation of the above fault parameters, the value of α^1 and α^2 at healthy nominal conditions is essentially zero.

The following intermittent time-varying fault in motor current is injected into the reaction wheel on the pitch axis as a sinusoidal variation in the motor torque gain k_t of that wheel:

$$k_t(t) = \begin{cases} k_t^{nom}, & t < 1000 \\ k_t^{nom} - 0.02 \sin\left(\frac{2\pi(t-1000)}{3000}\right), & 1000 \leq t \leq 4250 \\ k_t^{nom}, & 4250 < t \leq 6000 \end{cases} \quad (5-39)$$

where $k_t^{nom} = 0.029$ is the nominal value of the motor torque gain.

Time-varying bus voltage faults are injected and simulated as a sequence of instantaneous drops in the voltage of the power bus. Two types of faults are considered for the bus voltage including low-severity (or incipient) and high-severity faults that basically differ in terms of the severity of the voltage drop. Low severity bus voltage

faults include scenarios where the drop in the bus voltage is below 4V. These faults only cause higher power consumption in the ACS by making the wheel operate at a higher current. The low-severity faults will not make the ACS system unstable or out of control. The following sequence of low-severity bus voltage faults are injected over different time intervals in the reaction wheels of ACS (it is important to note that since the power bus is common to all loads in a satellite such as actuators, sensors, and payload instrumentation, bus voltage faults are also essentially common to all the three reaction wheels of the ACS):

$$V_{bus}(t) = \begin{cases} V_{bus}^{nom}, & 0 \leq t < 1000 \\ V_{bus}^{nom} - 1, & 1000 \leq t < 2240 \\ V_{bus}^{nom} - 4, & 2240 \leq t < 3100 \\ V_{bus}^{nom} - 3.5, & 3100 \leq t < 4390 \\ V_{bus}^{nom} - 2.5, & 4390 \leq t < 5100 \\ V_{bus}^{nom}, & 5100 \leq t \leq 6000 \end{cases} \quad (5-40)$$

where $V_{bus}^{nom} = 24V$ is the value of bus voltage under healthy operational mode.

The presence of high-severity bus voltage faults (i.e., drops of more than 5V in the bus voltage) makes the ACS system unstable and the satellite starts tumbling upon occurrence of these faults. The following sequence of high-severity bus voltage faults are injected into the ACS subsystem:

$$V_{bus}(t) = \begin{cases} V_{bus}^{nom}, & 0 \leq t < 1000 \\ V_{bus}^{nom} - 6, & 1000 \leq t < 2240 \\ V_{bus}^{nom} - 9.4, & 2240 \leq t < 3100 \\ V_{bus}^{nom} - 5.3, & 3100 \leq t < 4390 \\ V_{bus}^{nom} - 7.8, & 4390 \leq t < 5100 \\ V_{bus}^{nom}, & 5100 \leq t \leq 6000 \end{cases} \quad (5-41)$$

In the following subsections, we assume that full-state measurements are available from reaction wheels. More specifically, we assume that both current and speed of the

wheel are measured with appropriate sensors and are available for fault diagnosis. We will first test the diagnostic performance of the series-parallel FDII scheme under the aforementioned fault scenarios and then analyze its robustness with respect to measurements noise. Then, the same procedure is performed for the robust parallel FDII scheme.

All FDII validation results are obtained with Gaussian random noises for the current and speed measurements. The nominal levels (or intensities) of measurement noise for both state (i.e., current and speed) measurements are given in noise variance and noise power (in dB) in Table 5-3, and in terms of signal-to-noise ratio (SNR) in dB in Table 5-4. The definition of noise variance is clear. The other two indices are defined as follows:

Power of the noise (dB):

$$P_v(\text{dB}) = 10 \times \log_{10} \left(\frac{1}{T} \int_0^T |v(t)|^2 dt \right) \cong 10 \times \log_{10} \left(\frac{1}{T} \sum_{k=0}^{T/T_s} |v_k|^2 \right) \quad (5-42)$$

Signal-to-Noise Ratio (dB):

$$\text{SNR}(\text{dB}) = 10 \times \log_{10} \left(\frac{P_{\text{signal}}}{P_v} \right) \cong 10 \times \log_{10} \left(\frac{\sum_{k=0}^{T/T_s} |x_k|^2}{\sum_{k=0}^{T/T_s} |v_k|^2} \right) \quad (5-43)$$

where T is a specific period of time. In this thesis, T was set to be the orbit period.

The “nominal” noise intensity, which is set based on the typical noise levels of current and speed sensors available in the market, is a minimal noise level considered for the initial performance evaluation of the FDII schemes. However, two larger levels of noise – as compared to the nominal one – were also used to perform robustness analysis of the FDII schemes with respect to measurement noise. These noise levels are identified

in Table 5-3 and Table 5-4 as “medium” noise and “high” noise levels. The three aforementioned indices of noise intensity for these two noise levels are also given in Table 5-3 and Table 5-4. It is very important to note that the measurement noise power and the SNR of the “medium” and “high” noise levels are respectively 100 and 1000 times larger than that of the “nominal” noise conditions.

Table 5-3. Specifications of the various measurement noise levels used in the simulations.

Noise Level/Intensity	Measured Variable	Variance σ_v^2	Power P_v (dB)
<i>Nominal</i>	Current (v_i)	2×10^{-8}	-77
	Speed (v_ω)	0.009647	-10.16
<i>Medium</i> (in robustness analysis)	Current (v_i)	2×10^{-6}	-57
	Speed (v_ω)	0.9647	-0.16
<i>High</i> (in robustness analysis)	Current (v_i)	2×10^{-5}	-47
	Speed (v_ω)	9.6470	9.84

Table 5-4. Signal-to-noise ratio (SNR) corresponding to the various noise intensities in Table 5-3 and calculated for different fault scenarios.

Noise Level/Intensity	Measured Variable	Fault Scenario		
		Motor Current Fault	Low-Severity V_{bus} Fault	High-Severity V_{bus} Fault
<i>Nominal</i>	Current (v_i)	75.00 dB	74.57 dB	73.66 dB
	Speed (v_ω)	75.00 dB	74.76 dB	73.72 dB
<i>Medium</i> (in robustness analysis)	Current (v_i)	55.00 dB	54.57 dB	53.66 dB
	Speed (v_ω)	55.00 dB	54.76 dB	53.72 dB
<i>High</i> (in robustness analysis)	Current (v_i)	45.00 dB	44.57 dB	43.66 dB
	Speed (v_ω)	45.00 dB	44.76 dB	43.72 dB

It is important to note that the SNR index is provided in a separate table from the variance and the power. The reason is that as can be seen from the definition of SNR, the value of SNR not only depends on the noise intensity but also on the actual signal being measured. As a result, the SNR value would be dependent on the specific fault scenario being considered. Therefore, the SNR values corresponding to the three noise levels (i.e.,

nominal, medium, and high) are mentioned in a separate table (i.e., Table 5-4) for each fault scenario.

Indices of fault identification performance evaluation: Once a fault is correctly isolated, the FP estimate corresponding to the isolated fault can be taken as the indicator of the fault severity for fault identification purposes. In order to quantitatively assess the accuracy of fault identification, a number of performance indices have been used in this thesis that are based on evaluating the accuracy of FP estimates. These performance indices are basically average performance measures of the FP estimation error defined as:

$$e_k^\alpha = \alpha_k^i - \hat{\alpha}_k^i \quad (5-44)$$

where i is the index of the detected and isolated fault. The performance indices defined based on the above error include the root mean square of the error (RMSE), the mean of the error (ME), and the standard deviation of the error (STDE). These performance indicators are calculated as follows:

$$\text{RMSE:} \quad rms_\alpha = \sqrt{\frac{1}{N} \sum_{k=1}^N [e_k^\alpha]^2} \quad (5-45)$$

$$\text{ME:} \quad \bar{e}_\alpha = \frac{1}{N} \sum_{k=1}^N e_k^\alpha \quad (5-46)$$

$$\text{STDE:} \quad \sigma_\alpha = \sqrt{\frac{1}{N-1} \sum_{k=1}^N [e_k^\alpha - \bar{e}_\alpha]^2} \quad (5-47)$$

It should be noted that these performance indices are used for all FDII simulation results throughout this chapter.

5.5.1 Simulation Results for FDII Using the Series-Parallel Scheme

The series-parallel FDII scheme was applied to detect, isolate, and identify the aforementioned faults in the reaction wheel of the Pitch axis. Since two faults are considered in the reaction wheels, the bank of NPEs essentially consists of two NPEs; one NPE for FDII of V_{bus} fault and one NPE for FDII of k_t fault. Two one-hidden-layer feed-forward neural networks with four neurons in the hidden layer and one neuron in the output layer are used as NPEs. Sigmoidal activation functions were used for the neurons in the hidden layer, while linear neurons were used at the output layer. Neural network learning rates were selected as, $[\eta_w^1 \ \eta_v^1] = [1 \ 10^{-4}]$ and $[\eta_w^2 \ \eta_v^2] = [10^{-4} \ 10^{-7}]$ for the first and the second NPE in the bank of the series-parallel FDII scheme, respectively.

5.5.1.1 FDII of Motor Current Faults

In this section, the results of FDII in presence of the time-varying intermittent fault in the motor current over the time period $t \in [1000 \ 4250]$ seconds – given in equation (5-39) – are depicted. The measured speed and current of the reaction wheel and their estimates obtained from the two NPEs of the series-parallel FDII scheme are depicted in Figure 5-25. As can be seen from the figure, the results of the NPE for bus voltage fault are depicted on the left column and the results of the NPE for motor current fault are depicted on the right column. It is important to note that this convention is used throughout this chapter. These figures clearly show an extremely close match between the measured states and their corresponding estimates for both NPEs. Note also the effect of the faults on the states of the reaction wheel.

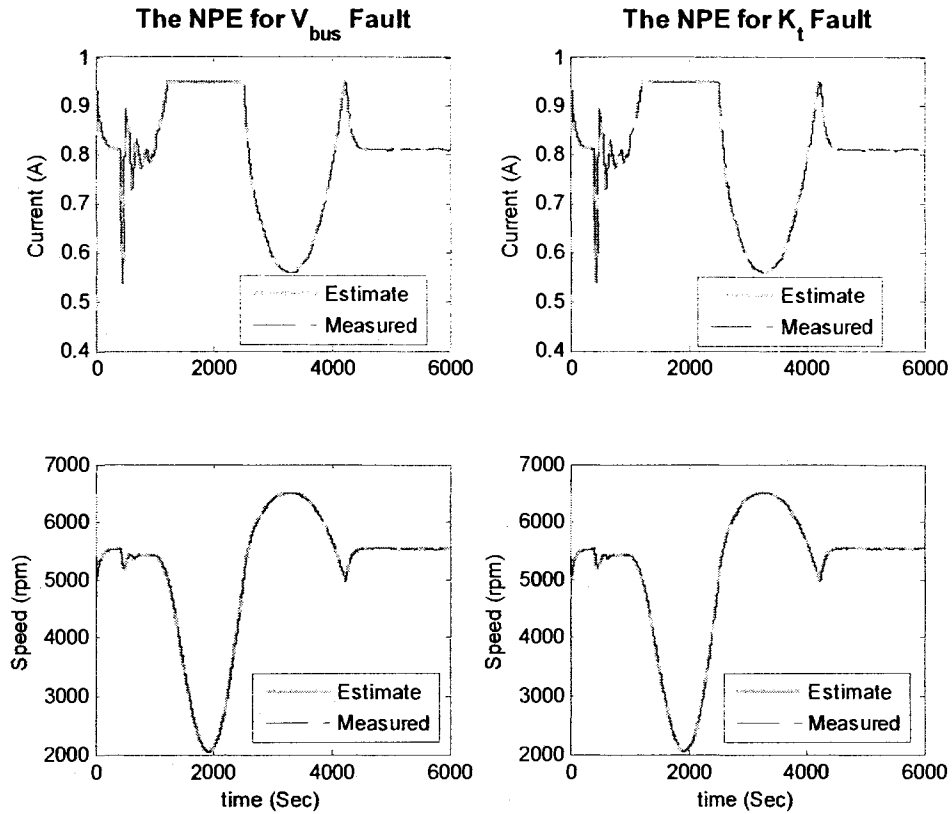


Figure 5-25. The estimated versus measured states using the series-parallel FDII scheme in presence of a time-varying fault in motor current over the time period $t \in [1000 \ 4250]$ second.

Figure 5-26 shows the residuals corresponding to the two NPEs in the bank. It is important to note that each NPE consists of two residual signals: (i) current residual and (ii) speed residual. These residuals are defined as $r_I^1 = I_k - \hat{I}_k^{\alpha_1}$ and $r_\omega^1 = \omega_k - \hat{\omega}_k^{\alpha_1}$ for the first NPE (i.e., the NPE for the FDII of V_{bus} faults), and $r_I^2 = I_k - \hat{I}_k^{\alpha_2}$ and $r_\omega^2 = \omega_k - \hat{\omega}_k^{\alpha_2}$ for the second NPE (i.e., the NPE for the FDII of K_t faults).

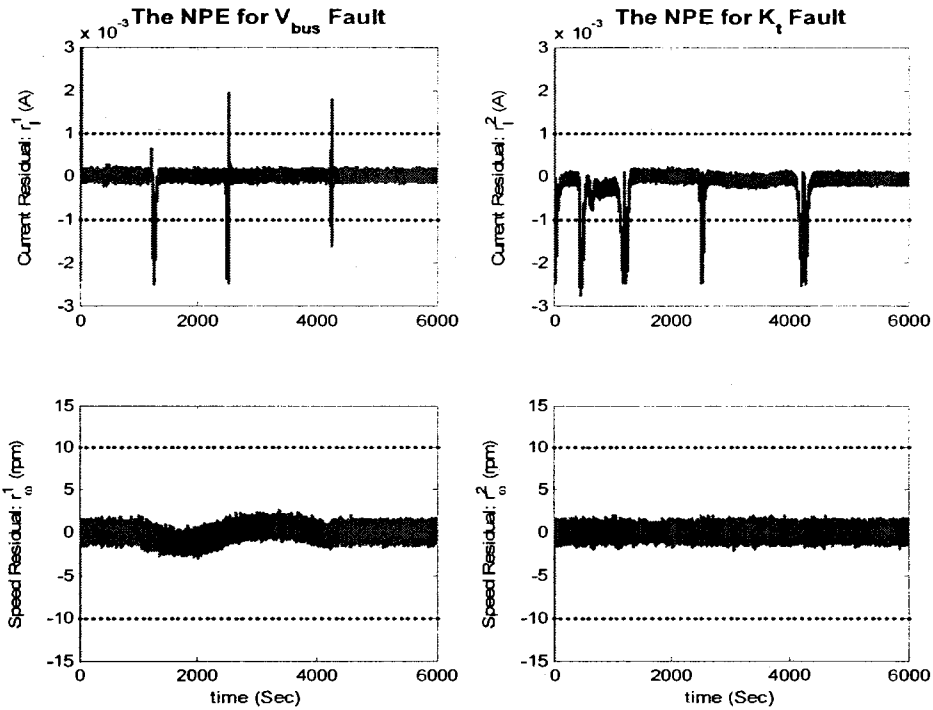


Figure 5-26. The residuals of the two NPEs of the series-parallel FDII scheme in presence of a time-varying fault in motor current over the time period $t \in [1000 \ 4250]$ second.

As was mentioned in Chapter 3, the residual thresholds must be set using the worst-case disturbance and noise analysis during the healthy period. Using this method, the residual thresholds are set to be almost four times bigger than the maximum effect of system noise and disturbances on the residual signal during healthy mode of operation. Accordingly, the threshold values were set to $\delta_i = \delta^1 = 10^{-3}$ (A) for the current residual and $\delta_\omega = \delta^2 = 10$ (rpm) for the speed residual. It should be noted that the residual thresholds are the same for all NPEs in the bank. It is also important to note that since the residual thresholds are set using the worst-case disturbance and noise analysis during healthy operations, the value of these thresholds may be changed if noise intensities are changed in the system. This issue will be further clarified in the robustness analysis section.

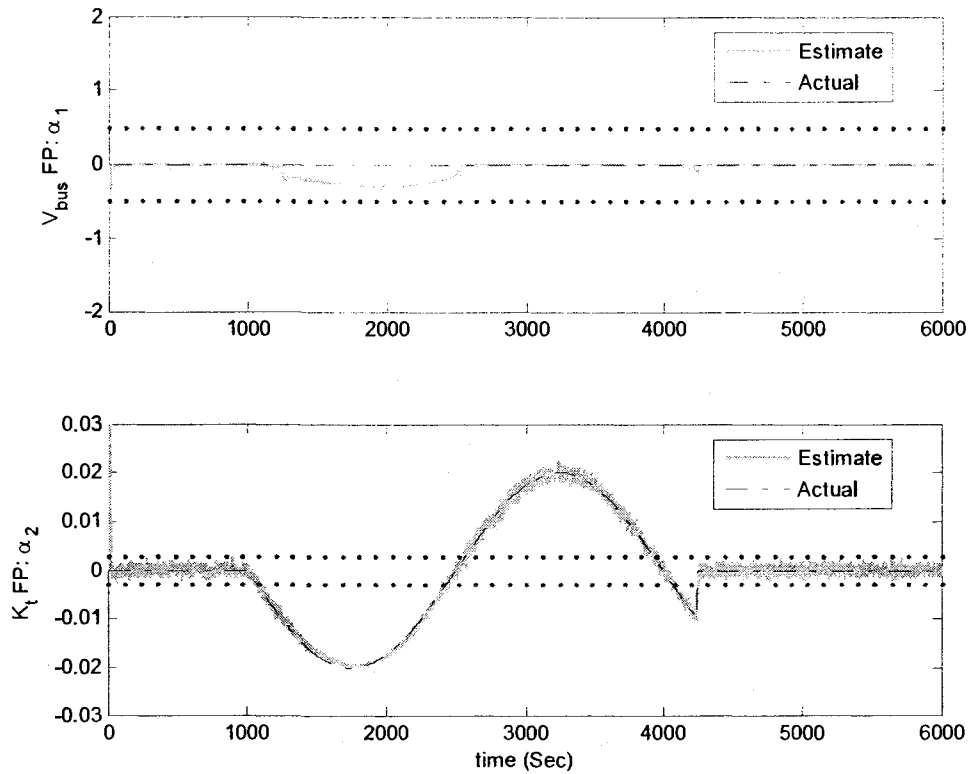


Figure 5-27. The estimated versus actual FPs using the series-parallel FDI scheme in presence of a time-varying fault in motor current over the time period $t \in [1000 \ 4250]$ second.

Figure 5-27 depicts the estimated versus actual values of the fault parameters α^1 and α^2 representing faults in V_{bus} and k_t , respectively. As can be seen in this figure, the fault parameters are very well estimated by the NPEs during both healthy and faulty periods. The FDI decision logic of the series-parallel scheme requires thresholds to be defined for FP estimates, as described in Chapter 3. The criterion for selecting FP thresholds was also mentioned in Chapter 3. Using that criterion, we select the thresholds to be $\varepsilon^1 = 0.5V$ for α^1 , and $\varepsilon^2 = 3 \times 10^{-3}$ for α^2 that accounts for almost 10.35% change in motor torque gain. It has been verified, through numerous simulations of the closed-loop ACS subsystem, that bus voltage faults with severity levels below 0.5V and motor torque gain variations in the order of 10% will not considerably degrade the closed-loop ACS

performance; hence the reliability and safety of the satellite is ensured and maintained. Indeed, the effect of such minor faults on the ACS system is a very slight increase in power consumption of the reaction wheels. It is also very important to note that as opposed to residual thresholds the FP thresholds always remain unchanged regardless of the noise or disturbance levels in the system. Instead, the FP thresholds are determined once at the design time and based on the inherent characteristics of the closed-loop system and the impact of each specific fault on the closed-loop system performance. In conclusion, throughout this thesis the FP thresholds are kept equal to the values mentioned above, namely $\varepsilon^1 = 0.5\text{V}$ for α^1 and $\varepsilon^2 = 3 \times 10^{-3}$ for α^2 .

It can be seen from Figure 5-27 that the estimate of the bus voltage FP has been incorrectly deviated from zero (though within threshold bounds) in presence of a fault in motor current. It is very important to keep in mind that this phenomenon will be observed for *most* of the fault scenarios and using both FDII schemes. Nevertheless, it should be noted that the FP estimates are not direct indicators for fault detection and isolation. More precisely, first the FDI decision logic of each algorithm is applied to find out the health state of the system. Once the health state of the system is determined and in case of presence of a fault the faulty component (or the fault source) is isolated, then the estimate of FP corresponding to the isolated fault is taken as an indicator of the fault severity.

Therefore, prior to interpreting the FP estimates, one has to obtain and analyze the results from the FDI decision logic for fault detection and isolation and then use the appropriate FP estimate for fault identification. The health state of the reaction wheel is determined using the FDI decision logic of the series-parallel scheme given in equation (3-35). The health state is depicted in Figure 5-28. Because of considering two types of

potential faults in the wheels, the health state can basically take three possible values including “0 for healthy”, “1 for faults in bus voltage” and “2 for faults in motor current”. However, it is also possible, though very rarely, that the FDI decision logic incorrectly indicates simultaneous presence of the two faults (it is said “incorrectly” because in this thesis it is assumed that faults do not occur concurrently). Therefore, the health state value equal to 3 is reserved for simultaneous presence of two faults. More precisely, whenever the health state is determined to be 3, it implies the existence of both faults has been determined by the FDII subsystem.

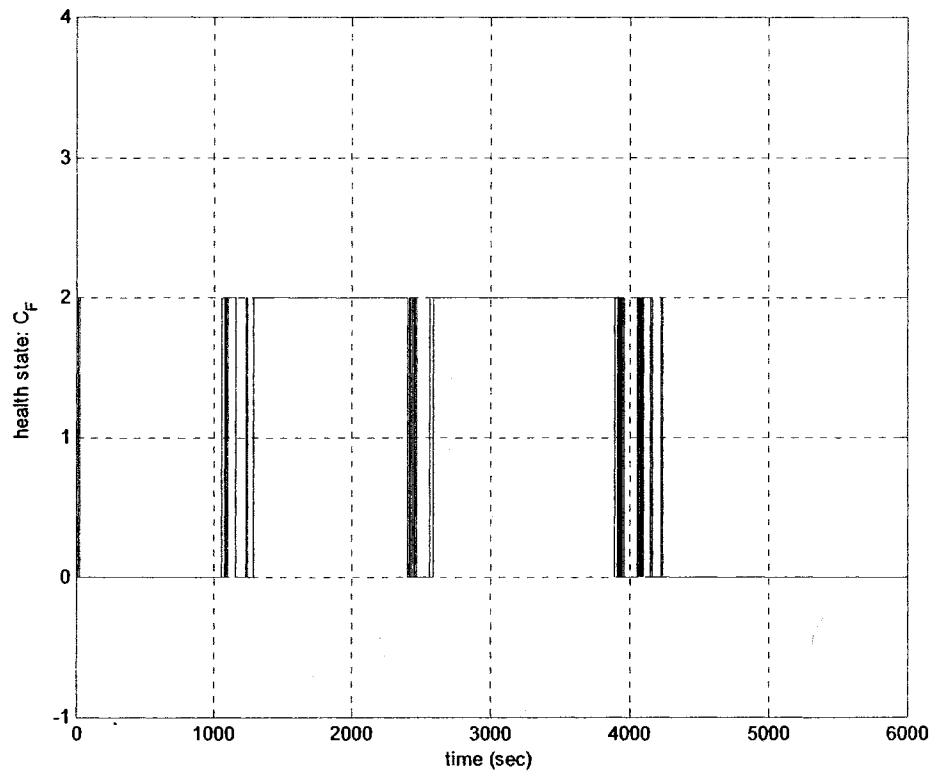


Figure 5-28. The health state of the RW using the series-parallel FDII scheme in presence of a time-varying fault in the motor current over the time period of $t \in [1000 \ 4250]$ second.

A number of observations can be made from Figure 5-28 as follows:

- The injected motor current fault has been correctly detected and isolated for the most of the faulty period.
- Only few false alarms are observed during the healthy period, namely prior to fault occurrence and after fault removal (or disappearance). It is also very important to note the robustness of the series-parallel FDII scheme to the transients of the closed-loop ACS system (i.e., the time it takes for the attitude to be stabilized, which is almost around 8 minutes or 500 seconds). It can be clearly seen from the figure that during the transient period (i.e., the first 500 seconds) there are only very few false alarms for a very short period of time. Being extremely robust to closed-loop system transients is indeed a notable advantage and capability of the serie-paralell FDII scheme.
- The first detection and isolation of the injected fault has taken place in only 54.3 seconds after fault occurrence. However, it was not persistent and some few *missed* alarms are observed until $t=1282.3$ seconds, where the fault has been persistently detected. Therefore, (a pessimistic) value of fault diagnosis delay is 282.3 seconds.
- A 100 second period of missed alarms over the period $t \in [2465 \ 2565]$ is also observed. It should be noted that these missed alarm occur around the zero-crossing of the fault parameter corresponding to the motor current, as can be seen in the actual FP of Figure 5-27. Hence, these missed alarms are, in fact, very reasonable because the fault is extremely small in that period and the system actually becomes momentarily healthy while the actual FP crosses zero value.
- Fault removal or disappearance has been persistently detected almost 13 seconds ahead of the actual fault removal (i.e., $t=4237$ seconds as compared to 4250 sec).

Now that the motor current fault has been correctly isolated, the FP estimate corresponding to this fault, namely $\hat{\alpha}^2$ (see Figure 5-27) can be taken to identify the fault severity. It should be noted that based on the isolation results, the bus voltage FP estimate, namely $\hat{\alpha}^1$ has to be neglected during the faulty period. The accuracy of motor current fault identification has been assessed using the afore-mentioned performance indices and the results are shown in Table 5-5. It can be clearly seen from this table that the motor current fault parameter (or the motor current fault severity) has been very accurately estimated with average errors in the order of less than 10^{-4} and standard deviations in the order of less than 10^{-3} , while the injected fault severity was varying between -0.02 to 0.02.

Table 5-5. The performance indices of motor current fault identification using the series-parallel FDII scheme in presence of intermittent motor current fault and with nominal noise levels.

	Pre-fault period $t \in [0 \ 1000] \text{sec}$	Faulty period $t \in [1000 \ 4250] \text{sec}$	Post-fault period $t \in [4250 \ 6000] \text{sec}$
RMSE	6.2663×10^{-4}	6.3787×10^{-4}	5.9962×10^{-4}
ME	-3.4188×10^{-5}	4.4874×10^{-6}	5.2092×10^{-5}
STDE	6.2571×10^{-4}	6.3786×10^{-4}	5.9737×10^{-4}

5.5.1.2 FDII of Incipient, Low-Severity Bus Voltage Faults

In this section, the results of FDII using the series-parallel scheme in presence of the sequence of low-severity bus voltage faults over the time period $t \in [1000 \ 5100]$ seconds - given in equation (5-40) – are depicted. The measured speed and current of the reaction wheel and their estimates obtained from the two NPEs of the series-parallel FDII scheme are compared in Figure 5-29. This figure shows a very close match between the measured states and their corresponding estimates from “the NPE for V_{bus} fault”. The

current estimates from the other NPE do not match the measurements over the faulty periods. This is reasonable because the results are obtained in presence of bus voltage fault, so only “the NPE for V_{bus} fault” has generated matching estimates for both of the states. Finally, note the effects of the bus voltage fault on the states of the reaction wheel.

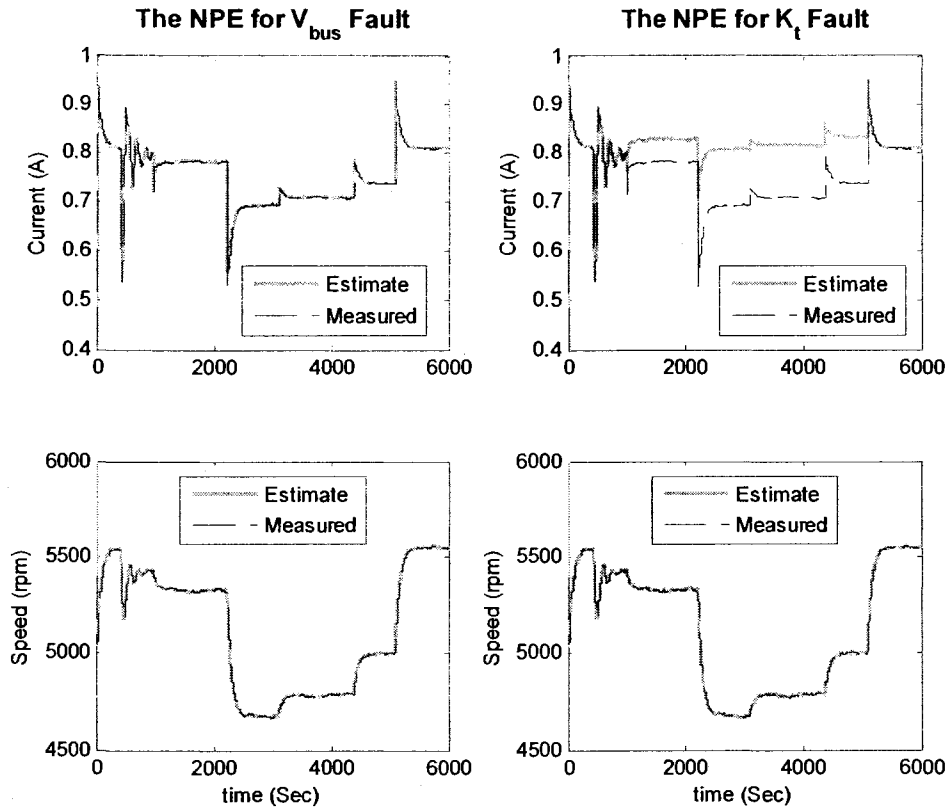


Figure 5-29. The estimated versus measured states using the series-parallel FDII scheme in presence of a sequence of low-severity bus voltage faults over the time period $t \in [1000 \ 5100]$ second.

Figure 5-30 shows the residuals of the two NPEs. As expected from the state estimates shown in Figure 5-29, only the two residuals of “the NPE for V_{bus} fault” remain within their corresponding thresholds. Since these results were obtained with nominal noise levels, the residual thresholds are essentially the same as the ones used for the motor current FDII in the previous section. As can be observed from Figure 5-30, both residuals of “the NPE for V_{bus} fault” have remained within their specified threshold bounds, except

for the current residual, where it has temporarily exceeded its corresponding threshold for a few times during the simulation period. These include once at the very beginning of the simulations due to closed-loop system transients and five times during the faulty period due to transients imposed by bus voltage fault initiation, change in the fault severity, and finally the fault removal.

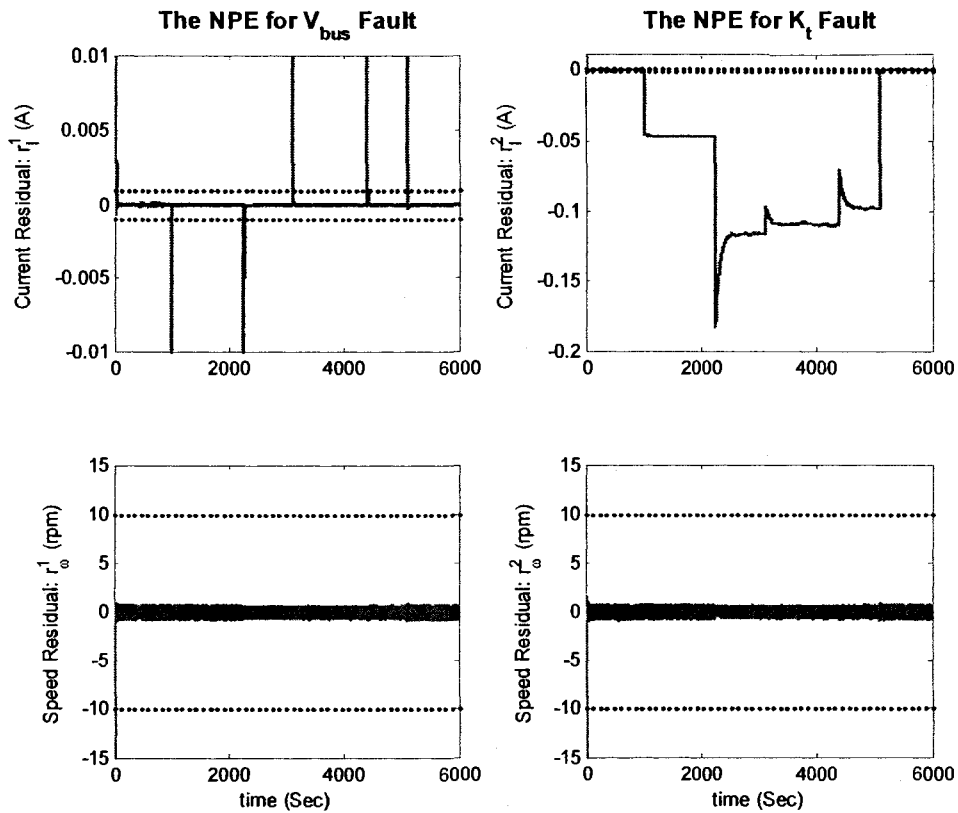


Figure 5-30. The residuals of the two NPEs of the series-parallel FDII scheme a sequence of low-severity bus voltage faults over the time period $t \in [1000 \ 5100]$ second.

As far as the residuals of “the NPE for K_t fault” are concerned, it can be seen from Figure 5-30 that the current residual has exceeded its threshold for the entire period of the presence of the bus voltage fault in the reaction wheel. Once again, this *correctly*

indicates that the fault model assigned to faults in motor current does not match the observations/measurements when a bus voltage fault is present in the system. Figure 5-31 is shown merely to provide a zoomed view of the current residual of “the NPE for K_t fault”.

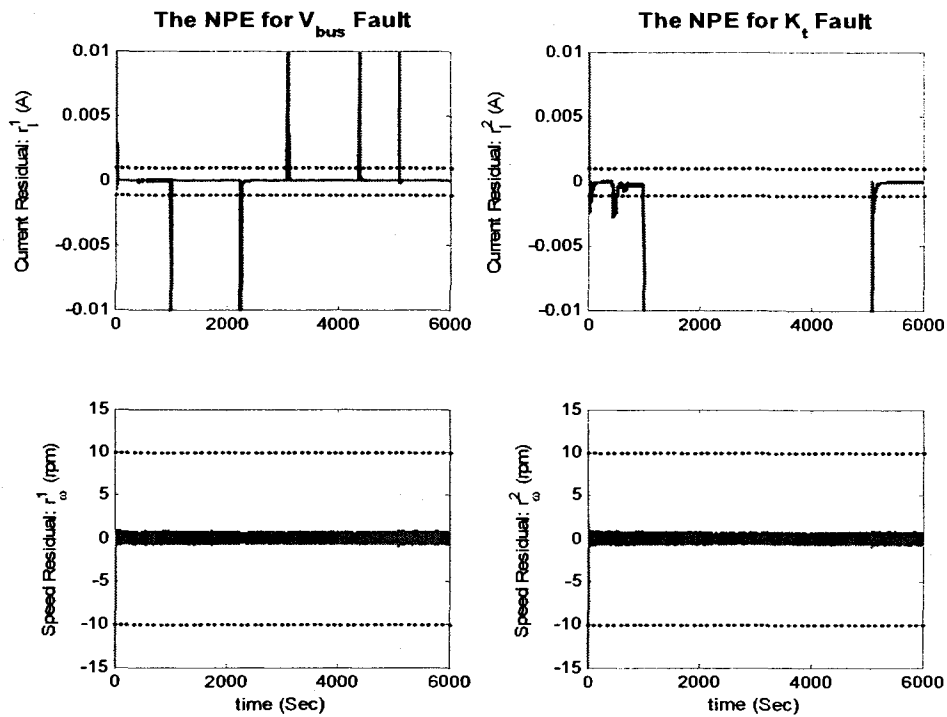


Figure 5-31. The residuals of the two NPEs of the series-parallel FDI scheme in presence of a sequence of low-severity bus voltage faults over the time period $t \in [1000 \ 5100]$ second; zoomed in for the current residual of ‘the NPE for K_t fault’.

Figure 5-32 depicts the estimated versus actual values of the fault parameters α^1 and α^2 representing faults in V_{bus} and k_t , respectively. As can be seen in this figure, the fault parameters are accurately estimated by the NPEs during both the healthy and faulty periods. More specifically, the bus voltage fault has been very precisely identified across all injected fault severity levels, including minor incipient faults such as 1V drop in the bus voltage.

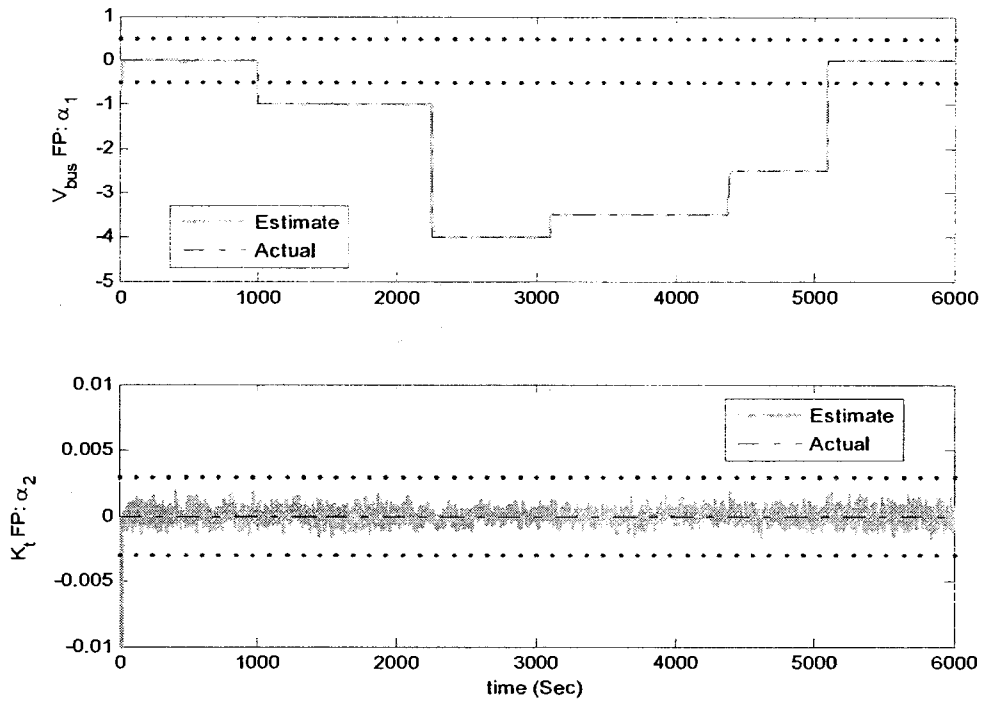
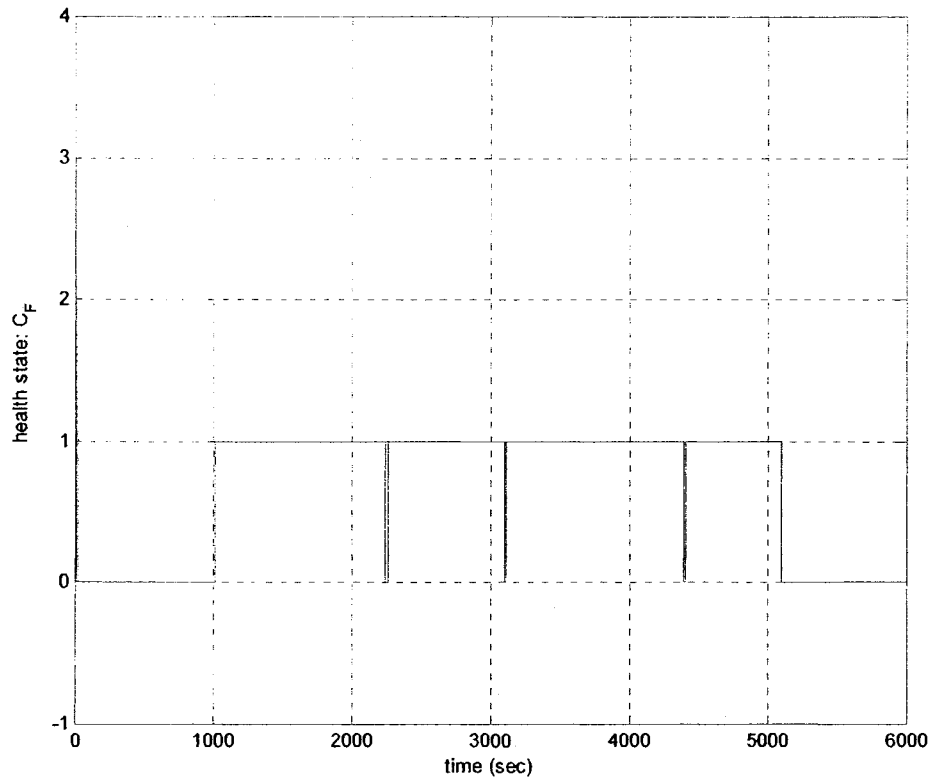


Figure 5-32. The estimated versus actual FPs using the series-parallel FDII scheme in presence of a sequence of low-severity bus voltage faults over the time period $t \in [1000 \ 5100]$ second.

It should be noted that even though in this fault scenario both FP estimates are accurate (i.e., $\hat{\alpha}^2$ is also very close to zero in presence of a fault in bus voltage and in absence of a fault in motor current), always *only one of the FP estimates* should be taken into account for fault identification, and that is the FP estimate that corresponds to the detected and isolated fault. Hence, first the health state of the system has to be determined using the FDI decision logic of the series-parallel scheme and then the FP estimate corresponding to the isolated fault has to be taken as the fault severity. The same logic shall be applied to the parallel FDII scheme.

Figure 5-33 depicts the health state of the reaction wheel obtained by applying the FDI decision logic of equation (3-35) for the series-parallel scheme.



- A sequence of intermittent missed alarms is also observed during the faulty period with short durations of 21 sec., 13.5 sec., and 12 sec., respectively. It should be noted that these missed alarms are indeed due to changes in the severity of the injected bus voltage fault.
- Fault removal or disappearance has been perfectly detected at $t=5100.05$ seconds, practically with *no* delay.

Now that the bus voltage fault has been correctly isolated, the FP estimate corresponding to this fault, namely $\hat{\alpha}^1$ (see Figure 5-32) must be taken as a measure of fault severity. On the other hand, the motor current FP estimate, namely $\hat{\alpha}^2$ has to be neglected during the faulty period. The accuracy of bus voltage fault identification has been assessed using the afore-mentioned performance indices and the results are shown in Table 5-6. It should be noted that all tables corresponding to bus voltage fault scenarios possess two extra rows as compared to the motor current fault scenarios. One of them shows the actual injected bus voltage drop for the healthy as well as different faulty periods and the other row shows the mean (or average) of the estimated drop over the same periods. The “average of estimated drop” is basically defined as:

$$\overline{\hat{\alpha}^2} = \frac{1}{N} \sum_{k=1}^N \hat{\alpha}_k^2 \quad (5-48)$$

The reason for using these two extra rows in case of bus voltage fault is that, as opposed to motor current faults, the bus voltage faults are piecewise constant. So, for healthy as well as faulty periods the fault severity can be represented by a single number. In consequence, the “average of estimated drop” can *directly* represent the estimated drop over each period by a *single* number. It should be noted, however, that using the above-mentioned definition of the “average of estimated drop” and because of the piece-wise

constant nature of the injected bus faults, the ME index becomes essentially the difference between the “actual V_{bus} drop” and the “average of estimated drop”; i.e.,

$$\text{ME} = \text{Actual } V_{bus} \text{ drop} - \text{Average of estimated drop}$$

It can be clearly seen from Table 5-6 that the bus voltage fault parameter (or the bus voltage fault severity) has been precisely estimated with average errors in the order of less than 10^{-2} V (or 10 mV) in “pre-fault period”, less than 2×10^{-3} V (or 2 mV) during all faulty periods, and less than 3×10^{-3} (or 3 mV) in “post-fault period”, while the actual injected faults are all in the order of Volts (i.e., 1 to 4 V). Furthermore, standard deviations are extremely small and are in the order of less than 4×10^{-4} V (or 400 μ V) during faulty periods, less than and 1.5×10^{-2} (or 15 mV) in “pre-fault period”, and less than 3×10^{-3} (or 3 mV) in “post-fault period”. All these performance indices clearly indicate that the series-parallel FDII scheme is extremely capable of accurately identifying fault severities, especially under “nominal” noise levels.

Table 5-6. The performance indices of fault identification using the series-parallel FDII scheme in presence of low-severity bus voltage fault and with nominal noise levels.

	Pre-fault period [0, 1000]s	1 st Faulty period [1000,2240]s	2 nd Faulty period [2240,3100]s	3 rd Faulty period [3100,4390]s	4 th Faulty period [4390,5100]s	Post-fault period [5100,6000]s
Actual V_{bus} drop	0	-1	-4	-3.5	-2.5	0
Average of estimated drop	-9.07×10^{-3}	-1.00	-4.00	-3.50	-2.50	-2.17×10^{-3}
RMSE	1.49×10^{-2}	1.05×10^{-3}	1.12×10^{-3}	1.19×10^{-3}	1.12×10^{-3}	2.91×10^{-3}
ME	9.07×10^{-3}	1.05×10^{-3}	1.06×10^{-3}	1.18×10^{-3}	1.11×10^{-3}	2.17×10^{-3}
STDE	1.20×10^{-2}	5.14×10^{-5}	3.72×10^{-4}	1.53×10^{-4}	1.95×10^{-4}	1.94×10^{-3}

5.5.1.3 FDII of High-Severity Bus Voltage Faults

In this section, the results of FDII in presence of the sequence of high-severity bus voltage faults over the time period $t \in [1000 \ 5100]$ seconds – given in equation (5-41) – are depicted. The measured speed and current of the reaction wheel and their estimates obtained from the NPEs of the series-parallel FDII scheme are shown in Figure 5-34. “The NPE for V_{bus} fault” generates state estimates very close to their respective measurements. However, the current estimate from “the NPE for K_t fault” does not match the measurements over the faulty periods. This is reasonable, since the results are obtained in presence of faults in the bus voltage. Finally, note the effect of the high-severity bus voltage faults on the states of the reaction wheel.

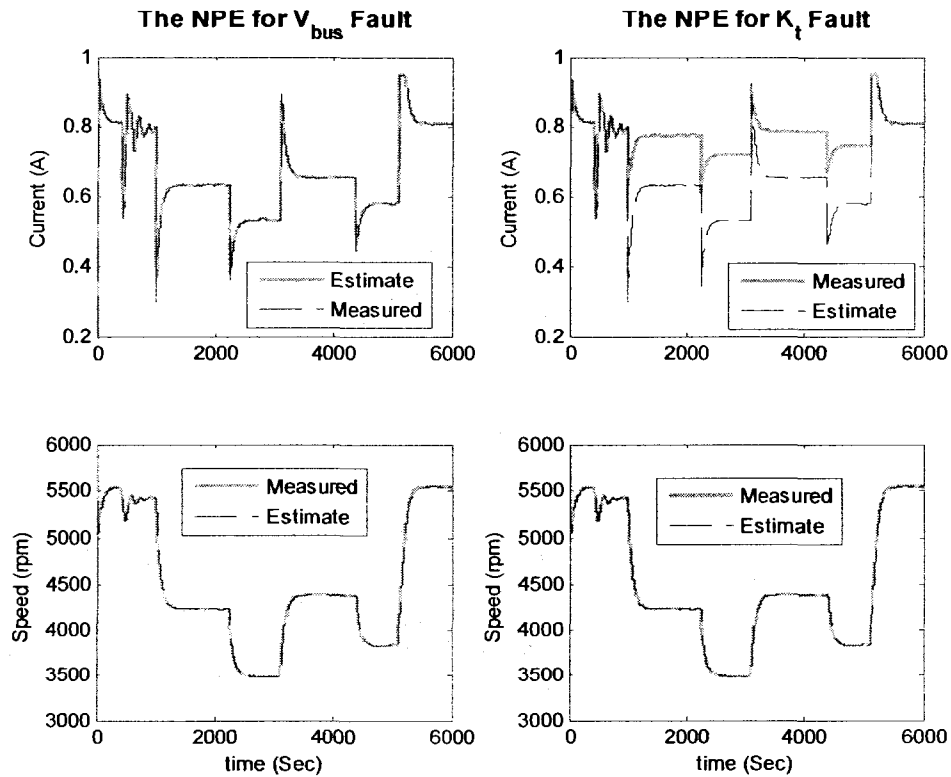


Figure 5-34. The estimated versus measured states using the series-parallel FDII scheme in presence of a sequence of high-severity bus voltage faults over the time period $t \in [1000 \ 5100]$ second.

Figure 5-35 shows the residuals of the two NPEs. As was expected from the state estimates shown in Figure 5-34, only the two residuals of “the NPE for V_{bus} fault” remain within their corresponding thresholds. Since these results were obtained with “nominal” noise levels, the residual thresholds are essentially the same as the ones used for motor current and low-severity bus voltage FDII in the previous sections. As can be observed from Figure 5-35, both residuals of “the NPE for V_{bus} fault” have remained within their specified threshold bounds, except for the current residual, where it has temporarily exceeded its corresponding threshold for a few times during the simulation period.

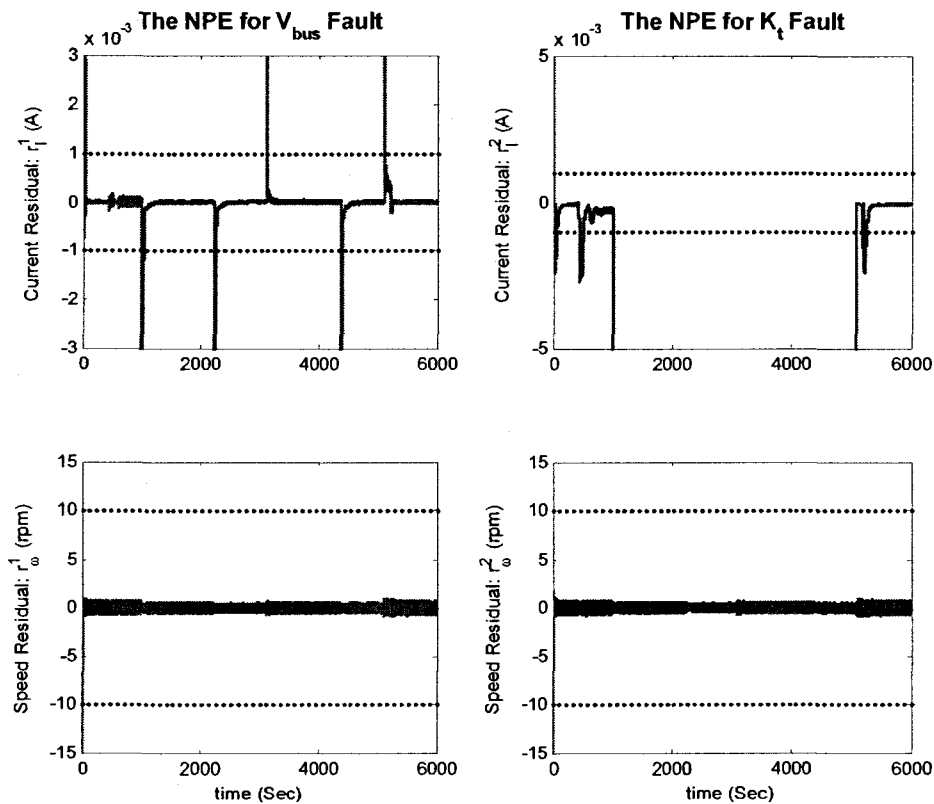


Figure 5-35. The residuals of the two NPEs of the *series-parallel* FDII scheme in presence of a sequence of *high-severity bus voltage faults* over the time period $t \in [1000 \ 5100]$ second; zoomed in for the current residual of “the NPE for K_t fault”.

Similar to the case of low-severity bus voltage faults, these are due to transients caused by bus voltage fault initiation, change in the fault severity, and finally the fault removal. It should be noted that the current residual of the “the NPE for K_t fault” has been zoomed in on the y -axis in Figure 5-35 in order to obtain a better visualization of this residual threshold exceeding the threshold. The original figure (without zooming for the current residual) is shown in Figure C-1 of Appendix C.

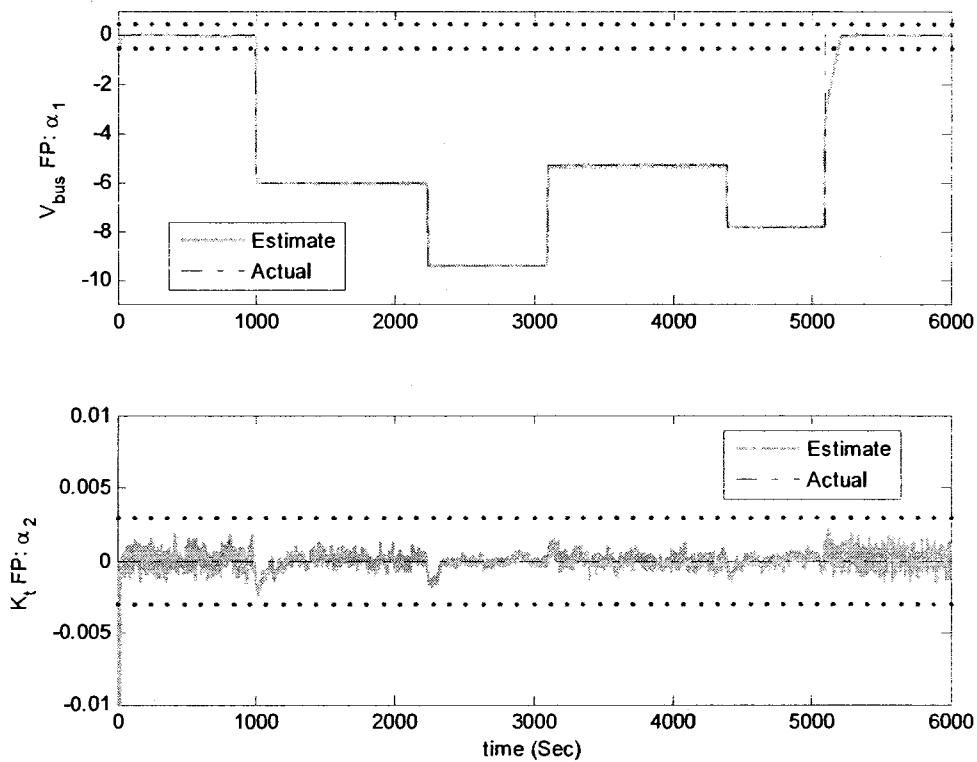


Figure 5-36. The estimated versus actual FPs using the series-parallel FDI scheme in presence of a sequence of high-severity bus voltage faults over the time period $t \in [1000 \ 5100]$ second.

Figure 5-36 depicts the estimated versus actual values of the fault parameters α^1 and α^2 . As can be seen in this figure, the fault parameters are accurately estimated by the NPEs during both healthy and faulty periods. More specifically, the bust voltage fault has been very precisely identified across all injected fault severity levels. Figure 5-37 depicts the

health state of the reaction wheel obtained by applying the FDI decision logic of equation (3-35) for the series-parallel scheme.

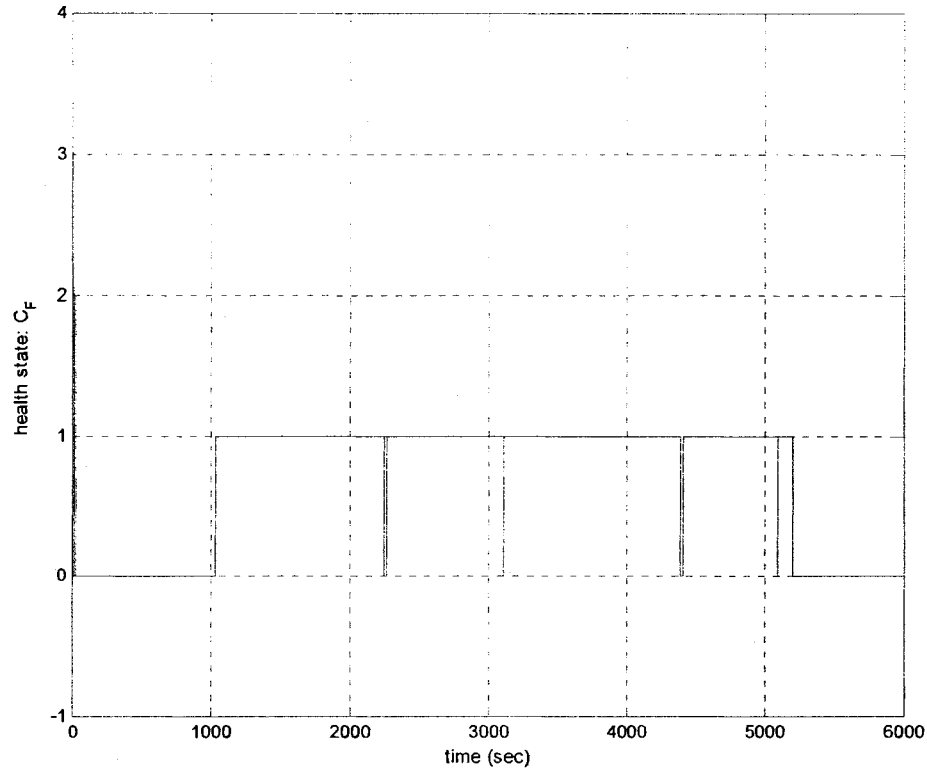


Figure 5-37. The health state of the RW using the series-parallel FDI scheme in presence of a sequence of high-severity bus voltage faults over the time period $t \in [1000 \ 5100]$ second.

A number of observations can be made from Figure 5-37 as follows:

- The injected sequence of high-severity bus voltage faults has been very well detected and isolated for almost the entire faulty period.
- There are very few false alarms prior to fault occurrence, which last *only* for 29.5 seconds after the beginning of simulations (compare to 29.3 seconds for low-severity bus voltage faults). Once again, this reveals that the series-parallel FDI scheme is extremely robustness to the transients of the closed-loop ACS.

- The delay in fault detection and isolation has been increased from 2.1 seconds for low-severity faults to 25.5 seconds for high-severity faults; however, it is still quite tolerable considering the rather slow dynamics of the satellite attitude.
- A sequence of intermittent missed alarms is also observed during the faulty period with short durations of 24 sec., 8 sec., and 16.5 sec., respectively. It should be noted that these missed alarms are indeed due to changes in the severity of the injected bus voltage faults.
- As opposed to the low-severity case (where fault removal or disappearance was perfectly detected with *no* delay), in presence of high-severity bus voltage faults, false alarms are observed even after fault removal. Indeed, the fault disappearance has been first correctly detected for 2 seconds after the actual fault removal time (i.e., 5100 seconds), but then a steady false alarm is observed for almost 96 seconds. Thereafter, fault removal has been persistently detected.

The accuracy of bus voltage fault identification has been assessed using the aforementioned performance indices and the results are shown in Table 5-7. It can be clearly seen from this table that the bus voltage fault parameter (or the bus voltage fault severity) has been precisely estimated with average errors, once again, in the order of less than 10^{-2} V (or 10 mV) in the “pre-fault” period, less than 2×10^{-3} V (or 2 mV) during all faulty periods, and less than 8×10^{-2} (or 80 mV) in the “post-fault” period, while the actual injected faults are all in the order of a few Volts (i.e., 5.3 to 9.4 V). The mean error in the “post-fault” period is clearly larger than in case of low-severity faults, which can also be easily observed by comparing the “post-fault” period of Figure 5-32 and Figure 5-36. Furthermore, the standard deviations are extremely small and are in the order of

less than 7×10^{-4} V (or 700 μ V) during faulty periods and less than and 1.5×10^{-2} (or 15 mV) in the “pre-fault” period. The considerable increase of the STDE during the “post-fault” period, from less than 3 mV in case of low-severity faults to more than 280 mV in case of high-severity faults is indeed due to the relatively long transient period of bus voltage FP estimate, as can be seen in Figure 5-36. All performance indices given in Table 5-7 clearly indicate that the series-parallel FDII scheme is extremely capable of precisely identifying high-severity bus voltage faults, especially under “nominal” noise levels.

Table 5-7. The performance indices of fault identification using the series-parallel FDII scheme in presence of high-severity bus voltage fault subject to nominal noise levels.

	Pre-fault period [0, 1000]s	1 st Faulty period [1000,2240]s	2 nd Faulty period [2240,3100]s	3 rd Faulty period [3100,4390]s	4 th Faulty period [4390,5100]s	Post-fault period [5100,6000]s
Actual V_{bus} drop	0	-6	-9.4	-5.3	-7.8	0
Average of estimated drop	-9.07×10^{-3}	-6.001	-9.402	-5.301	-7.801	-7.48×10^{-2}
RMSE	1.49×10^{-2}	1.41×10^{-3}	1.78×10^{-3}	1.52×10^{-3}	1.58×10^{-3}	2.92×10^{-1}
ME	9.07×10^{-3}	1.34×10^{-3}	1.71×10^{-3}	1.49×10^{-3}	1.43×10^{-3}	7.48×10^{-2}
STDE	1.18×10^{-2}	4.60×10^{-4}	5.06×10^{-4}	3.31×10^{-4}	6.87×10^{-4}	2.83×10^{-1}

5.5.2 Robustness Analysis of the Series-Parallel FDII Scheme with Respect to Measurement Noise

In this section, the robustness of the series-parallel FDII scheme with respect to measurement noise is extensively analyzed and investigated. Towards this objective, the simulations in the previous sections, which were carried out under “nominal” noise level, are repeated again with higher levels of noise, namely “medium” and “high” noise levels in reaction wheel’s current and speed measurements according to Table 5-3 and Table

5-4. Then, the robustness of the series-parallel scheme in both FDI and fault severity estimation subject to different noise levels are compared using the health state variable C_k^F and the FP estimation performance indices (i.e., RMSE, ME, and STDE), respectively. It should be noted that the robustness analysis is performed separately for each fault scenario. It is important to note that the state estimates and the residuals of the NPEs are not depicted throughout the robustness analysis section. Instead, they are shown in Appendix C.

5.5.2.1 FDII of Motor Current Faults

In the following, the robustness of the series-parallel FDII scheme is analyzed in presence of the intermittent time-varying motor current fault given in equation (5-39), subject to A) *medium* level of measurement noise (i.e., SNR=55dB for both current and speed), and B) *high* level of measurement noise (i.e., SNR=45dB for both current and speed).

A) Medium Level/Intensity of Measurement Noise (SNR = 55dB): The state estimates and the residuals corresponding to the NPEs for V_{bus} and K_1 faults are shown in Figure C-2 and Figure C-3 of Appendix C, respectively. As can be seen from Figure C-3, the residual thresholds are set to $\delta_j = \delta^1 = 8 \times 10^{-3} (A)$ for the current residual and $\delta_\omega = \delta^2 = 80 (rpm)$ for the speed residual. This shows eight times increase in both current and speed residual thresholds as compared to the case of “nominal” noise level. This is due to the fact that the residual thresholds are set using the worst-case disturbance and noise analysis during *healthy* operations.

Figure 5-38 depicts the FP estimates versus their actual values. As can be observed from this figure, the increased level of noise has a considerable impact on the motor

current FP estimate, i.e. $\hat{\alpha}^2$. Indeed, the motor current FP estimate shows very large oscillations (or variance) during both healthy and faulty periods. The magnitude of these oscillations is so high that the motor current FP estimate frequently exceeds its corresponding threshold.

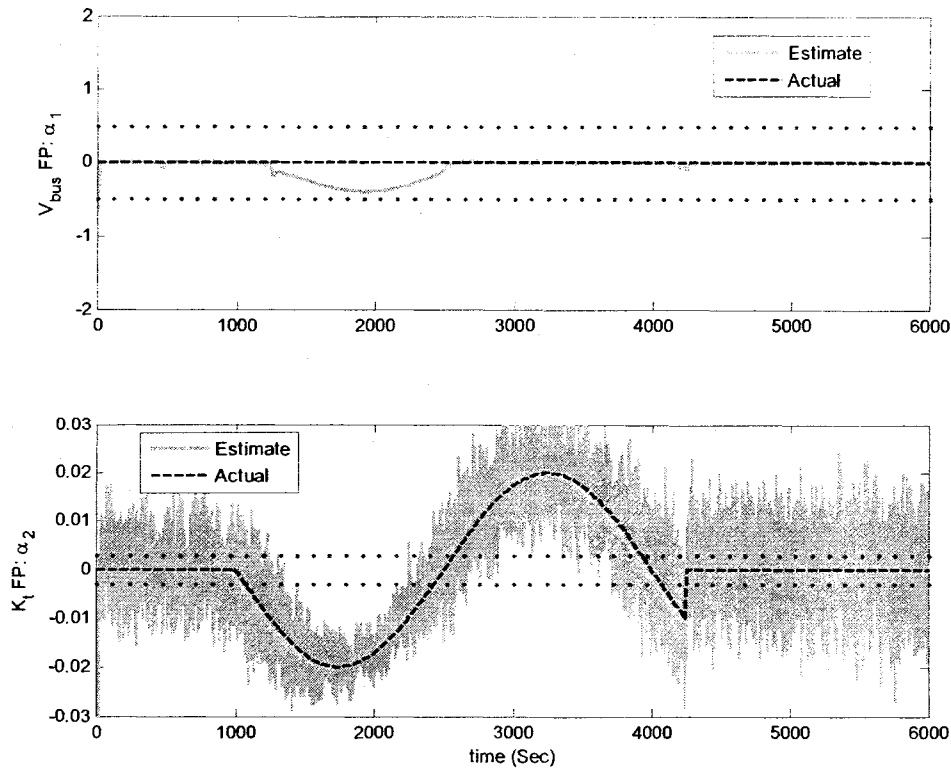


Figure 5-38. The estimated versus actual FPs using the series-parallel FDII in presence of motor current fault over the period $t \in [1000 \ 4250]$ sec., subject to *medium* noise level (SNR=55 dB).

Figure 5-39 shows the health state of the reaction wheel in presence of the time-varying intermittent fault in motor current over the time period $t \in [1000 \ 4250]$ and subject to medium noise level. As can be clearly seen from this figure, the health state of the system frequently oscillates between 0 (i.e., healthy) and 2 (i.e., fault in the motor current) during both “pre-fault” and “post-fault” periods, thus creating a large number of

false alarms. These frequent oscillations in the health state of the reaction wheel (or frequent false alarms) are indeed due to the above mentioned large oscillations in the motor current FP estimate, which are in turn due to high level of measurement noise. Furthermore, the period of *missed alarms* has been increased from 100 seconds (i.e., $t \in [2465 \ 2565]$ in Figure 5-28) in case of “nominal” noise level to almost 600 seconds in case of “medium” noise level (i.e., $t \in [2300 \ 2900]$ in Figure 5-39). In conclusion, the increase in the level of measurement noise considerably deteriorates the detection and isolation performance of the series-parallel FDI scheme.

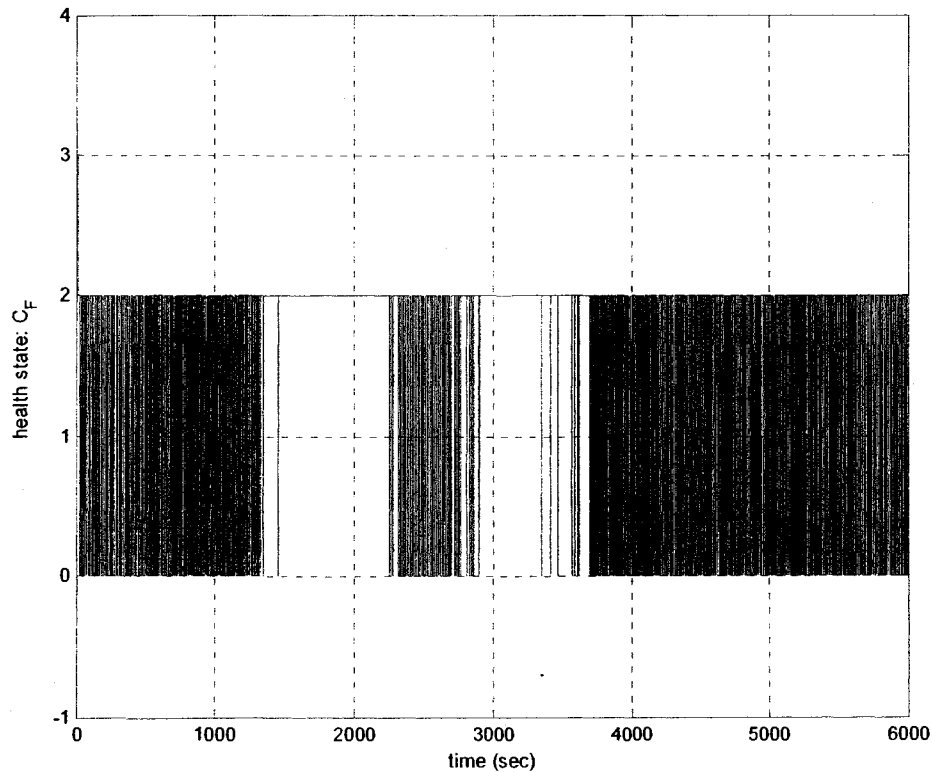


Figure 5-39. The health state of the RW using the series-parallel FDI scheme in presence of motor current fault over the period $t \in [1000 \ 4250]$ sec., subject to *medium* noise level (SNR=55 dB).

One way of significantly reducing the false alarms is to apply a simple Moving-Window Mean Filter (MWMF) to the motor current FP estimate. The mathematical representation of this filtering technique is as follows:

$$\hat{\alpha}_k^{2,fil} = \frac{1}{N_{fil}} \sum_{k=k_1}^{k_2} \hat{\alpha}_k^2; \forall k_1 \leq k \leq k_2 \quad (5-49)$$

$$k_1 = j.N_{fil} + 1; \quad k_2 = (j+1).N_{fil}; \quad j = 0, 1, \dots$$

where $\hat{\alpha}_k^{2,fil}$ denotes the filtered motor current FP estimate and N_{fil} denotes the fixed window length of the MWMF in terms of the number of time steps. It can be inferred from the above formulation of MWMF that the *filtered* motor current FP estimate, namely $\hat{\alpha}_k^{2,fil}$, is piece-wise constant. The use of *moving average filtering* instead of MWMF has also been investigated in this thesis. However, the MWMF outperforms the moving average filter even though the latter produces smooth – as opposed to piece-wise constant – results for the motor current FP estimate.

The result of filtering the motor current FP estimate is shown in Figure 5-40. It can be clearly seen in this figure that the filtered motor current FP estimate is much smoother than the non-filtered one shown in Figure 5-38. Clearly, the use of a window-based filter introduces a delay in fault diagnosis. After numerous testing of MWMF with various window lengths, the best filtering result was achieved using a window length of $N_{fil} = 400$ time steps. Therefore, considering the sampling time of $T_s = 50m\text{sec}$, the additional delay in diagnosis introduced due to filtering is equal to *only* $400 \times T_s = 20$ seconds. This additional delay in fault diagnosis is quite tolerable considering that many of the false alarms as well as missed alarms have been removed using the filtered FP, as can be seen from Figure 5-41.

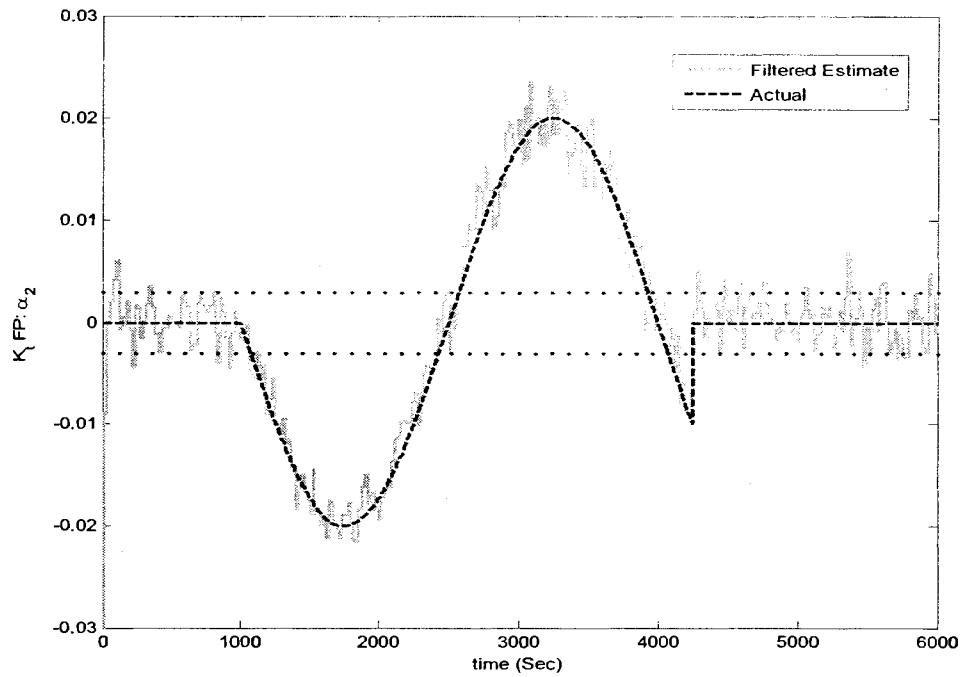


Figure 5-40. Moving-window filtered version of the estimated motor current FP versus its actual value using the series-parallel FDI scheme in presence of motor current fault over the time period $t \in [1000 \ 4250]$ sec., subject to *medium* noise level (SNR=55 dB).

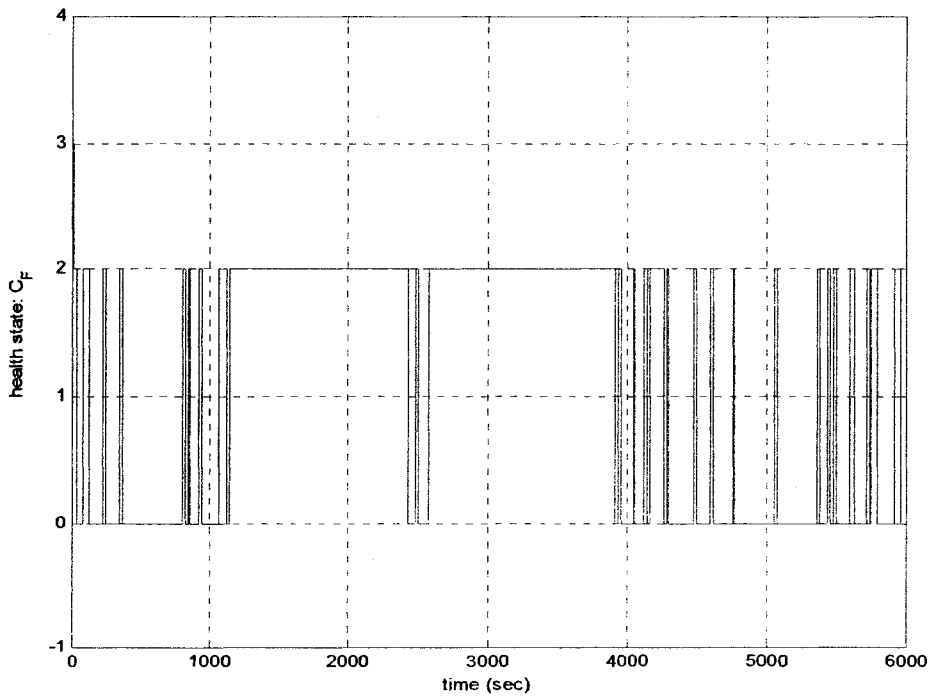


Figure 5-41. The health state of the RW using the series-parallel FDI scheme in presence of motor current fault over the time period $t \in [1000 \ 4250]$ sec, subject to *medium* noise level (SNR=55 dB) and with moving-window mean filtering of the motor current FP estimate.

B) High Level/Intensity of Measurement Noise (SNR = 45dB): The state estimates and the residuals corresponding to the NPEs for V_{bus} and K_t faults are shown in Figure C-4 and Figure C-5 of Appendix C, respectively. As can be seen from Figure C-5, the residual thresholds are set to $\delta_i = \delta^1 = 0.03 (A)$ for the current residual and $\delta_\omega = \delta^2 = 200 (rpm)$ for the speed residual. This shows almost three times increase in current and speed residual thresholds as compared to the case of “nominal” noise level. Once again, this is due to the fact that the residual thresholds are set using the worst-case disturbance and noise analysis during *healthy* operations.

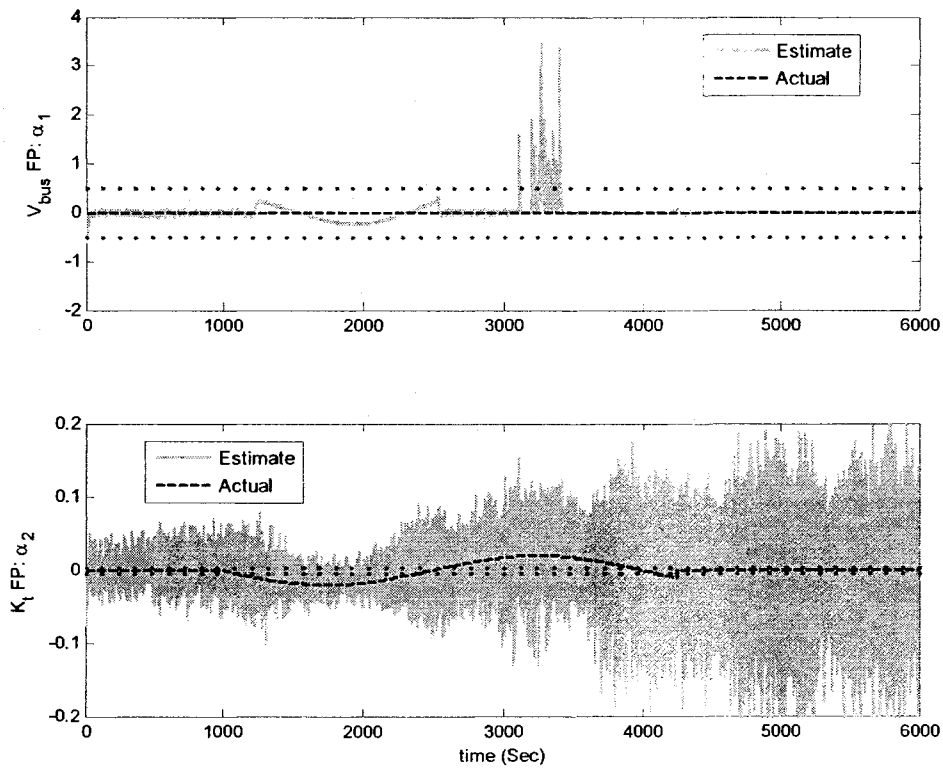


Figure 5-42. The estimated versus actual FPs using the series-parallel FDI in presence of motor current fault over the time period $t \in [1000 \ 4250]$ sec., subject to *high* noise level (SNR=45 dB).

Figure 5-42 depicts the FP estimates versus their actual values. As can be observed from this figure, the “high” level of measurement noise has a very large impact on the motor current FP estimate, i.e. $\hat{\alpha}^2$. Indeed, the motor current FP estimate shows very large oscillations (or variance) during both healthy and faulty periods. Consequently, the motor current FP estimate frequently and largely exceeds its corresponding threshold. The magnitude of these oscillations is so high that filtering the motor current FP estimate using the MWMF cannot reduce the impact of measurement noise on the FDII performance. Furthermore, the bus voltage FP estimate intermittently exceeds its corresponding threshold over the time period $t \in [3100 \ 3400]$, which is *incorrect* since there is *no* fault in the bus voltage. Therefore, the series-parallel FDII scheme completely fails to diagnose and identify motor current faults in presence of “high” measurement noise levels (or low SNR values).

The three performance indices of fault identification, namely RMSE, ME, and STDE corresponding to the motor current FP estimate subject to various noise levels are compared in Table 5-8, Table 5-9, and Table 5-10, respectively. The performance indices are compared over three time periods, namely “Pre-fault period”, “Faulty period”, and “Post-fault period”. It can be seen from these tables that across *all* time periods, the increase in the level of measurement noise has created a *significant* increase in *all* three performance indices. For example, it can be observed from Table 5-8 that a change in SNR by a factor of 1000 (i.e., from the “nominal” to the “high” noise level) results in changes in the RMSE index by factors of 27, 46, and 89 over the “Pre-fault period”, “Faulty period”, and “Post-fault period”, respectively.

Table 5-8. Comparison of the RMSE of the motor current FP estimation using the series-parallel FDII scheme subject to various noise levels and in presence of intermittent motor current fault.

Noise Level (SNR)	Pre-fault period $t \in [0 \ 1000]$ sec	Faulty period $t \in [1000 \ 4250]$ sec	Post-fault period $t \in [4250 \ 6000]$ sec
<i>Nominal</i> (75 dB)	6.2663×10^{-4}	6.3787×10^{-4}	5.9962×10^{-4}
<i>Medium</i> (55 dB)	4.6380×10^{-3} Filt.:(2.1292×10^{-3})	4.6157×10^{-3} Filt.:(2.2368×10^{-3})	5.8943×10^{-3} Filt.:(2.1813×10^{-3})
<i>High</i> (45 dB)	1.7037×10^{-2}	2.9358×10^{-2}	5.3681×10^{-2}

The sensitivity of the ME index with respect to measurement noise is even worse than that of the RMSE index. As can be observed from Table 5-9, a change in SNR by a factor of 1000 results in increase of the ME index by factors of 95, 930, and 69 over the “Pre-fault period”, “Faulty period”, and “Post-fault period”, respectively.

Table 5-9. Comparison of the ME of the motor current FP estimation using the series-parallel FDII scheme subject to various noise levels and in presence of intermittent motor current fault.

Noise Level (SNR)	Pre-fault period $t \in [0 \ 1000]$ sec	Faulty period $t \in [1000 \ 4250]$ sec	Post-fault period $t \in [4250 \ 6000]$ sec
<i>Nominal</i> (74 dB)	-3.4188×10^{-5}	4.4874×10^{-6}	5.2092×10^{-5}
<i>Medium</i> (54 dB)	-1.6480×10^{-4} Filt.:(-1.6464×10^{-4})	-5.5290×10^{-4} Filt.:(-5.6718×10^{-4})	-3.0165×10^{-4} Filt.:(-3.0607×10^{-4})
<i>High</i> (44 dB)	-3.2413×10^{-3}	-4.1785×10^{-3}	-3.5906×10^{-3}

Finally, as can be observed from Table 5-10, a 1000 times increase in the level of measurement noise causes 26, 45, and 90 times increase in the standard deviation of the fault identification error over the “Pre-fault period”, “Faulty period”, and “Post-fault period”, respectively.

Table 5-10. Comparison of the STDE of FP estimation using the series-parallel FDII scheme subject to various noise levels and in presence of intermittent motor current fault.

Noise Level (SNR)	Pre-fault period $t \in [0 \ 1000]$ sec	Faulty period $t \in [1000 \ 4250]$ sec	Post-fault period $t \in [4250 \ 6000]$ sec
Nominal (74 dB)	6.2571×10^{-4}	6.3786×10^{-4}	5.9737×10^{-4}
Medium (54 dB)	4.6350×10^{-3} Filt.: (2.1229×10^{-3})	4.5825×10^{-3} Filt.: (2.1637×10^{-3})	5.8866×10^{-4} Filt.: (2.1597×10^{-3})
High (44 dB)	1.6726×10^{-2}	2.9060×10^{-2}	5.3561×10^{-2}

5.5.2.2 FDII of Low-Severity Bus Voltage Faults

In the following, the robustness of the series-parallel FDII scheme is analyzed in presence of the intermittent sequence of low-severity bus voltage faults given in equation (5-40), subject to A) *medium* level of measurement noise (i.e., SNR=54.57dB for the motor current and SNR=54.76dB for the speed of the wheel), and B) *high* level of measurement noise (i.e., SNR=44.57dB for the motor current and SNR=44.76dB for the speed of the wheel).

A) Medium Level/Intensity of Measurement Noise (Current SNR = 54.57 dB and Speed SNR = 54.76 dB): The state estimates and the residuals corresponding to the NPEs for V_{bus} and K_t faults are shown in Figure C-6 and Figure C-7 of Appendix C, respectively. Similar to the case of FDII of motor current faults subject to “medium” noise level, the residual thresholds are set to $\delta_i = \delta^1 = 8 \times 10^{-3}$ (A) for the current residual and $\delta_\omega = \delta^2 = 80$ (rpm) for the speed residual, as can be seen from Figure C-7.

Figure 5-43 depicts the FP estimates versus their actual values. As can be observed from this figure, even though the increased level of noise does not affect the bus voltage FP estimate, it has a considerable impact on the motor current FP estimate. Indeed, the

motor current FP estimate shows very large oscillations (or variance) during both healthy periods and in presence of fault in the bus voltage. The magnitude of these oscillations is so high that the motor current FP estimate frequently exceeds its corresponding threshold even though *no* faults exist in the motor current.

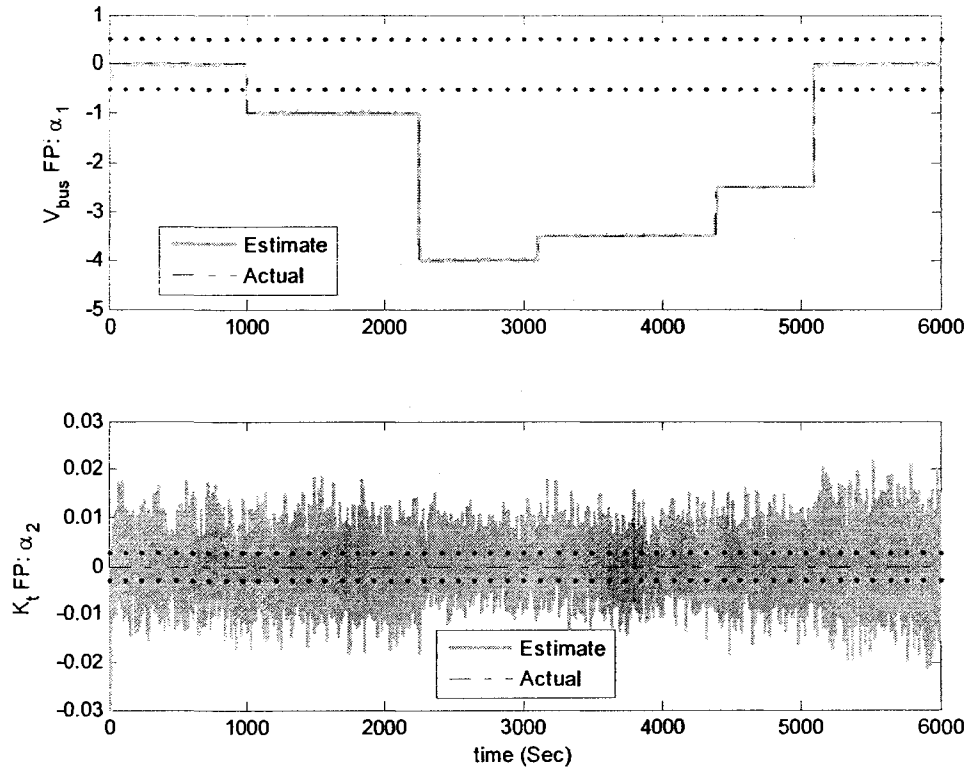


Figure 5-43. The estimated versus actual FPs using the series-parallel FDH in presence of a sequence of low-severity bus voltage faults over the time period $t \in [1000 \ 5100]$ sec., subject to medium noise level (Current SNR=54.57 dB and Speed SNR=54.76 dB).

Figure 5-44 shows the health state of the reaction wheel. As can be clearly seen from this figure, the health state of the system frequently oscillates between 0 (i.e., healthy) and 2 (i.e., fault in the motor current) during both “pre-fault” and “post-fault” periods, thus creating a large number of *false alarms*. These frequent oscillations in the health state of the reaction wheel (or frequent false alarms) are indeed due to the above

mentioned large oscillations in the motor current FP estimate, which are in turn due to high level of measurement noise.

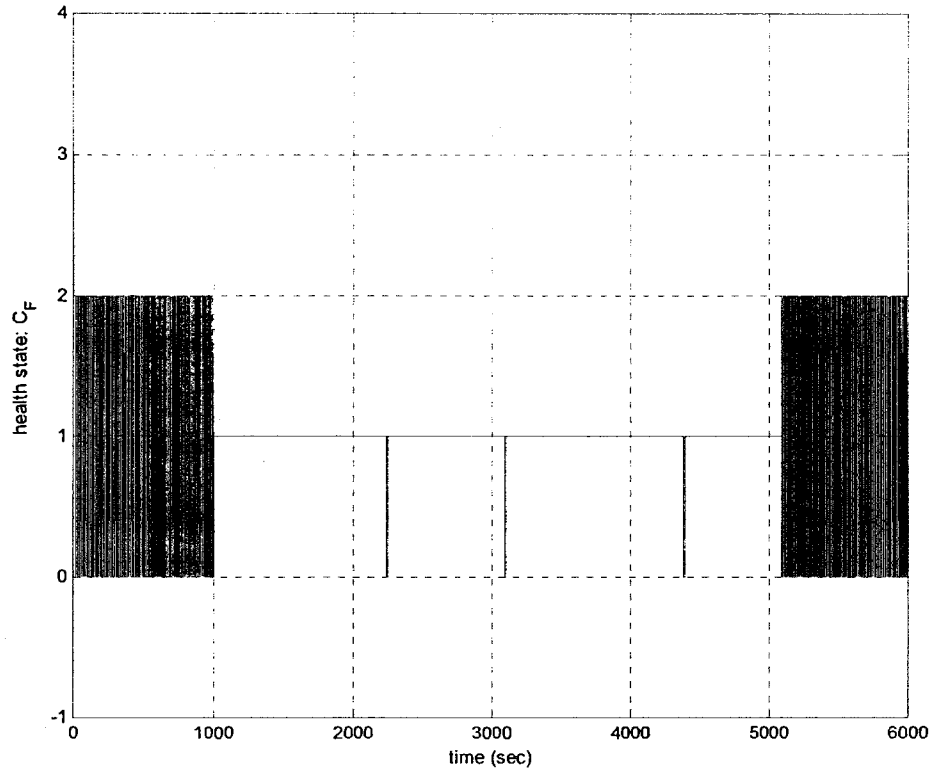


Figure 5-44. The health state of the RW using the series-parallel FDII scheme in presence of a sequence of *low-severity* bus voltage faults over the time period $t \in [1000 \ 5100]$ sec., subject to *medium* noise level (Current SNR=54.57 dB and Speed SNR=54.76 dB).

Once again, many of these false alarms can be removed by filtering the current FP estimate using the MWMF filtering technique. The result of this filtering on the current FP estimate can be seen in Figure 5-45.

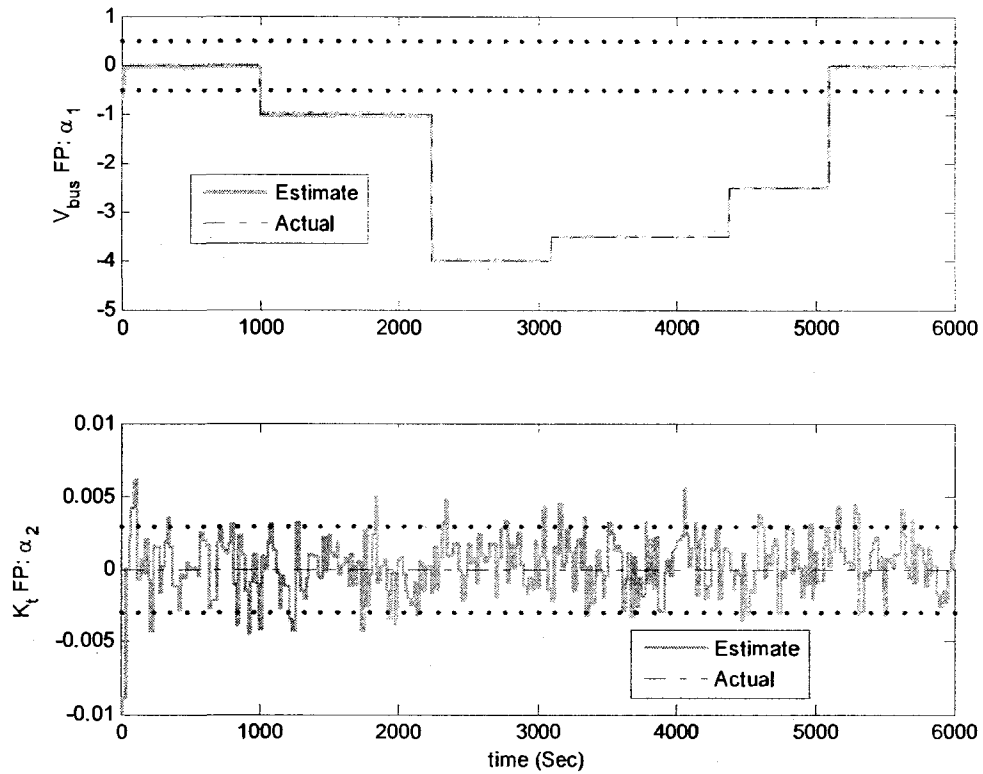


Figure 5-45. Moving-window filtered version of the estimated motor current FP versus its actual value using the series-parallel FDII scheme in presence of a sequence of *low-severity* bus voltage faults over the time period $t \in [1000 \ 5100]$ sec., subject to *medium* noise level (Current SNR=54.57 dB and Speed SNR=54.76 dB).

The identified health state of the reaction wheel using the filtered FP estimate is also shown in Figure 5-46. Note that many of the false alarms in both “pre-fault” and “post-fault” periods have been removed using the filtered FP, as can be seen from Figure 5-46.

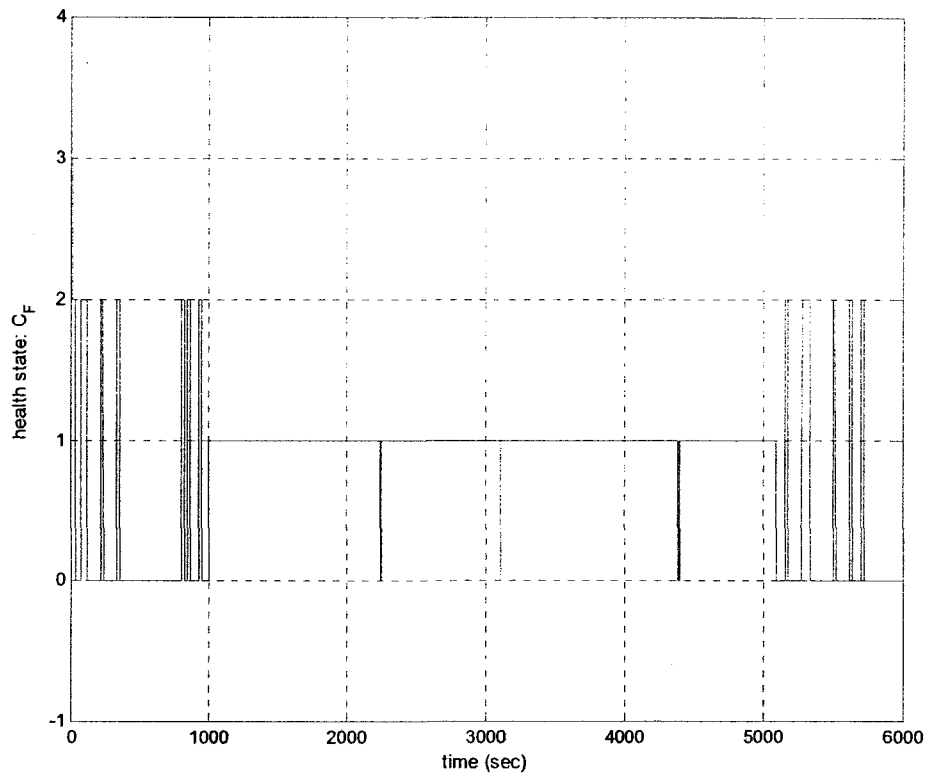


Figure 5-46. The health state of the RW using the series-parallel FDII scheme in presence of a sequence of *low-severity* bus voltage faults over the time period $t \in [1000 \ 5100]$ sec., subject to *medium* noise level (Current SNR=54.57 dB and Speed SNR=54.76 dB), and with moving-window mean filtering of the motor current FP estimate.

B) High Level/Intensity of Measurement Noise (Current SNR = 44.57 dB and Speed SNR = 44.76 dB): The state estimates and the residuals corresponding to the NPEs for V_{bus} and K_t faults are shown in Figure C-8 and Figure C-9 of Appendix C, respectively. Note that the values of the residual thresholds essentially remain equal to the values used for FDII of the motor current fault subject to “high” noise level (i.e., $\delta_j = \delta^1 = 0.03$ (A) for the current residual and $\delta_\omega = \delta^2 = 200$ (rpm) for the speed residual). Indeed, it is very important to note that the value of the residual thresholds for the series-parallel FDII scheme is dependent *only* on the measurement noise (as well as disturbance) level and is *irrelevant* to the fault that is injected into the system.

Figure 5-47 depicts the FP estimates versus their actual values, where the MWMF filter has already been applied to the motor current FP estimate. It can be easily seen from this figure that the motor current FP estimate exceeds its corresponding threshold at many points during both healthy and faulty periods.

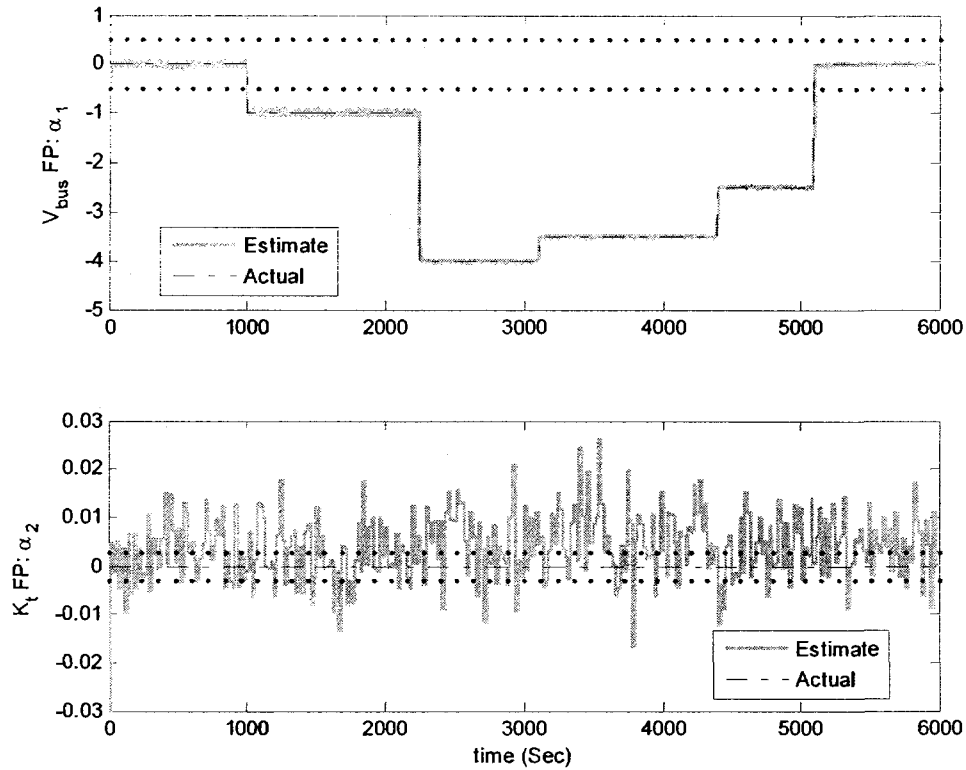


Figure 5-47. The estimated versus actual FPs using the series-parallel FDII in presence of a sequence of low-severity bus voltage faults over the time period $t \in [1000 \ 5100]$ sec., subject to high noise level (Current SNR=44.57 dB and Speed SNR=44.76 dB).

The health state of the reaction wheel identified by the series-parallel FDII scheme using the filtered FP estimate is shown in Figure 5-48. Note that for most of the “pre-fault” and “post-fault” periods the health state of the wheel is *incorrectly* detected as being faulty (i.e., presence of a fault in the motor current). Hence, for most of these two periods, the series-parallel FDII scheme generates *false alarms*. Moreover, a number of

misidentifications of the health state of the wheel can also be observed over the time period $t \in [1000 \ 2000]$ seconds. More specifically, the health state of the wheel is identified as being 3 for a few points within that period, which *wrongly* indicates simultaneous presence of both bus voltage and motor current faults. In conclusion, the “high” level of measurement noise has significantly deteriorated the FDI performance of the series-parallel FDII scheme.

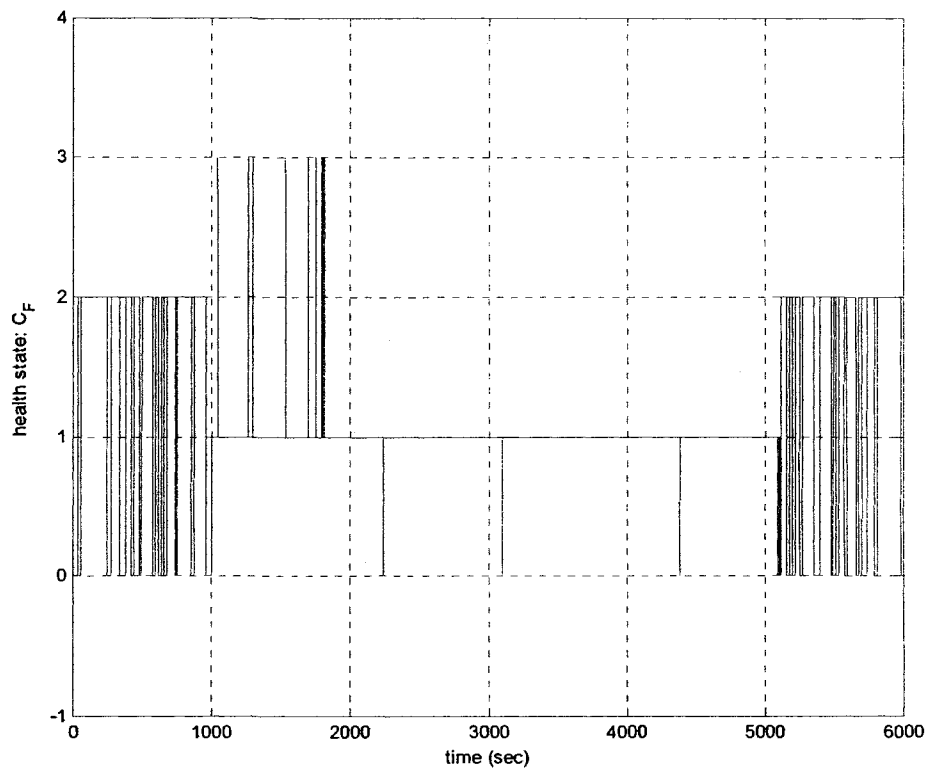


Figure 5-48. The health state of the RW using the series-parallel FDII scheme in presence of a sequence of *low-severity* bus voltage faults over the time period $t \in [1000 \ 5100]$ sec., subject to *high* noise level (Current SNR=44.57 dB and Speed SNR=44.76 dB).

The three performance indices of fault identification, namely RMSE, ME, and STDE corresponding to the bus voltage FP estimate subject to various noise levels are compared in Table 5-11, Table 5-12, and Table 5-13, respectively. Due to the piece-wise constant

nature of bus voltage faults, the performance indices are compared over six time periods including two healthy periods, namely “Pre-fault” and “Post-fault” periods, and four faulty periods each corresponding to a specific value of the bus voltage drop (or severity of the bus voltage fault). It can be seen from the three tables that across *almost all* time periods, the increase in the level of measurement noise has created a slight increase in *all* performance indices. The only exception is the “post-fault” period, where the ME index decreases as the measurement noise level increases, as can be seen from Table 5-12.

Table 5-11. Comparison of the RMSE of the bus voltage FP estimation using the series-parallel FDII scheme subject to various noise levels and in presence of a sequence of low-severity bus voltage faults.

Noise Level	Pre-fault period [0, 1000]s	1 st Faulty period [1000,2240]s	2 nd Faulty period [2240,3100]s	3 rd Faulty period [3100,4390]s	4 th Faulty period [4390,5100]s	Post-fault period [5100,6000]s
<i>Nominal</i>	1.49×10^{-2}	1.05×10^{-3}	1.12×10^{-3}	1.19×10^{-3}	1.12×10^{-3}	2.91×10^{-3}
<i>Medium</i>	1.68×10^{-2}	9.41×10^{-3}	4.01×10^{-3}	4.11×10^{-3}	4.34×10^{-3}	8.82×10^{-3}
<i>High</i>	2.80×10^{-2}	2.83×10^{-2}	1.18×10^{-2}	1.41×10^{-2}	9.01×10^{-3}	1.15×10^{-2}

Table 5-12. Comparison of the ME of the bus voltage FP estimation using the series-parallel FDII scheme subject to various noise levels and in presence of a sequence of low-severity bus voltage faults.

Noise Level	Pre-fault period [0, 1000]s	1 st Faulty period [1000,2240]s	2 nd Faulty period [2240,3100]s	3 rd Faulty period [3100,4390]s	4 th Faulty period [4390,5100]s	Post-fault period [5100,6000]s
<i>Nominal</i>	9.07×10^{-3}	1.34×10^{-3}	1.71×10^{-3}	1.49×10^{-3}	1.43×10^{-3}	7.48×10^{-2}
<i>Medium</i>	8.97×10^{-3}	1.29×10^{-3}	1.45×10^{-3}	1.62×10^{-3}	1.38×10^{-3}	1.45×10^{-3}
<i>High</i>	7.90×10^{-3}	1.62×10^{-3}	2.28×10^{-3}	2.48×10^{-3}	1.71×10^{-3}	-9.17×10^{-5}

Table 5-13. Comparison of the STDE of the bus voltage FP estimation using the series-parallel FDII scheme subject to various noise levels and in presence of a sequence of low-severity bus voltage faults.

Noise Level	Pre-fault period [0, 1000]s	1 st Faulty period [1000,2240]s	2 nd Faulty period [2240,3100]s	3 rd Faulty period [3100,4390]s	4 th Faulty period [4390,5100]s	Post-fault period [5100,6000]s
<i>Nominal</i>	1.18×10^{-2}	4.60×10^{-4}	5.06×10^{-4}	3.31×10^{-4}	6.87×10^{-4}	2.83×10^{-3}
<i>Medium</i>	1.42×10^{-2}	9.32×10^{-3}	3.74×10^{-3}	3.78×10^{-3}	4.11×10^{-3}	8.71×10^{-3}
<i>High</i>	2.68×10^{-2}	2.84×10^{-2}	1.16×10^{-2}	1.11×10^{-2}	8.85×10^{-3}	1.55×10^{-2}

It should be noted that the sensitivity of the bus voltage fault identification to measurement noise is much less than that of the motor current fault identification. This is

due to the fact that the bus voltage FP estimate is much more robust than the motor current FP estimate with respect to measurement noise. Nevertheless, as mentioned above, the detection and isolation (or FDI) performance of the series-parallel scheme is very sensitive to measurement noise.

5.5.2.3 FDII of High-Severity Bus Voltage Faults

In the following, the robustness of the series-parallel FDII scheme is analyzed in presence of the intermittent sequence of high-severity bus voltage faults given in equation (5-41), subject to A) *medium* level of measurement noise (i.e., SNR=53.66dB for the motor current and SNR=53.72dB for the speed of the wheel), and B) *high* level of measurement noise (i.e., SNR=43.66dB for the motor current and SNR=43.72dB for the speed of the wheel).

A) Medium Level/Intensity of Measurement Noise (Current SNR = 53.66 dB and Speed SNR = 53.72 dB): The state estimates and the residuals corresponding to the NPEs for V_{bus} and K_t faults are shown in Figure C-10 and Figure C-11 of Appendix C, respectively. Needless to say, the residual thresholds corresponding to the “medium” noise level are $\delta_I = \delta^1 = 8 \times 10^{-3}$ (A) for the current residual and $\delta_\omega = \delta^2 = 80$ (rpm) for the speed residual, as can be seen from Figure C-11.

Figure 5-49 depicts the FP estimates versus their actual values, where the MWMF filter has already been applied to the motor current FP estimate. It can be easily seen from this figure that the motor current FP estimate exceeds its corresponding threshold at only few points during both healthy and faulty periods.

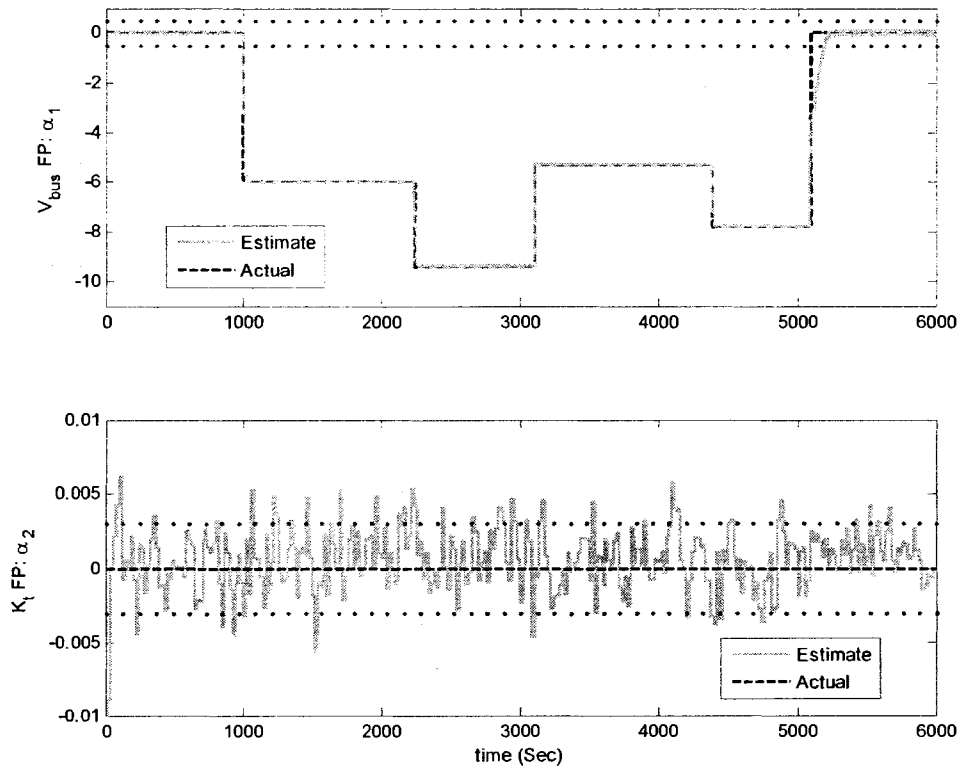


Figure 5-49. The estimated versus actual FPs using the series-parallel FDII in presence of a sequence of high-severity bus voltage faults over the time period $t \in [1000 \ 5100]$ sec., subject to medium noise level (Current SNR=53.66 dB and Speed SNR=53.72 dB).

Figure 5-50 shows the health state of the reaction wheel in presence of the high-severity bus voltage faults and subject to “medium” noise level. As compared to the result of “nominal” noise level depicted in Figure 5-37, a number of additional *false alarms* are now generated by the series-parallel FDII scheme especially in “pre-fault” and “post-fault” periods. These *false alarms* are due to sensitivity of the series-parallel scheme to measurements noise.

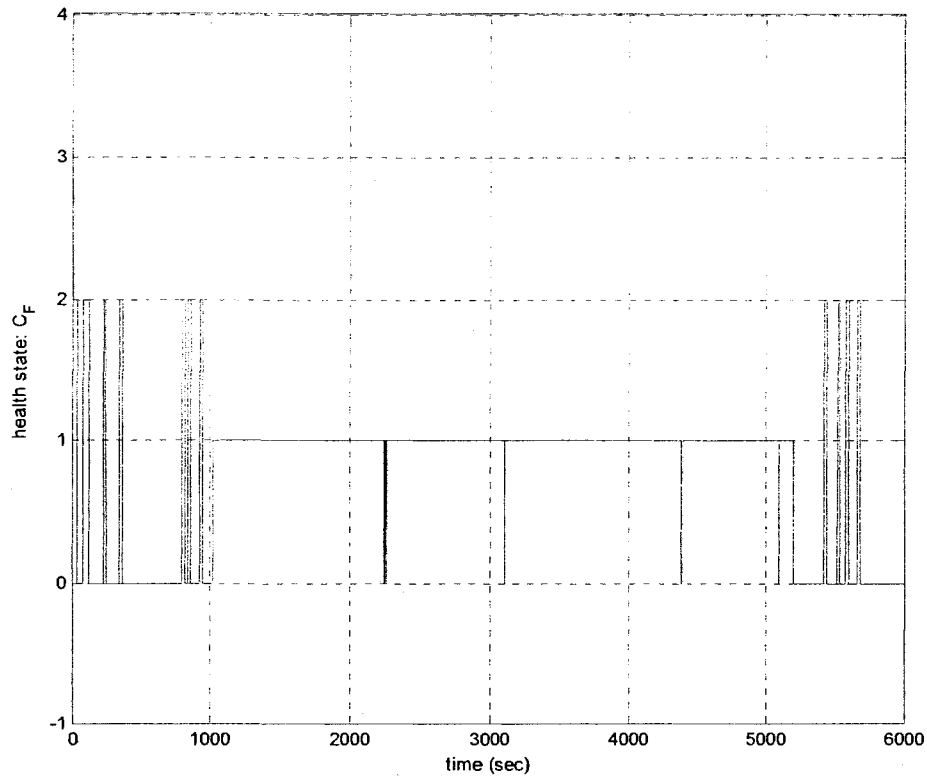


Figure 5-50. The health state of the RW using the series-parallel FDI scheme in presence of a sequence of *high-severity* bus voltage faults over the time period $t \in [1000 \ 5100]$ sec., subject to *medium* noise level (Current SNR=53.66 dB and Speed SNR=53.72 dB).

B) High Level/Intensity of Measurement Noise (Current SNR = 43.66 dB and Speed

SNR = 43.72 dB): The state estimates and the residuals corresponding to the NPEs for V_{bus} and K_t faults are shown in Figure C-12 and Figure C-13 of Appendix C, respectively. Note that the values of the residual thresholds corresponding to the “high” noise level are $\delta_I = \delta^1 = 0.03$ (A) for the current residual and $\delta_\omega = \delta^2 = 200$ (rpm) for the speed residual, as can be seen from Figure C-13.

Figure 5-51 depicts the FP estimates versus their actual values, where the MWMF filter has already been applied to the motor current FP estimate. It can be easily seen from this figure that the motor current FP estimate exceeds its corresponding threshold at many

points during both healthy and faulty periods. Furthermore, note that the bus voltage FP estimate has *wrongly* exceeded its corresponding threshold for the entire “post-fault” period.

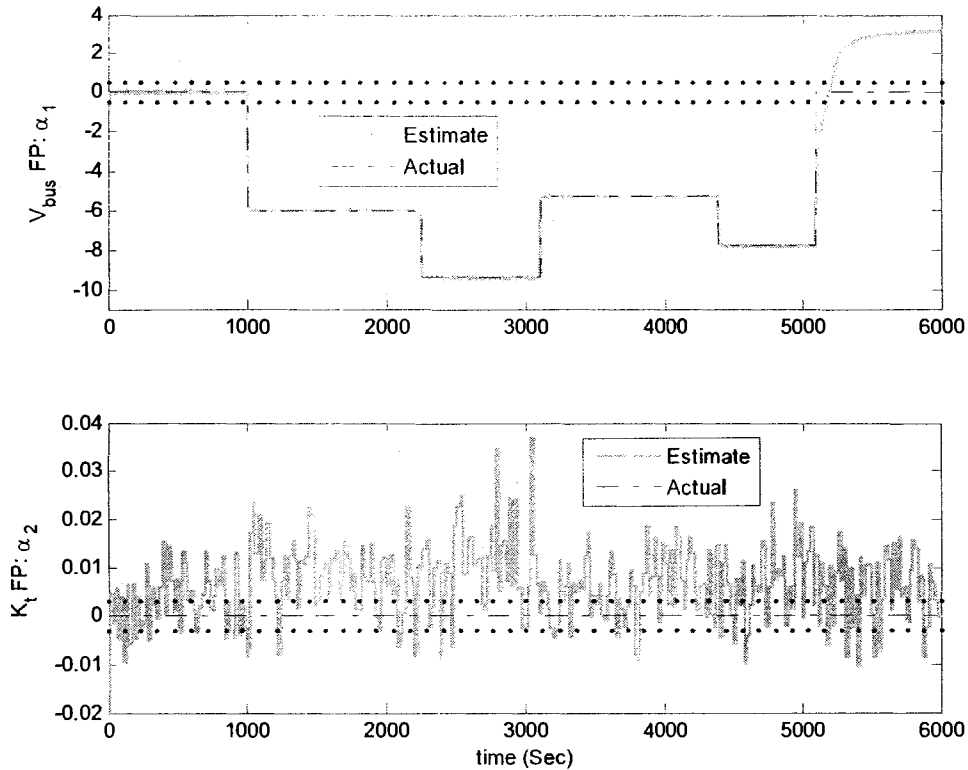


Figure 5-51. The estimated versus actual FPs using the series-parallel FDII in presence of a sequence of *high-severity* bus voltage faults over the time period $t \in [1000 \ 5100]$ sec., subject to *high* noise level (Current SNR=43.66 dB and Speed SNR=43.72 dB).

The health state of the reaction wheel identified by the series-parallel FDII scheme using the filtered FP estimate is shown in Figure 5-48. Note that for most of the “pre-fault” and “post-fault” periods the health state of the wheel is *incorrectly* detected as being faulty. More specifically, there are many *false alarms* in the “pre-fault” period that *wrongly* indicate the presence of fault in the motor current, and the false alarms in the “post-fault” period indicate either the presence of motor current fault or simultaneous

presence of both motor current and bus voltage faults (i.e., the health state is equal to 3). Surprisingly, the FDI performance of the series-parallel scheme during the faulty periods (i.e., presence of high-severity bus voltage faults) is practically *unchanged* as compared to Figure 5-37 for the “nominal” noise level. Nonetheless, the FDI performance of the series-parallel FDI scheme has been significantly deteriorated (i.e., generation of many false alarms during “pre-fault” and “post-fault” periods) due to the “high” level of measurement noise.

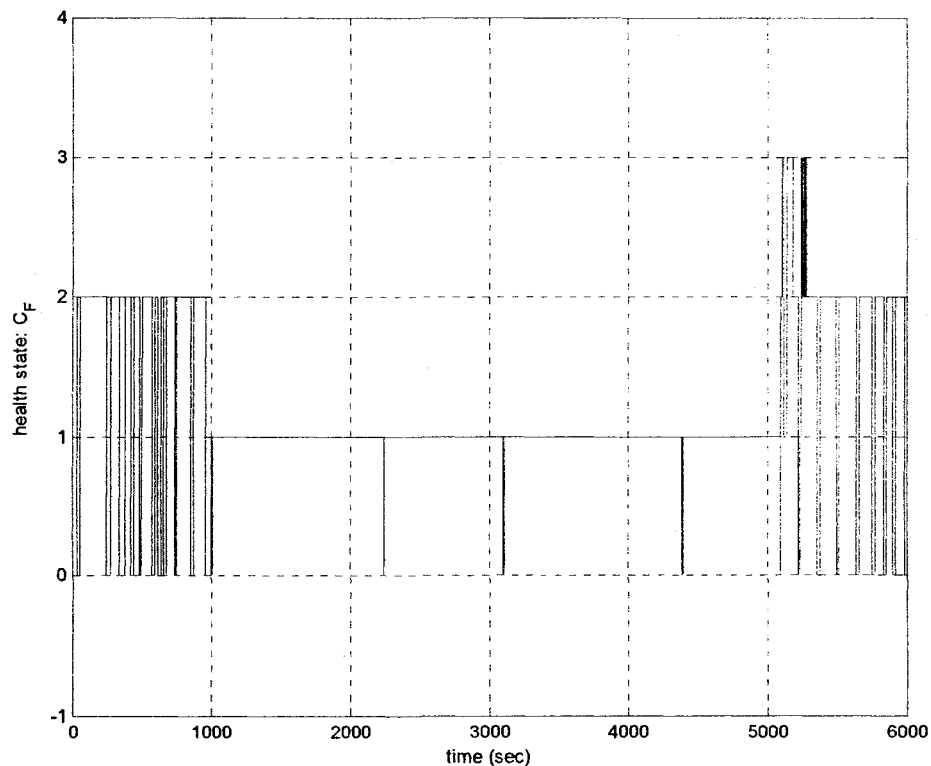


Figure 5-52. The health state of the RW using the series-parallel FDI scheme in presence of a sequence of *high-severity* bus voltage faults over the time period $t \in [1000 \ 5100]$ sec., subject to *high* noise level (Current SNR=43.66 dB and Speed SNR=43.72 dB).

The three performance indices of fault identification, namely RMSE, ME, and STDE corresponding to the bus voltage FP estimate subject to various noise levels are compared

in Table 5-14, Table 5-15, and Table 5-16, respectively. It can be seen from the three tables that, other than a few exceptions, the increase in the level of measurement noise creates a *slight* increase in the performance indices. The increase of the performance indices is more significant for the STDE index during the faulty periods. Furthermore, it should be noted that in the “post-fault” period, the “high” level of noise has created a *very large* increase in all three performance indices.

Table 5-14. Comparison of the RMSE of the bus voltage FP estimation using the series-parallel FDII scheme subject to various noise levels and in presence of a sequence of high-severity bus voltage faults.

Noise Level	Pre-fault period [0, 1000]s	1 st Faulty period [1000,2240]s	2 nd Faulty period [2240,3100]s	3 rd Faulty period [3100,4390]s	4 th Faulty period [4390,5100]s	Post-fault period [5100,6000]s
<i>Nominal</i>	1.49×10^{-2}	1.41×10^{-3}	1.78×10^{-3}	1.52×10^{-3}	1.58×10^{-3}	2.92×10^{-1}
<i>Medium</i>	1.68×10^{-2}	4.2×10^{-3}	4.60×10^{-3}	1.28×10^{-2}	4.53×10^{-3}	2.90×10^{-1}
<i>High</i>	2.80×10^{-2}	1.21×10^{-2}	1.29×10^{-2}	1.99×10^{-2}	1.11×10^{-2}	2.72

Table 5-15. Comparison of the ME of the bus voltage FP estimation using the series-parallel FDII scheme subject to various noise levels and in presence of a sequence of high-severity bus voltage faults.

Noise Level	Pre-fault period [0, 1000]s	1 st Faulty period [1000,2240]s	2 nd Faulty period [2240,3100]s	3 rd Faulty period [3100,4390]s	4 th Faulty period [4390,5100]s	Post-fault period [5100,6000]s
<i>Nominal</i>	9.07×10^{-3}	1.34×10^{-3}	1.71×10^{-3}	1.49×10^{-3}	1.43×10^{-3}	7.48×10^{-2}
<i>Medium</i>	8.97×10^{-3}	1.62×10^{-3}	2.10×10^{-3}	1.98×10^{-3}	1.69×10^{-3}	7.29×10^{-2}
<i>High</i>	7.90×10^{-3}	2.19×10^{-3}	2.89×10^{-3}	3.45×10^{-3}	2.26×10^{-3}	-2.52

Table 5-16. Comparison of the STDE of the bus voltage FP estimation using the series-parallel FDII scheme subject to various noise levels and in presence of a sequence of high-severity bus voltage faults.

Noise Level	Pre-fault period [0, 1000]s	1 st Faulty period [1000,2240]s	2 nd Faulty period [2240,3100]s	3 rd Faulty period [3100,4390]s	4 th Faulty period [4390,5100]s	Post-fault period [5100,6000]s
<i>Nominal</i>	1.18×10^{-2}	4.60×10^{-4}	5.06×10^{-4}	3.31×10^{-4}	6.87×10^{-4}	2.83×10^{-1}
<i>Medium</i>	1.42×10^{-2}	3.88×10^{-3}	4.90×10^{-3}	1.27×10^{-2}	4.2×10^{-3}	2.81×10^{-1}
<i>High</i>	2.69×10^{-2}	1.19×10^{-2}	1.25×10^{-2}	1.96×10^{-2}	1.09×10^{-2}	1.03

In conclusion, the above robustness analysis reveals that the series-parallel FDII scheme is very sensitive to measurement noise, especially in fault detection and isolation. More

specifically, subject to high levels of measurement noise, the series-parallel FDII scheme generates many *false alarms*. Furthermore, while the bus voltage fault identification is slightly sensitive to the measurement noise level, the motor current fault identification performance significantly deteriorates in presence of high noise levels.

5.5.3 Simulation Results for FDII Using the Parallel Scheme

The parallel FDII scheme was applied to detect, isolate, and identify the aforementioned motor current and bus voltage faults in the reaction wheel of the Pitch axis. Similar to the series-parallel scheme, the bank of NPEs consists of two NPEs; one NPE for FDII of V_{bus} fault and one NPE for FDII of k_r fault. Two one-hidden-layer feed-forward neural networks with four neurons in the hidden layer and one neuron in the output layer are used as NPEs. Sigmoidal activation functions were used for the neurons in the hidden layer, while linear neurons were used at the output layer. Neural network learning rates were selected as, $[\eta_w^1 \ \eta_v^1] = [0.7 \ 0.7]$ and $[\eta_w^2 \ \eta_v^2] = [5 \times 10^{-8} \ 5 \times 10^{-8}]$ for the first and the second NPE in the bank of the parallel FDII scheme, respectively.

5.5.3.1 FDII of Motor Current Faults

In this section, the results of FDII in presence of the time-varying intermittent fault in motor current over the time period $t \in [1000 \ 4250]$ seconds – given in equation (5-39) – are depicted. The measured speed and current of the reaction wheel and their estimates obtained from the two NPEs of the parallel FDII scheme are depicted in Figure 5-53. Figure 5-25. *Only* “the NPE for k_r fault” shows a close match between the measured and the estimated values of *both* states of the reaction wheel during both healthy and faulty periods. However, “the NPE for V_{bus} fault” fails to correctly estimate the speed of the wheel during the faulty period. This was expected since the motor current fault was injected into the reaction wheel.

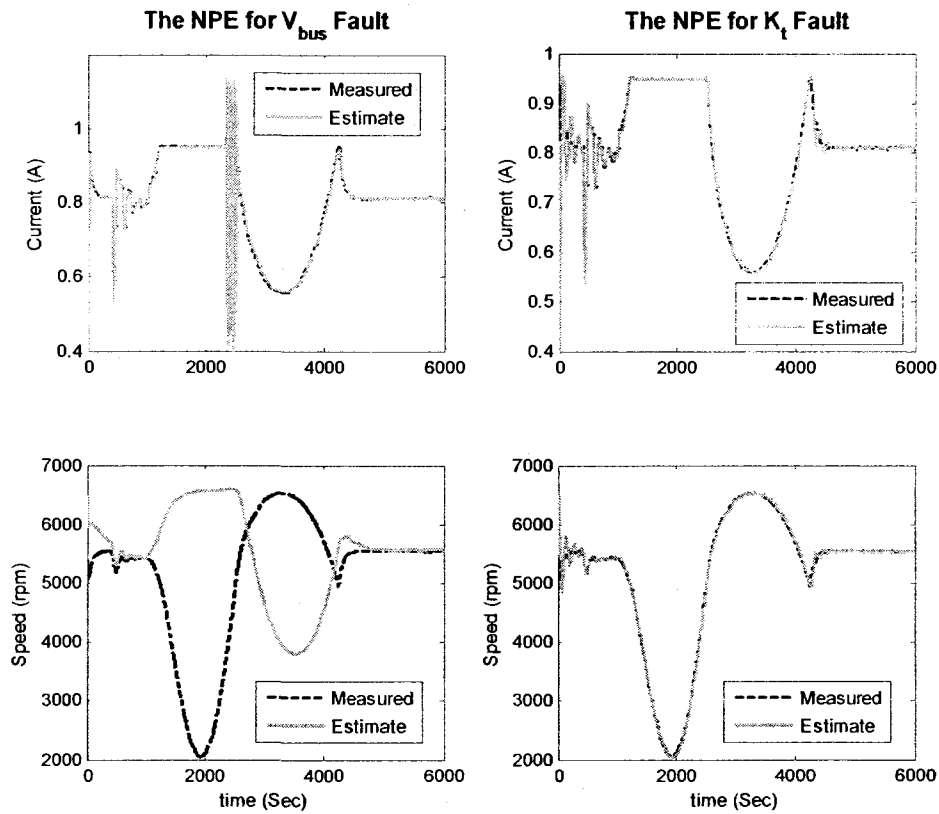


Figure 5-53. The estimated versus measured states using the parallel FDII scheme in presence of a time-varying fault in motor current over the time period $t \in [1000 \ 4250]$ second.

Figure 5-54 shows the residuals corresponding to the two NPEs in the bank. As was mentioned in Chapter 3, the residual thresholds must be set using the worst-case disturbance and noise analysis during the healthy period. Using this method, the residual thresholds are set to be almost four times bigger than the maximum effect of system noise and disturbances on the residual signal during healthy mode of operation. Accordingly, the threshold values were set to $\delta_I = \delta^1 = 0.025(A) = 25(mA)$ for the current residual and $\delta_\omega = \delta^2 = 200(rpm)$ for the speed residual. It should be noted that the residual thresholds are the same for all NPEs in the bank.

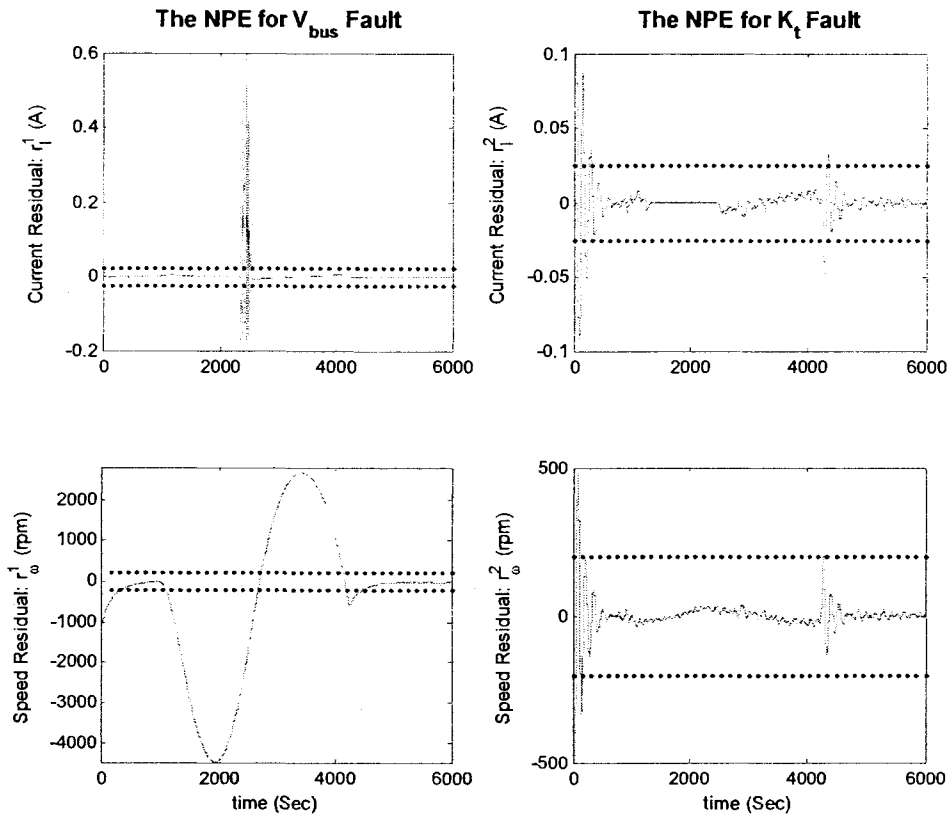


Figure 5-54. The residuals of the two NPEs of the parallel FDII scheme in presence of a time-varying fault in motor current over the time period $t \in [1000 \ 4250]$ second.

The health state of the reaction wheel is determined using the FDI decision logic of the parallel scheme given in equation (3-41). As opposed to the series-parallel scheme, the FP estimates are not required for fault detection and isolation in the parallel scheme and they are only used for fault identification. The health state is depicted in Figure 5-55. A number of observations can be made from this figure as follows:

- The injected motor current fault has been correctly detected and isolated for the most of the faulty period. The only exceptions are the *missed alarms* over two time periods: $t \in [2686.5 \ 2741]$ sec. and $t \in [4151 \ 4201]$ sec., which are both less than 60 seconds.
- As opposed to the series-parallel scheme, the parallel FDII is very sensitive to closed-loop system transients. This can be observed from the *false alarms* prior to fault

occurrence in the time period $t \in [0 \ 374]$ sec. and after fault removal (or disappearance) in the time period $t \in [4250 \ 4499]$ sec. Hence, the *false alarms* due to closed-loop system transients extend for 374 seconds in the “pre-fault” period and for almost 250 seconds in the “post-fault” period. Indeed, as was mentioned in Chapter 3, the sensitivity to closed-loop system transients is a fundamental disadvantage of the parallel FDII scheme. This *lack of robustness* to closed-loop system transients is due to the slow convergence rate of the parallel FDII scheme, as can be observed from the speed estimates of “the NPE for V_{bus} fault” over the “pre-fault” and “post-fault” periods.

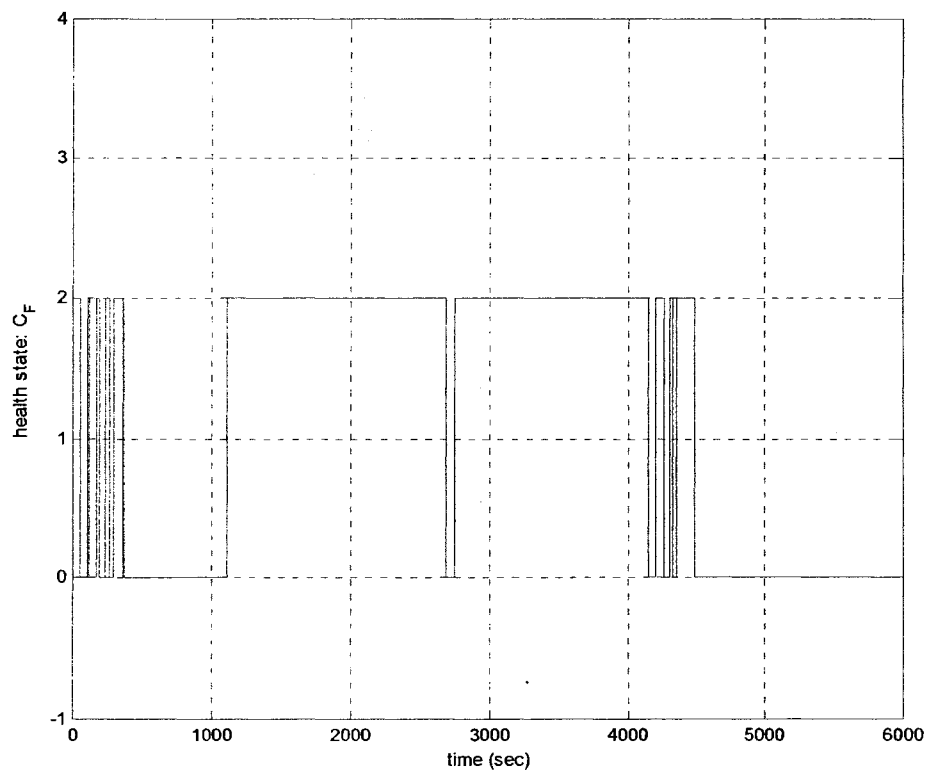


Figure 5-55. The health state of the RW using the parallel FDII scheme in presence of a time-varying fault in motor current over the time period of $t \in [1000 \ 4250]$ second.

- The first detection and isolation of the injected fault has persistently taken place at $t=1108.2$ sec. Therefore, the value of fault diagnosis delay is 108.2 seconds. Hence, the parallel scheme is faster in persistence FDI of the motor current fault than the series-parallel scheme. Note that the first detection of the motor current fault using the series-parallel scheme took only 54.3 seconds, however, the persistence detection and isolation took place in 282.3 seconds, which is more than twice bigger than the delay of the parallel scheme.

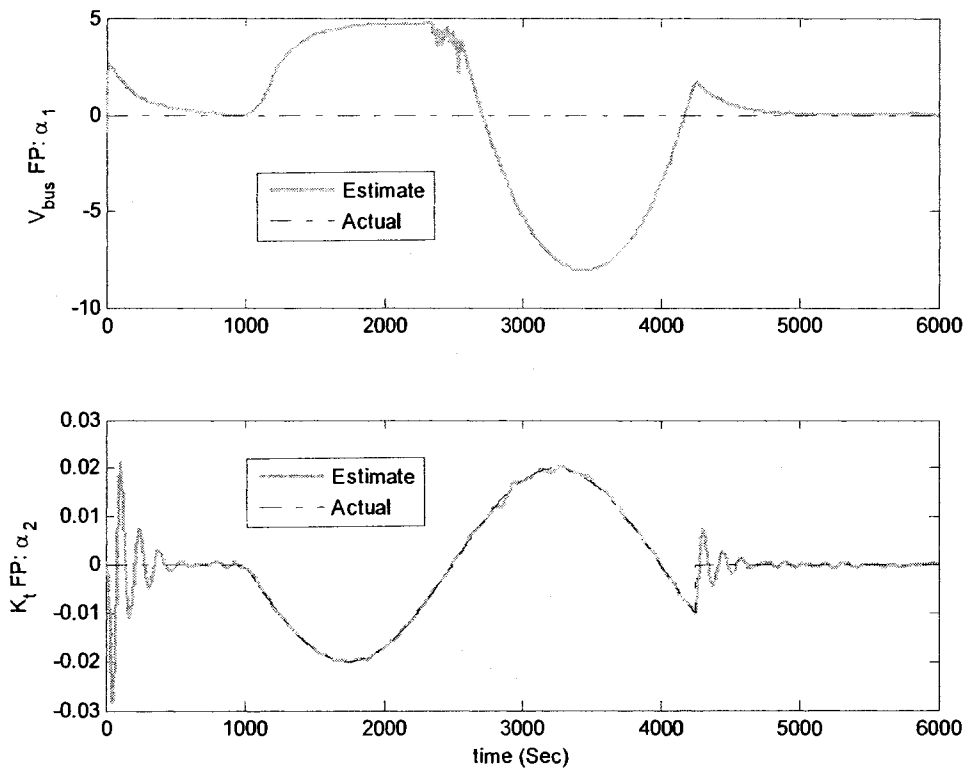


Figure 5-56. The estimated versus actual FPs using the parallel FDI scheme in presence of a time-varying fault in motor current over the time period $t \in [1000 \ 4250]$ second.

Once a fault has been detected and isolated, the fault severity can be estimated using the FP estimates. Figure 5-56 depicts the estimated versus actual values of the fault parameters. It is very important to note that at each instant of time, the value of the fault

parameter that corresponds to the isolated fault must be taken as a measure of fault severity. If the health state of the system is identified as being healthy, both fault parameters must be taken into account. Hence, since the health state of the reaction wheel has never been identified as 1 (i.e., fault in the bus voltage) in Figure 5-55, the bus voltage FP estimate in Figure 5-56 should always be neglected. Moreover, note the transient in the motor current FP estimate at the beginning of the “pre-fault” and “post-fault” periods, which are due to the afore-mentioned impact of the closed-loop system transients on the performance of the parallel FDII scheme.

The accuracy of motor current fault identification has been assessed using the three performance indices and the results are shown in Table 5-17. It can be clearly seen from this table that the motor current severity has been very accurately estimated with average errors in the order of less than 5×10^{-5} and standard deviations in the order of less than 4×10^{-4} , while the injected fault severity was varying between -0.02 to 0.02. It is important to note that the parallel scheme is slightly more accurate than the series-parallel scheme in identifying the severity of the motor current faults.

Table 5-17. The performance indices of motor current fault identification using the parallel FDII scheme in presence of intermittent motor current fault and subject to nominal noise levels.

	Pre-fault period $t \in [0 \ 1000] \text{sec}$	Faulty period $t \in [1000 \ 4250] \text{sec}$	Post-fault period $t \in [4250 \ 6000] \text{sec}$
RMSE	3.5848×10^{-4}	3.866×10^{-4}	3.9839×10^{-4}
ME	1.9183×10^{-5}	-3.3165×10^{-5}	4.9591×10^{-5}
STDE	3.5799×10^{-4}	3.8518×10^{-4}	3.9530×10^{-4}

5.5.3.2 FDII of Low-Severity Bus Voltage Faults

In this section, the results of FDII using the parallel scheme in presence of the sequence of low-severity bus voltage faults over the time period $t \in [1000 \ 5100]$ seconds - given in equation (5-40) – are depicted. The measured speed and current of the reaction wheel

and their estimates obtained from the two NPEs of the parallel FDII scheme are compared in Figure 5-57. This figure shows a very close match between the measured values and the estimates of *both* states from *only* “the NPE for V_{bus} fault”. More specifically, the current estimates from “the NPE for K_t fault” do not match the measurements especially over the faulty periods. This is reasonable because the results are obtained in presence of bus voltage fault, so only “the NPE for V_{bus} fault” has generated matching estimates for both of the states. Finally, note the transient of the speed estimate from “the NPE for V_{bus} fault” at the beginning of the simulations.

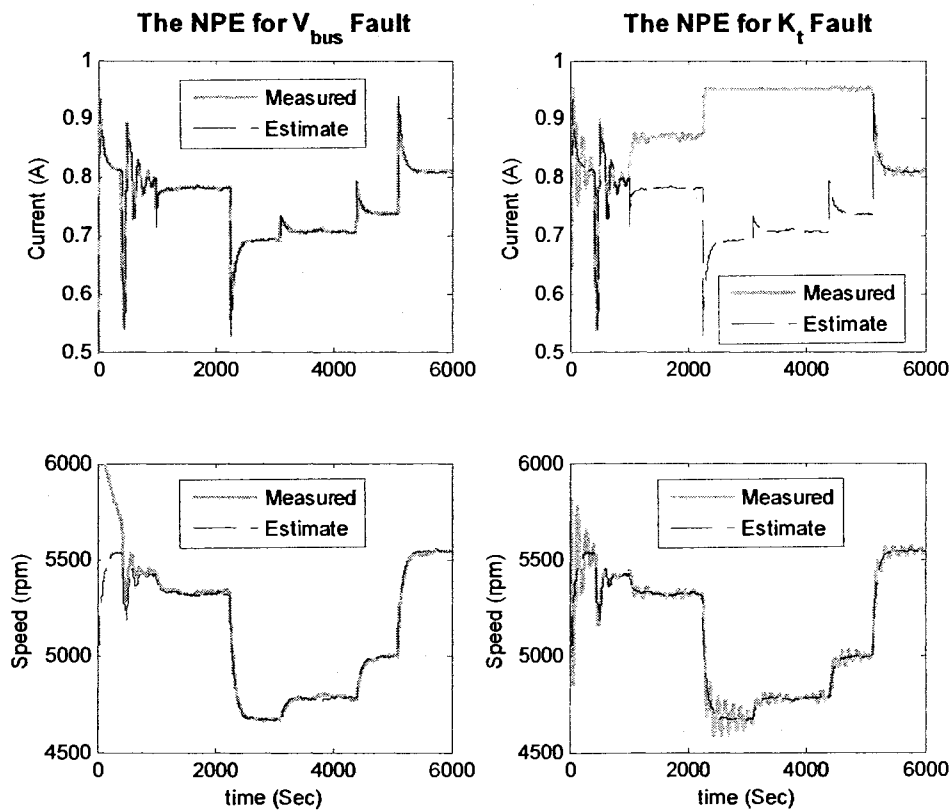


Figure 5-57. The estimated versus measured states using the parallel FDII scheme in presence of a sequence of low-severity bus voltage faults over the time period $t \in [1000 \ 5100]$ second.

Figure 5-58 shows the residuals of the two NPEs of the parallel scheme. As expected from the state estimates shown in Figure 5-57, only the two residuals of “the NPE for

V_{bus} fault” remain within their corresponding thresholds. The residual thresholds are essentially the same as the ones used for the motor current FDII using the parallel scheme presented in the previous section. As can be observed from Figure 5-58, both residuals of “the NPE for V_{bus} fault” have remained within their specified threshold bounds, except for the current residual, where it has sporadically exceeded its corresponding threshold for a few times during the simulation period. These include once at the very beginning of the simulations due to closed-loop system transients and five times during the faulty period due to transients imposed by bus voltage fault initiation, change in the fault severity, and finally the fault removal. Furthermore, as compared to the series-parallel scheme, it takes a longer time for the speed residual of the parallel scheme to converge to within its threshold bounds after the initiation of the simulation.

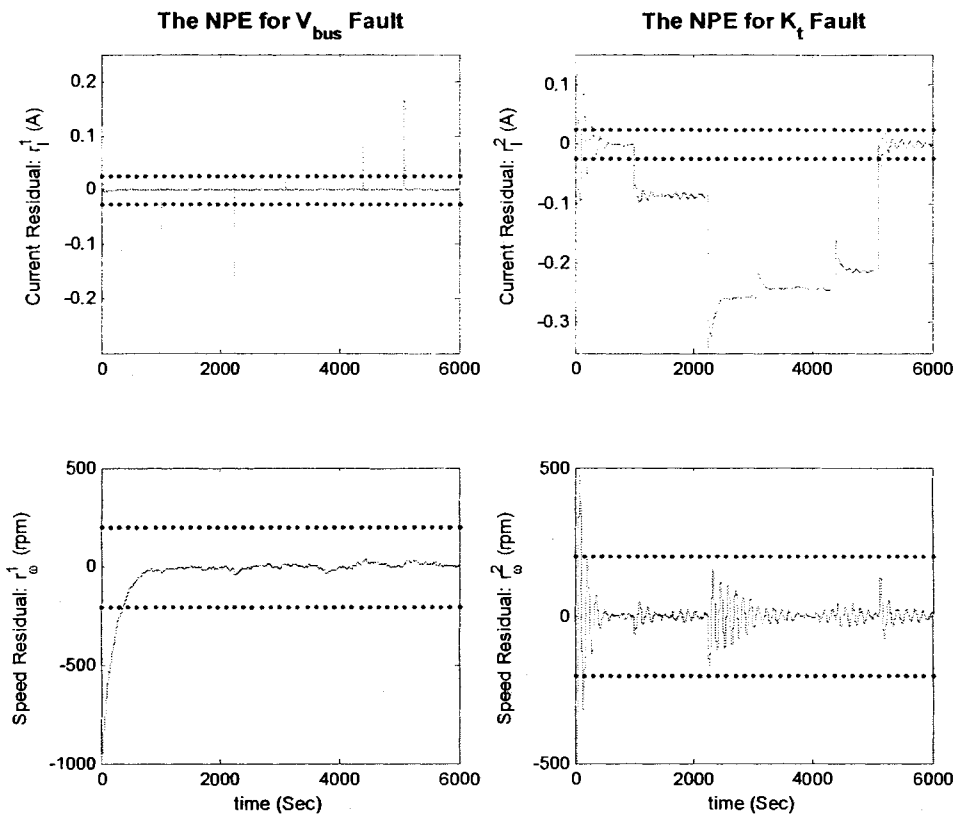


Figure 5-58. The residuals of the two NPEs of the parallel FDI scheme in presence of a sequence of low-severity bus voltage faults over the time period $t \in [1000 \ 5100]$ second.

As far as the residuals of “the NPE for K_t fault” are concerned, it can be seen from Figure 5-30 that the current residual has exceeded its threshold for the entire period of the presence of the bus voltage fault in the reaction wheel.

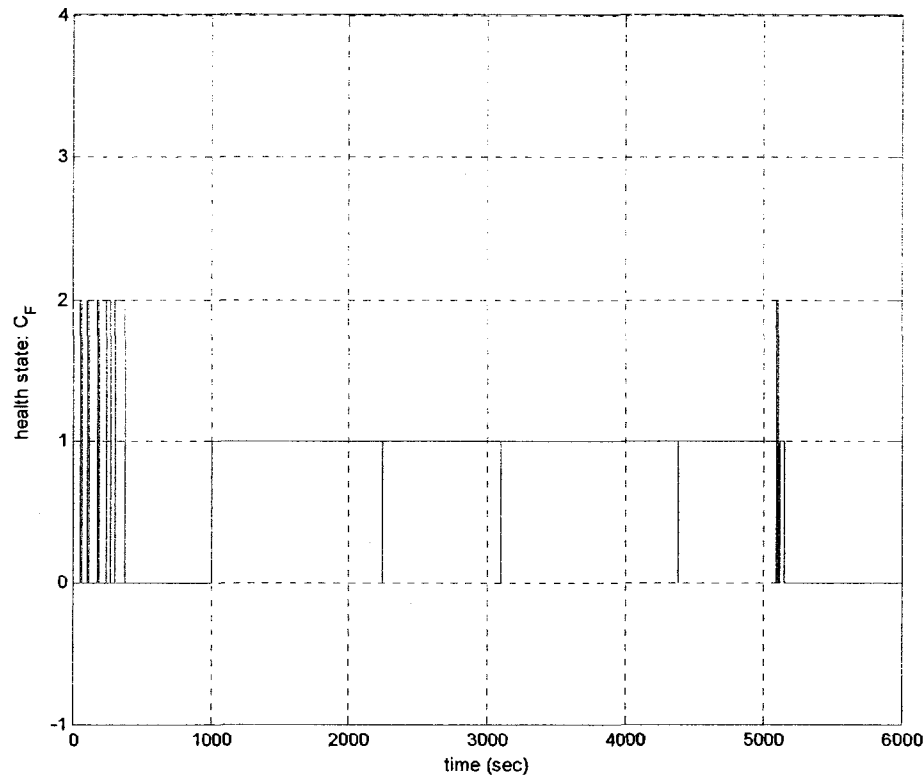


Figure 5-59. The health state of the RW using the parallel FDII scheme in presence of a sequence of low-severity bus voltage faults over the time period $t \in [1000 \ 5100]$ second.

Figure 5-59 depicts the health state of the reaction wheel obtained by applying the FDI decision logic of equation (3-41) for the parallel scheme. A number of observations can be made from this figure as follows:

- The injected sequence of low-severity (or incipient) bus voltage faults has been correctly detected and isolated for almost the entire period of bus voltage fault presence.
- A number of false alarms exist prior to fault occurrence, which last for 380.1 seconds after the start of the simulations. Compared to the settling time of the closed-loop ACS system (which is equal to almost 500 seconds), this reveals that the parallel FDII scheme is sensitive to the transients of the closed-loop ACS. Moreover, note that two short duration false alarms are also observed after fault removal including: (i) a false alarm

indicating motor current fault for almost 6 seconds over the period $t \in [5100.30 \ 5106.9]$ sec. and (ii) a false alarm indicating bus voltage fault for almost 31 seconds over the period $t \in [5115.4 \ 5146]$ sec.

- The delay in fault detection and isolation is *only* 4.2 seconds, which is twice bigger than that of the series-parallel scheme.
- A sequence of intermittent missed alarms is also observed during the faulty period with very short durations of 8 sec., 2 sec., and 4.5 sec., respectively. It should be noted that these missed alarms are indeed due to changes in the severity of the injected bus voltage fault. It is important to note that the durations of the missed alarms of the parallel scheme are shorter than those of the series-parallel scheme, namely 21 sec., 13.5 sec., and 12 sec.
- Fault removal or disappearance has been perfectly detected at $t=5100.05$ seconds, practically with *no* delay. However, there are few short duration of false alarms, which were mentioned in the above.

Figure 5-60 depicts the estimated versus actual values of the fault parameters. Now that the bus voltage fault has been correctly isolated, the FP estimate corresponding to this fault, namely $\hat{\alpha}^1$ (see Figure 5-60) must be taken as a measure of fault severity. As can be seen in Figure 5-60, the bus voltage fault has been very precisely identified across all injected fault severity levels, including minor incipient faults such as 1V drop in the bus voltage. Once again, note the transient of the bus voltage FP estimate at the start of the simulation.

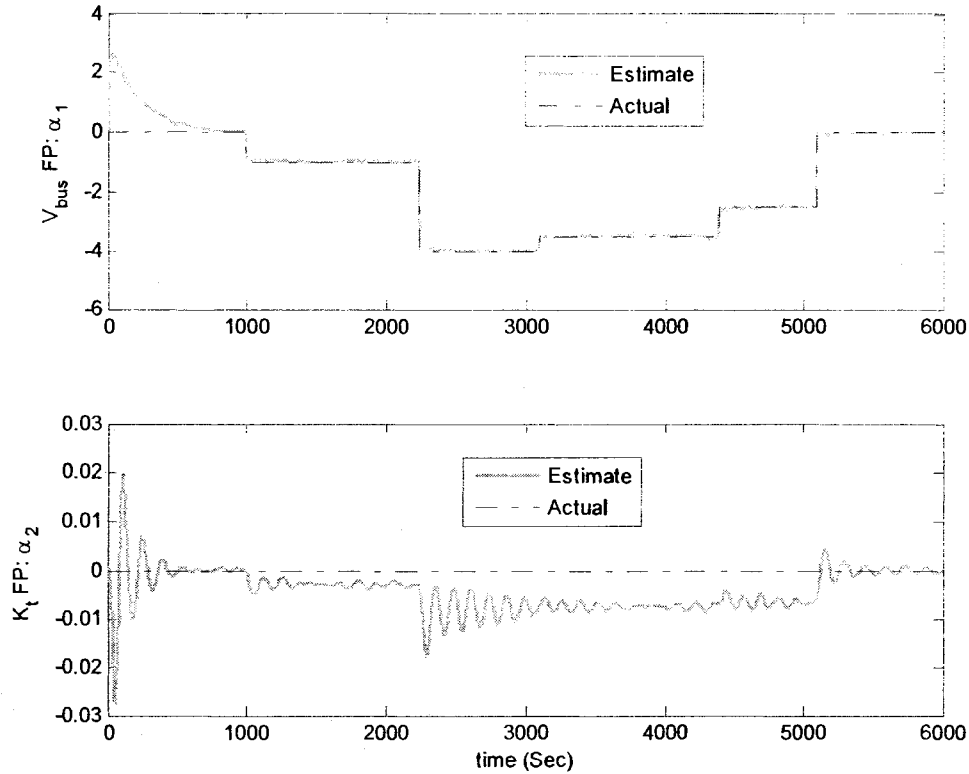


Figure 5-60. The estimated versus actual FPs using the parallel FDI scheme in presence of a sequence of low-severity bus voltage faults over the time period $t \in [1000 \ 5100]$ second.

The accuracy of the bus voltage fault identification has been assessed using the aforementioned four performance indices and the results are shown in Table 5-18. It can be clearly seen from Table 5-18 that the bus voltage fault severity has been accurately estimated with average errors in the order of less than 10^{-1} V (or 100 mV) in “pre-fault period”, less than 3×10^{-2} V (or 30 mV) during all faulty periods, and 30.4 mV in “post-fault period”, while the actual injected faults are all in the order of Volts (i.e., 1 to 4 V). Furthermore, the standard deviations are relatively small and are in the order of less than 4×10^{-2} V (or 40 mV) during faulty periods, in the order of 5×10^{-2} V (or 50 mV) in “pre-fault period”, and less than 3×10^{-2} (or 30 mV) in “post-fault period”. All these

performance indices clearly indicate that the parallel FDII scheme is capable of accurately identifying fault severities, especially under “nominal” noise levels. Nonetheless, the parallel scheme is less accurate than the series-parallel scheme in identifying the low-severity bus voltage faults.

Table 5-18. The performance indices of fault identification using the parallel FDII scheme in presence of low-severity bus voltage fault and subject to nominal noise levels.

	Pre-fault [0, 1000]s	1 st Faulty period [1000,2240]s	2 nd Faulty period [2240,3100]s	3 rd Faulty period [3100,4390]s	4 th Faulty period [4390,5100]s	Post-fault [5100,6000]s
Actual V_{bus} drop	0	-1	-4	-3.5	-2.5	0
Average of Estimated drop	0.0885	-0.9715	-3.9854	-3.4889	-2.5210	-0.0304
RMSE	0.1024	0.0346	0.0363	0.0401	0.0358	0.0406
ME	-0.0885	-0.0285	-0.0146	-0.0111	0.0210	0.0304
STDE	0.0516	0.0196	0.0332	0.0385	0.0289	0.0268

5.5.3.3 FDII of High-Severity Bus Voltage Faults

In this section, the results of FDII in presence of the sequence of high-severity bus voltage faults over the time period $t \in [1000 \ 5100]$ seconds – given in equation (5-41) – are depicted. The measured speed and current of the reaction wheel and their estimates obtained from the NPEs of the parallel FDII scheme are shown in Figure 5-61. “The NPE for V_{bus} fault” generates state estimates very close to their respective measurements. However, the current estimate from “the NPE for K_1 fault” does not match its respective measurement over the faulty periods. This is reasonable, since the results are obtained in presence of high-severity faults in the bus voltage.

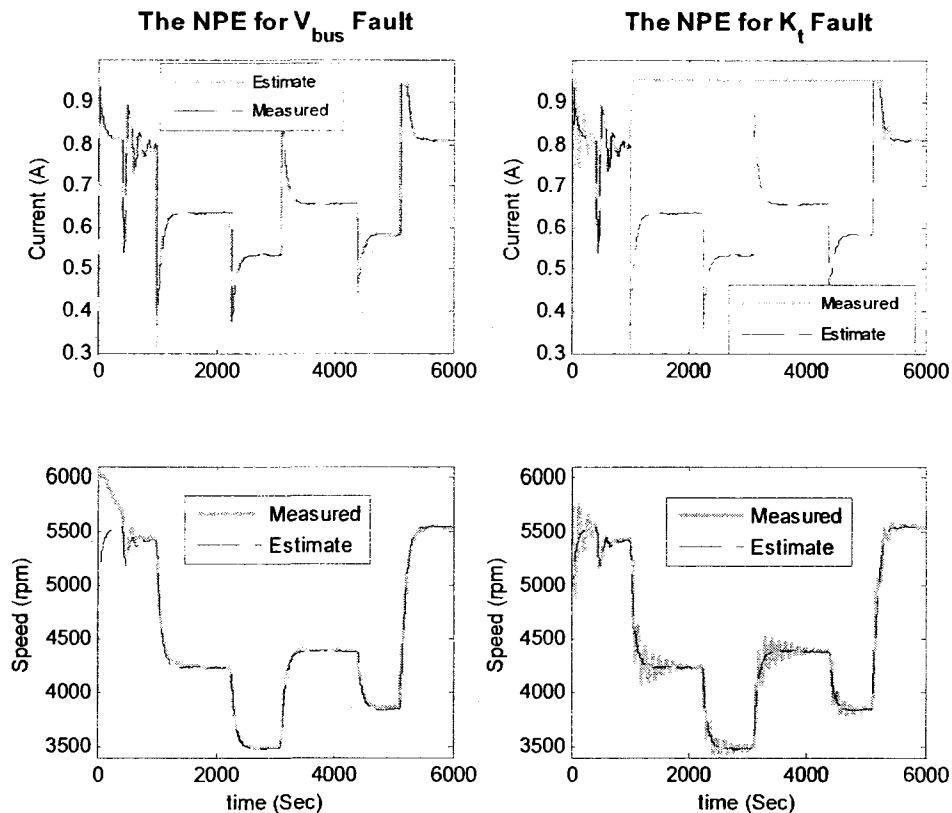


Figure 5-61. The estimated versus measured states using the parallel FDII scheme in presence of a sequence of high-severity bus voltage faults over the time period $t \in [1000 \ 5100]$ second.

Figure 5-62 shows the residuals of the two NPEs. As was expected from the state estimates shown in Figure 5-61, only the two residuals of “the NPE for V_{bus} fault” remain within their corresponding thresholds except for a few times in the current residual. These are due to transients caused by the initiation of the bus voltage fault, the change in the fault severity, and finally the fault removal. It should be noted that the arguments previously mentioned for the low-severity bus voltage faults are as well applicable to the high-severity bus voltage faults.

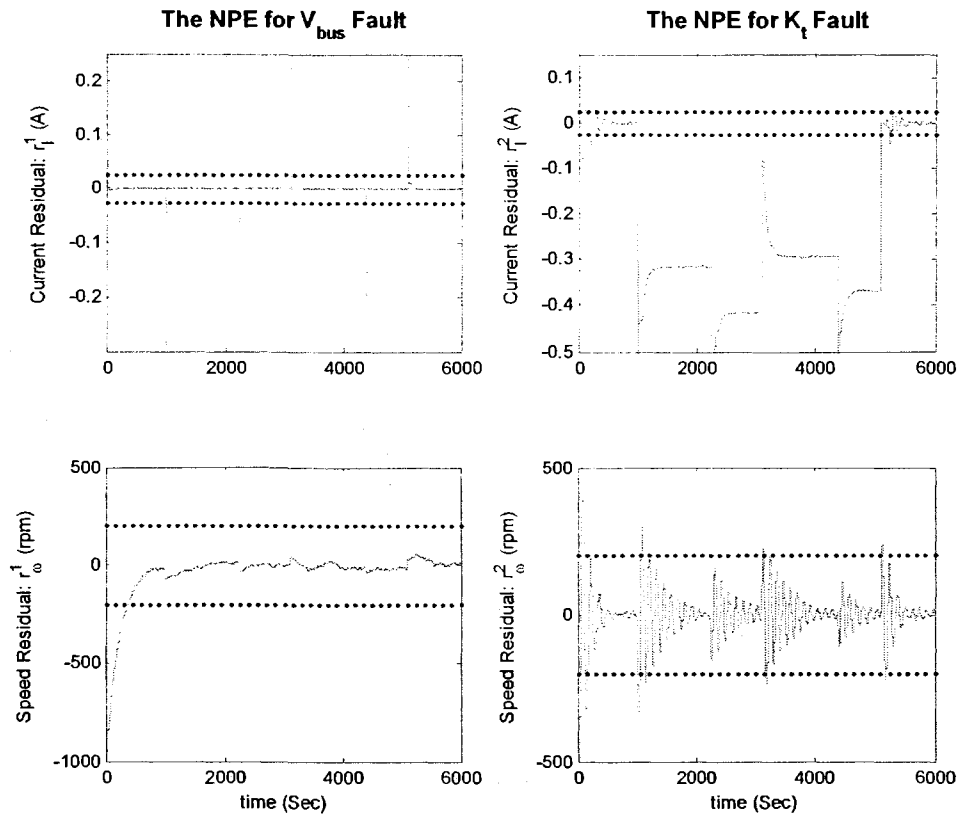


Figure 5-62. The residuals of the two NPEs of the parallel FDII scheme a sequence of high-severity bus voltage faults over the time period $t \in [1000 \ 5100]$ second.

Figure 5-63 depicts the health state of the reaction wheel obtained by applying the FDI decision logic of the parallel scheme given in equation (3-41). A number of observations can be made from this figure as follows:

- The injected sequence of high-severity bus voltage faults has been correctly detected and isolated for almost the entire period of bus voltage fault presence.
- A number of false alarms exist prior to fault occurrence, which last for 380 seconds after the start of the simulations. This, once again, reveals that the parallel FDII scheme is sensitive to the transients of the closed-loop ACS. Moreover, some false alarms exist after fault removal, which last for almost 225 seconds until $t=5325$ sec.

- The delay in fault detection and isolation is *only* 8.5 seconds, which is twice bigger than the delay of the parallel scheme in detecting and isolating low-severity bus voltage faults.
- A sequence of intermittent missed alarms is also observed during the faulty period with very short durations of 8 sec., 8 sec., and 7.5 sec., respectively. It should be noted that these missed alarms are indeed due to changes in the severity of the injected bus voltage fault.

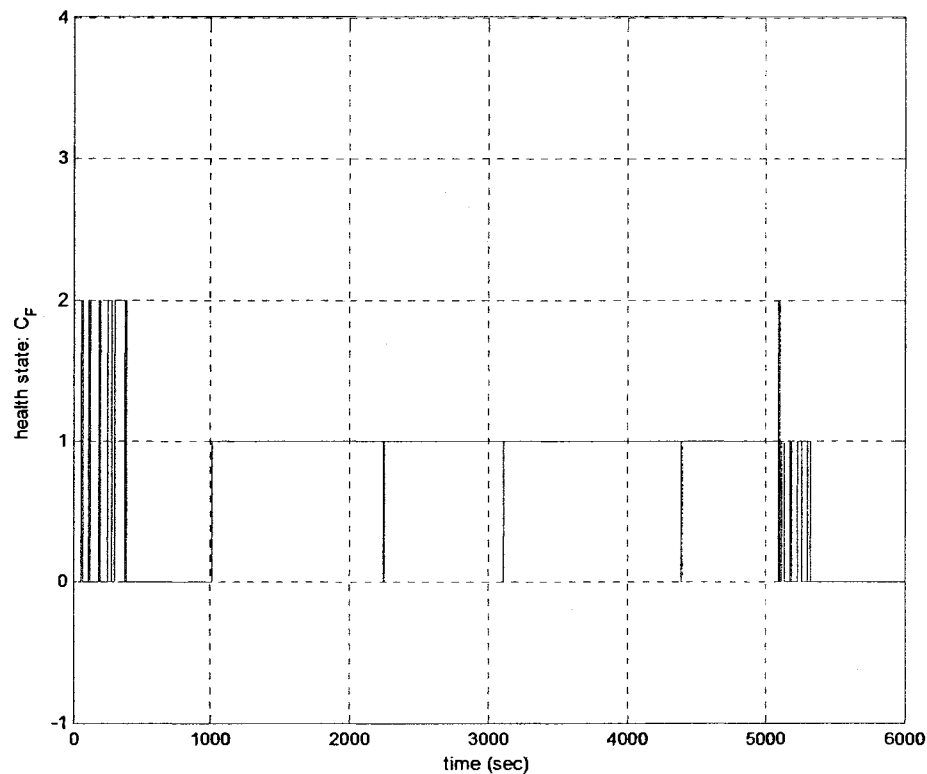


Figure 5-63. The health state of the RW using the parallel FDII scheme in presence of a sequence of high-severity bus voltage faults over the time period $t \in [1000 \ 5100]$ second.

Figure 5-64 depicts the estimated versus actual values of the fault parameters α^1 and α^2 . The accuracy of the parallel scheme in identifying the high-severity bus voltage faults has been assessed using the afore-mentioned performance indices and the results are shown

in Table 5-19. It can be clearly seen from this table that the bus voltage fault severity has been precisely estimated with average errors, once again, in the order of less than 10^{-1} V (or 100 mV) in the “pre-fault” period, less than 6.5×10^{-2} V (or 65 mV) during all faulty periods, and in the order of 3.5×10^{-2} (or 35 mV) in the “post-fault” period, while the actual injected faults are all in the order of a few Volts (i.e., 5.3 to 9.4 V).

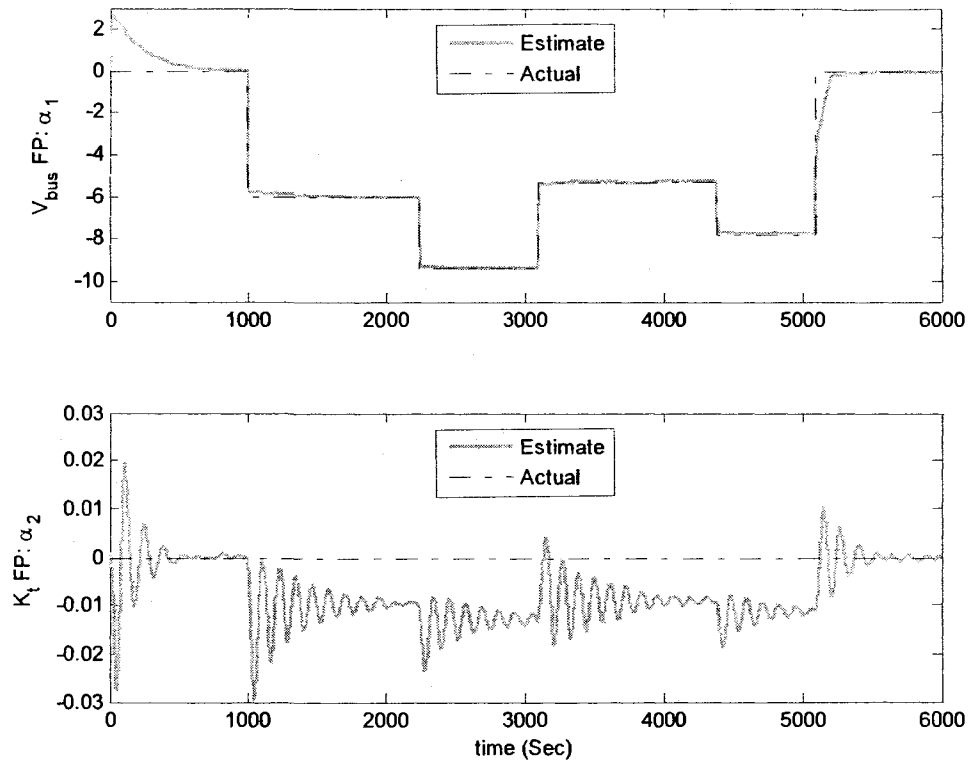


Figure 5-64. The estimated versus actual FPs using the parallel FDII scheme in presence of a sequence of high-severity bus voltage faults over the time period $t \in [1000 \ 5100]$ second.

All performance indices given in Table 5-19 clearly indicate that the parallel FDII scheme is capable of accurately identifying high-severity bus voltage faults, especially under “nominal” noise levels.

Table 5-19. The performance indices of fault identification using the parallel FDII scheme in presence of high-severity bus voltage fault and subject to nominal noise levels.

	Pre-fault [0, 1000]s	1 st Faulty period [1000,2240]s	2 nd Faulty period [2240,3100]s	3 rd Faulty period [3100,4390]s	4 th Faulty period [4390,5100]s	Post-fault [5100,6000]s
Actual V_{bus} drop	0	-6	-9.4	-5.3	-7.8	0
Average of Estimated drop	0.0885	-5.9555	-9.3823	-5.2858	-7.7389	-0.0348
RMSE	0.1024	0.0831	0.0314	0.0462	0.0639	0.0532
ME	-0.0885	-0.0445	0.0177	-0.0142	-0.0611	0.0348
STDE	0.0516	0.0701	0.0206	0.0440	0.0186	0.0401

5.5.4 Robustness Analysis of the Parallel FDII Scheme with Respect to Measurement Noise

In this section, the robustness of the parallel FDII scheme with respect to measurement noise is extensively analyzed and investigated. Hence, the simulations that were carried out for the parallel scheme subject to the “nominal” noise level are repeated again with higher levels of noise, namely “medium” and “high” noise levels, according to Table 5-3 and Table 5-4. Then, the performance of the parallel FDII scheme in terms of FDI and fault severity estimation subject to different noise levels are compared using the health state variable C_k^F and the FP estimation performance indices (i.e., RMSE, ME, and STDE), respectively. It should be noted that the robustness assessment of the parallel FDII scheme is performed separately for each fault scenario.

5.5.4.1 FDII of Motor Current Faults

In the following, the robustness of the parallel scheme is analyzed in presence of the intermittent time-varying motor current fault given in equation (5-39), subject to A)

medium level of measurement noise (i.e., SNR=55dB for both current and speed), and B) *high* level of measurement noise (i.e., SNR=45dB for both current and speed).

A) Medium Level/Intensity of Measurement Noise (SNR = 55dB): The state estimates and the residuals corresponding to the NPEs for V_{bus} and K_t faults are shown in Figure C-14 and Figure C-15 of Appendix C, respectively. As can be seen from Figure C-15, the residual thresholds are set to $\delta_I = \delta^1 = 0.025(A) = 25(mA)$ for the current residual and $\delta_\omega = \delta^2 = 200(rpm)$ for the speed residual. Hence, both current and speed residual thresholds are kept equal to their respective values under the “nominal” noise level. It should be noted that, as opposed to the series-parallel scheme, the residual thresholds of the parallel scheme are much less dependent on the noise level. This is indeed due to the fact that the parallel FDII scheme is very robust to measurement noise.

Figure 5-65 shows the health state of the reaction wheel in presence of the intermittent time-varying motor current fault over the time period $t \in [1000 \ 4250]$ and subject to the “medium” noise level. By comparing Figure 5-65 with Figure 5-55, one can easily see that even an increase of SNR with a factor of 100 does *not* practically deteriorate (or only very slightly deteriorates) the FDI performance of the parallel scheme. The slight deteriorations in the FDI performance due to the increased level of measurement noise include: (i) the duration of the *false alarms* in the “pre-fault” period due to transients of the closed-loop ACS have been extended from 374 seconds (under the “nominal” noise level) to 385 seconds and (ii) the false alarms in the “post-fault” period have been extended up to $t=4520$ second as compared to $t=4499$ second under the “nominal” noise level. Nevertheless, the FDI delay has been reduced to 100 seconds as compared to 108.2 seconds under the “nominal” noise level.

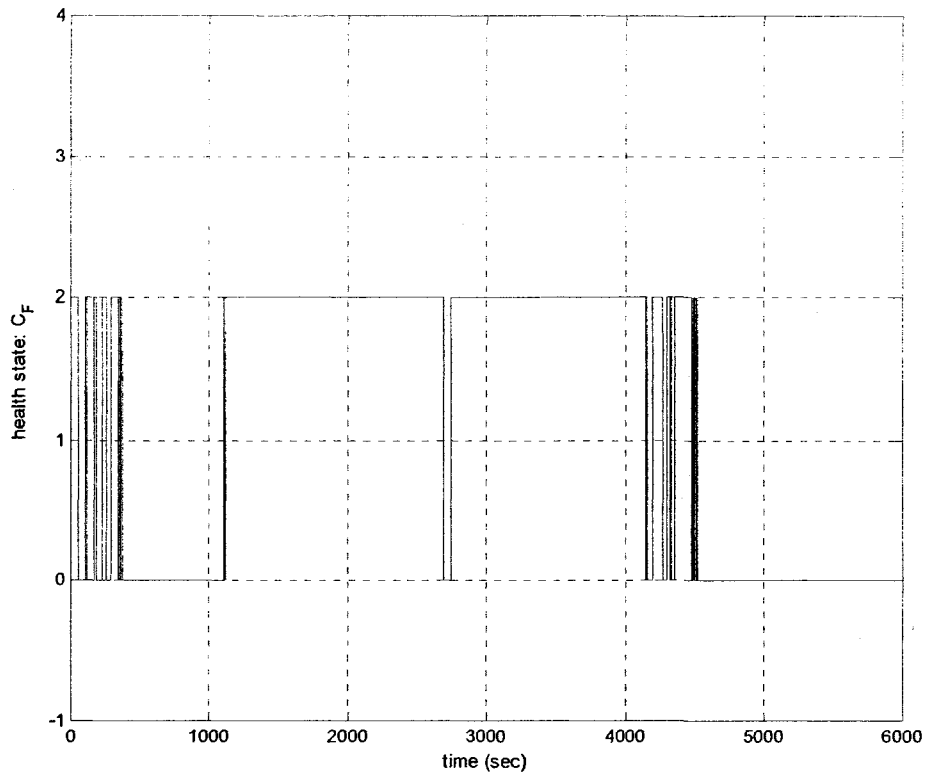


Figure 5-65. The health state of the RW using the parallel FDII scheme in presence of motor current fault over the period $t \in [1000 \ 4250]$ sec., subject to *medium* noise level (SNR=55 dB).

Figure 5-66 depicts the FP estimates versus their actual values. As can be observed from this figure, the increased level of noise has a very small impact on the motor current FP estimate, i.e. $\hat{\alpha}^2$. In particular, comparing Figure 5-66 with Figure 5-56 reveals that even with the increase of SNR with a factor of 100, the motor current FP estimate remains practically unchanged.

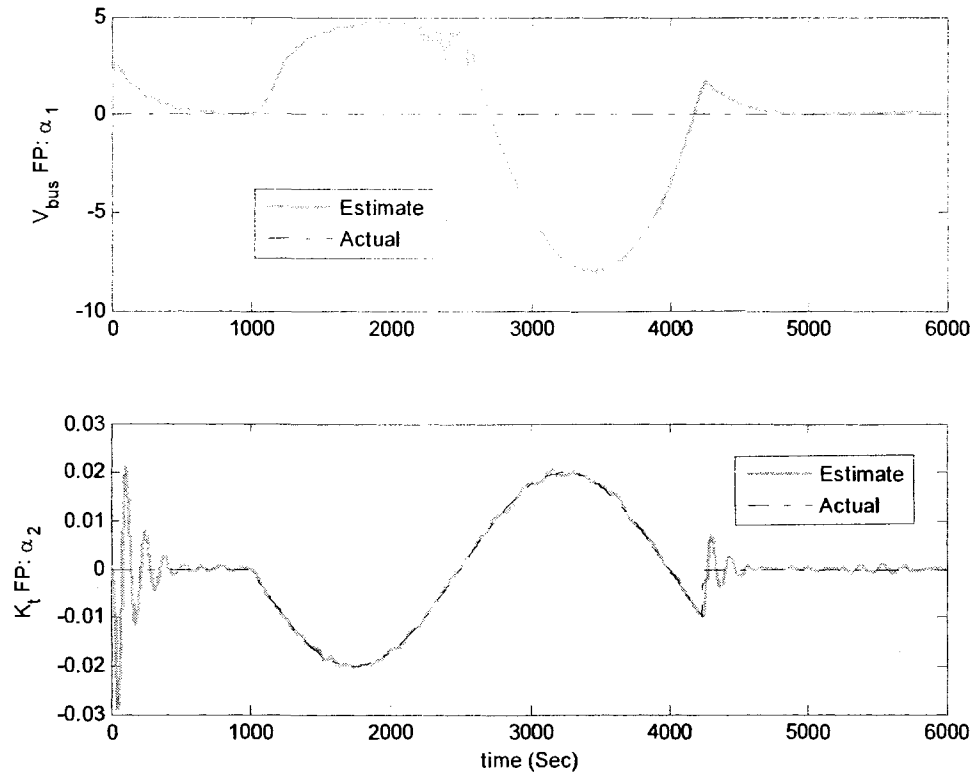


Figure 5-66. The estimated versus actual FPs using the parallel FDI in presence of motor current fault over the period $t \in [1000 \ 4250]$ sec., subject to *medium* noise level (SNR=55 dB).

B) High Level/Intensity of Measurement Noise (SNR = 45dB): The state estimates and the residuals corresponding to the NPEs for V_{bus} and K_t faults are shown in Figure C-16 and Figure C-17 of Appendix C, respectively. As was mentioned previously, the residual thresholds of the parallel scheme remain unchanged due to the robustness of the parallel scheme, and are thus equal to $\delta_i = \delta^1 = 0.025(A) = 25(mA)$ for the current residual and $\delta_\omega = \delta^2 = 200(rpm)$ for the speed residual.

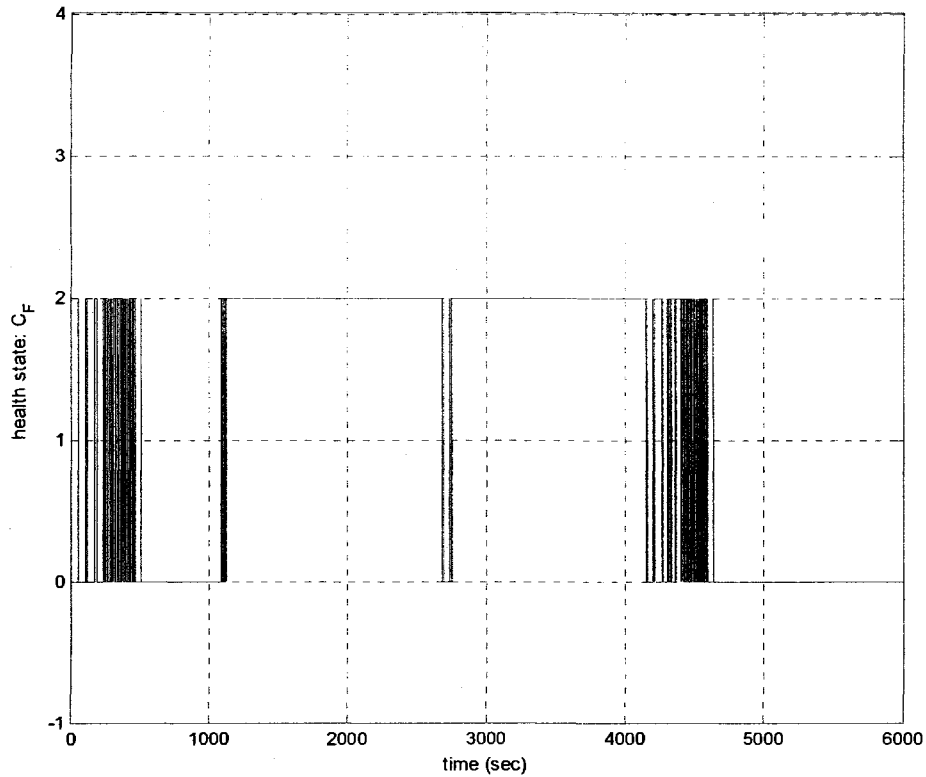


Figure 5-67. The health state of the RW using the parallel FDI scheme in presence of motor current fault over the period $t \in [1000 \ 4250]$ sec., subject to *high* noise level (SNR=45 dB).

Figure 5-67 shows the health state of the reaction wheel in presence of the intermittent time-varying motor current fault over the time period $t \in [1000 \ 4250]$ and subject to the “high” noise level. Once again, comparing Figure 5-67 with Figure 5-55 reveals that even an increase of SNR with a factor of 1000 has a relatively small impact on the FDI performance of the parallel scheme. As compared to the case of “nominal” noise level depicted in Figure 5-55, the deteriorations in the FDI performance due to the “high” noise level include: (i) the duration of the *false alarms* in the “pre-fault” period due to transients of the closed-loop ACS have been extended from 374 seconds (under the “nominal” noise level) to 465 seconds and (ii) the false alarms in the “post-fault” period have been extended up to $t=4600$ second as compared to $t=4499$ second under the

“nominal” noise level, and finally (iii) the FDI delay has been increased from 108.2 seconds under the “nominal” noise level to 120.4 seconds under the “high” noise level. Nonetheless, the above-mentioned deteriorations are negligible as compared to those observed for the series-parallel scheme.

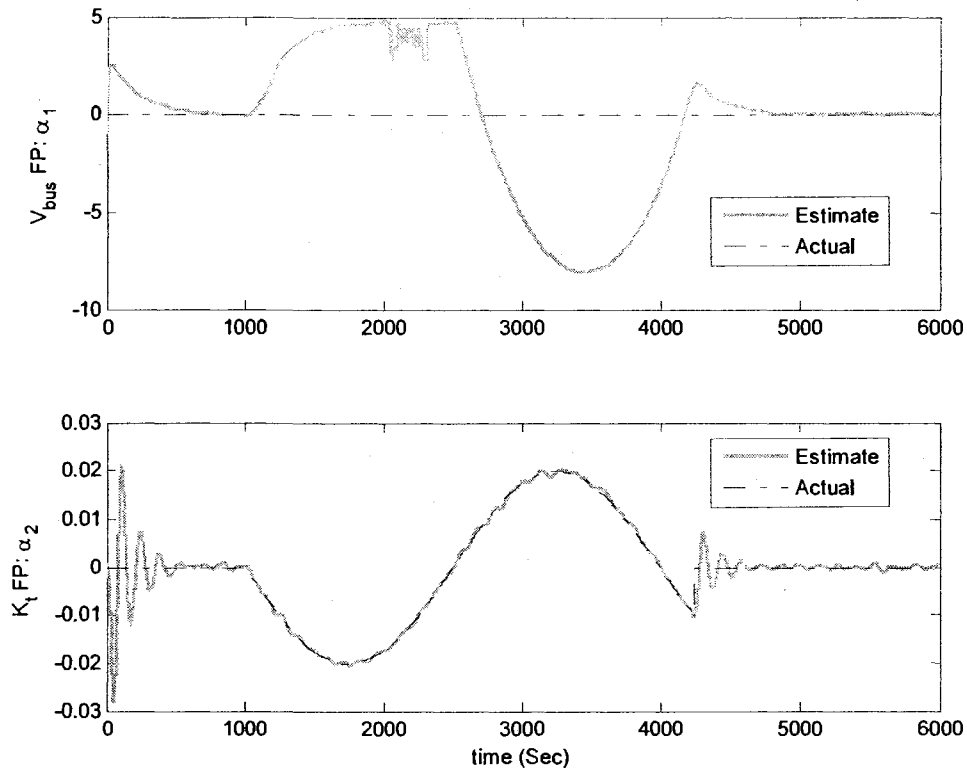


Figure 5-68. The estimated versus actual FPs using the parallel FDI in presence of motor current fault over the time period $t \in [1000 \ 4250]$ sec., subject to *high* noise level (SNR=45 dB).

Figure 5-68 depicts the FP estimates versus their actual values. As can be observed from this figure, the increased level of noise has a small impact on the motor current FP estimate especially at the steady state of both “pre-fault” and “post-fault” periods. More specifically, comparing Figure 5-68 with Figure 5-56 reveals that the motor current FP estimate slightly deteriorates even with an increase of SNR with a factor of 1000.

The three performance indices of fault identification, namely RMSE, ME, and STDE corresponding to the motor current FP estimate subject to various noise levels are compared in Table 5-20, Table 5-21, and Table 5-22, respectively. It can be clearly seen from the three tables that the order of the performance indices has remained unchanged across all time periods even with the increase in the level of measurement noise. For instance, the RMSE index in Table 5-20 has remained in the order of 10^{-4} for all noise levels across all time periods.

Table 5-20. Comparison of the RMSE of the motor current FP estimation using the parallel FDII scheme subject to various noise levels and in presence of intermittent motor current fault

Noise Level (SNR)	Pre-fault period $t \in [0 \ 1000]$sec	Faulty period $t \in [1000 \ 4250]$sec	Post-fault period $t \in [4250 \ 6000]$sec
<i>Nominal</i> (75 dB)	3.5848×10^{-4}	3.866×10^{-4}	3.9839×10^{-4}
<i>Medium</i> (55 dB)	4.1429×10^{-4}	3.8274×10^{-4}	3.7182×10^{-4}
<i>High</i> (45 dB)	3.6911×10^{-4}	4.2064×10^{-4}	4.1193×10^{-4}

The only significant exception is the “pre-fault” period of Table 5-21, where the ME index has been increased with a factor of almost 3.7 due to the increase of SNR with a factor of 100 (i.e., comparing the ME index under the “medium” noise level with that of the “nominal” noise level). Moreover, the ME index has been increased with a factor of almost 4.27 due to the increase of SNR with a factor of 1000 (i.e., “high” noise level). Similar to the RMSE index, the STDE index has also remained in the order of 10^{-4} for all noise levels across all time periods, as can be observed from Table 5-22.

Table 5-21. Comparison of the ME of the motor current FP estimation using the parallel FDII scheme subject to various noise levels and in presence of intermittent motor current fault.

Noise Level (SNR)	Pre-fault period $t \in [0 \ 1000]$ sec	Faulty period $t \in [1000 \ 4250]$ sec	Post-fault period $t \in [4250 \ 6000]$ sec
<i>Nominal</i> (75 dB)	1.9183×10^{-5}	-3.3165×10^{-5}	4.9591×10^{-5}
<i>Medium</i> (55 dB)	-7.0704×10^{-5}	-1.2692×10^{-5}	5.7889×10^{-5}
<i>High</i> (45 dB)	-8.1501×10^{-5}	-1.9495×10^{-5}	-1.0237×10^{-6}

Table 5-22. Comparison of the STDE of FP estimation using the parallel FDII scheme subject to various noise levels and in presence of intermittent motor current fault.

Noise Level (SNR)	Pre-fault period $t \in [0 \ 1000]$ sec	Faulty period $t \in [1000 \ 4250]$ sec	Post-fault period $t \in [4250 \ 6000]$ sec
<i>Nominal</i> (75 dB)	3.5799×10^{-4}	3.8518×10^{-4}	3.9530×10^{-4}
<i>Medium</i> (55 dB)	4.0824×10^{-4}	3.8253×10^{-4}	3.6730×10^{-4}
<i>High</i> (45 dB)	3.6002×10^{-4}	4.2019×10^{-4}	4.1194×10^{-4}

In conclusion, the performance of the parallel scheme in detection, isolation and identification of motor current faults is very robust to measurement noise.

5.5.4.2 FDII of Low-Severity Bus Voltage Faults

In the following, the robustness of the parallel FDII scheme is analyzed in presence of the intermittent sequence of low-severity bus voltage faults given in equation (5-40), subject to A) *medium* level of measurement noise (i.e., SNR=54.57dB for the motor current and SNR=54.76dB for the speed of the wheel), and B) *high* level of measurement noise (i.e., SNR=44.57dB for the motor current and SNR=44.76dB for the speed of the wheel).

A) Medium Level/Intensity of Measurement Noise (Current SNR = 54.57 dB and Speed SNR = 54.76 dB): The state estimates and the residuals corresponding to the NPEs for V_{bus} and K_t faults are shown in Figure C-18 and Figure C-19 of Appendix C,

respectively. Similar to the case of FDII of motor current faults subject to “medium” noise level, the residual thresholds of the parallel scheme are set to $\delta_i = \delta^1 = 8 \times 10^{-3}$ (A) for the current residual and $\delta_\omega = \delta^2 = 80$ (rpm) for the speed residual, as can be seen from Figure C-19.

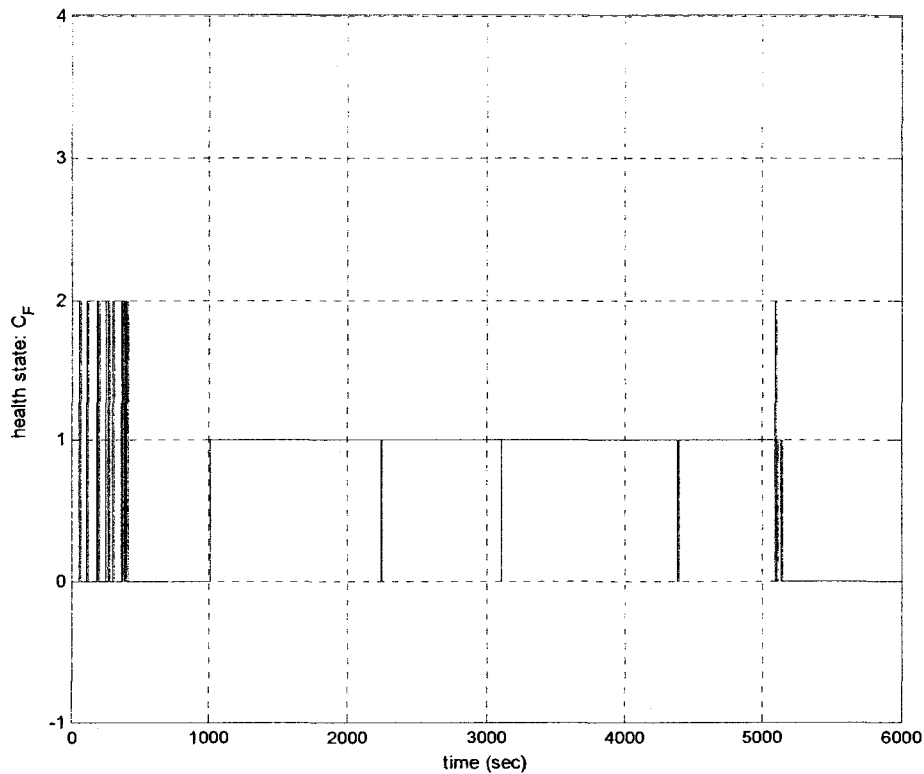


Figure 5-69. The health state of the RW using the parallel FDII scheme in presence of a sequence of *low-severity* bus voltage faults over the time period $t \in [1000 \ 5100]$ sec., subject to *medium* noise level (Current SNR=54.57 dB and Speed SNR=54.76 dB).

Figure 5-69 shows the health state of the reaction wheel. As compared to the case of “nominal” noise level depicted in Figure 5-59, the deteriorations in the FDI performance due to the “medium” noise level are practically negligible and include: (i) the duration of the *false alarms* in the “pre-fault” period due to the transients of the closed-loop ACS have been extended from 380.1 seconds (under the “nominal” noise level) to 411

seconds; (ii) the FDI delay has been very slightly increased from 4.2 seconds under the “nominal” noise level to 4.5 seconds under the “medium” noise level; and (iii) the duration of the last missed alarm during the “faulty” period (among the three missed alarms in that period) has been very slightly increased from 4.5 seconds under the “nominal” noise level to 5 seconds under the “medium” noise level. Furthermore, it should be noted that the health state in the “post-fault” period does not show any significant change to the increased level of measurement noise. One can clearly observe that the above-mentioned deteriorations are negligible as compared to those observed for the series-parallel scheme, thus confirming the extreme robustness of the parallel scheme to measurement noise.

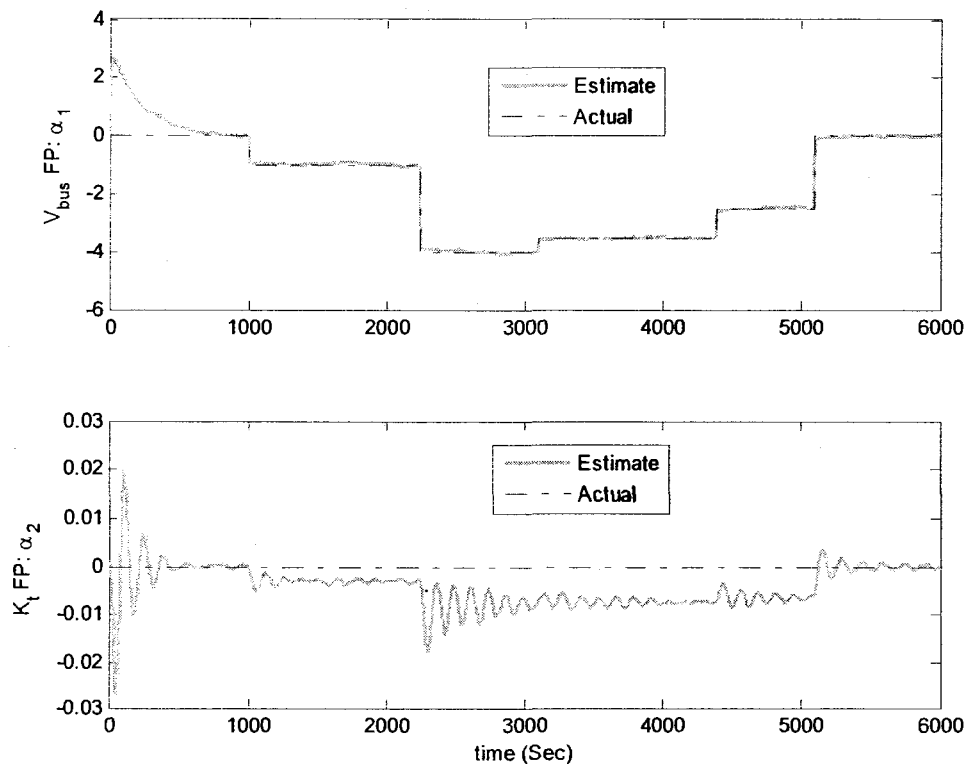


Figure 5-70. The estimated versus actual FPs using the parallel FDII in presence of a sequence of low-severity bus voltage faults over the time period $t \in [1000 \ 5100]$ sec., subject to medium noise level (Current SNR=54.57 dB and Speed SNR=54.76 dB).

Figure 5-70 depicts the estimated versus actual values of the fault parameters under the “medium” noise level. As can be observed from this figure, the increased level of noise has a very small impact on the bus voltage FP estimate, i.e. $\hat{\alpha}^1$. More specifically, comparing Figure 5-70 with Figure 5-60 reveals that even with the increase of SNR with a factor of 100, the bus voltage FP estimate remains practically unchanged.

B) High Level/Intensity of Measurement Noise (Current SNR = 44.57 dB and Speed

SNR = 44.76 dB): The state estimates and the residuals corresponding to the NPEs for V_{bus} and K_t faults are shown in Figure C-20 and Figure C-21 of Appendix C, respectively. As was mentioned previously, the residual thresholds of the parallel scheme remain unchanged due to the robustness of the parallel scheme, and are thus equal to $\delta_I = \delta^1 = 0.025(A) = 25(mA)$ for the current residual and $\delta_\omega = \delta^2 = 200(rpm)$ for the speed residual.

Figure 5-71 shows the health state of the reaction wheel in presence of the sequence of low-severity bus voltage faults – given in equation (5-40) – and subject to the “high” noise level. As compared to the case of “nominal” noise level depicted in Figure 5-59, small deteriorations can be observed in the FDI performance due to the “high” noise level, including: (i) the duration of the *false alarms* in the “pre-fault” period due to the transients of the closed-loop ACS have been extended from 380.1 seconds (under the “nominal” noise level) to 516 seconds; (ii) the health state in the “post-fault” period shows *false alarms* for almost 190 seconds after fault removal as compared to 46 seconds under the “nominal” noise level; (iii) the FDI delay has been very slightly increased from 4.2 seconds under the “nominal” noise level to 5.1 seconds under the “high” noise level; and (iv) the duration of the first and the last missed alarm during the “faulty” period

(among the three missed alarms in that period) has been very slightly increased from 8 and 4.5 seconds under the “nominal” noise level to 9.5 and 6 seconds under the “high” noise level, respectively. However, considering the increase of SNR with a factor of 1000, one can easily conclude that the FDI performance of the parallel scheme is very slightly sensitive to measurement noise. Moreover, the above-mentioned deteriorations are negligible as compared to those observed for the series-parallel scheme, thus confirming the robustness of the parallel scheme with respect to measurement noise.

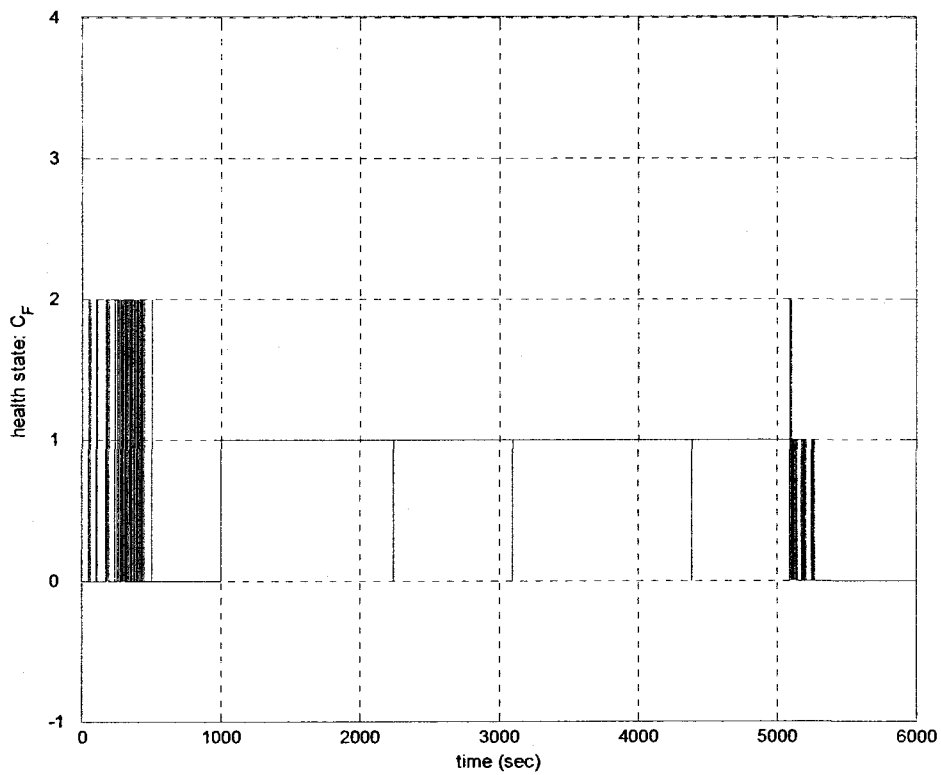


Figure 5-71. The health state of the RW using the parallel FDI scheme in presence of a sequence of *low-severity* bus voltage faults over the time period $t \in [1000 \ 5100]$ sec., subject to *high* noise level (Current SNR=44.57 dB and Speed SNR=44.76 dB).

Figure 5-72 depicts the estimated versus actual values of the fault parameters under the “high” noise level. As can be observed from this figure, the increased level of noise has a

small impact on the bus voltage FP estimate, i.e. $\hat{\alpha}^1$. More specifically, comparing Figure 5-72 with Figure 5-60 reveals that transient period of the bus voltage FP estimate becomes slightly longer due to the increase of SNR with a factor of 1000.

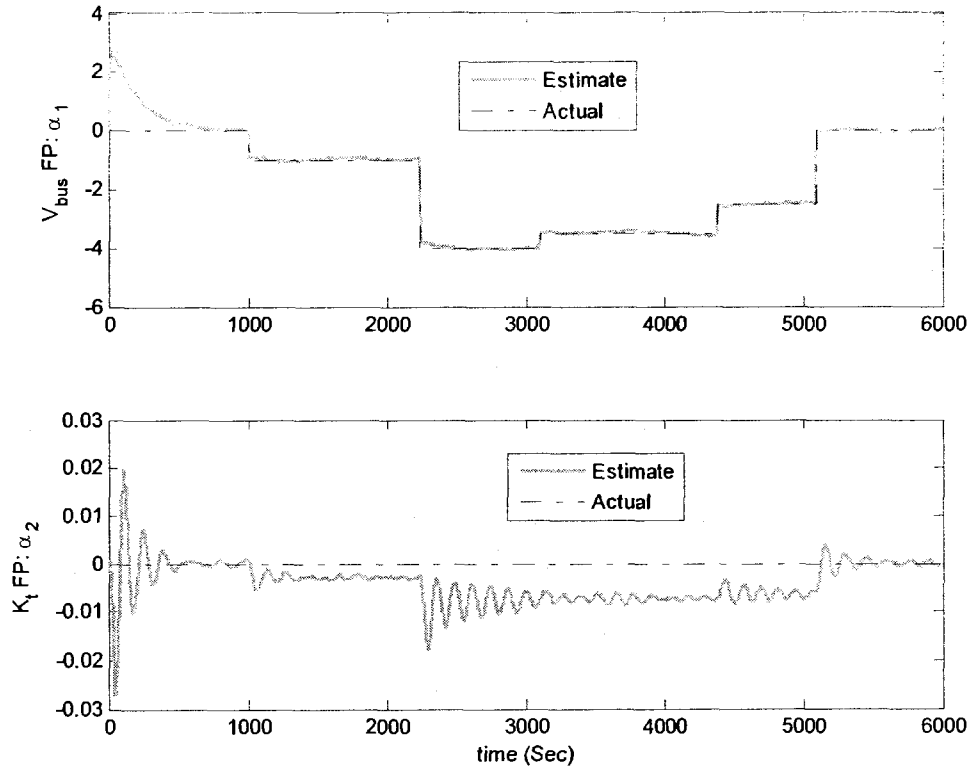


Figure 5-72. The estimated versus actual FPs using the parallel FDI in presence of a sequence of low-severity bus voltage faults over the time period $t \in [1000 \ 5100]$ sec., subject to high noise level (Current SNR=44.57 dB and Speed SNR=44.76 dB).

The three performance indices of fault identification, namely RMSE, ME, and STDE corresponding to the bus voltage FP estimate subject to various noise levels are compared in Table 5-23, Table 5-24, and Table 5-25, respectively. It can be clearly seen from the three tables that *no* significant increase has occurred in the order of the performance indices across all time periods even with the increase of the level of measurement noise with factors of 100 and 1000.

Table 5-23. Comparison of the RMSE of the bus voltage FP estimation using the parallel FDII scheme subject to various noise levels and in presence of a sequence of low-severity bus voltage faults.

Noise Level	Pre-fault period [0, 1000]s	1 st Faulty period [1000,2240]s	2 nd Faulty period [2240,3100]s	3 rd Faulty period [3100,4390]s	4 th Faulty period [4390,5100]s	Post-fault period [5100,6000]s
<i>Nominal</i>	0.1024	0.0346	0.0363	0.0401	0.0358	0.0406
<i>Medium</i>	0.0752	0.0586	0.0496	0.0253	0.0369	0.0256
<i>High</i>	0.0803	0.0586	0.0504	0.0489	0.0371	0.0361

Table 5-24. Comparison of the ME of the bus voltage FP estimation using the parallel FDII scheme subject to various noise levels and in presence of a sequence of low-severity bus voltage faults.

Noise Level	Pre-fault period [0, 1000]s	1 st Faulty period [1000,2240]s	2 nd Faulty period [2240,3100]s	3 rd Faulty period [3100,4390]s	4 th Faulty period [4390,5100]s	Post-fault period [5100,6000]s
<i>Nominal</i>	-0.0885	-0.0285	-0.0146	-0.0111	0.0210	0.0304
<i>Medium</i>	-0.0451	-0.0435	-0.0062	-0.0156	-0.0142	0.0140
<i>High</i>	-0.0689	-0.0376	3.62×10^{-4}	-0.0096	0.0058	-0.0112

Table 5-25. Comparison of the STDE of the bus voltage FP estimation using the parallel FDII scheme subject to various noise levels and in presence of a sequence of low-severity bus voltage faults.

Noise Level	Pre-fault period [0, 1000]s	1 st Faulty period [1000,2240]s	2 nd Faulty period [2240,3100]s	3 rd Faulty period [3100,4390]s	4 th Faulty period [4390,5100]s	Post-fault period [5100,6000]s
<i>Nominal</i>	0.0516	0.0196	0.0332	0.0385	0.0289	0.0268
<i>Medium</i>	0.0602	0.0392	0.0492	0.0199	0.0340	0.0215
<i>High</i>	0.0412	0.0450	0.0504	0.0479	0.0367	0.0343

Hence, it can be concluded that the performance of the parallel scheme in detection, isolation and identification of low-severity bus voltage faults is very robust to measurement noise.

5.5.4.3 FDII of High-Severity Bus Voltage Faults

In the following, the robustness of the parallel FDII scheme is analyzed in presence of the intermittent sequence of low-severity bus voltage faults given in equation (5-40), subject to A) *medium* level of measurement noise (i.e., SNR=53.66dB for the motor current and

SNR=53.72dB for the speed of the wheel), and B) *high* level of measurement noise (i.e., SNR=43.66dB for the motor current and SNR=43.72dB for the speed of the wheel).

A) Medium Level/Intensity of Measurement Noise (Current SNR = 53.66 dB and Speed SNR = 53.72 dB): The state estimates and the residuals corresponding to the NPEs for V_{bus} and K_t faults are shown in Figure C-22 and Figure C-23 of Appendix C, respectively. Needless to say, the residual thresholds of the parallel scheme remain as $\delta_i = \delta^1 = 8 \times 10^{-3}$ (A) for the current residual and $\delta_\omega = \delta^2 = 80$ (rpm) for the speed residual, as can be seen from Figure C-23.

Figure 5-73 depicts the health state of the reaction wheel in presence of the sequence of high-severity bus voltage faults – given in equation (5-41) – and subject to the “medium” noise level. As compared to the case of “nominal” noise level depicted in Figure 5-63Figure 5-59, minor deteriorations can be observed in the FDI performance of the parallel scheme due to the “medium” noise level, including: (i) the duration of the *false alarms* in the “pre-fault” period due to the transients of the closed-loop ACS have been extended from 380 seconds (under the “nominal” noise level) to 411 seconds; (ii) the FDI delay has been very slightly increased from 8.5 seconds under the “nominal” noise level to 10 seconds under the “medium” noise level; and (iii) the *false alarms* in the “post-fault” period have been extended up to $t=5387$ second as compared to $t=5325$ second under the “nominal” noise level (i.e., 62 seconds extension in the period of *false alarms* after fault removal). Finally, it should be noted that the durations of the three missed alarms during the “faulty” period have remained precisely equal to those under the “nominal” noise level. One can clearly observe that the above-mentioned deteriorations are negligible as compared to those observed for the series-parallel scheme.

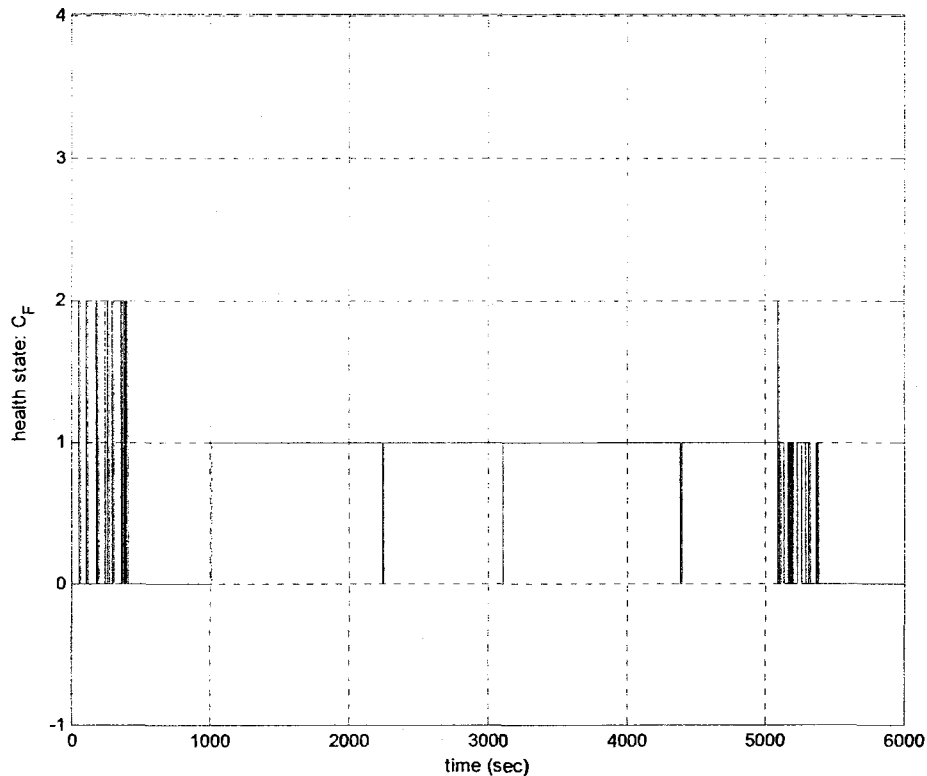


Figure 5-73. The health state of the RW using the parallel FDI scheme in presence of a sequence of *high-severity* bus voltage faults over the time period $t \in [1000 \ 5100]$ sec., subject to *medium* noise level (Current SNR=53.66 dB and Speed SNR=53.72 dB).

Figure 5-74 depicts the estimated versus actual values of the fault parameters under the “medium” noise level. Comparing Figure 5-74 with Figure 5-64 reveals that the bus voltage FP estimate remains practically unchanged even with the increase of SNR with a factor of 100.

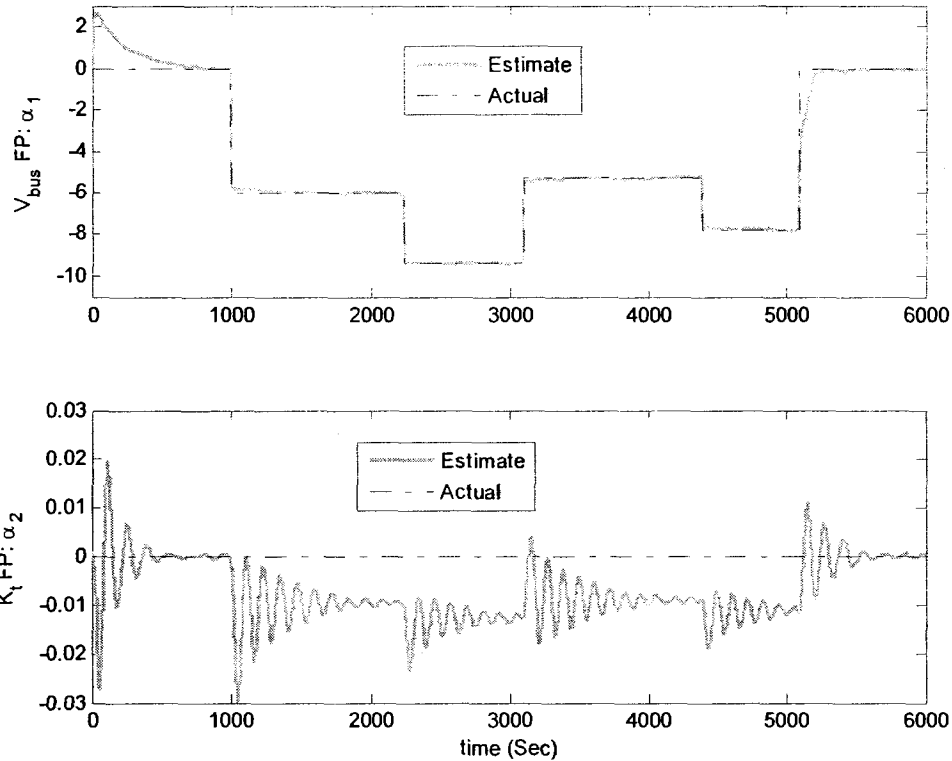


Figure 5-74. The estimated versus actual FPs using the parallel FDII in presence of a sequence of high-severity bus voltage faults over the time period $t \in [1000 \ 5100]$ sec., subject to medium noise level (Current SNR=53.66 dB and Speed SNR=53.72 dB).

B) High Level/Intensity of Measurement Noise (Current SNR = 43.66 dB and Speed SNR = 43.72 dB): The state estimates and the residuals corresponding to the NPEs for V_{bus} and K_t faults are shown in Figure C-24 and Figure C-25 of Appendix C, respectively. As was mentioned many times in the previous sections, the residual thresholds of the parallel scheme remain unchanged due to the robustness of the parallel scheme, and are thus equal to $\delta_t = \delta^1 = 0.025(A) = 25(mA)$ for the current residual and $\delta_\omega = \delta^2 = 200(rpm)$ for the speed residual, as can be observed from Figure C-25.

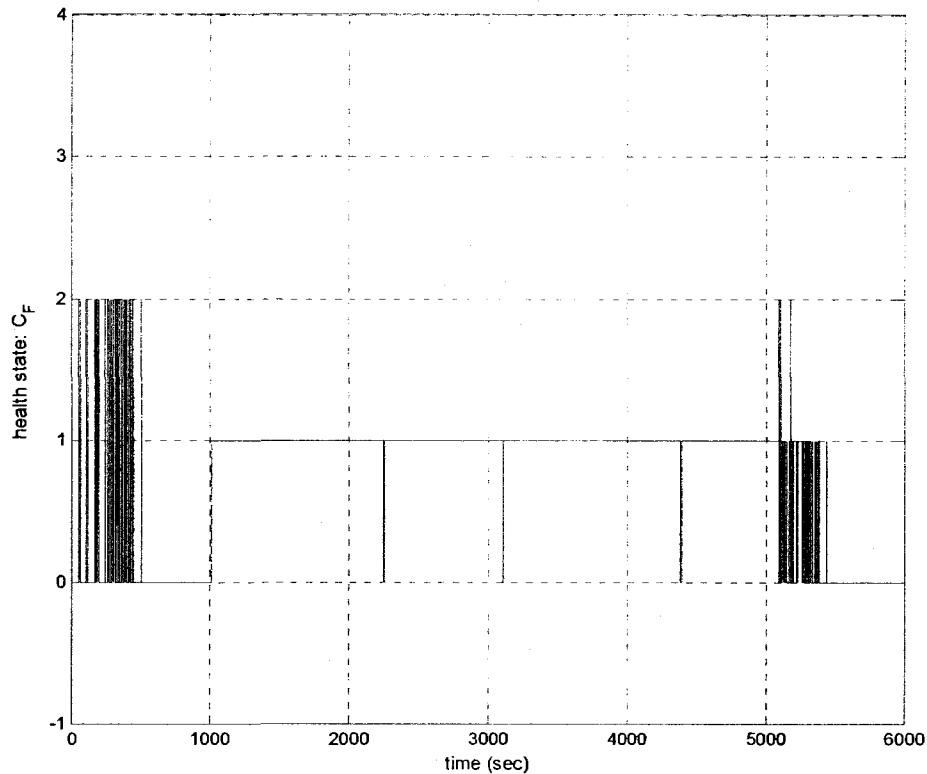


Figure 5-75. The health state of the RW using the parallel FDI scheme in presence of a sequence of high-severity bus voltage faults over the time period $t \in [1000 \ 5100]$ sec., subject to high noise level (Current SNR=43.66 dB and Speed SNR=43.72 dB).

Figure 5-75 depicts the health state of the reaction wheel in presence of the sequence of high-severity bus voltage faults – given in equation (5-41) – and subject to the “high” noise level. As compared to the case of “nominal” noise level depicted in Figure 5-63Figure 5-59, minor deteriorations can be observed in the FDI performance of the parallel scheme due to the increase of the noise level (or SNR) with a factor of 1000, including: (i) the duration of the *false alarms* in the “pre-fault” period due to the transients of the closed-loop ACS have been extended from 380 seconds (under the “nominal” noise level) to 455 seconds; (ii) the FDI delay has been slightly increased from 8.5 seconds under the “nominal” noise level to 12 seconds under the “high” noise level; (iii) the *false alarms* in the “post-fault” period have been extended up to $t=5400$ second

as compared to $t=5325$ second under the “nominal” noise level (i.e., 75 seconds extension in the period of *false alarms* after fault removal); and finally (iv) the durations of the three missed alarms during the “faulty” period have been slightly increased from 8, 8, and 7.5 seconds under the “nominal” noise level to 9, 10, and 9.5 seconds under the “high” noise level, respectively. One can clearly observe that the above-mentioned deteriorations are insignificant as compared to those observed for the series-parallel scheme and considering the increase of the SNR with a factor of 1000. Hence, the FDI performance of the parallel scheme is robust with respect to measurement noise.

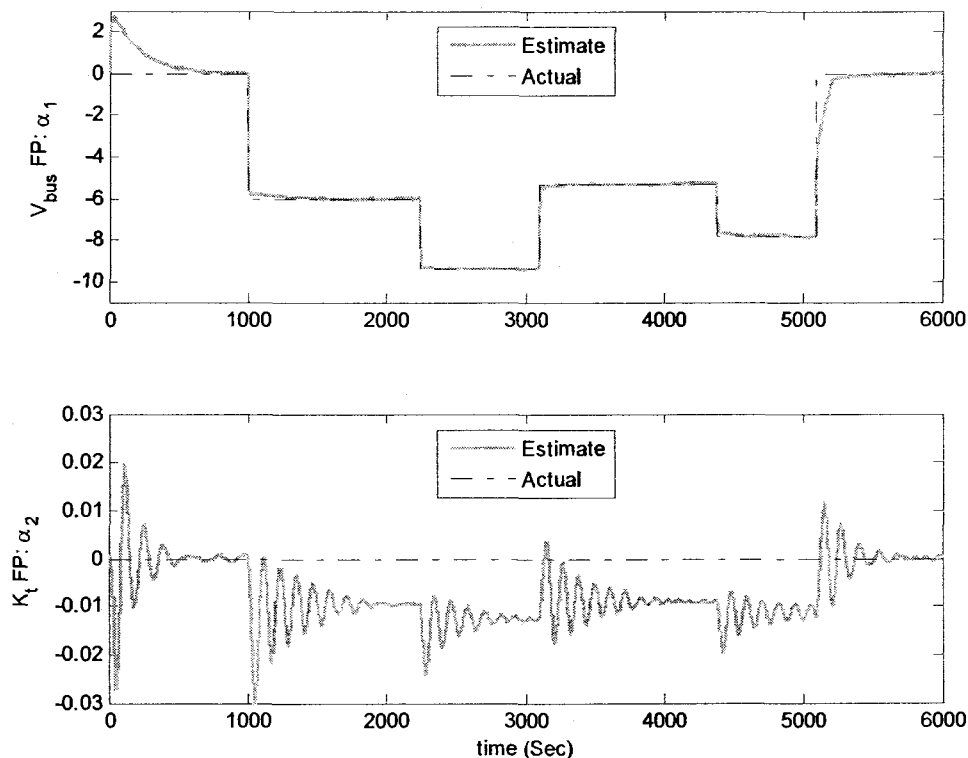


Figure 5-76. The estimated versus actual FPs using the parallel FDI in presence of a sequence of high-severity bus voltage faults over the time period $t \in [1000 \ 5100]$ sec., subject to high noise level (Current SNR=43.66 dB and Speed SNR=43.72 dB).

Figure 5-76 depicts the estimated versus actual values of the fault parameters under the “high” noise level. Comparing Figure 5-76 with Figure 5-64 reveals that the bus voltage

FP estimate remains practically unchanged, except for a very small increase of the transient period, even with the increase of SNR with a factor of 1000.

The three performance indices of fault identification, namely RMSE, ME, and STDE corresponding to the bus voltage FP estimate subject to various noise levels are compared in Table 5-26, Table 5-27, and Table 5-28Table 5-23, respectively. It can be clearly seen from the three tables that *no* significant increase has occurred in the order of the performance indices across all time periods even with the increase of the SNR with factors of 100 and 1000.

Table 5-26. Comparison of the RMSE of the bus voltage FP estimation using the parallel FDII scheme subject to various noise levels and in presence of a sequence of high-severity bus voltage faults.

Noise Level	Pre-fault period [0, 1000]s	1 st Faulty period [1000,2240]s	2 nd Faulty period [2240,3100]s	3 rd Faulty period [3100,4390]s	4 th Faulty period [4390,5100]s	Post-fault period [5100,6000]s
<i>Nominal</i>	0.1024	0.0831	0.0314	0.0462	0.0639	0.0532
<i>Medium</i>	0.0752	0.0710	0.0292	0.0573	0.0493	0.0757
<i>High</i>	0.0803	0.0664	0.0267	0.0459	0.0463	0.0528

Table 5-27. Comparison of the ME of the bus voltage FP estimation using the parallel FDII scheme subject to various noise levels and in presence of a sequence of high-severity bus voltage faults.

Noise Level	Pre-fault period [0, 1000]s	1 st Faulty period [1000,2240]s	2 nd Faulty period [2240,3100]s	3 rd Faulty period [3100,4390]s	4 th Faulty period [4390,5100]s	Post-fault period [5100,6000]s
<i>Nominal</i>	-0.0885	-0.0445	0.0177	-0.0142	-0.0611	0.0348
<i>Medium</i>	-0.0451	-0.0074	0.0114	0.0179	-0.0269	0.0680
<i>High</i>	-0.0689	-0.0280	-0.0034	0.0244	-0.0093	0.0327

Table 5-28. Comparison of the STDE of the bus voltage FP estimation using the parallel FDII scheme subject to various noise levels and in presence of a sequence of high-severity bus voltage faults.

Noise Level	Pre-fault period [0, 1000]s	1 st Faulty period [1000,2240]s	2 nd Faulty period [2240,3100]s	3 rd Faulty period [3100,4390]s	4 th Faulty period [4390,5100]s	Post-fault period [5100,6000]s
<i>Nominal</i>	0.0516	0.0701	0.0206	0.0440	0.0186	0.0401
<i>Medium</i>	0.0602	0.0706	0.0269	0.0545	0.0413	0.0334
<i>High</i>	0.0412	0.0602	0.0265	0.0388	0.0454	0.0415

Therefore, similar to the case of low-severity bus voltage faults, it can be concluded that the performance of the parallel scheme in detection, isolation and identification of high-severity bus voltage faults is robust to measurement noise.

5.6 Simulation Results for FDII with Partial-State Measurement

In this section, the performance of both series-parallel and parallel FDII schemes in diagnosing the motor current and bus voltage faults is evaluated under partial-state measurements of the reaction wheel. More precisely, it is assumed that only the speed of the wheel is measured by an appropriate sensor and the current must be estimated using the neural state estimator (NSE) presented in Chapter 4. This is a reasonable assumption, since current sensors are often more sensitive than speed sensors. Furthermore, current sensors are usually more prone to measurement inaccuracies and faults as compared to speed sensors. For instance, most current sensors maintain their specified precision over only a certain dynamic range of currents and their accuracy deteriorates beyond that range.

In the following, first the performance of the NSE (depicted in Figure 4-4) in estimating the motor current from speed measurements is assessed under healthy conditions of the reaction wheel. For the sake of completeness, the performance of the NSE under healthy conditions is evaluated at both low and high speeds of the wheel. Then, the state estimation performance of the NSE is evaluated in presence of faults in the reaction wheel in order to assess the fault tolerance capability of the NSE. The fault scenarios considered for this purpose are precisely the same as the motor current fault and the low-severity and high-severity bus voltage faults given in equations (5-39), (5-40) and (5-41), respectively. It is very important to note that the NSE used in the simulations consists of a one-hidden-layer feedforward neural network with one neuron in the input layer, four neurons in the hidden layer, and two neurons in the output layer. Sigmoidal activation functions are used for the neurons in the hidden layer, while linear neurons are

used in output layer. The parameters of the NSE are set to $\eta_w^{obs} = \eta_v^{obs} = 10^{-3}$ for the learning rates of the output and hidden layer weights, and the parameter β in equation (4-36) is set to 0.1.

Finally, the performance of the two proposed FDII schemes, namely the series-parallel and the parallel, are evaluated in presence of the same fault scenarios utilized under full-state measurements but this time using the estimate of the motor current (obtained from the NSE) instead of its measurement. In other words, the fault diagnosis performance of the integration of the *hybrid* NPEs and the FTO (i.e., the Kalman filter structure preserving NSE) depicted in Figure 4-1 and Figure 4-2 are assessed under partial-state measurements of the reaction wheel. The parameter values of the NPEs and the NSE used in the simulations are exactly the same as the values mentioned in above.

5.6.1 State Estimation under Healthy Conditions

As was mentioned in the above, the state estimation performance of the NSE under healthy conditions is evaluated at both low and high speeds of the wheel.

5.6.1.1 Three Satellite Slew Maneuvers at Low Speeds of the Wheel

First, the ability of the NSE in estimating the motor current of the reaction wheel using only speed measurement is assessed under healthy conditions at low speeds of the wheel (i.e., around 40 *rpm*) and subject to three slew-maneuvers of the satellite. As can be observed from Figure 5-77, both current and speed estimates very closely match their respective measurements. In particular, the current estimate quickly converges to its actual value even with a relatively large initial estimation error.

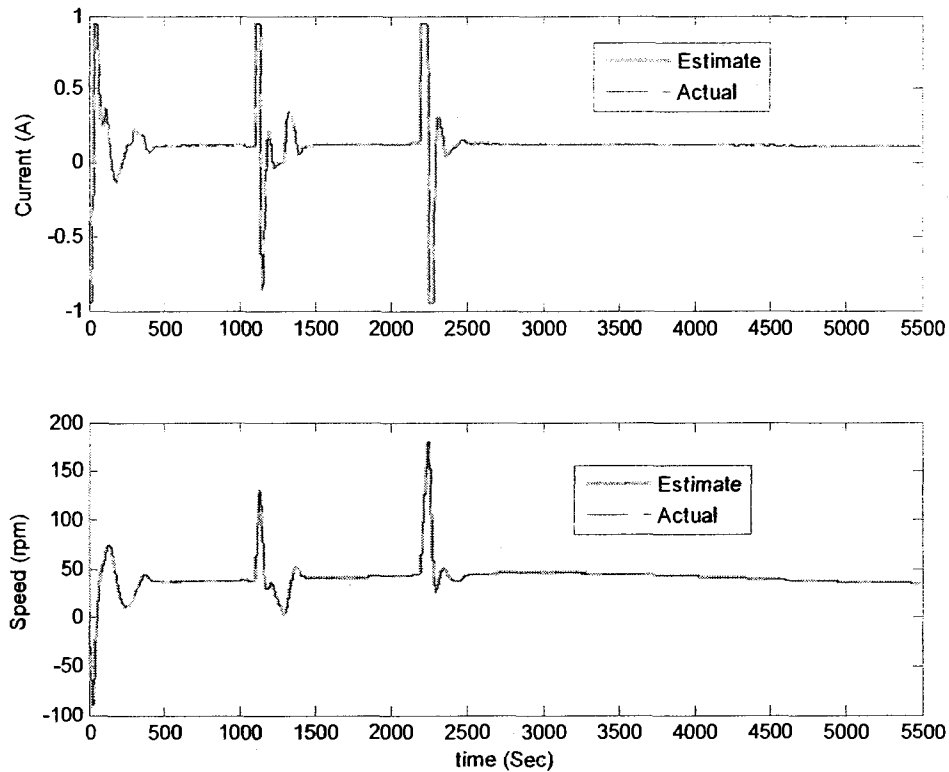


Figure 5-77. The current and speed estimates from the full-order FTO versus their actual values using only speed measurements subject to 3 satellite slew-manuevers at low speeds of the wheel.

Nevertheless, the initial current estimation error cannot be observed in Figure 5-77 due to the scales of the axes. In order to obtain a better view and more details of the situation, the graph of current estimate versus its actual value is separately zoomed in on the y -axis as well as the time axis (for the first 2 seconds of the simulation), as depicted in Figure 5-78. In the bottom graph of this figure, one can easily see the fast convergence rate of the current estimates even in presence of almost 0.3 (A) initial estimation error.

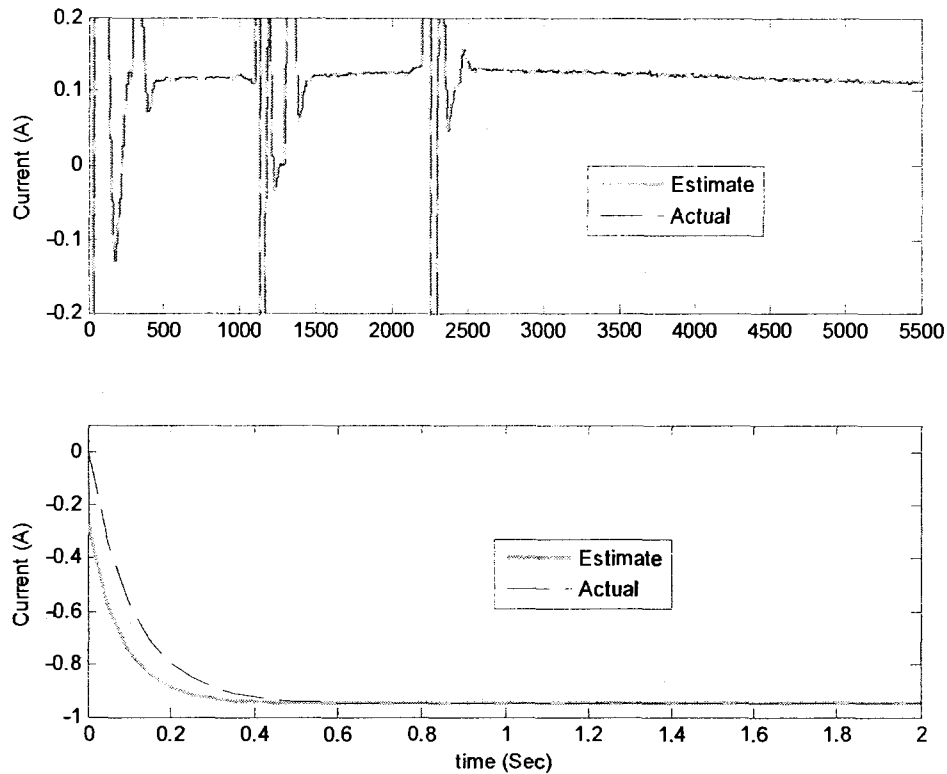


Figure 5-78. The current estimate from the full-order FTO versus its actual value using only speed measurements subject to 3 satellite slew-maneuvers at low speeds of the wheel; top figure: zoomed in on the y-axis, bottom figure: zoomed in on the time-axis for the first 2 seconds.

5.6.1.2 One Slew-Maneuver of the Satellite at High Speeds of the Wheel

In this section, the ability of the NSE in estimating the motor current is assessed under healthy conditions of the reaction wheel at high speeds of the wheel (i.e., around 570 rpm) and subject to one slew-maneuver of the satellite. As can be observed from Figure 5-79, both current and speed estimates very closely match their respective measurements.

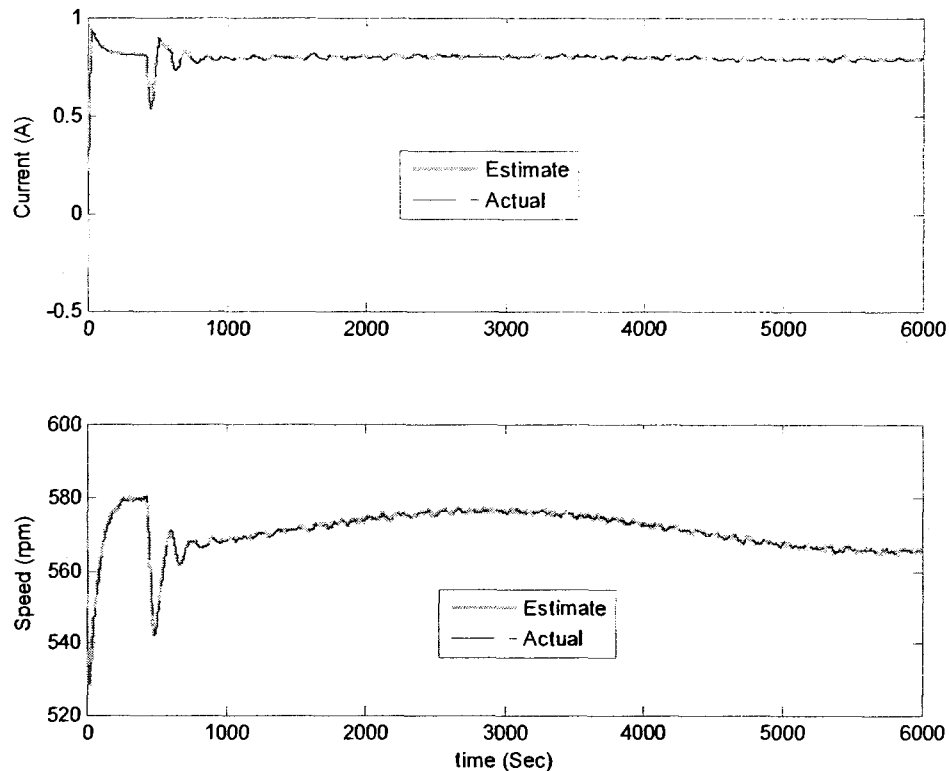


Figure 5-79. The current and speed estimates from the full-order FTO versus their actual values using only speed measurements subject to 1 slew-maneuver of the satellite at high speeds of the wheel.

In particular, the current estimate quickly converges to its actual value even with a relatively large initial estimation error. However, this convergence cannot be observed in Figure 5-79. Hence, similar to the previous case, the graph of the current estimate versus its actual value is zoomed in on both y-axis and time axis (for the first 3 seconds of the simulation), as depicted in Figure 5-80. It can be clearly observed in the bottom graph of this figure that the current estimate quickly converges to its actual value even in presence of approximately 0.3 (A) initial estimation error. In conclusion, under nominal healthy conditions, the Kalman filter structure preserving NSE is capable of precisely estimating the motor current of the reaction wheel from only speed measurements at both low and high speeds of the wheel.

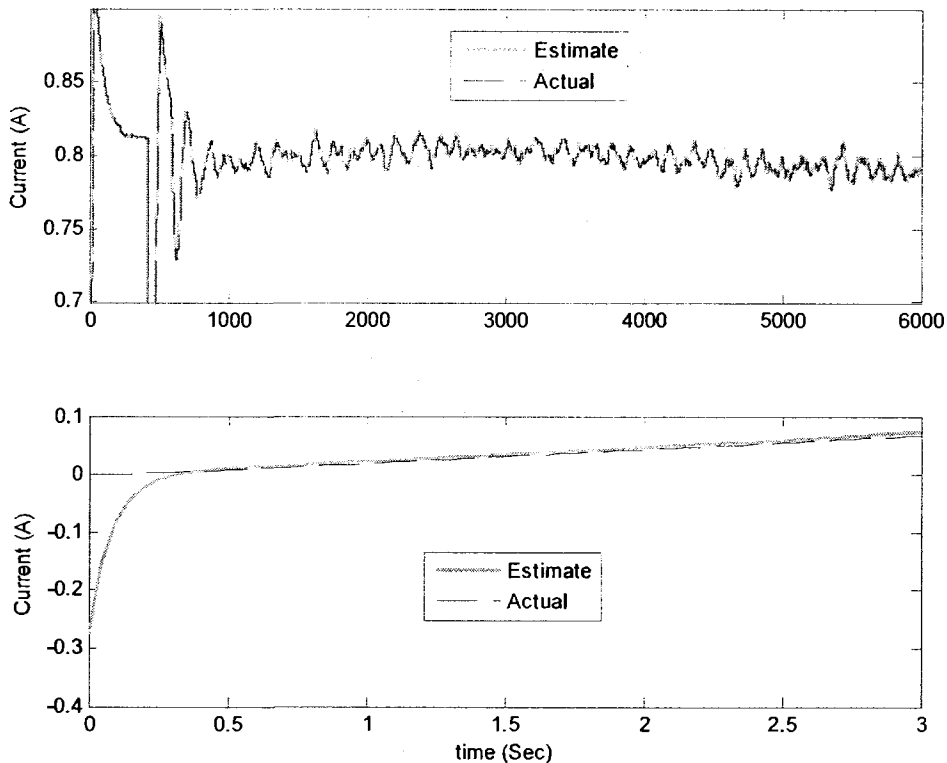


Figure 5-80. The current estimate from the full-order FTO versus its actual value using only speed measurements subject to 1 slew-maneuver of the satellite at high speeds of the wheel; top figure: zoomed in on the y-axis, bottom figure: zoomed in on the time-axis for the first 3 seconds.

5.6.2 State Estimation in Presence of Faults

The objective of this section is to evaluate the fault tolerance capability of the NSE. Therefore, the performance of the NSE in estimating the motor current is assessed in presence of faults in the motor current as well as the bus voltage of the reaction wheel. The fault scenarios considered include the motor current fault in equation (5-39), and the low-severity and high-severity bus voltage faults given in equations (5-40) and (5-41), respectively.

5.6.2.1 State Estimation in Presence of Motor Current Fault

First, the intermittent time-varying motor current fault given in equation (5-39) is injected into the reaction wheel and the NSE is used to estimate the motor current based on only

the speed measurements. Due to its special importance, only the the current estimate versus its actual value is depicted in Figure 5-81. The speed estimate versus its actual value is shown in Figure C-26 of Appendix C. It can be observed from Figure 5-81 that the current estimate very closely matches its actual value even in presence of the motor current fault over the time period $t \in [1000 \ 4250]$ second. Hence, the NSE is robust (or tolerant) to faults in the motor current.

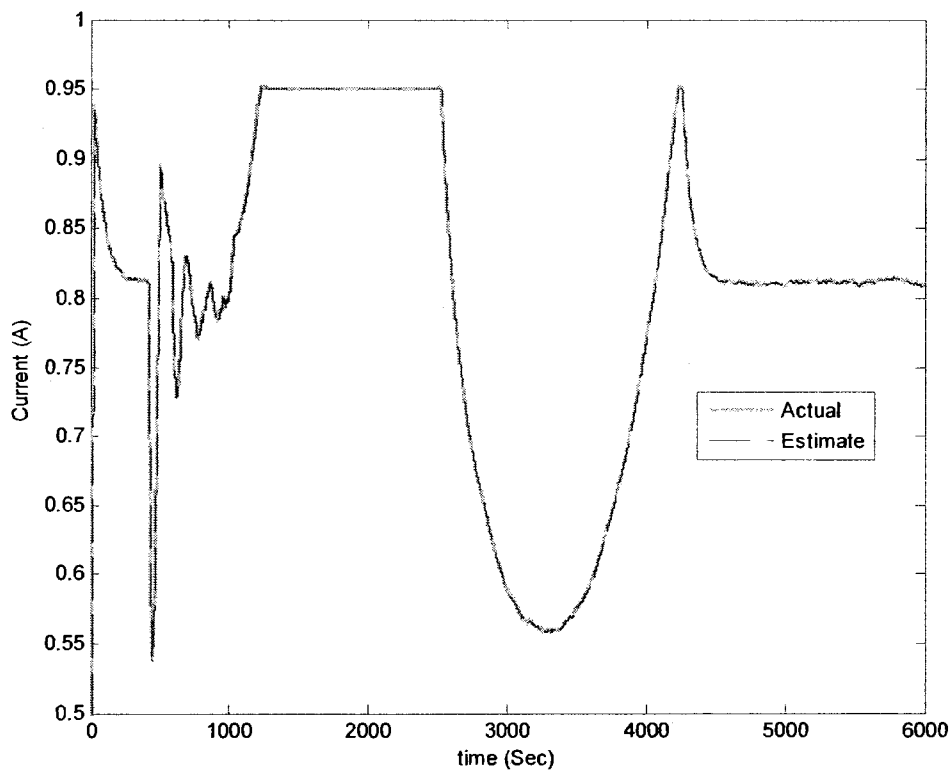


Figure 5-81. The current estimate from the full-order FTO versus its actual value using only speed measurements in presence of a time-varying fault in motor current over the time period of $t \in [1000 \ 4250]$ second.

5.6.2.2 State Estimation in Presence of Low-Severity Bus Voltage Faults

In this section, the intermittent sequence of low-severity bus voltage faults given in equation (5-40) is injected into the reaction wheel and the NSE is used to estimate the

motor current based on the speed measurements. The speed estimate versus its actual value is depicted in Figure C-27 of Appendix C. Moreover, the current estimate versus its actual value is shown in Figure 5-82.

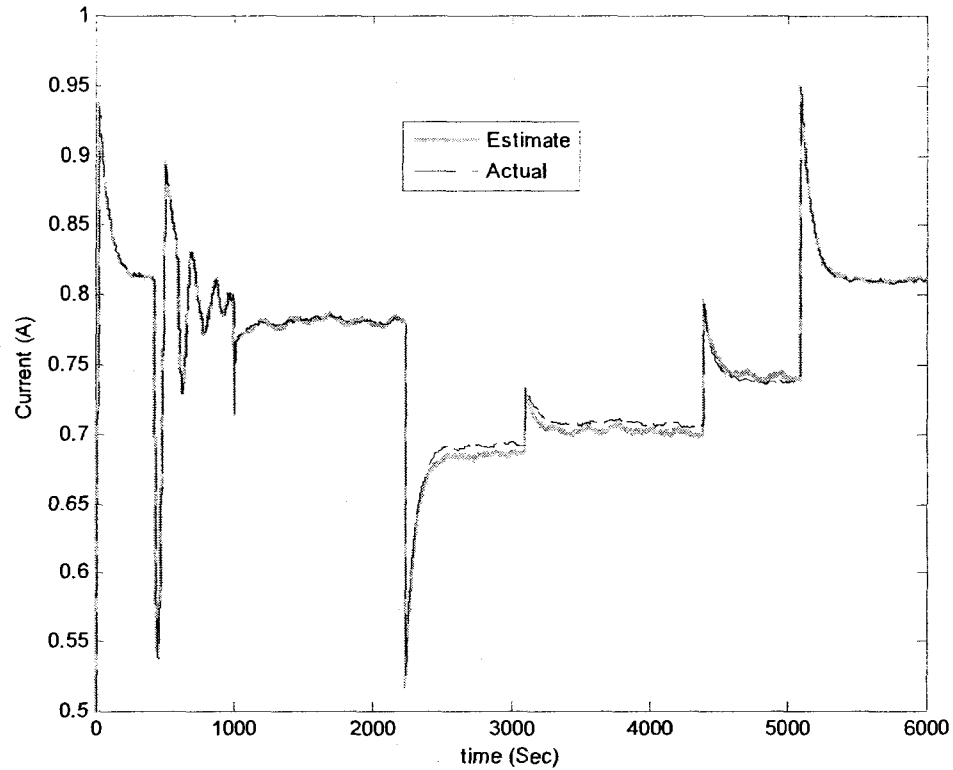


Figure 5-82. The current estimate from the full-order FTO versus its actual value using only speed measurements in presence of a sequence of low-severity bus voltage faults over the time period $t \in [1000 \ 5100]$ second.

It can be clearly seen from Figure 5-82 that as the severity of the bus voltage faults increases, the motor current estimates become less accurate. More specifically, the motor current estimates are more deviated from their actual values over the second and the third faulty periods (where the bus voltage drops are 4 and 3.5 Volts, respectively) as compared to the other two faulty periods (i.e., 1V drop in the first faulty period and 2.5V drop in the last faulty period) as well as the healthy period. Nevertheless, the current

estimates are yet accurate enough to be used as inputs to the FDII schemes without causing problems in fault diagnosis, as will be demonstrated later in the text.

5.6.2.3 Estimation in Presence of High-Severity Bus Voltage Faults

In this section, the intermittent sequence of high-severity bus voltage faults given in equation (5-41) is injected into the reaction wheel and the NSE is used to estimate the motor current based on the speed measurements. The speed estimate versus its actual value is depicted in Figure C-28 of Appendix C. Furthermore, the current estimate versus its actual value is shown in Figure 5-83.

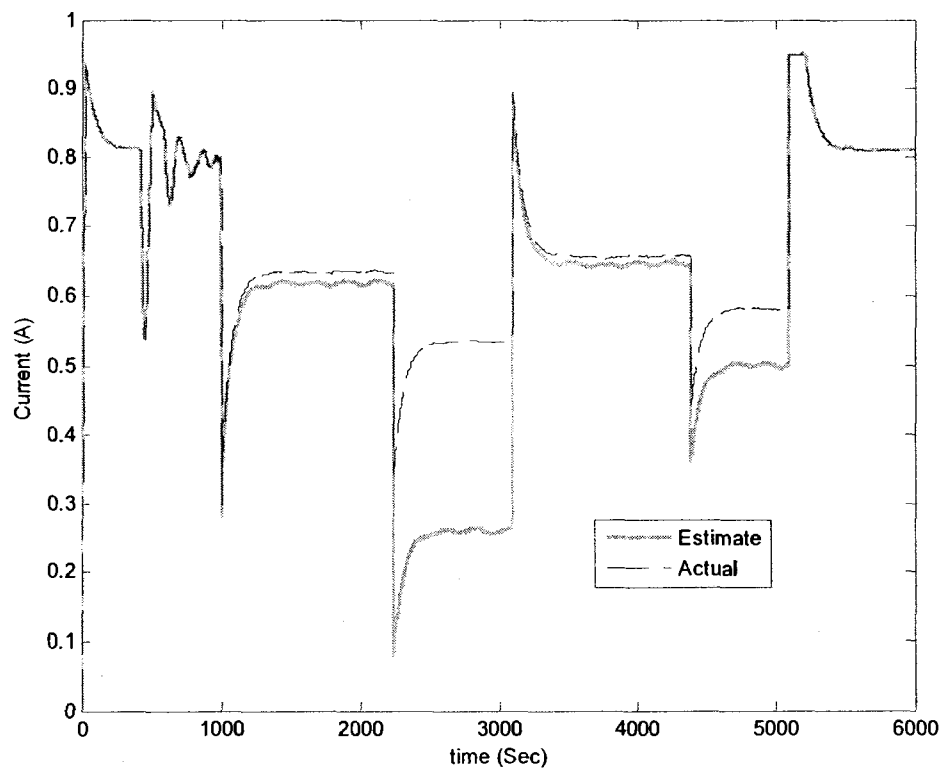


Figure 5-83. The current estimate from the full-order FTO versus its actual value using only speed measurements in presence of a sequence of high-severity bus voltage faults over the time period $t \in [1000 \ 5100]$ second.

Once again, it can be clearly observed from Figure 5-83 that under high-severity levels of the bus voltage fault, the NSE fails to accurately estimate the motor current. More specifically, in the second and the last faulty periods (corresponding to 9.4V and 7.8V drop in bus voltage, respectively), the current estimates are completely biased. Hence, it can be concluded that the NSE is robust (or tolerant) with respect to bus voltage faults only within a certain bound on the bus voltage fault severity. Based on the simulation results presented in above, this bound is within zero to 6V drop in the bus voltage. Therefore, presence of bus voltage faults with severity levels beyond 6V make the NSE unable to accurately estimate the reaction wheel current using only wheel speed measurements.

5.6.3 FDII Using Estimates of the Current from the NSE

In this section, the performance of the two proposed FDII schemes, namely the series-parallel and the parallel, are evaluated in presence of the three fault scenarios mentioned in above (and given in equations (5-39) to (5-41)) and based on only speed measurements. Hence, due to unavailability of current measurements, the estimate of the motor current obtained from the NSE is fed as an input to the FDII schemes. In the following, the performance of the proposed FDII schemes under partial-state measurements (i.e., only speed measurements from the reaction wheel) is evaluated separately in presence of each fault scenario. Furthermore, it should be noted that all the simulation results presented in the following are obtained under the “nominal” noise level.

5.6.3.1 FDII of Motor Current Faults Using the Series-Parallel Scheme

In this section, the results of FDII using the series-parallel scheme in presence of the intermittent time-varying motor current fault – given in equation (5-39) – under the partial-state measurements of the reaction wheel are presented. The results are obtained utilizing the speed measurements from the sensors and the motor current estimates from the NSE.

The residuals corresponding to the NPEs for V_{bus} and K_t fault is depicted in Figure C-29 of Appendix C. These residuals are obtained using equation (4-5) for the case of partial state measurements (i.e., the measurement of only the speed of the wheel). The residual thresholds are essentially the same as the ones used for the series-parallel scheme under the full-state measurement assumption and subject to the “nominal” noise level.

Figure 5-84 depicts the estimated value of the fault parameters, generated by the series-parallel scheme under partial-state measurements, versus their actual values. The FP thresholds are also set equal to the values of the FP thresholds utilized for the series-parallel scheme under the full-state measurement assumption. As compared to the result of full-state measurements depicted in Figure 5-27, one can easily observe that the performance of the series-parallel scheme in estimating the FPs has remained practically unchanged. This is mainly due to the fact that the NSE is robust (or tolerant) with respect to faults in the motor current.

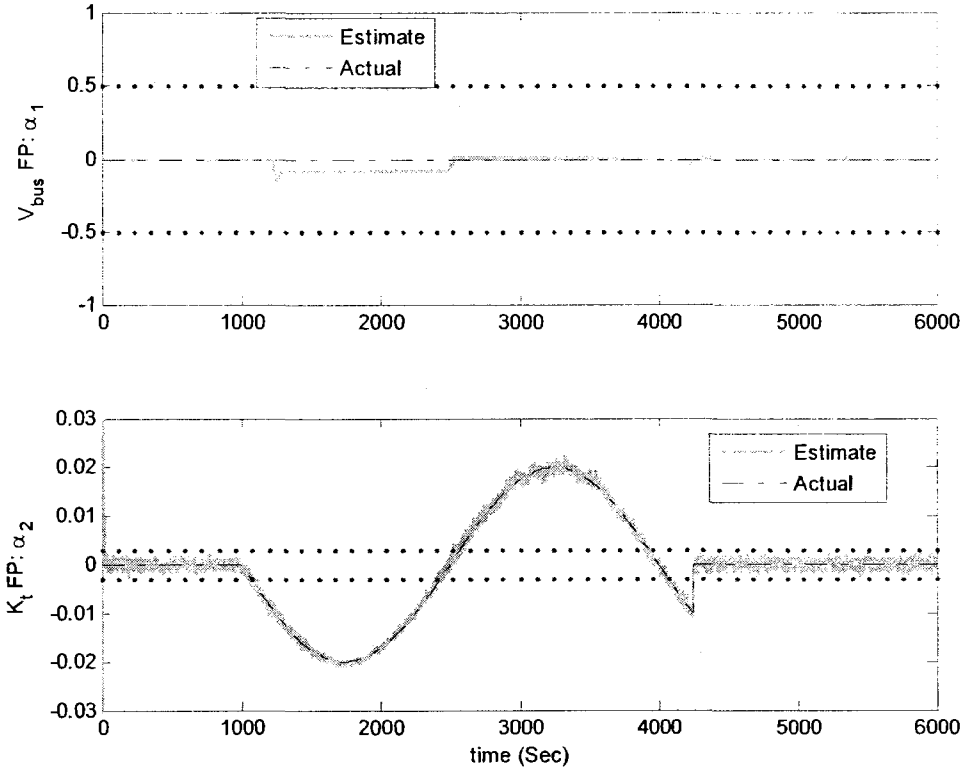


Figure 5-84. The estimated versus actual FPs using the series-parallel FDI scheme in presence of a time-varying fault in motor current over the time period $t \in [1000 \ 4250]$ second under partial-state measurements (i.e., measured speed and estimated current from the FTO).

Figure 5-85 depicts the health state of the reaction wheel under partial-state measurements. As compared to the similar result under full-state measurements depicted in Figure 5-28, the following observations can be made:

- (i) The fault diagnosis delay has been increased from 54.3 seconds under full-state measurements to 65 seconds under partial-state measurements.
- (ii) The time of persistently detecting the motor current fault removal (or disappearance) has been changed from $t=4237$ second under full-state measurements to $t=4245$ second under partial-state measurements.

(iii) The number of missed alarms has been slightly increased under full-state measurements. More precisely, a number of *new* missed alarms can be observed over the time periods $t \in [2408 \ 2580]$ sec. and $t \in [3900 \ 4080]$ sec.

Nevertheless, the above deteriorations in the FDI performance of the series-parallel scheme due to partial-state measurements are insignificant. Therefore, it can be concluded that the detection and isolation performance of the series-parallel scheme is practically unchanged under partial-state measurements.

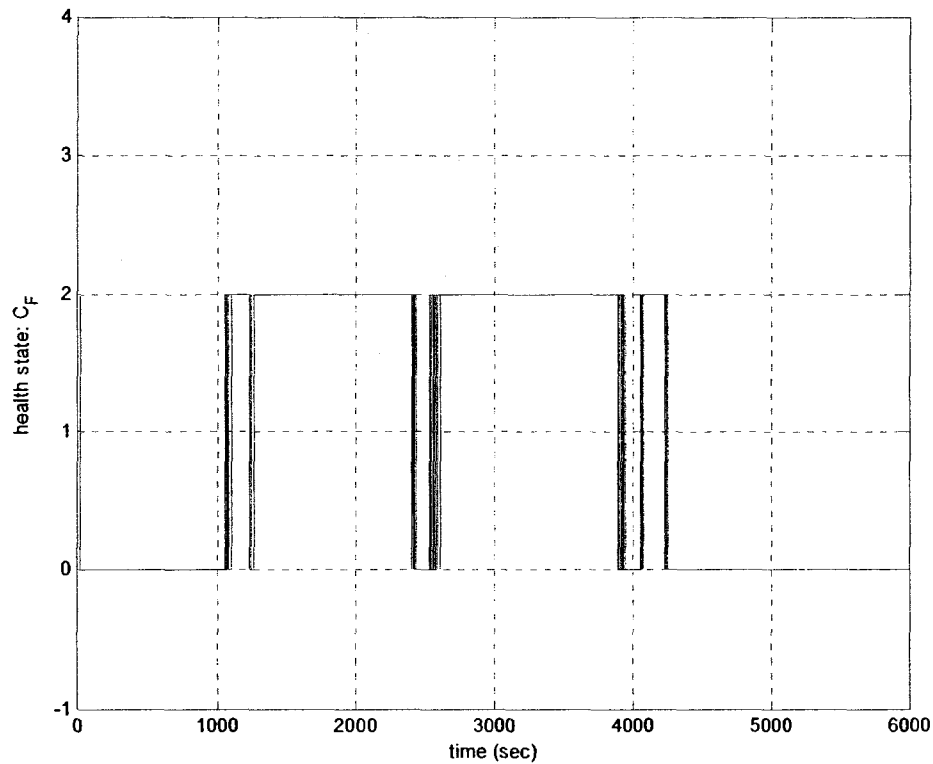


Figure 5-85. The health state of the RW using the series-parallel FDI scheme in presence of a time-varying fault in motor current over the time period of $t \in [1000 \ 4250]$ second under partial-state measurements (i.e., measured speed and estimated current from the FTO).

Finally, Table 5-29 shows the three performance indices of fault identification, namely RMSE, ME, and STDE, corresponding to the severity estimation of the motor current fault using the series-parallel scheme under partial-state measurements. As compared to

its counterpart under full-state measurements (i.e., Table 5-5), it can be easily concluded that the partial availability of the states has *not* significantly affected the fault identification performance of the series-parallel scheme across almost all time periods. The only exception includes the ME index over the “pre-fault” period, which has been increased by almost a factor of 3.1 under partial-state measurements.

Table 5-29. The performance indices of motor current fault identification using the series-parallel FDII scheme in presence of intermittent motor current fault and under partial-state measurements (i.e., measured speed and estimated current from the FTO).

	Pre-fault period $t \in [0 \ 1000] \text{sec}$	Faulty period $t \in [1000 \ 4250] \text{sec}$	Post-fault period $t \in [4250 \ 6000] \text{sec}$
RMSE	5.7919×10^{-4}	5.9243×10^{-4}	6.2504×10^{-4}
ME	1.0531×10^{-4}	9.6095×10^{-6}	7.8485×10^{-6}
STDE	5.6955×10^{-4}	5.9236×10^{-4}	6.2500×10^{-4}

Nonetheless, it can be concluded from the above results that the performance of the series-parallel scheme in conjunction with the NSE in diagnosing faults in the motor current under partial state measurements is very similar to that of the series-parallel scheme alone under full-state measurements. It should also be noted that this conclusion is valid for a relatively range of fault severities in the motor current.

5.6.3.2 FDII of Motor Current Faults Using the Parallel Scheme

In this section, the results of FDII using the parallel scheme in presence of the intermittent time-varying motor current fault – given in equation (5-39) – under the partial-state measurements of the reaction wheel are presented. The results are obtained utilizing the speed measurements from the sensors and the motor current estimates from the NSE.

The residuals corresponding to the NPEs for V_{bus} and K_t fault is depicted in Figure C-30 of Appendix C. These residuals are obtained using equation (4-5) for the case of

partial state measurements. The residual thresholds are essentially the same as the ones used for the parallel scheme under the full-state measurement assumption.

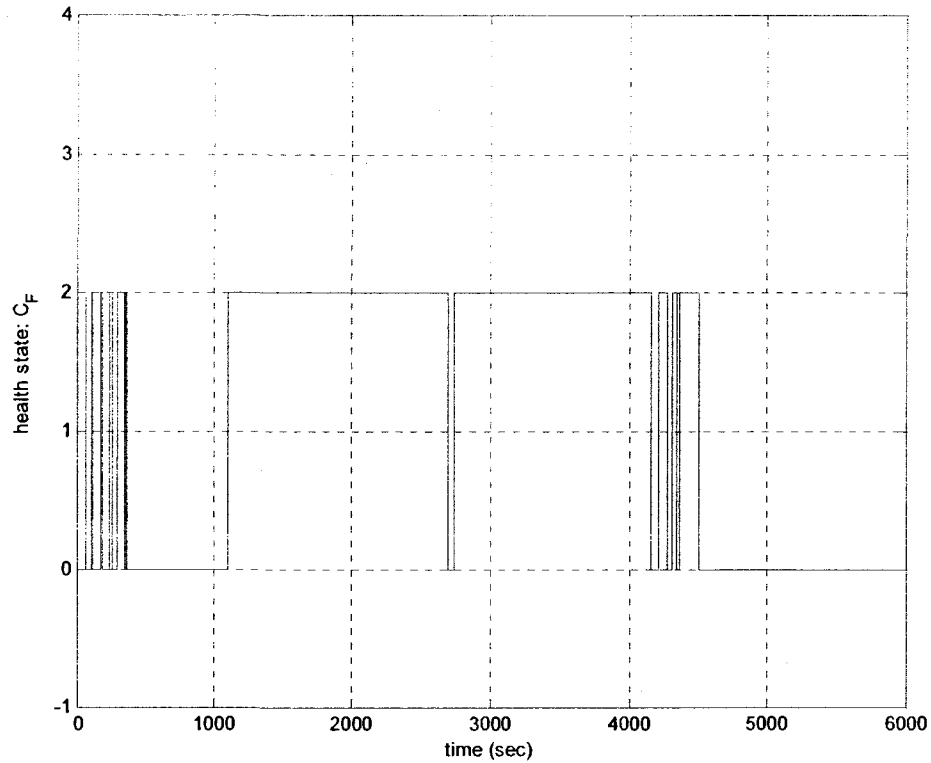


Figure 5-86. The health state of the RW using the parallel FDII scheme in presence of a time-varying fault in motor current over the time period of $t \in [1000 \ 4250]$ second under partial-state measurements (i.e., measured speed and estimated current from the FTO).

As was mentioned previously, the health state in the parallel scheme is obtained using only the residual signals and the FP estimates are needed only to identify the severity of a detected and isolated fault. Hence, the health state is depicted prior to the FP estimates in the parallel scheme. Figure 5-86 depicts the health state of the reaction wheel under partial-state measurements. As compared to the similar result under full-state measurements depicted in Figure 5-55, the following observations can be made:

- (i) Surprisingly, the fault diagnosis delay has been reduced from 108.2 seconds under full-state measurements to 105 seconds under partial-state measurements.

(ii) The time of persistently detecting the motor current fault removal (or disappearance) has been changed from $t=4499$ second under full-state measurements to $t=4507$ second under partial-state measurements.

(iii) Surprisingly, the duration of false alarms due to the transients of the closed-loop ACS has been reduced from 374 seconds under full-state measurements to 365 seconds under partial-state measurements.

Therefore, it can be clearly seen that the detection and isolation performance of the parallel scheme is *by no means* affected by the partial availability of states.

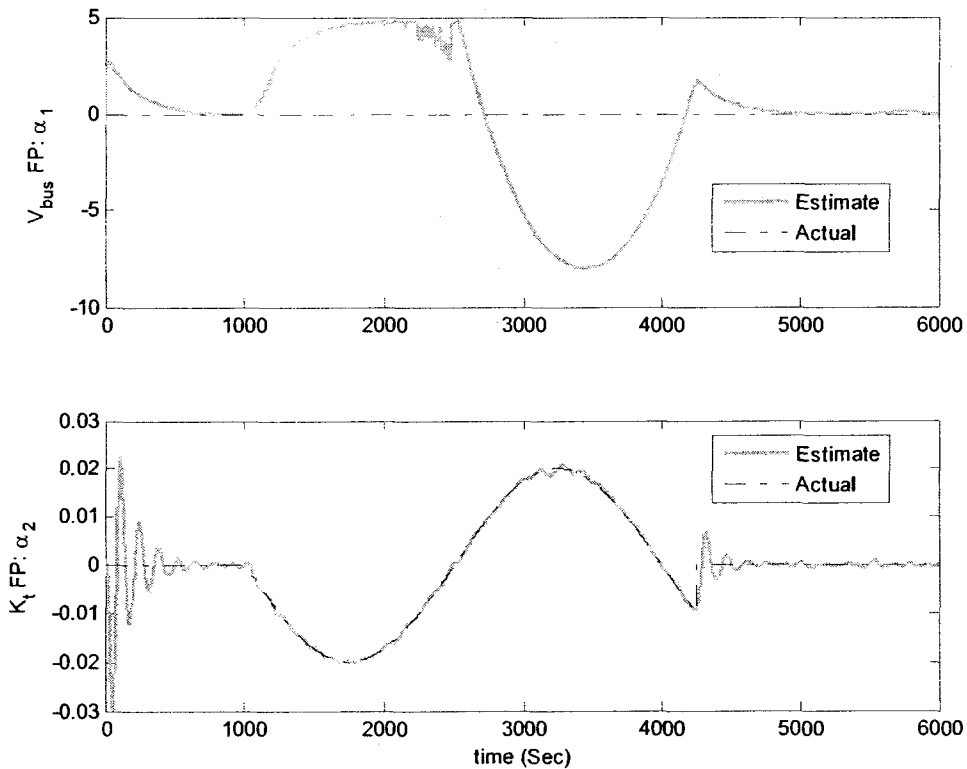


Figure 5-87. The estimated versus actual FPs using the parallel FDI scheme in presence of a time-varying fault in motor current over the time period $t \in [1000 \ 4250]$ second under partial-state measurements (i.e., measured speed and estimated current from the FTO).

Figure 5-87 depicts the estimated value of the fault parameters, generated by the parallel scheme under partial-state measurements, versus their actual values. As compared to the

result of full-state measurements depicted in Figure 5-56, one can easily observe that the performance of the series-parallel scheme in estimating the FPs has remained practically unchanged. This is mainly due to the fact that the NSE is robust (or tolerant) with respect to faults in the motor current.

Table 5-30. The performance indices of motor current fault identification using the parallel FDII scheme in presence of intermittent motor current fault and under partial-state measurements (i.e., measured speed and estimated current from the FTO).

	Pre-fault period $t \in [0 \ 1000] \text{sec}$	Faulty period $t \in [1000 \ 4250] \text{sec}$	Post-fault period $t \in [4250 \ 6000] \text{sec}$
RMSE	3.8713×10^{-4}	4.6638×10^{-4}	3.8081×10^{-4}
ME	1.0637×10^{-5}	-4.1341×10^{-5}	7.6425×10^{-5}
STDE	3.8701×10^{-4}	4.6455×10^{-4}	3.7307×10^{-4}

Finally, Figure 5-30 shows the three performance indices of fault identification, namely RMSE, ME, and STDE, corresponding to the identification of the motor current fault using the parallel scheme under partial-state measurements. As compared to its counterpart under full-state measurements (i.e., Table 5-17), it can be clearly seen that the partial availability of the states has a *very small* impact on the fault identification performance of the parallel scheme across all time periods.

5.6.3.3 FDII of Low-Severity Bus Voltage Faults Using the Series-Parallel Scheme

In this section, the results of FDII using the series-parallel scheme in presence of the intermittent sequence of low-severity bus voltage faults – given in equation (5-40) – under the partial-state measurements of the reaction wheel are presented. The results are obtained utilizing the speed measurements from the sensors and the motor current estimates from the NSE. The residuals corresponding to the NPEs for V_{bus} and K_t fault is

depicted in Figure C-31 and Figure C-32 of Appendix C. As was mentioned previously, these residuals are obtained using equation (4-5).

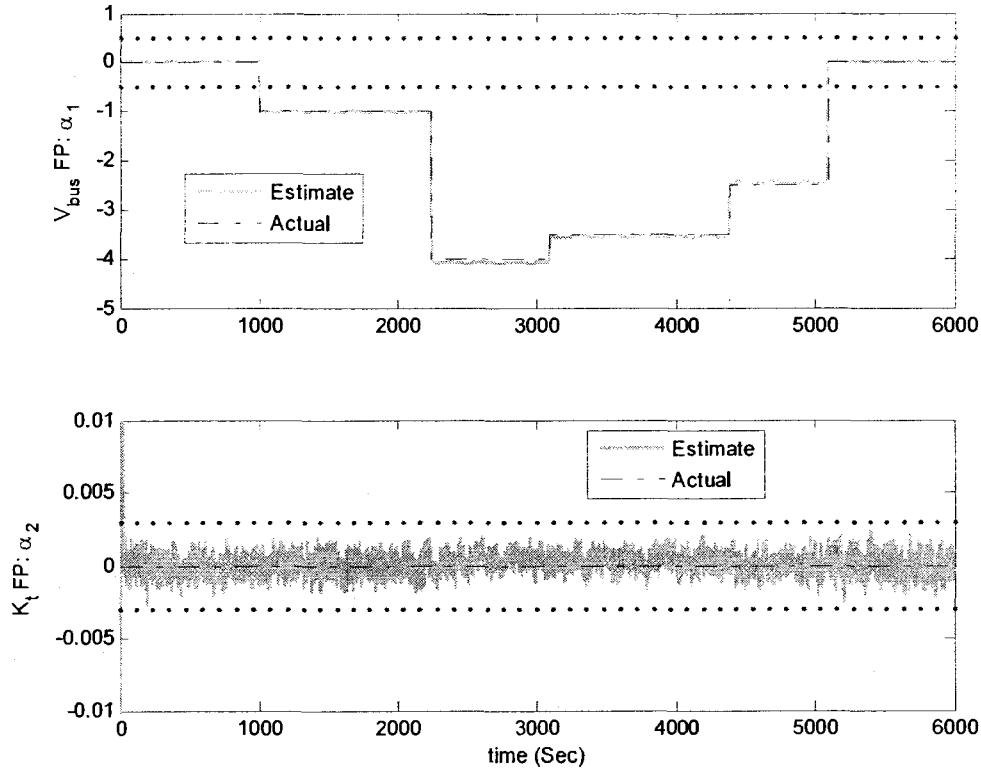


Figure 5-88. The estimated versus actual FPs using the series-parallel FDI scheme in presence of a sequence of low-severity bus voltage faults over the time period $t \in [1000 \ 5100]$ second under partial-state measurements (i.e., measured speed and estimated current from the FTO).

Figure 5-88 depicts the estimated fault parameters, generated by the series-parallel scheme under partial-state measurements, versus their actual values. As compared to the result of full-state measurements depicted in Figure 5-32, the performance of the series-parallel scheme in estimating the FPs is slightly deteriorated especially over the time periods with higher severity of the bus voltage fault. This is mainly due to the fact that the performance of the NSE in estimating the motor current deteriorates as the severity of the bus voltage fault increases.

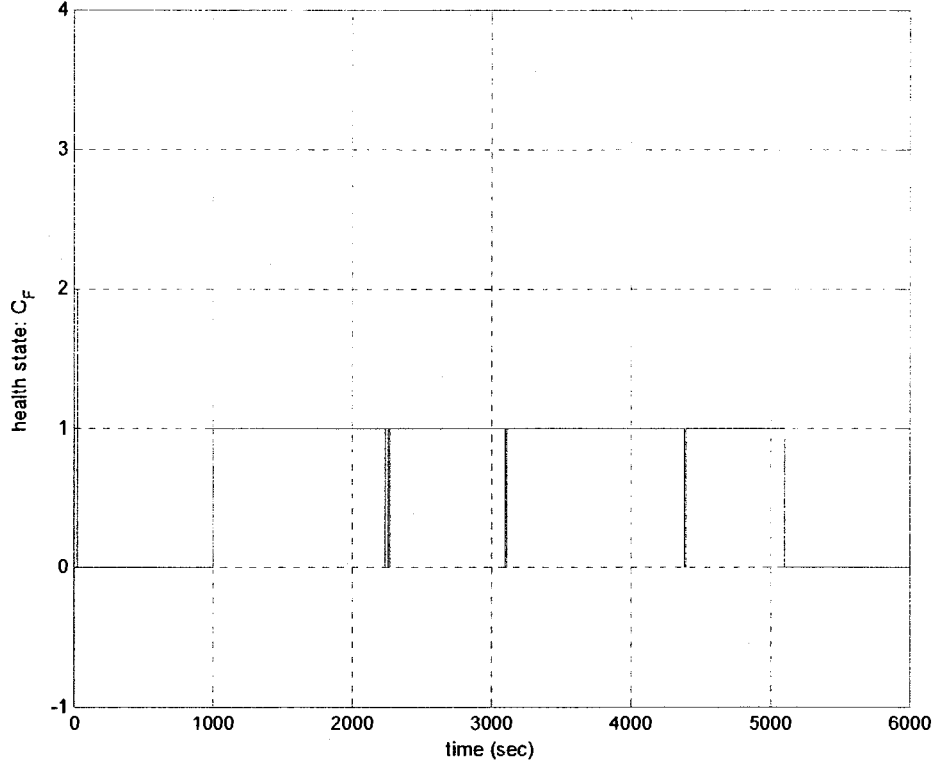


Figure 5-89. The health state of the RW using the series-parallel FDI scheme in presence of a sequence of low-severity bus voltage faults over the time period $t \in [1000 \ 5100]$ second under partial-state measurements (i.e., measured speed and estimated current from the FTO).

Figure 5-89 depicts the health state of the reaction wheel under partial-state measurements. As compared to the similar result under full-state measurements depicted in Figure 5-33, it can be clearly concluded that the detection and isolation performance of the series-parallel scheme is practically unchanged due to the partial availability of the states. The only deterioration in the performance of the series-parallel scheme is in the duration of the three missed alarms during the faulty period, which have been slightly increased from 21, 13.5, and 12 seconds under full-state measurements to 25, 15, and 15 seconds under partial-state measurements, respectively.

Table 5-31. The performance indices of fault identification using the series-parallel FDI scheme in presence of low-severity bus voltage fault and under partial-state measurements (i.e., measured speed and estimated current from the FTO).

	Pre-fault period [0, 1000]s	1 st Faulty period [1000,2240]s	2 nd Faulty period [2240,3100]s	3 rd Faulty period [3100,4390]s	4 th Faulty period [4390,5100]s	Post-fault period [5100,6000]s
Actual V_{bus} drop	0	-1	-4	-3.5	-2.5	0
Average of estimated drop	-0.0018	-1.0108	-4.0813	-3.5621	-2.4623	-1.3808×10^{-4}
RMSE	0.0020	0.0178	0.0825	0.0637	0.0403	1.5463×10^{-4}
ME	0.0018	0.0108	0.0813	0.0621	-0.0377	-1.3808×10^{-4}
STDE	7.7438×10^{-4}	0.0141	0.0140	0.0141	0.0144	6.9597×10^{-5}

Finally, Table 5-31 shows the three performance indices of fault identification, namely RMSE, ME, and STDE, corresponding to the estimation of the bus voltage fault severity using the series-parallel scheme under partial-state measurements. As compared to its counterpart under full-state measurements (i.e., Table 5-6), it can be clearly seen that the partial availability of the states has slightly affected the identification performance of the series-parallel scheme across almost all time periods, especially over the second, the third, and the fourth faulty periods, where the severity of the bus voltage fault is relatively high. It is important to note that over the healthy periods (i.e., the “pre-fault” and the “post-fault” periods) as well as the first faulty period with low-severity bus voltage fault, the identification performance of the series-parallel scheme has not been deteriorated.

In conclusion, while the performance of the series-parallel scheme in detecting and isolating the low-severity bus voltage faults has not been practically affected due to partial availability of the states, the identification (or fault severity estimation) performance has been deteriorated especially over the faulty periods with higher bus voltage fault severities.

5.6.3.4 FDII of Low-Severity Bus Voltage Faults Using the Parallel Scheme

In this section, the results of FDII using the parallel scheme in presence of the intermittent sequence of low-severity bus voltage faults – given in equation (5-40) – under the partial-state measurements of the reaction wheel are presented. The results are obtained utilizing the speed measurements from the sensors and the motor current estimates from the NSE. The residuals corresponding to the NPEs for V_{bus} and K_t fault is depicted in Figure C-33 of Appendix C. As was mentioned previously, these residuals are obtained using equation (4-5).

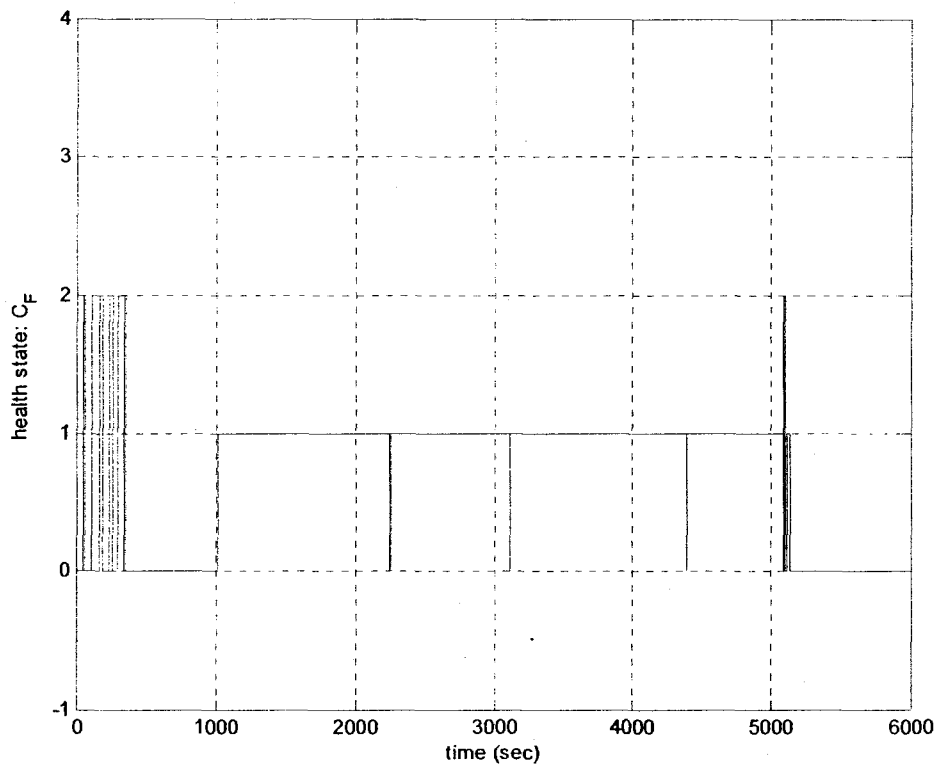


Figure 5-90. The health state of the RW using the parallel FDII scheme in presence of a sequence of low-severity bus voltage faults over the time period $t \in [1000 \ 5100]$ second under partial-state measurements (i.e., measured speed and estimated current from the FTO).

Figure 5-90 depicts the health state of the reaction wheel under partial-state measurements. As compared to the similar result under full-state measurements depicted in Figure 5-59, the following observations can be made:

- (i) Surprisingly, the fault diagnosis delay is very slightly decreased from 4.2 seconds under full-state measurements to 4 seconds under partial-state measurements.
- (ii) The time of persistently detecting the motor current fault removal (or disappearance) has been changed from $t=5146$ second under full-state measurements to $t=5142.5$ second under partial-state measurements.
- (iii) The duration of false alarms due to the transients of the closed-loop ACS has been reduced from 380.1 seconds under full-state measurements to 357 seconds under partial-state measurements.

Therefore, it can be clearly seen that the detection and isolation performance of the parallel scheme is even *very slightly* enhanced using the motor current estimates from the NSE rather than the actual measurements of the current. Nevertheless, this is not true for the fault identification performance of the parallel scheme, as can be observed from Figure 5-91. In this figure, the estimated value of the fault parameters, generated by the parallel scheme under partial-state measurements, is depicted versus their actual values. As compared to the result of full-state measurements depicted in Figure 5-60, one can easily observe that the identification performance of the parallel scheme is deteriorated especially over the time periods where the severity of the bus voltage fault is relatively high.

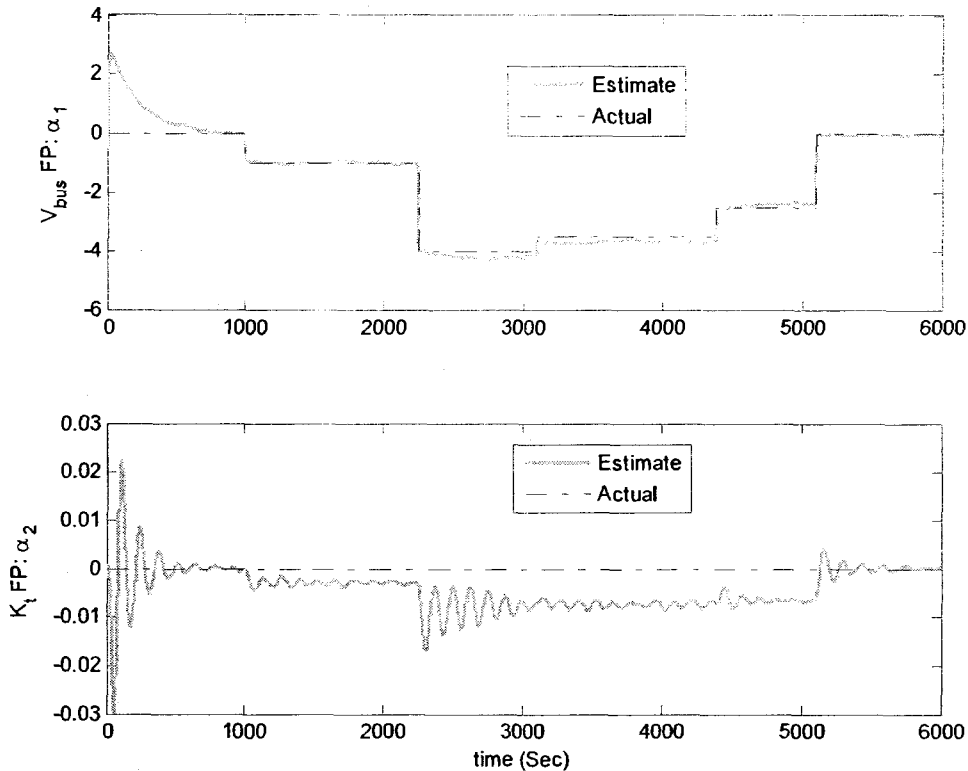


Figure 5-91. The estimated versus actual FPs using the parallel FDII scheme in presence of a sequence of low-severity bus voltage faults over the time period $t \in [1000 \ 5100]$ second under partial-state measurements (i.e., measured speed and estimated current from the FTO).

Table 5-32 shows the three performance indices of fault identification, namely RMSE, ME, and STDE, corresponding to the identification of the bus voltage fault severity using the parallel scheme under partial-state measurements. As compared to its counterpart under full-state measurements (i.e., Table 5-18), it can be clearly seen that the partial availability of the states has affected the identification performance of the parallel scheme across almost all time periods, especially over the second, the third, and the fourth faulty periods, where the severity of the bus voltage fault is relatively high.

In conclusion, similar to the series-parallel scheme, the performance of the parallel scheme in detecting and isolating the low-severity bus voltage faults has not been practically affected due to partial availability of the states; however, the identification (or

fault severity estimation) performance has been deteriorated especially over the faulty periods with higher bus voltage fault severities. For example, the fault severity over the second faulty period is estimated as 4.20V, while the actual drop of the bus voltage is 4V. It is important to note that the amount of the deterioration in fault identification of the parallel scheme is higher than that of the series-parallel scheme.

Table 5-32. The performance indices of fault identification using the parallel FDII scheme in presence of low-severity bus voltage fault and under partial-state measurements (i.e., measured speed and estimated current from the FTO).

	Pre-fault period [0, 1000]s	1 st Faulty period [1000,2240]s	2 nd Faulty period [2240,3100]s	3 rd Faulty period [3100,4390]s	4 th Faulty period [4390,5100]s	Post-fault period [5100,6000]s
Actual V_{bus} drop	0	-1	-4	-3.5	-2.5	0
Average of estimated drop	0.0672	-0.9892	-4.2020	-3.7045	-2.4302	-0.0320
RMSE	0.0949	0.0351	0.2117	0.2088	0.0936	0.0371
ME	-0.0672	-0.0181	0.2020	0.2045	-0.0698	0.0320
STDE	0.0670	0.0334	0.0635	0.0421	0.0624	0.0188

5.6.3.5 FDII of High-Severity Bus Voltage Faults Using the Series-Parallel Scheme

In this section, the results of FDII using the series-parallel scheme in presence of the intermittent sequence of high-severity bus voltage faults – given in equation (5-41) – under the partial-state measurements of the reaction wheel are presented. The results are obtained utilizing the speed measurements from the sensors and the motor current estimates from the NSE. The residuals corresponding to the NPEs for V_{bus} and K_t fault is depicted in Figure C-34 and Figure C-35 of Appendix C. Needless to say, these residuals are obtained using equation (4-5).

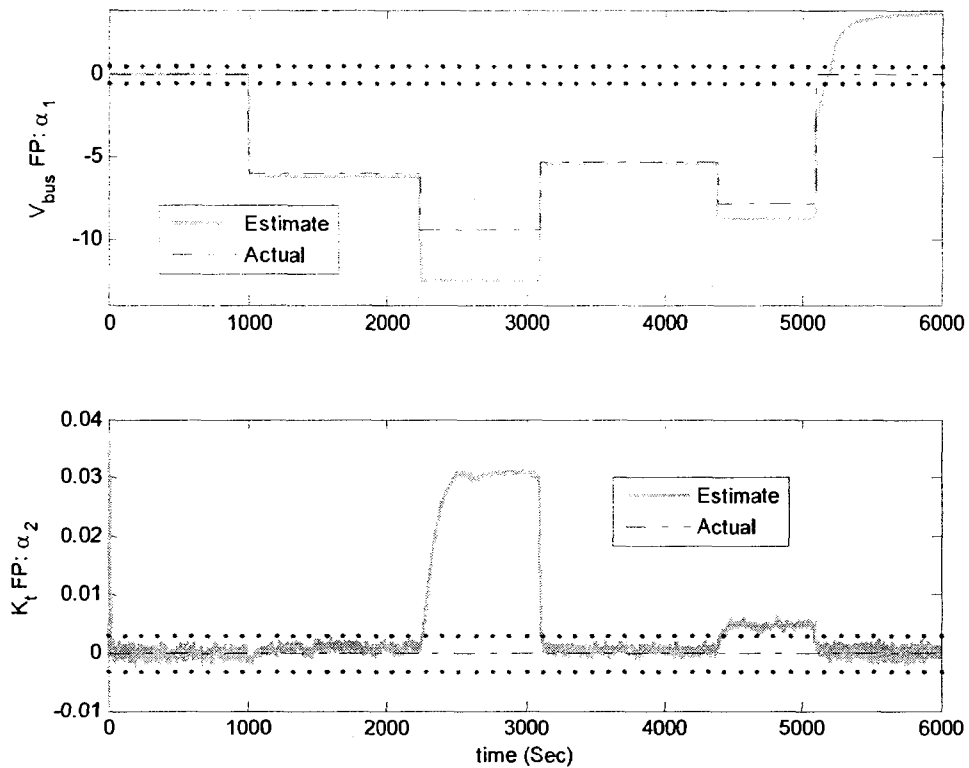


Figure 5-92. The estimated versus actual FPs using the series-parallel FDI scheme in presence of a sequence of high-severity bus voltage faults over the time period $t \in [1000 \ 5100]$ second under partial-state measurements (i.e., measured speed and estimated current from the FTO).

Figure 5-92 and Figure 5-93 respectively represent the estimated fault parameters and the health state of the reaction wheel, generated by the series-parallel scheme under partial-state measurements. As compared to the results of full-state measurements depicted in Figure 5-36 and Figure 5-37, the performance of the series-parallel scheme in both fault isolation and fault parameter estimation has been significantly deteriorated especially over the time periods with severities beyond 6V. More specifically, the number of short-duration missed alarms has been clearly increased especially over the third faulty period. Furthermore, even though the presence of the bus voltage fault has been correctly detected and isolated over the second faulty period (see Figure 5-93), the fault severity has been wrongly estimated as 12.54V while the actual value of the bus voltage drop is

9.4V, as can be seen from Table 5-33. This is equivalent to almost 33.5% error in fault identification (or severity estimation). Similarly, the bus voltage fault has been correctly detected and isolated over the fourth faulty period; however, while the actual value of the bus voltage drop is 7.8V the severity of the fault is estimated as 8.75V, which is equivalent to almost 12.25% error in fault identification. It is important to note that the performance deteriorations in the FDII of the high-severity bus voltage faults are due to the fact that the performance of the NSE in estimating the motor current from speed measurements significantly deteriorates as the severity of the bus voltage fault exceeds beyond 6V.

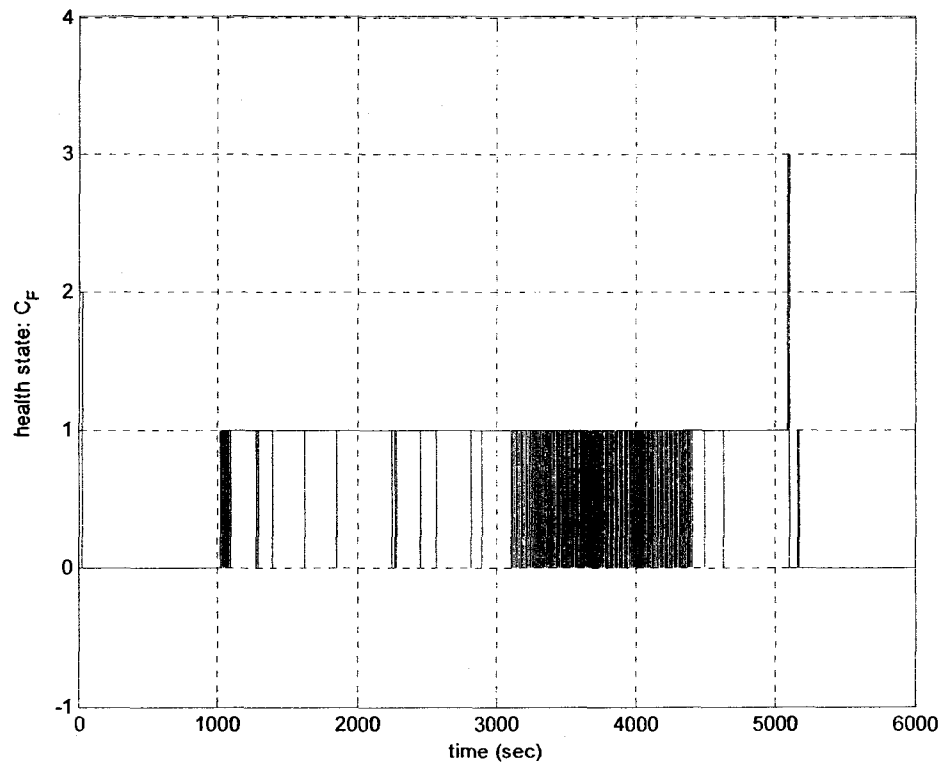


Figure 5-93. The health state of the RW using the series-parallel FDII scheme in presence of a sequence of high-severity bus voltage faults over the time period $t \in [1000 \ 5100]$ second under partial-state measurements (i.e., measured speed and estimated current from the FTO).

Table 5-33. The performance indices of fault identification using the series-parallel FDII scheme in presence of high-severity bus voltage fault and under partial-state measurements (i.e., measured speed and estimated current from the FTO).

	Pre-fault period [0, 1000]s	1 st Faulty period [1000,2240]s	2 nd Faulty period [2240,3100]s	3 rd Faulty period [3100,4390]s	4 th Faulty period [4390,5100]s	Post-fault period [5100,6000]s
Actual V_{bus} drop	0	-6	-9.4	-5.3	-7.8	0
Average of estimated drop	-0.0017	-6.1876	-12.5473	-5.4336	-8.7350	3.0516
RMSE	0.0018	0.1888	3.1474	0.1355	0.9352	3.2581
ME	0.0017	0.1876	3.1473	0.1336	0.9350	-3.0516
STDE	7.2735×10^{-4}	0.0208	0.0210	0.0222	0.0220	1.1416

In conclusion, the performance of the series-parallel scheme in FDII of high-severity bus voltage faults significantly deteriorates as the severity of the fault increases. It should also be noted that the deterioration in the performance is more significant for fault identification rather than fault detection and isolation (FDI).

5.6.3.6 FDII of High-Severity Bus Voltage Faults Using the Parallel Scheme

In this section, the results of FDII using the parallel scheme in presence of the intermittent sequence of high-severity bus voltage faults – given in equation (5-41) – under the partial-state measurements of the reaction wheel are presented. The results are obtained utilizing the speed measurements from the sensors and the motor current estimates from the NSE. The residuals corresponding to the NPEs for V_{bus} and K_t fault is depicted in Figure C-36 of Appendix C. Once again, the residuals are obtained using equation (4-5).

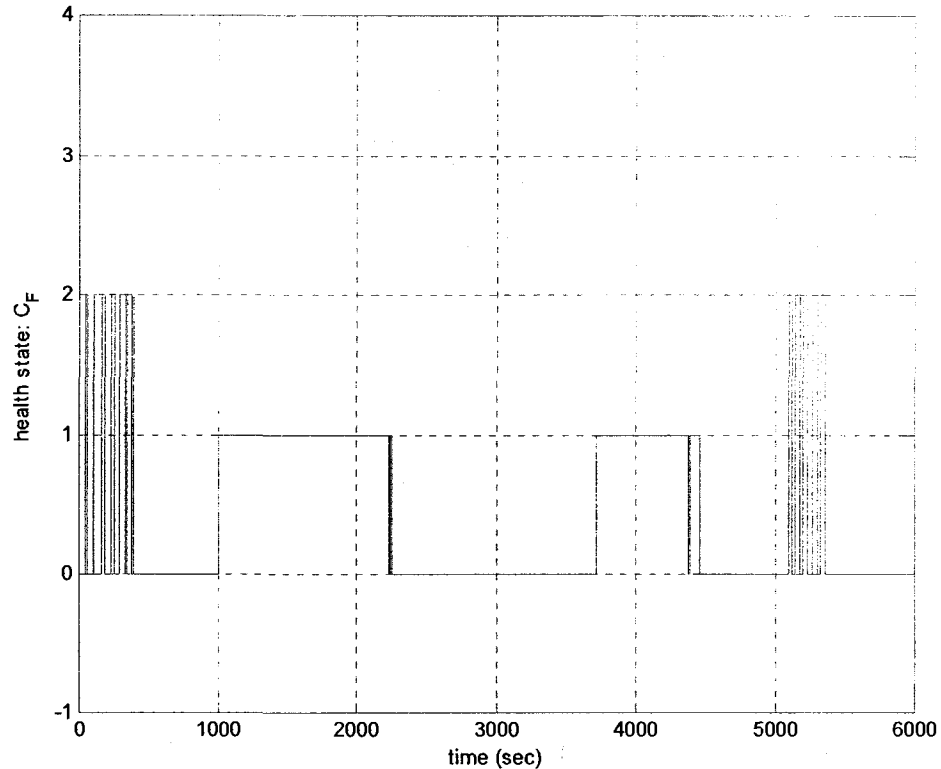


Figure 5-94. The health state of the RW using the parallel FDI scheme in presence of a sequence of high-severity bus voltage faults over the time period $t \in [1000 \ 5100]$ second under partial-state measurements (i.e., measured speed and estimated current from the FTO).

Figure 5-94 and Figure 5-95 respectively represent the health state of the reaction wheel and the estimated fault parameters versus their actual values, generated by the parallel scheme under partial-state measurements. As compared to the results of full-state measurements depicted in Figure 5-63 and Figure 5-64, the performance of the parallel scheme in both fault isolation and fault parameter estimation has been clearly deteriorated especially over the time periods with severities beyond 6V. More specifically, the following deteriorations are observed:

- (i) The duration of the false alarms due to the transients of the closed-loop ACS has been slightly increased from 380 seconds under full-state measurements to 390 seconds under partial-state measurements.

(ii) The fault diagnosis delay has been slightly increased from 8.5 seconds under full-state measurements to 12 seconds under partial-state measurements.

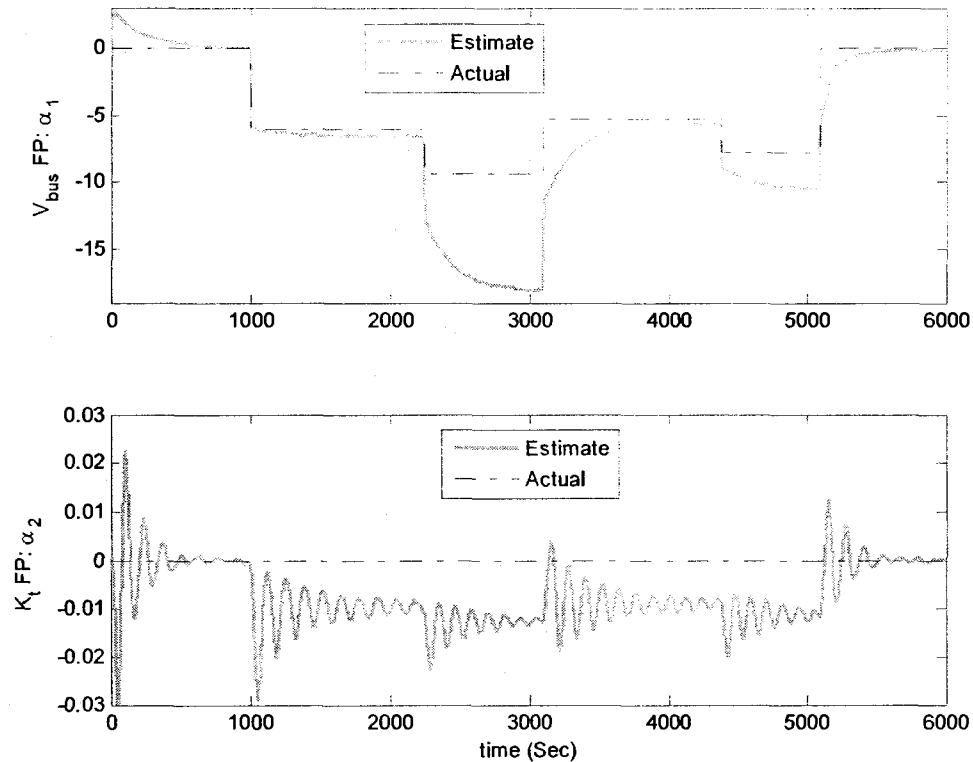


Figure 5-95. The estimated versus actual FPs using the parallel FDII scheme in presence of a sequence of high-severity bus voltage faults over the time period $t \in [1000 \ 5100]$ second under partial-state measurements (i.e., measured speed and estimated current from the FTO).

(iii) As far as the detection and isolation performance of the parallel scheme is concerned, the second faulty period is completely missed, as can be observed from Figure 5-94. Furthermore, the third faulty period is missed for the first 620 seconds (i.e., over the time period $t \in [3100 \ 3720]$ sec.) but is later correctly detected and isolated. Finally, the fourth faulty period is correctly detected and isolated for *only* the first 75 seconds and is then missed until the end of the faulty period (i.e., up to fault removal time). Hence, it can be concluded that the parallel scheme is indeed unable to detect and isolate high-severity bus voltage faults under partial-state measurements.

(iv) Since the high-severity bus voltage faults with severities beyond 6V are not detected and isolated, there is no point of discussing the impact of the partial availability of the states on the identification performance of the parallel scheme. Nonetheless, Table 5-34 shows the accuracy of fault identification based on the three performance indices, namely RMSE, ME, and STDE. It can be clearly observed from this table that over the second faulty period, the fault severity has been wrongly estimated as 17.06V while the actual value of the bus voltage drop is only 9.4V, which is almost equivalent to 81.5% error in fault identification (or severity estimation). Similarly, while the actual value of the bus voltage drop over the fourth faulty period is 7.8V, the severity of the fault is estimated as 10.12V, which is equivalent to almost 30% error in fault identification.

Table 5-34. The performance indices of fault identification using the parallel FDII scheme in presence of high-severity bus voltage fault and under partial-state measurements (i.e., measured speed and estimated current from the FTO).

	Pre-fault period [0, 1000]s	1 st Faulty period [1000,2240]s	2 nd Faulty period [2240,3100]s	3 rd Faulty period [3100,4390]s	4 th Faulty period [4390,5100]s	Post-fault period [5100,6000]s
Actual V_{bus} drop	0	-6	-9.4	-5.3	-7.8	0
Average of estimated drop	0.0794	-6.4739	-17.0594	-5.7759	-10.1156	-0.1469
RMSE	0.1084	0.4915	7.7383	0.4864	2.3450	0.1583
ME	-0.0794	0.4739	7.6594	0.4759	2.3156	0.1469
STDE	0.0738	0.1304	1.1024	0.1007	0.3704	0.0591

In conclusion, the performance of the parallel scheme in FDII of high-severity bus voltage faults drastically deteriorates as the severity of the fault increases. It is important to note that this deterioration in the FDII of high-severity bus voltage faults under partial state measurements is more significant in the parallel scheme than the series-parallel scheme.

5.7 Conclusions

In this chapter, the proposed FDII methodology was employed for fault diagnosis of reaction wheel actuators of the attitude control subsystem (ACS) of a 3-axis stabilized LEO satellite. To be able to properly verify and validate the effectiveness of the proposed FDII techniques, first a high-fidelity ACS simulator of a 3-axis stabilized satellite was developed. The ACS simulator consisted of the nonlinear model of the spacecraft attitude dynamics, a high-fidelity nonlinear model of reaction wheels, and the mathematical models of environmental disturbances acting upon the satellite. Furthermore, a decentralized PID control strategy was designed to stabilize the spacecraft attitude and thus provide the necessary framework for validating the FDII algorithm.

Following the convergence verification of the ACS for both attitude stabilization and slew manoeuvring, faults were characterized and then injected in one of the reaction wheels of the ACS – associated to the pitch axis. The faulty ACS system was simulated in order to generate faulty data of the closed-loop ACS. It was assumed that the reaction wheel actuators are prone to two different types of faults including faults in the bus voltage and faults in the motor current. Faults in the motor current were modeled and injected intermittently as time-varying variations in the reaction wheel's motor torque gain. The fault injection model used for motor current faults enabled us to assess the performance of the proposed FDII schemes in presence of a continuum of fault severities from very minor, incipient faults (due to, for instance, wear and tear of the motor) to up to 70% reduction in the motor torque gain. On the other hand, faults in the bus voltage were modeled and injected as a sequence of intermittent drops in the voltage of power bus. Both low-severity (or incipient) and high-severity faults were considered for the bus

voltage. Low-severity bus voltage faults correspond to drops in the voltage up to 4 Volts. The low-severity bus voltage faults do *not* de-stabilize the ACS system, however, they make the wheel operate at higher currents and thus increase power consumption by the reaction wheel. On the other hand, the high-severity bus voltage faults make the closed-loop ACS unstable and thus the satellite starts tumbling between $\pm 90^\circ$ once the severity of the bus voltage fault exceeds beyond 4 Volts.

Numerous simulation results were presented for evaluating the performance of the proposed fault diagnosis schemes in detecting, isolating, and identifying faults in the reaction wheels of the ACS and in presence of external disturbances and measurement noise. The simulation results demonstrated the effectiveness of the proposed fault diagnosis schemes. Numerous qualitative and quantitative observations were made in Chapter 5 regarding the performance capabilities of each FDII scheme. Furthermore, a comprehensive analysis was performed on the robustness of the two FDII schemes with respect to measurement noise. It was observed that the FDII performance of the *parallel* scheme is extremely robust to measurement noise, hence making it suitable for health monitoring of systems with even very noisy sensors (i.e., very low SNR). On the contrary, the series-parallel scheme was very sensitive to measurement noise. Instead, it displayed fast convergence rates and was very robust to closed-loop system transients. Hence, the series-parallel scheme is desirable for (high SNR) systems requiring very short delays in fault diagnosis and/or systems requiring frequent commanding. In practice, the choice of the appropriate FDII scheme is imposed by the specifications and the requirements of the specific problem at hand.

Finally, the performance of the FDII schemes under partial-state measurements was validated using simulations. It was assumed that only the speed of the wheel is measured and the motor current was estimated from the speed measurements using the neural state estimator (NSE). First, the performance of the NSE was verified under the nominal healthy conditions of the reaction wheel. More specifically, it was shown that the motor current estimates generated by the NSE very quickly converge to their actual values even in presence of a relatively large initial estimation error. Then, faults were injected into the reaction wheel and the performance of the NSE was evaluated over the faulty periods in order to verify the robustness (or tolerance) of the NSE with respect to faults. It was shown that the NSE is completely tolerant with respect to the motor current faults. However, the performance of the NSE deteriorates as the severity of the bus voltage faults increases. More precisely, it was concluded that the NSE is robust (or tolerant) to bus voltage faults with severities below 6V. Beyond that severity level, the motor current estimates start to significantly deviate from their actual values. Numerous observations and conclusions were made regarding the performance capabilities of the FDII schemes under partial-state measurements using the NSE for estimating the unmeasured state of the reaction wheel (i.e., the motor current). In summary, it was concluded that the performance of both FDII schemes remain practically unchanged in presence of both motor current faults (over a wide range of severities) and bus voltage faults with severities below 6V. However, the identification (or severity estimation) performance of the series-parallel scheme as well as the overall performance (i.e., including detection, isolation, and identification performance) of the parallel scheme significantly deteriorates as the severity of the bus voltage faults exceeds 6V.

Chapter 6:

6 Conclusions and Future Work

In this thesis, the problem of fault diagnosis in components and actuators of nonlinear systems was considered. A fault diagnosis system at its best must be able to not only detect the presence and isolate the location of faults in a system but also identify them (i.e., estimate their severities) once they are detected and isolated. Hence, a diagnostic system is also equivalently called a fault detection, isolation, and identification (FDII) system. While the importance of fault detection and isolation (FDI) is evident for health monitoring of engineering systems, the importance of fault identification has not been equally recognized in the literature. Consequently, fewer theoretical and practical contributions in the domain of fault identification or severity estimation exist in the literature, especially for nonlinear systems. However, it was shown in Chapter 1 that identification of fault severities is a cornerstone to fault prognosis and subsequently to develop a condition-based maintenance (CBM) system. Furthermore, it was shown that the accurate fault identification is an invaluable asset for fault tolerant control systems, in general, and is a necessity for implementing *active* fault accommodation and recovery procedures, in particular.

In view of these substantiations, and the ever-increasing demand for both autonomous fault tolerant control of safety-critical (and mission-critical) systems and CBM in especially mass-producing industries and OEMs, in this thesis a novel integrated *hybrid*

solution to the problem of fault diagnosis for components of nonlinear systems has been presented. Unlike most existing fault diagnosis techniques, the proposed solution is able to *simultaneously* detect, isolate, and identify the severity of faults in system components within a single unified diagnostic module. The developed FDII solution takes advantage of both *a priori* mathematical model information of the system and the adaptive nonlinear approximation capability of computational intelligence techniques especially neural networks. In Chapter 2, a comprehensive survey and analysis of the two major analytical redundancy-based approaches to fault diagnosis, namely the model-based and the computational intelligence (CI)-based approaches, was presented, which differ mainly in terms of the form of *a priori* knowledge or information being employed for diagnosis. Furthermore, some of the diagnostic methodologies were presented in order to describe as to how the three tasks of detection, isolation and identification are achieved within each framework. Once again, it should be noted that the FDII methodology that has been proposed in this thesis is an integrated *hybrid* approach that simultaneously exploits the benefits of both model-based and CI-based approaches.

In order to achieve fault identification, faults were modelled through parameterization of the nominal mathematical model of the system with a set of fault parameters (FPs), where each FP is an indication of a particular fault in the system. It was discussed, however, that such a *multi-parameter* fault model is not sufficient for fault isolation. Hence, to enable fault isolation a set of *single-parameter* fault models were extracted from the *multi-parameter* ones. Once the set of single-parameter fault models were derived, the problem of FDII in nonlinear systems was formulated as an on-line nonlinear parameter estimation problem with FPs as the *unknown* parameters to be estimated.

Various nonlinear parameter estimation methods were then reviewed in Chapter 3 and a solution based on neural networks was then proposed. The rationale for choosing neural networks for on-line nonlinear parameter estimation has been their universal function approximation capability and the availability of well-established and well-understood weight adaptation laws.

Therefore, the core of the proposed *hybrid* nonlinear FDII solution is a bank of adaptive neural parameter estimators (NPE), where each NPE in the bank was designed based on a separate single-parameter fault model. At each instant of time, the NPEs provide estimates of the *unknown* fault parameters (FP), which in conjunction with the output residuals determine the health state of the system being monitored. The residuals were defined as the difference between the actual measurements and the output estimates (or predictions) generated by the single-parameter fault models using their respective FP estimates from NPEs. It should be noted that the actual FP values are essentially *unknown*, so their estimates have to be used for predictions. The fault parameter estimation was based on on-line minimization of instantaneous output estimation error.

First, subject to the availability of full state measurements, two NPE structures, namely series-parallel and parallel, have been proposed and their respective FDI decision logics and weight update laws have been provided in Chapter 3. Each FDII scheme was shown to exhibit an exclusive set of desirable attributes. Furthermore, simple neural network architecture and straightforward weight adaptation laws make both proposed FDII schemes suitable for real-time implementation of on-line health monitoring systems. It should be noted that the robust parallel FDII scheme is a major contribution of this

thesis, being proposed for the first time in the literature. Furthermore, the novelty aspects of the series-parallel scheme have also been mentioned in Chapters 1 and 3.

In Chapter 4, the proposed FDII schemes were extended to systems with partial state measurement. The practical significance and motivations of such an extension were discussed in Chapter 4. The notion of fault tolerant observer (FTO) was introduced, which enables estimating the *unmeasured* states of the system even in presence of faults in the system. In other words, state estimates from an FTO are *robust* to faults. In order to systematically design an FTO, the literature on optimal filtering and state estimation was extensively reviewed and analyzed. Accordingly, a Kalman structure preserving neural state estimator (NSE) was designed and developed that adaptively estimates system states by constantly minimizing instantaneous observation error. The self-adapting and self-learning capability of neural networks has been exploited in the proposed NSE in order to achieve robustness with respect to faults. Due to presence of output feedback in the architecture of the NSE and on-line nature of the proposed FTO, the update laws were derived using the on-line recursive back-propagation algorithm. The details of the weight update laws have been provided in Chapter 4.

Finally, the proposed FDII methodology was employed for fault diagnosis of reaction wheel actuators of the attitude control subsystem (ACS) of a 3-axis stabilized LEO satellite. While taking the extremely important role of stabilizing the attitude of a satellite, reaction wheels are sensitive devices that are vulnerable to different sources of faults. Therefore, the existence of a reliable fault diagnosis system that constantly monitors the health state of these actuators is crucial especially for autonomous satellite operations. To be able to properly verify and validate the effectiveness of the proposed

FDII techniques, first a high-fidelity ACS simulator of a 3-axis stabilized satellite was developed. The ACS simulator consisted of the nonlinear model of the spacecraft attitude dynamics, a high-fidelity nonlinear model of reaction wheels, and the mathematical models of environmental disturbances acting upon the satellite. Furthermore, a decentralized PID control strategy was designed to stabilize the spacecraft attitude and thus provide the necessary framework for validating the FDII algorithm.

Following the convergence verification of the ACS for both attitude stabilization and slew manoeuvring, faults were characterized and then injected in one of the reaction wheels of the ACS – associated to the pitch axis. The faulty ACS system was simulated in order to generate faulty data of the closed-loop ACS. It was assumed that the reaction wheel actuators are prone to two different types of faults including faults in the bus voltage and faults in the motor current. Faults in the motor current were modeled and injected intermittently as time-varying variations in the reaction wheel's motor torque gain. The fault injection model used for motor current faults enabled us to assess the performance of the proposed FDII schemes in presence of a continuum of fault severities from very minor, incipient faults (due to, for instance, wear and tear of the motor) to up to 70% reduction in the motor torque gain. On the other hand, faults in the bus voltage were modeled and injected as a sequence of intermittent drops in the voltage of power bus. Both low-severity (or incipient) and high-severity faults were considered for the bus voltage.

Numerous simulation results were presented for evaluating the performance of the proposed fault diagnosis schemes in detecting, isolating, and identifying faults in the reaction wheels of the ACS and in presence of external disturbances and measurement

noise. The simulation results demonstrated the effectiveness of the proposed fault diagnosis schemes. Numerous qualitative and quantitative observations were made in Chapter 5 regarding the performance capabilities of each FDII scheme. Furthermore, a comprehensive analysis was performed on the robustness of the two FDII schemes with respect to measurement noise. It was observed that the FDII performance of the *parallel* scheme is extremely robust to measurement noise, hence making it suitable for health monitoring of systems with even very noisy sensors (i.e., very low SNR). On the contrary, the series-parallel scheme was very sensitive to measurement noise. Instead, it displayed fast convergence rates and was very robust to closed-loop system transients. Hence, the series-parallel scheme is desirable for (high SNR) systems requiring very short delays in fault diagnosis and/or systems requiring frequent commanding. In practice, the choice of the appropriate FDII scheme is imposed by the specifications and the requirements of the specific problem at hand.

Finally, the performance of the FDII schemes under partial-state measurements was validated using simulations. It was assumed that only the speed of the wheel is measured and the motor current was estimated from the speed measurements using the neural state estimator (NSE). First, the performance of the NSE was verified under the nominal healthy conditions of the reaction wheel. More specifically, it was shown that the motor current estimates generated by the NSE very quickly converge to their actual values even in presence of a relatively large initial estimation error. Then, faults were injected into the reaction wheel and the performance of the NSE was evaluated over the faulty periods in order to verify the robustness (or tolerance) of the NSE with respect to faults. It was shown that the NSE is completely tolerant with respect to the motor current faults.

However, the performance of the NSE deteriorates as the severity of the bus voltage faults increases. More precisely, it was concluded that the NSE is robust (or tolerant) to bus voltage faults with severities below 6V. Beyond that severity level, the motor current estimates start to significantly deviate from their actual values. Numerous observations and conclusions were made regarding the performance capabilities of the FDII schemes under partial-state measurements using the NSE for estimating the unmeasured state of the reaction wheel (i.e., the motor current). In summary, it was concluded that the performance of both FDII schemes remain practically unchanged in presence of both motor current faults (over a wide range of severities) and bus voltage faults with severities below 6V. However, the identification (or severity estimation) performance of the series-parallel scheme as well as the overall performance (i.e., including detection, isolation, and identification performance) of the parallel scheme significantly deteriorates as the severity of the bus voltage faults exceeds 6V.

A large number of potential future works can be envisaged for this thesis due to the widespread applicability of fault diagnosis, prognosis, and health management (DPHM) technologies across various science and engineering applications, in general, and the divers set of mathematical tools and methodologies employed in the design of proposed FDII approach, in particular. Nonetheless, the future research directions can basically be classified into two distinct categories: (i) future work with short to medium-term objectives and (ii) future work with medium to long-term objectives. In the following, we will discuss and investigate each category of future research directions separately:

(i) Future work with short to medium-term objectives: This future research direction aims at further enhancing the capabilities of the FDII methodology proposed in

this thesis. These enhancements may take place at various levels and from different perspectives. Some examples include:

- Extending the mathematical merit and rigour of the proposed FDII approach. More specifically, derivation of mathematical proofs and isolability conditions for the fault isolation decision logic of the two series-parallel and parallel FDII schemes. Furthermore, rigorous derivation of convergence proofs for fault parameter estimation can be envisaged as a future work, which is compounded due to nonlinearity of the problem, black-box nature of neural networks and the inherent coupling between estimation and adaptation of neural filters.
- Derivation of formal and analytical results/proofs for robustness of the parallel FDII scheme with respect to measurement noise,
- Extending the robustness of the proposed FDII to other sources of uncertainties, especially modeling errors.
- Derivation of a concrete mathematical proof for the convergence of the proposed FTO under certain severity levels of faults in the system,
- Enhance the capability of FDII under partial-state measurement. As was observed in the simulation results for fault diagnosis in reaction wheels, the proposed fault tolerant observer becomes less accurate under bus voltage faults, in general, and completely fails to correctly estimate system states in presence of high severity levels of bus voltage fault. So, enhancements are required to address these shortcomings. This can be accomplished in two ways: (i) by investigating the robustness of the proposed FTO to a general set of fault scenarios and to make it robust to higher levels of fault severities, and (ii) to collaboratively perform fault

tolerant state estimation in concurrence with fault parameter estimation. This idea is, in essence, very similar to the *dual estimation* problem (or *joint state and parameter* estimation problem) in the Kalman filtering literature (see Haykin [49]).

(ii) Future work with medium to long-term objectives: This future research direction aims at improving the technological merit of the proposed FDII methodology and bringing it to the next level of technological development, with the objective of addressing the ever-increasing demands of modern engineering systems. Examples of such technological shifts include:

- Fault prognosis,
- Condition-based maintenance (CBM),
- Active fault tolerant control,
- Fault diagnosis, recovery and accommodation

References

- [1] S. Simani, C. Fantuzzi, and R. J. Patton, *Model-based Fault Diagnosis in Dynamic Systems Using Identification Techniques*, London, Great Britain, Springer-Verlag, 2003.
- [2] G. G. Yen and L. W. Ho, "Online multiple model-based fault diagnosis and accommodation," *IEEE Transactions on Industrial Electronics*, vol. 50, no. 2, pp. 296-312, 2003.
- [3] G. Vachtsevanos, F. L. Lewis, M. Roemer, A. Hess, and B. Wu, *Intelligent Fault Diagnosis and Prognosis for Engineering Systems*. Hoboken, New Jersey: John Wiley & Sons Inc., 2006.
- [4] J. S. Mitchell, "Five to ten year vision for CBM, ATP Fall Meeting – Condition Based Maintenance Workshop," USA, Atlanta, GA, 1998.
- [5] S. K. Yang, "A condition-based failure-prediction and processing-scheme for preventive maintenance," *IEEE Trans. on Reliability*, vol. 52, no. 3, pp. 373-383, 2003.
- [6] S. Wu, N. Gebraeel, M. A. Lawley, and Y. Yih, "A neural network integrated decision support system for condition-based optimal predictive maintenance policy," *IEEE Trans. on Systems, Man and Cybernetics, Part A*, vol. 37, no. 2, pp. 226-236, 2007.
- [7] M. Bengtsson, "Condition based maintenance system technology – where is development heading?" in *Proceedings of the 17th European Maintenance Congress*, Barcelona, Spain, 2004.
- [8] M. G. Thurston, "An Open Standard for Web-Based Condition-Based Maintenance Systems", AUTOTESTCON Proceedings, pp. 401-415, Valley Forge, PA, 2001.
- [9] Web reference: <http://www.mimosa.org>
- [10] M. R. Maurya, R. Rengaswamy, and V. Venkatasubramanian, "Fault diagnosis using dynamic trend analysis: A review and recent developments," *Engineering Applications of Artificial Intelligence*, vol. 20, no. 2, pp. 133-146, 2007.
- [11] J.T. Cheung and G. Stephanopoulos, "Representation of process trends-Part I. A formal representation framework," *Computers and Chemical Engineering*, vol. 14 no. 4/5, pp. 495–510, 1990.

- [12] R. Rengaswamy and V. Venkatasubramanian, "A syntactic pattern recognition approach for process monitoring and fault diagnosis," *Engineering Applications of Artificial Intelligence*, vol. 8, no. 1, pp. 35–51, 1995.
- [13] J. Wong, K. McDonald and A. Palazoglu, "Classification of process trends based on fuzzified symbolic representation and hidden Markov models," *Journal of Process Control*, vol. 8, no. 5, pp. 395–408, 1998.
- [14] B. R. Bakshi and G. Stephanopoulos, "Representation of process trends—III. Multi-scale extraction of trends from process data," *Computers and Chemical Engineering* vol. 18, no. 4, pp. 267–302, 1994.
- [15] W. Sun, A. Palazoglu, and J. A. Romagnoli, "Detecting abnormal process trends by wavelet-domain hidden Markov models," *AIChE Journal* vol. 49, no. 1, pp. 140–150, 2003.
- [16] J. Colomer, J. Melendez, F. I. Gamero, "Pattern recognition based on episodes and DTW. Application to diagnosis of a level control system," in *Proceedings of the 16th International Workshop on Qualitative Reasoning*, Barcelona, Catalonia, Spain, 2002.
- [17] S. Dash, R. Rengaswamy, and V. Venkatasubramanian, "Fuzzy-logic based trend classification for fault diagnosis of chemical processes," *Computers and Chemical Engineering*, vol. 27, no. 3, pp. 347–362, 2003.
- [18] Z. K. Peng, "Application of the Wavelet transform in machine condition monitoring and fault diagnostics," *Mechanical Systems and Signal Processing*, vol. 18, pp. 199–221, 2004.
- [19] B. Liu and S. F. Ling, "Machinery diagnostic based on Wavelet packets," *Journal of Vibration and Control*, vol. 3, pp. 5–17, 1997.
- [20] J. Lin and M. J. Zou, "Gearbox fault diagnosis using adaptive Wavelet filter," *Mechanical Systems and Signal Processing*, vol. 17, no. 6, pp. 1259–1269, 2003.
- [21] K. Loparo, "Bearing fault diagnosis based on wavelet transform and fuzzy inference," *Mechanical Systems and Signal Processing*, vol. 18, pp. 1077–1095, 2004.
- [22] J. C. Garcia-Prada, C. Castejon, and O. J. Lara, "Incipient bearing fault diagnosis using DWT for feature extraction," *Proceedings of 12th IFToMM World Congress*, Besancon, France, 2007.
- [23] R. V. Beard, "Failure accommodation in linear systems through self reorganization," Ph. D. dissertation, Massachusetts Institute of Technology, Mass., USA, 1971.

- [24] J. Chen and R. J. Patton, *Robust Model-based Fault Diagnosis for Dynamic Systems*, Kluwer Academic, Norwell, Massachusetts, 1999.
- [25] J. Gertler, *Fault Detection and Diagnosis in Engineering Systems*, Marcel Dekker, Basel, Switzerland, 1998.
- [26] R. Isermann, "Process fault detection and diagnosis methods," in *Proceedings of IFAC symposium SAFERPROCESS'94*, vol. 2, Helsinki, Finland, pp. 597-612, 1994.
- [27] R. J. Patton, C. Lopez-Toribio, and F. J. Uppal, "Artificial intelligence approaches to fault diagnosis," *IEE Colloquium on Condition Monitoring: Machinery, External Structures and Health*, vol. 5, pp. 1-18, 1999.
- [28] J. Korbicz, J. M. Koscielny, Z. Kowalczyk, and W. Cholewa, *Fault Diagnosis: Models, Artificial Intelligence, Applications*. Heidelberg, Germany: Springer-Verlag, 2004.
- [29] R. Rengaswamy, D. Mylaraswamy, V. Venkatasubramanian, and K. E. Arzen, "A comparison of model-based and neural network-based diagnostic methods," *Engineering Applications of Artificial Intelligence*, vol. 14, pp. 808-818, 2001.
- [30] N. Kuipel and P. M. Frank, "A fuzzy FDI decision-making system for the support of the human operator," in *Proceedings of the IFAC Symposium SAFEPROCESS'97*, Hull, UK, pp. 721-726, Pergamon Press, 1998.
- [31] C. Nan, F. Khan, and M. T. Iqbal, "Real-time fault diagnosis using knowledge-based expert system," *Process Safety and Environmental Protection*, vol. 86, no. 1, pp. 55-71, 2008.
- [32] S. M. El-Shal and A. S. Morris, "A fuzzy expert system for fault detection in statistical process control of industrial processes," *IEEE Trans. on Systems, Man Cybernetics-Part C*, vol. 30, no. 2, pp. 281-289, 2000.
- [33] L. F. Mendonca, J. M. G. Sa da Costa, and J. M. C. Sousa, "Fault detection and diagnosis using fuzzy methods," in *Proceedings of European Control Conference (ECC'2003)*, pp. 1-6, Session fault diagnosis 2, Cambridge, United Kingdom, 2003.
- [34] H. Monsef, A. M. Ranjbar, and S. Jadid, "Fuzzy rule-based expert system for power system fault diagnosis," *IEE Proceedings Generation, Transmission & Distribution*, vol. 144, no. 2, pp. 186-192, 1997.
- [35] E. Y. Chow and A. S. Willsky, "Issues in the development of a general algorithm for reliable failure detection," in *Proceedings of the 19th Conference on Decision & Control*, vol. 19, Albuquerque, NM, pp. 1006-1112, 1980.

- [36] A. S. Willsky and H. L. Jones, "Generalized likelihood ratio approach to detection and estimation of jumps in linear systems", *IEEE Trans. Automatic Control*, vol. 21, no. 1, pp. 108-112, 1976.
- [37] M. Basseville and I. V. Nikiforov, *Detection of Abrupt Changes: Theory and Application*. New York: Prentice-Hall Inc., 1993.
- [38] R. Da and C. F. Lin, "Failure detection of dynamical systems with the state χ^2 test," *Journal of Guidance, Control & Dynamics*, vol. 17, no. 2, pp. 271-277, 1994.
- [39] P. M. Frank and X. Ding, "Survey of robust residual generation and evaluation methods in observer-based fault detection systems," *Journal of Process Control*, vol. 7, no. 6, pp. 403-424, 1997.
- [40] H. Schneider and P. M. Frank, "Observer-based supervision and fault detection in robots using nonlinear and fuzzy-logic residual evaluation," *IEEE Trans. on Control System Technology*, vol. 4, no. 3, pp. 274-282, 1996.
- [41] F. Gustafsson, *Adaptive Filtering and Change Detection*. West Sussex, England, John Wiley & Sons, 2000.
- [42] X. Zhang, M. M. Polycarpou, and T. Parisini, "A robust detection and isolation scheme for abrupt and incipient faults in nonlinear systems," *IEEE Trans. on Automatic Control*, vol. 47, no. 4, pp. 576-593, 2002.
- [43] H. Hammouri, M. Kinnaert, and E. H. El Yaagoubi, "Application of nonlinear observers to fault detection and isolation," A book chapter in *New Directions in Nonlinear Observer Design*, Springer, Berlin / Heidelberg, pp. 423-443, 1999.
- [44] P. M. Frank, G. Schrier, and E. Alcorta Garcia, "Nonlinear observers for fault detection and isolation," A book chapter in *New Directions in Nonlinear Observer Design*, Springer, Berlin / Heidelberg, pp. 399-422, 1999.
- [45] C. Edwards, S. K. Spurgeon and R. J. Patton, "Sliding mode observers for fault detection and isolation," *Automatica*, vol. 36, pp. 541-553, 2000.
- [46] H. Hammouri, M. Kinnaert, and E. H. El Yaagoubi, "Observer-based approach to fault detection and isolation for nonlinear systems," *IEEE Trans. on Automatic Control*, vol. 44, no. 10, pp. 1879-1884, 1999.
- [47] E. A. Wan and R. van der Merwe, "The unscented Kalman filter for nonlinear estimation," in *Proceedings of IEEE Symposium on Adaptive Systems for Signal Processing, Communication and Control*, Lake Louise, Alberta, Canada, 2000.
- [48] S. J. Julier and J. K. Uhlmann, "A New Extension of the Kalman Filter to Nonlinear Systems," in *Proceedings of AeroSense: The 11th International*

Symposium on Aerospace/Defence Sensing, Simulation and Controls, Orlando, FL, 1997.

- [49] S. Haykin, *Kalman Filtering and Neural Networks*, John Wiley & Sons, New York, 2001.
- [50] K. V. Ling and K. W. Lim, "Receding horizon recursive state estimation," *IEEE Trans. on Automatic Control*, vol. 44, pp. 1750-1753, 1999.
- [51] C. V. Rao, J. B. Rawlings, and D. Q. Mayne, "Constrained state estimation for nonlinear discrete-time systems: stability and moving horizon approximations," *IEEE Trans. on Automatic Control*, vol. 48, no. 2, pp. 246-258, 2003.
- [52] A. Alessandri, M. Baglietto, G. Battistelli, and T. Parisini, "Receding-horizon estimation for noisy nonlinear discrete-time systems," in *Proceedings of the 42nd IEEE Conference on Decision and Control*, vol. 6, pp. 5825-5830, Maui, Hawaii USA, 2003.
- [53] A. Alessandri, "Fault diagnosis for nonlinear systems using a bank of neural estimators," *Computers in Industry*, vol. 52, no. 3, pp. 271-289, 2003.
- [54] M. Desai and A. Ray, "A fault detection and isolation methodology," in *Proceedings of the 20th IEEE Conference on Decision and Control*, vol. 20, pp. 1363-1369, 1981.
- [55] E. Chow, and A. Willsky, "Analytical redundancy and the design of robust failure detection systems," *IEEE Trans. on Automatic Control*, vol. 29, no. 7, pp. 603-614, 1984.
- [56] M. Desai and A. Ray, "A fault detection and isolation methodology - theory and application," in *Proceedings of the American Control Conference*, pp. 262-270, 1984.
- [57] S. K. Neguang, P. Zhang, and S. Ding, "Parity based fault estimation for nonlinear systems: An LMI approach," in *Proceedings of American Control Conference*, Minneapolis, Minnesota, USA, pp. 5141-5146, 2006.
- [58] C. Christophe, V. Cocquempot, and B. Jiang, "Link between high gain observer-based residual and parity space one," in *Proceedings of the American Control Conference*, Anchorage, AK, pp. 2100-2105, 2002.
- [59] C. Christophe, "Link between high-gain observer-based and parity space residuals for FDI," *Transactions of the Institute of Measurement and Control*, vol. 26, no. 4, pp. 325-337, 2004.
- [60] R. Isermann, "Fault diagnosis via parameter estimation and knowledge processing," *Automatica*, vol. 29, no. 4, pp. 815-835, 1994.

- [61] A. P. Wang and H. Wang, "Fault diagnosis for nonlinear systems via neural networks and parameter estimation," in *Proceedings of International Conference on Control and Automation*, Budapest, Hungary, pp. 559-563, 2005.
- [62] R. Patton, F. Upal, and C. Lopez-Toribio, "Soft computing approaches to fault diagnosis for dynamic systems: A survey," in *Proceedings of 4th IFAC Symposium on Fault Detection, Supervision and Safety for Tech. Processes*, Budapest, pp. 298-311, 2000.
- [63] J. Korbicz, J. M. Koscielnly, Z. Kowalczyk, and W. Cholewa, *Fault Diagnosis: Models, Artificial Intelligence, Applications*, Springer-Verlag, Berlin, Heidelberg, 2004.
- [64] V. Palade, C. D. Bocaniala, and L. C. Jain, *Computational Intelligence in Fault Diagnosis*, Springer-Verlag, London, 2006.
- [65] K. S. Narendra and K. Parthasarathy, "Identification and control of dynamical systems using neural networks," *IEEE Trans. on Neural Networks*, vol. 1, pp. 4-27, March 1990.
- [66] P. S. Maybeckand and P.D. Hanlon, "Performance enhancement of a multiple model adaptive Estimator," *IEEE Transaction on Aerospace and Electronic Systems*, Vol.31, No.4, pp.1240-1254, 1995.
- [67] Y. Zhang and Xiao, "Detection and Diagnosis of Sensor and Actuator Failures using Interacting multiple-model estimator," *Proceedings of the 36th IEEE Conference on Decision and Control*, pp. 4475-4480, San Diego, CA, Dec. 1997.
- [68] K. Narendra and J. Balakrishnan, "Adaptive Control Using Multiple Models," *IEEE Transaction on Automatic Control*, Vol. 42, N0.2, pp.171-187, 1997.
- [69] A. Alessandri, "Fault diagnosis for nonlinear systems using a bank of neural estimators," *Computers in industry*, vol. 52, pp. 271-289, 2003.
- [70] E. Sobhani-Tehrani, K. Khorasani, S. Tafazoli, "Dynamic Neural Network-based Estimator for Fault Diagnosis in Reaction Wheel Actuator of Satellite Attitude Control System," *Proc. Int. Joint Conf. on Neural Networks*, pp. 2347-2352, 2005.
- [71] J. D. Boskovic and R. K. Mehra, "Stabel adaptive multiple model-based control design for accommodation of sensor failures," in *Proceedings of the American Control Conference*, Anchorage, AK, pp. 2046-2051, 2002.
- [72] J. D. Boskovic, S. E. Bergstrom, and R. K. Mehra, "Retrofit reconfigurable flight control in the presence of control effector damage," in *Proceedings of the American Control Conference*, vol. 4, pp. 2652 - 2657, 2003.
- [73] "Capabilities in the area of flight-critical systems." Available on the Web at http://www.ssci.com/Technology/FCS/SofC_nop.pdf

- [74] J. Lunze and J. Schroder, "State observation and diagnosis of discrete-event systems described by stochastic automata," *Discrete Event Dynamic Systems: Theory and Applications*, vol. 11, pp. 319-369, 2000.
- [75] J. Lunze and J. Schroder, "Sensor and actuator fault diagnosis of systems with discrete inputs and outputs," *IEEE Transactions on Systems, Man, and Cybernetics –Part B*, vol. 34, no. 2, 2004.
- [76] G. Besancon and H. Hammouri, "On uniform observation of nonuniformly observable systems," *Sys. Control Lett.*, vol. 29, pp. 9-19, 1996.
- [77] R. Seliger and P. M. Frank, "Robust component fault detection and isolation in nonlinear dynamic systems using nonlinear unknown input observers," *Proceedings of the IFAC/IMAC Symposium SAFERPROCESS'91*, Baden-Baden, Germany, pp. 313-318, 1991.
- [78] X. Ding and P. M. Frank, "An adaptive observer-based fault detection scheme for nonlinear systems," in *Proceedings of the 12th IFAC World Congress*, Sydney, Australia, pp. 63-68, 1993.
- [79] H. Yang and M. Saif, "Nonlinear adaptive observer design for fault detection," in *Proceedings of the American Control Conference*, Seattle, pp. 1136-1139, 1995.
- [80] R. Sreedhar, B. Fernandez, and G. Y. Masada, "Robust fault detection in nonlinear systems using sliding mode observers," *Proceedings of the 2nd IEEE Conference on Control Applications*, Vancouver, BC, Canada, pp. 716-721, 1993.
- [81] A. Alessandri, M. Caccia, and G. Veruggio, "Fault detection of actuator faults in unmanned underwater vehicles," *Control Engineering Practice*, vol. 7, no. 3, pp. 357-368, 1999.
- [82] F. Caliskan and Ch. M. Hajiyev, "EKF based surface fault detection and reconfiguration in aircraft control systems," in *Proceedings of the American Control Conference*, Chicago, Illinois, pp. 1220-1224, 2000.
- [83] A. Okatan, Ch. Hajiyev, and U. Hajiyeva, "Kalman filter innovation sequence based fault detection in LEO satellite attitude determination and control system," *3rd International Conference on Recent Advances in Space Technologies*, pp. 411-416, 2007.
- [84] N. Tudoroiu, E. Sobhani-Tehrani, and K. Khorasani, "Interactive bank of unscented Kalman filters for fault detection and isolation in reaction wheel actuators of satellite attitude control system," in *Proceedings of the 32nd IEEE Conference on Industrial Electronics*, Paris, France, pp. 264-269, 2006.
- [85] P. Li and V. Kadiramanathan, "Particle filtering based likelihood ratio approach to fault diagnosis in nonlinear stochastic systems," *IEEE Transactions on Systems,*

Man, and Cybernetics, Part C: Applications and Reviews, vol. 31, no. 3, pp. 337-343, 2001.

- [86] R. N. Clark, "Instrument fault detection," *IEEE Transaction on Aerospace and Electronics*, vol. AES-14, no. 3, pp. 456-465, 1978.
- [87] D W. Chen and M. Saif, "Observer-based strategies for actuator fault detection, isolation and estimation for certain class of nonlinear systems," *IET Control Theory and Applications*, vol. 1, no. 6, pp. 1672-1680, 2007.
- [88] K. A. Laparo, M. C. Buchner, and K. S. Vasudeva, "Leak detection in an experimental heat exchanger process: A multiple model approach," *IEEE Transactions on Automatic Control*, vol. 36, no. 2, pp. 167-177, 1991.
- [89] T. E. Menke and P. S. Maybeck, "Sensor/actuator failure detection in the Vista F-16 by multiple model adaptive estimation," *IEEE Transactions on Aerospace and Electronic Systems*, vol. 31, no. 4, pp. 1218-1229, 1995.
- [90] H. A. P. Blom and Y. Bar-Shalom, "The interacting multiple model algorithm for systems with markovian switching coefficients," *IEEE Trans. Automatic Control*, vol. 33, no. 8, pp. 780-783, Aug. 1988.
- [91] Y. Bar-Shalom, X. R. Li, and T. Kirubarajan, *Estimation with Applications to Tracking and Navigation*, John Wiley & Sons, New York, NY, 2001.
- [92] R. K. Mehra, C. Rago, and S. Seereeram, "Failure detection and identification using a nonlinear interactive multiple model (IMM) filtering approach with aerospace applications," in *Proceedings of the 11th IFAC Symposium on System Identification*, Fukuoka, Japan, 1997.
- [93] Y. Zhang and Xiao, "Detection and Diagnosis of Sensor and Actuator Failures using Interacting multiple-model estimator," *Proceedings of the 36th IEEE Conference on Decision and Control*, pp. 4475-4480, San Diego, CA, Dec. 1997.
- [94] N. Tudoroiu and K. Khorasani, "Fault detection and diagnosis for satellite's attitude control system using an interactive multiple model (IMM) approach," in *Proceedings of the 2005 Conference on Control Applications*, Toronto, Canada, August 2005.
- [95] P. M. Frank, "Fault diagnosis in dynamic systems using analytical and knowledge-based redundancy: a survey and some new results," *Automatica*, vol. 26, no. 3, pp. 459-474, 1990.
- [96] R. V. Beard, "Failure accommodation in linear systems through self-reorganization," *Ph.D. dissertation*, Massachusetts Institute of Technology, Cambridge, MA, 1971.

- [97] H. L. Jones, "Failure detection in linear systems," *Ph.D. dissertation*, Massachusetts Institute of Technology, Cambridge, MA, 1973.
- [98] M. A. Massoumnia, "A geometric approach to the synthesis of failure detection filters," *IEEE Transactions on Automatic Control*, vol. AC-31, pp. 839-846, 1986.
- [99] M. A. Massoumnia, G. C. Verghese, and A. S. Willsky, "Failure detection and identification," *IEEE Transactions on Automatic Control*, vol. 34, pp. 316-321, 1989.
- [100] C. D. Persis and A. Isidori, "A geometric approach to nonlinear fault detection and isolation," *IEEE Transactions on Automatic Control*, vol.46, no. 6, pp. 853-865, 2001.
- [101] A. Isidori, *Nonlinear Control Systems*, Springer Verlag, New York, 3rd ed., 1995.
- [102] C. P. Tan, and C. Edwards, "Sliding mode observers for reconstruction of simultaneously actuator and sensor faults," in *Proceedings of the Conference on Decision and Control*, Maui, Hawaii USA, pp. 1455-1460, 2003,
- [103] V. Palade, C. D. Bocaniala, and L. J. (Eds), *Computational Intelligence in Fault Diagnosis*. London: Springer-Verlag, 2006.
- [104] E. J. Zampino, "Application of fault-tree analysis to troubleshooting the NASA GRC icing research tunnel," in *Proceedings of the Annual Reliability and Maintainability Symposium*, pp. 16-22, 2001.
- [105] P. A. Crosetti, "Fault tree analysis with probability evaluation," *IEEE Transactions on Nuclear Science*, vol. 18, no. 1, pp. 465-471, 1971.
- [106] A. L. Dexter, "Fuzzy model-based fault diagnosis," *IEE Proceedings – Control Theory and Applications*, vol. 142, no. 6, pp. 545-550, 1995.
- [107] L. Mendonca, J. Sousa, and J. S. de Costa, "Fault detection and isolation of industrial processes using optimized fuzzy models," in *Computational Intelligence for Fault Diagnosis*, pp. 81-194, Springer-Verlag, London, 2006.
- [108] G. V. Cybenko, "Approximation by superpositions of a sigmoidal function," *Mathematics of Control, Signals and Systems*, vol. 2, no. 4, pp. 303-314, 1989.
- [109] B. Li, M.-Y. Chow, Y. Tipsuan, and J. S. Hung, "Neural-network-based motor rolling bearing fault diagnosis," *IEEE Transactions on Industrial Electronics*, vol. 47, no. 5, pp. pp. 1060-1069, 2000.
- [110] R. J. Patton, J. Chen, and T. M. Siew, "Fault diagnosis in nonlinear dynamic systems via neural networks," in *Proceedings of the IEE International Conference on Control*, pp. 1346-1351, 1994.

- [111] K. Funahashi and Y. Nakamura, "Approximation of dynamical systems by continuous time recurrent neural networks," *Neural Networks*, vol. 6, pp. 801-806, 1993.
- [112] C. Ku and K. Y. Lee, "Diagonal recurrent neural networks for dynamic systems control," *IEEE Transactions on Neural Networks*, vol. 6, no. 1, pp. 144-156, 1995.
- [113] A. Atiya and A. Parlos, "Nonlinear system identification using spatiotemporal neural networks," in *Proceedings of the International Joint Conference on Neural Networks (IJCNN)*, Baltimore, MD, pp. 504-509, 1992.
- [114] J. C. Principe and M. A. Motter, "A gamma memory neural network for system identification," in *Proceedings of the IEEE World Congress on Computational Intelligence*, vol. 5, pp. 3232-3237, 1994.
- [115] A. Yazdizadeh and K. Khorasani, "Nonlinear system identification using embedded dynamic neural networks," in *Proceedings in IEEE World Congress on Computational Intelligence*, pp. 378-383, 1998.
- [116] A. Waibel, T. Hanazawa, G. Hinton, K. Shikano, and K. J. Lang, "Phoneme recognition using time-delay neural networks," *IEEE Transactions on Acoustic, Speech and Signal Processing*, vol. 37, no. 3, pp. 328 - 339, 1989.
- [117] A. Yazdizadeh, *Identification of Nonlinear Systems Using Dynamic Neural Networks*, Ph.D. thesis, Department of Electrical and Computer Engineering, Concordia, Montreal, Canada, 1997.
- [118] F. Abdollahi, H. A. Talebi, and R. V. Patel, "Stable identification of nonlinear systems using neural networks: theory and experiments," *IEEE/ASME Trans. on Mechatronics*, vol. 11, no. 4, pp. 488-495, 2006.
- [119] M. Brown and C. J. Harris, *Neurofuzzy Adaptive Modeling and Control*, Prentice-Hall International Series in System and Control Engineering, 1995.
- [120] Z. Xiaodong, M. M. Polycarpou and T. Parisini, "A robust detection and isolation scheme for abrupt and incipient faults in nonlinear systems," *IEEE Transactions on Auto. Control*, vol. 47, no. 4, pp. 576 - 593, April 2002.
- [121] H. A. Talebi and K. Khorasani, "An intelligent sensor and actuator fault detection and isolation scheme for nonlinear systems," in *Proceedings of the 46th IEEE Conference on Decision and Control*, New Orleans, LA, 2621-2625.
- [122] K. Watanabe and D. M. Himmelblau, "Instrument fault detection in systems with uncertainties," *International Journal System Science*, vol. 13, no. 2, pp. 137-158, 1982.

- [123] R. J. Patton, S. W. Willcox, and S. J. Winter, "A parameter insensitive technique for aircraft sensor fault analysis," *Journal of Guidance, Control, and Dynamics*, vol. 10, no. 3, pp. 359–367, 1987.
- [124] X. Lou, A. S. Willsky, and G. C. Verghese, "Optimally robust redundancy relations for failure detection in uncertain systems," *Automatica*, vol. 22, no. 3, pp. 333–344, 1986.
- [125] Q. Wu and M. Saif, "Robust fault detection and diagnosis for a multiple satellite formation flying system using second order sliding mode and wavelet networks," in *Proceedings of the American Control Conference*, New York City, USA, pp. 426-431, 2007.
- [126] J. Korbicz, K. Patan, and A. Obuchowicz, "Dynamic neural networks for process modeling in fault detection and isolation systems," *International Journal of Applied Math. and Comp. Science*, vol. 9, no. 3, pp. 519-546, 1999.
- [127] J. J. Gertler, "Survey of model-based failure detection and isolation in complex plants," *IEEE Control System Magazine*, vol. 8, pp. 3–11, Dec. 1988.
- [128] A. S. Abutaleb, "A genetic algorithm for the maximum likelihood estimation of the parameters of sinusoids in a noisy environment," *Journal of Circuits, Systems, and Signal Processing*, vol. 16, no. 1, pp. 69-81, 1997.
- [129] L. Yao and W. Sethares, "Nonlinear parameter estimation via the genetic algorithm," *IEEE Transaction on Signal Processing*, vol. 42, no. 4, pp. 927-935.
- [130] H. Singer, "Parameter estimation of nonlinear stochastic differential equations: simulated maximum likelihood versus extended Kalman filter and Ito-Taylor expansion," *Journal of Computational and Graphical Statistics*, vol. 11, no. 4, pp. 972-995, 2002.
- [131] A. Houacine, "Regularized fast recursive-least squares algorithms for finite memory filtering," *IEEE Transactions on Signal Processing*, vol. 40, pp. 758-769, 1992.
- [132] G. Haupt, N. Kasdin, G. Keiser, and B. Parkinson, "An optimal recursive iterative algorithm for discrete-time nonlinear least-squares estimation," *AIAA-95-3218*, pp. 404-417, 1995. Also available online at:
http://einstein.stanford.edu/content/sci_papers/papers/HauptG_1995_57.pdf
- [133] S. J. Julier, J. K. Uhlmann, and H. E. Durrant-Whyte, "A new approach for filtering nonlinear systems," in *Proceedings of the American Control Conference*, Seattle, Washington, pp. 1628-1632, 1995.
- [134] M. Darouach, M. Zasadzinski, and S. J. Xu, "Full order observers for linear systems with unknown inputs," *IEEE Transaction on Automatic Control*, vol. 39, no. 3, pp. 606-609, 1994.

- [135] J. Wunnenberg, "Observer-based fault detection in dynamic systems," *PhD Thesis*, University of Duisburg, Germany, 1990.
- [136] D. Koenig and S. Mammar, "Design of a class of reduced order unknown inputs nonlinear observer for fault diagnosis," *Proceedings of the American Control Conference*, Arlington, VA, pp. 2143-2147, 2001.
- [137] A. M. Pertew, H. J. Marquez, and Q. Zhao, " H_∞ synthesis of unknown input observers for nonlinear Lipschitz systems," *International Journal of Control*, vol. 78, no. 15, pp. 1155-1165, 2005.
- [138] D. Koenig, "Observer design for unknown input nonlinear descriptor systems via convex optimization," *IEEE Transactions on Automatic Control*, vol. 51, no. 6, pp. 1047-1052, 2006.
- [139] S. Mondal, G. Chakraborty, and K. Bhattacharyya, "A full-order Luenberger-like observer for nonlinear systems with unknown inputs," in *Proceedings of the International Conference on Advances in Control and Optimization of Dynamical Systems*, Bangalore, India, pp. 107-120, 2007.
- [140] N. Wiener, *Extrapolation, Interpolation, and Smoothing of Stationary Time Series, with Engineering Applications*, Cambridge, MA: MIT Press, 1949.
- [141] A. H. Jazwinski, *Stochastic Processes and Filtering Theory*, Prentice Hall, Englewood Cliffs, NJ, 1979.
- [142] A. Papoulis, U. Pillai, *Probability, Random Variables, and Stochastic Processes*, McGraw-Hill, 2002.
- [143] S. Haykin, P. Yee, and E. Derbez, "Optimum nonlinear filtering," *IEEE Transaction on Signal Processing*, vol. 45, no. 11, 1997.
- [144] D. Manolakis, F. Ling, and J. G. Proakis, "Efficient time-recursive least-squares algorithms for finite-memory adaptive filtering," *IEEE Transactions on Systems and Circuits*, vol. 34, no. 4, pp. 400-408, 1987.
- [145] M. Niedzwiecki, "Multiple-model approach to finite memory adaptive filtering," *IEEE Transactions on Signal Processing*, vol. 40, no. 2, pp. 470-473, 1992.
- [146] T. Parisini and R. Zoppoli, "Neural networks for nonlinear state estimation," *International Journal of Robust Control*, vol. 4, pp. 231-248, 1994.
- [147] A. Jazwinski, "Limited memory optimal filtering," *IEEE Transactions on Automatic Control*, vol. 13, no. 5, pp. 558-563, 1968.
- [148] J. T. Lo, "Synthetic approach to optimal filtering," *IEEE Transactions on Neural Networks*, vol. 5, no. 5, pp. 803-811, 1994.

- [149] P. J. Werbos, "Backpropagation through time: What it does and how to do it," *Proceedings of the IEEE*, vol. 78, no. 10, pp. 1550-1560, 1990.
- [150] A. Alessandri, T. Parisini, and R. Zoppoli, "Neural approximators for nonlinear finite-memory state estimation," *International Journal of Control*, vol. 67, no. 2, pp. 275-301, 1997.
- [151] R. Zoppoli, M. Sanguineti, and T. Parisini, "Approximating networks and extended Ritz method for the solution of functional optimization problems," *Journal of Optimization Theory and Applications*, vol. 112, no. 2, pp. 403-439, 2002.
- [152] J. R. Wertz and W. J. Larson, "Space mission analysis and design," 3rd ed., Dordrecht, Netherlands; Boston: Kluwer, 1999.
- [153] C. Brown, *Elements of Spacecraft Design*, AIAA Educational Series, 2002.
- [154] R. Gessner, B. Kusters, A. Hefler, R. Eilenberger, J. Hartmann, and M. Schmidt, "Hierarchical FDIR concepts in S/C systems," available on-line at: http://www.google.ca/search?hl=en&q=Hierarchical+FDIR+concepts+in+S%2FC+systems&meta=lr%3Dlang_en%7Clang_fa
- [155] A. Barua and K. Khorasani, "Intelligent model-based hierarchical fault diagnosis for satellite formations," in *Proceedings of the IEEE Conference on Systems, Man, and Cybernetics*, Montreal, Canada, pp. 3191-3196, 2007.
- [156] T. Magill, "Optimal adaptive estimation of sampled stochastic processes," *IEEE Transactions on Automatic Control*, vol. 10, no. 4, pp. 434-439, 1965.
- [157] M. Sampath, R. Sengupta, S. Lafortune, K. Sinnamohideen and D. Teneketzis, "Failure diagnosis using discrete-event models", *IEEE Transactions on Control System Technology*, vol. 4, pp. 105-124, 1996.
- [158] R. Debouk, S. Lafortune and D. Teneketzis, "Coordinated decentralized protocols for failure diagnosis of discrete event systems", *Discrete Event Dynamic Systems*, vol. 10, pp. 33-86, 2000.
- [159] D. Bernard, R. Doyle, E. Riedel, N. Rouquette, J. Wyatt, M. Lowry, and P. Nayak, "Autonomy and software technology on NASA's Deep Space One," *IEEE Intelligent Systems and Their Applications*, vol. 14, no. 3, pp. 10-15, 1999.
- [160] H. A. Talebi and K. Khorasani, "A robust fault detection and isolation scheme with application to magnetorquer type actuators for satellites," in *Proceedings of the IEEE Conference on Systems, Man, and Cybernetics*, Montreal, Canada, pp. 3165-3170, 2007.
- [161] T. Jiang, K. Khorasani, and S. Tafazoli, "Parameter estimation-based fault detection, isolation and recovery for nonlinear satellite models," Accepted for

publication in *IEEE Transactions on Control Systems Technology*. Available in electronic form on IEEE website.

- [162] Q. Wu and M. Saif, "Observer-based robust fault detection and diagnosis for a satellite system with flexible appendages," in *Proceedings of the IEEE Conference on Decision and Control*, San Diego, CA, pp. 2183-2188, 2006.
- [163] H. A. Talebi and R. V. Patel, "An intelligent fault detection and recovery scheme for reaction wheel actuator of satellite attitude control systems," in *Proceedings of the IEEE International Conference on Control Applications*, Munich, Germany, pp. 3282-3287, 2006.
- [164] Z. Q. Li, L. Ma, and K. Khorasani, "A dynamic neural network-based reaction wheel fault diagnosis for satellites," in *Proceedings of the International Joint Conference on Neural Networks (IJCNN)*, Vancouver, Canada, pp. 3714-3721, 2006.
- [165] N. Meskin and K. Khorasani, "Fault detection and isolation in a redundant reaction wheels configuration of a satellite," in *Proceedings of the IEEE Conference on Systems, Man, and Cybernetics*, Montreal, Canada, pp. 3153-3158, 2007.
- [166] S. W. Shepperd, "Quaternion from rotation matrix," *Journal of guidance and control*, vol. 1, no. 3, pp. 223-224, 1978.
- [167] B. Bialke, "High Fidelity Mathematical Modeling of Reaction Wheel Performance," *Advances in the Astronautical Sciences*, pp. 483-496, 1998.
- [168] M. J. Sidi, *Spacecraft Dynamics and Control-A Practical Engineering Approach*, Cambridge University Press, 1997.
- [169] B. Wie, *Space vehicle dynamics and control*, AIAA, 1998.
- [170] J. D. Böskovi, Sai-Ming Li and R. K. Mehra, "Robust adaptive variable structure control of spacecraft under control input saturation," *Journal of Guidance, Control, and Dynamics*, vol. 24, No. 1, pp. 14-22, 2001.
- [171] J. Crassidis, S. V. Vadali, and F. L. Markley, "Optimal variable-structure control tracking of spacecraft maneuvers," *AIAA*, Web reference: <http://www.acsu.buffalo.edu/~johnc/fmet99.pdf>
- [172] S. W. Piche, "Steepest descent algorithms for neural network controller and filters," *IEEE Transactions on Neural Networks*, vol. 5, no. 2, pp. 198-212, 1994.
- [173] Y. M. Zhang and J. Jiang, "Active fault-tolerant control system against partial actuator failures," *IEE Proceedings on Control Theory Applications*, vol. 149, no. 1, 2002.

Appendix A

Ordered Partial Derivatives (From Piche [172])

For adapting discrete-time dynamical systems and, in particular, to update the weights of a neural network with dynamic elements using steepest descent, a partial derivative of the associated dynamical system must be calculated. Because a dynamical system contains feedback, the calculation of this derivative can be quite complex. The ordered partial derivative, which is a partial derivative whose constant and varying terms are defined using ordered set of equations, provides a mathematical tool for easily finding derivatives of complex dynamical systems.

To define the ordered derivative, the concept of an ordered set of equations must first be introduced. Let $\{z_1, \dots, z_i, \dots, z_j, \dots, z_n\}$ be a set of n equations. This set of equations is defined to be an ordered set of equations if each variable z_i is a function only of the variables $\{z_1, \dots, z_{i-1}\}$. Thus, the equation for any variable of an ordered set of equations can be written as

$$z_i = f_i(z_1, \dots, z_{i-1}) \quad (\text{A-1})$$

Because of the ordered nature of this set of equations, the variables $\{z_1, \dots, z_{i-1}\}$ must be calculated before z_i can be computed. As an example, the following three equations from an ordered set of equations:

$$\begin{aligned} z_1 &= 1 \\ z_2 &= 3z_1 \\ z_3 &= z_1 + 2z_2 \end{aligned} \quad (\text{A-2})$$

When calculating a partial derivative it is necessary to specify which variables are held constant and which are allowed to vary. Typically, if this is not specified, it is assumed

that all variables are held constant except those terms appearing in the denominator of the partial derivative. This is the convention adopted in this paper; thus, the partial derivatives of z_3 with respect to z_1 , $\frac{\partial z_3}{\partial z_1}$, is 1.

An ordered partial derivative is a partial derivative whose constant and varying terms are determined using an ordered set of equations. The constant terms of the ordered partial derivative of z_j with respect to z_i , which is denoted $\frac{\partial^+ z_j}{\partial z_i}$ in order to distinguish it from an ordinary partial derivative, are $\{z_1, \dots, z_{i-1}\}$. The varying terms are $\{z_i, \dots, z_j, \dots, z_n\}$. Using mathematical notation, the ordered partial derivative is defined as:

$$\frac{\partial^+ z_j}{\partial z_i} = \frac{\partial z_j}{\partial z_i} \Big|_{\{z_1, \dots, z_{i-1}\}} \quad (\text{A-3})$$

Using this definition, the following two properties of the ordered derivative can easily be shown

$$\frac{\partial^+ z_{i+1}}{\partial z_i} = \frac{\partial z_{i+1}}{\partial z_i} \quad (\text{A-4})$$

and

$$\frac{\partial^+ z_j}{\partial z_i} = 0 \quad \text{if } j < i \quad (\text{A-5})$$

When $j > i+1$, the ordered derivative is found using either of the following two chain rule expansions:

$$\frac{\partial^+ z_j}{\partial z_i} = \frac{\partial z_j}{\partial z_i} + \sum_{k=i+1}^{j-1} \frac{\partial^+ z_j}{\partial z_k} \frac{\partial z_k}{\partial z_i} \quad (\text{A-6})$$

and

$$\frac{\partial^+ z_j}{\partial z_i} = \frac{\partial z_j}{\partial z_i} + \sum_{k=i+1}^{j-1} \frac{\partial z_j}{\partial z_k} \frac{\partial^+ z_k}{\partial z_i} \quad (\text{A-7})$$

As an example, applying either the first (equation (A-6)) or the second (equation (A-7)) chain rule expansions to the ordered set of equations given in (A-2), the ordered partial

derivative of z_3 with respect to z_1 , $\frac{\partial^+ z_3}{\partial z_1}$ is 7.

Appendix B

Attitude Reference System and Coordinate Frames (Wertz [152])

In general, to determine a satellite's attitude with respect to another body, a reference system must be used. While any reference system will provide valid answers if it is applied consistently, it is desirable to choose a convenient reference frame. An appropriate reference frame simplifies calculations and reduces the obscuring of physical theory by numerous algebraic/geometrical transformations. Throughout this chapter, the following four reference frames are utilized. It is important to note that the x , y , and z notation that may have been used in each frame of reference is independent of the other reference frames.

1) Spacecraft fixed/body reference frame \mathfrak{S}_B : The body frame is a body-fixed frame of reference. Its origin is located at the spacecraft center of mass and its orientation is based on the spacecraft geometry. For example, as depicted Figure B-1, the x and y axes are along the two coordinates of the solar panels on the bottom side of the satellite and the z axis is along the height and completes the orthogonal triad.

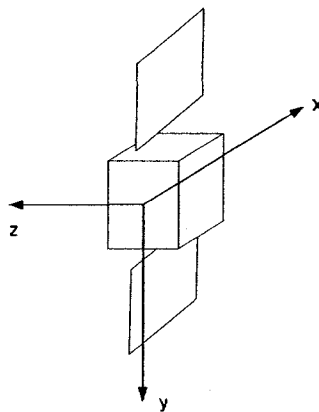


Figure B - 1. Spacecraft fixed/body reference frame.

2) **Spacecraft principal axes reference frame:** The principal frame is a body-fixed frame of reference. Its origin is located at the spacecraft's center of mass and its orientation is along the principal directions of the satellite body. Note that the principal directions are the eigenvectors of the spacecraft's Inertia matrix and that the dynamic equations can be expressed more conveniently in this frame.

3) **Orbital reference frame (RPY frame):** The orbital reference frame is shown in Figure B-2. As can be seen in this figure, it is the well-known Earth-pointing reference system where the x -axis (Roll) is perpendicular to nadir and along the satellite's velocity vector (i.e., tangential to the orbit), the z -axis (Yaw) points towards the center of the Earth, and the y -axis (Pitch) is perpendicular to the orbit plane with positive direction towards south pole completing the orthogonal right-hand triad. It should be noted that the RPY frame is a rotating frame with the speed of rotation equal to the satellite's rotation speed around the Earth. Representing the attitude of a satellite with respect to the rotating orbital frame makes the design and implementation of an attitude control law much more convenient.

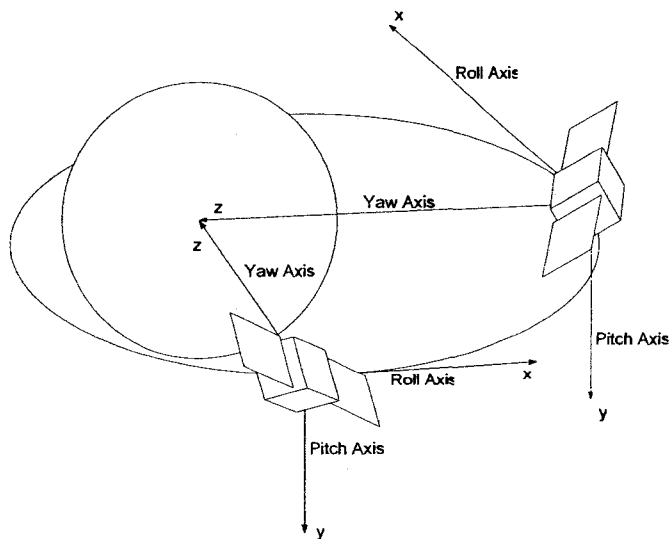


Figure B - 2. Orbital reference frame or RPY (Roll-Pitch-Yaw) frame.

4) Inertial (Earth-fixed) reference frame: This is the non-rotating Earth-fixed frame that has its origin located at the center of the Earth. As shown in Figure B-3, its x -axis points through the Greenwich Meridian in the equatorial plane, z -axis is in the same direction as the Earth's rotation axis, and its y -axis completes the right-hand triad.

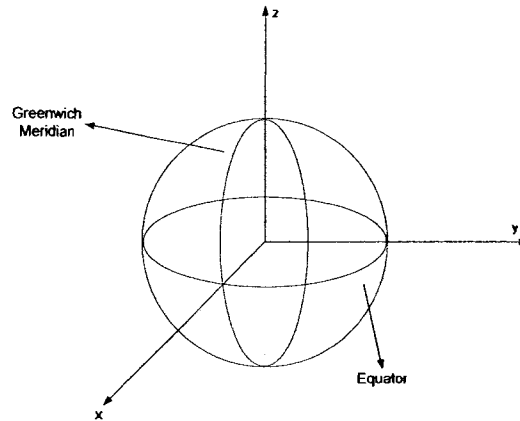


Figure B - 3. Inertial (or Earth-fixed) reference frame.

Appendix C

Extra Figures of FDII Results

In this Appendix, the reaction wheel states and their estimates from the *hybrid* FDII schemes under various fault scenarios and noise levels are depicted.

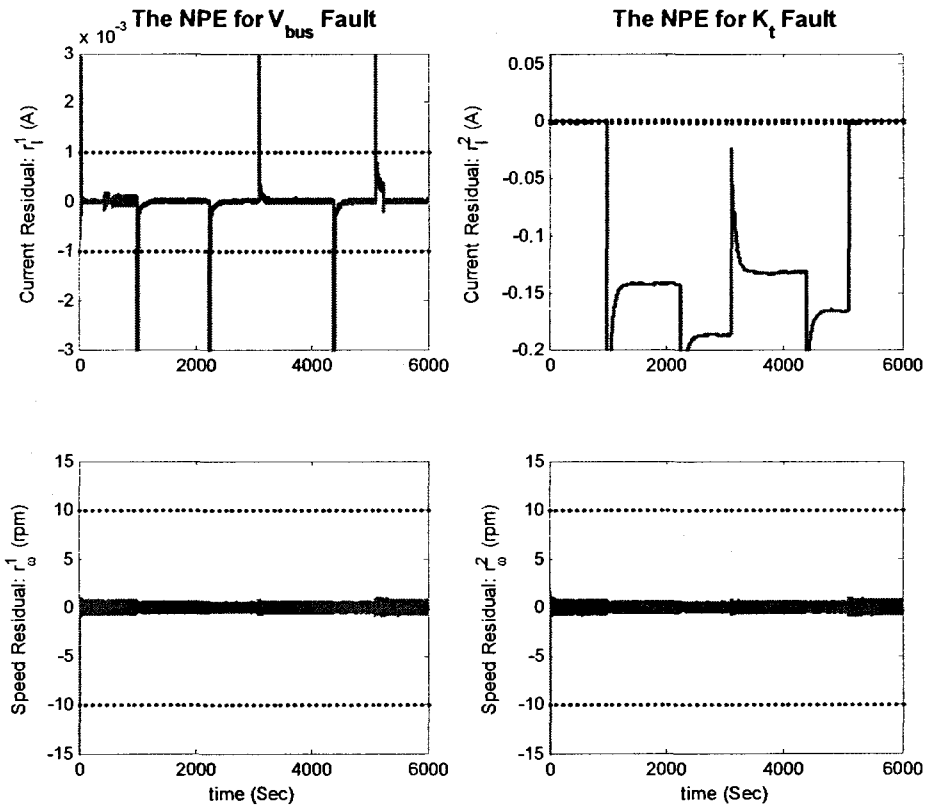


Figure C-1. The residuals of the two NPEs of the *series-parallel* FDII scheme in presence of a sequence of *high-severity bus voltage faults* over the time period $t \in [1000 \ 5100]$ second.

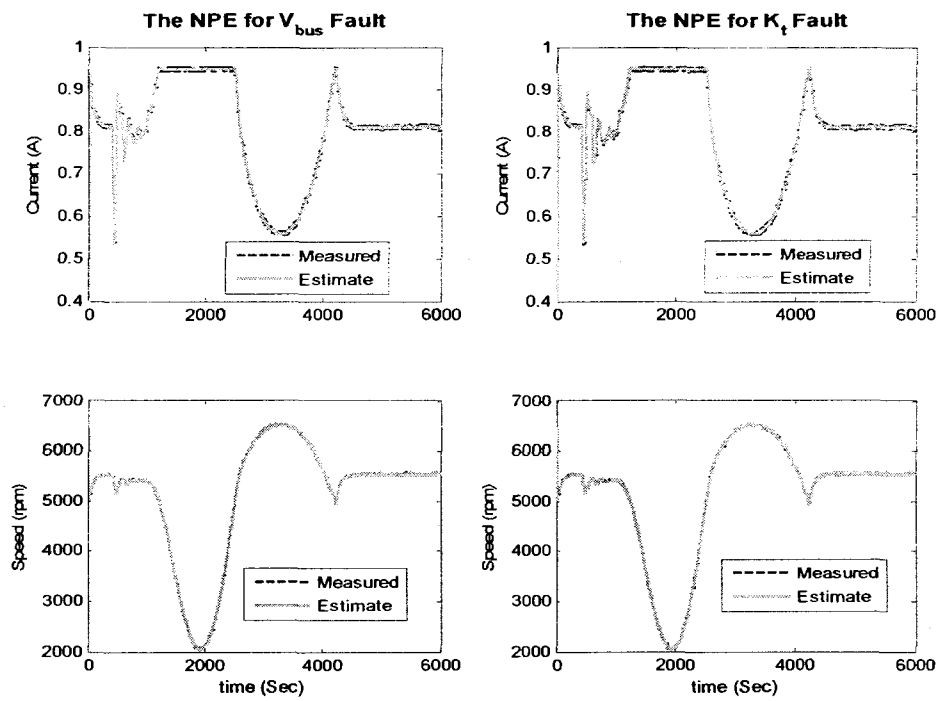


Figure C-2. The estimated versus measured states using the *series-parallel* FDI scheme in presence of motor current fault over the time period $t \in [1000 \ 4250]$ sec., subject to *medium* noise level (SNR=55 dB).

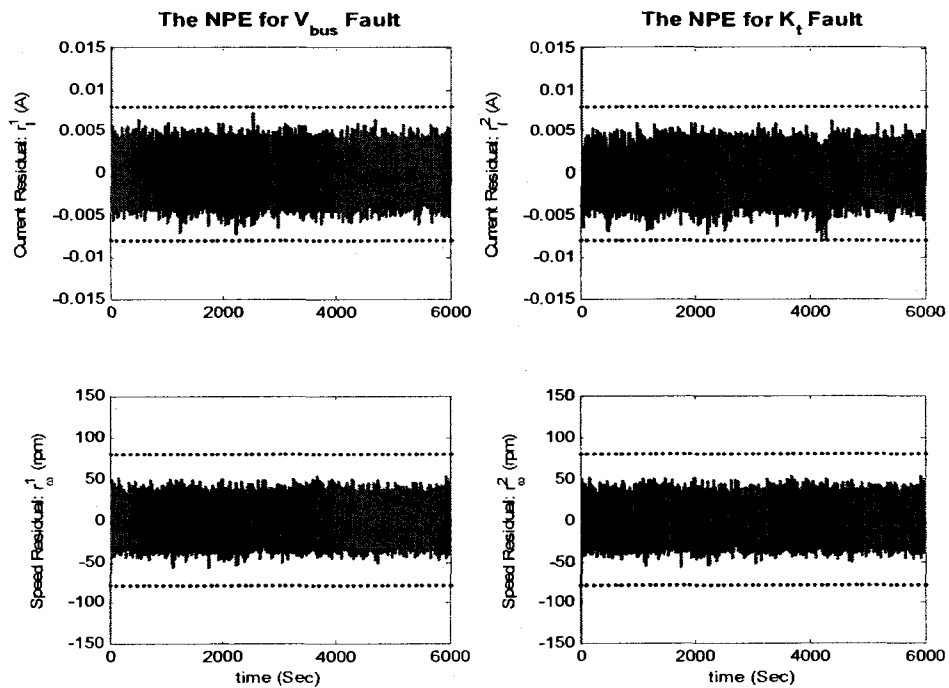


Figure C-3. The residuals of the two NPEs of the *series-parallel* FDI scheme in presence of motor current fault over the period $t \in [1000 \ 4250]$ sec., subject to *medium* noise level (SNR=55 dB).

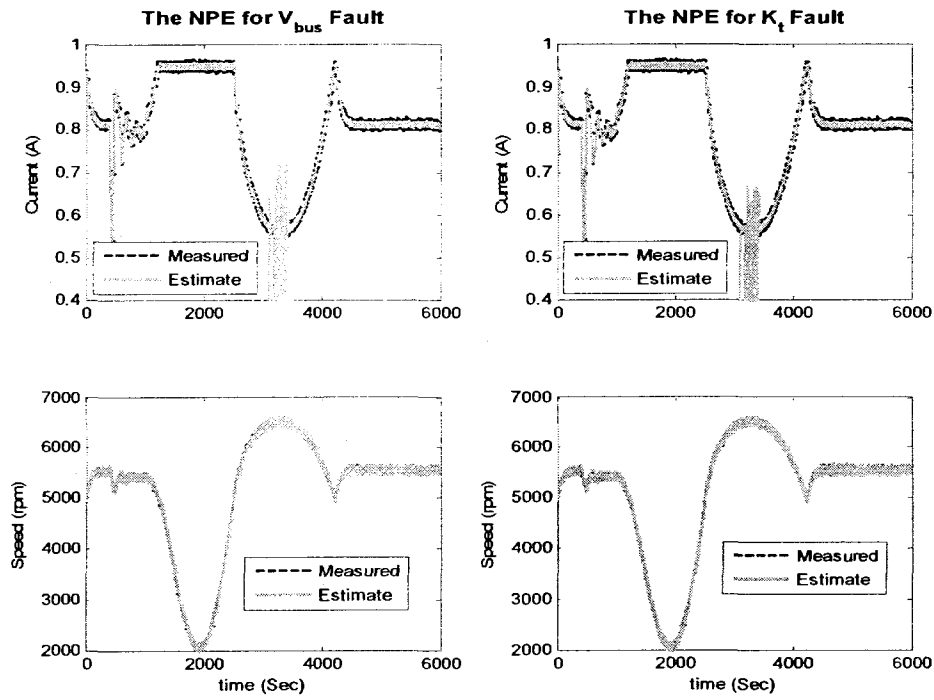


Figure C-4. The estimated versus measured states using the *series-parallel* FDII scheme in presence of motor current fault over the time period $t \in [1000 \ 4250]$ sec., subject to *high* noise level (SNR=45 dB).

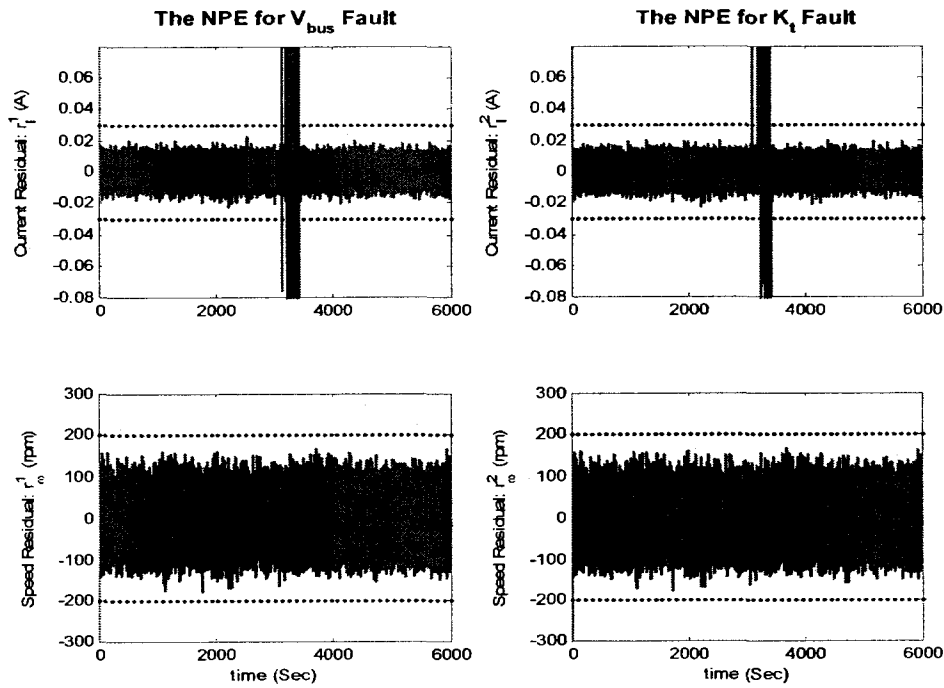


Figure C-5. The residuals of the two NPEs of the *series-parallel* FDII scheme in presence of motor current fault over the time period $t \in [1000 \ 4250]$ sec., subject to *high* noise level (SNR=45 dB).

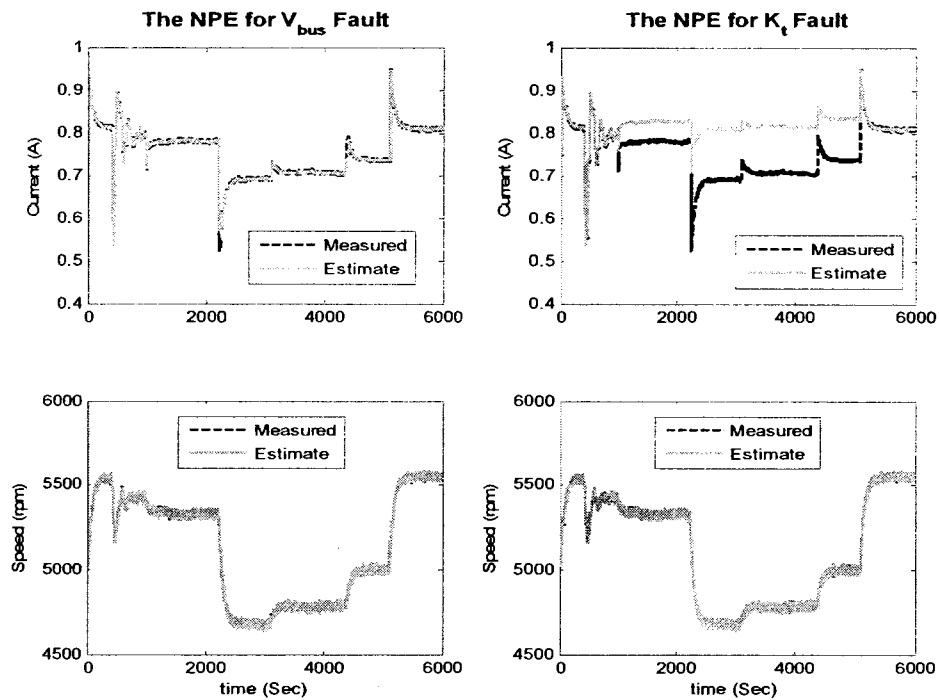


Figure C-6. The estimated versus measured states using the *series-parallel* FDII scheme in presence of a sequence of *low-severity* bus voltage faults over the time period $t \in [1000 \ 5100]$ sec., subject to *medium* noise level (Current SNR=54.57 dB and Speed SNR=54.76 dB).

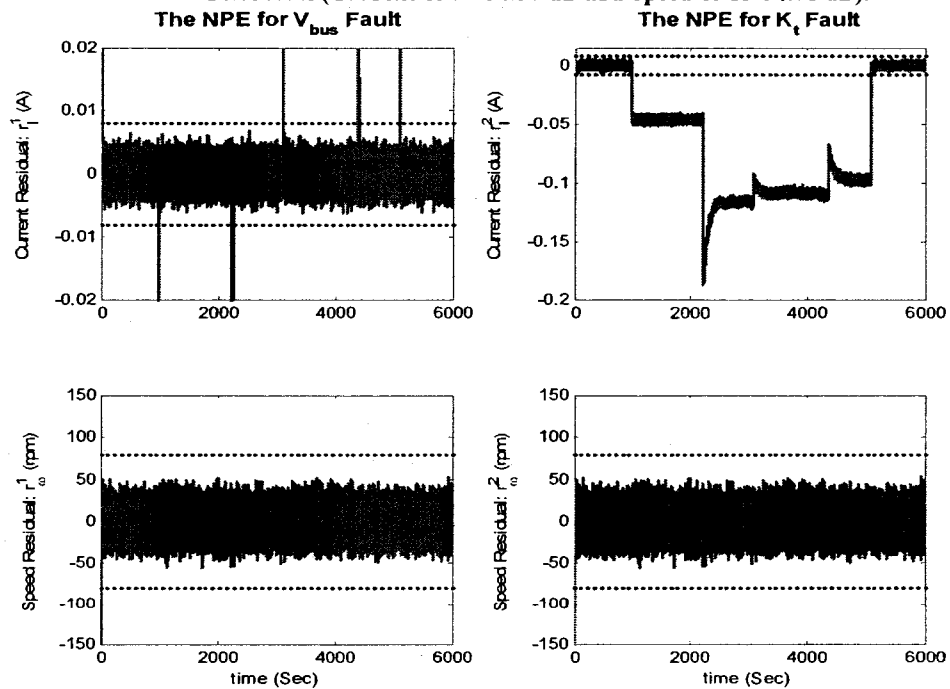


Figure C-7. The residuals of the two NPEs of the *series-parallel* FDII scheme in presence of a sequence of *low-severity* bus voltage faults over the time period $t \in [1000 \ 5100]$ seconds, subject to *medium* noise level (Current SNR=54.57 dB and Speed SNR=54.76 dB).

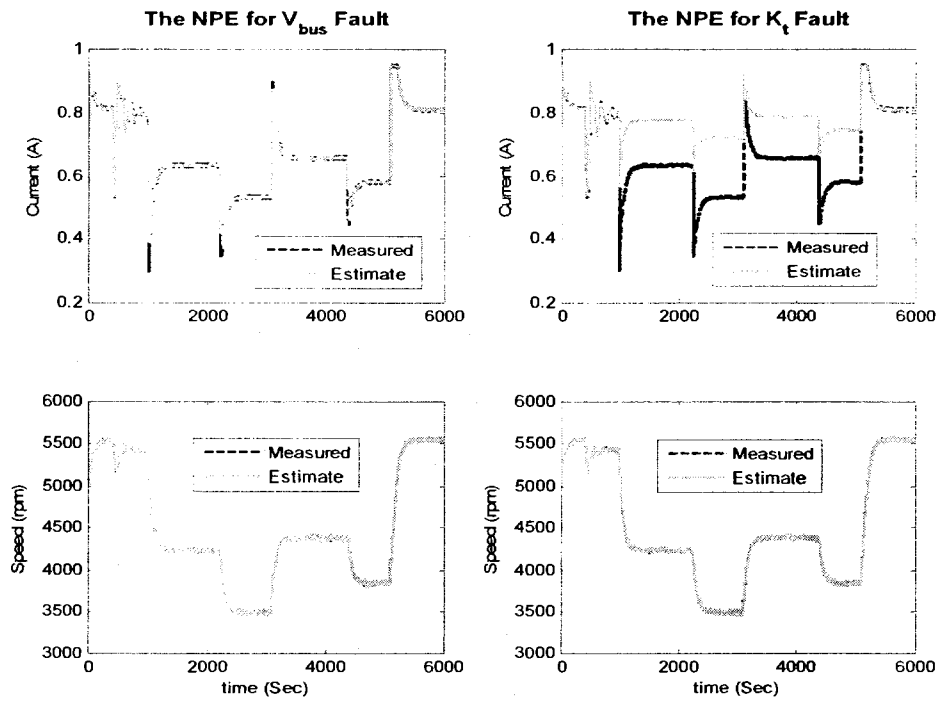


Figure C-10. The estimated versus measured states using the *series-parallel* FDI scheme in presence of a sequence of *high-severity* bus voltage faults over the time period $t \in [1000 \ 5100]$ sec., subject to *medium* noise level (Current SNR=53.66 dB and Speed SNR=53.72 dB).

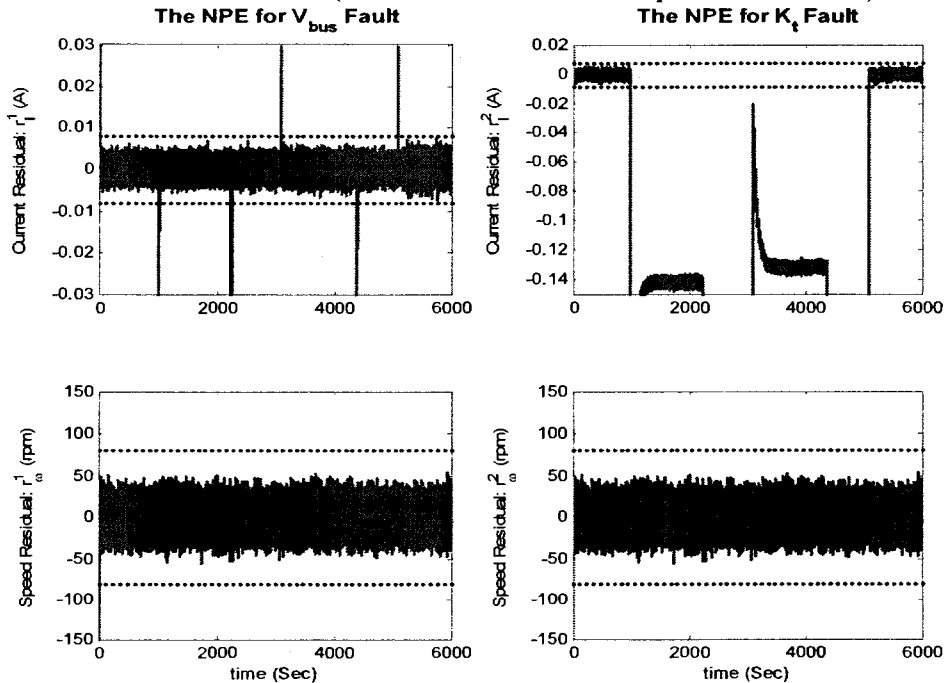


Figure C-11. The residuals of the two NPEs of the *series-parallel* FDI scheme in presence of a sequence of *high-severity* bus voltage faults over the time period $t \in [1000 \ 5100]$ sec., subject to *medium* noise level (Current SNR=53.66 dB and Speed SNR=53.72 dB).

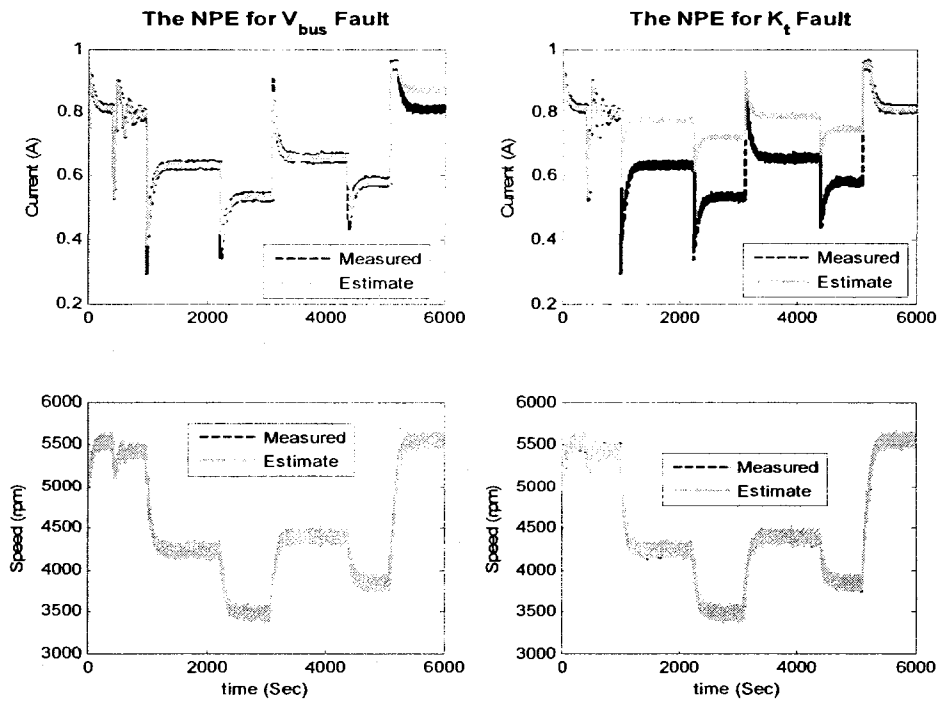


Figure C-12. The estimated versus measured states using the *series-parallel* FDII scheme in presence of a sequence of *high-severity* bus voltage faults over the time period $t \in [1000 \ 5100]$ sec., subject to *high* noise level (Current SNR=43.66 dB and Speed SNR=43.72 dB).

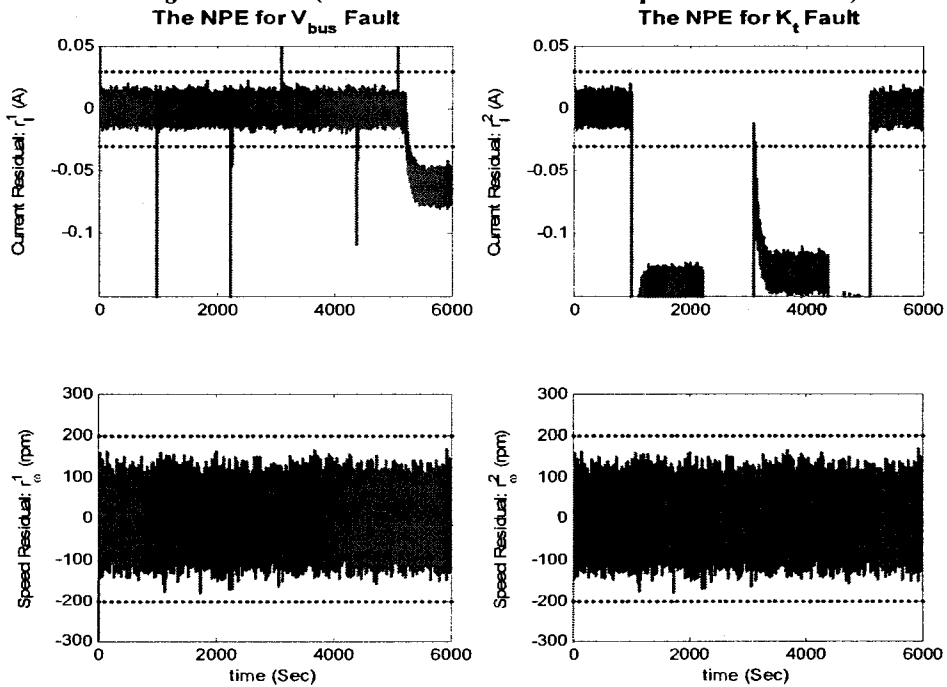


Figure C-13. The residuals of the two NPEs of the *series-parallel* FDII scheme in presence of a sequence of *high-severity* bus voltage faults over the time period $t \in [1000 \ 5100]$ sec., subject to *high* noise level (Current SNR=43.66 dB and Speed SNR=43.72 dB).

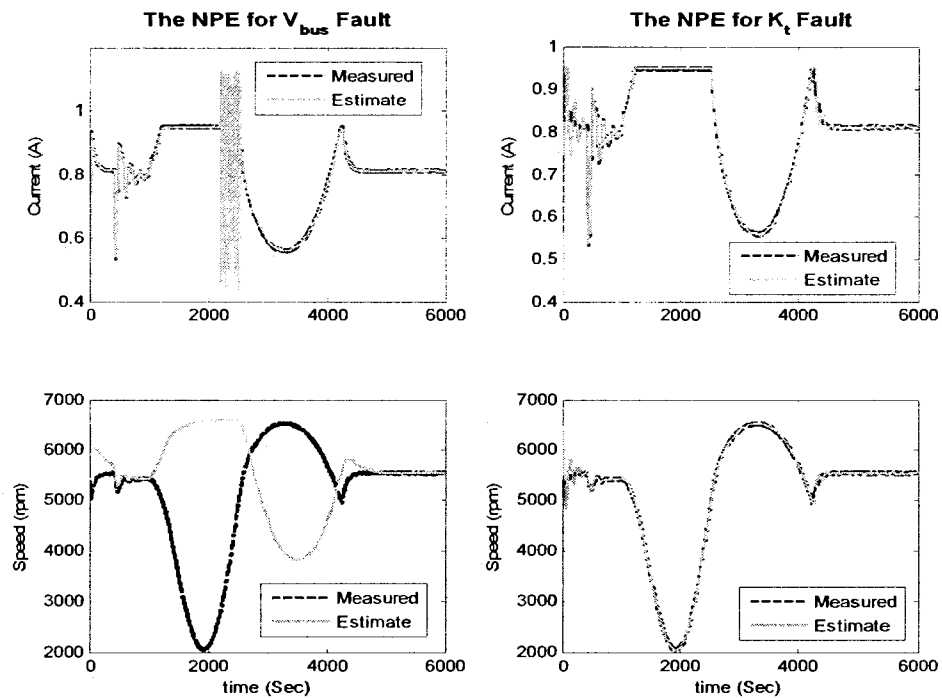


Figure C-14. The estimated versus measured states using the *parallel* FDI scheme in presence of motor current fault over the time period $t \in [1000 \ 4250]$ sec., subject to *medium* noise level (SNR=55 dB).

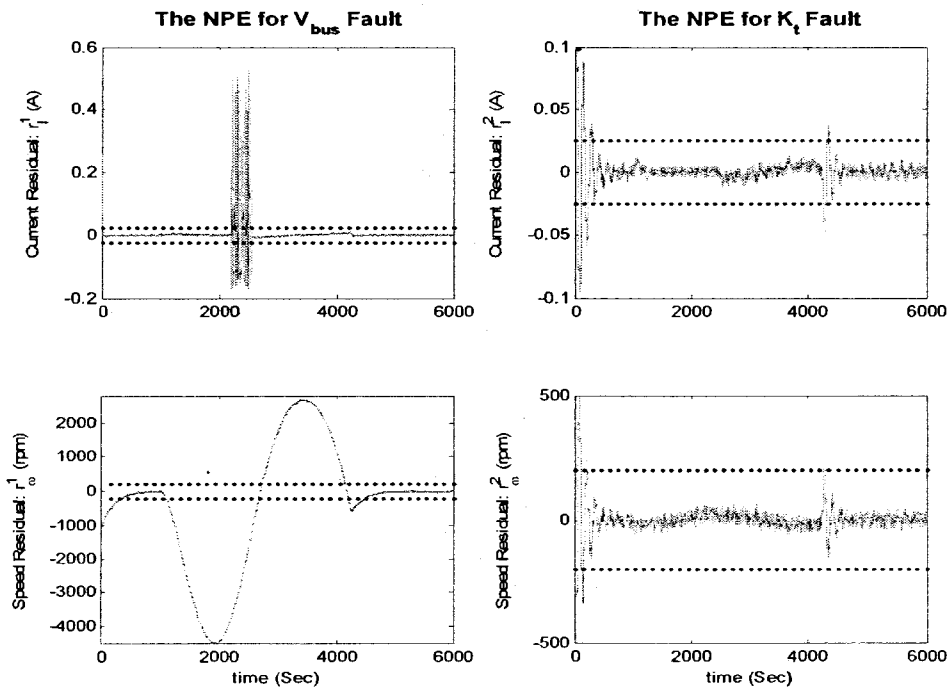


Figure C-15. The residuals of the two NPEs of the *parallel* FDI scheme in presence of motor current fault over the period $t \in [1000 \ 4250]$ sec., subject to *medium* noise level (SNR=55 dB).

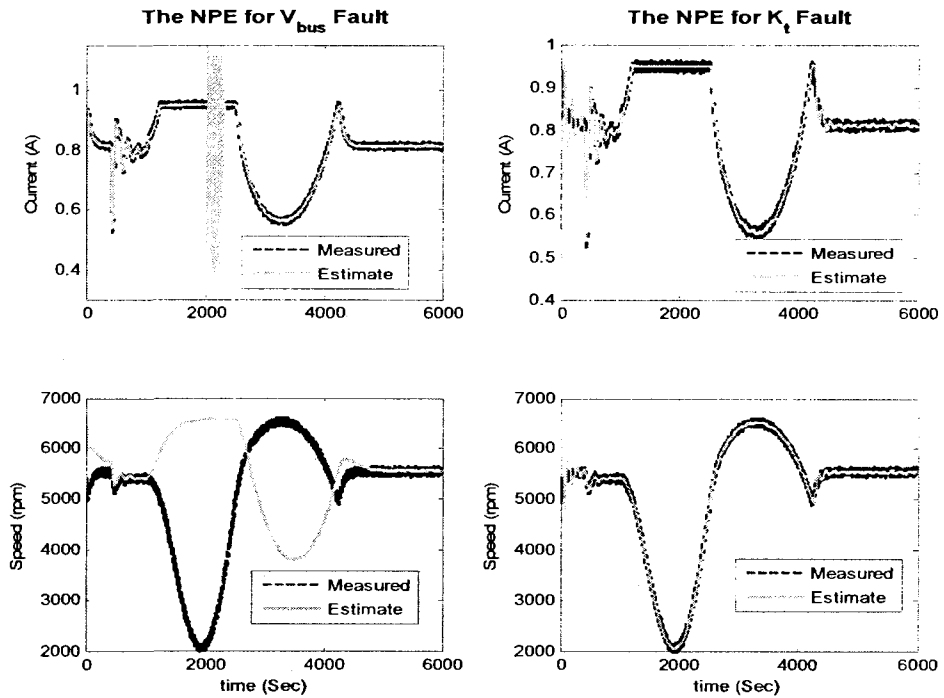


Figure C-16. The estimated versus measured states using the *parallel* FDII scheme in presence of motor current fault over the time period $t \in [1000 \ 4250]$ sec., subject to *high* noise level (SNR=45 dB).

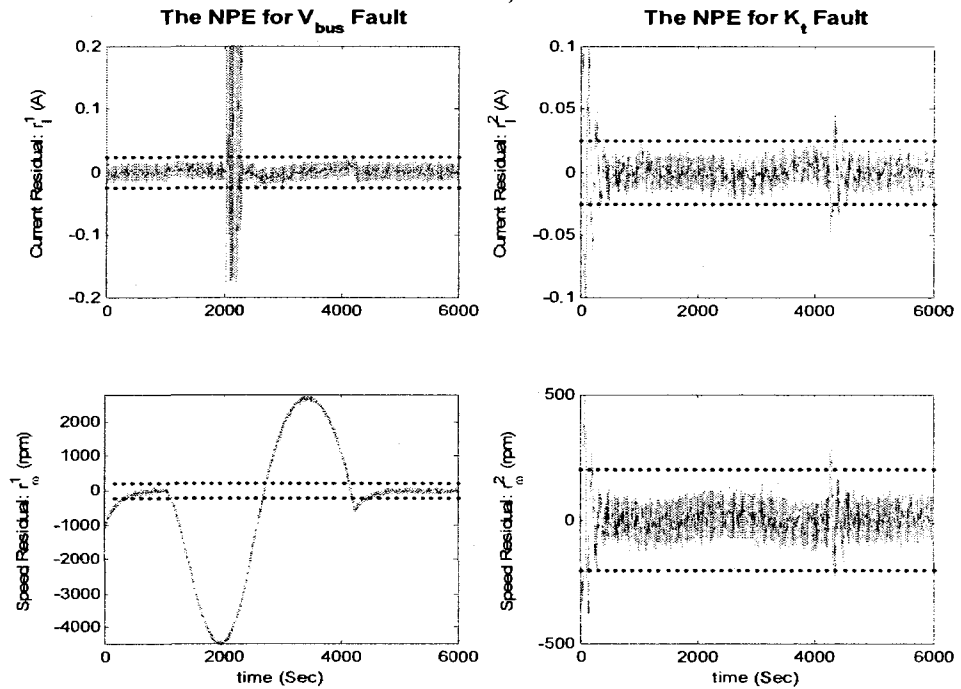


Figure C-17. The residuals of the two NPEs of the *parallel* FDII scheme in presence of motor current fault over the time period $t \in [1000 \ 4250]$ sec., subject to *high* noise level (SNR=45 dB).

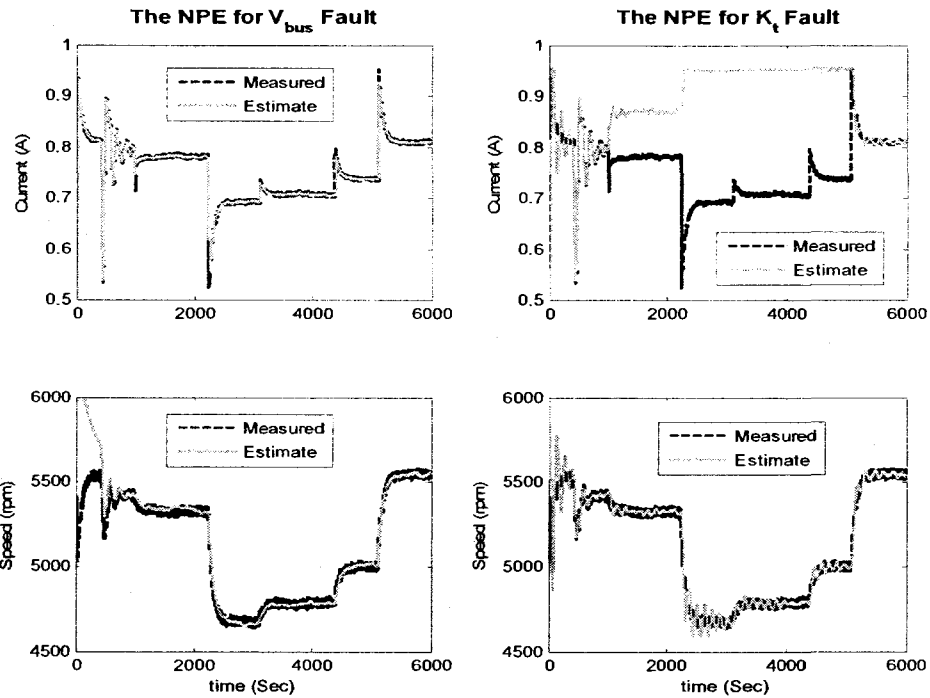


Figure C-18. The estimated versus measured states using the *parallel* FDII scheme in presence of a sequence of *low-severity bus voltage faults* over the time period $t \in [1000 \ 5100]$ sec., subject to *medium noise level* (Current SNR=54.57 dB and Speed SNR=54.76 dB).

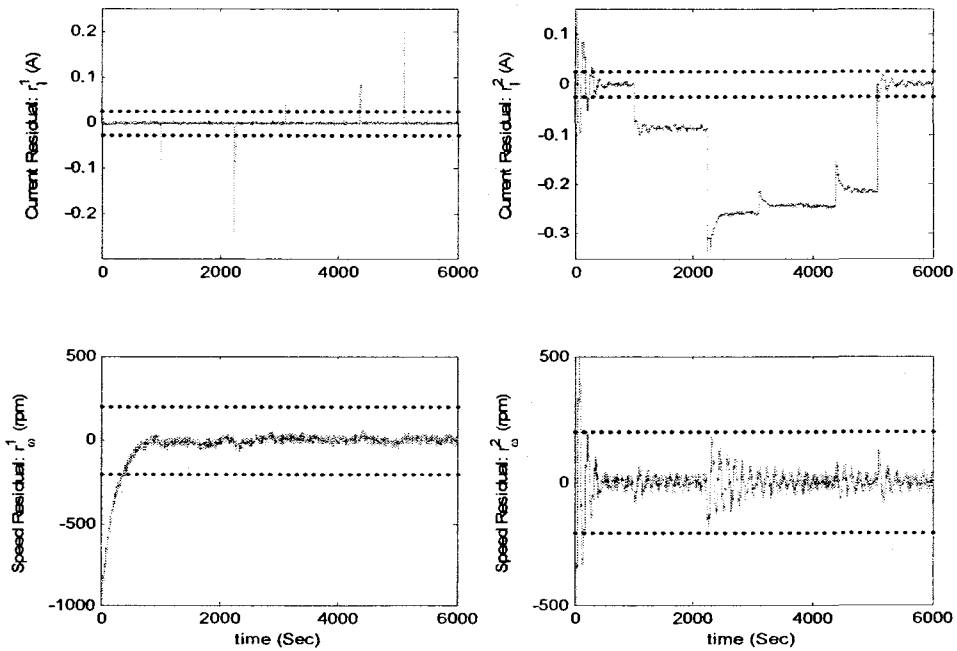


Figure C-19. The residuals of the two NPEs of the *parallel* FDII scheme in presence of a sequence of *low-severity bus voltage faults* over the time period $t \in [1000 \ 5100]$ seconds, subject to *medium noise level* (Current SNR=54.57 dB and Speed SNR=54.76 dB).

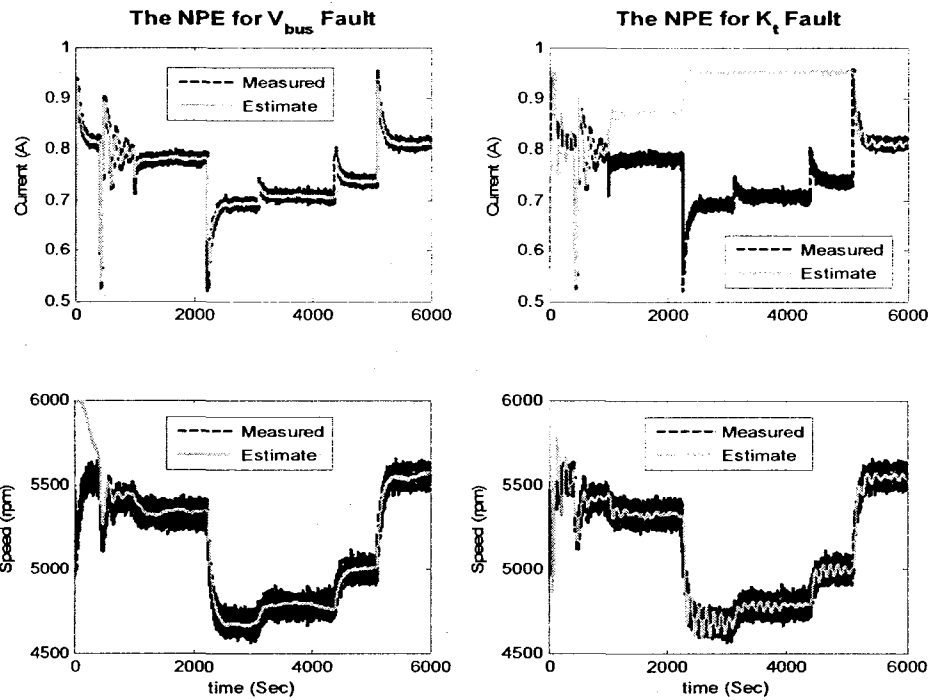


Figure C-20. The estimated versus measured states using the *parallel* FDH scheme in presence of a sequence of *low-severity bus voltage faults* over the time period $t \in [1000 \ 5100]$ sec., subject to *high noise level* (Current SNR=44.57 dB and Speed SNR=44.76 dB).

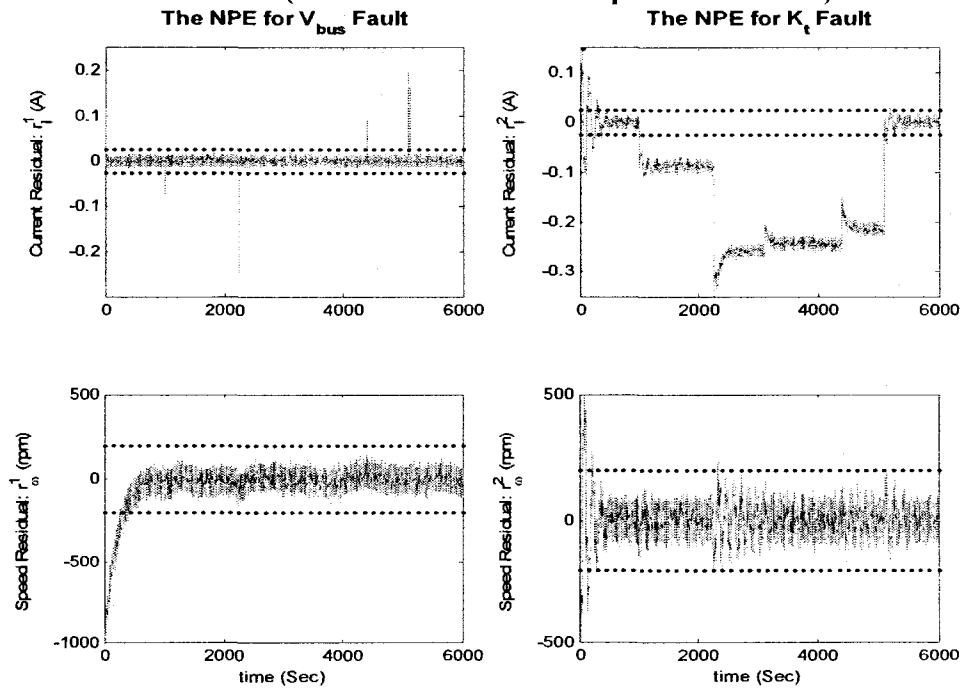


Figure C-21. The residuals of the two NPEs of the *parallel* FDH scheme in presence of a sequence of *low-severity bus voltage faults* over the time period $t \in [1000 \ 5100]$ sec., subject to *high noise level* (Current SNR=44.57 dB and Speed SNR=44.76 dB).

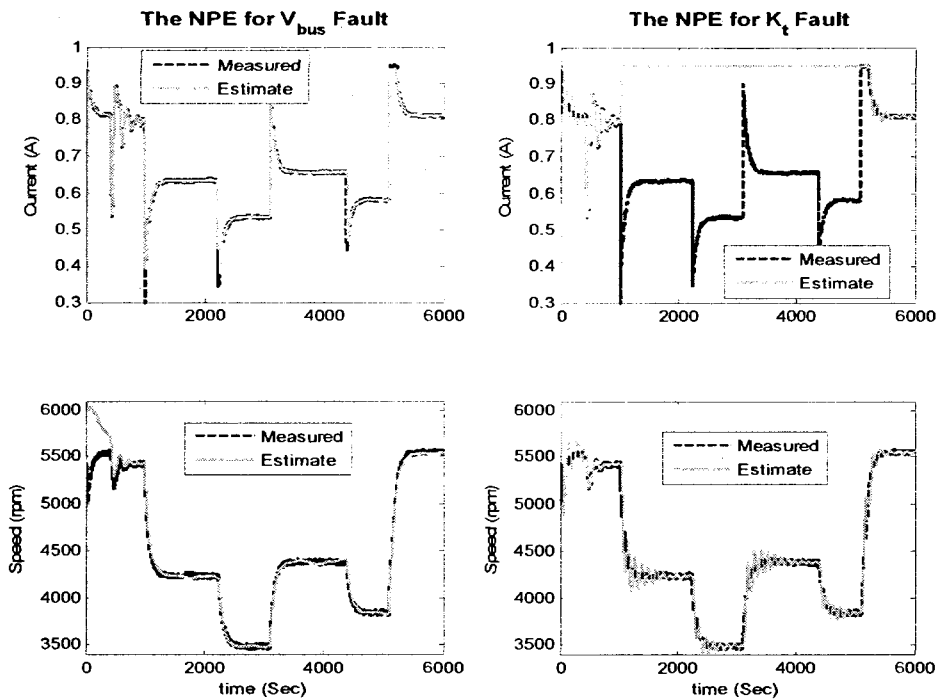


Figure C-22. The estimated versus measured states using the *parallel* FDII scheme in presence of a sequence of *high-severity* bus voltage faults over the time period $t \in [1000 \ 5100]$ sec., subject to *medium* noise level (Current SNR=54.57 dB and Speed SNR=54.76 dB).

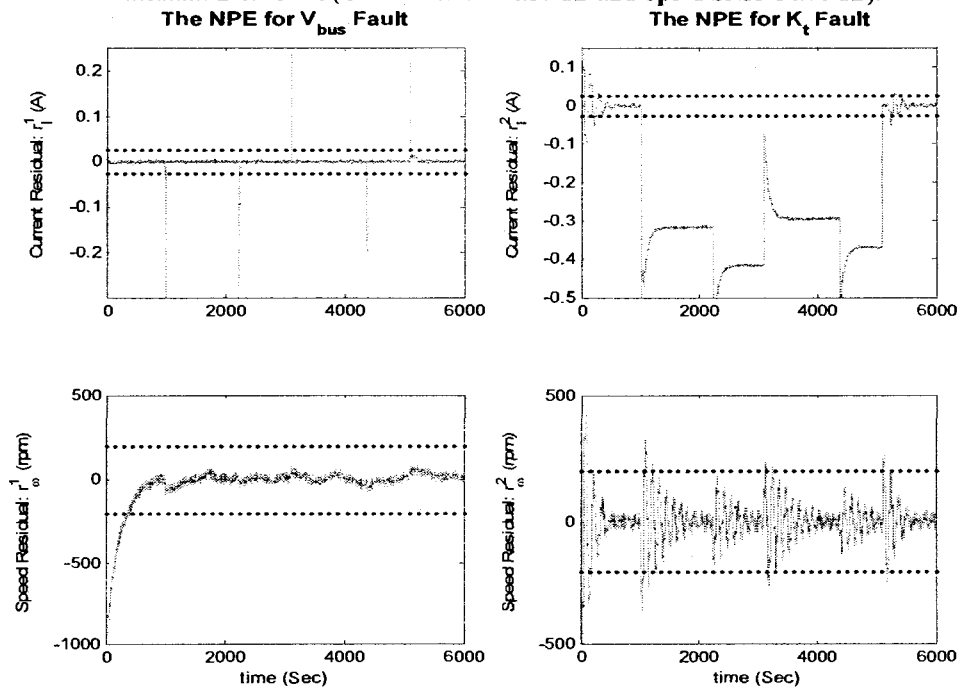


Figure C-23. The residuals of the two NPEs of the *parallel* FDII scheme in presence of a sequence of *high-severity* bus voltage faults over the time period $t \in [1000 \ 5100]$ sec., subject to *medium* noise level (Current SNR=53.66 dB and Speed SNR=53.72 dB).

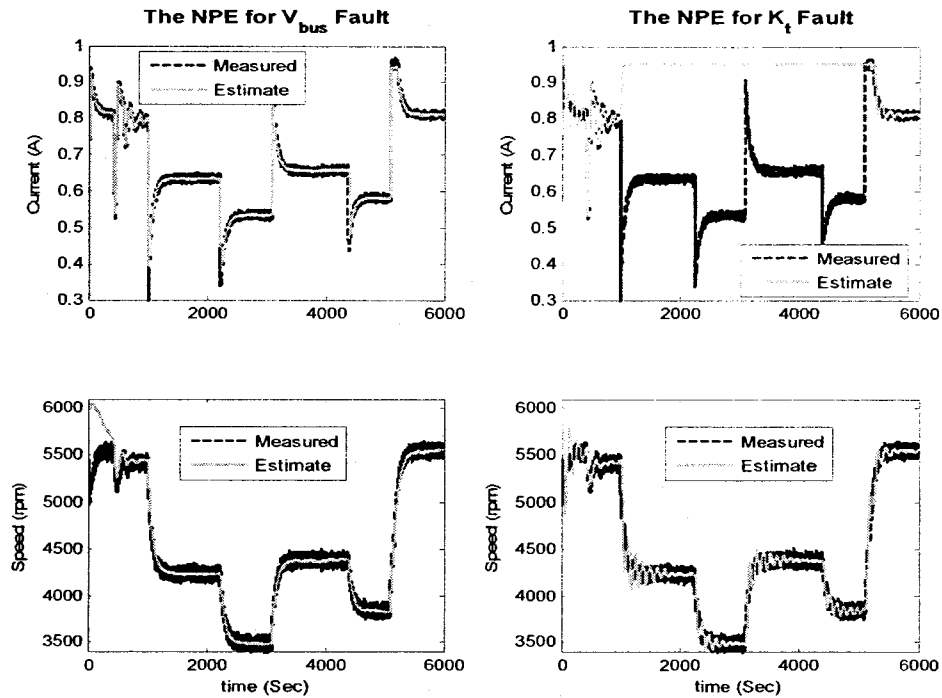


Figure C-24. The estimated versus measured states using the *parallel* FDI scheme in presence of a sequence of *high-severity bus voltage faults* over the time period $t \in [1000 \ 5100]$ sec., subject to *high noise level* (Current SNR=44.57 dB and Speed SNR=44.76 dB).

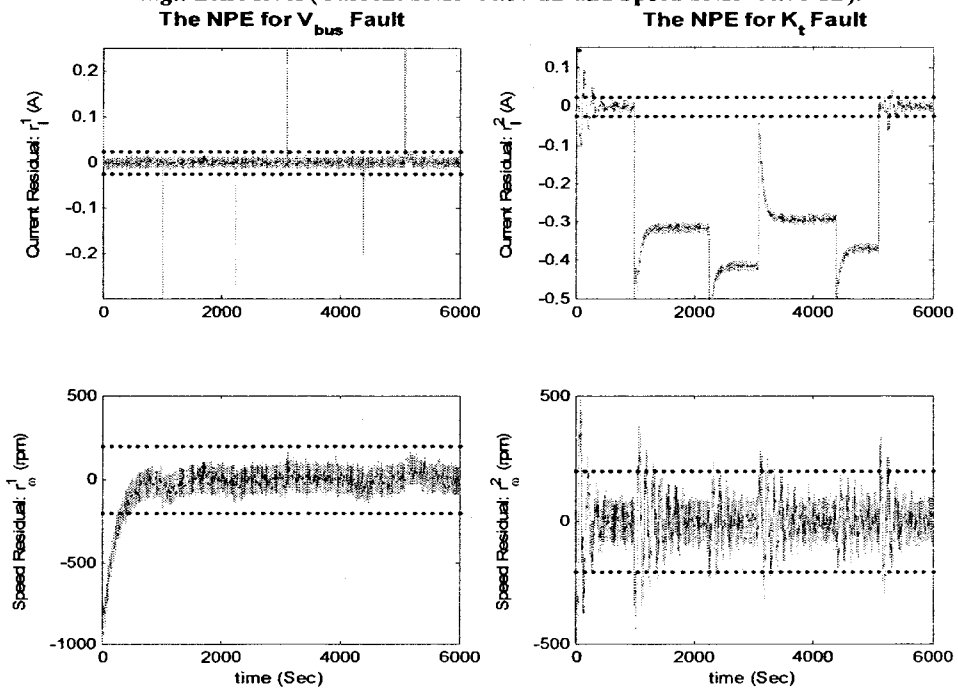


Figure C-25. The residuals of the two NPEs of the *parallel* FDI scheme in presence of a sequence of *high-severity bus voltage faults* over the time period $t \in [1000 \ 5100]$ sec., subject to *high noise level* (Current SNR=43.66 dB and Speed SNR=43.72 dB).

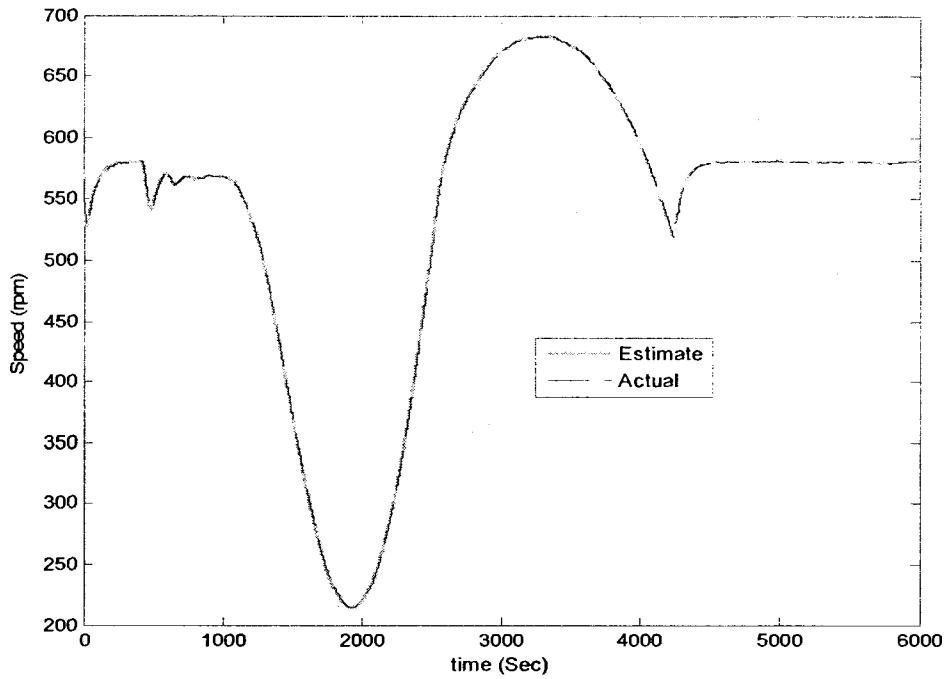


Figure C-26. Speed estimate from the full-order FTO versus its actual value using only speed measurements in presence of a time-varying fault in motor current over the time period of $t \in [1000 \ 4250]$ second.

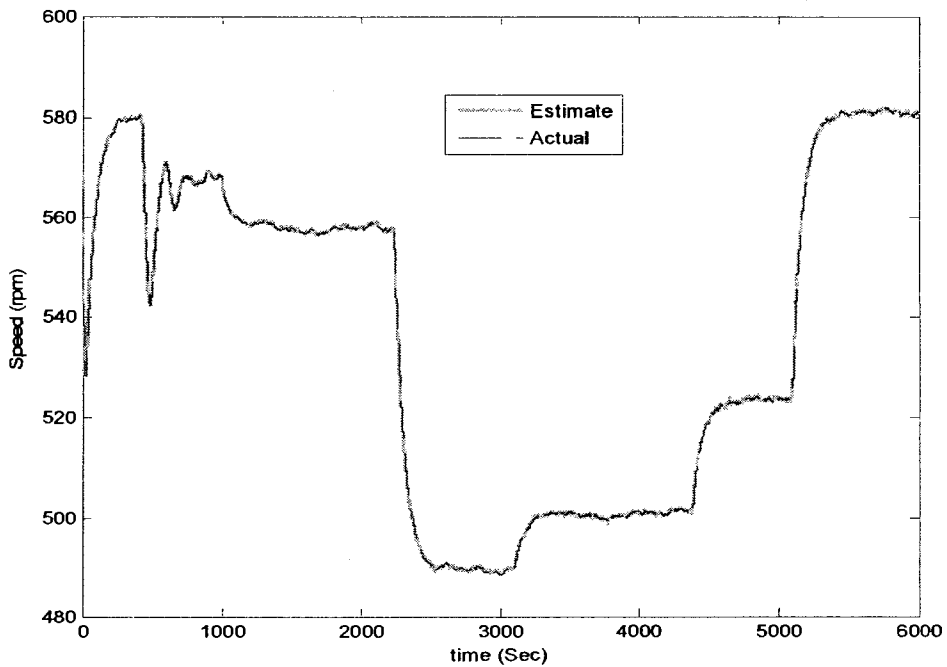


Figure C-27. Speed estimate from the full-order FTO versus its actual value using only speed measurements in presence of a sequence of low-severity bus voltage faults over the time period $t \in [1000 \ 5100]$ second.

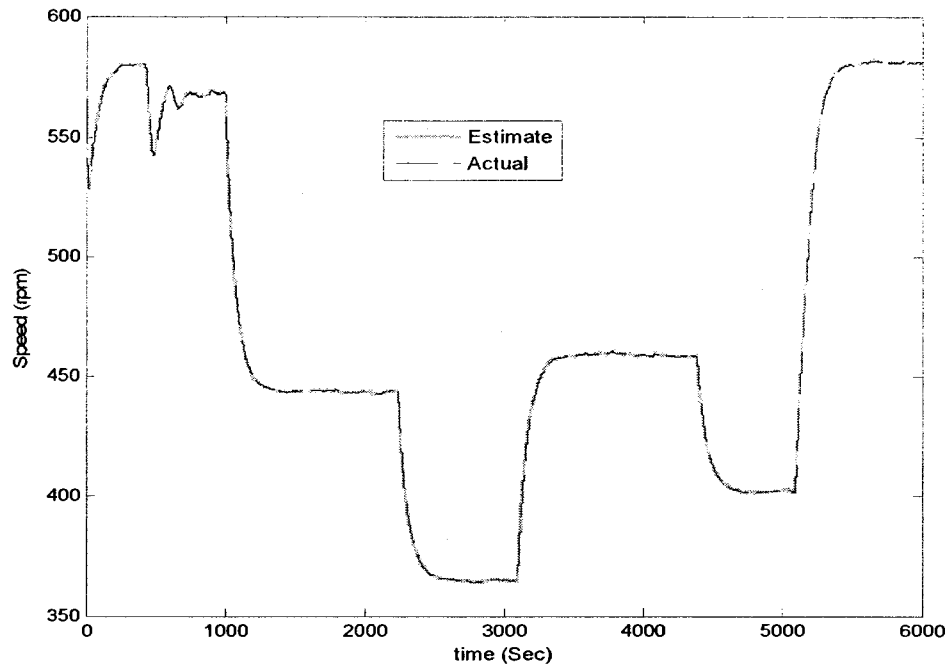


Figure C-28. Speed estimate from the full-order FTO versus its actual value using only speed measurements in presence of a sequence of high-severity bus voltage faults over the time period $t \in [1000 \ 5100]$ second.

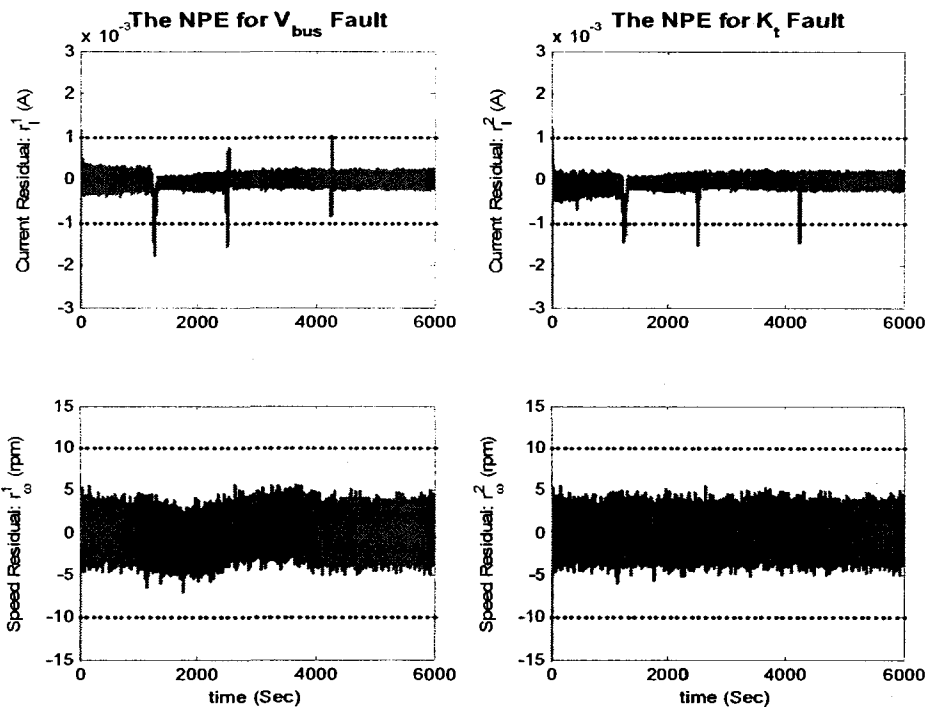


Figure C-29. The residuals of the two NPEs of the series-parallel FDII scheme in presence of a time-varying fault in motor current over the time period $t \in [1000 \quad 4250]$ second under partial-state measurements (i.e., measured speed and estimated current from the FTO).

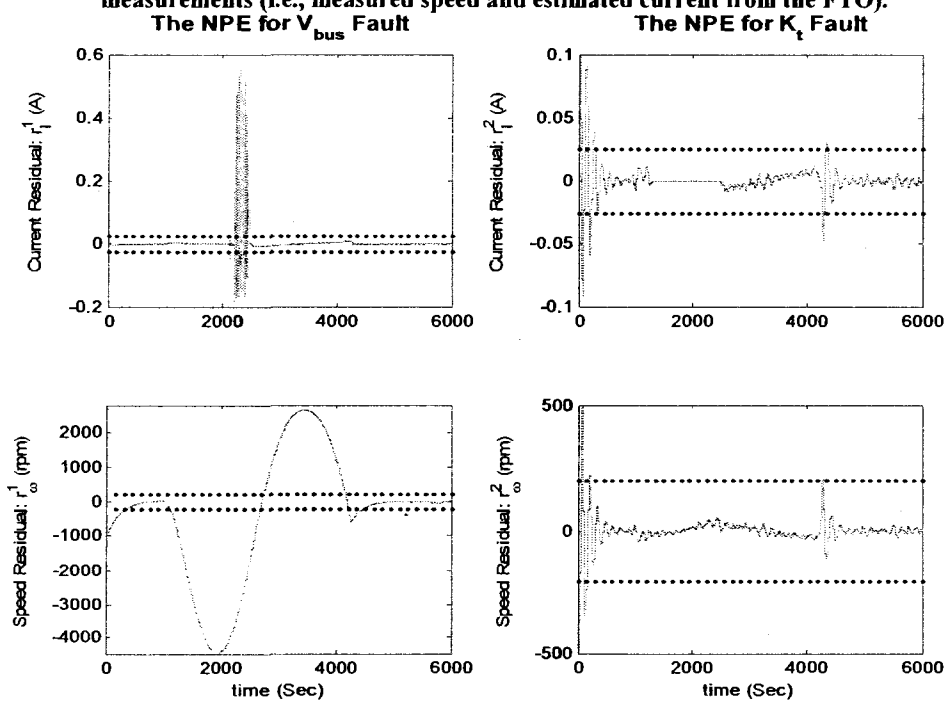


Figure C-30. The residuals of the two NPEs of the parallel FDII scheme in presence of a time-varying fault in motor current over the time period $t \in [1000 \quad 4250]$ second under partial-state measurements (i.e., measured speed and estimated current from the FTO).

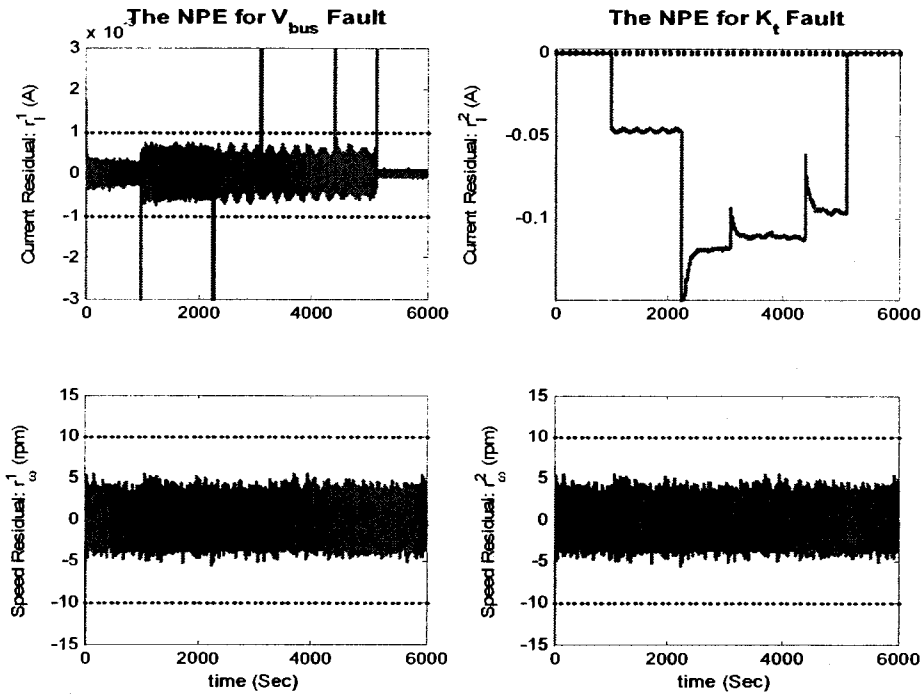


Figure C-31. The residuals of the two NPEs of the series-parallel FDI scheme in presence of a sequence of low-severity bus voltage faults over the time period $t \in [1000 \ 5100]$ second under partial-state measurements (i.e., measured speed and estimated current from the FTO).

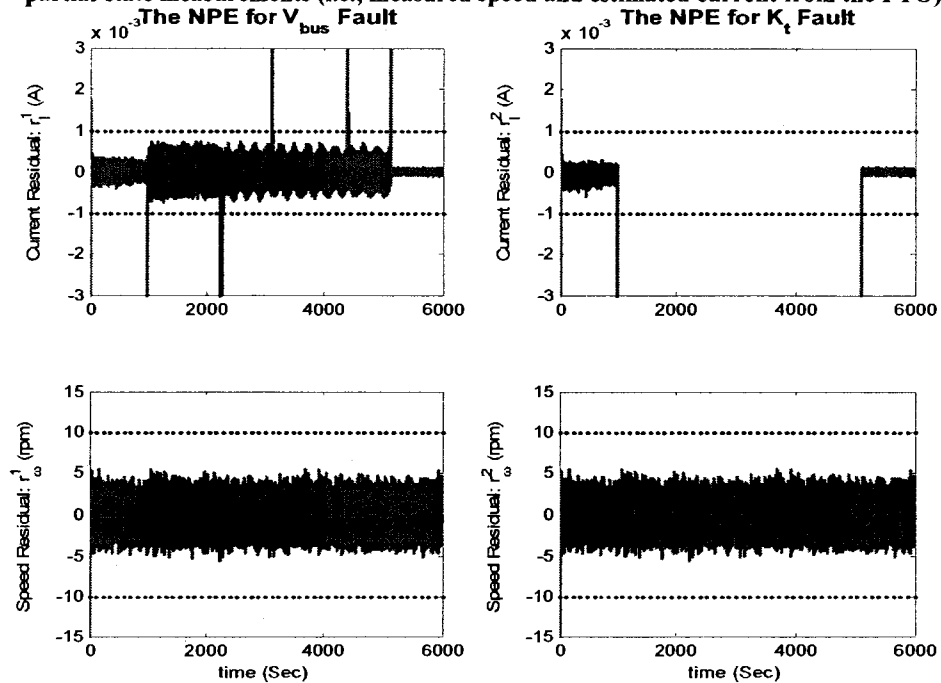


Figure C-32. The residuals of the two NPEs of the series-parallel FDI scheme in presence of a sequence of low-severity bus voltage faults over the time period $t \in [1000 \ 5100]$ second under partial-state measurements (i.e., measured speed and estimated current from the FTO); zoomed in for the current residual of “the NPE for K_t fault”.

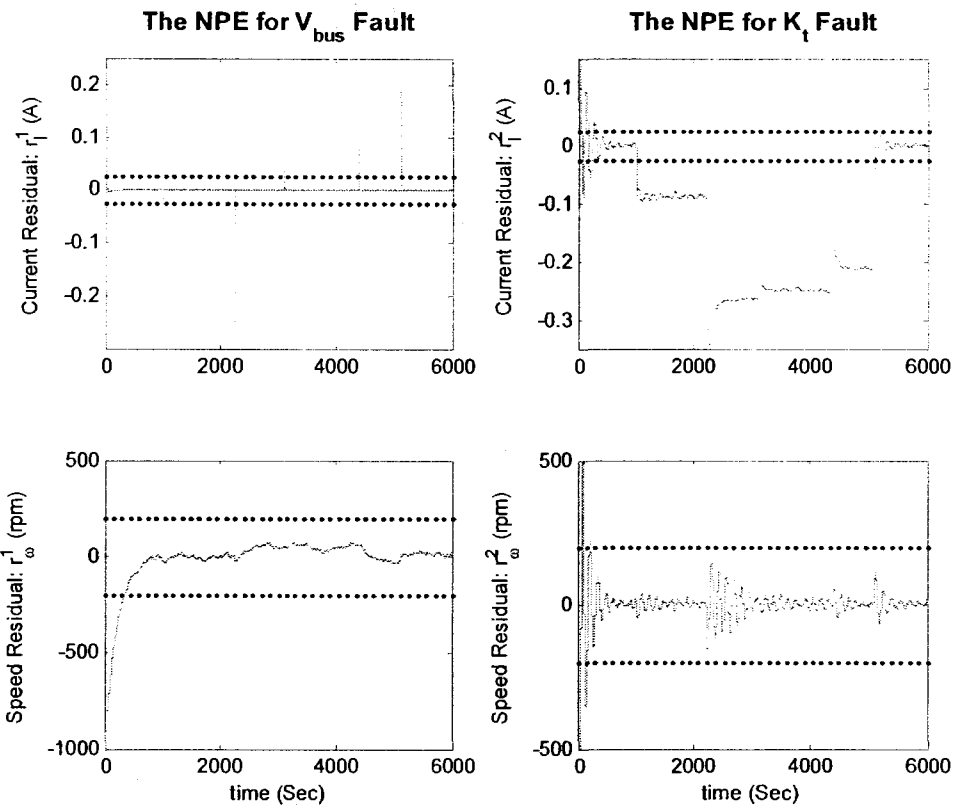


Figure C-33. The residuals of the two NPEs of the parallel FDII scheme in presence of a sequence of low-severity bus voltage faults over the time period $t \in [1000 \ 5100]$ second under partial-state measurements (i.e., measured speed and estimated current from the FTO).

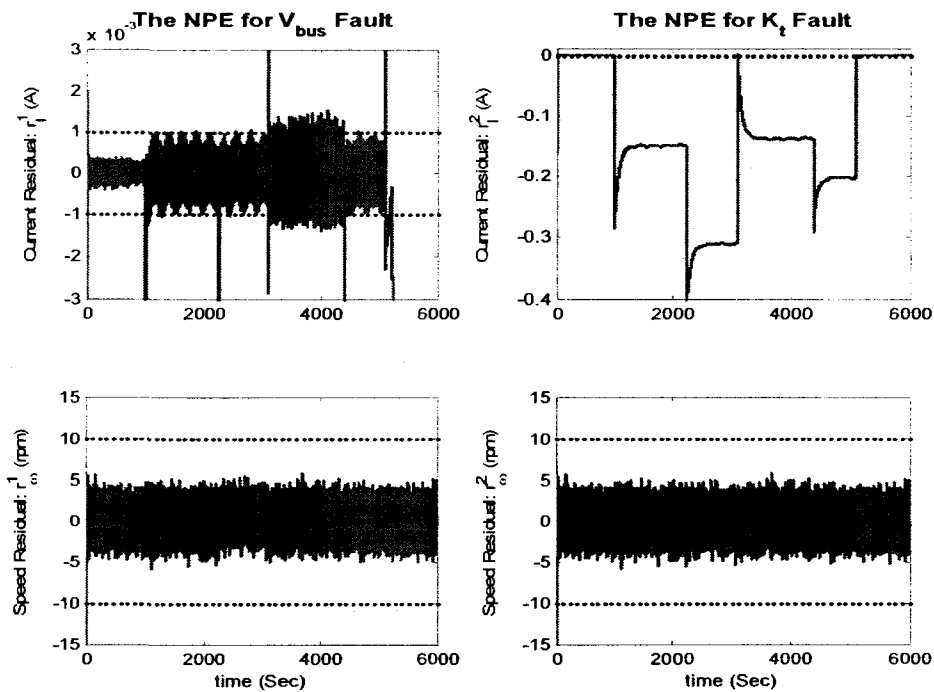


Figure C-34. The residuals of the two NPEs of the *series-parallel* FDII scheme in presence of a sequence of *high-severity bus voltage faults* over the time period $t \in [1000 \ 5100]$ second under partial-state measurements (i.e., measured speed and estimated current from the FTO).

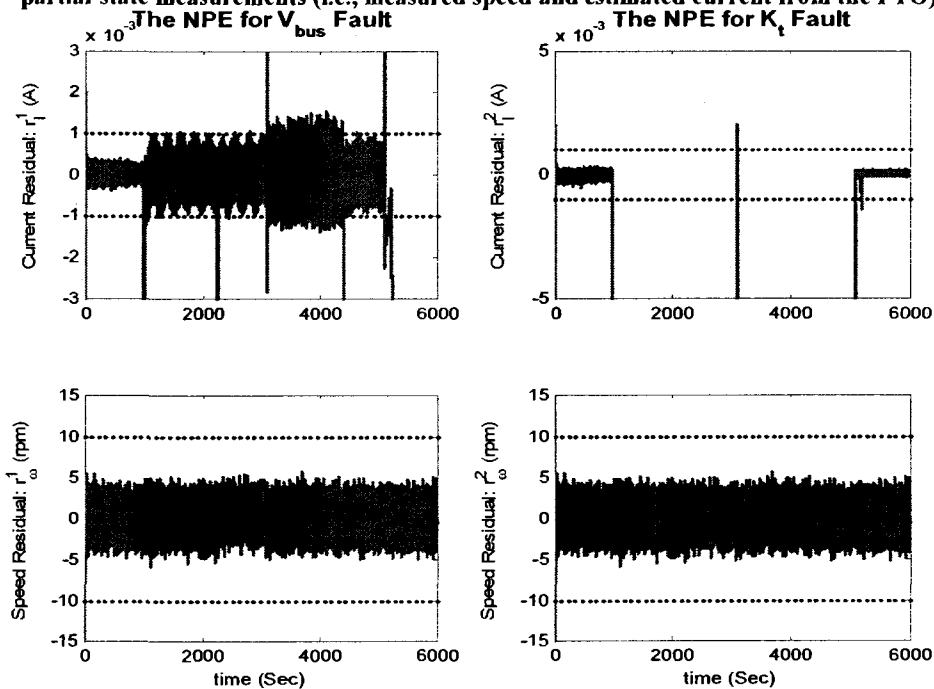


Figure C-35. The residuals of the two NPEs of the *series-parallel* FDII scheme in presence of a sequence of *high-severity bus voltage faults* over the time period $t \in [1000 \ 5100]$ second under partial-state measurements (i.e., measured speed and estimated current from the FTO); zoomed in for the current residual of “the NPE for K_t fault”.

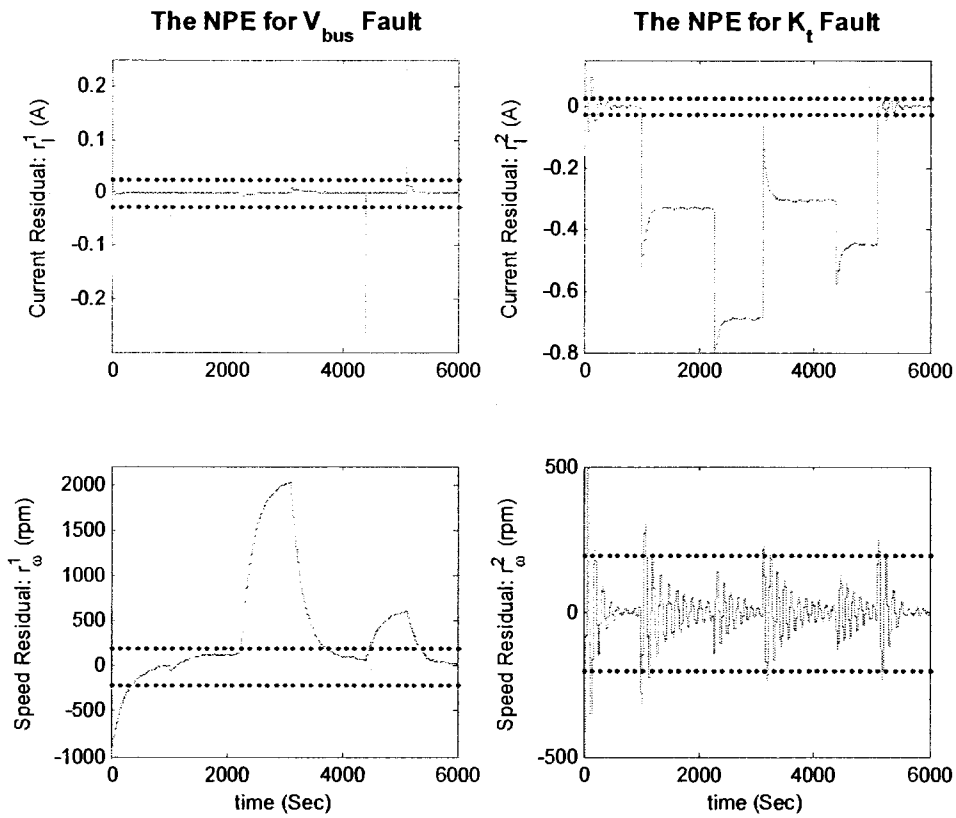


Figure C-36. The residuals of the two NPEs of the parallel FDII scheme in presence of a sequence of high-severity bus voltage faults over the time period $t \in [1000 \ 5100]$ second under partial-state measurements (i.e., measured speed and estimated current from the FTO).